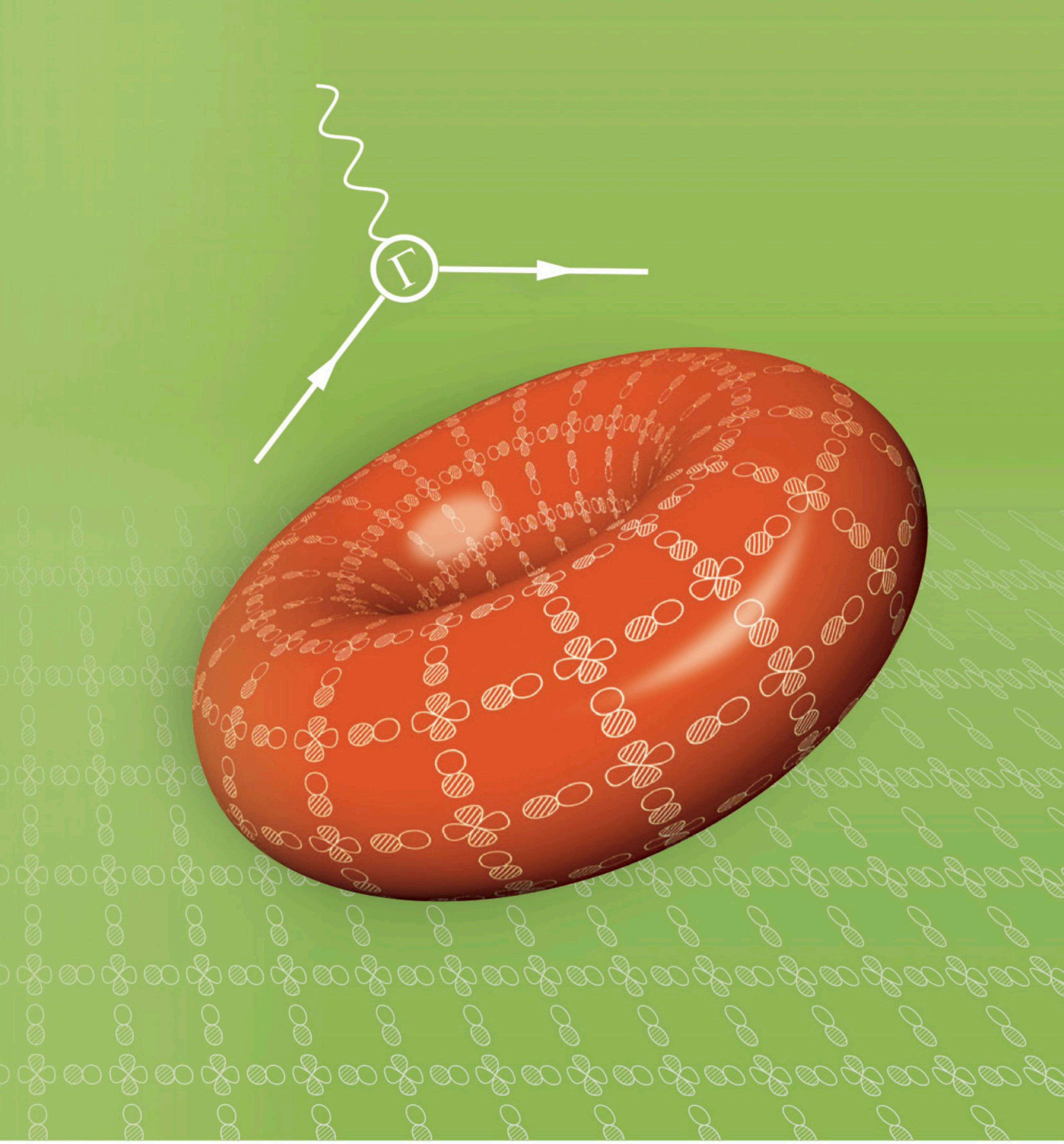

Correlations and Phase Transitions

Eva Pavarini and Erik Koch (Eds.)

JÜLICH
Forschungszentrum

Schriften des Forschungszentrums Jülich
Reihe Modeling and Simulation Band / Volume 14

Forschungszentrum Jülich GmbH
Institute for Advanced Simulation

Lecture Notes of the Autumn School on Correlated Electrons 2024

Eva Pavarini and Erik Koch (Eds.)

Correlations and Phase Transitions

Autumn School organized by
the Institute for Advanced Simulation
at Forschungszentrum Jülich
16 – 20 September 2024

Schriften des Forschungszentrums Jülich
Modeling and Simulation

Band / Volume 14

ISSN 2192-8525

ISBN 978-3-95806-751-6

Bibliographic information published by the Deutsche Nationalbibliothek.
Die Deutsche Nationalbibliothek lists this publication in the Deutsche Nationalbibliografie; detailed bibliographic data are available in the Internet at http://dnb.d-nb.de.

Publisher: Forschungszentrum Jülich GmbH
Institute for Advanced Simulation

Cover Design: Grafische Medien, Forschungszentrum Jülich GmbH

Printer: Kern GmbH, Bexbach

Distributor: Forschungszentrum Jülich
Zentralbibliothek, Verlag
52425 Jülich
Phone +49 (0)2461 61-5368 · Fax +49 (0)2461 61-6103
e-mail: zb-publikation@fz-juelich.de
www.fz-juelich.de/zb

Schriften des Forschungszentrums Jülich
Reihe Modeling and Simulation, Band / Volume 14

ISSN 2192-8525
ISBN 978-3-95806-751-6

Contents

Preface

Emergent phenomena are the essence of condensed-matter physics and at the same time what makes the behavior of correlated materials appealing for applications. They are, however, hard to understand at a fundamental level. It is the interplay of several competing interactions—none of which can be treated as a mere perturbation, leading to the emergence of effective interactions—that makes their description a grand challenge. Addressing it requires mastery of a wide spectrum of theoretical concepts, ranging from materials modeling using first-principles approaches to advanced many-body methods based on dynamical mean-fields, stochastic simulations and renormalization techniques. The concepts of symmetry, topological invariance and the classification of transitions between phases are of crucial importance to bring order to the plethora of observed phenomena. The goal of this year's school is to provide students with an overview of the state-of-the-art in the field of emergent phases in strongly correlated systems and the many techniques used to investigate them. After introducing the fundamental models and concepts, lectures will turn to emergent phenomena, focusing on superconductivity, Kondo behavior, Mott phases, quantum magnetism, and Kosterlitz-Thouless transitions. Experimental lectures will explore phenomena under normal and extreme conditions.

A school of this size and scope requires backing from many sources. We are very grateful for all the practical and financial support we have received. The Institute for Advanced Simulation at the Forschungszentrum Jülich and the Jülich Supercomputer Centre provided the major part of the funding and were vital for the organization of the school as well as for the production of this book. The Institute for Complex Adaptive Matter (ICAM) continued also this year to endorse the school and supplied additional funds.

The nature of a school makes it desirable to have the lecture notes available when the lectures are given. This way students get the chance to work through the lectures thoroughly while their memory is still fresh. We are therefore extremely grateful to the lecturers that, despite tight deadlines, provided their manuscripts in time for the production of this book. We are confident that the lecture notes collected here will not only serve the participants of the school but will also be useful for other students entering the exciting field of strongly-correlated materials.

We are grateful to Mrs. H. Lexis of the Verlag des Forschungszentrum Jülich and to Mrs. D. Mans of the Grafische Betriebe for providing their expert support in producing the present volume on a tight schedule. We heartily thank our students and postdocs who helped with proofreading the manuscripts, often on quite short notice: Elaheh Adibi, Amit Chauhan, Qiwei Li, and Xue-Jing Zhang.

Finally, our special thanks go to Dipl.-Ing. R. Hölzle for his invaluable advice on the innumerable questions concerning the organization of such an endeavor, and to Mrs. L. Snyders for expertly handling all practical issues.

Eva Pavarini and Erik Koch

August 2024

1 Particle-Hole Symmetries in Condensed Matter

Martin R. Zirnbauer
Institute of Theoretical Physics
University of Cologne
Zülpicher Str. 77a, 50937 Köln

Contents

E. Pavarini and E. Koch (eds.)
Correlations and Phase Transitions
Modeling and Simulation Vol. 14
Forschungszentrum Jülich, 2024, ISBN 978-3-95806-751-6
http://www.cond-mat.de/events/correl24

1 Introduction

Symmetries have played a major role in the development of physics from ancient history to modern times – be it as exact symmetries leading to exact conservation laws by Noether's theorem and its variants, or as approximate symmetries providing a guide to the essential features of a physical system. In the twentieth century, a major physics strand was the development of the Landau theory (or Landau-Wilson-Ginzburg paradigm) of phase transitions. The hypothesis there was that thermodynamic phases and phase transitions between them can be characterized by the appearance (or disappearance) of a so-called order parameter breaking a continuous or discrete symmetry. Now in recent decades that Landau paradigm was challenged by the discovery of a variety of *topological states* of matter and quantum phase transitions, where different phases are not distinguished by symmetry breaking but rather by some kind of topological invariant taking different values in different phases. Intriguingly, this challenge to the Landau framework has in turn been counter-challenged in recent years: it is currently being investigated [1] whether topological (non-Landau) phase transitions could still be subsumed under a generalized Landau framework invoking a generalized symmetry concept called *higher-form symmetries*, where the conserved "charges" may be magnetic fluxes and or higher-dimensional analogs thereof. Motivated by that general setting, the present lecture focuses on just one detail out of the grand picture: *particle-hole symmetry* as one of the anti-unitary symmetries that play a role in the classification of so-called symmetry-protected topological phases.

In developing the concept of symmetries and their consequences, we are somewhat hampered by the fact that there exists no consensus as to what exactly is meant by a "symmetry" in quantum mechanics. Therefore, our lecture begins with an attempt to offer various definitions and clarifications. Quantum symmetries in our sense act primarily on quantum states, and by Wigner's Theorem they lift to unitary or anti-unitary operations on the Fock-Hilbert space of the quantum system. Since the energy of a stable system (quantum or not) is bounded from below by the ground-state energy (which we may take to be zero), it follows that any operation of symmetry must transform positive-energy eigenstates into other positive-energy eigenstates. So, operations that anticommute with the Hamiltonian (and hence reverses the sign of the energy) cannot qualify as symmetries. Examples of such non-symmetries are chiral "symmetry" or sublattice "symmetry", and Bogoliubov-deGennes "symmetry". We also emphasize that there exists no such thing as a gauge "symmetry"; in fact, gauge invariance can never be broken, neither explicitly nor spontaneously, whereas symmetries can be.

The cacophony of language is particularly severe in the case of particle-hole symmetries. Major review articles say that *every superconductor is particle-hole symmetric*. We strongly discourage the use of such language, as it confuses the notion of symmetry with a structural element of the theoretical formalism. In a similar vein, particle-hole symmetries (usually of antilinear type) must not be confused with the linear symmetry of charge conjugation, which plays a prominent role in the relativistic quantum theory of the Dirac field (as part of the CPT theorem). Understood in our sense, the transformation of a particle-hole symmetry exchanges particle-like excitations of a Fermi-liquid state with hole-like excitations. Acting on a single band, it transforms the Fock vacuum into the totally occupied state. As such it can be a symmetry of the ground state only in a situation of half filling. An informative comparison is with the operation of time-reversal symmetry T: while T acts on (charge density, current density, electric field, magnetic field) as $(\rho, j; E, B) \mapsto (\rho, -j; E, -B)$, a particle-hole symmetry acts as $(\rho, j; E, B) \mapsto (-\rho, j; -E, B)$. Complementary to the anti-unitary symmetry of time reversal, particle-hole symmetries are phenomenologically relevant for systems in zero electric field but nonzero magnetic field.

The present lecture is an excerpt from a review article [2] written a few years ago. Following our basic definitions and list of non-symmetries, we will illustrate the notion of particle-hole symmetry at the example of the Su-Schrieffer-Heeger model and the Kitaev-Majorana chain. Then, simplifying some of the mathematical abstractions in [2], we define particle-hole symmetry *invariantly*, i.e., without fixing any preferred single-particle basis of Hilbert space. We finish the lecture with the fascinating story of composite fermions in the half-filled lowest Landau level.

2 What's a symmetry in quantum mechanics?

In the general setting of quantum theory (and other theories, for that matter) one has two basic structures: *observables* and *states*. These are dual to each other in that there is a *pairing* between them, viz. the operation of taking the expectation value of an observable in a state,

$$\text{observables} \ \otimes \ \text{states} \to \text{real numbers}. \tag{1}$$

Physical observables are realized as self-adjoint operators $A = A^\dagger$ on a Hilbert space V. The same goes for states, by what is known as the state's density matrix, ρ, a positive self-adjoint operator of unit trace:

$$\rho = \rho^\dagger, \quad 0 \le \rho \le 1, \quad \mathrm{Tr}_V\, \rho = 1. \tag{2}$$

Adopting the Hilbert-space realization, one writes the pairing (1) as a trace:

$$A \otimes \rho \mapsto \mathrm{Tr}_V\, \rho A. \tag{3}$$

The (square of the) overlap between two states (sometimes called the "transition probability" for short) is

$$W_{f \leftarrow i} = \mathrm{Tr}_V \ \rho_f \rho_i \,. \tag{4}$$

The observables $A, B, \ldots$ of quantum theory form an associative algebra: $(AB)C = A(BC)$. For present purposes, note that an *automorphism* of the operator algebra is a transformation $A \mapsto S(A)$ that preserves the operator product,

$$S(AB) = S(A)S(B). \tag{5}$$

Since the algebra of quantum observables is an algebra over $\mathbb{C}$ (the complex numbers) one distinguishes between two kinds of automorphism:

$$S \text{ linear}: \quad S(\lambda A) = \lambda S(A) \quad (\lambda \in \mathbb{C}), \tag{6}$$

$$S \text{ antilinear}: \quad S(\lambda A) = \bar{\lambda} S(A). \tag{7}$$

Remark. The bar operation $\lambda \to \bar{\lambda}$ denotes complex conjugation, i.e. the operation fixing the real axis and inverting the imaginary axis:

$$(\mathrm{Re}\,\lambda, \mathrm{Im}\,\lambda) \mapsto (\mathrm{Re}\,\lambda, -\,\mathrm{Im}\,\lambda). \tag{8}$$

It should be stressed that (8) is just one out of many automorphisms of $\mathbb{C}$, and from the algebraic viewpoint there is nothing special about the real axis. Indeed, reflection at any line through zero in $\mathbb{C}$ does the same job. If there is only one copy of $\mathbb{C}$ in play, one will simply define the real axis to be that special line of reflection! This freedom of simplification no longer exists for a complex vector space $V \cong \mathbb{C}^n$ of dimension $n > 1$, as one can make different choices of "real axis" in the different subspaces of V. This prompts a warning: in the absence of further structure, no *a priori* notion of complex conjugation exists for a complex vector space V with $\dim V > 1$.

Now, what do we mean by a *symmetry* in quantum mechanics? There are two sets of requirements. The first set is this:

- A symmetry operation, S, is a transformation of the space of states, $0 \leq \rho \mapsto S(\rho) \geq 0$.
- S leaves all transition probabilities invariant:

$$\mathrm{Tr}_V\, S(\rho_f) S(\rho_i) = \mathrm{Tr}_V\, \rho_f \rho_i\,. \tag{9}$$

Note that we have been careful to introduce symmetry operations S as transformation on the space of states or density matrices. This prompts the natural question whether S [subject to condition (9)] lifts to an operator on the Hilbert space V. In other words, one asks whether there exists an operator $\widehat{S}: \ V \to V,\ \psi \mapsto \widehat{S}\psi$ such that

$$S(\rho) = \widehat{S} \circ \rho \circ \widehat{S}^{-1}. \tag{10}$$

The answer to this question turns out to be YES and is known as *Wigner's Theorem* (see [3] for an old and [4] for a modern proof). One has to distinguish between two cases. For a given S, the operator $\widehat{S}$ is either *unitary*,

$$\big\langle \widehat{S}\psi_f, \widehat{S}\psi_i \big\rangle = \langle \psi_f, \psi_i \rangle, \tag{11}$$

or *anti-unitary*,

$$\big\langle \widehat{S}\psi_f, \widehat{S}\psi_i \big\rangle = \overline{\langle \psi_f, \psi_i \rangle}. \tag{12}$$

Here, $\langle \psi_f, \psi_i \rangle$ denotes the Hermitian scalar product of the quantum Hilbert space V.

Having introduced the basics of symmetry operations on states, let us now turn to the dual side of physical observables. On general grounds, an operation $\rho \mapsto S(\rho)$ on states induces an operation $A \mapsto S'(A)$ on observables. This comes about because the pairing between states and observables is required to be invariant: the expectation value of the symmetry-transformed observable $S'(A)$ in the symmetry-transformed state $S(\rho)$ must be equal to the expectation value of A in the state ρ. In the realization of both A and ρ as operators on V, this forces that

$$S'(A) = \widehat{S} \circ A \circ \widehat{S}^{-1}. \tag{13}$$

Remark. It follows that a symmetry operation is automatically an automorphism of the algebra of observables: $S'(AB) = S'(A)S'(B)$.

Next comes an important inference. Recall that the density matrix ρ of any state (pure or mixed) in quantum mechanics is a semi-positive self-adjoint operator of unit trace. In particular, ρ has the property $\rho \geq 0$, and this property has to be preserved by symmetry transformations. By the principle of invariant pairing between states and observables, it follows that a symmetry operation takes a semi-positive observable A to another such observable:

$$A \geq 0 \Rightarrow S'(A) = \widehat{S} A \widehat{S}^{-1} \geq 0. \tag{14}$$

Now, any Hamiltonian H in quantum mechanics must be bounded from below (or else the theory would not have a ground state) to be acceptable. As an operator bounded from below, H can be made positive by shifting the zero on the energy axis. Applied to the Hamiltonian, Eq. (14) says that $H \geq 0$ remains positive under any symmetry transformation. Thus an operation (such as "chiral symmetry" or "sublattice symmetry", see Sect. 4) that reverses the sign of the Hamiltonian does not qualify as a symmetry.

The set of symmetry operations we have described so far is a large set containing many "silly" operations that are of little practical consequence and interest. We shall now sharpen the symmetry concept by adding a restriction: by a symmetry (in the true and final sense) we mean an operation that leaves the quantum dynamics invariant (i.e., maps solutions to solutions). Then, to decide the question of symmetry or no symmetry, we need a model of quantum dynamics. For a prototype we may look at the Schrödinger equation of single-particle quantum mechanics,

$$\mathrm{i}\hbar\, \partial_t \psi = H \psi\, . \tag{15}$$

We see that if ψ is a solution of Eq. (15) and $\psi \mapsto \widehat{S}\psi$ is a unitary operation, then $\widehat{S}\psi$ is a solution if the operator $\widehat{S}$ commutes with the Hamiltonian:

$$\widehat{S} \circ H \circ \widehat{S}^{-1} = H. \tag{16}$$

In the case of an anti-unitary operation, $\widehat{S}\, \mathrm{i} \widehat{S}^{-1} = -\mathrm{i}$, we still have a symmetry if Eq. (16) holds, provided that one qualification is made: solutions with time running forward get transformed by $\widehat{S}$ to solutions with time running backward, as $\mathrm{i} \to -\mathrm{i}$ is to be compensated by $\partial_t \to -\partial_t$.

In summary, a symmetry in quantum mechanics is subject to two conditions: (i) acting on the space of states it preserves all transition probabilities, and (ii) acting on the space of observables it commutes with the Hamiltonian, or the generator of the quantum dynamics.

3 Quantum billiard with magnetic fluxes

While our focus in the main part of this lecture will be on anti-unitary symmetries of particle-hole type, let us begin with a few words on a famous (and non-controversial) cousin, namely time reversal T. By non-relativistic reduction of the time-reversal operation on Dirac spinors, T acts on spinful electrons as an antilinear operation with square $T^2 = -1$. The presence of the minus sign has an important consequence known as *Kramers degeneracy*, as follows. Let T be a symmetry ($TH = HT$). Then if ψ is an eigenvector of H, so is $T\psi$. Assuming the proportionality $T\psi \overset{?}{=} \lambda\psi$ ($\lambda \in \mathbb{C}$), one quickly gets a contradiction with $T\lambda = \bar{\lambda}T$ and $T^2 = -1$. It follows that ψ and $T\psi$ must be linearly independent. Thus they form a so-called Kramers pair $\{\psi, T\psi\}$ of degenerate energy eigenvectors. (As a brief aside, this kind of Kramers pair rose to prominence in recent activities on the quantum spin Hall effect.)

We now present an example showing that T-symmetry may have non-trivial consequences even in the absence of spin (when $T^2 = +1$). Consider the quantum chaotic billiard of a spinless free particle moving in a compact domain with von Neumann boundary conditions at the concave boundary. Let the billiard have fourfold rotational symmetry. Assume that the quantum particle is charged and that four magnetic flux insertions with alternating circulation reduce the rotational symmetry to a twofold one as shown in Fig. 1.

The group of unitary symmetries of this system is $\mathbb{Z}_2 = \{\mathrm{Id}, R_\pi\}$, consisting of the neutral element and rotation through π about the central point. In this simple example, the Hilbert space of a single particle decomposes into two subspaces: the R_π-even and the R_π-odd states.

The magnetic billiard also has two anti-unitary symmetries; these are time reversal followed by rotation through either $+\pi/2$ or $-\pi/2$ (to restore the magnetic circulation). Denote the first of these by $T' \equiv R_{\pi/2} \circ T$. Because time reversal commutes with space rotations, so does T'. Moreover, the anti-unitary operator T' squares to R_π and thus to $+1$ on the R_π-even and -1 on the R_π-odd sector. As a result, there exists a qualitative difference between the energy spectra for the two sectors: the R_π-even eigenstates generically come with non-degenerate energy eigenvalues, whereas the R_π-odd eigenstates organize into Kramers doublets. (Speaking the language of the Tenfold Way [5], the R_π-even sector is of symmetry type AI, while the R_π-odd sector is of symmetry type AII.)

4 “Symmetries” that aren’t symmetries

Having given a reasonably precise definition and a simple example of what we mean by a symmetry, we now address the real-life complication that “symmetry” is often used in a sloppy and even misleading sense.

The literature often speaks of gauge “symmetries”. This prompts us to emphasize that electromagnetic gauge invariance is not a symmetry in our sense. Rather, gauge invariance is simply a consistency condition, which arises because one prefers (for convenience, not by necessity) to work with gauge-dependent quantities, even though the physics is gauge-invariant and a formulation avoiding gauge fields altogether would in principle be feasible. (Indeed, mathematically

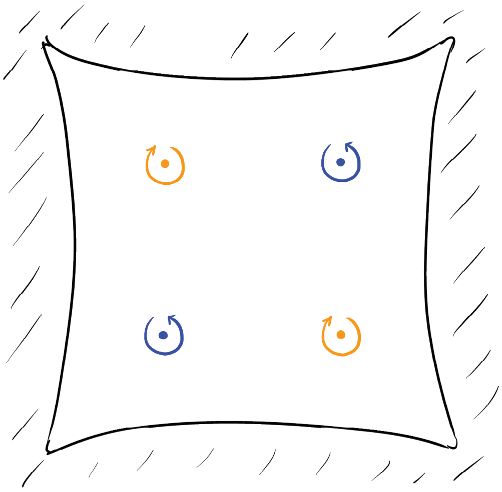

Fig. 1: *Quantum billiard with four magnetic flux insertions that alternate in circulation. The symmetry group is* $G = \mathbb{Z}_4 = \{T'^0,\ T'^1,\ T'^2,\ T'^3\}$ *generated by time reversal in combination with rotation by an angle of* $\pi/2$.

speaking, the wave functions of quantum mechanics are sections of a complex vector bundle and as such invariant under gauge transformations.) The crux of the matter can be explained by way of an informative analogy: in principle, a vector v in a vector space is invariantly defined, but in practice one expresses it by its components with respect to one basis or another:

$$v = \sum e_i\, v^i = \sum \tilde{e}_i\, \tilde{v}^i. \tag{17}$$

Choosing a fixed basis $\{e_i\}$ is like "fixing the gauge", and changing to another basis $\{\tilde{e}_i\}$ amounts to making a gauge transformation. Gauge invariance in this context is the simple fact that any expression with physical meaning can depend on the components v^i or $\tilde{v}^i$ only in a way that allows the expression to be rewritten in terms of the invariantly defined vector v (without invoking any basis). Once it is understood that gauge invariance is no more than a consistency condition, it is clear that:

- Gauge "symmetries" can never be broken, neither explicitly nor spontaneously (whereas symmetries can be broken).
- Gauge "symmetries" do not entail any conservation laws (whereas continuous symmetries do, by Noether's principle).

In particular, the conservation of electric charge should not be attributed to local $\mathrm{U}(1)$ electromagnetic gauge invariance (as is often done). We will not go deeper into this subject here, but refer our audience to the literature [6, 7].

Our next non-symmetry is chiral "symmetry", also known as a sublattice "symmetry" in the condensed matter context. So, assuming the setting of a lattice, consider a bipartite system whose Hilbert space V decomposes as $V = V_A \oplus V_B$. Let the Hamiltonian be off-diagonal with respect to that decomposition:

$$H = H_{A\leftarrow B} + H_{B\leftarrow A}\,. \tag{18}$$

If one defines a so-called sublattice transformation S by reversing the sign of the wave function, say, on the B-sublattice $S: \ \psi_A + \psi_B \mapsto \psi_A - \psi_B$, then S anticommutes with H:

$$SH = -HS. \tag{19}$$

This is an example of a chiral or sublattice "symmetry". Since S does not commute with the Hamiltonian, it is not a true symmetry in our sense. (It can, however, be turned into a symmetry in a suitable many-fermion setting; cf. Sect. 6.)

Another non-symmetry to be mentioned here is the particle-hole "symmetry" of the Bogoliubov-deGennes equations for a superconductor treated in the Hartree-Fock-Bogoliubov mean-field approximation. To spell that out, we invoke the formalism of second quantization (which we assume to be understood). Written in terms of the creation ($c^\dagger$) and annihilation (c) operators for some choice of single-particle basis, the second-quantized Hamiltonian is of the general form

$$H = \sum_{ij} \left(A_{ij} c_i^\dagger c_j + \tfrac{1}{2} B_{ij} c_i^\dagger c_j^\dagger + \tfrac{1}{2} C_{ij} c_i c_j \right), \quad \overline{A_{ij}} = A_{ji}, \ C_{ij} = \overline{B_{ji}} = -C_{ji}\,. \tag{20}$$

The information contained in H can be recast as a matrix with block structure by organizing the expression as

$$H = \tfrac{1}{2} \sum_{ij} \begin{pmatrix} c_i^\dagger & c_i \end{pmatrix} \begin{pmatrix} A_{ij} & B_{ij} \\ C_{ij} & -\overline{A_{ij}} \end{pmatrix} \begin{pmatrix} c_j \\ c_j^\dagger \end{pmatrix} + \text{const.} \tag{21}$$

The resulting matrix h,

$$h \equiv \begin{pmatrix} A & B \\ C & -\overline{A} \end{pmatrix}, \tag{22}$$

or written in tensor-product notation,

$$h = A \otimes \tfrac{1}{2}(1+\sigma_3) + B \otimes \sigma_+ + C \otimes \sigma_- - \overline{A} \otimes \tfrac{1}{2}(1-\sigma_3), \tag{23}$$

is Hermitian ($h^\dagger = h$), and by construction it <u>always</u> satisfies the relation

$$h = -\Sigma_1 \, \overline{h} \, \Sigma_1\,, \quad \Sigma_1 = \mathbf{1} \otimes \sigma_1\,. \tag{24}$$

The matrix h is known the Bogoliubov-deGennes (BdG) "Hamiltonian", and the relation (24) is sometimes called the "particle-hole symmetry" of the BdG Hamiltonian – with the bizarre corollary that *every superconductor is particle-hole symmetric* (?!). In actual fact, neither is h a Hamiltonian, as it is not bounded from below in general, nor is the relation (24) a symmetry in the proper sense. Indeed, that relation is no more than a reflection of ($h = h^\dagger$ and) the canonical anticommutation (CAR) relations for fermion Fock operators:

$$c_i^\dagger c_j^\dagger + c_j^\dagger c_i^\dagger = 0 = c_i c_j + c_j c_i\,, \quad c_i^\dagger c_j + c_j c_i^\dagger = \delta_{ij}\,. \tag{25}$$

Since these CAR relations constitute an algebraic foundation that cannot ever be violated, the relation (24) should really be attributed to the *structure* of the theoretical formalism, not to any symmetry of the Hamiltonian.

5 The conundrum of charge conjugation

Having gone through a list of popular "symmetries" that aren't symmetries, we now turn to a true symmetry which, however, is not a particle-hole symmetry: charge conjugation.

Charge conjugation is a symmetry operation of the relativistic quantum theory of the Dirac field. It is one of the protagonists of the CPT-theorem, which states that any relativistic QFT with "reasonable" properties must be invariant under the combined operations of charge conjugation, parity transformation, and time reversal. A main stay in the realm of particle physics, charge conjugation has also come up in condensed matter physics, although it is of little relevance there. Let us spend a few words about it.

For a newcomer to the field, the situation with charge conjugation C may seem somewhat confusing. One the one hand, charge conjugation can be seen as an operation that transforms solutions of the Dirac equation to other solutions. As such, it is anti-unitary [8]. Indeed, the Dirac equation for a relativistic Dirac particle with mass m and momentum p is

$$\mathrm{i}\hbar\,\partial_t\psi = h\psi\,, \quad h = \beta mc^2 + c\sum \alpha_l\, p_l\,, \quad p_l = \frac{1}{\mathrm{i}}\frac{\partial}{\partial x_l} \tag{26}$$

(in zero electromagnetic field). A popular choice for the Dirac matrices β and α_l is

$$\beta = \begin{pmatrix} \mathbf{1} & 0 \\ 0 & -\mathbf{1} \end{pmatrix}, \quad \alpha_l = \begin{pmatrix} 0 & \sigma_l \\ \sigma_l & 0 \end{pmatrix} \quad (l = 1, 2, 3).$$

For that choice, one checks that solutions $t \mapsto \psi(\cdot, t)$ of the Dirac equation map to solution $t \mapsto C\psi(\cdot, t)$ (with the time t still running forward) by the transformation

$$C\psi = \beta\alpha_2\overline{\psi}, \tag{27}$$

which is antilinear. On the other hand, authoritative texts [9] state that charge conjugation is a linear operation, hence a <u>unitary</u> symmetry of the quantized Dirac field theory.

What's the resolution of this conundrum? In short, it is necessary to distinguish between two closely related but different notions. The anti-unitary operation C in (27) is no more (and no less) than a symmetry of the Dirac equation, which for present purposes is best viewed as a classical field equation. To arrive at a satisfactory quantum theory, some processing needs to be done; in particular, one has to come up with a good Fock vacuum (the "Dirac sea" of filled negative-energy states) converting the sign-indefinite h of the Dirac equation into an operator bounded from below. It turns out that the appropriate process of quantization does not take the anti-unitary symmetry C of the Dirac equation (26) to an operation acting on the Fock-Hilbert space of the quantum theory. To obtain something meaningful, C must be composed with a second antilinear operation (essentially, the Dirac ket-to-bra bijection, a.k.a. Fréchet-Riesz isomorphism), so that the finished product, $\widehat{C}$, is complex linear and unitary.

For a quick diagnostic of what's wrong with C, one observes that $Ch = -hC$. Thus in view of our mantra that *symmetries always commute with the Hamiltonian*, we have to concede that (i) either h is not the Hamiltonian, or (ii) C cannot be a symmetry. We'll leave it at that here and refer to the Appendix for more detail.

The take-away message here is that charge conjugation, properly understood as an operation on Fock-Hilbert space, is a unitary transformation. A brief characterization is

$$(\rho, j) \xrightarrow{C} (-\rho, -j), \quad \big(E, B\big) \xrightarrow{C} \big(-E, -B\big). \tag{28}$$

In most (if not all) condensed matter settings of interest, at least one of the components E, B of the electromagnetic field will be present. Therefore, charge conjugation symmetries are of little relevance to condensed matter physics.

To summarize, particle-hole symmetry should not be confused with charge conjugation symmetry. The latter is unitary whereas the former is anti-unitary. The electromagnetic field (E, B) is sent by the latter to $(-E, -B)$, but by the former to $(-E, B)$.

6 Su-Schrieffer-Heeger model

Building on the non-example of chiral "symmetry", we now develop our first example of a true symmetry of particle-hole type. We adopt an informal style (relegating the more formal aspects to the following section) and first convey the basic and general idea.

Let us recycle from Sect. 4 the setting of a bipartite system (with sublattices A and B) and Hilbert space decomposition $V = V_A \oplus V_B$. We then second-quantize the Hamiltonian of Eq. (18) as an operator acting on the fermionic Fock space generated by V:

$$H = \sum_{ij} \Big(c_{Ai}^\dagger H_{Ai,Bj}\, c_{Bj} + c_{Bj}^\dagger H_{Bj,Ai}\, c_{Ai} \Big) \,. \tag{29}$$

Consider now transforming the operator algebra by an automorphism K which is defined by

$$K(c_{Ai}) = c_{Ai}^\dagger \,, \quad K(c_{Bj}) = -c_{Bj}^\dagger \,, \tag{30}$$

in conjunction with the property of being antilinear and involutive:

$$K(H_{Ai,Bj}) = \overline{H_{Ai,Bj}} \,, \quad K^2 = \text{Id}. \tag{31}$$

It is easy to see that this operation K leaves the Hamiltonian invariant:

$$\begin{aligned} K(H) &= \sum_{ij} \Big(K(c_{Ai}^\dagger) K(H_{Ai,Bj}) K(c_{Bj}) + K(c_{Bj}^\dagger) K(H_{Bj,Ai}) K(c_{Ai}) \Big) \\ &= \sum_{ij} \Big(c_{Ai} H_{Bj,Ai} \, (-c_{Bj}^\dagger) - c_{Bj} H_{Ai,Bj} \, c_{Ai}^\dagger \Big) \quad = \ H, \end{aligned} \tag{32}$$

where in the last step we used the CAR relations to restore normal ordering, putting annihilation operators in the right and creation operators in the left position. K satisfies all the structural requirements posited in the opening section (i.e., it is an automorphism of the operator algebra and preserves all transition probabilities). Hence the relation $K(H) = H$ tells us that K is a symmetry of the many-fermion system with Hamiltonian H. Since K is antilinear, the symmetry is of anti-unitary type. We note that K is qualitatively different from the anti-unitary symmetry of time reversal T: the latter transforms creation operators amongst themselves and annihilation operators amongst themselves, whereas the former mixes/exchanges creation with annihilation operators. (For that reason, K was called a "mixing symmetry" in the foundational paper [5].)

Let us now take the general setting of a bipartite system and specialize it to a model actively studied in contemporary condensed matter physics. For this we associate one single-particle state with each site of a one-dimensional chain of sites labeled by the integers $n \in \mathbb{Z}$. The single-particle states on even sites ($n \in 2\mathbb{Z}$) span the subspace V_A, those on odd sites span V_B. The Hamiltonian is a kinetic energy of hopping between adjacent sites

$$H_{\text{kin}} = \sum_{n\in\mathbb{Z}} \left(t_{n+1,n}\, c_{n+1}^\dagger c_n + t_{n,n+1}\, c_n^\dagger c_{n+1} \right), \quad t_{n,n+1} = \overline{t_{n+1,n}}. \tag{33}$$

This Hamiltonian has the particle-hole symmetry $K(H_{\text{kin}}) = H_{\text{kin}}$ given by

$$K(c_n) = (-1)^n c_n^\dagger , \quad K(c_n^\dagger) = (-1)^n c_n , \quad K(\mathrm{i}) = -\mathrm{i}\,. \tag{34}$$

Notice that there is no condition on the hopping amplitudes $t_{n,n+1}$: these can be complex and even n-dependent in some random way and K will still be a symmetry.

We now take a closer look at translation-invariant systems with real hopping: $t_{n,n+1} \equiv -t_0 \in \mathbb{R}_+$. In that case, it is useful to transform to the momentum representation by introducing

$$a_k = \sum_{n\in\mathbb{Z}} \mathrm{e}^{-\mathrm{i}kn} c_n , \quad a_k^\dagger = \sum_{n\in\mathbb{Z}} \mathrm{e}^{+\mathrm{i}kn} c_n^\dagger \quad (k \in \mathbb{R}/2\pi\mathbb{Z}). \tag{35}$$

Note that these momentum-space operators satisfy the anticommutation relations

$$a_k^\dagger a_{k'} + a_{k'} a_k^\dagger = 2\pi\, \delta(k-k'). \tag{36}$$

The Hamiltonian $H \equiv H_{\text{kin}}$ of the translation-invariant system then takes the diagonal form

$$H = \int \frac{dk}{2\pi}\, \varepsilon(k)\, a_k^\dagger a_k , \quad \varepsilon(k) = -t_0 \cos k. \tag{37}$$

In the momentum basis, the operation K of particle-hole symmetry acts as

$$K(a_k) = a_{k+\pi}^\dagger , \quad K(a_k^\dagger) = a_{k+\pi} , \quad K(\mathrm{i}) = -\mathrm{i}\,. \tag{38}$$

Note that $K(H) = H$ holds more generally for any k-odd dispersion relation $\varepsilon(k\pm\pi) = -\varepsilon(k)$. The situation is illustrated graphically in Fig. 2 for the cosine band $\varepsilon(k) = -t_0 \cos k$. The figure also indicates the fact that the lift $\widehat{K}$ of K to the many-fermion Fock space leaves the free-fermion ground state invariant only if the cosine band is at half filling.

Finally, in order to arrive at the Su-Schrieffer-Heeger (SSH, [10]) model, one staggers the hopping amplitude:

$$0 < t_0 = t_{2n-1,2n} < t_1 = t_{2n,2n+1}. \tag{39}$$

Thus the chain alternates between weak bonds (with hopping amplitude t_0) and strong bonds (amplitude $t_1 > t_0$). The alternation reduces the group of translation symmetries from $\mathbb{Z}$ to $2\mathbb{Z}$

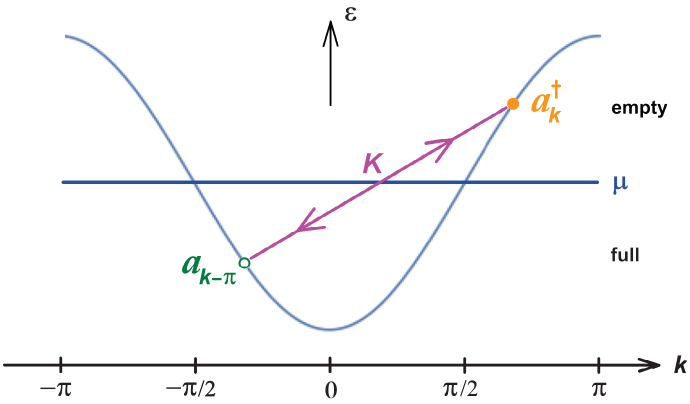

Fig. 2: *Particle-hole symmetry of the cosine band at half filling. The particle-hole transformation K exchanges the single-particle creation operator at momentum k with the single-hole creation operator at the shifted momentum $k \pm \pi$.*

(translation by two lattice sites). A good way to handle the situation is to double the unit cell in real space (and cut the Brillouin zone in momentum space in half). The single band of before then splits into two bands, and the staggered hopping opens an energy gap between the two. At half filling, the upper one is a *conduction* band, the lower one a *valence* band.

Let us now discuss some physical consequences of the particle-hole symmetry of the SSH model. When the Fermi energy lies in the gap between the conduction and valence bands, the SSH model is an example of a topological (band) insulator in one space dimension. Such systems have been under active investigation over the last two decades. More specifically, the SSH model represents a so-called *symmetry-protected topological phase* (SPT phase), with the protecting symmetry being the particle-hole symmetry K. Let us give a brief exposition.

By a principle known as *bulk-boundary correspondence*, the hallmark of any SPT phase is the appearance of gapless edge modes in a system with boundary (when there is something “topological” and non-trivial about the ground state of the bulk system without boundary). In the case of the SSH model, it is quite easy to exhibit the relevant effect. For that purpose, consider the SSH model on the half-space lattice $\mathbb{N} \cup \{0\}$ (i.e. the positive integers including zero). Let the bond between the boundary site $n = 0$ and its neighbor $n = 1$ be weak (t_0), the bond between $n = 1$ and $n = 2$ strong (t_1), and so on. Then it is easy to check that the operator

$$\psi = \sum_{n \geq 0} (-t_0/t_1)^n \, c_{2n}^\dagger \tag{40}$$

commutes with the SSH Hamiltonian H, and so does its adjoint $\psi^\dagger$:

$$\big[H, \psi\big] = 0 = \big[H, \psi^\dagger\big]. \tag{41}$$

Thus, when acting on the ground state of H (or any eigenstate, for that matter), the operators ψ / $\psi^\dagger$ create/annihilate an excitation of zero energy. Since $t_0 < t_1$, the magnitude $\left|-t_0/t_1\right|^n = \mathrm{e}^{-n/\xi}$ ($\xi > 0$) of the coefficients in the sum (40) decreases exponentially with increasing distance from the boundary $n = 0$. In other words, the operator ψ creates a zero mode exponentially localized near the system boundary. That’s the gapless edge mode of the SSH model.

One may now ask: is the gapless edge mode a fluke/outlier unique to the SSH Hamiltonian H, or is there some robustness to the phenomenon, i.e., does the gapless feature survive when we deform H to, say, complex or even disordered hopping amplitudes? A detailed look into this question is outside the scope of the present 90 minute lecture. So, we just state the known outcome [11]: the gapless edge mode does remain in place as long as the deformation preserves particle-hole symmetry and leaves the energy gap of the bulk system open. Owing to their topological protection by symmetry, we can make the gapless edge disappear only by tuning the system through a phase transition where the energy gap of the bulk system closes.

Let us add a little precision to this story. One can imagine stacking a number N of identical SSH chains, all with boundary at $n = 0$. Then instead of one gapless edge mode we have N such modes. When we couple the chains within the parameter space of the free-fermion Hamiltonian, all N modes are known to remain gapless (as long as particle-hole symmetry is preserved and the bulk energy gap is kept open). What happens when electron-electron interactions are turned on (still preserving the particle-hole symmetry)? The answer is that interactions can change the number N of gapless edge modes without passing through a phase transition, but the change $\varDelta N$ is always an integer multiple of 4. In other words, the topological classification of one-dimensional topological insulators with particle-hole symmetry (known as symmetry class AIII in the Tenfold Way) is $\mathbb{Z}/4\mathbb{Z}$. So, we can take away the message that the anti-unitary symmetry of particle-hole transformation has some utility!

7 Kitaev-Majorana chain

Another example of interest can be generated by varying the previous one. Let us take the Hamiltonian H_{kin} of Eq. (29) and add pair creation and annihilation terms:

$$H_{BD\text{I}} = H_{\text{kin}} + \sum_{n\in\mathbb{Z}} \big(\varDelta_{n+1,n}\, c_{n+1}^\dagger c_n^\dagger + \varDelta_{n,n+1}\, c_n c_{n+1} \big), \quad \varDelta_{n,n+1} = \overline{\varDelta_{n+1,n}}\,. \tag{42}$$

This extended Hamiltonian still has the particle-hole symmetry K of Eq. (34) for any choice of pairing amplitudes $\varDelta_{n+1,n}$ (randomly depending on n). It can serve as the Hamiltonian for a superconductor (of spinless or spin-polarized electrons with zero chemical potential) in the Hartree-Fock-Bogoliubov (HFB) mean-field approximation.

Let us insert a quick comment on notation and language. The previous example (SSH) featured two symmetries: the $\mathrm{U}(1)$ symmetry behind particle-number conservation and a particle-hole symmetry K. In the present case, the $\mathrm{U}(1)$ symmetry is gone; this change modifies the symmetry class from AIII to BDI in the Tenfold Way [5].

The Hamiltonian $H_{BD\text{I}}$ is very easy to analyze (and still informative) when the hopping and pairing amplitudes are chosen in a special translation-invariant way, so that

$$H_{BD\text{I}} \equiv H = t \sum_{n\in\mathbb{Z}} \big(c_{n+1} - c_{n+1}^\dagger \big) \big(c_n + c_n^\dagger \big). \tag{43}$$

We refer to this H as the Hamiltonian of the *Kitaev-Majorana chain*. We can characterize its ground state fully by the complex lines A_k of its quasi-particle annihilation operators. By

Fourier transformation these are

$$A_k = \mathbb{C}\alpha_k\,, \quad \alpha_k = \sum\nolimits_n \mathrm{e}^{\mathrm{i}kn}\left(\mathrm{i}\sin(k/2)\,c_n + \cos(k/2)\,c_n^\dagger\right).$$

Indeed, one easily checks that the α_k obey the commutation relation $[H,\,\alpha_k] = -t\alpha_k$ and thus lower the energy by $t > 0$. The state of lowest energy, known as the superconducting ground state in the HFB mean-field approximation, is the one annihilated by all these energy-lowering operators. Note that although α_k is double-valued as a function of $k \in \mathbb{R}/2\pi\mathbb{Z}$, the fiber bundle of complex lines $A_k = \mathbb{C}\alpha_k$ is well-defined. (Mathematically speaking, we are facing a line bundle in a non-trivial isomorphism or K-theory class. The "square-root nature" of the α_k signals the existence of a topological invariant which is robust against deformation and, by bulk-boundary correspondence, protects gapless edge modes of Majorana type.)

Application of the particle-hole transformation (34) to the annihilation operators α_k gives

$$KA_kK^{-1} = A_{\pi-k}\,. \tag{44}$$

This means that the superconducting ground state is particle-hole symmetric, as K transforms the set of quasi-particle annihilation operators amongst themselves. (It should be mentioned that this property gets lost when the chemical potential moves away from zero.)

8 Lifting ph-symmetry to Fock space

To achieve a satisfactory understanding of the workings of particle-hole symmetry K, we need its lift $\widehat{K}$ to the fermionic Fock space $\mathcal{F} = \bigwedge(V)$, i.e. a mapping $\widehat{K}\,:\ \mathcal{F} \to \mathcal{F}$ such that

$$K(A) = \widehat{K} \circ A \circ \widehat{K}^{-1}. \tag{45}$$

The lift $\widehat{K}$ can be described at various levels of sophistication. Here, to keep things simple, we shall restrict our setting to that of a finite-dimensional single-particle Hilbert space V. (This setting encompasses the SSH chain of finite length and the lowest Landau level of a quantum Hall system with finite area.) For the general case of infinite dimension, we refer our audience to the technical chapters of the review article [2].

The transformation K of a particle-hole symmetry is a concatenation of two operations: (i) a system-dependent transformation, say Γ, which arises already in the initial setup of a single-particle Hilbert space V, and (ii) a universal operation that we refer to as *particle-hole conjugation*. In the example of the SSH chain, Γ is the momentum shift $k \to k \pm \pi$ (or, more generally, the sublattice transformation $\psi_A + \psi_B \mapsto \psi_A - \psi_B$); while particle-hole conjugation is always the same, namely the operation, say $A \mapsto A^\flat$, of switching between creation and annihilation operators ($a_k \leftrightarrow a_k^\dagger$). We hasten to add that particle-hole conjugation differs from Hermitian conjugation (even though the two coincide on Fock operators: $a_k^\flat \equiv a_k^\dagger$). Indeed, particle-hole conjugation is an algebra automorphism whereas Hermitian conjugation $A \mapsto A^\dagger$ is an algebra *anti*-automorphism, viz.

$$(AB)^\flat = A^\flat B^\flat \quad \text{vs.} \quad (AB)^\dagger = B^\dagger A^\dagger. \tag{46}$$

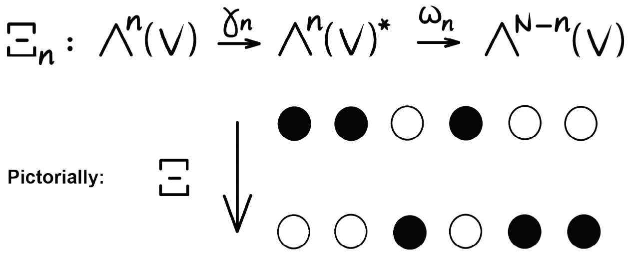

Fig. 3: *Transforming n particles into n holes, the antilinear operator Ξ_n of particle-hole conjugation is invariantly defined as the concatenation of the Fréchet-Riesz isomorphism γ_n with the wedge isomorphism ω_n. In the occupation-number representation with respect to any orthonormal single-particle basis, it takes filled orbitals to empty ones and vice versa. Consequently, particle-hole conjugation can never be a symmetry of any Fermi liquid.*

In brief, our story is going to unfold as follows. A short calculation [similar to that in Eq. (32)] shows that the universal operation of particle-hole conjugation sends every traceless Hermitian one-body Hamiltonian to its negative ($H^\flat = -H$). If the (non-universal) operator Γ anticommutes with the single-particle Hamiltonian (cf. chiral "symmetry"), then the concatenation K of Γ and particle-hole conjugation leaves the Hamiltonian of the second-quantized theory invariant,

$$K(H) = \big(\Gamma(H)\big)^\flat = H, \tag{47}$$

and is thus a particle-hole symmetry of H. As we shall see, the mapping $A \mapsto A^\flat$ is necessarily complex antilinear. Typically, Γ is complex linear (the case of charge conjugation being an exception). If so, the concatenation K is an anti-unitary operation. That will be the upshot of the current section.

After this overture with road map, we turn to the main agenda point here: constructing the Fock space lift, $\Xi : \mathcal{F} \to \mathcal{F}$, of particle-hole conjugation:

$$A^\flat = \Xi \circ A \circ \Xi^{-1}. \tag{48}$$

To give a very simple (if preliminary) description of Ξ, fix some orthonormal single-particle basis and work in the occupation number representation of $\mathcal{F}$, i.e., express states in Fock space as linear combinations of the basic states that have each single-particle state either occupied or empty. In this representation, the lift Ξ of particle-hole conjugation flips all occupations ($0 \leftrightarrow 1$), see the lower part of Fig. 3. This is the rough picture of Ξ. From that picture, it is more or less clear that such Ξ will swap creation with annihilation operators as desired. For the fine picture, we must take into account possible sign factors (due to the fermion algebra) that may have to be built into Ξ.

In an effort to be pedagogical, we defer the precise (and invariant) description of Ξ until later and stick for now with the occupation number representation w.r.t. a fixed orthonormal basis, which we label by $i \in \{1, \ldots, N\}$. Adopting Dirac notation, we denote the Fock vacuum by $|\mathrm{vac}\rangle$, and we express n-particle states with definite occupation numbers as

$$\Phi_n = c_{i_1}^\dagger c_{i_2}^\dagger \cdots c_{i_n}^\dagger |\mathrm{vac}\rangle. \tag{49}$$

Now since our Hilbert space V is assumed to be finite-dimensional, we can also speak about the state of total filling (i.e., the state with maximal particle number $N = \dim V$, where every single-particle state is occupied). That state, $|\text{sea}\rangle$, is only unique up to normalization and phase. So we make some fixed choice of $|\text{sea}\rangle$. Then the particle-hole conjugate $\varXi \varPhi_n$ is defined to be the state vector which is empty for each single-particle state occupied in the $\varPhi_n$ of Eq. (49):

$$\varXi \varPhi_n = c_{i_1} c_{i_2} \cdots c_{i_n} |\text{sea}\rangle . \tag{50}$$

(Notice that the order of the index sequence remains unchanged.) This expression for $\varXi \varPhi_n$ supersedes the hand-waving definition of $\varXi$ ($\bullet \leftrightarrow \circ$) of before, by specifying the sign factors involved. It is good enough for most practical purposes. Nonetheless, as careful thinkers we wish to convince ourselves that $\varXi$ actually exists as an invariantly defined (hence basis-independent) operation. That will occupy us for the rest of this section.

The invariant definition of $\varXi$ uses two isomorphisms, which we refer to as “Fréchet-Riesz” and “wedge”. We begin with the former. As a quantum mechanical Hilbert space, V is equipped with a Hermitian scalar product and hence an antilinear mapping

$$\gamma : \; V \to V^*, \quad v \mapsto \langle v, \cdot \rangle \, . \tag{51}$$

In physics, this mapping is also known as the Dirac ket-to-bra bijection, $|v\rangle \mapsto \langle v|$. It immediately generalizes to an antilinear Fock-space isomorphism

$$\gamma_n : \; \mathcal{F}_n \equiv \bigwedge^n(V) \to \mathcal{F}_n^* = \bigwedge^n(V)^* \cong \bigwedge^n(V^*) \tag{52}$$

by distributing γ over exterior products:

$$v_1 \wedge \cdots \wedge v_n \mapsto \gamma v_1 \wedge \cdots \wedge \gamma v_n \, . \tag{53}$$

This defines the Fréchet-Riesz isomorphism γ_n .

The definition of the wedge isomorphism is a little more involved. Recall that we have fixed a choice of fully occupied state vector $\psi_{\text{sea}} \in \bigwedge^N(V)$. By taking an n-particle wave function ψ_n and wedging it (by exterior multiplication, which includes antisymmetrization) with an $(N-n)$-particle wave function ψ_{N-n}, we get some complex multiple of ψ_{sea}. Thus we may define

$$B : \; \mathcal{F}_n \otimes \mathcal{F}_{N-n} \to \mathbb{C}, \quad \psi_n \otimes \psi_{N-n} \mapsto B(\psi_n, \psi_{N-n}) \tag{54}$$

by the identification

$$\psi_n \wedge \psi_{N-n} \equiv B(\psi_n, \psi_{N-n}) \, \psi_{\text{sea}} \, . \tag{55}$$

The pairing B is complex bilinear and non-degenerate. Therefore, by a basic principle of linear algebra, it gives us a linear isomorphism

$$\omega_n : \; \mathcal{F}_n^* \to \mathcal{F}_{N-n}, \tag{56}$$

called *wedge isomorphism*, by the definition

$$\omega_n^{-1}(\psi_{N-n}) = B(\cdot, \psi_{N-n}) \in \mathcal{F}_n^* \, . \tag{57}$$

The finished product [12] of invariantly defined particle-hole conjugation ξ (restricted to the n-particle subspace $\mathcal{F}_n \subset \mathcal{F}$) then is the two-step process

$$\Xi_n : \ \mathcal{F}_n \xrightarrow{\gamma_n} \mathcal{F}_n^* \xrightarrow{\omega_n} \mathcal{F}_{N-n} \, . \tag{58}$$

Remark. Our informed audience may recognize some similarity between Ξ and the Hodge star operator $\star$ on differential forms in Riemannian geometry. The difference is that, given our setting in quantum mechanics, we are operating over $\mathbb{C}$ (not $\mathbb{R}$) and Ξ is antilinear (not linear).

9 Half-filled lowest Landau level

We have stressed that the universal operation of plain particle-hole conjugation can never be a symmetry of a Fermi liquid state or anything close to a free-fermion ground state. Recall the simple reason: particle-hole conjugation redistributes the population from the Fermi sea to the Fermi non-sea. Therefore, in order to stabilize the free-fermion or Fermi liquid ground state, a system-specific second transformation (Γ) must be applied.

Of course this no-go argument is void for interacting systems far from the free-fermion limit. The remainder of this lecture will be devoted to one rather spectacular example of a strongly correlated system – the half-filled lowest Landau level – where plain particle-hole conjugation does take the role of a symmetry.

To begin with history, it was Girvin [13] who pointed out the relevance of particle-hole conjugation for the physics of the quantum Hall effect (QHE). Recall that QHE takes place in a two-dimensional electron gas subject to a magnetic field. In the limit of a very strong magnetic field, one may project the single-electron Hilbert space to the lowest Landau level (LLL), say V_0 . Adopting the symmetric gauge for a homogeneous magnetic field of strength $B = -|B| \, dx \wedge dy$, the LLL wave functions are given by complex-analytic functions ψ of the dimensionless variable $z = (x + \mathrm{i}y)/\ell$. Here $\ell = \sqrt{\hbar/|eB|}$ is the magnetic length, and x, y are Cartesian coordinates for the plane $\mathbb{R}^2$. The Hermitian scalar product on V_0 is

$$\langle \psi, \psi' \rangle_{V_0} = \int d\mu(z) \, \overline{\psi(z)} \, \psi'(z), \quad d\mu(z) = \frac{|dx \, dy|}{2\pi\ell^2} \, \mathrm{e}^{-|z|^2/2}. \tag{59}$$

The description of V_0 is particularly simple in the case of a disk-shaped system. There, if the magnetic flux totals N flux quanta, V_0 is spanned by the N functions z^j for $j = 0, 1, \ldots, N-1$. The many-electron wave function $\psi_{\mathrm{sea}} \in \bigwedge^N (V_0)$ for the state of total filling can be expressed as a normalized Vandermonde determinant,

$$\psi_{\mathrm{sea}}(z_1, z_2, \ldots, z_N) = \mathcal{N}^{-1/2} \prod_{1 \le i < j \le N} (z_i - z_j). \tag{60}$$

Particle-hole conjugation $\Xi_n : \ \bigwedge^n (V_0) \to \bigwedge^{N-n} (V_0)$ here takes the concrete form

$$(\Xi_n \Psi)(z_{n+1}, \ldots, z_N) = \int \prod_{j=1}^{n} d\mu(z_j) \, \overline{\Psi(z_1, \ldots, z_n)} \, \psi_{\mathrm{sea}}(z_1, \ldots, z_n, z_{n+1}, \ldots, z_N). \tag{61}$$

Thus a complex-analytic and skew-symmetric function of n variables is particle-hole conjugated to another such function of $N-n$ variables. It is not difficult to see that Eq. (61) amounts to the same as (58).

9.1 Symmetry under particle-hole conjugation

The hallmark of quantum dynamics projected to the lowest Landau level (or any Landau level, for that matter) is that the kinetic energy of the charge carriers is totally quenched (if disorder or inhomogeneities in the background potential can be neglected), leaving no one-body component in the Hamiltonian of the bulk system. Now since the particle-hole conjugation operator Ξ sign-inverts the local charge density with respect to half filling, $\Xi Q(x) \Xi^{-1} = -Q(x)$, any residual two-body charge-charge (or current-current) interaction, in particular the Coulomb interaction, commutes with Ξ.

In the sequel, we assume our Hamiltonian H to be exactly particle-hole conjugation symmetric ($\Xi H = H \Xi$). Under that assumption, we would expect the ground state Ψ_0 to be particle-hole conjugation symmetric ($\Xi \Psi_0 \in \mathbb{C}\Psi_0$) at half filling. If so, we face an immediate complication from the free-fermion perspective: since Ξ exchanges filled single-particle levels with empty ones, a ground state invariant under Ξ cannot be of Fermi-liquid type (at least not in the original electron degrees of freedom).

The theoretical treatment of the subject took off in 1993 with the work of Halperin–Lee–Read (HLR, [14]), who did propose a Fermi-liquid ground state for the lowest Landau level at half filling. Converting electrons into composite fermions by a procedure called magnetic flux attachment, they argued that the latter could form a Fermi sea; the rough picture was that, by attaching two (fictitious) flux quanta to each electron, one cancels the background magnetic field on average, thus allowing the composite fermions to move as free fermions, at half filling. The technical step of flux attachment is carried out by introducing a fictitious gauge field, a, and adding to the field-theory Lagrangian a Chern-Simons term $a \wedge da$.

Although the HLR proposal was quite successful in fitting the observed phenomena, one bothersome issue remained: there exists no manifest particle-hole symmetry in the HLR field-theory Lagrangian. That's a serious worry because, as explained above, the Coulomb interaction projected to the lowest Landau level does have the particle-hole conjugation symmetry Ξ. Now much light and renewed interest has been thrown on the issue by a recent proposal of Son [15], which we summarize briefly.

9.2 Son's proposal and its physical meaning

Son [15] starts by observing that, for the purpose of developing a low-energy effective theory, one may realize the lowest Landau level as the subspace of zero modes of a massless Dirac fermion ψ, say with charge $q = +|e|$, in a homogeneous magnetic field:

$$S = \mathrm{i}\hbar c \int dt \int d^2 r \; \bar{\psi}\, \gamma^\mu \big(\partial_\mu - \mathrm{i} q A_\mu / \hbar\big) \psi + \cdots , \tag{62}$$

where the ellipses indicate residual interaction terms. In fact, adopting the symmetric gauge $A = |B|\big(x^1dx^2 - x^2dx^1\big)/2$ for $B = |B|\, dx^1 \wedge dx^2$, and choosing the gamma matrices $\gamma^0 = \sigma_3$, $\gamma^1 = \mathrm{i}\sigma_2$, $\gamma^2 = -\mathrm{i}\sigma_1$, one arrives at a Dirac Hamiltonian D of the form

$$D \propto \begin{pmatrix} 0 & \partial_z - \bar{z}/4 \\ \partial_{\bar{z}} + z/4 & 0 \end{pmatrix}, \quad z = \big(x^1 + \mathrm{i}x^2\big)\sqrt{|eB|/\hbar}\,,$$

and the zero modes of this Hamiltonian,

$$\psi_0 = \begin{pmatrix} f(z) \\ 0 \end{pmatrix} \mathrm{e}^{-|z|^2/4}, \quad \partial_{\bar{z}} f(z) = 0,$$

are in bijection with the states spanning the lowest Landau level; see above.

For the relativistic system (62), one has command of the discrete symmetry operations of charge conjugation C, parity P, and time reversal T. The product CT is antilinear in second quantization and sends the electromagnetic field (E, B) to $(-E, B)$. Thus it is an anti-unitary symmetry of the massless Dirac fermion (62) in zero electric field E and for any magnetic field B. It is straightforward to check that CT coincides with our operation Ξ of particle-hole conjugation upon restriction to the zero-energy Landau level of the theory (62).

Let us emphasize once again that a Ξ-symmetric half-filled Fermi-liquid ground state does not exist, neither in the quantum Hall electron variables nor in the low-energy equivalent theory (62). In view of that no-go situation, one is motivated to look for a good change of variables by which to develop a Fermi-liquid description of some sort.

Assuming the starting point (62), Son [15] performs a so-called fermionic particle-vortex transformation to pass to a dual formulation (known as QED_3) by another Dirac field ξ coupled to a dynamical gauge field a (which coincides with the Chern-Simons dynamical gauge field a of HLR but for a pseudoscalar multiplicative factor, the Hall conductivity at half-filling):

$$S_{\text{dual}} = 2\pi\mathrm{i}\hbar v_F \int dt \int d^2r \; \bar{\xi}\gamma^\mu\big(\partial_\mu - 2\mathrm{i}a_\mu/q\big)\,\xi + \int A \wedge da + \cdots\,, \tag{63}$$

where we adopt the convention $dx^0 = v_F\, dt$ and $\partial_0 = v_F^{-1}\partial_t$, as our physical system with characteristic speed v_F has only Galilean invariance (not Lorentz invariance). The dynamical gauge field $a = a_\mu dx^\mu$ is a gauge potential for the charge-current two-form $J = da$ of the two-dimensional electron gas. In particular, its time component a_0 is proportional to the orbital magnetization m of the 2D electron gas. The two-component spinor field ξ in (63) is called the Dirac composite fermion. It has the physical dimension of length^{-1}, and it is charge-neutral as it does not couple directly to the external gauge field A. In view of the fundamental duality between magnetic flux and electric charge, the coupling to the charge one-form a suggests that ξ carries an emergent magnetic flux. In fact, what ξ carries is *vorticity*, a quantity tied to the presence of magnetic flux; see below.

The half-filled lowest Landau level features a nonzero orbital magnetization $\langle m\rangle$, and according to (63) the magnetization $\langle m\rangle \sim \langle a_0\rangle$ as the time-component of a acts as a chemical potential for the Dirac composite fermion ξ. Therefore one may well expect the latter to form a Fermi-liquid ground state by populating a Fermi sea up to the chemical potential $\langle m \rangle$.

Let us now take a closer look at the objects of the dual theory (63). For the benefit of our audience, we here adopt component notation (with respect to a Cartesian basis), assuming familiarity with epsilon tensors and the summation convention. We write

$$J = \tfrac{1}{2} J_{\mu\nu}\, dx^\mu \wedge dx^\nu , \quad J_{\mu\nu} = \epsilon_{\mu\nu\lambda} J^\lambda , \quad J^0 = \rho_{\text{exc}} , \quad J^l = j^l \ (l = 1, 2), \tag{64}$$

with j^l the components of the electric current vector field and $\rho_{\text{exc}} \equiv \rho$ the excess electric charge density with respect to half filling, and we put

$$a = a_\mu dx^\mu = m dt - \epsilon_{il}\, p^i dx^l . \tag{65}$$

The equation $J = da$ then splits into three equations:

$$\rho = -\partial_i p^i , \quad j^l = \epsilon^{il} \partial_i m + \partial_t p^l \quad (l = 1, 2). \tag{66}$$

The physical interpretation of the dynamical gauge field a should now be clear: p^i are the components an electric polarization vector field $\vec{p}$, and m is an orbital magnetization function for the 2D electron gas. These are determined only up to gauge transformations

$$m \mapsto m + \partial_t \phi , \quad p^l \mapsto p^l - \epsilon^{il} \partial_i \phi , \tag{67}$$

by a pseudoscalar function ϕ with the physical dimension of electric charge.

Turning to the Dirac composite-fermion field ξ, we expand on the statement that ξ carries vorticity by way of an emergent magnetic field. To start the argument, we observe that S_{dual} in (63) has a symmetry under global $\mathrm{U}(1)$ phase rotations (not to be confused with gauge transformations $a \mapsto a + d\phi$ and $\xi \mapsto \mathrm{e}^{2\mathrm{i}\phi/q}\xi$),

$$\xi(x) \mapsto \mathrm{e}^{\mathrm{i}\theta} \xi(x), \quad \bar{\xi}(x) \mapsto \mathrm{e}^{-\mathrm{i}\theta} \bar{\xi}(x), \tag{68}$$

which entails a conserved current:

$$\partial_\mu \Phi^\mu = 0, \quad \Phi^\mu = \bar{\xi} \gamma^\mu \xi . \tag{69}$$

Hence, the physical meaning of ξ hinges on the interpretation of the conservation law implied by $\partial_\mu \Phi^\mu = 0$. To uncover it, we introduce

$$b_{12} = \frac{2h}{q} \Phi^0 , \quad e_i = \frac{2h}{q} v_F \epsilon_{ij} \Phi^j \quad (h = 2\pi\hbar, \ i = 1, 2). \tag{70}$$

The continuity equation (69) then takes the form

$$\partial_t b_{12} + \partial_1 e_2 - \partial_2 e_1 = 0 , \tag{71}$$

which can be interpreted as Faraday's law of induction (written in components and transcribed to 2+1 space-time dimensions), with the consequence that the total space integral of b_{12} is independent of time. To reinforce the Faraday interpretation, we do an integration by parts, $\int A \wedge da = \int dA \wedge a$, and we decompose the electromagnetic field strength into its electric and magnetic parts: $dA = B + E \wedge dt$. We then see that the coupling $a_\mu \Phi^\mu$ between the dynamical gauge field a_μ and the conserved current Φ^μ enters into the dual action (63) as a shift:

$$B \to B + b\,, \quad E \to E + e \quad (b = b_{12}\, dx^1 \wedge dx^2,\ e = e_i\, dx^i). \tag{72}$$

Thus b and e are to be interpreted as *emergent magnetic and electric fields*. Moreover, taking the dual action (63) for granted, we see that the functional integral over a_0 pins the emergent magnetic field b to the external magnetic field B:

$$B_{\text{eff}} \equiv b + B = 0. \tag{73}$$

This constraint indicates that the conservation law $\int b \propto \int \Phi^0\, d^2r = \text{const}$ reflects the conservation of magnetic flux, $\int B = \text{const}$. Now, which conserved property of the electron gas is tied to the total external magnetic flux? There exists only one good answer to this question: the integrated *vorticity*, viz. the total number of zeroes in the one-body density matrix for the many-electron wave function; see [2] for more detail.

A follow-up comment concerns the factor of 2 in the expression $\nabla_\mu = \partial_\mu - 2\mathrm{i}\, a_\mu / q$ for the covariant derivative in (63). By canonical quantization of the Dirac composite field ξ, the presence of this factor means that single-particle excitations of ξ carry *two* emergent magnetic flux quanta $2h/q$ and hence two vortices due to the constraint (73). (The argument for that uses the Dirac quantization condition, stating that the lattice of quantized electric charges is h-reciprocal to the lattice of quantized magnetic fluxes.)

To add some perspective, it had long been appreciated that the LLL composite fermion is a composite object made from one electric charge quantum (electron) and two magnetic flux quanta (vortices). The traditional approach of HLR was to build the theory around the electron degrees of freedom and attach Chern-Simons magnetic flux as a subsidiary feature. The more recent approach of Son turned the emphasis around, by taking the vortex degrees of freedom (which carry magnetic flux but no electric charge) as primary and coupling them to fluctuations in the charge current J via the magnetization/polarization one-form a. Although the physical predictions turn out to be quite similar, the change of approach does make for some differences. For one, the number of composite fermions in the HLR approach is given by the number of electrons, whereas in Son's proposal it is given by half the number of magnetic flux quanta. For another, the realization of symmetries is different; see the next subsection.

9.3 Symmetry considerations

We now address the symmetry aspects of Son's proposal and especially the issue of particle-hole (conjugation) symmetry. Since particle-hole conjugation Ξ is realized in the (zero Landau level of the) Dirac fermion representation (62) by CT, we shall elucidate the corresponding operation CT in the dual representation (63).

As we are going to see, the operation of time reversal T is realized on the fermionic vortex field ξ in an unfamiliar way that makes the symmetry aspects quite striking. To spell them out, we begin by reviewing how T acts on the electromagnetic gauge field A and on the charge current J. The guiding principle here is that the field-matter interaction $A \wedge J$ must transform as a space-time density, so that

$$S_{\text{int}} = \int A \wedge J = \frac{1}{2} \int A_\mu dx^\mu \wedge J_{\nu\lambda}\, dx^\nu \wedge dx^\lambda = \int A_\mu J^\mu |d^3 x| \tag{74}$$

is invariant under <u>all</u> space-time diffeomorphisms including those that are orientation reversing, and is invariant under time reversal in particular. Now the two-form $J = da$ for the charge 3-current (in 2+1 dimensions) is a *time-even* differential form, which means that it transforms under time reversal T by straight pullback: $J \mapsto +T^* J$. It then follows from $J = da$ and $T^* \circ d = d \circ T^*$ that the magnetization/polarization one-form $a = a_\mu dx^\mu$ is also time-even: $a \mapsto +T^* a$; in components we have

$$T: \; a_0(\mathbf{r},t) \mapsto -a_0(\mathbf{r},-t), \quad a_l(\mathbf{r},t) \mapsto +a_l(\mathbf{r},-t) \quad (l = 1,2). \tag{75}$$

In contrast, the electromagnetic gauge field A is a *time-odd* one-form; thus it transforms under time reversal by negative pullback ($A \mapsto -T^* A$) or

$$T: \; A_0(\mathbf{r},t) \mapsto +A_0(\mathbf{r},-t), \quad A_l(\mathbf{r},t) \mapsto -A_l(\mathbf{r},-t) \quad (l = 1,2). \tag{76}$$

(Of course, the opposite behavior of $J \mapsto +T^* J$ versus $A \mapsto -T^* A$ is just what is needed in order for $A \wedge J = A_\mu J^\mu |d^3 x|$ to transform as a scalar under time reversal.)
The sign-opposite transformation law for a as compared with A has a surprising effect. To see that most clearly, consider the first-quantized Hamiltonian h of the vortex field ξ in a given gauge field $a = m dt - p$:

$$h(p,m) = \hbar v_F \sum_{l=1}^{2} \sigma_l \left(\frac{1}{\mathrm{i}} \frac{\partial}{\partial x^l} + \frac{2}{q} p_l \right) - \frac{2\hbar}{q} m, \tag{77}$$

where $m = v_F a_0$ is the local magnetization, and $p = \sum p_l \, dx^l$ is the local polarization, treated here as a co-vector field (or form). To determine how T acts on ξ, one observes that if ξ is a solution of the Dirac equation $\mathrm{i}\hbar\, \partial_t \xi = h\xi$, then by time-reversal invariance (or equivariance) so is $T\xi$. There exist two different scenarios by which to realize that equivariance condition. The standard scenario is that T commutes with both h and $\mathrm{i}\hbar\, \partial_t$. Since ∂_t changes sign under $t \mapsto -t$, this means that T must be antilinear ($T\mathrm{i} = -\mathrm{i}T$). The second scenario for time-reversal symmetry of the Dirac equation is that T *anti*commutes with both $\mathrm{i}\hbar\, \partial_t$ and the Hamiltonian h. Given Eq. (77), it is clear that the time-even property of a, namely $T: \; m \mapsto -m$ and $p_l \mapsto +p_l$ ($l = 1,2$), forces the latter scenario. Thus in the present instance, time reversal is realized as an operation that is complex *linear* ($T\mathrm{i} = +\mathrm{i}T$) and anticommutes with the vortex-field Hamiltonian h. Explicitly,

$$T: \; \xi(\mathbf{r},t) \mapsto \sigma_3 \xi(\mathbf{r},-t), \quad h(p,m) \mapsto \sigma_3 h(p,-m) \sigma_3 = -h(p,m). \tag{78}$$

This is how time reversal acts (in first quantization, i.e., viewing the Dirac equation as a classical field equation) on the fermionic vortex field ξ of the dual representation.

The other factor of the symmetry operation CT is charge conjugation C. We recall that the electromagnetic gauge field A transforms under C as $A \mapsto -A$. In order for the field-matter interaction $\int A \wedge da$ to be charge-conjugation invariant, the dynamical gauge field a must conform to the same transformation law as A (thus, $C: \; a \mapsto -a$). This is achieved by the antilinear transformation

$$C: \; \xi \mapsto \sigma_1 \bar{\xi}. \tag{79}$$

It follows that C anticommutes with the operator $\mathrm{i}\hbar\,\partial_t - h$ and hence reverses the sign of h:

$$C: \; h(p,m) \mapsto \sigma_1 \, \overline{h(-p,-m)} \, \sigma_1 = -h(p,m). \tag{80}$$

Next, we turn to the combined operation CT. By the properties of its factors C and T, the product CT is an antilinear symmetry of the first-quantized Hamiltonian:

$$CT: \; h(p,m) \mapsto \sigma_2 \, \overline{h(-p,m)} \, \sigma_2 = +h(p,m). \tag{81}$$

Note that the emphasis here is on *symmetry* (as opposed to antisymmetry $h \mapsto -h$). The field-matter interaction $\int A \wedge J$ for $J = da$,

$$\int A \wedge da = \int dA \wedge a = \int (B + E \wedge dt) \wedge (m\,dt - p), \tag{82}$$

augments the vortex-field Hamiltonian by a term

$$h_{\text{int}} = \int (Bm - E \wedge p), \tag{83}$$

which is invariant under both T and C. The combined action of these operations on the electromagnetic field and the dynamical gauge field is

$$(E,B) \xrightarrow{CT} (-E,B), \quad (p,m) \xrightarrow{CT} (-p,m). \tag{84}$$

Now from our condensed-matter perspective, the electromagnetic field is to be regarded as a given background (not to be transformed). We then see that CT remains a symmetry for $E \equiv 0$ (zero external electric field) and any magnetic field B.

We can now deliver the (symmetry) punch line of Son's proposal. In the original formulation (62) by a massless Dirac fermion projected to the zero Landau level, the operator CT acted as particle-hole conjugation Ξ. Thus it exchanged particles and holes (or antiparticles) when acting on the Fock space of the second-quantized theory, thereby posing an obstruction to the existence of any Fermi-liquid ground state (with symmetry Ξ). Now in the dual representation (63) this obstruction has disappeared! Indeed, the operation CT on the fermionic vortex field ξ and the dynamical gauge field a is a proper symmetry of the Hamiltonian; when acting on the Fock space constructed by canonical quantization of the dual theory (63), it sends particles, or particle-like excitations of the vortex field, to particles, and it sends antiparticles to antiparticles. In Son's language, the Dirac composite fermion ξ is its own antiparticle. This, then, is how CT (alias particle-hole conjugation) may emerge as a symmetry of a Fermi-liquid ground state.

9.4 Microscopic picture of the composite fermion

To augment the field-theoretic symmetry considerations, which may seem quite abstract, we now offer a glimpse of the microscopic picture of the Dirac composite fermion. From experiment and theory one knows that the composite fermion at half filling ($\nu = 1/2$) is a charge-neutral excitation made, roughly speaking, from one electron and two fictitious magnetic flux quanta. How is this crude picture refined in view of Son's proposal?

For quantum Hall states and other systems with an energy gap where the quantum adiabatic theorem holds, one knows that the adiabatic insertion of a magnetic flux line (in 3D, or flux point in 2D), with circulation equal to that of the strong magnetic background field, expands the electron gas radially outward from the point of insertion. (We expect this to be still true for the gapless system of the half-filled lowest Landau level.) The adiabatic flux insertion gives rise to spectral flow resulting in a zero (or vortex) of the many-electron wave function. Adopting the symmetric gauge with respect to the insertion point, z_0, one can express the effect of flux insertion as multiplication by the operator

$$U_{z_0} = \prod\nolimits_j (z_j - z_0), \tag{85}$$

where z_j ($j = 1, 2, ...$) are the electron coordinates of the holomorphic representation; see the very beginning of this Section. In the occupation-number representation $\mathbf{n} = \{n_0, n_1, n_2, ...\}$ w.r.t. the single-particle basis $(z - z_0)^l \mathrm{e}^{-|z-z_0|^2/4}$ ($l = 0, 1, 2, ...$), the effect of the vortex operator U_{z_0} is a shift $\mathbf{n} \mapsto \{0, n_0, n_1, \ldots\}$ leaving the zero orbital ($l = 0$) vacant. The vacancy amounts to a local charge deficit: for filling fraction ν, that deficit is $-\nu e$. Thus, the electric charge of a vortex excitation at half filling is $-e/2$.

Now from the particle-hole conjugation symmetry of the half-filled LLL, we expect the vortex-type excitation of charge $-e/2$ to be accompanied by its antiparticle, the “antivortex”. Centered at position z_1, the antivortex is created by the particle-hole conjugate operator

$$U^\flat_{z_1} = \Xi U_{z_1} \Xi^{-1}. \tag{86}$$

By construction, an antivortex excitation carries the opposite charge ($+e/2$) and the same energy, provided that the ground state is particle-hole symmetric. Doing a short calculation in the occupation-number representation of above, one finds that $U^\flat_{z_1}$ has the same effect as U_{z_1} but for one characteristic difference: while U_{z_1} leaves the zero orbital (w.r.t. z_1) always empty, the particle-hole conjugate $U^\flat_{z_1}$ leaves it always occupied. Thus $U^\flat_{z_1}$ creates a vortex with charge deficit $-e/2$ centered at z_1 and at the same time adds an electron in the zero orbital at z_1, thereby producing a total charge increment of $+e/2$.

Given the basic building blocks of U_{z_0} and $U^\flat_{z_1}$, Wang and Senthil (WS, [16]) proposed to think of Son's composite fermion as a (more or less loosely) bound state of one vortex and one antivortex. Indeed, (i) there is an attractive electric force between a vortex and an antivortex, (ii) the total charge of a bound pair at $\nu = 1/2$ is zero, and (iii) the bound vortex-antivortex pair is its own antiparticle as the vortex component gets transformed under particle-hole conjugation to the antivortex component; cf. Fig. 4.

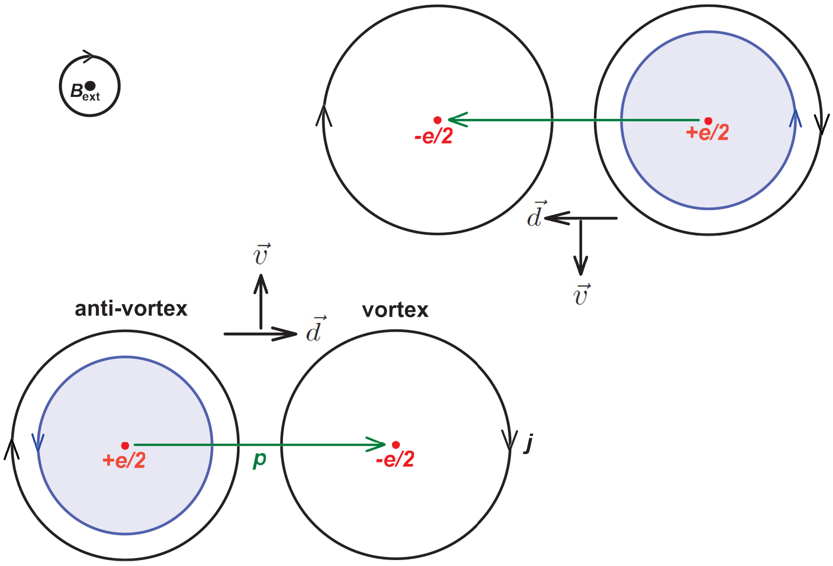

Fig. 4: *Semiclassical picture at $\nu = 1/2$ of a composite fermion (left-hand side) and its particle-hole conjugate (right-hand side). The composite fermion is an electric dipole made from a vortex with positive charge $-e/2$ and an antivortex with negative charge $+e/2$. In a state of motion, the velocity $\vec{v}$ and the dipole moment $\vec{d}$ form an orthogonal pair positively oriented with respect to B_{ext}.*

The composite fermions of observable consequence are those in a state of rapid motion (at the Fermi speed of the composite Fermi liquid). These carry an electric dipole moment $\vec{d}$ proportional to the relative position $z_1 - z_0$, and the dipole vector $\vec{d}$ is perpendicular to the velocity $\vec{v}$ of the motion – a phenomenon known as "spin-momentum" locking and anticipated in early work by N. Read [17]. Assuming the limit of large separation $|z_1 - z_0|$ between the vortex and antivortex constituents, WS argued that the process of adiabatically transporting a composite fermion around the Fermi surface, or rotating its k-vector through 2π, gives a Berry phase of π. (The latter had been recognized as an important ingredient [18, 15] for the correct phenomenology of the composite Fermi liquid.) It should be added that while the whole scenario sounds very plausible, its details still await confirmation by rigorous work.

Appendix

A Charge conjugation explained

In order to appreciate the symmetry of charge conjugation, one needs some understanding of the process of canonical quantization of the Dirac field. The latter requires three pieces of basic input: (i) the complex phase space W of classical solutions of the free Dirac equation, (ii) an invariantly defined symmetric bilinear form $B : \ W \otimes W \to \mathbb{C}$ (in order to construct the canonical anticommutation relations for the Dirac field), and (iii) a compatible complex structure J on the space $W_\mathbb{R}$ of real fields (to construct the proper ground state upon which to build the Fock space of physical electron and positron states of the Dirac field).

In this appendix, we focus on the first input, (i), as this already provides plenty of insight into the intricacies of charge conjugation. A key point is that one should think of the (complex) Dirac field as an object with two parts to it: a spinor part ψ that solves the free Dirac equation

$$D\psi = 0, \quad D = -\mathrm{i}\hbar\gamma^\mu\partial_\mu + mc, \tag{87}$$

and a *co-spinor* part $\widetilde{\psi}$ that solves the adjoint equation,

$$\widetilde{\psi} \circ D = 0. \tag{88}$$

(You may think of the spinor as a column vector and of the co-spinor as a row vector.) In other words, the complex phase space for the Dirac field is a direct sum $W = V \oplus \widetilde{V}$ of two subspaces: that of the spinor solutions ($\psi \in V$), and that of the co-spinor solutions ($\widetilde{\psi} \in \widetilde{V}$). The elements of the complex phase space W of solutions are pairs: $\big(\psi, \widetilde{\psi}\big) \in V \oplus \widetilde{V}$.

Now the Dirac operator D is formally adjoint to $D^\dagger = \gamma^0 D \gamma^0$. Therefore, the co-spinor $\widetilde{\psi} = \psi^\dagger\gamma^0$ solves the adjoint equation (88) if the spinor ψ solves Eq. (87). We say that the complex vector space W has a real subspace $W_\mathbb{R}$ spanned by the "real" solutions $\big(\psi, \widetilde{\psi}\big) = \big(\psi, \psi^\dagger\gamma^0\big)$.

To construct the quantum theory of the Dirac field, one has to work with the complex phase space W of solutions, as follows. One separates the spinor solutions ψ into their positive-frequency and negative-frequency parts, $\psi = \psi_+ + \psi_-$, by a so-called mode expansion (here indicated in schematic notation):

$$\psi_+ = \int d^3k\, u(k)\, \mathrm{e}^{-\mathrm{i}\omega_k t}, \quad \psi_- = \int d^3k\, v(k)\, \mathrm{e}^{+\mathrm{i}\omega_k t} \quad (\omega_k > 0). \tag{89}$$

This defines a decomposition $V = V_+ \oplus V_-$. The same procedure applied to the co-spinor solutions defines a decomposition $\widetilde{V} = \widetilde{V}_+ \oplus \widetilde{V}_-$. (We remark that by the bilinear form B not here specified, one has the duality $V_\pm^* \cong \widetilde{V}_\mp$.)

By the process of canonical quantization one turns elements of (more precisely: the coefficients appearing in the mode expansion of)

- V_+ into electron creation operators,
- V_- into positron annihilation operators,

- $\widetilde{V}_+ \cong V_-^*$ into positron creation operators,
- $\widetilde{V}_- \cong V_+^*$ into electron annihilation operators.

The Fock space of the quantized Dirac field then is the exterior algebra

$$\mathcal{F} = \bigwedge \big(V_+ \oplus \widetilde{V}_+\big) = \bigwedge \big(V_+ \oplus V_-^*\big). \tag{90}$$

Given this information, we can explain how charge conjugation works.
The operator $\psi \mapsto C\psi = \gamma^2 \bar{\psi}$ of Eq. (27) defines a mapping

$$C : \; V_\pm \to V_\mp \,, \tag{91}$$

which swaps positive-frequency and negative-frequency solutions. Thus, upon quantization, it takes an electron creation operator $\psi \in V_+$ and turns it into a positron annihilation operator $C\psi \in V_-$ (and vice versa). Such an operator does not act on the Fock space $\mathcal{F}$ of physical states. To obtain an operator that does act on $\mathcal{F}$, one needs to compose C with the mapping, say C', from spinor solutions to co-spinor solutions:

$$C' : \; V_\mp \to \widetilde{V}_\pm \,, \quad \psi \mapsto \psi^\dagger \gamma^0. \tag{92}$$

Note that C' involves complex conjugation (via †) and hence switches between positive-frequency and negative-frequency solutions. Both C and C' are antilinear, so their concatenation $\widehat{C} = C' \circ C \; : \; V_\pm \to \widetilde{V}_\pm$ is complex linear. Altogether, $\widehat{C}$ maps electron creation operators to positron creation operators (and likewise for the annihilation operators). That's the unitary symmetry $\widehat{C}$ of charge conjugation of the relativistic Dirac field. (We re-iterate that $\widehat{C}$ is not a good model for anything of much relevance in condensed matter physics.)

References

[1] J. McGreevy, Annu. Rev. Cond. Matt. Phys. **14**, 57 (2023)

[2] M.R. Zirnbauer, J. Math. Phys. **62**, 021101 (2021)

[3] V. Bargmann, J. Math. Phys. **5**, 862 (1964)

[4] D.S. Freed, *On Wigner's Theorem*, arXiv:1112.2133 (2011)

[5] P. Heinzner, A. Huckleberry and M.R. Zirnbauer, Commun. Math. Phys. **257**, 725 (2005)

[6] T. Tao, `terrytao.wordpress.com/2008/09/27/what-is-a-gauge`

[7] M. Greiter, Ann. Phys. **319**, 217 (2005)

[8] B. Thaller, *The Dirac equation* (Springer, Berlin, 1991)

[9] S. Weinberg, *The Quantum Theory of Fields*, Vol. 1 (CUP, Cambridge, 2005)

[10] W.P. Su, J.R. Schrieffer and A.J. Heeger, Phys. Rev. Lett. **42**, 1698 (1979)

[11] L. Fidkowski and A. Kitaev, Phys. Rev. B **83**, 075103 (2011)

[12] For brevity, we have suppressed one annoying detail: to get all the sign factors right, we need to give an n-dependent sign to ψ_{sea} in Eq. (55); see [2].

[13] S.M. Girvin, Phys. Rev. B **29**, 6012 (1984)

[14] B.I. Halperin, P.A. Lee and N. Read, Phys. Rev. B **47**, 7312 (1993)

[15] D.T. Son, Phys. Rev. X **5**, 031027 (2015)

[16] C. Wang and T. Senthil, Phys. Rev. B **93**, 085110 (2016)

[17] N. Read, Semicond. Sci. Technol. **9**, 1859 (1994)

[18] F.D.M. Haldane, Phys. Rev. Lett. **93**, 206602 (2004)

2 Mean-Field Theory: Hartree-Fock and BCS

Erik Koch
Institute for Advanced Simulation
Forschungszentrum Jülich

Contents

E. Pavarini and E. Koch (eds.)
Correlations and Phase Transitions
Modeling and Simulation Vol. 14
Forschungszentrum Jülich, 2024, ISBN 978-3-95806-751-6
http://www.cond-mat.de/events/correl24

1 Many-electron states

One of the great surprises of quantum mechanics is the existence of indistinguishable objects. Classically this is not possible: objects can always be distinguished at least by their position in space, meaning that indistinguishable objects must be identical. This is Leibniz' Principle of the Identity of Indiscernibles [1]. For quantum objects, however, the uncertainty principle makes the distinction of particles by their position impossible. This allows for the existence of elementary particles. They form the basic units of all matter. So, quite remarkably, all the different objects we know are made of indistinguishable building blocks.

In the formalism of quantum mechanics, indistinguishability means that no observable lets us distinguish one of these particles from the other. This means that every observable for, e.g., electrons, must treat each electron in the same way. Thus, in principle, observables must act on all electrons in the universe. In practice we can, of course, distinguish electrons localized on the moon from those in our lab to an excellent approximation. Thus, for all practical purposes, we can restrict our description to the electrons in the system under consideration, assuming that the differential overlap with all other electrons vanishes. Any observable $M(x_1,\dots,x_N)$ for the N electrons in our system must then be symmetric under permutations of the variables x_i.

The consequences are straightforward: An observable $M(x)$ acting on a single-particle degree of freedom x must act on all indistinguishable particles in the same way, i.e., $\sum_i M(x_i)$. Likewise, a two-body observable $M(x,x')$ must act on all pairs in the same way, $\sum_{i,j} M(x_i,x_j)$ with $M(x,x') = M(x',x)$. We can thus write any observable in the form

$$M(\mathbf{x}) = M^{(0)} + \sum_i M^{(1)}(x_i) + \frac{1}{2!}\sum_{i\neq j} M^{(2)}(x_i,x_j) + \frac{1}{3!}\sum_{i\neq j\neq k} M^{(3)}(x_i,x_j,x_k) + \cdots \tag{1}$$

$$= M^{(0)} + \sum_i M^{(1)}(x_i) + \sum_{i<j} M^{(2)}(x_i,x_j) + \sum_{i<j<k} M^{(3)}(x_i,x_j,x_k) + \cdots\,, \tag{2}$$

where the summations can be restricted since the operators must be symmetric in their arguments, while for two or more identical coordinates the operator is really one of lower order: $M^{(2)}(x_i,x_i)$, e.g., only acts on a single coordinate and should be included in $M^{(1)}$.

For the many-body wavefunctions $\Psi(x_1,x_2,\cdots)$ the situation is slightly more complex. Since the probability density $|\Psi(x_1,x_2,\cdots)|^2$ is an observable, the wavefunction should transform as one-dimensional (irreducible) representations of the permutation group. Which irreducible representation applies to a given type of elementary particle is determined by the spin-statistics theorem [2,3]: The wavefunctions of particles with integer spin are symmetric, those of particles with half-integer spin change sign when two arguments are exchanged. From an arbitrary N-particle wavefunction we thus obtain a many-electron wavefunction by antisymmetrizing

$$\mathcal{A}\Psi(x_1,\dots,x_N) := \frac{1}{\sqrt{N!}}\sum_P (-1)^P \Psi\left(x_{p(1)},\dots,x_{p(N)}\right)\,, \tag{3}$$

where $(-1)^P$ is the parity of the permutation P that maps $n\to p(n)$. Since there are $N!$ different permutations, this can easily become an extremely costly operation. Remarkably, a product of

N single-electron states φ_α can be antisymmetrized much more efficiently (in $\mathcal{O}(N^3)$ steps) by writing it in the form of a determinant

$$\Phi_{\alpha_1,\dots,\alpha_N}(x_1,\dots,x_N) := \frac{1}{\sqrt{N!}}\begin{vmatrix} \varphi_{\alpha_1}(x_1) & \varphi_{\alpha_2}(x_1) & \cdots & \varphi_{\alpha_N}(x_1) \\ \varphi_{\alpha_1}(x_2) & \varphi_{\alpha_2}(x_2) & \cdots & \varphi_{\alpha_N}(x_2) \\ \vdots & \vdots & \ddots & \vdots \\ \varphi_{\alpha_1}(x_N) & \varphi_{\alpha_2}(x_N) & \cdots & \varphi_{\alpha_N}(x_N) \end{vmatrix}. \tag{4}$$

For $N{=}1$ the Slater determinant is simply the one-electron orbital $\Phi_\alpha(x) = \varphi_\alpha(x)$ while for $N{=}2$ we get the familiar expression $\Phi_{\alpha,\alpha'}(x,x') = \big(\varphi_\alpha(x)\varphi_{\alpha'}(x') - \varphi_{\alpha'}(x)\varphi_\alpha(x')\big)/\sqrt{2}$ for the two-electron Slater determinant.

Slater determinants are important because they can be used to build a basis of the many-electron Hilbert space. To see how, we consider a complete set of orthonormal single-electron states

$$\sum_n \overline{\varphi_n(x)}\,\varphi_n(x') = \delta(x{-}x')\ \text{(complete)} \qquad \int\! dx\,\overline{\varphi_n(x)}\,\varphi_m(x) = \delta_{n,m}\ \text{(orthonormal)}\,. \tag{5}$$

To expand an arbitrary N-particle function $a(x_1,\dots,x_N)$, we start by considering it as a function of x_1 with $x_2,\dots,x_N$ kept fixed. We can then expand it in the complete set $\{\varphi_n\}$ as

$$a(x_1,\dots,x_N) = \sum_{n_1} a_{n_1}(x_2,\dots,x_N)\,\varphi_{n_1}(x_1)$$

with expansion coefficients that depend on the remaining coordinates

$$a_{n_1}(x_2,\dots,x_N) = \int\! dx_1\,\overline{\varphi_{n_1}(x_1)}\,a(x_1,x_2,\dots,x_N).$$

These, in turn, can be expanded as a functions of x_2

$$a_{n_1}(x_2,\dots,x_N) = \sum_{n_2} a_{n_1,n_2}(x_3,\dots,x_N)\,\varphi_{n_2}(x_2).$$

Repeating this, we obtain the expansion of a in product states

$$a(x_1,\dots,x_N) = \sum_{n_1,\dots,n_N} a_{n_1,\dots,n_N}\,\varphi_{n_1}(x_1)\cdots\varphi_{n_N}(x_N)$$

with

$$a_{n_1,\dots,n_N} = \int\! dx_1\cdots\int\! dx_N\,\overline{\varphi_{n_1}(x_1)}\cdots\overline{\varphi_{n_N}(x_N)}\,a(x_1,\dots,x_N).$$

For an antisymmetric N-particle function Ψ the expansion coefficients are thus antisymmetric under permutation of the indices: $a_{n_{p(1)},\dots,n_{p(N)}} = (-1)^P a_{n_1,\dots,n_N}$. Fixing some particular order of the indices, e.g., $n_1 < n_2 < \ldots < n_N$, we thus get an expansion in Slater determinants

$$\Psi(x_1,\dots,x_N) = \sum_{n_1<\ldots<n_N} a_{n_1,\dots,n_N}\sqrt{N!}\,\Phi_{n_1,\dots,n_N}(x_1,\dots,x_N).$$

Since we can write any antisymmetric function as such a configuration-interaction expansion, the set of Slater determinants

$$\Big\{\Phi_{n_1,\dots,n_N}(x_1,\dots,x_N)\,\Big|\; n_1 < n_2 < \cdots < n_N\Big\} \tag{6}$$

forms a basis of the N-electron Hilbert space. Since the overlap of two Slater determinants

$$\int d\boldsymbol{x}\, \overline{\Phi_{\alpha_1,\dots,\alpha_N}(\boldsymbol{x})}\, \Phi_{\beta_1,\dots,\beta_N}(\boldsymbol{x}) = \frac{1}{N!}\sum_{P,P'}(-1)^{P+P'}\prod_n \int dx_n\, \overline{\varphi_{\alpha_{p(n)}}(x_n)}\, \varphi_{\alpha_{p'(n)}}(x_n)$$
$$= \begin{vmatrix} \langle\varphi_{\alpha_1}|\varphi_{\beta_1}\rangle & \cdots & \langle\varphi_{\alpha_1}|\varphi_{\beta_N}\rangle \\ \vdots & \ddots & \vdots \\ \langle\varphi_{\alpha_N}|\varphi_{\beta_1}\rangle & \cdots & \langle\varphi_{\alpha_N}|\varphi_{\beta_N}\rangle \end{vmatrix} \tag{7}$$

is the determinant of the overlap of the constituent orbitals, the Slater determinants (6) form a complete orthonormal basis of the N-electron Hilbert space when the orbitals $\varphi_n(x)$ are a complete orthonormal basis of the one-electron Hilbert space.

While we use a set of N one-electron orbitals $\varphi_n(x)$ to define an N-electron Slater determinant $\Phi_{\alpha_1,\dots,\alpha_N}(\boldsymbol{x})$, this representation is not unique: Any unitary transformation among the N occupied orbitals will not change the determinant. Thus, strictly, a Slater determinant is not determined by the set of indices we usually give, but, up to a phase, by the N-dimensional subspace spanned by the orbitals $\varphi_1, \dots, \varphi_N$ in the single-electron Hilbert space. The projector to this space is the one-body density matrix

$$\Gamma^{(1)}(x,x') = N\int dx_2\cdots dx_N\, \overline{\Phi(x,x_2,\dots,x_N)}\,\Phi(x',x_2,\dots,x_N)\,. \tag{8}$$

To see this, we expand the Slater determinant along its first row

$$\Phi_{\alpha_1\cdots\alpha_N}(x_1,\dots,x_N) = \frac{1}{\sqrt{N}}\sum_{n=1}^{N}(-1)^{1+n}\,\varphi_{\alpha_n}(x_1)\,\Phi_{\alpha_{i\neq n}}(x_2,\dots,x_N)\,, \tag{9}$$

where $\Phi_{\alpha_{i\neq n}}(x_2,\dots,x_N)$ is the determinant with the first row and the n-th column removed, which can be written as $N{-}1$-electron Slater determinants with orbital α_n removed. Inserting this into (8) we find

$$\Gamma^{(1)}_{\Phi}(x,x') = \sum_{n=1}^{N}\overline{\varphi_{\alpha_n}(x)}\,\varphi_{\alpha_n}(x')\,, \tag{10}$$

which is the expansion of the one-body density matrix in eigenfunctions (natural orbitals), with eigenvalues (natural occupation numbers) either one or zero. Any many-electron wavefunction $\Psi(\boldsymbol{x})$ with the same one-body density matrix $\Gamma^{(1)}_{\Phi}$ equals the Slater determinant $\Phi(\boldsymbol{x})$ up to a phase, i.e., $|\langle\Psi|\Phi\rangle| = 1$.

We can generalize this procedure and calculate higher order density matrices by introducing the generalized Laplace expansion

$$\Phi_{\alpha_1\cdots\alpha_N}(\mathrm{x}) = \frac{1}{\sqrt{\binom{N}{p}}}\sum_{n_1<\cdots<n_p}(-1)^{1+\sum_i n_i}\,\Phi_{\alpha_{n_1}\cdots\alpha_{n_p}}(x_1,\dots,x_p)\Phi_{\alpha_{i\notin\{n_1,\dots,n_p\}}}(x_{p+1},\dots,x_N),$$

which is obtained by writing the permutation of all N indices as a permutation of $N{-}p$ indices and the remaining p indices separately, summing over all distinct sets of p indices. This allows us to evaluate arbitrary matrix elements and higher order density matrices [4]. But as can be seen from the above expansion, the expressions very quickly get quite cumbersome. Fortunately there is a representation that is much better suited to handling antisymmetric wavefunctions. It is called second quantization.

2 Second quantization

Second quantization is the generalization of the Dirac notation to many-electron states [5, 6]. The idea is to separate the wavefunction into coordinate and state, $\varphi_\alpha(x) = \langle x|\alpha\rangle$, and absorb the coordinate in the operators, so that expectation values are rewritten as

$$\int dx\, \overline{\varphi_\alpha(x)} M(x) \varphi_\beta(x') = \langle\alpha| \int dx\, |x\rangle M(x) \langle x|\beta\rangle =: \langle\alpha|\hat{M}|\beta\rangle.$$

For many-electron systems the coordinates are represented by the field-operators $\hat{\Psi}(x)$. To implement antisymmetry, they need to anticommute $\hat{\Psi}(x)\hat{\Psi}(x') = -\hat{\Psi}(x')\hat{\Psi}(x)$. They can be thought of as removing an electron with coordinates $x{=}(\boldsymbol{r},\sigma)$ from the system. Applying them on a state with no electrons thus gives zero. Their conjugate operators insert an electron to the system. The entire formalism is defined by a compact set of properties of the vacuum state $|0\rangle$ and the anticommutation relations of the field operators:

$$\boxed{\begin{array}{rl} \hat{\Psi}(x)|0\rangle = 0 & \left\{\hat{\Psi}(x),\, \hat{\Psi}(x')\right\} = 0 = \left\{\hat{\Psi}^\dagger(x),\, \hat{\Psi}^\dagger(x')\right\} \\ \langle 0|0\rangle = 1 & \left\{\hat{\Psi}(x),\, \hat{\Psi}^\dagger(x')\right\} = \delta(x{-}x') \end{array}} \tag{11}$$

where the curly braces denote the anti-commutator $\{A,\, B\} := A\,B{+}B\,A$. As a direct consequence we obtain the Pauli principle: $\hat{\Psi}^\dagger(x)\hat{\Psi}^\dagger(x) = 0$.

2.1 Creation and annihilation operators

For a single-electron state $\varphi_\alpha(x)$ we can define an operator

$$c^\dagger_\alpha := \int dx\, \varphi_\alpha(x)\, \hat{\Psi}^\dagger(x), \tag{12}$$

that inserts an electron at position x weighted with the amplitude $\varphi_\alpha(x)$ — hence called creation operator for state $|\alpha\rangle$. Note that the creation operators transform in the same way as the single-electron states they represent, not like operators in first quantization,

$$|\tilde{\alpha}_i\rangle = \sum_\mu |\alpha_\mu\rangle\, U_{\mu i} \qquad \rightsquigarrow \qquad \tilde{c}^\dagger_{\tilde{\alpha}_i}|0\rangle = \sum_\mu c^\dagger_{\alpha_\mu}|0\rangle\, U_{\mu i} = \left(\sum_\mu c^\dagger_{\alpha_\mu} U_{\mu i}\right)|0\rangle. \tag{13}$$

The anticommutator with the field annihilator just gives back the single-electron wavefunction

$$\left\{\hat{\Psi}(x),\, c^\dagger_\alpha\right\} = \int dx'\, \varphi_\alpha(x')\, \left\{\hat{\Psi}(x),\, \hat{\Psi}^\dagger(x')\right\} = \varphi_\alpha(x)\,. \tag{14}$$

Thus, together with their adjoints, the annihilation operators,

$$c_\alpha := \int dx\, \overline{\varphi_\alpha(x)}\, \hat{\Psi}(x), \tag{15}$$

they form the algebra

$$\begin{aligned} c_\alpha|0\rangle &= 0 \qquad & \big\{c_\alpha,\, c_\beta\big\} &= 0 = \big\{c^\dagger_\alpha,\, c^\dagger_\beta\big\} \\ \langle 0|0\rangle &= 1 \qquad & \big\{c_\alpha,\, c^\dagger_\beta\big\} &= \langle\alpha|\beta\rangle \end{aligned} \tag{16}$$

The notation of second quantization has two principal advantages: (i) it is impossible to write unphysical states which are not antisymmetric or operators which are not acting on all electrons in the same way, and (ii) operators are independent of particle number, so that it becomes straightforward to work in Fock space. This simplifies many-body calculations significantly.

2.2 Representation of Slater determinants

We have now all the tools in place to write the Slater determinant (4) in second quantization, using the creation operators to specify the occupied orbitals and the field operators to give the coordinates for the real-space representation:

$$\Phi_{\alpha_1\alpha_2\ldots\alpha_N}(x_1,x_2,\ldots,x_N) = \frac{1}{\sqrt{N!}}\,\big\langle 0\big|\,\hat{\Psi}(x_1)\hat{\Psi}(x_2)\ldots\hat{\Psi}(x_N)\;\; c^\dagger_{\alpha_N}\ldots c^\dagger_{\alpha_2}c^\dagger_{\alpha_1}\big|0\big\rangle. \tag{17}$$

Note how writing the Slater determinant as an expectation value of annihilation and creation operators nicely separates the coordinates on the left from the orbitals on the right. This is just the desired generalization of the Dirac notation $\varphi(x) = \langle x|\varphi\rangle$.
Not surprisingly, the proof of (17) is by induction. As a warm-up we consider the case of a single-electron wavefunction ($N = 1$). Using the anticommutation relation (14), we see that

$$\big\langle 0\big|\,\hat{\Psi}(x_1)\,c^\dagger_{\alpha_1}\big|0\big\rangle = \big\langle 0\big|\,\varphi_{\alpha_1}(x_1) - c^\dagger_{\alpha_1}\hat{\Psi}(x_1)\big|0\big\rangle = \varphi_{\alpha_1}(x_1). \tag{18}$$

For the two-electron state $N = 2$, we anticommute $\hat{\Psi}(x_2)$ in two steps to the right

$$\begin{aligned} \big\langle 0\big|\,\hat{\Psi}(x_1)\hat{\Psi}(x_2)\,c^\dagger_{\alpha_2}c^\dagger_{\alpha_1}\big|0\big\rangle &= \big\langle 0\big|\,\hat{\Psi}(x_1)\big(\varphi_{\alpha_2}(x_2) - c^\dagger_{\alpha_2}\hat{\Psi}(x_2)\big)c^\dagger_{\alpha_1}\big|0\big\rangle \\ &= \big\langle 0\big|\,\hat{\Psi}(x_1)c^\dagger_{\alpha_1}\big|0\big\rangle\,\varphi_{\alpha_2}(x_2) - \big\langle 0\big|\,\hat{\Psi}(x_1)c^\dagger_{\alpha_2}\hat{\Psi}(x_2)c^\dagger_{\alpha_1}\big|0\big\rangle \\ &= \varphi_{\alpha_1}(x_1)\varphi_{\alpha_2}(x_2) - \varphi_{\alpha_2}(x_1)\varphi_{\alpha_1}(x_2). \end{aligned} \tag{19}$$

We see how anticommuting automatically produces the appropriate signs for the antisymmetric wavefunction. Dividing by $\sqrt{2}$, we obtain the desired two-electron Slater determinant.
The general case of an N-electron state works just the same. Anti-commuting $\hat{\Psi}(x_N)$ all the way to the right produces $N-1$ terms with alternating sign

$$\begin{aligned} \big\langle 0\big|\,\hat{\Psi}(x_1)\cdots\hat{\Psi}(x_{N-1})\hat{\Psi}(x_N)\,c^\dagger_{\alpha_N}c^\dagger_{\alpha_{N-1}}\cdots c^\dagger_{\alpha_1}\big|0\big\rangle \;=& \\ + \qquad & \big\langle 0\big|\,\hat{\Psi}(x_1)\cdots\hat{\Psi}(x_{N-1})\,c^\dagger_{\alpha_{N-1}}\cdots c^\dagger_{\alpha_1}\big|0\big\rangle \quad \varphi_{\alpha_N}(x_N) \\ - \qquad & \big\langle 0\big|\,\hat{\Psi}(x_1)\cdots\hat{\Psi}(x_{N-1})\,\textstyle\prod_{n\neq N-1} c^\dagger_{\alpha_n}\big|0\big\rangle \quad \varphi_{\alpha_{N-1}}(x_N) \\ \vdots \qquad & \\ (-1)^{N-1} \qquad & \big\langle 0\big|\,\hat{\Psi}(x_1)\cdots\hat{\Psi}(x_{N-1})\,c^\dagger_{\alpha_N}\;\cdots\; c^\dagger_{\alpha_2}\big|0\big\rangle \quad \varphi_{\alpha_1}(x_N)\,. \end{aligned}$$

Using (17) for the $N-1$-electron states, this is nothing but the Laplace expansion of

$$D = \begin{vmatrix} \varphi_{\alpha_1}(x_1) & \varphi_{\alpha_2}(x_1) & \cdots & \varphi_{\alpha_N}(x_1) \\ \varphi_{\alpha_1}(x_2) & \varphi_{\alpha_2}(x_2) & \cdots & \varphi_{\alpha_N}(x_2) \\ \vdots & \vdots & \ddots & \vdots \\ \varphi_{\alpha_1}(x_N) & \varphi_{\alpha_2}(x_N) & \cdots & \varphi_{\alpha_N}(x_N) \end{vmatrix}$$

along the Nth row. Dividing by $\sqrt{N!}$ we see that we have shown (17) for N-electron states, completing the proof by induction.

Given this representation of Slater determinants it is easy to eliminate the coordinates so we can work with N-electron states rather than N-electron wavefunctions—just as in Dirac notation. In particular we can rewrite the basis of Slater determinants (6) into a basis of product states

$$\left\{ c^\dagger_{n_N} \cdots c^\dagger_{n_1} |0\rangle \;\middle|\; n_1 < \cdots < n_N \right\}, \tag{20}$$

which allows us to express any N-electron state as

$$|\Psi\rangle = \sum_{n_1 < \cdots < n_N} a_{n_1,\dots,n_N}\, c^\dagger_{n_N} \cdots c^\dagger_{n_1} |0\rangle. \tag{21}$$

2.3 Representation of n-body operators

To work with N-electron states rather than Slater determinants, we also have to rewrite the N-electron operators $M(\boldsymbol{x})$ appropriately. This is easily done by incorporating the coordinates that we have separated from the Slater determinants into the operators such that the expectation values remain unchanged. This is, again, analogous to the Dirac formalism:

$$\int dx\, \overline{\varphi_n(x)}\, M(x)\, \varphi_m(x) = \langle \varphi_n | \underbrace{\int dx\, |x\rangle M(x) \langle x|}_{=:\hat{M}} \varphi_m\rangle = \langle \varphi_n | \hat{M} | \varphi_m \rangle. \tag{22}$$

For N-electron Slater determinants it becomes

$$\begin{aligned} &\int dx_1 \cdots dx_N\, \overline{\Phi_{\beta_1\cdots\beta_N}(x_1,\cdots,x_N)}\, M(x_1,\dots,x_N)\, \Phi_{\alpha_1\cdots\alpha_N}(x_1,\cdots,x_N) \\ =&\int dx_1 \cdots dx_N \langle 0| c_{\beta_1} \cdots c_{\beta_N} \hat{\Psi}^\dagger(x_N) \cdots \hat{\Psi}^\dagger(x_1)|0\rangle M(x_1,\dots,x_N) \langle 0| \hat{\Psi}(x_1) \cdots \hat{\Psi}(x_N) c^\dagger_{\alpha_N} \cdots c^\dagger_{\alpha_1}|0\rangle \\ &= \big\langle 0 \big| c_{\beta_1} \cdots c_{\beta_N}\, \hat{M}\, c^\dagger_{\alpha_N} \cdots c^\dagger_{\alpha_1} \big| 0 \big\rangle \end{aligned}$$

with the representation of the n-body operator in terms of field operators

$$\hat{M} := \frac{1}{N!} \int dx_1 \cdots x_N\, \hat{\Psi}^\dagger(x_N) \cdots \hat{\Psi}^\dagger(x_1)\, M(x_1,\cdots,x_N)\, \hat{\Psi}(x_1) \cdots \hat{\Psi}(x_N)\,. \tag{23}$$

Note that this particular form of the operator is only valid when applied to N-electron states, since we have used that the N annihilation operators bring us to the zero-electron space, where $|0\rangle\langle 0| = \mathbb{1}$. Keeping this in mind, we can work entirely in terms of our algebra (11).

To see what (23) means, we look, in turn, at the different n-body parts of $M(\boldsymbol{x})$, (2):

$$M(\mathbf{x}) = M^{(0)} + \sum_i M^{(1)}(x_i) + \sum_{i<j} M^{(2)}(x_i, x_j) + \sum_{i<j<k} M^{(3)}(x_i, x_j, x_k) + \cdots \tag{24}$$

We start with the simplest case, the zero-body operator, which, just a number $M^{(0)}$. Operating on an N-electron wavefunction, it gives

$$\begin{aligned}
\hat{M}^{(0)} &= \frac{M^{(0)}}{N!} \int dx_1 dx_2 \cdots x_N\, \hat{\Psi}^\dagger(x_N) \cdots \hat{\Psi}^\dagger(x_2) \hat{\Psi}^\dagger(x_1)\, \hat{\Psi}(x_1) \hat{\Psi}(x_2) \cdots \hat{\Psi}(x_N) \\
&= \frac{M^{(0)}}{N!} \int \qquad dx_2 \cdots x_N\, \hat{\Psi}^\dagger(x_N) \cdots \hat{\Psi}^\dagger(x_2) \qquad \hat{N} \qquad \hat{\Psi}(x_2) \cdots \hat{\Psi}(x_N) \\
&= \frac{M^{(0)}}{N!} \int \qquad dx_2 \cdots x_N\, \hat{\Psi}^\dagger(x_N) \cdots \hat{\Psi}^\dagger(x_2) \qquad 1 \qquad \hat{\Psi}(x_2) \cdots \hat{\Psi}(x_N) \\
&\vdots \\
&= \frac{M^{(0)}}{N!}\, 1 \cdot 2\, \cdots\, N = M^{(0)}\,,
\end{aligned} \tag{25}$$

where we have used that the operator

$$\int dx\, \hat{\Psi}^\dagger(x) \hat{\Psi}(x) = \hat{N}$$

counts the creation/annihilation operators: Applied to the vacuum state it gives $\hat{N}\,|0\rangle = 0$, while its commutator with any creation operator produces that operator

$$[\hat{N},\, c_n^\dagger] = \int dx\, [\hat{\Psi}^\dagger(x)\hat{\Psi}(x),\, c_n^\dagger] = \int dx\, \hat{\Psi}^\dagger(x)\, \{\hat{\Psi}(x),\, c_n^\dagger\} = \int dx\, \hat{\Psi}^\dagger(x)\, \varphi_n(x) = c_n^\dagger. \tag{26}$$

where we have used the simple relation $[AB,\, C] = A\{B,\, C\} - \{A,\, C\}B$. Commuting with an annihilator we pick up a minus sign $[\hat{N},\, \hat{\Psi}(x)] = -\hat{\Psi}(x)$, i.e., $\hat{N}\hat{\Psi}(x) = \hat{\Psi}(x)\big(\hat{N}-1\big)$. Thus, commuting $\hat{N}$ through a general product state, we obtain for each creation operator that we encounter a copy of the state, while for each annihilator we obtain minus that state, giving in total the original state times the difference in the number of creation and annihilation operators.

Remarkably, while we started from an operator acting on N-electron states, the resulting operator in second quantized form is independent of the number of electrons. We will see that this is an important general feature of operators in second quantization which makes working in Fock spaces amazingly simple.

We note that (25) just means that the overlap of two Slater determinants (7) is equal to that of the corresponding product states

$$\int d\boldsymbol{x}\, \overline{\Phi_{\alpha_1,\ldots,\alpha_N}(\boldsymbol{x})}\, \Phi_{\beta_1,\ldots,\beta_N}(\boldsymbol{x}) = \big\langle 0\big|\, c_{\alpha_1} \cdots c_{\alpha_N}\, c_{\beta_N}^\dagger \cdots c_{\beta_1}^\dagger \big|0\big\rangle. \tag{27}$$

2.3.1 One-body operators

Next we consider one-body operators $\sum_j M^{(1)}(x_j)$

$$\begin{aligned}\hat{M}^{(1)} &= \frac{1}{N!}\int dx_1\cdots dx_N\,\hat{\Psi}^\dagger(x_N)\cdots\hat{\Psi}^\dagger(x_1)\sum_j M^{(1)}(x_j)\,\hat{\Psi}(x_1)\cdots\hat{\Psi}(x_N)\\ &= \frac{1}{N!}\sum_j\int dx_j\,\hat{\Psi}^\dagger(x_j)\,M^{(1)}(x_j)\,(N{-}1)!\,\hat{\Psi}(x_j)\\ &= \frac{1}{N}\sum_j\int dx_j\,\hat{\Psi}^\dagger(x_j)\,M^{(1)}(x_j)\,\hat{\Psi}(x_j)\\ &= \int dx\quad\hat{\Psi}^\dagger(x)\;M^{(1)}(x)\;\hat{\Psi}(x)\end{aligned} \tag{28}$$

Here we have first anticommuted $\hat{\Psi}^\dagger(x_j)$ all the way to the left and $\hat{\Psi}(x_j)$ to the right. Since these take the same numbers of anticommutations, there is no sign involved. In between these field operators we are left with a zero-body operator for $N{-}1$ electrons, producing, when $\hat{M}^{(1)}$ acts on an N-electron state, a factor of $(N{-}1)!$. Again we notice that we obtain an operator that no longer depends on the number of electrons, i.e., that is valid in the entire Fock space.

Expanding the field-operators in a complete orthonormal set $\hat{\Psi}(x)=\sum_n\varphi_n(x)\,c_n$ gives

$$\hat{M}^{(1)} = \sum_{n,m}\int dx\,\overline{\varphi_n(x)}\,M(x)\,\varphi_m(x)\;c_n^\dagger c_m = \sum_{n,m}\langle\varphi_n|M^{(1)}|\varphi_m\rangle\,c_n^\dagger c_m = \sum_{n,m}c_n^\dagger\,M^{(1)}_{nm}\,c_m. \tag{29}$$

The matrix elements $M^{(1)}_{nm}=\langle\varphi_n|M^{(1)}|\varphi_m\rangle$ transform like a single-electron matrix $\boldsymbol{M}^{(1)}$: From (13) and writing the annihilation operators as a column vector $\boldsymbol{c}$ we see that

$$\hat{M}^{(1)} = \boldsymbol{c}^\dagger\,\boldsymbol{M}^{(1)}\,\boldsymbol{c} \;=\boldsymbol{c}^\dagger\boldsymbol{U}^\dagger\,\boldsymbol{U}\boldsymbol{M}^{(1)}\boldsymbol{U}^\dagger\,\boldsymbol{U}\boldsymbol{c} = \tilde{\boldsymbol{c}}^\dagger\,\tilde{\boldsymbol{M}}^{(1)}\,\tilde{\boldsymbol{c}}\,. \tag{30}$$

Once we have arrived at the representation in terms of orbitals, we can restrict the orbital basis to a non-complete set. This simply gives the operator in the variational (Fock) subspace spanned by the orbitals.

We note that the expression (29) not only works for local operators but also for differential operators like the momentum or kinetic energy: we have taken care not to exchange the order of $M^{(1)}$ and one of its field operators. We can write truly non-local operators in a similar way. As an example, the one-body density operator is given by

$$\hat{\Gamma}^{(1)}(x;x') = \hat{\Psi}^\dagger(x)\hat{\Psi}(x') \tag{31}$$

so that one coordinate is not integrated over, rather setting it to x in the bra and x' in the ket. In an orthonormal basis it becomes

$$\hat{\Gamma}^{(1)}(x;x') = \sum_{n,m}\overline{\varphi_n(x)}\,\varphi_m(x')\,c_n^\dagger c_m\,. \tag{32}$$

2.3.2 Two-body operators

For the two-body operators $\sum_{i<j} M^{(2)}(x_i, x_j)$ we proceed in the familiar way, anti-commuting first the operators with the coordinates involved in $M^{(2)}$ all the way to the left and right, respectively. This time we are left with a zero-body operator for $N{-}2$ electrons:

$$\begin{aligned}
\hat{M}^{(2)} &= \frac{1}{N!}\int dx_1\cdots dx_N\,\hat{\Psi}^\dagger(x_N)\cdots\hat{\Psi}^\dagger(x_1)\sum_{i<j} M^{(2)}(x_i,x_j)\,\hat{\Psi}(x_1)\cdots\hat{\Psi}(x_N)\\
&= \frac{1}{N!}\sum_{i<j}\int dx_i dx_j\,\hat{\Psi}^\dagger(x_j)\hat{\Psi}^\dagger(x_i)\,M^{(2)}(x_i,x_j)\,(N{-}2)!\,\hat{\Psi}(x_i)\hat{\Psi}(x_j)\\
&= \frac{1}{N(N{-}1)}\sum_{i<j}\int dx_i dx_j\,\hat{\Psi}^\dagger(x_j)\hat{\Psi}^\dagger(x_i)\,M^{(2)}(x_i,x_j)\,\hat{\Psi}(x_i)\hat{\Psi}(x_j)\\
&= \qquad\frac{1}{2}\int dx\;dx'\;\hat{\Psi}^\dagger(x')\;\hat{\Psi}^\dagger(x)\;\;M^{(2)}(x,x')\;\;\hat{\Psi}(x)\;\hat{\Psi}(x')
\end{aligned}$$

Expanding in an orthonormal basis, we get

$$\begin{aligned}
\hat{M}^{(2)} &= \frac{1}{2}\sum_{n,n',m,m'}\int dx dx'\,\overline{\varphi_{n'}(x')\varphi_n(x)}\,M^{(2)}(x,x')\,\varphi_m(x)\varphi_{m'}(x')\quad c^\dagger_{n'}c^\dagger_n c_m c_{m'}\\
&= \frac{1}{2}\sum_{n,n',m,m'}\langle\varphi_n\varphi_{n'}|M^{(2)}|\varphi_m\varphi_{m'}\rangle\quad c^\dagger_{n'}c^\dagger_n c_m c_{m'}
\end{aligned} \tag{33}$$

where the exchange of the indices in the second line is a consequence of the way the Dirac state for two electrons is usually written: first index for the first coordinate, second index for the second, while taking the adjoint of the operators changes their order. $M_{nn',mm'} = \langle\varphi_n\varphi_{n'}|M^{(2)}|\varphi_m\varphi_{m'}\rangle$ transforms like a fourth-order tensor: Transforming to a different basis (13) gives

$$\tilde{M}^{(2)}_{\nu\nu',\mu\mu'} = \sum_{n,n',m,m'} U^\dagger_{\nu n}U^\dagger_{\nu' n'}M_{nn',mm'}U_{m\mu}U_{m'\mu'}\,. \tag{34}$$

Form the symmetry of the two-body operator $M^{(2)}(x,x') = M^{(2)}(x',x)$ follows $M_{nn',mm'} = M_{n'n,m'm}$. Moreover, $M_{nn,mm'}$ will not contribute to $\hat{M}^{(2)}$ since $c^\dagger_n c^\dagger_n = \{c^\dagger_n,\, c^\dagger_n\}/2 = 0$, and likewise for $M_{nn',mm}$.

Note that the representation (33) is not quite as efficient as it could be: The terms with n and n' and/or m and m' exchanged connect the same basis states. Collecting these terms by introducing an ordering of the operators and using the symmetry of the matrix elements we obtain

$$\hat{M}^{(2)} = \sum_{n'>n,\,m'>m} c^\dagger_{n'}c^\dagger_n\underbrace{\left(M^{(2)}_{nn',mm'} - M^{(2)}_{n'n,mm'}\right)}_{=:\breve{M}^{(2)}_{nn',mm'}}c_m c_{m'}\,. \tag{35}$$

Since the states $\{c^\dagger_{n'}c^\dagger_n|0\rangle \mid n' > n\}$ form a basis of the two-electron Hilbert space, considering nn' as the index of a basis state, the $\breve{M}^{(2)}_{nn',mm'}$ form a two-electron matrix $\breve{\boldsymbol{M}}^{(2)}$.

The procedure of rewriting operators in second quantization obviously generalizes to observables acting on more than two electrons in the natural way. We note that, while we started from a form of the operators (24) that was explicitly formulated in an N-electron Hilbert space, the results (25), (29), and (33) are of the same form no matter what value N takes. Thus these operators are valid not just on some N-electron Hilbert space, but on the entire Fock space. This is a particular strength of the second-quantized formalism.

2.4 Transforming the orbital basis

We noted in (13) that the creators transform in the same way as the orbitals they represent

$$|\beta_i\rangle = U|\alpha_i\rangle = \sum_j |\beta_j\rangle\langle\alpha_j|\alpha_i\rangle = \sum_\mu |\alpha_\mu\rangle \underbrace{\langle\alpha_\mu|U|\alpha_i\rangle}_{=:U_{\mu i}} \quad\rightsquigarrow\quad c^\dagger_{\beta_i} = \sum_\mu c^\dagger_{\alpha_\mu}\, U_{\mu i}\,, \tag{36}$$

so the "operators" really transform like states. Writing the transformation matrix as $\boldsymbol{U} = e^{\boldsymbol{M}}$, where $\boldsymbol{M}$ is anti-Hermitian, $\boldsymbol{M}^\dagger = -\boldsymbol{M}$ when $\boldsymbol{U}$ is unitary, but can be any matrix when $\boldsymbol{U}$ is merely invertible, we can write the basis transformation in a form appropriate for operators:

$$c^\dagger_{\beta_i} = e^{\boldsymbol{c}^\dagger\boldsymbol{M}\boldsymbol{c}}\, c^\dagger_{\alpha_\mu}\, e^{-\boldsymbol{c}^\dagger\boldsymbol{M}\boldsymbol{c}}\,. \tag{37}$$

To see this, we use the Baker-Campbell-Hausdorff formula in the form

$$e^{\lambda A} B\, e^{-\lambda A} = B + \lambda\,[A,\,B] + \frac{\lambda^2}{2!}[A,\,[A,\,B]] + \frac{\lambda^3}{3!}\Big[A,\,\big[A,\,[A,\,B]\big]\Big] + \cdots\,, \tag{38}$$

where the expansion coefficients follow by taking the derivatives of the left hand side at $\lambda = 0$, together with the commutator

$$[c^\dagger_{\alpha_\mu} c_{\alpha_\nu},\, c^\dagger_{\alpha_\kappa}] = c^\dagger_{\alpha_\mu}\,\delta_{\nu,\kappa} \tag{39}$$

from which we obtain for the repeated commutators

$$\Big[\sum_{\mu,\nu} M_{\mu\nu} c^\dagger_{\alpha_\mu} c_{\alpha_\nu},\, \sum_\kappa c^\dagger_{\alpha_\kappa}\,\big(M^n\big)_{\kappa i}\Big] = \sum_{\mu\nu\kappa} c^\dagger_{\alpha_\mu}\, M_{\mu\nu}\,\delta_{\nu,\kappa}\,\big(M^n\big)_{\kappa i} = \sum_\mu c^\dagger_{\alpha_\mu}\,\big(M^{n+1}\big)_{\mu i}\,. \tag{40}$$

To keep the derivation simple, we have chosen to transform an operator from the orthonormal basis that we also used to write the exponential operator. Being linear, the transform works, of course, the same for an arbitrary creation operator.

Using this form of the basis transformation and noticing that $e^{-\boldsymbol{c}^\dagger\boldsymbol{M}\boldsymbol{c}}|0\rangle = |0\rangle$, we immediately see that acting with the exponential of a one-body operator on a product state results in another product state

$$e^{\boldsymbol{c}^\dagger\boldsymbol{M}\boldsymbol{c}}\prod c^\dagger_{\alpha_n}|0\rangle = \prod e^{\boldsymbol{c}^\dagger\boldsymbol{M}\boldsymbol{c}}\, c^\dagger_{\alpha_n} e^{-\boldsymbol{c}^\dagger\boldsymbol{M}\boldsymbol{c}}|0\rangle = \prod c^\dagger_{\beta_n}|0\rangle\,. \tag{41}$$

This is, e.g., used when working in the interaction picture. Anticommutators with transformed operators, (36), are simply $\big\{c_{\alpha_j},\, e^{\boldsymbol{c}^\dagger\boldsymbol{M}\boldsymbol{c}}\, c^\dagger_{\alpha_i}\, e^{-\boldsymbol{c}^\dagger\boldsymbol{M}\boldsymbol{c}}\big\} = \langle\alpha_j|e^M|\alpha_i\rangle$.

Annihilation operators, being the adjoint of the creators, transform in just the expected way

$$c_{\beta_i} = e^{-\boldsymbol{c}^\dagger\boldsymbol{M}^\dagger\boldsymbol{c}}\, c_{\alpha_\mu}\, e^{\boldsymbol{c}^\dagger\boldsymbol{M}^\dagger\boldsymbol{c}}\,, \tag{42}$$

which means that for unitary transformations, where $\boldsymbol{M}$ is anti-Hermitian, creators and annihilators transform in the same way. Note that in the imaginary-time formalism the annihilators are, via analytic continuation, chosen to transform in the same way as the creators, making them different from the adjoint of the creators.

3 Variational methods

The variational principle and the Schrödinger equation are equivalent. Consider the energy expectation value as a wave-function functional

$$E[\Psi] = \frac{\langle\Psi|H|\Psi\rangle}{\langle\Psi|\Psi\rangle}\,. \tag{43}$$

Its variation is

$$E[\Psi{+}\delta\Psi] = E[\Psi] + \frac{\langle\delta\Psi|H|\Psi\rangle + \langle\Psi|H|\delta\Psi\rangle}{\langle\Psi|\Psi\rangle} - \langle\Psi|H|\Psi\rangle\,\frac{\langle\delta\Psi|\Psi\rangle + \langle\Psi|\delta\Psi\rangle}{\langle\Psi|\Psi\rangle^2} + \mathcal{O}^2. \tag{44}$$

The first-order term vanishes for $H|\Psi\rangle = E[\Psi]\,|\Psi\rangle$, which is the Schrödinger equation. Since the eigenfunctions

$$H|\Psi_n\rangle = E_n|\Psi_n\rangle\,, \tag{45}$$

can be chosen to form an orthonormal basis, we can expand any wavefunction as

$$|\Psi\rangle = \sum_n |\Psi_n\rangle\,\langle\Psi_n|\Psi\rangle \tag{46}$$

and determine, as long as $\langle\Psi|\Psi\rangle \neq 0$, its energy expectation value

$$\frac{\langle\Psi|H|\Psi\rangle}{\langle\Psi|\Psi\rangle} = \frac{\sum_{m,n}\langle\Psi|\Psi_m\rangle\langle\Psi_m|H|\Psi_n\rangle\langle\Psi_n|\Psi\rangle}{\sum_{m,n}\langle\Psi|\Psi_m\rangle\langle\Psi_m|\Psi_n\rangle\langle\Psi_n|\Psi\rangle} = \frac{\sum_n E_n\left|\langle\Psi_n|\Psi\rangle\right|^2}{\sum_n\left|\langle\Psi_n|\Psi\rangle\right|^2}\,. \tag{47}$$

Since by definition no eigenenergy can be lower than the ground state energy E_0, we immediately see that the energy expectation value can never drop below the ground state energy

$$\frac{\langle\Psi|H|\Psi\rangle}{\langle\Psi|\Psi\rangle} = \frac{\sum_n E_n\left|\langle\Psi_n|\Psi\rangle\right|^2}{\sum_n\left|\langle\Psi_n|\Psi\rangle\right|^2} \geq \frac{\sum_n E_0\left|\langle\Psi_n|\Psi\rangle\right|^2}{\sum_n\left|\langle\Psi_n|\Psi\rangle\right|^2} = E_0\,. \tag{48}$$

We can use the same argument to generalize this variational principle: Assume we have arranged the eigenenergies in ascending order, $E_0 \leq E_1 \leq \cdots$, then the energy expectation value for a wavefunction that is orthogonal to the n lowest eigenstates, can not drop below E_n

$$\frac{\langle\Psi_{\perp_n}|H|\Psi_{\perp_n}\rangle}{\langle\Psi_{\perp_n}|\Psi_{\perp_n}\rangle} \geq E_n \quad \text{if } \langle\Psi_i|\Psi_{\perp_n}\rangle = 0 \text{ for } i = 0,\dots,n{-}1. \tag{49}$$

This generalized variational principle is, of course, only of practical use if we know something about the eigenstates, e.g., when we can use symmetries to ensure orthogonality.
For an ab-initio Hamiltonian of N electrons in the field of nuclei of charge Z_α at position $\boldsymbol{R}_\alpha$,

$$H = -\frac{1}{2}\sum_i \Delta_i - \sum_{i,\alpha}\frac{Z_\alpha}{|\boldsymbol{r}_i - \boldsymbol{R}_\alpha|} + \sum_{i<j}\frac{1}{|\boldsymbol{r}_i - \boldsymbol{r}_j|} + \sum_{\alpha<\beta}\frac{Z_\alpha Z_\beta}{|\boldsymbol{R}_\alpha - \boldsymbol{R}_\beta|}\,, \tag{50}$$

the Schrödinger equation is a partial differential equation. In second quantization it becomes a linear-algebra problem: We introduce an orbital basis set $\{\varphi_k\,|\,k\}$, which for simplicity we assume here to be orthonormal, from which we construct an orthonormal basis of N-electron product states, $\{\Phi_{k_1,\dots,k_N}\,|\,k_1<\cdots<k_N\}$. To simplify the notation we sort the basis states, e.g., lexicographically in the orbital indices $\boldsymbol{k}=(k_1,\dots,k_N)$ and define the row vector of basis states $|\boldsymbol{\Phi}\rangle := \big(|\Phi_{\mathbf{1}}\rangle, |\Phi_{\mathbf{2}}\rangle,\dots\big)$. The expansion of a state $|\Psi\rangle$ in this basis can then be written as

$$|\Psi\rangle = \sum_{k_1<\cdots<k_N} a_{k_1,\dots,k_N}\,|\Phi_{k_1,\dots,k_N}\rangle = \sum_i a_i\,|\Phi_i\rangle = |\boldsymbol{\Phi}\rangle\,\boldsymbol{a}\,, \tag{51}$$

where $\boldsymbol{a}$ is the vector of expansion coefficients. Likewise we can write the Schrödinger equation as a matrix eigenvalue problem

$$\boldsymbol{H}\boldsymbol{a} = \langle\boldsymbol{\Phi}|\hat{H}|\boldsymbol{\Phi}\rangle\boldsymbol{a} = \begin{pmatrix} \langle\Phi_1|\hat{H}|\Phi_1\rangle & \langle\Phi_1|\hat{H}|\Phi_2\rangle & \cdots \\ \langle\Phi_2|\hat{H}|\Phi_1\rangle & \langle\Phi_2|\hat{H}|\Phi_2\rangle & \cdots \\ \vdots & \vdots & \ddots \end{pmatrix} \begin{pmatrix} a_1 \\ a_2 \\ \vdots \end{pmatrix} = E \begin{pmatrix} a_1 \\ a_2 \\ \vdots \end{pmatrix} = E\boldsymbol{a}\,. \tag{52}$$

From the eigenvectors of the matrix $\boldsymbol{H}$ we easily recover the eigenstates of the Hamiltonian

$$\boldsymbol{H}\boldsymbol{a}_n = E_n\boldsymbol{a}_n \quad \rightsquigarrow \quad \hat{H}|\Psi_n\rangle = E_n|\Psi_n\rangle \quad \text{with } |\Psi_n\rangle = |\boldsymbol{\Phi}\rangle\,\boldsymbol{a}_n\,. \tag{53}$$

Unfortunately, for an ab-initio Hamiltonian like (50) we need an infinite orbital basis set, so that the Hamiltonian matrix $\boldsymbol{H}$ is infinite dimensional. A pragmatic approach to allow for computer simulations is to simply restrict the calculation to a finite basis $|\tilde{\boldsymbol{\Phi}}\rangle := \big(|\tilde{\Phi}_1\rangle,\dots,|\tilde{\Phi}_{\tilde{L}}\rangle\big)$, i.e., work with a finite matrix $\tilde{\boldsymbol{H}} := \langle\tilde{\boldsymbol{\Phi}}|\hat{H}|\tilde{\boldsymbol{\Phi}}\rangle$ of dimension $\tilde{L}$. The crucial question is then how the eigenstates

$$\tilde{\boldsymbol{H}}\tilde{\boldsymbol{a}}_n = \tilde{E}_n\tilde{\boldsymbol{a}}_n \quad \rightsquigarrow \quad |\tilde{\Psi}_n\rangle := |\tilde{\boldsymbol{\Phi}}\rangle\,\tilde{\boldsymbol{a}}_n \tag{54}$$

are related to those of H. The answer is surprisingly simple [7]: The eigenvalues of $\tilde{\boldsymbol{H}}$, ordered as $\tilde{E}_0 \le \tilde{E}_1 \le \cdots \le \tilde{E}_{\tilde{L}-1}$, are variational with respect to those of H:

$$E_n \le \tilde{E}_n \quad \text{for } n\in\{0,\dots,\tilde{L}-1\}\,. \tag{55}$$

To show this, we construct a state in $\mathrm{span}\,\big(|\tilde{\Psi}_0\rangle,\dots,|\tilde{\Psi}_n\rangle\big)$, which by construction has an energy expectation value $\le \tilde{E}_n$, that is orthogonal to the exact eigenstates $|\Psi_0\rangle,\dots,|\Psi_{n-1}\rangle$, so that by the generalized variational principle its expectation value is $\ge E_n$. Being the non-zero solution of $n-1$ linear equations with n variables, such a state certainly exists, hence $E_n \le \tilde{E}_n$.

The convergence of the matrix eigenvalues with increasing basis size is surprisingly regular. Let us extend our original basis of $\tilde{L}$ states by an additional $L-\tilde{L}$ states. Then, repeating the above argument with the L-dimensional problem taking the role of $\hat{H}$, we obtain (55) with E_n being the eigenvalues of the L-dimensional Hamiltonian matrix $\boldsymbol{H}$. Since $\boldsymbol{H}$ now is finite, we can use the same argument for $-\boldsymbol{H}$, obtaining

$$-\,E_{L-i} \le -\tilde{E}_{\tilde{L}-i} \quad \text{for } i\in\{1,\dots,\tilde{L}\}. \tag{56}$$

Taking the two inequalities together we obtain

$$E_n \le \tilde{E}_n \le E_{n+(L-\tilde{L})} \quad \text{for } n\in\{0,\dots,\tilde{L}-1\}. \tag{57}$$

For the special case $L = \tilde{L}+1$ of adding a single basis state, this is the Hylleraas-Undheim/MacDonald nesting property for eigenvalues in successive approximations

$$E_1 \leq \tilde{E}_1 \leq E_2 \leq \tilde{E}_2 \leq \cdots \leq \tilde{E}_L \leq E_{L+1}\,. \tag{58}$$

For a finite basis sets of K single-electron functions the dimension of (52) for an N-electron problem increase extremely rapidly: There are $K \cdot (K-1) \cdot (K-2) \cdots (K-(N-1))$ ways of picking N indices out of K. Since we only use one specific ordering of these indices, we still have to divide by $N!$ to obtain the number of such determinants:

$$\dim \mathcal{H}_K^{(N)} = \frac{K!}{N!(K-N)!} = \binom{K}{N}\,. \tag{59}$$

For $N = 25$ electrons and $K = 100$ orbitals the dimension already exceeds 10^{23}.
To get reliable results, we simply have to systematically increase the basis until the change in the desired eigenvalues becomes smaller than the accuracy required by the physical problem. The art is, of course, to devise clever basis sets such that this is achieved already for bases of manageable dimensions.

3.1 Non-interacting electrons

Even when considering a system of N non-interacting electrons we have to solve the large matrix eigenvalue problem (52). Writing the non-interacting Hamiltonian in the basis used for the CI expansion (51) we obtain

$$\hat{H} = \sum_{n,m} H_{nm}\, c_n^\dagger c_m\,,$$

which, in general, has non-vanishing matrix elements between Slater determinants that differ in at most one operator. But we can simplify things drastically by realizing that we can choose any single-electron basis for the CI expansion. If we choose the eigenstates of the single-electron matrix H_{nm} as basis, the second-quantized Hamiltonian becomes

$$\hat{H} = \sum_{n,m} \big(\varepsilon_n\, \delta_{n,m}\big) c_n^\dagger c_m = \sum_n \varepsilon_n\, c_n^\dagger c_n\,.$$

In this basis all off-diagonal matrix elements vanish and the CI Hamiltonian (52) is diagonal. Thus all $\binom{K}{N}$ eigenstates are Slater determinants

$$|\Phi_{\boldsymbol{n}}\rangle = c_{n_N}^\dagger \cdots c_{n_1}^\dagger |0\rangle \qquad \text{with eigenenergy} \quad E_{\boldsymbol{n}} = \sum_i \varepsilon_{n_i}\,. \tag{60}$$

This shows that choosing an appropriate basis for a CI expansion is crucial. A good general strategy should thus be to solve the matrix problem (52) and at the same time look for the basis set (of given size) that minimizes the variational energy. This is the idea of the multi-configurational self-consistent field method (MCSCF) [8]. In the following we will restrict ourselves to the simplest case where the many-body basis consists of a single Slater determinant. This is the Hartree-Fock method.

3.2 Hartree-Fock theory

The idea of the Hartree-Fock approach is to find an approximation to the ground-state of the N-electron problem by minimizing the total-energy wave-function functional (43) allowing only N-electron Slater determinants as variational functions. Since expectation values of Slater determinants are determined by their one-body density matrix, this means that we want to find the occupied subspace for which (43) is minimized.

To perform these variations we represent unitary transformations of the orbital basis as in Sec. 2.4 (related to the Thouless representation of Slater determinants [9])

$$\hat{U}(\lambda) = e^{i\lambda\hat{M}} \qquad \text{with} \quad \hat{M} = \sum_{\alpha,\beta} M_{\alpha\beta}\, c^\dagger_\alpha c_\beta \quad \text{hermitian}\,. \tag{61}$$

Using the Hausdorff expansion (38), the variation of the energy expectation value becomes

$$\begin{aligned} E(\lambda) &= \langle\varPhi|e^{i\lambda\hat{M}}\,\hat{H}\,e^{-i\lambda\hat{M}}|\varPhi\rangle \\ &= \langle\varPhi|\hat{H}|\varPhi\rangle + i\lambda\langle\varPhi|[\hat{H},\,\hat{M}]|\varPhi\rangle + \frac{(i\lambda)^2}{2}\langle\varPhi|\big[[\hat{H},\,\hat{M}],\,\hat{M}\big]|\varPhi\rangle + \cdots \end{aligned} \tag{62}$$

The energy functional is stationary for $\varPhi^{\mathrm{HF}}$ when

$$\langle\varPhi^{\mathrm{HF}}|[\hat{H},\,\hat{M}]|\varPhi^{\mathrm{HF}}\rangle = 0 \tag{63}$$

for every hermitian single-electron operator $\hat{M}$. This condition is most easily understood when we work with orthonormal orbitals $\{|\varphi\rangle|\,n\}$ from which the Slater determinant can be constructed: $|\varPhi^{\mathrm{HF}}\rangle = c^\dagger_N\cdots c^\dagger_1|0\rangle$. Then (63) is equivalent to

$$\langle\varPhi^{\mathrm{HF}}|[\hat{H},\,c^\dagger_n c_m + c^\dagger_m c_n]|\varPhi^{\mathrm{HF}}\rangle = 0 \quad \forall\, n,\, m$$

(in fact, $n \geq m$ suffices). Since

$$c^\dagger_n c_m|\varPhi^{\mathrm{HF}}\rangle = \left\{\begin{array}{cl} \delta_{n,m}|\varPhi^{\mathrm{HF}}\rangle & \text{if } n,\, m \in \{1,\dots,N\} \\ 0 & \text{if } m \quad \notin \{1,\dots,N\} \end{array}\right. ,$$

i.e., (63) is automatically fulfilled if both n and m are either occupied or unoccupied (virtual). This is not unexpected since transformations among the occupied or virtual orbitals, respectively, do not change the Slater determinant. The condition thus reduces to

$$\langle\varPhi^{\mathrm{HF}}|c^\dagger_m c_n \hat{H}|\varPhi^{\mathrm{HF}}\rangle = 0 \quad \forall\, m \in \{1,\dots,N\},\, n \notin \{1,\dots,N\}\,. \tag{64}$$

In other words, for the Hamiltonian there are no matrix elements between the stationary Slater determinant and determinants that differ from it in one orbital. This condition that for the Hartree-Fock determinant the Hamiltonian does not produce single excitations is called the Brillouin theorem.

Let us consider a Hamiltonian with one- and two-body terms

$$\hat{H} = \sum_{n,m} c^\dagger_n\, T_{nm}\, c_m + \sum_{n>n',m>m'} c^\dagger_n c^\dagger_{n'}\,\big(U_{nn',mm'} - U_{nn',m'm}\big)\, c_{m'} c_m$$

Then for each $n > N \geq m$ the singly-excited term

$$\Big(T_{nm} + \sum_{m'\leq N}\big(U_{nm',mm'} - U_{nm',m'm}\big)\Big)c_n^\dagger c_m|\Phi^{\mathrm{HF}}\rangle = 0$$

must vanish. This is the same condition as for a non-interacting Hamiltonian with matrix elements

$$F_{nm} = T_{nm} + \sum_{m'\leq N}\left(U_{nm',mm'} - U_{nm',m'm}\right). \tag{65}$$

$\boldsymbol{F}$ is called the Fock matrix. It depends, via the summation over occupied states, i.e., the density matrix, on the Slater determinant it is acting on. So we cannot simply diagonalize the single-electron matrix $\boldsymbol{F}$ since this will, in general, give a different determinant. Instead we need to find a Slater determinant for which $\boldsymbol{F}$ is diagonal (in fact, it is sufficient if it is block-diagonal in the occupied and virtual spaces). This is typically done by constructing a new Slater determinant from the N lowest eigenstates of $\boldsymbol{F}$ and iterating. Alternatively, we can use, e.g., steepest descent methods to minimize the expectation value directly or optimizing the one-body density matrix [10, 11]. At self-consistency the Fock matrix is diagonal with eigenvalues

$$\varepsilon_m^{\mathrm{HF}} = \Big(T_{mm} + \sum_{m'\leq N}\underbrace{\left(U_{mm',mm'} - U_{mm',m'm}\right)}_{=:\Delta_{mm'}}\Big) = \Big(T_{mm} + \sum_{m'\leq N}\Delta_{mm'}\Big) \tag{66}$$

and the Hartree-Fock energy is given by

$$\langle\Phi^{\mathrm{HF}}|\hat{H}|\Phi^{\mathrm{HF}}\rangle = \sum_{m\leq N}\Big(T_{mm} + \sum_{m'<m}\Delta_{mm'}\Big) = \sum_{m\leq N}\Big(T_{mm} + \frac{1}{2}\sum_{m'\leq N}\Delta_{mm'}\Big).$$

Removing an electron from the occupied orbital φ_a changes the energy expectation value by

$$\langle\Phi^{\mathrm{HF}}_{a\,\mathrm{rem}}|\hat{H}|\Phi^{\mathrm{HF}}_{a\,\mathrm{rem}}\rangle - \langle\Phi^{\mathrm{HF}}|\hat{H}|\Phi^{\mathrm{HF}}\rangle = -\Big(T_{aa} + \frac{1}{2}\sum_{m'\leq N}\Delta_{am'}\Big) - \frac{1}{2}\sum_{m\neq a\leq N}\Delta_{ma} = -\varepsilon_a^{\mathrm{HF}}. \tag{67}$$

When we assume that removing an electron does not change the orbitals, which should be a good approximation in the limit of many electrons $N \gg 1$, this gives the ionization energy (Koopmans' theorem). Likewise, the energy expectation value of an excited Slater determinant $\Phi^{\mathrm{HF}}_{a\to b}$ with an electron moved from orbital $a \leq N$ to orbital $b > N$ is

$$\varepsilon^{\mathrm{HF}}_{a\to b} = \langle\Phi^{\mathrm{HF}}_{a\to b}|\hat{H}|\Phi^{\mathrm{HF}}_{a\to b}\rangle - \langle\Phi^{\mathrm{HF}}|\hat{H}|\Phi^{\mathrm{HF}}\rangle = \varepsilon_b^{\mathrm{HF}} - \varepsilon_a^{\mathrm{HF}} - \Delta_{ab} \tag{68}$$

It can be interpreted as the energy of a state with an electron-hole excitation, again neglecting relaxation effects. For the Coulomb interaction

$$\begin{aligned}\Delta_{ab} = \frac{1}{2}(\Delta_{ab} + \Delta_{ba}) &= \frac{1}{2}\left(\left\langle\varphi_a\varphi_b\left|\frac{1}{r-r'}\right|\varphi_a\varphi_b - \varphi_b\varphi_a\right\rangle + \left\langle\varphi_b\varphi_a\left|\frac{1}{r-r'}\right|\varphi_b\varphi_a - \varphi_a\varphi_b\right\rangle\right)\\ &= \frac{1}{2}\left\langle\varphi_a\varphi_b - \varphi_b\varphi_a\left|\frac{1}{r-r'}\right|\varphi_a\varphi_b - \varphi_b\varphi_a\right\rangle > 0\end{aligned}$$

so that the third term in (68) describes the attraction between the excited electron and the hole.

3.2.1 Homogeneous electron gas

Since the homogeneous electron gas is translation invariant it is natural to write the Hamiltonian (for states with homogeneous charge density) in the basis of plane waves $\langle r,\sigma|\boldsymbol{k},\sigma\rangle = (2\pi)^{-3/2}\,e^{i\boldsymbol{k}\cdot\boldsymbol{r}}$

$$\hat{H} = \sum_\sigma \int d\boldsymbol{k}\,\frac{|\boldsymbol{k}^2|}{2} c^\dagger_{\boldsymbol{k},\sigma}c_{\boldsymbol{k},\sigma} + \frac{1}{2(2\pi)^3}\sum_{\sigma,\sigma'}\int d\boldsymbol{k}\int d\boldsymbol{k}'\int' d\boldsymbol{q}\,\frac{4\pi}{|\boldsymbol{q}|^2} c^\dagger_{\boldsymbol{k}-\boldsymbol{q},\sigma}c^\dagger_{\boldsymbol{k}'+\boldsymbol{q},\sigma'}c_{\boldsymbol{k}',\sigma'}c_{\boldsymbol{k},\sigma}\,, \tag{69}$$

where the prime on the $\boldsymbol{q}$ integral means that $\boldsymbol{q}=0$ is excluded since the homogeneous contribution to the Coulomb repulsion of the electrons is cancelled by its attraction with the homogeneous neutralizing background charge density. It seems reasonable to consider as an ansatz a Slater determinant $|\Phi_{k_F}\rangle$ of all plane-wave states with momentum below some Fermi momentum, $|\boldsymbol{k}| < k_F$. The charge density for such a determinant follows, using the anticommutator of the field operator

$$\{\hat{\Psi}^\dagger_\sigma(\boldsymbol{r}),\,c_{\boldsymbol{k},\sigma}\} = \int d\boldsymbol{r}'\,\frac{e^{-i\boldsymbol{k}\cdot\boldsymbol{r}}}{(2\pi)^{3/2}}\,\{\hat{\Psi}^\dagger_\sigma(\boldsymbol{r}),\,\hat{\Psi}_\sigma(\boldsymbol{r}')\} = \frac{e^{-i\boldsymbol{k}\cdot\boldsymbol{r}}}{(2\pi)^{3/2}}\,,$$

from the diagonal of the density matrix

$$n_\sigma(\boldsymbol{r}) = \langle\Phi^{\mathrm{HF}}|\hat{\Psi}^\dagger_\sigma(\boldsymbol{r})\hat{\Psi}_\sigma(\boldsymbol{r})|\Phi^{\mathrm{HF}}\rangle = \int_{|\boldsymbol{k}|<k_F} d\boldsymbol{k}\,\left|\frac{e^{i\boldsymbol{k}\cdot\boldsymbol{r}}}{(2\pi)^{3/2}}\right|^2 = \frac{k_F^3}{6\pi^2}\,. \tag{70}$$

It is independent of position, so $|\Phi_{k_F}\rangle$ looks like an appropriate ansatz for a homogeneous system. Moreover, it fulfills the stationarity condition (64): To create just a single excitation one of the creation operators in the Coulomb term of (69) must fill one of the annihilated states, i.e., $\boldsymbol{q}=0$ or $\boldsymbol{q}=\boldsymbol{k}-\boldsymbol{k}'$. But this implies that the term is diagonal with $\boldsymbol{q}=0$ giving the direct and $\boldsymbol{q}=\boldsymbol{k}-\boldsymbol{k}'$ the exchange contribution. Since the $\boldsymbol{q}=0$ term is not present in the Hamiltonian, the eigenenergies of the Fock matrix are just the sum of the kinetic and the exchange terms

$$\varepsilon^{\mathrm{HF}}_{k,\sigma} = \frac{|\boldsymbol{k}|^2}{2} - \frac{1}{4\pi^2}\int_{|\boldsymbol{k}'|<k_F} d\boldsymbol{k}'\,\frac{1}{|\boldsymbol{k}-\boldsymbol{k}'|^2} = \frac{k^2}{2} - \frac{k_F}{\pi}\left(1 + \frac{k_F^2-k^2}{2k_Fk}\ln\left|\frac{k_F+k}{k_F-k}\right|\right) \tag{71}$$

It depends only on $k=|\boldsymbol{k}|$. Interestingly the slope of $\varepsilon^{\mathrm{HF}}_{\boldsymbol{k},\sigma}$ becomes infinite for $k\to k_F$. Thus, the density of states $D(\varepsilon_k)d\varepsilon = 4\pi k^2\,dk$, given by

$$D^{\mathrm{HF}}_\sigma(\varepsilon) = 4\pi k^2\left(\frac{d\varepsilon^{\mathrm{HF}}_{k,\sigma}}{dk}\right)^{-1} = 4\pi k^2\left(k - \frac{k_F}{\pi k}\left(1 - \frac{k_F^2+k^2}{2k_Fk}\ln\left|\frac{k_F+k}{k_F-k}\right|\right)\right)^{-1} \tag{72}$$

vanishes at the Fermi level (see Fig. 1). This is not quite what we expect from a respectable electron gas... It is clearly a defect of the Hartree-Fock approximation.

Instead of calculating the energy expectation value also directly in k-space, it is instructive to look at the exchange term in real space. To evaluate the electron-electron repulsion we need the diagonal of the 2-body density matrix, which is given in terms of the one-body density matrix

$$\langle\Phi_{k_F}|\hat{\Psi}^\dagger_{\sigma'}(\boldsymbol{r}')\hat{\Psi}^\dagger_\sigma(\boldsymbol{r})\hat{\Psi}_\sigma(\boldsymbol{r})\hat{\Psi}_{\sigma'}(\boldsymbol{r}')|\Phi_{k_F}\rangle = \det\begin{pmatrix}\Gamma^{(1)}_{\sigma\sigma}(\boldsymbol{r},\boldsymbol{r}) & \Gamma^{(1)}_{\sigma\sigma'}(\boldsymbol{r},\boldsymbol{r}')\\ \Gamma^{(1)}_{\sigma'\sigma}(\boldsymbol{r}',\boldsymbol{r}) & \Gamma^{(1)}_{\sigma'\sigma'}(\boldsymbol{r}',\boldsymbol{r}')\end{pmatrix},$$

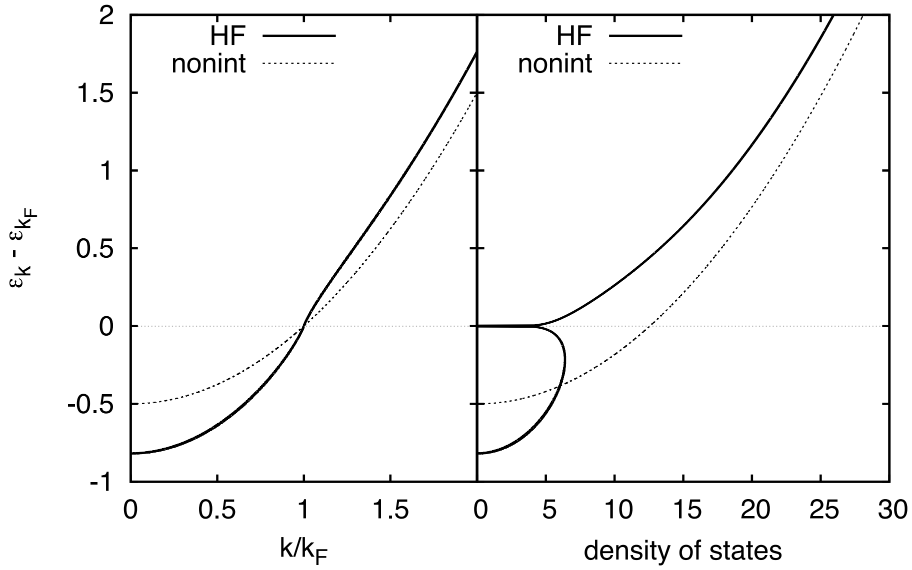

Fig. 1: *Hartree-Fock eigenvalues and density of states for the homogeneous solution $|\Psi_{k_F}\rangle$ of the homogeneous electron gas compared to non-interacting values.*

where the one-body density matrix vanishes unless $\sigma' = \sigma$ where it is evaluated as in (70)

$$\begin{aligned}
\Gamma_{\sigma\sigma}(\boldsymbol{r},\boldsymbol{r}') &= \langle \Phi_{k_F}|\hat{\Psi}^\dagger_\sigma(\boldsymbol{r})\hat{\Psi}_\sigma(\boldsymbol{r}')|\Phi_{k_F}\rangle \\
&= \int_{|\boldsymbol{k}|<k_F} d\boldsymbol{k}\,\frac{e^{-i\boldsymbol{k}\cdot(\boldsymbol{r}-\boldsymbol{r}')}}{(2\pi)^3} = \frac{1}{4\pi^2}\int_0^{k_F} dk\,k^2\int_{-1}^{1} d\cos\theta\,e^{ik|\boldsymbol{r}-\boldsymbol{r}'|\cos\theta} \\
&= \frac{k_F^3}{2\pi^2}\underbrace{\frac{\sin x - x\cos x}{x^3}}_{\xrightarrow{x\to 0} 1/3} = 3n_\sigma\,\frac{\sin x - x\cos x}{x^3}
\end{aligned} \tag{73}$$

with $x = k_F|\boldsymbol{r}-\boldsymbol{r}'|$. Dividing the 2-body density matrix by n_σ^2 and subtracting the direct term (which is canceled by the contribution of the background charge) we obtain the exchange hole [11]

$$g_x(r,0) - 1 = -9\left(\frac{\sin k_F r - k_F r\cos k_F r}{(k_F r)^3}\right)^2. \tag{74}$$

It is shown in Fig. 2. The exchange energy per spin is then the Coulomb interaction of the charge density with its exchange hole

$$E_x = \frac{1}{2}\int d\boldsymbol{r}\,n_\sigma\int d\boldsymbol{r}' n_\sigma\frac{g_x(r,r')-1}{|\boldsymbol{r}-\boldsymbol{r}'|} = \frac{1}{2}\underbrace{\int d\boldsymbol{r}\,n_\sigma}_{=N}\int d\tilde{\boldsymbol{r}}\,n_\sigma\,\frac{g_x(\tilde{r},0)-1}{\tilde{r}}\,.$$

The exchange energy per electron of spin σ is thus

$$\varepsilon_x^\sigma = \frac{4\pi n_\sigma}{2}\int_0^\infty dr\,r^2\,\frac{g(r,0)-1}{r} = -\frac{9\cdot 4\pi n_\sigma}{2k_F^2}\underbrace{\int_0^\infty dx\,\frac{(\sin x - x\cos x)^2}{x^5}}_{=1/4} = -\frac{3k_F}{4\pi}\,. \tag{75}$$

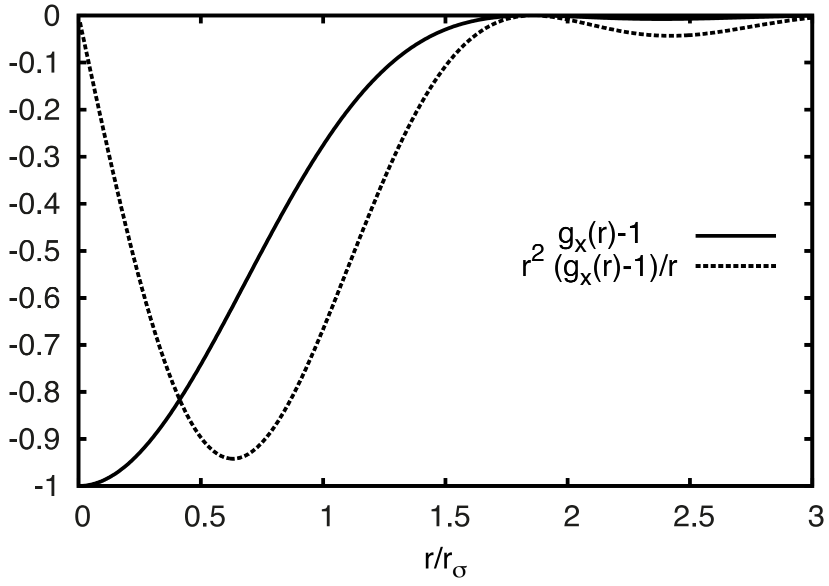

Fig. 2: *Exchange hole for a paramagnetic homogeneous electron gas in units of the spin Wigner-Seitz radius* $k_F\, r_\sigma = (9\pi/2)^{1/3}$. *In addition, the dotted line shows the contribution of the exchange hole to the Coulomb repulsion energy of Eq. (75).*

Together with the kinetic energy per electron of spin σ

$$\varepsilon^\sigma_{\text{kin}} = 4\pi \int_0^{k_F} dk\, k^2\, \frac{k^2}{2} \Big/ 4\pi \int_0^{k_F} dk\, k^2 = \frac{3k_F^2}{10} \tag{76}$$

we obtain the total energy per electron

$$\varepsilon_{\text{HF}} = \frac{n_\uparrow\big(\varepsilon^\uparrow_{\text{kin}}+\varepsilon^\uparrow_x\big) + n_\downarrow\big(\varepsilon^\downarrow_{\text{kin}}+\varepsilon^\downarrow_x\big)}{n_\uparrow + n_\downarrow} = \frac{3(6\pi^2)^{2/3}}{10}\frac{n_\uparrow^{5/3}+n_\downarrow^{5/3}}{n} - \frac{3}{4}\left(\frac{6}{\pi}\right)^{1/3}\frac{n_\uparrow^{4/3}+n_\downarrow^{4/3}}{n}\,.$$

While the kinetic energy is lowest when $n_\uparrow = n_\downarrow$, exchange favors spin polarization. For reasonable electron densities the kinetic energy dominates, only at extremely low densities exchange dominates and the solution would be ferromagnetic.

A ferromagnetic Slater determinant would, of course, have two different Fermi momenta, $k_F^\uparrow \neq k_F^\downarrow$. It also would break the symmetry of the Hamiltonian under spin rotations. This is an example of how we can lower the energy expectation value by allowing Slater determinants that break a symmetry of the system. When we do not restrict the symmetry of the Slater determinant, the approach is called unrestricted Hartree-Fock. For the electron gas this approach actually gives Hartree-Fock states that even break translational symmetry, see, e.g., [12].

3.2.2 Hubbard model

As a simple example to illustrate the difference between restricted and unrestricted Hartree-Fock we consider the Hubbard model with two sites, $i = 1, 2$, between which the electrons can hop with matrix element $-t$ and with an on-site Coulomb repulsion U

$$\hat{H} = -t\sum_\sigma \left(c^\dagger_{2\sigma}c_{1\sigma} + c^\dagger_{1\sigma}c_{2\sigma}\right) + U \sum_{i\in\{1,2\}} n_{i\uparrow}n_{i\downarrow}\,. \tag{77}$$

The number of electrons N and the total spin projection S_z are conserved, so the Fock space Hamiltonian is block-diagonal in the Hilbert spaces with fixed number of up- and down-spin electrons $N_\uparrow$ and $N_\downarrow$ with dimensions

N	0	1		2			3		4	
$N_\uparrow$	0	1	0	2	1	0	2	1	2	
$N_\downarrow$	0	0	1	0	1	2	1	2	2	
dim	1	2	2	1	4	1	2	2	1	16

Exact solutions: The Hamiltonian for $N=N_\uparrow=1$ is easily constructed. By introducing the basis states $c^\dagger_{1\uparrow}|0\rangle$ and $c^\dagger_{2\uparrow}|0\rangle$, we obtain the Hamiltonian matrix

$$\Big\langle 0\Big| \begin{pmatrix} c_{1\uparrow} \\ c_{2\uparrow} \end{pmatrix} \hat{H} \begin{pmatrix} c^\dagger_{1\uparrow} & c^\dagger_{2\uparrow} \end{pmatrix} \Big|0\Big\rangle = \begin{pmatrix} 0 & -t\,\langle 0|c_{1\uparrow}\, c^\dagger_{1\uparrow} c_{2\uparrow}\, c^\dagger_{2\uparrow}|0\rangle \\ -t\,\langle 0|c_{2\uparrow}\, c^\dagger_{2\uparrow} c_{1\uparrow}\, c^\dagger_{1\uparrow}|0\rangle & 0 \end{pmatrix} = \begin{pmatrix} 0 & -t \\ -t & 0 \end{pmatrix}.$$

This is easily diagonalized giving the familiar bonding and antibonding solution

$$|\varphi_\pm\rangle = \frac{1}{\sqrt{2}}\big(c^\dagger_{1\uparrow} \pm c^\dagger_{2\uparrow}\big)\,|0\rangle = c^\dagger_{\pm\uparrow}|0\rangle\,. \tag{78}$$

For $N_\uparrow = 1 = N_\downarrow$, we obtain a non-trivial interacting system

$$\Big\langle 0\Big| \begin{pmatrix} c_{1\uparrow}c_{2\downarrow} \\ c_{2\uparrow}c_{1\downarrow} \\ c_{1\uparrow}c_{1\downarrow} \\ c_{2\uparrow}c_{2\downarrow} \end{pmatrix} \hat{H} \begin{pmatrix} c^\dagger_{2\downarrow}c^\dagger_{1\uparrow} & c^\dagger_{1\downarrow}c^\dagger_{2\uparrow} & c^\dagger_{1\downarrow}c^\dagger_{1\uparrow} & c^\dagger_{2\downarrow}c^\dagger_{2\uparrow} \end{pmatrix} \Big|0\Big\rangle = \begin{pmatrix} 0 & 0 & -t & -t \\ 0 & 0 & -t & -t \\ -t & -t & U & 0 \\ -t & -t & 0 & U \end{pmatrix}. \tag{79}$$

To diagonalize the matrix, we transform the basis into linear combinations of covalent and ionic states

$$|\mathrm{cov}_\pm\rangle = \frac{1}{\sqrt{2}}\big(c^\dagger_{2\downarrow}c^\dagger_{1\uparrow} \pm c^\dagger_{1\downarrow}c^\dagger_{2\uparrow}\big)|0\rangle \tag{80}$$

$$|\mathrm{ion}_\pm\rangle = \frac{1}{\sqrt{2}}\big(c^\dagger_{1\downarrow}c^\dagger_{1\uparrow} \pm c^\dagger_{2\downarrow}c^\dagger_{2\uparrow}\big)|0\rangle \tag{81}$$

It is then easy to verify that $|\mathrm{cov}_-\rangle$ is an eigenstate with eigenvalue $\varepsilon_{\mathrm{cov}_-}=0$ and that $|\mathrm{ion}_-\rangle$ has eigenenergy $\varepsilon_{\mathrm{ion}_-}=U$. The remaining two states mix

$$\begin{pmatrix} \langle \mathrm{cov}_+| \\ \langle \mathrm{ion}_+| \end{pmatrix} \hat{H} \begin{pmatrix} |\mathrm{cov}_+\rangle & |\mathrm{ion}_+\rangle \end{pmatrix} = \frac{1}{2}\left(U - \begin{pmatrix} U & 4t \\ 4t & -U \end{pmatrix}\right). \tag{82}$$

Rewriting the matrix

$$\begin{pmatrix} U & 4t \\ 4t & -U \end{pmatrix} = \sqrt{U^2+16t^2}\begin{pmatrix} \cos\Theta & \sin\Theta \\ \sin\Theta & -\cos\Theta \end{pmatrix}, \tag{83}$$

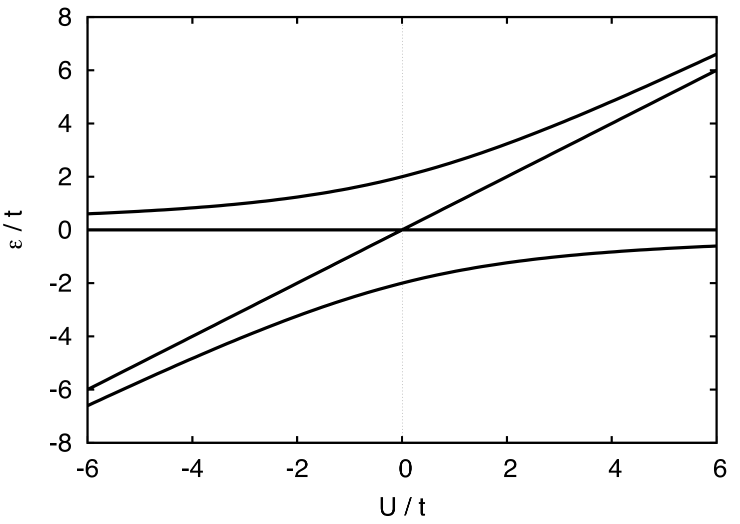

Fig. 3: *Spectrum of the two-site Hubbard model as a function of U/t.*

we find the ground state of the half-filled two-site Hubbard model

$$|\mathrm{gs}\rangle = \cos\Theta/2\,|\mathrm{cov}_+\rangle + \sin\Theta/2\,|\mathrm{ion}_+\rangle \tag{84}$$

$$= \frac{1}{\sqrt{2}}\Big(\cos\tfrac{\Theta}{2}\,c^\dagger_{2\downarrow}c^\dagger_{1\uparrow} + \cos\tfrac{\Theta}{2}\,c^\dagger_{1\downarrow}c^\dagger_{2\uparrow} + \sin\tfrac{\Theta}{2}\,c^\dagger_{1\downarrow}c^\dagger_{1\uparrow} + \sin\tfrac{\Theta}{2}\,c^\dagger_{2\downarrow}c^\dagger_{2\uparrow}\Big)\,|0\rangle \tag{85}$$

with an energy of $\varepsilon_{\mathrm{gs}} = (U - \sqrt{U^2{+}16t^2})/2$. Without correlations ($U = 0 \rightsquigarrow \Theta = \pi/2$), all basis states have the same prefactor, so we can factorize the ground state, writing it as a product $c^\dagger_{+\downarrow}c^\dagger_{+\uparrow}|0\rangle$ of the operators defined in (78). For finite U this is no longer possible. In the strongly correlated limit $U \gg t$ ($\Theta \searrow 0$) the ground state becomes the maximally entangled state $|\mathrm{cov}_+\rangle$ and can not even approximately be expressed as a two-electron Slater determinant.

Hartree-Fock: We now want to see what Hartree-Fock can do in such a situation. Since the Hamiltonian is so simple, we can directly minimize the energy expectation value. The most general ansatz is a Slater determinant of an orbital $\varphi(\theta_\uparrow) = \sin(\theta_\uparrow)\,\varphi_1 + \cos(\theta_\uparrow)\,\varphi_2$ for the spin-up, and $\varphi(\theta_\downarrow) = \sin(\theta_\downarrow)\,\varphi_1 + \cos(\theta_\downarrow)\,\phi_2$ for the spin-down electron:

$$|\Phi(\theta_\uparrow,\theta_\downarrow)\rangle = \Big(\sin(\theta_\downarrow)\,c^\dagger_{1\downarrow} + \cos(\theta_\downarrow)\,c^\dagger_{2\downarrow}\Big)\Big(\sin(\theta_\uparrow)\,c^\dagger_{1\uparrow} + \cos(\theta_\uparrow)\,c^\dagger_{2\uparrow}\Big)\,|0\rangle\;. \tag{86}$$

The energy expectation value as a function of the parameters θ_σ is then

$$\begin{aligned}\langle\Phi(\theta_\uparrow,\theta_\downarrow)|\hat{H}|\Phi(\theta_\uparrow,\theta_\downarrow)\rangle =& -2t\,(\sin\theta_\uparrow\sin\theta_\downarrow + \cos\theta_\uparrow\cos\theta_\downarrow)\,(\cos\theta_\uparrow\sin\theta_\downarrow + \sin\theta_\uparrow\cos\theta_\downarrow)\\ &+ U\left(\sin^2\theta_\uparrow\sin^2\theta_\downarrow + \cos^2\theta_\uparrow\cos^2\theta_\downarrow\right)\;.\end{aligned} \tag{87}$$

If the Slater determinant respects the symmetry of the molecule under the exchange of sites (mirror symmetry of the H_2 molecule), it follows that the Hartree-Fock orbitals for both spins are the bonding state φ_+ ($\theta = \pi/4$). This is the *restricted Hartree-Fock* solution. The corresponding energy is $E(\pi/4,\pi/4) = -2t{+}U/2$. The unrelaxed excited determinants are obtained

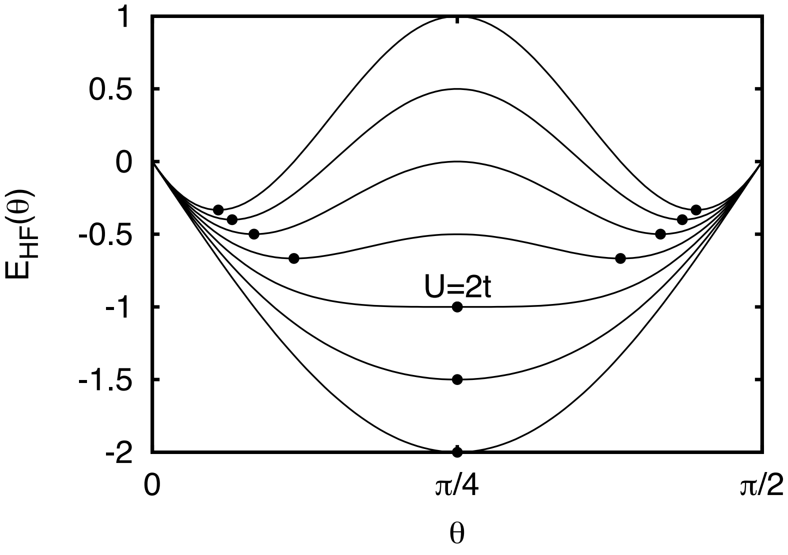

Fig. 4: *Energy expectation value for a Slater determinant $\Phi(\theta, \pi/2-\theta)$ for $U=0,\ t,\ 2t,\ \dots,\ 6t$. When $U \leq 2t$ the minimum is at $\theta = \pi/4$. This is the Hartree-Fock solution with the bonding orbitals φ_+ occupied. For $U \geq 2t$, $\theta = \pi/4$ is still an extremal point (restricted Hartree-Fock solution), but an energy minimum is only attained when the symmetry is broken (unrestricted Hartree-Fock solution).*

by replacing occupied orbitals φ_+ with φ_-. Altogether we obtain the restricted Hartree-Fock spectrum

$$\begin{aligned} E(\ \ \pi/4,\ \ \pi/4) &= \ -2t + U/2 \\ E(\ \ \pi/4,-\pi/4) &= \qquad\quad U/2 \\ E(-\pi/4,\ \ \pi/4) &= \qquad\quad U/2 \\ E(-\pi/4,-\pi/4) &= \ \ \ 2t + U/2 \end{aligned} \tag{88}$$

Comparing to the energy for a state with both electrons of the same spin ($E = 0$), we see that there is no spin-triplet, i.e., Hartree-Fock breaks the spin symmetry [13]. The states (88) are *spin-contaminated* [14]. Even worse, the Hartree-Fock ground state, and consequently all the states, are independent of U. The weight of the ionic states is always $1/2$, leading to an increase of the energy with $U/2$.

To avoid this, we can allow the Hartree-Fock solution to break the symmetry of the molecule (*unrestricted Hartree-Fock*), putting, e.g., more of the up-spin electron in the orbital on site 1 and more of the down-spin electron in orbital 2. In an extended system this corresponds to an antiferromagnetic spin-density wave. For $U < 2t$ this does not lead to a state of lower energy. For larger U, however, there is a symmetry-broken ground state

$$\Phi_{\mathrm{UHF}} = \Phi(\theta,\, \pi/2-\theta) \quad \text{with} \quad \theta(U) = \frac{\pi}{4} \pm \frac{1}{2}\arccos\left(\frac{2t}{U}\right). \tag{89}$$

Its energy is $E_{\mathrm{UHF}} = -2t^2/U$. Still there is no triplet state (spin contamination) and, for $U \to \infty$, the overlap with the true singlet ground state goes to $\left|\langle\Phi_{\mathrm{UHF}}|\Psi_-\rangle\right|^2 = 1/2$.

From Fig. 4 it might appear that there are just two degenerate unrestricted Hartree-Fock determinants. But, remembering that we can chose the spin quantization axis at will, we see that by rotating the spins by an angle α about the axis $\hat{n}$ (see App. A.2)

$$R_{\hat{n}}(\alpha) = e^{-i\hat{n}\cdot\vec{\sigma}\,\alpha/2} = \cos(\alpha/2) - i\sin(\alpha/2)\,\hat{n}\cdot\vec{\sigma}$$

we can produce a continuum of degenerate solutions $\hat{R}_{\hat{n}}(\alpha)|\Phi_{\mathrm{UHF}}\rangle$. As an example we consider the state we obtain when we rotate the spin quantization axis from the $\hat{z}$ into the $\hat{x}$ direction

$$R_{\hat{y}}(-\pi/2) = \frac{1}{\sqrt{2}}\begin{pmatrix} 1 & 1 \\ -1 & 1 \end{pmatrix}$$

which transforms the creation operators according to (13) as

$$\left(c^\dagger_{i\uparrow},\, c^\dagger_{i\downarrow}\right) R_{\hat{y}}(-\pi/2) = \left(\frac{1}{\sqrt{2}}\big(c^\dagger_{i\uparrow}{-}c^\dagger_{i\downarrow}\big),\, \frac{1}{\sqrt{2}}\big(c^\dagger_{i\uparrow}{+}c^\dagger_{i\downarrow}\big)\right).$$

The determinant (86) thus transforms to

$$\hat{R}_{\hat{y}}(-\pi/2)|\Phi(\theta_\uparrow,\theta_\downarrow)\rangle = \frac{1}{2}\Big(s_\downarrow\big(c^\dagger_{1\uparrow}{+}c^\dagger_{1\downarrow}\big) + c_\downarrow\big(c^\dagger_{2\uparrow}{+}c^\dagger_{2\downarrow}\big)\Big)\Big(s_\uparrow\big(c^\dagger_{1\uparrow}{-}c^\dagger_{1\downarrow}\big) + c_\uparrow\big(c^\dagger_{2\uparrow}{-}c^\dagger_{2\downarrow}\big)\Big)|0\rangle \quad (90)$$

where we introduced the abbreviations $s_\sigma = \sin\theta_\sigma$ and $c_\sigma = \cos\theta_\sigma$. Since the Hamiltonian (77) is invariant under spin rotations, $\hat{R}_{\hat{y}}(-\pi/2)\,\hat{H}\,\hat{R}^\dagger_{\hat{y}}(-\pi/2) = \hat{H}$, the energy expectation value of the rotated state is still given by (87).

Attractive Hubbard model For negative U allowing the spin orbitals to differ, $\Phi(\theta,\,\pi/2{-}\theta)$, does not lower the energy expectation value. The minimum is always obtained for the restricted Hartree-Fock determinant $\Phi(\pi/4,\,\pi/4)$. In fact, for the attractive Hubbard model rather than breaking spin symmetry, we should try to break the charge symmetry: For $U < -2t$ the ansatz $\Phi(\theta,\theta)$ minimizes the energy for the two states $\theta(U) = \pi/4 \pm \arccos(-2t/U)$ with energy $E(U) = 2t^2/U + U$. Thus, the unrestricted Hartree-Fock ground state breaks the charge symmetry, i.e., is a charge-density wave state. On the other hand, looking back to (90) we see that $\Phi(\theta,\theta)$ is invariant under the spin rotation. This is actually true for any $\hat{R}_{\hat{n}}(\alpha)$ so that the unrestricted Hartree-Fock ground state of the attractive Hubbard model does not break spin symmetry.

It seems strange that for the attractive model we only find two unrestricted Hartree-Fock states, while for the repulsive model we have a continuum of states. To find the ’missing’ states we consider a new kind of transformation that mixes creation and annihilation operators: When we exchange the role of the creation and annihilation operators for the up spins only, i.e.,

$$\tilde{c}^\dagger_{i\uparrow} = (-1)^i c_{i\uparrow} \quad \text{and} \quad \tilde{c}^\dagger_{i\downarrow} \to c^\dagger_{i\downarrow}, \quad (91)$$

the Hamiltonian (77) transforms into a two-site Hubbard model with the sign of U reversed

$$\hat{H} = -t\sum_\sigma \left(\tilde{c}^\dagger_{2\sigma}\tilde{c}_{1\sigma} + \tilde{c}^\dagger_{1\sigma}\tilde{c}_{2\sigma}\right) - U\sum_{i\in\{1,2\}} \tilde{n}_{i\uparrow}\tilde{n}_{i\downarrow} + U(\tilde{n}_{1\downarrow} + \tilde{n}_{2\downarrow}). \quad (92)$$

Let us see what happens to the Slater determinant (86) when we apply the same transformation. In doing this, we have to remember that the vacuum state must vanish when acted on with an annihilator. For $|0\rangle$ this is no longer true for the transformed operators, but we can easily write down a state

$$|\tilde{0}\rangle = c^\dagger_{2\uparrow}c^\dagger_{1\uparrow}|0\rangle \tag{93}$$

that behaves as a suitable vacuum state: $\tilde{c}_{i\sigma}|\tilde{0}\rangle = 0$ and $\langle\tilde{0}|\tilde{0}\rangle$. We can then rewrite the transformed Slater determinant (86) as

$$\begin{aligned}|\tilde{\Phi}(\theta_\uparrow,\theta_\downarrow)\rangle &= \Big(\sin(\theta_\downarrow)\,\tilde{c}^\dagger_{1\downarrow} + \cos(\theta_\downarrow)\,\tilde{c}^\dagger_{2\downarrow}\Big)\Big(\sin(\theta_\uparrow)\,\tilde{c}^\dagger_{1\uparrow} + \cos(\theta_\uparrow)\,\tilde{c}^\dagger_{2\uparrow}\Big)\,|\tilde{0}\rangle \\ &= \Big(\sin(\theta_\downarrow)\,c^\dagger_{1\downarrow} + \cos(\theta_\downarrow)\,c^\dagger_{2\downarrow}\Big)\Big(-\sin(\theta_\uparrow)\,c_{1\uparrow} + \cos(\theta_\uparrow)\,c_{2\uparrow}\Big)\,c^\dagger_{2\uparrow}c^\dagger_{1\uparrow}|0\rangle \\ &= \Big(\sin(\theta_\downarrow)\,c^\dagger_{1\downarrow} + \cos(\theta_\downarrow)\,c^\dagger_{2\downarrow}\Big)\Big(+\sin(\theta_\uparrow)\,c^\dagger_{2\uparrow} + \cos(\theta_\uparrow)\,c^\dagger_{1\uparrow}\Big)\,|0\rangle\ .\end{aligned}$$

Thus, the transformation takes the unrestricted state $|\Phi(\theta,\pi/2-\theta)\rangle$ for the repulsive Hubbard model into the unrestricted state $|\Phi(\theta,\theta)\rangle$ for the attractive Hubbard model. Transforming the rotated state (90) in the same way, we find something remarkable:

$$\begin{aligned}&\frac{1}{2}\Big(s_\downarrow\big(\tilde{c}^\dagger_{1\uparrow}+\tilde{c}^\dagger_{1\downarrow}\big) + c_\downarrow\big(\tilde{c}^\dagger_{2\uparrow}+\tilde{c}^\dagger_{2\downarrow}\big)\Big)\Big(s_\uparrow\big(\tilde{c}^\dagger_{1\uparrow}-\tilde{c}^\dagger_{1\downarrow}\big) + c_\uparrow\big(\tilde{c}^\dagger_{2\uparrow}-\tilde{c}^\dagger_{2\downarrow}\big)\Big)\,|\tilde{0}\rangle \\ &= \frac{1}{2}\Big(s_\downarrow\big(-c_{1\uparrow}+c^\dagger_{1\downarrow}\big) + c_\downarrow\big(c_{2\uparrow}+c^\dagger_{2\downarrow}\big)\Big)\Big(s_\uparrow\big(-c_{1\uparrow}-c^\dagger_{1\downarrow}\big) + c_\uparrow\big(c_{2\uparrow}-c^\dagger_{2\downarrow}\big)\Big)\,c^\dagger_{2\uparrow}c^\dagger_{1\uparrow}|0\rangle \\ &= \frac{1}{2}\Big(\big(s_\downarrow c_\uparrow+c_\downarrow s_\uparrow\big)\big(c^\dagger_{1\downarrow}c^\dagger_{1\uparrow}+c^\dagger_{2\downarrow}c^\dagger_{2\uparrow}\big)|0\rangle + 2\big(s_\downarrow s_\uparrow c^\dagger_{1\downarrow}c^\dagger_{2\uparrow}+c_\downarrow c_\uparrow c^\dagger_{2\downarrow}c^\dagger_{2\uparrow}\big)|0\rangle \\ &\qquad\qquad + \big(s_\downarrow c_\uparrow-c_\downarrow s_\uparrow\big)\big(c^\dagger_{2\downarrow}c^\dagger_{1\downarrow}c^\dagger_{2\uparrow}c^\dagger_{1\uparrow}-1\big)|0\rangle \Big).\end{aligned}$$

The energy expectation value of this state is by construction the same as for the charge-density state. For $\theta_\downarrow = \pi/2-\theta_\uparrow$ the new state has a uniform density, but the wavefunction no longer has a well-defined particle number, i.e., it breaks particle number conservation. It is still a product state in the transformed operators and vacuum, but it is a state in Fock space. States of this type are the key to describing superconductivity.

3.3 BCS theory

Next we consider the BCS Hamiltonian

$$\hat{H}_{\mathrm{BCS}} = \sum_{\boldsymbol{k}\sigma} \varepsilon_{\boldsymbol{k}}\, c^\dagger_{\boldsymbol{k}\sigma}c_{\boldsymbol{k}\sigma} - \sum_{\boldsymbol{k}\boldsymbol{k}'} G_{\boldsymbol{k}\boldsymbol{k}'}\, c^\dagger_{\boldsymbol{k}\uparrow}c^\dagger_{-\boldsymbol{k}\downarrow}c_{-\boldsymbol{k}'\downarrow}c_{\boldsymbol{k}'\uparrow} \tag{94}$$

with an attractive interaction between pairs of electrons of opposite spin and momentum (Cooper pairs). We now want to see if we can use the idea of product states in Fock space that we encountered for the attractive Hubbard model. To start, let us consider the determinant of plane-wave states that we used for the homogeneous electron gas $|\Phi_{k_F}\rangle$. Since all states with momentum below k_F are occupied, we have

$$c^\dagger_{\boldsymbol{k}\sigma}|\Phi_{k_F}\rangle = 0\ \text{ for } |\boldsymbol{k}| < k_F \text{ and } \quad c_{\boldsymbol{k}\sigma}|\Phi_{k_F}\rangle = 0\ \text{ otherwise.}$$

Thus $|\Phi_{k_F}\rangle$ behaves like a vacuum state for the transformed operators

$$\tilde{c}_{\boldsymbol{k}\sigma} = \Theta(k_F - |\boldsymbol{k}|)\, c^\dagger_{\boldsymbol{k}\sigma} + \Theta(|\boldsymbol{k}| - k_F)\, c_{\boldsymbol{k}\sigma} = \begin{cases} c^\dagger_{\boldsymbol{k}\sigma} & \text{for } |\boldsymbol{k}| < k_F \\ c_{\boldsymbol{k}\sigma} & \text{for } |\boldsymbol{k}| > k_F \end{cases}$$

Allowing the operators to mix, we can generalize this transformation to

$$\begin{aligned} b_{\boldsymbol{k}\uparrow} &= u_k c_{\boldsymbol{k}\uparrow} - v_k c^\dagger_{-\boldsymbol{k}\downarrow} \\ b_{\boldsymbol{k}\downarrow} &= u_k c_{\boldsymbol{k}\downarrow} + v_k c^\dagger_{-\boldsymbol{k}\uparrow} \end{aligned}$$

Notice how states with $(\boldsymbol{k},\, \sigma)$ and $(-\boldsymbol{k}, -\sigma)$ are mixed. The corresponding creation operators are the adjoints, $b^\dagger_{k\sigma} = \overline{u}_k c^\dagger_{k\sigma} - 2\sigma \overline{v}_k c_{-k,-\sigma}$, where $\sigma = \pm 1/2$. These Bogoliubov-Valatin operators fulfill the canonical anticommutation relations

$$\{b_{\boldsymbol{k}\sigma},\, b_{\boldsymbol{k}'\sigma'}\} = 0 = \{b^\dagger_{\boldsymbol{k}\sigma},\, b^\dagger_{\boldsymbol{k}'\sigma'}\} \quad \text{and} \quad \{b_{\boldsymbol{k}\sigma},\, b_{\boldsymbol{k}'\sigma'}\} = \delta(\boldsymbol{k} - \boldsymbol{k}')\, \delta_{\sigma,\sigma'}$$

when (the non-trivial anticommutators are $\{b_{\boldsymbol{k}\uparrow},\, b_{-\boldsymbol{k}\downarrow}\}$ and $\{b_{\boldsymbol{k}\sigma},\, b^\dagger_{\boldsymbol{k}\sigma}\}$)

$$|u_k|^2 + |v_k|^2 = 1\,. \tag{95}$$

A vacuum state for the new operators can be constructed from the generalized product state $\prod_{\boldsymbol{k}\sigma} b_{\boldsymbol{k}\sigma}|0\rangle$. Expanding the operators

$$b_{-\boldsymbol{k}\uparrow} b_{\boldsymbol{k}\downarrow} b_{\boldsymbol{k}\uparrow} b_{-\boldsymbol{k}\downarrow}|0\rangle = v_k(u_k + v_k\, c^\dagger_{-\boldsymbol{k}\uparrow} c^\dagger_{\boldsymbol{k}\downarrow})\, v_k(u_k + v_k\, c^\dagger_{\boldsymbol{k}\uparrow} c^\dagger_{-\boldsymbol{k}\downarrow})\; |0\rangle$$

and calculating the norm

$$\langle 0|(\overline{u}_k + \overline{v}_k\, c_{-\boldsymbol{k}\downarrow} c_{\boldsymbol{k}\uparrow})(\overline{u}_k + \overline{v}_k\, c_{\boldsymbol{k}\downarrow} c_{-\boldsymbol{k}\uparrow})(u_k + v_k\, c^\dagger_{-\boldsymbol{k}\uparrow} c^\dagger_{\boldsymbol{k}\downarrow})(u_k + v_k\, c^\dagger_{\boldsymbol{k}\uparrow} c^\dagger_{-\boldsymbol{k}\downarrow})|0\rangle = \big(|u_k|^2 + |v_k|^2\big)^2$$

we see from (95) that the BCS wavefunction

$$|\mathrm{BCS}\rangle = \prod_{\boldsymbol{k}} (u_k + v_k\, c^\dagger_{\boldsymbol{k}\uparrow} c^\dagger_{-\boldsymbol{k}\downarrow})\; |0\rangle \tag{96}$$

is the (normalized) vacuum for the Bogoliubov-Valatin operators.
To calculate physical expectation values we express the electron operators as

$$\begin{aligned} c_{\boldsymbol{k}\uparrow} &= \overline{u}_k b_{\boldsymbol{k}\uparrow} + v_k b^\dagger_{-\boldsymbol{k}\downarrow} \\ c_{\boldsymbol{k}\downarrow} &= \overline{u}_k b_{\boldsymbol{k}\downarrow} - v_k b^\dagger_{-\boldsymbol{k}\uparrow} \end{aligned}$$

The expectation value for the occupation of a plane-wave state, e.g., is

$$\langle \mathrm{BCS}|\hat{n}_{\boldsymbol{k}\uparrow}|\mathrm{BCS}\rangle = \langle \mathrm{BCS}|(u_k b^\dagger_{\boldsymbol{k}\uparrow} + \overline{v}_k b_{-\boldsymbol{k}\downarrow})(\overline{u}_k b_{\boldsymbol{k}\uparrow} + v_k b^\dagger_{-\boldsymbol{k}\downarrow})|\mathrm{BCS}\rangle = |v_k|^2 = \langle \mathrm{BCS}|\hat{n}_{-\boldsymbol{k}\downarrow}|\mathrm{BCS}\rangle.$$

Unlike the electron gas Slater determinant $|\Phi_{k_F}\rangle$, where $n_{\boldsymbol{k}\sigma}$ is 1 below k_F and vanishes above, varying the parameter v_k in the BCS wavefunction allows us to get arbitrary momentum distributions $\langle n_{\boldsymbol{k}\sigma}\rangle$. Since the BCS wavefunction has contributions in all particle sectors with an even number of electrons, there are also less-conventional expectation values, e.g.,

$$\langle \mathrm{BCS}|c^\dagger_{\boldsymbol{k}\uparrow} c^\dagger_{-\boldsymbol{k}\downarrow}|\mathrm{BCS}\rangle = \langle \mathrm{BCS}|(u_k b^\dagger_{\boldsymbol{k}\uparrow} + \overline{v}_k b_{-\boldsymbol{k}\downarrow})(u_k b^\dagger_{-\boldsymbol{k}\downarrow} - \overline{v}_k b_{\boldsymbol{k},\uparrow})|\mathrm{BCS}\rangle = \overline{v}_k u_k = \overline{\langle c_{-\boldsymbol{k}\downarrow} c_{\boldsymbol{k}\uparrow}\rangle}.$$

When minimizing the energy expectation value, we have to introduce a chemical potential μ that is chosen to give the desired number of particles $N = \sum_{\boldsymbol{k}\sigma} |v_k|^2$. We get

$$\langle \mathrm{BCS}|\hat{H}-\mu\hat{N}|\mathrm{BCS}\rangle = \sum_{\boldsymbol{k}\sigma} (\varepsilon_{\boldsymbol{k}}-\mu)\,|v_k|^2 - \sum_{\boldsymbol{k},\boldsymbol{k}'} G_{\boldsymbol{k}\boldsymbol{k}'}\,\overline{v}_k u_k v_{k'} \overline{u}_{k'}\,, \tag{97}$$

where the last term is real since $G_{\boldsymbol{k}\boldsymbol{k}'} = G_{\boldsymbol{k}'\boldsymbol{k}}$. Writing the Bogoliubov coefficients in polar coordinates, $u_k = |u_k|e^{i\alpha_k}$ and $v_k = |v_k|e^{i(\alpha_k+\varphi_k)}$, we obtain

$$\langle \mathrm{BCS}|\hat{H}-\mu\hat{N}|\mathrm{BCS}\rangle = \sum (\varepsilon_{\boldsymbol{k}}-\mu)\,|v_k|^2 - \sum G_{\boldsymbol{k}\boldsymbol{k}'}\,|v_k||u_k||v_{k'}||u_{k'}|\cos(\varphi_{k'}-\varphi_k), \tag{98}$$

which is minimized when the relative phase φ_k is independent of k, i.e., all Cooper pairs in (96) are *phase coherent* (while the α_k merely contribute to the global phase)

$$|\mathrm{BCS}(\varphi)\rangle = \prod \big(|u_k| + |v_k|e^{i\varphi} c^\dagger_{\boldsymbol{k}\uparrow} c^\dagger_{-\boldsymbol{k}\downarrow}\big)|0\rangle. \tag{99}$$

Their overlap is $\langle \mathrm{BCS}(\varphi')|\mathrm{BCS}(\varphi)\rangle = \prod_{\boldsymbol{k}} \big(|u_k|^2 + |v_k|^2 e^{i(\varphi'-\varphi)}\big)$ so that in the thermodynamic limit they are orthogonal for $\varphi \neq \varphi'$. For a fixed phase φ the particle number fluctuates $\langle \hat{N}^2\rangle - \langle \hat{N}\rangle^2 = 4\sum_{\boldsymbol{k}} |v_k|^2|u_k|^2 < 2\langle \hat{N}\rangle$. Since the phase of a state with $N/2$ Cooper pairs is $e^{i\varphi N/2}$, we can project out states with fixed number of electrons by integrating over φ

$$|\mathrm{BCS}_N\rangle = \frac{1}{\sqrt{2\pi}} \int_0^{2\pi} d\varphi\, e^{-i\varphi N/2}\,|\mathrm{BCS}(\varphi)\rangle.$$

It remains to minimize (97) with respect to the absolute values, written as $|u_k| = \sin\Theta_k$ and $|v_k| = \cos\Theta_k$ with $\Theta_k \in [0,\pi/2)$. Setting the derivative of

$$\langle \mathrm{BCS}|\hat{H}-\mu\hat{N}|\mathrm{BCS}\rangle = \sum_{\boldsymbol{k}\sigma} (\varepsilon_{\boldsymbol{k}}-\mu)\frac{1+\cos 2\Theta_k}{2} - \sum_{\boldsymbol{k}\boldsymbol{k}'} G_{\boldsymbol{k}\boldsymbol{k}'} \frac{\sin 2\Theta_k}{2}\frac{\sin 2\Theta_{k'}}{2}$$

with respect to Θ_k to zero we find the system of equations

$$\tan 2\Theta_k = -\frac{\sum_{\boldsymbol{k}'} G_{\boldsymbol{k}\boldsymbol{k}'} \sin(2\Theta_{k'})/2}{\varepsilon_{\boldsymbol{k}}-\mu} = -\frac{\Delta_{\boldsymbol{k}}}{\varepsilon_{\boldsymbol{k}}-\mu} = \frac{\Delta_{\boldsymbol{k}}}{\mu-\varepsilon_{\boldsymbol{k}}} \tag{100}$$

where we have introduced the gap function $\Delta_{\boldsymbol{k}}$. Using $(\cos x)^2 = 1/\big(1+(\tan x)^2\big)$ we obtain the momentum distribution

$$\langle n_{\boldsymbol{k}\sigma}\rangle = |v_k|^2 = \frac{1}{2}\big(1+\cos 2\Theta_k\big) = \frac{1}{2}\left(1 - \frac{\varepsilon_{\boldsymbol{k}}-\mu}{\sqrt{(\varepsilon_{\boldsymbol{k}}-\mu)^2 + \Delta_{\boldsymbol{k}}^2}}\right). \tag{101}$$

For $\Delta_{\boldsymbol{k}} \equiv 0$ this is just the step function of a Fermi gas, for finite Δ the transition is more smooth. We still have to determine the parameters μ and $\Delta_{\boldsymbol{k}}$. The chemical potential is fixed by

$$N = \sum_{\boldsymbol{k}} 2|v_k|^2 = \sum_{\boldsymbol{k}} \left(1 - \frac{\varepsilon_{\boldsymbol{k}}-\mu}{\sqrt{(\varepsilon_{\boldsymbol{k}}-\mu)^2 + \Delta_{\boldsymbol{k}}^2}}\right) \tag{102}$$

while for $\Delta_{\boldsymbol{k}}$ we obtain from (100) and (101) the self-consistent gap equations

$$\Delta_{\boldsymbol{k}} = \sum_{\boldsymbol{k}'} G_{\boldsymbol{k}\boldsymbol{k}'} \frac{\sin 2\Theta_k}{2} = \frac{1}{2}\sum_{\boldsymbol{k}'} G_{\boldsymbol{k}\boldsymbol{k}'} \tan 2\Theta_{k'} \cos 2\Theta_{k'} = -\frac{1}{2}\sum_{\boldsymbol{k}'} \frac{G_{\boldsymbol{k}\boldsymbol{k}'}\Delta_{\boldsymbol{k}'}}{\sqrt{(\varepsilon_{\boldsymbol{k}'}-\mu)^2 + \Delta_{\boldsymbol{k}'}^2}}\,. \tag{103}$$

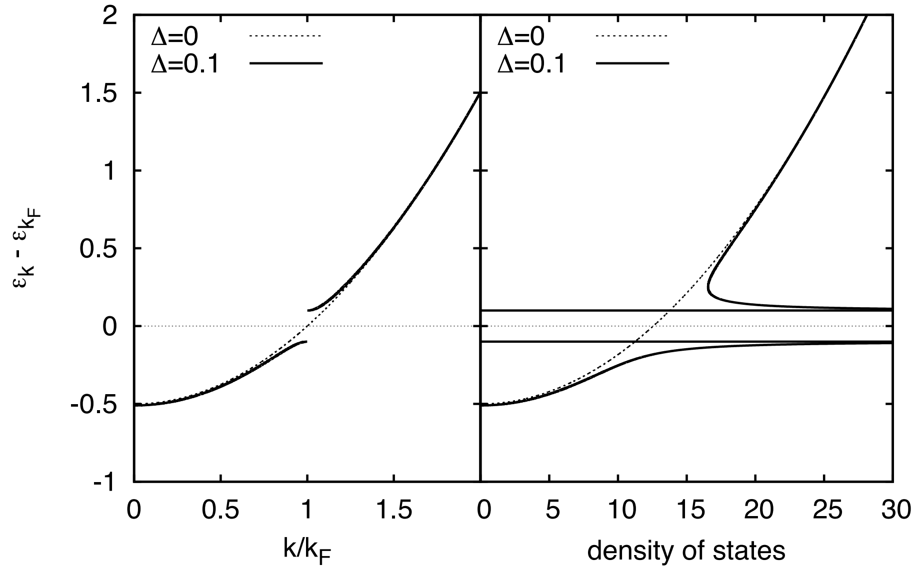

Fig. 5: *Quasi-electron energy and density of states for the BCS state with and without gap.*

To see that Δ is indeed a gap, consider the (unrelaxed) quasi-electron states ($\varepsilon_{\boldsymbol{k}} > \mu$)

$$|\boldsymbol{k}\uparrow\rangle = \frac{1}{u_k} c^\dagger_{\boldsymbol{k}\uparrow}|\mathrm{BCS}\rangle = b^\dagger_{\boldsymbol{k}\uparrow}|\mathrm{BCS}\rangle. \tag{104}$$

Adding an electron of momentum $\boldsymbol{k}$ destroys its Cooper pair, changing $\langle n_{\boldsymbol{k}\uparrow}+n_{\boldsymbol{k}\downarrow}\rangle$ from $2|v_k^2|$ to 1 and removing the interaction of the pair with all others:

$$\begin{aligned}\langle \boldsymbol{k}\uparrow|\hat{H}-\mu\hat{N}|\boldsymbol{k}\uparrow\rangle - \langle\mathrm{BCS}|\hat{H}-\mu\hat{N}|\mathrm{BCS}\rangle &= (\varepsilon_{\boldsymbol{k}}-\mu)\,(1-2|v_k|^2) + 2\Delta_{\boldsymbol{k}}|v_k||u_k|\\ &= (\varepsilon_{\boldsymbol{k}}-\mu)\,(-\cos 2\Theta_k) + \Delta_{\boldsymbol{k}}\sin 2\Theta_k = \sqrt{(\varepsilon_{\boldsymbol{k}}-\mu)^2+\Delta^2}.\end{aligned}$$

For $\Delta_{\boldsymbol{k}} \equiv 0$ we recover Koopmans' Hartree-Fock result, while for $\Delta_{\boldsymbol{k}} > 0$ a gap opens around the Fermi level. Fig. 5 compares the quasi-electron dispersion and the corresponding density of states for the two cases, assuming, for simplicity, a k-independent gap $\Delta_{\boldsymbol{k}} \equiv \Delta$.

4 Conclusion

We have seen that second quantization is a remarkably useful formalism. With just a few simple rules for the field operators and the corresponding vacuum, it converts dealing with many-electron states to straightforward algebraic manipulations. Moreover it is naturally suited for performing calculations in variational spaces spanned by a finite basis of orbitals. But its advantages go beyond a mere simplification. By abstracting from the coordinate representation, it allows us to express many-body operators in a way that is independent of the number of electrons. Because of this it becomes possible to consider Fock-space wavefunctions which do not have a definite number of electrons. This allows us to consider unrestricted mean-field states that not only break spatial or spin symmetries but also particle conservation. This additional freedom allows us to extend the concept of a Slater determinant to product states in Fock space, an example of which is the BCS wavefunction.

A Appendix

A.1 Non-orthonormal basis

A general one-electron basis of functions $|\chi_n\rangle$ will have an overlap matrix $S_{nm} = \langle\chi_n|\chi_m\rangle$ that is positive definite (and hence invertible) and hermitian. The completeness relation is

$$\mathbb{1} = \textstyle\sum_{k,l} |\chi_k\rangle (S^{-1})_{kl} \langle\chi_l| \,. \tag{105}$$

With it we can easily write the Schrödinger equation $\hat{H}|v\rangle = \varepsilon|v\rangle$ in matrix form

$$\sum_k \underbrace{\langle\chi_i|H|\chi_k\rangle}_{=:H_{ik}} \underbrace{\sum_l (S^{-1})_{kl}\langle\chi_l|v\rangle}_{=:v_k} \langle\chi_i|\hat{H}|v\rangle = \varepsilon\langle\chi_i|v\rangle = \varepsilon \sum_k \underbrace{\langle\chi_i|\chi_k\rangle}_{=S_{ik}} \underbrace{\sum_l (S^{-1})_{kl}\langle\chi_l|v\rangle}_{=v_k} \,. \tag{106}$$

Collecting all components, this becomes the generalized eigenvalue problem $\boldsymbol{Hv} = \varepsilon\boldsymbol{Sv}$. From the solution $\boldsymbol{v}$ we can easily construct $|v\rangle = \sum v_k|\chi_k\rangle$. It is, however, often more convenient to have an orthonormal basis, so that we do not have to deal with the overlap matrices in the definition of the second quantized operators or the generalized eigenvalue problem.

To orthonormalize the basis $\{|\chi_n\rangle\}$, we need to find a basis transformation $\boldsymbol{T}$ such that

$$|\varphi_n\rangle := \textstyle\sum_m |\chi_m\rangle\, T_{mn} \qquad \text{with} \quad \langle\varphi_n|\varphi_m\rangle = \delta_{mn} \,. \tag{107}$$

This implies that $\boldsymbol{T}^\dagger\boldsymbol{S}\boldsymbol{T} = \mathbb{1}$, or equivalently $\boldsymbol{S}^{-1} = \boldsymbol{T}\boldsymbol{T}^\dagger$. This condition does not uniquely determine $\boldsymbol{T}$. In fact there are many orthonormalization techniques, e.g., Gram-Schmidt orthonormalization or Cholesky decomposition.

Usually we will have chosen the basis functions $|\chi_n\rangle$ for a physical reason, e.g., atomic orbitals, so that we would like the orthonormal basis functions to be as close to the original basis as possible, i.e, we ask for the basis transformation $\boldsymbol{T}$ that minimizes

$$\begin{aligned}\sum_n \big\| |\varphi_n\rangle - |\chi_n\rangle \big\|^2 &= \sum_n \Big\| \sum_m |\chi_m\rangle (T_{mn} - \delta_{mn}) \Big\|^2 \\ &= \mathrm{Tr}\,(\boldsymbol{T}^\dagger - \mathbb{1})\,\boldsymbol{S}\,(\boldsymbol{T} - \mathbb{1}) = \mathrm{Tr}\,(\underbrace{\boldsymbol{T}^\dagger\boldsymbol{S}\boldsymbol{T}}_{=\mathbb{1}} - \boldsymbol{T}^\dagger\boldsymbol{S} - \boldsymbol{S}\boldsymbol{T} + \boldsymbol{S}) \,.\end{aligned} \tag{108}$$

Given an orthonormalization $\boldsymbol{T}$, we can obtain any other orthonormalization $\tilde{\boldsymbol{T}}$ by performing a unitary transformation, i.e., $\tilde{\boldsymbol{T}} = \boldsymbol{T}\boldsymbol{U}$. Writing $\boldsymbol{U} = \exp(i\lambda\boldsymbol{M})$ with $\boldsymbol{M}$ a Hermitian matrix, we obtain the variational condition

$$0 \overset{!}{=} \mathrm{Tr}\,(+i\boldsymbol{M}\boldsymbol{T}^\dagger\boldsymbol{S} - i\boldsymbol{S}\boldsymbol{T}\boldsymbol{M}) = i\,\mathrm{Tr}\,(\boldsymbol{T}^\dagger\boldsymbol{S} - \boldsymbol{S}\boldsymbol{T})\boldsymbol{M}, \tag{109}$$

which is fulfilled for $\boldsymbol{S}\boldsymbol{T} = \boldsymbol{T}^\dagger\boldsymbol{S}$, i.e., $\boldsymbol{S}\boldsymbol{T}^2 = \boldsymbol{T}^\dagger\boldsymbol{S}\boldsymbol{T} = \mathbb{1}$. The second variation at $\boldsymbol{T} = \boldsymbol{S}^{-1/2}$

$$\frac{1}{2}\,\mathrm{Tr}\,(\boldsymbol{M}^2\boldsymbol{S}^{1/2} + \boldsymbol{S}^{1/2}\boldsymbol{M}^2) > 0 \tag{110}$$

is positive, since $\boldsymbol{S}$ and the square of the hermitian matrix $\boldsymbol{M}$ are both positive definite. Hence the Löwdin symmetric orthogonalization [15]

$$\boldsymbol{T}_{\text{Löwdin}} = \boldsymbol{S}^{-1/2} \tag{111}$$

minimizes the modification of the basis vectors due to orthogonalization.

A.2 Pauli matrices

The spin matrices were defined by Pauli [16] as

$$\sigma_x = \begin{pmatrix} 0 & 1 \\ 1 & 0 \end{pmatrix} \quad \sigma_y = \begin{pmatrix} 0 & -\mathrm{i} \\ \mathrm{i} & 0 \end{pmatrix} \quad \sigma_z = \begin{pmatrix} 1 & 0 \\ 0 & -1 \end{pmatrix}$$

They are hermitian and unitary, so that $\sigma_j^2 = \sigma_j \sigma_j^\dagger = \mathbb{1}$. Moreover, $\det \sigma_j = -1$ and $\operatorname{Tr} \sigma_j = 0$. By explicit multiplication we find $\sigma_x \sigma_y = \mathrm{i}\sigma_z$, from which we get the more symmetric equation $\sigma_x \sigma_y \sigma_z = \mathrm{i}$. These relations are cyclic, which is easily seen by repeatedly using $\sigma_j^2 = \mathbb{1}$

$$\sigma_x\sigma_y = \mathrm{i}\sigma_z \overset{\cdot\sigma_z}{\rightsquigarrow} \sigma_x\sigma_y\sigma_z = \mathrm{i} \overset{\sigma_x\cdot}{\rightsquigarrow} \sigma_y\sigma_z = \mathrm{i}\sigma_x \overset{\cdot\sigma_x}{\rightsquigarrow} \sigma_y\sigma_z\sigma_x = \mathrm{i} \overset{\sigma_y\cdot}{\rightsquigarrow} \sigma_z\sigma_x = \mathrm{i}\sigma_y \overset{\cdot\sigma_y}{\rightsquigarrow} \sigma_z\sigma_x\sigma_y = \mathrm{i}\,.$$

Exchanging two adjacent indices changes the sign, e.g., multiplying $\sigma_x\sigma_y\sigma_z = \mathrm{i}$ from the left with $\sigma_y\sigma_x$ gives $\sigma_y\sigma_x{=}{-}\mathrm{i}\sigma_z$, which is again cyclic in the indices. We note that the multiplication table of the matrices $-\mathrm{i}\sigma_j$ is the same as the that of the basic quaternions. We can summarize the products of the Pauli matrices in the form

$$\big(\vec{a}\cdot\vec{\sigma}\big)\big(\vec{b}\cdot\vec{\sigma}\big) = \sum a_j b_k\, \sigma_j\sigma_k = \big(\vec{a}\cdot\vec{b}\big)\mathbb{1} + \mathrm{i}\big(\vec{a}\times\vec{b}\big)\cdot\vec{\sigma}\,. \tag{112}$$

From the products follow the familiar commutation relations $[\sigma_x,\, \sigma_y] = 2\mathrm{i}\sigma_z$ (cyclic), while the anticommutators are $\{\sigma_j,\, \sigma_k\} = 2\delta_{j,k}\,\mathbb{1}$.

Together with the unit matrix, the Pauli matrices form a basis of the four-dimensional algebra of complex $2{\times}2$ matrices and we can write

$$\begin{pmatrix} m_{11} & m_{12} \\ m_{21} & m_{22} \end{pmatrix} = M = m_0\mathbb{1} + \vec{m}\cdot\vec{\sigma} = \begin{pmatrix} m_0{+}\,m_z & m_x{-}\mathrm{i}m_y \\ m_x{+}\mathrm{i}m_y & m_0{-}\,m_z \end{pmatrix} \tag{113}$$

with $2m_0 = m_{11}{+}m_{22}$, $2m_z = m_{11}{-}m_{22}$, $2m_x = m_{12}{+}m_{21}$, and $2m_x = \mathrm{i}(m_{12}{-}m_{21})$, which can be written as $2m_j = \operatorname{Tr} M\sigma_j$, with $\sigma_0 := \mathbb{1}$. When the m_0 and $\vec{m}$ are real, M is hermitian. Matrix products are easily evaluated using (112). As a simple example we find

$$(m_0\mathbb{1} + \vec{m}\cdot\vec{\sigma})(m_0\mathbb{1} - \vec{m}\cdot\vec{\sigma}) = m_0^2 - m_x^2 - m_y^2 - m_z^2 = \det M$$

(remember $\det \alpha\mathbb{1}_N = \alpha^N$). Thus, when $\det M \neq 0$, the inverse of M is

$$M = m_0\mathbb{1} + \vec{m}\cdot\vec{\sigma} \quad \rightsquigarrow \quad M^{-1}{=}(m_0\mathbb{1} - \vec{m}\cdot\vec{\sigma})/\det M. \tag{114}$$

For a unitary matrix $U{=}\,u_0{+}\vec{u}{\cdot}\vec{\sigma}$ with $\det U = 1$ we then see from $U^\dagger = u_0^*{+}\vec{u}^{\,*}{\cdot}\vec{\sigma} \overset{!}{=} u_0{-}\vec{u}{\cdot}\vec{\sigma}$ that u_0 must be real and $\vec{u} = \mathrm{i}\vec{n}$ imaginary, so that $1 = \det U = u_0^2 + \|\vec{n}\|^2$, which allows us to write $u_0 = \cos\alpha$ and $\vec{n} = \sin\alpha\ \hat{n}$ with unit vector $\hat{n} := \vec{n}/\|\vec{n}\|$ and $\alpha \in [0, 2\pi)$. Thus any special unitary $2{\times}2$ matrix $U{\in}\,\mathrm{SU}(2)$ can be written, using $(\hat{n}\cdot\vec{\sigma})^2{=}\,\mathbb{1}$ from (112) in the power series,

$$U_{\hat{n},\alpha} = \cos\alpha\,\mathbb{1} + \mathrm{i}\sin\alpha\ (\hat{n}\cdot\vec{\sigma}) = \exp\!\big(\mathrm{i}\alpha\,\hat{n}\cdot\vec{\sigma}\big). \tag{115}$$

General unitary matrices with $\det U = \mathrm{e}^{\mathrm{i}\alpha_0}$ have the form $U = \mathrm{e}^{\mathrm{i}\alpha_0/2} U_{\hat{n},\alpha}$.

The U are related to rotations of vectors $\vec{a} \in \mathbb{R}^3$ via $U(\vec{a}\cdot\vec{\sigma})U^\dagger$. To see this we remember that $\vec{a}\cdot\vec{\sigma}$ is a hermitian 2×2 matrix with zero trace. By the cyclic property of the trace $\operatorname{Tr} U(\vec{a}\cdot\vec{\sigma})U^\dagger = \operatorname{Tr}\vec{a}\cdot\vec{\sigma}$, so that there exists a unique $\vec{a}_U$ with $U(\vec{a}\cdot\vec{\sigma})U^\dagger = \vec{a}_U\cdot\vec{\sigma}$. This mapping $\vec{a}\to\vec{a}_U$ is linear, $U\big((c\vec{a}+\vec{b})\cdot\vec{\sigma}\big)U^\dagger = cU(\vec{a}\cdot\vec{\sigma})U^\dagger + U(\vec{b}\cdot\vec{\sigma})U^\dagger$, and preserves the inner product

$$\vec{a}\cdot\vec{b} = \tfrac{1}{2}\operatorname{Tr}(\vec{a}\cdot\vec{\sigma})(\vec{b}\cdot\vec{\sigma}) = \tfrac{1}{2}\operatorname{Tr} U(\vec{a}\cdot\vec{\sigma})U^\dagger\, U(\vec{b}\cdot\vec{\sigma})U^\dagger = \tfrac{1}{2}\operatorname{Tr}(\vec{a}_U\cdot\vec{\sigma})(\vec{b}_U\cdot\vec{\sigma}) = \vec{a}_U\cdot\vec{b}_U$$

so that it must be a proper rotation, $\vec{a}_U = R_U\,\vec{a}$ with $R_U\in \mathrm{SO}(3)$. To identify which rotation, we consider the special case $\vec{a}_\| = c_a\hat{n}$ for which, by (112), $\vec{a}_\|\cdot\vec{\sigma}$ commutes with $\hat{n}\cdot\vec{\sigma}$ so that $U(\vec{a}_\|\cdot\vec{\sigma})U^\dagger = \vec{a}_\|\cdot\vec{\sigma}$, i.e., $\hat{n}$ is the axis of rotation. To find the rotation angle ϑ, we consider a unit vector $\hat{a}_\perp$ perpendicular to $\hat{n}$, for which, using $(\hat{a}_\perp\cdot\vec{\sigma})(\hat{n}\cdot\vec{\sigma}) = \mathrm{i}(\hat{a}_\perp\times\hat{n})\cdot\vec{\sigma}$ and $\operatorname{Tr}\vec{v}\cdot\vec{\sigma}=0$,

$$\begin{aligned}\cos\vartheta &= \hat{a}_\perp\cdot R_U\hat{a}_\perp = \tfrac{1}{2}\operatorname{Tr}(\hat{a}_\perp\cdot\vec{\sigma})U(\hat{a}_\perp\cdot\vec{\sigma})U^\dagger\\ &= \tfrac{1}{2}\operatorname{Tr}(\hat{a}_\perp\cdot\vec{\sigma})(\cos\alpha+\mathrm{i}\sin\alpha\,(\hat{n}\cdot\vec{\sigma}))\;\;(\hat{a}_\perp\cdot\vec{\sigma})(\cos\alpha-\mathrm{i}\sin\alpha\,(\hat{n}\cdot\vec{\sigma}))\\ &= \tfrac{1}{2}\operatorname{Tr}\big(\cos\alpha\,\hat{a}_\perp-\sin\alpha\,(\hat{a}_\perp\times\hat{n})\big)\cdot\vec{\sigma}\quad\big(\cos\alpha\,\hat{a}_\perp+\sin\alpha\,(\hat{a}_\perp\times\hat{n})\big)\cdot\vec{\sigma}\\ &= \big(\cos\alpha\,\hat{a}_\perp-\sin\alpha\,(\hat{a}_\perp\times\hat{n})\big)\cdot\big(\cos\alpha\,\hat{a}_\perp+\sin\alpha\,(\hat{a}_\perp\times\hat{n})\big) = (\cos\alpha)^2-(\sin\alpha)^2 = \cos2\alpha\end{aligned}$$

Hence, $U_{\hat{n},\alpha}\in\mathrm{SU}(2)$ induces a rotation $R_U\in\mathrm{SO}(3)$ about the axis $\hat{n}$ through the angle $\vartheta=2\alpha$. Therefore, matrices in $\mathrm{SU}(2)$ are commonly written using the angle of rotation $\vartheta\in[0,4\pi)$ instead of $\alpha\in[0,2\pi)$ as $U(\hat{n},\vartheta)=\exp(\mathrm{i}\frac{\vartheta}{2}\,\hat{n}\cdot\vec{\sigma})$. We see, in particular, that the two matrices $U(\hat{n},\vartheta)$ and $U(\hat{n},\vartheta{+}2\pi) = -U(\hat{n},\vartheta)$ in $\mathrm{SU}(2)$ induce the same rotation $R_{-U}=R_U\in\mathrm{SO}(3)$.

Diagonalizing a hermitian 2×2 matrix $M = m_0\mathbb{1}+\vec{m}\cdot\vec{\sigma}$ is now simple: just rotate $\hat{m}\to\hat{z}$

$$U\big(m_0\mathbb{1}+\|\vec{m}\|\,(\hat{m}\cdot\vec{\sigma})\big)U^\dagger = m_0\mathbb{1}+\|\vec{m}\|\,\sigma_z$$

from which we easily read off the eigenvalues

$$\varepsilon_\pm = m_0\pm\|\vec{m}\| = \frac{m_{11}{+}m_{22}}{2}\pm\sqrt{\frac{(m_{11}{-}m_{22})^2}{4}+|m_{12}|^2} = \tfrac{1}{2}\operatorname{Tr}M\pm\sqrt{\big(\tfrac{1}{2}\operatorname{Tr}M\big)^2-\det M},$$

while the eigenvalues are the columns vectors of $U^\dagger = \big(\boldsymbol{v}_+,\,\boldsymbol{v}_-\big)$

$$m_0\mathbb{1}+\vec{m}\cdot\vec{\sigma} = U^\dagger\big(m_0\mathbb{1}+\|\vec{m}\|\,\sigma_z\big)U = m_0\mathbb{1}+\|\vec{m}\|\,\big(\boldsymbol{v}_+,\boldsymbol{v}_-\big)\,\sigma_z\begin{pmatrix}\boldsymbol{v}_+^\dagger\\ \boldsymbol{v}_-^\dagger\end{pmatrix}$$

We still need to determine a U that rotates $\hat{m}\to\hat{z}$. The rotation axis should be orthogonal to both vectors, i.e., $\hat{n} = \hat{z}\times\hat{m}/\|\hat{z}\times\hat{m}\| = (m_x\hat{y}{-}m_y\hat{x})/\sqrt{m_x^2{+}m_y^2}$, so that the rotation angle $\vartheta\in[0,\pi]$ is determined by $\cos\vartheta = \hat{m}\cdot\hat{z} = m_z/\|\vec{m}\|$. Using also the other spherical coordinates $m_x = \|\vec{m}\|\sin\vartheta\cos\varphi$ and $m_y = \|\vec{m}\|\sin\vartheta\sin\varphi$, we get $\hat{n} = \cos\varphi\,\hat{y}-\sin\varphi\,\hat{x}$ so that

$$U(\hat{n},\vartheta) = \begin{pmatrix}\cos\frac{\vartheta}{2}+\mathrm{i}n_z\sin\frac{\vartheta}{2} & (n_y{+}\mathrm{i}n_x)\sin\frac{\vartheta}{2}\\ -(n_y{-}\mathrm{i}n_x)\sin\frac{\vartheta}{2} & \cos\frac{\vartheta}{2}-\mathrm{i}n_z\sin\frac{\vartheta}{2}\end{pmatrix} = \begin{pmatrix}\cos\frac{\vartheta}{2} & +\mathrm{e}^{-\mathrm{i}\varphi}\sin\frac{\vartheta}{2}\\ -\mathrm{e}^{+\mathrm{i}\varphi}\sin\frac{\vartheta}{2} & \cos\frac{\vartheta}{2}\end{pmatrix}$$

from which we read off the eigenvectors as the columns of $U^\dagger$ (which you may want to check for simple cases like $M=\sigma_z$, σ_x or σ_y)

$$\boldsymbol{v}_+ = \begin{pmatrix}\cos\frac{\vartheta}{2}\\ +\mathrm{e}^{+\mathrm{i}\varphi}\sin\frac{\vartheta}{2}\end{pmatrix}\text{ and }\boldsymbol{v}_- = \begin{pmatrix}-\mathrm{e}^{-\mathrm{i}\varphi}\sin\frac{\vartheta}{2}\\ \cos\frac{\vartheta}{2}\end{pmatrix}\text{ with }\begin{aligned}\varphi &= \arg(m_{21}){=}-\arg(m_{12})\\ \vartheta &= \arccos\frac{m_{11}{-}m_{22}}{\varepsilon_+{-}\varepsilon_-}\end{aligned}. \tag{116}$$

A more symmetric form of the eigenvectors may be obtained by writing $\mathrm{e}^{\mp\mathrm{i}\varphi/2}\boldsymbol{v}_\pm$.

A.3 Some useful commutation relations

Commuting an operator through a product of operators is straightforward

$$\begin{aligned}
AB_1\cdots B_N &= [A,\,B_1]\,B_2\cdots B_N + B_1AB_2\cdots B_N \\
&= [A,\,B_1]\,B_2\cdots B_N + B_1[A,\,B_2]\cdots B_N + B_1B_2A\cdots B_N \\
&\;\vdots \\
&= \sum_{n=1}^{N}\prod_{i=1}^{n-1}B_i\;\;[A,\,B_n]\prod_{i=n+1}^{N}B_i + B_1\cdots B_NA
\end{aligned}$$

while, working analogously, anticommuting introduces alternating signs

$$\begin{aligned}
AB_1\cdots B_N &= \{A,\,B_1\}\,B_2\cdots B_N - B_1AB_2\cdots B_N \\
&= \{A,\,B_1\}\,B_2\cdots B_N - B_1\{A,\,B_2\}\cdots B_N - B_1B_2A\cdots B_N \\
&\;\vdots \\
&= \sum_{n=1}^{N}(-1)^{n-1}\prod_{i=1}^{n-1}B_i\;\;\{A,\,B_n\}\prod_{i=n+1}^{N}B_i + (-1)^NB_1\cdots B_NA
\end{aligned}$$

The following special cases are particularly useful

$$\begin{aligned}
[A,\,BC] &= [A,\,B]\,C\;+\;B\,[A,\,C] \\
&= \{A,\,B\}C - B\{A,\,C\} \\
[AB,\,C] &= A\,[B,\,C]\;+\;[A,\,C]\,B \\
&= A\{B,\,C\} - \{A,\,C\}B \\
[AB,\,CD] &= A\;[B,\,C]\,D + AC\;[B,\,D]\;+\;[A,C]\;DB + C\;[A,\,D]\,B \\
&= A\{B,\,C\}D - AC\{B,\,D\} + \{A,C\}DB - C\{A,\,D\}B
\end{aligned}$$

Important examples are $\left[c_i^\dagger c_j,\,c_\gamma^\dagger\right] = \langle j|\gamma\rangle\,c_i^\dagger$ and $\left[c_i^\dagger c_j,\,c_\gamma\right] = -\langle i\,|\gamma\rangle\,c_j$.
For the commutator of products of creation and annihilation operators appearing in one- and two-body operators we find

$$\left[c_i^\dagger c_j,\,c_\alpha^\dagger c_\beta\right] = \left[c_i^\dagger c_j,\,c_\alpha^\dagger\right]c_\beta + c_\alpha^\dagger\left[c_i^\dagger c_j,\,c_\beta\right] = \langle j|\alpha\rangle\,c_i^\dagger c_\beta - \langle\beta|i\rangle\,c_\alpha^\dagger c_j$$

and

$$\left[c_i^\dagger c_j^\dagger c_k c_l,\,c_\alpha^\dagger c_\beta\right] = \langle l|\alpha\rangle\,c_i^\dagger c_j^\dagger c_k c_\beta + \langle k|\alpha\rangle\,c_i^\dagger c_j^\dagger c_\beta c_l - \langle\beta|j\rangle\,c_i^\dagger c_\alpha^\dagger c_k c_l - \langle\beta|i\rangle\,c_\alpha^\dagger c_j^\dagger c_k c_l\,.$$

References

[1] P. Forrest: *The Identity of Indiscernibles*, in The Stanford Encyclopedia of Philosophy `http://plato.stanford.edu/entries/identity-indiscernible/`

[2] W. Pauli: *The connection between spin and statistics*, Phys. Rev. **58**, 716 (1940)

[3] R.F. Streater and A.S. Wightman: *PCT, Spin and Statistics, and All That* (Benjamin, New York, 1964)

[4] P.-O. Löwdin: *Quantum Theory of Many-Particle Systems I*, Phys. Rev. **97**, 1474 (1955)

[5] P. Jordan and O. Klein: *Zum Mehrkörperproblem in der Quantenmechanik*, Z. Physik **45**, 751 (1927)

[6] P. Jordan and E. Wigner: *Über das Paulische Äquivalenzverbot*, Z. Physik **47**, 631 (1928)

[7] R. Peierls: *Surprises in Theoretical Physics* (Princeton University Press, 1979)

[8] P. Jorgensen and J. Simons: *Second Quantization-Based Methods in Quantum Chemistry* (Academic Press, New York, 1981)

[9] D.J. Thouless: *Stability conditions and nuclear rotations in the Hartree-Fock theory*, Nucl. Phys. **21**, 225 (1960)

[10] Le Thi Hoai: *Product wave-functions in Fock-space* (MSc Thesis, German Research School for Simulation Sciences, 2015)

[11] E. Koch: *Many-Electron States* in [17]

[12] S. Zhang and D.M. Ceperley: *Hartree-Fock Ground State of the Three-Dimensional Electron Gas*, Phys. Rev. Lett. **100**, 236404 (2008)

[13] E. Koch: *Exchange Mechanisms* in [18]

[14] A. Szabo and N.S. Ostlund: *Modern Quantum Chemistry* (McGraw Hill, New York, 1989)

[15] P.-O. Löwdin: *On the Non-Orthogonality Problem Connected with the Use of Atomic Wave Functions in the Theory of Molecules and Crystals,* J. Chem. Phys. **18**, 365 (1950)

[16] W. Pauli jr.: *Zur Quantenmechanik des magnetischen Elektrons*, Z. Phys. **43**, 601 (1927)

[17] E. Pavarini, E. Koch, and U. Schollwöck (Eds.):
Emergent Phenomena in Correlated Matter,
Reihe Modeling and Simulation, Vol. 3 (Forschungszentrum Jülich, 2013)
`http://www.cond-mat.de/events/correl13`

[18] E. Pavarini, E. Koch, F. Anders, and M. Jarrell (Eds.): *From Models to Materials*,
Reihe Modeling and Simulation, Vol. 2 (Forschungszentrum Jülich, 2012)
`http://www.cond-mat.de/events/correl12`

3 Understanding the Hubbard Model with Simple Calculations

Richard T. Scalettar
University of California Davis
Department of Physics and Astronomy
One Shields Ave., Davis, CA 95616

Contents

E. Pavarini and E. Koch (eds.)
Correlations and Phase Transitions
Modeling and Simulation Vol. 14
Forschungszentrum Jülich, 2024, ISBN 978-3-95806-751-6
http://www.cond-mat.de/events/correl24

1 Introduction

The Hubbard Hamiltonian,

$$\hat{\mathcal{H}} = -t \sum_{\langle \mathbf{jl} \rangle \sigma} \left(\hat{c}^{\dagger}_{\mathbf{l}\sigma} \hat{c}_{\mathbf{j}\,\sigma} + \hat{c}^{\dagger}_{\mathbf{j}\,\sigma} \hat{c}_{\mathbf{l}\sigma} \right) + U \sum_{\mathbf{l}} \left(\hat{n}_{\mathbf{l}\uparrow} - \frac{1}{2} \right) \left(\hat{n}_{\mathbf{l}\downarrow} - \frac{1}{2} \right) - \mu \sum_{\mathbf{l}} \hat{n}_{\mathbf{l}\sigma} \tag{1}$$

describes the 'hopping' of two species of fermions, spin $\sigma = \uparrow, \downarrow$, between neighboring sites $\langle \mathbf{jl} \rangle$ of a lattice, and interacting, when on the same site l, with an energy U. Here $\hat{n}_{\mathbf{l}\sigma} = \hat{c}^{\dagger}_{\mathbf{l}\sigma} \hat{c}_{\mathbf{l}\sigma}$ is the fermion number operator and μ is the chemical potential. I am going to assume familiarity with the basic properties of fermion creation and destruction operators $\hat{c}^{\dagger}_{\mathbf{l}\sigma}$ and $\hat{c}_{\mathbf{l}\sigma}$, including, for example, their anticommutation relations, $\{\hat{c}^{\dagger}_{\mathbf{l}\sigma}, \hat{c}_{\mathbf{j}\sigma'}\} = \delta_{\mathbf{jl}} \delta_{\sigma\sigma'}$ and $\{\hat{c}^{\dagger}_{\mathbf{l}\sigma}, \hat{c}^{\dagger}_{\mathbf{j}\sigma'}\} = 0$. We have written the interaction in 'particle-hole symmetric form'. This corresponds, up to an irrelevant constant term in the energy, to a simple shift in the chemical potential μ from the alternate expression $U \sum_{\mathbf{l}} \hat{n}_{\mathbf{l}\uparrow} \hat{n}_{\mathbf{l}\downarrow}$. We will see why this is more symmetric in section 6, and the deep implications of such symmetries in section 7.

A discussion of the Hubbard Hamiltonian is a truly immense undertaking. From a temporal point of view it encompasses a six decade history spanning the work of Hubbard, Anderson and Mott in the 1960's through a host of materials to which it has been applied: transition metal oxides, heavy fermions, cuprate superconductors, etc. [1]. Indeed, in the last 15 years a major focus of the Atomic and Molecular (AMO) community has been on realizing and characterizing the Hubbard model in systems of ultracold atoms [2, 3]. Attempts to solve the Hubbard model computationally have driven a rich set of stories in inhomogeneous Hartree-Fock (magnetism and stripe formation) [4], quantum Monte Carlo (QMC) [5] (including antiferromagnetic order, d-wave superconductivity, and the 'sign problem'), density matrix renormalization group (DMRG) methods (stripes and superconductivity) [6], and machine learning (ML) [7]. A recent review summarizes the breadth of these developments, applications and connections [8].

From a pedagogical point of view, then, the danger of a lecture (or even several lectures) on the Hubbard model is the temptation to focus on sophisticated techniques and applications. The audience can easily be left with a sense of the breadth and excitement of the field, but not with a concrete ability to '*do something*'.

The objectives of this lecture are to provide some specific calculations which shed light on the basic physics of the Hubbard model. We will begin with the non-interacting limit, i.e., obtaining the 'band structure' of the Hubbard model. We will emphasize that this already allows contact with some fascinating phenomena – localization by disorder, Fermi surface nesting and a divergence of the density of states linked to magnetism and superconductivity, and flat bands in which the electron energy is independent of momentum.

We will also describe two very interesting aspects of the non-interacting case. First, we will consider what happens when the motion of fermions to the left and to the right is unbalanced (the 'Hatano-Nelson' model). In this case the Hamiltonian is non-Hermitian! Second, we will relate a special choice of hoppings which can realize the surprising phenomenon of 'perfect quantum state transfer'.

After discussing the $U = 0$ limit, and these two interesting situations, we will examine the opposite limit when $t = 0$, or, more generally, the strong coupling case $U \gg t$. This will give us insight into a fundamental feature of the Hubbard model, the 'Mott plateau', where the density gets frozen at half-filling for an extended range of chemical potential, a signature of an insulating phase arising from interactions.

The final objective is to describe the consequences of a set of canonical transformations which can be performed on the Hubbard model. We will see these allow us to discern surprising and not immediately intuitive physics in some parameter regimes from the more evident physics in others. Our first illustration will be on the by now well-known connections between magnetism in the repulsive Hubbard models and s-wave superconductivity and charge density wave formation in the attractive Hubbard model. We will then turn to a recent discovery of a transformation which leads to a rigorous demonstration of pair density wave formation, a phase of matter which has proven elusive to achieve both experimentally and theoretically.

2 A classical mechanics prelude

Let's begin with a familiar, but seemingly completely unrelated problem, which will prove to have close mathematical analogies with the non-interacting Hubbard model. Consider a one-dimensional array of N uniform masses m connected to their neighbors by uniform springs γ. Newton's equations of motion for this mass-spring system are,

$$m\frac{d^2x_l}{dt^2} = -\gamma\big(x_l - x_{l+1}\big) - \gamma\big(x_l - x_{l-1}\big)\,, \tag{2}$$

where $x_l(t)$ is the displacement from equilibrium of mass l at time t. We will not boldface the site indices when we are in one dimension. We solve this problem with the *ansatz* $x_l(t) = a_l\, e^{i\omega t}$ which reduces the N coupled differential equations to N coupled algebraic equations for the amplitudes a_l. After cancelling the common factor of $e^{i\omega t}$ from all the terms, we find

$$m\,\omega^2\, a_l = \gamma\big(a_l - a_{l+1}\big) + \gamma\big(a_l - a_{l-1}\big)\,. \tag{3}$$

These equations are solved by introducing normal mode coordinates labeled by k,

$$a_l = e^{-ikl} a_0, \tag{4}$$

yielding the normal mode frequencies,

$$m\,\omega^2(k) = 2\gamma\big(1 - \cos(k)\big)\,. \tag{5}$$

Here we have now used notation emphasizing that the frequency depends on the 'momentum' k. (We will come back shortly to why calling k the momentum makes sense.)

Eq. (5) is an embarrassment of riches. From a collection of N linear equations (Eqs. (3)) we have an *infinite* set of solutions labeled by the continuous parameter k. Something is wrong, and it's because we did not treat the boundary conditions carefully. Equations (3) are only true for the masses which have both left and right neighbors, $l=2,3,\cdots N{-}1$. The two masses at the end have only a single neighbor if we adopt 'open boundary conditions' (obc). Here instead we use 'periodic boundary conditions' (pbc), and link oscillator $l=1$ to oscillator $l=N$ with an extra spring of potential energy $\frac{1}{2}\gamma(x_1{-}x_N)^2$. Then Eqs. (3) apply to *all* x_l, but only if we demand that $x_0 \equiv x_N$ and $x_1 \equiv x_{N+1}$.

This solves our problem of too many solutions, since it quantizes the previously unrestricted allowed values of momentum by requiring $e^{ikN}=1$ or, in other words, $k \in \frac{2\pi}{N}\{1,2,\cdots,N\}$. Because cosine is periodic, it is equivalent to set

$$k \in \frac{2\pi}{N}\left\{-\frac{N}{2}{+}1, -\frac{N}{2}{+}2\cdots\frac{N}{2}\right\} \qquad \text{(pbc)},$$

which has the advantage of making k symmetric about $k=0$.

It is useful to consider two special cases. When $k=0$, all masses have identical displacements $a_l = a_0$. The entire chain is shifted rigidly and $\omega(k)=0$. This is an example of a zero frequency 'Goldstone mode' associated with the translational invariance of our mass-spring system. Because only inter-mass springs are present, there is no potential tying any mass to a particular location in space. As a consequence the energy is invariant under a simultaneous translation of all the masses. Put another way, the choice of origin is irrelevant, the equations are unchanged by a constant shift of all the coordinates, $x_l \to x_l{+}c$. On the other hand, when $k=\pi$ the masses alternate $a_l = a_0\, e^{i\pi l} = a_0(-1)^l$. This results in the largest normal mode frequency (energy), $\omega^2 = 4k/m$. There is an interesting analogy with quantum mechanics here. If you sketch a_l versus l for this highest energy mode, you see there is a node between every mass. a_l wiggles as fast as possible. Similarly, in quantum mechanics we know that wiggly wave functions are associated with *high* kinetic energy.

One can also solve the open boundary condition case. The 'dispersion relation' giving the functional form for $\omega(k)$ is unchanged, but the N allowed momenta are shifted slightly to

$$k \in \frac{2\pi}{N{+}1}\{0,1,2,\cdots N{-}1\} \qquad \text{(obc)}.$$

The pbc case is a bit more simple, so we use it here. Besides simplicity, it is also the case that properties measured in finite length N chains with pbc are closer to the thermodynamic limit $N=\infty$ than obc. Specifically, finite size corrections often go as $1/N^2$ with periodic and $1/N$ with open boundary conditions.

A closing observation is that this solution of coupled oscillators all goes horribly wrong in the presence of anharmonicity. Indeed, even a single anharmonic oscillator, the problem of $F=ma$ with $V(x)=\frac{1}{2}kx^2+\frac{1}{4}ux^4$ is intractable. As we shall see below, the presence of interactions, i.e., quartic terms in the fermion creation and annihilation operators, $U\hat{n}_{1\uparrow}\hat{n}_{1\downarrow} = U\hat{c}^\dagger_{1\uparrow}\hat{c}_{1\uparrow}\hat{c}^\dagger_{1\downarrow}\hat{c}_{1\downarrow}$, analogous to the fourth power ux^4, is precisely what makes the Hubbard model impossible to solve for U non-zero.

That's a long time spent on classical mechanics! But we will see now that the exact same mathematics underlies the solution of the non-interacting Hubbard model.

3 The Hubbard model at $U = 0$

3.1 The 1D case (linear chain)

Let's write down the non-interacting ($U = 0$) Hubbard model for a 1D chain.

$$\hat{\mathcal{H}} = -t \sum_l \left(\hat{c}_l^\dagger \hat{c}_{l+1} + \hat{c}_{l+1}^\dagger \hat{c}_l \right) - \mu \sum_l \hat{c}_l^\dagger \hat{c}_l \, . \tag{6}$$

Because we will not have any interactions for this section, we have suppressed the spin index σ on the fermionic operators. That is, since U is the only thing that connects fermions with $\sigma = \uparrow$ to fermions with $\sigma = \downarrow$, when $U = 0$ we can just solve each spin sector independently.

Now just as we defined normal mode coordinates for the positions of our masses we can also here define linear combinations

$$\hat{c}_k^\dagger \equiv \frac{1}{\sqrt{N}} \sum_l e^{ikl} \, \hat{c}_l^\dagger \tag{7}$$

and their inverse,

$$\hat{c}_l^\dagger \equiv \frac{1}{\sqrt{N}} \sum_l e^{-ikl} \, \hat{c}_k^\dagger . \tag{8}$$

Note the resemblance between Eqs. (7) and (4). The fermion creation operator transformation is, however, a little more subtle than the classical mechanics case, because we must be sure that our new operators $\hat{c}_k$ obey the same fermionic anti-commutation relations as the originals. It is easy to prove this from the identities

$$\frac{1}{N} \sum_l e^{i(k-k')l} = \delta_{kk'} \tag{9}$$

and

$$\frac{1}{N} \sum_k e^{i(l-l')k} = \delta_{ll'} \tag{10}$$

which hold for the discrete allowed momenta $k, k' \in \frac{2\pi}{N}\{-\frac{N}{2}+1, -\frac{N}{2}+2, \cdots, \frac{N}{2}\}$. Equations (9) and (10) are the discrete analogs of the familiar orthogonality relations used in Fourier transforms.

We refer to a change of operators which preserves the commutation relations, such as Eq. (7), as a canonical transformation. This too is analogous language to classical mechanics, where a canonical transformation preserves the Poisson brackets. The last section of this chapter will focus on this topic.

Plugging the transformation Eq. (8) into the Hamiltonian, Eq. (6), and making use of Eqs. (9) and (10) yields

$$\hat{\mathcal{H}} = \sum_k \left(E(k) - \mu \right) \hat{c}_k^\dagger \hat{c}_k \tag{11}$$

where

$$E(k) = -2t\cos(k)\,. \tag{12}$$

The similarity between the right-hand sides of Eqs. (5) and (12) should be evident, from the appearance of $\cos(k)$ and the identification $2\gamma \leftrightarrow -\mu$. The energy levels of the 1D Hubbard chain range from $-2t \leq E(k) \leq +2t$. One refers to this range as the (1D chain) 'bandwidth' $W = 4t$.

It is interesting to think about the structure on Eq. (11). The Hamiltonian does not 'mix' different values of momentum k. When an electron of momentum k is destroyed, all that can happen is that an electron with the *same* momentum be created. This is the analog of the classical mechanical principal that normal modes do not mix: A system set into oscillation in a particular normal mode remains in that mode forever, and none of the others ever get excited.

Concerning the left-hand sides, one can wonder why the frequency/energy appears linearly in Eq. (12) in the quantum problem, whereas it was quadratic in the coupled oscillator calculation Eq. (5). The answer, of course, lies in the fact that Newton's equations involve $\frac{d^2}{dt^2}$, whereas the Schrödinger equation involves only $\frac{\partial}{\partial t}$.

We have exploited the translation invariance of the oscillator system and the Hubbard Hamiltonian to guess (make an *ansatz*) to extract the normal modes/band structure. In the absence of such symmetries the problem becomes one of diagonalizing a matrix.

Put another way, we can write the Hubbard Hamiltonian as

$$\hat{\mathcal{H}} = \begin{pmatrix} \hat{c}_1^\dagger & \hat{c}_2^\dagger & \hat{c}_3^\dagger & \hat{c}_4^\dagger & \hat{c}_5^\dagger & \cdots \end{pmatrix} \begin{pmatrix} -\mu & -t & 0 & 0 & 0 & \cdots \\ -t & -\mu & -t & 0 & 0 & \cdots \\ 0 & -t & -\mu & -t & 0 & \cdots \\ 0 & 0 & -t & -\mu & -t & \cdots \\ 0 & 0 & 0 & -t & -\mu & \cdots \\ \vdots & \vdots & \vdots & \vdots & \vdots & \ddots \end{pmatrix} \begin{pmatrix} \hat{c}_1 \\ \hat{c}_2 \\ \hat{c}_3 \\ \hat{c}_4 \\ \hat{c}_5 \\ \vdots \end{pmatrix}. \tag{13}$$

We happen to know (if we have some experience with tri-diagonal matrices) the eigenvalues and eigenvectors of the matrix in Eq. (13). The eigenvalues are just the $E(k)$ in Eq. (12), and the matrix of eigenvectors has entries $\Psi_{kl} = e^{ikl}$. I have used the notation Ψ deliberately, because these eigenvectors are quite literally the familiar plane-wave solutions of the free particle Schrödinger equation (on a discrete lattice). This justifies our referring to k as the momentum.

If we had not known this similarity transformation, we would have proceeded by diagonalizing the matrix by calling an appropriate BLAS/LAPACK routine. While we should avoid solving the eigenproblem numerically if an analytic solution is available, it is worth emphasizing it is not at all a big deal. We shall see the utility of this way of thinking in terms of matrix diagonalization when we discuss localized modes in the non-interacting Hubbard model.

Equation (12) gives the energy of a single electron, that is, the energy of the state $|k\rangle = c_k^\dagger|\mathrm{vac}\rangle$. It remains to discuss the computation of the energy with M electrons. The prescription is simple: if several electrons are present, the state $|\,k_1\,k_2\,\cdots k_M\,\rangle = c_{k_1}^\dagger c_{k_2}^\dagger \cdots c_{k_M}^\dagger|\mathrm{vac}\rangle$ has energy

$E(k_1) + E(k_2) + \cdots E(k_M)$. Of course the Pauli principle forbids any of the k_i from being the same for a given spin species.

If we are interested in the ground state of M electrons, we fill up (occupy) the states of lowest energy. The 'Fermi Energy' is the highest energy that is occupied for M particles. The seemingly mysterious choice of the minus sign in front of the hopping parameter t makes momentum $k = 0$ have the lowest energy, with a Fermi surface enclosing it.

Once we have the dispersion relation in hand, a very important quantity is the density of states $N(\omega)$. In words, $N(\omega)\,d\omega$ gives the number of $E(k)$ values which lie between ω and $\omega{+}d\omega$. Formally,

$$N(\omega) \equiv \frac{1}{N} \sum_k \delta\big(\omega - E(k)\big). \tag{14}$$

We can easily get $N(\omega)$ in the limit $N \to \infty$ where the k values become continuous

$$N(\omega) = \frac{1}{2\pi} \int_{-\pi}^{+\pi} dk\, \delta\big(\omega + 2t\cos(k)\big) = \frac{1}{\sqrt{4t^2 - \omega^2}}\,. \tag{15}$$

We have used the prescription $\frac{1}{N}\sum_k \to \frac{1}{2\pi}\int dk$ in going from a sum over discrete values separated by $2\pi/N$, to an integral. $N(\omega)$ diverges at $\omega = \pm 2t$ where the dispersion relation $E(k) = -2t\cos(k)$ is flat, an observation familiar from textbook discussions of band theory.

3.2 The 2D square lattice

On a 2D square lattice, the noninteracting Hubbard Hamiltonian is

$$\hat{\mathcal{H}} = -t \sum_{l_x,l_y} \big(\hat{c}^\dagger_{l_x,l_y} \hat{c}_{l_x+1,l_y} + \hat{c}^\dagger_{l_x+1,l_y} \hat{c}_{l_x,l_y} + \hat{c}^\dagger_{l_x,l_y} \hat{c}_{l_x,l_y+1} + \hat{c}^\dagger_{l_x,l_y+1} \hat{c}_{lx,l_y}\big) - \mu \sum_{l_x l_y} \hat{c}^\dagger_{l_x,l_y} \hat{c}_{l_x,l_y} \tag{16}$$

Although it is useful to work through the algebra for practice, the result is pretty reasonable, and we will just quote it. The process is just to redo the steps of the previous section with $l \to l_x, l_y$. The result is

$$\hat{\mathcal{H}} = \sum_{k_x,k_y} \big(E(k_x,k_y) - \mu\big) \hat{c}^\dagger_{k_x,k_y} \hat{c}_{k_x,k_y} \tag{17}$$

where

$$E(k_x,k_y) = -2t\cos(k_x) - 2t\cos(k_y) \tag{18}$$

gives the energy of an electron of momentum k_x, k_y. The energy levels of the Hubbard model on a square lattice range from $-4\,t \leq E(k_x,k_y) \leq +4\,t$. The bandwidth is $W = 8\,t$.

For many fermions, we again get the energy by just summing up the single particle levels out to a maximum Fermi Energy. However, in $d > 1$ one can ask for the shape of the contour of the boundary between the occupied and unoccupied k_x, k_y. This is referred to as the 'Fermi surface' (FS). For small k_x, k_y we can expand the cosines in Eq. (18)

$$E(k_x,k_y) \sim -4t + t\big(k_x^2 + k_y^2\big) \tag{19}$$

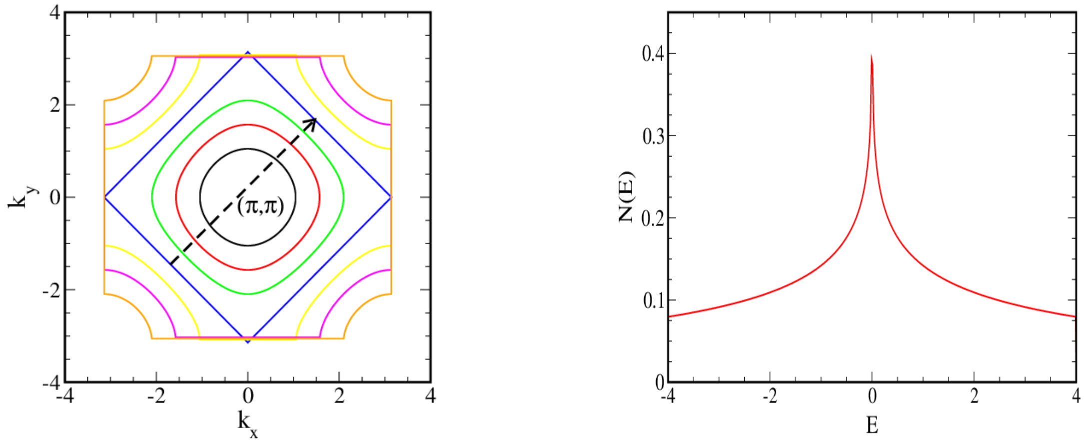

Fig. 1: *Left: The Fermi surfaces of the Hubbard model an a square lattice with nearest neighbor hopping for different numbers of particles (filling). They begin as circles at low density but evolve into a rotated square at half-filling. Right: The density of states $N(\omega)$ of the Hubbard model on a square lattice with nearest neighbor hopping. There is a divergence ('van Hove singularity') of $N(\omega)$ at $\omega = 0$ (half filling).*

and see that the FS is a circle about $(k_x, k_y) = (0, 0)$. Thinking in analogy with $E(k) = \hbar^2\left(k_x^2+k_y^2\right)/2m$ we see that the effective mass of the fermions $m = 1/(2t)$ (setting $\hbar = 1$).

In general $E(k)$ is not quadratic and the FS does not have a circular topology (sphere in three dimensions). Indeed, the FS's for different fillings (number of fermions) are shown in the left panel of Fig. 1. An interesting feature of the dispersion relation of Eq. (18) is 'perfect nesting'.

As seen in the left panel of Fig. 1, when the interior of the FS encompasses half of the allowed momenta (and hence the lattice is half-filled), the FS is a 'rotated square' and has the feature that a single wave-vector $(k_x, k_y) = (\pi, \pi)$ connects many points on the FS. The second is a 'van Hove singularity' in the density of states. At half-filling, $N(\omega{=}0)$ diverges. See the right panel of Fig. 1.

It turns out that both of these properties make the square lattice Hubbard model particularly prone to assuming ordered phases when the interaction U is turned on. The rough reason appeals to your knowledge of second order perturbation theory, where you know the effect of a perturbation $\hat{V}$ is to shift the energy E_n of eigenstate $|n\rangle$ by $E_n^{(2)} = \sum_{m\neq n} \frac{|\langle n|\hat{V}|m\rangle|^2}{E_n-E_m}$. If there are many states with $E_m = E_n$ the effect of $\hat{V}$ will be very large. This is precisely what happens with perfect nesting. The van-Hove singularity in $N(\omega)$ has been suggested to be implicated in high superconducting transition temperatures. That is, thinking of the BCS formula for the critical temperature in terms of the coupling constant λ and the density of states, $T_c \sim e^{-1/\lambda N(\omega)}$, we see that a large $N(\omega)$ suggests a large T_c.

We conclude by noting that there are materials, like the cuprate superconductors, for which the square lattice is considered appropriate: the copper atoms in the CuO$_2$ planes reside on a square lattice.

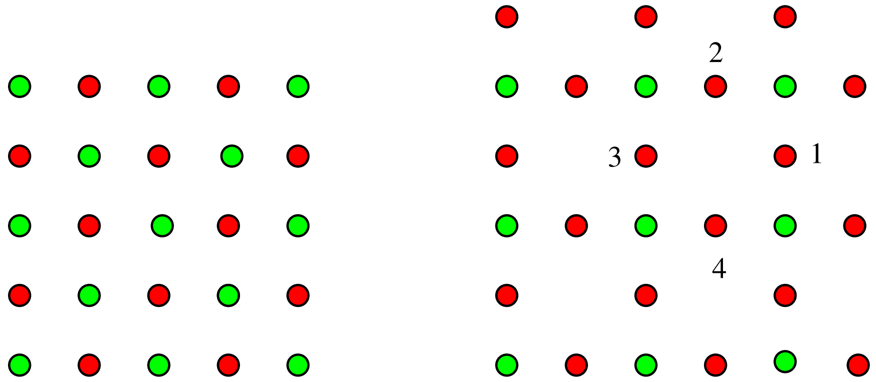

Fig. 2: *<u>Left</u>: The square lattice can be decomposed into two groups $\mathcal{A}$ and $\mathcal{B}$ of sites, colored as red and green, such that the neighbors of a red site are only green and vice-versa. The geometry is said to be 'bipartite'. <u>Right</u>: The Lieb lattice is also bipartite, but note there are twice as many red sites as green sites.*

3.3 The Lieb lattice and "flat bands"

An interesting feature of the square lattice is that its sites can be divided into two sublattices (red and green in the left panel of Fig. 2) such that the nearest neighbors of red sites are always green and the nearest neighbors of green sites are always red. Such a geometry is said to be 'bipartite'. This property has deep implications for the physics, most fundamentally its consistency with antiferromagnetic order. In a model where the energy is minimized by neighboring spins pointing in opposite directions, one can place the electrons so that those with up spins occupy one sublattice and those with down spins reside on the other sublattice with no frustration (neighboring sites with high energy because their spins are in the same direction).

The honeycomb lattice describing the positions of the carbon atoms in a sheet of graphene is also bipartite. In both the square and honeycomb cases, the numbers of red and green sites are identical. We will next consider the Hubbard model on a Lieb lattice, shown in the right panel of Fig. 2. Although we blitzed through going from a 1D chain to a 2D square lattice, it is worth being a bit more careful with this one, because going to momentum space does not quite complete the process of diagonalization.

Aside: The serious student of the Hubbard model would do well to compute $E(k_x, k_y)$ for a honeycomb geometry. This is useful 'technical' practice, as dealing with axes which are not parallel to $\hat{x}$ and $\hat{y}$ requires some care. It is also of course important physically towards the understanding of graphene. Just as the dispersion relation of the square lattice has interesting properties like Fermi nesting, the honeycomb lattice hosts Dirac fermions, electrons whose kinetic energy is linear in their momenta.

For the Lieb lattice, the repeating structure contains a three atom basis. In transforming to momentum space we must include a 'band' index for the basis, in addition to momentum. The resulting Hamiltonian is diagonal in (k_x, k_y) but the three basis states of given (k_x, k_y) mix with the 3×3 matrix

$$\begin{pmatrix} 0 & -t\big(1+e^{ik_x}\big) & -t\big(1+e^{ik_y}\big) \\ -t\big(1+e^{-ik_x}\big) & 0 & 0 \\ -t\big(1+e^{-ik_y}\big) & 0 & 0 \end{pmatrix}. \tag{20}$$

Diagonalizing this matrix completes the process of identifying the single particle states. The crucial and surprising feature is that one of the energy bands has $E(k_x, k_y) = 0$: The (kinetic) energy is independent of momentum. A plot of energy versus momentum yields a horizontal line, i.e., a 'flat band'.

One can actually understand the origin of the zero energy states in real space. Consider the four sites enumerated as $1, 2, 3, 4$ in Fig. 2(right). Imagine a wavefunction with nonzero components only on these four sites, and make those components all of equal magnitude, but alternating in sign so that the entries for sites $1, 3$ are positive and those for $2, 4$ are negative. It is fairly easy to see that if you apply the real space Hamiltonian matrix of Eq. (13), but generalized to hopping on the Lieb lattice, the result is the zero vector: Because only sites $1, 2, 3, 4$ have nonzero components. hopping is possible only to the four green sites which adjoin them. However, because of the sign alternation of the components in the original vector, there is a perfect cancellation of the hopping. It is clear that this numbering $1, 2, 3, 4$ can be performed around *any* of the 'holes' in the Lieb geometry. There is an eigenvector of zero eigenvalue for each unit cell.

The Lieb lattice is also often considered as a more refined picture of the cuprates, because the oxygen atoms of a CuO_2 sheet lie on the midpoints of the bonds of the square array of copper atoms, just as the red circles in Fig. 2. The flat band is entirely of 'oxygen' origin, as the construction above demonstrates.

3.4 Localization by disorder

Examining Eqs. (6) and (13), it is clear that disorder in the chemical potentials (making the energy for a fermion to occupy a particular location site-dependent) can be simply incorporated by changing the matrix elements $\mu \to \mu_l$. The transformation Eq. (7) no longer diagonalizes the Hamiltonian, as translation invariance is broken. However the diagonalization can still be accomplished numerically.

A very interesting phenomenon occurs. While the plane wave eigenstates in the absence of randomness extend throughout the lattice, the eigenstates in the presence of disorder can be 'localized', meaning that the components of the eigenstate are significant only on a fraction of the sites and exponentially small elsewhere.

Figure 3 shows the square of the ground state wavefunction for a 1D chain of $N = 1024$ sites for different ranges Δ of the random chemical potential (site energy) $-\Delta/2 < \mu_l < +\Delta/2$ and no interactions ($U = 0$). Wave functions have been shifted so that their maximum amplitude is at the lattice center $x = N/2 = 512$. In 1D all wavefunctions fall off exponentially for an arbitrarily small Δ. The same is true in 2D, though it was a very challenging assertion to prove [9]. In 3D, the eigenstates near the center of the DOS are delocalized, and those at the

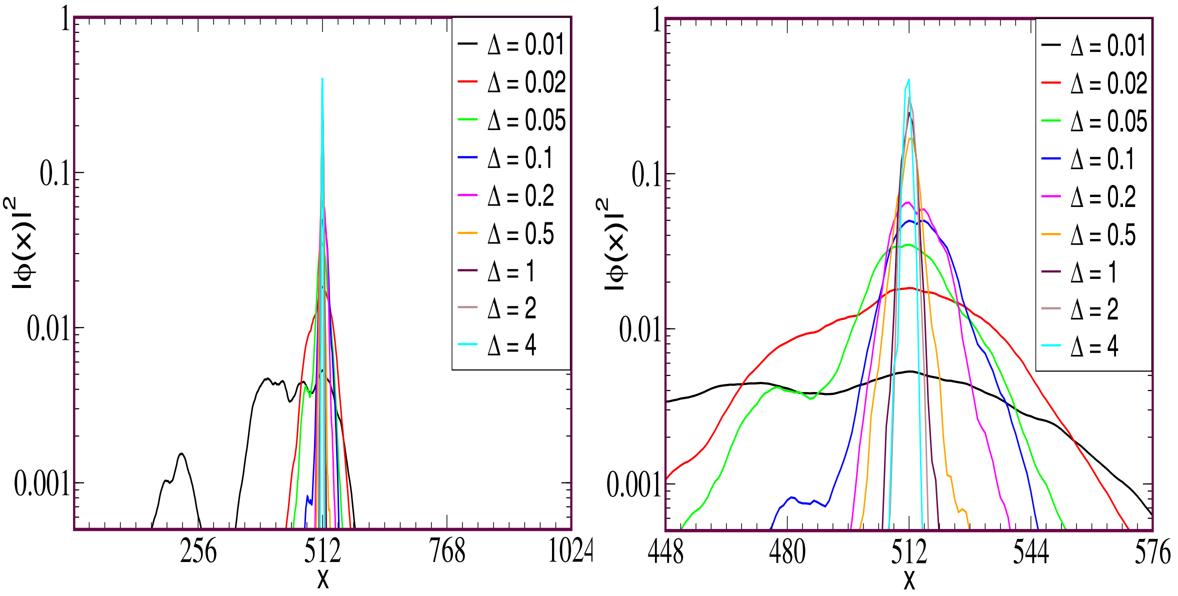

Fig. 3: *Left: Square of amplitude of the ground state wavefunction for a disordered 1D chain. As the disorder amplitude Δ decreases, the wavefunction is increasingly spread out, but it remains localized for any nonzero Δ. Right: Same data but blown up near the lattice center. Note the logarithmic scale on the vertical axes.*

edges (high and low energies) are localized. The energy separating these cases is referred to as the 'mobility edge.' Detailed numerical work is reviewed in [10].

Here one can continue the analogy with classical systems. A beautiful discussion of Maradudin describes localization about a single defect mass in a 1D mass-spring chain [11].

There is a lot to unpack in the comments above, and indeed there was a long effort to understand the nature of localization in two dimensions. Indeed, a major theme of condensed matter physics for nearly three decades concerned whether non-zero U could result in delocalization in 2D [12]. But the main message for us here is that many aspects of this deep and beautiful chapter of condensed matter physics conform to the title of this chapter: From a computational perspective they boil down to the very familiar and simple question of diagonalizing a matrix!

4 The Hatano-Nelson model

A recently emerging area of interest concerns non-Hermitian Hamiltonians [13–15]. The simple methods we have introduced give us a foothold into this field as well. For concreteness, let's consider the 'Hatano-Nelson Hamiltonian' in one dimension

$$\hat{\mathcal{H}} = -t \sum_{l=1}^{L} \left(e^{h}\, \hat{c}^{\dagger}_{l+1} \hat{c}_{l} + e^{-h}\, \hat{c}^{\dagger}_{l} \hat{c}_{l+1} \right) + \sum_{l} \mu_l\, \hat{c}^{\dagger}_{l} \hat{c}_{l} \quad . \tag{21}$$

which is obtained from the Hubbard model of Eq. (6) by introducing a hopping which is different for fermions moving to the left and to the right. The parameter h controls the degree of anisotropy in the hopping, and μ_l are random site energies. Periodic boundary conditions connect sites 1 and L.

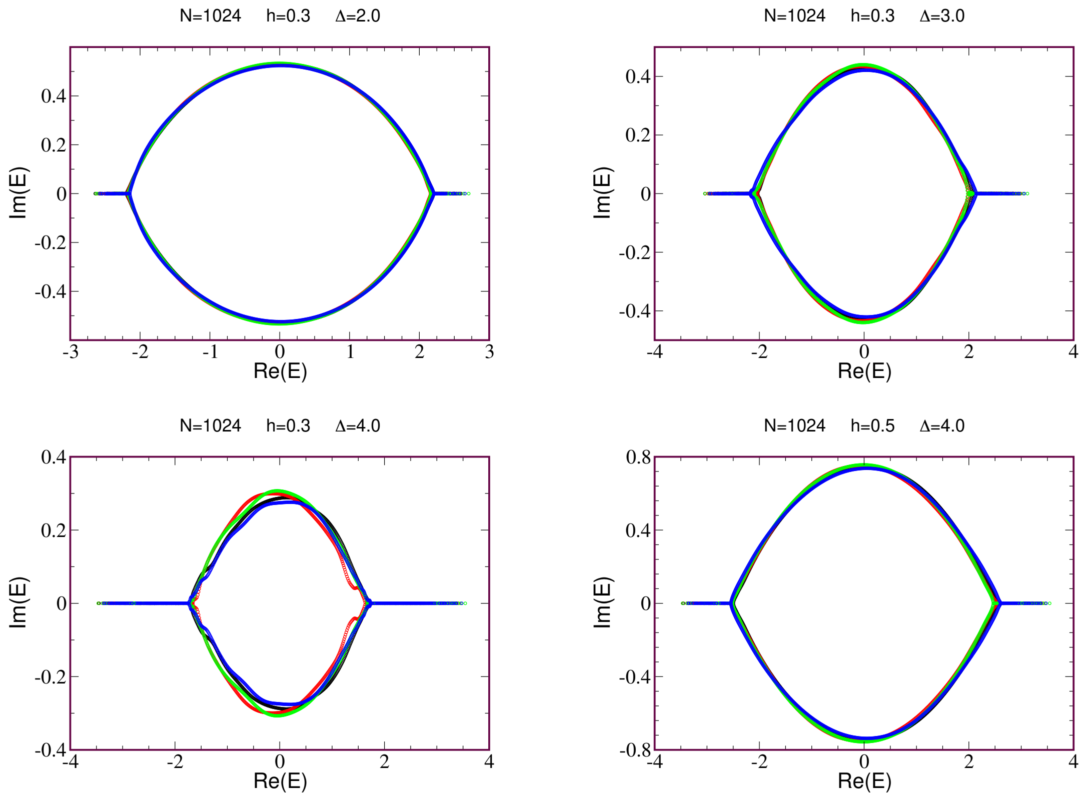

Fig. 4: *Eigenvalues of the Hatano-Nelson Hamiltonian for an $N = 1024$ site chain. The random chemical potentials are chosen from a box distribution $-\varDelta < \mu_l < +\varDelta$. Four disorder realizations are shown in each figure. As the disorder $\varDelta$ increases at fixed h, the real 'wings' become longer. As h increases at fixed $\varDelta$, the imaginary part of the eigenvalues grows.*

In the case where there is no disorder, $\mu_l = 0$, we can try the same canonical transformation as Eq. (7), which leads to eigenvalues then having the form

$$E(k) = -t\big(e^{-h-ik} + e^{h+ik}\big) = -2t\big(\cosh(h)\cos(k) + \mathrm{i}\sinh(h)\sin(k)\big). \tag{22}$$

As k varies from 0 to 2π (in steps of $1/L$) this describes an ellipse centered at the origin of the complex plane. The length of the ellipse along the real axis is $4t\cosh(h)$ and along the imaginary axis, $4t\sinh(h)$. The periodic boundary conditions are crucial. Without them one can do a 'gauge transformation', or in more elementary language a redefinition of the eigenvectors, which makes h disappear from the problem: $\tilde{v}_l = e^{-hl}v_l$. Then the matrix is Hermitian, with all real eigenvalues.

As remarked earlier, in the presence of disorder the transformation of Eq. (7) no longer works. Instead one simply diagonalizes the matrix,

$$H = \begin{pmatrix} \mu_1 & -t\,e^{h} & 0 & 0 & 0 & \cdots & -t\,e^{-h} \\ -t\,e^{-h} & \mu_2 & -t\,e^{h} & 0 & 0 & \cdots & 0 \\ 0 & -t\,e^{-h} & \mu_3 & -t\,e^{h} & 0 & \cdots & 0 \\ \vdots & \vdots & \vdots & & & \vdots & \ddots \\ -t\,e^{h} & 0 & 0 & 0 & 0 & -t\,e^{-h} & \mu_L \end{pmatrix}. \tag{23}$$

When disorder is present, the original elliptical distribution in the complex plane develops 'wings' extending out along the real axis, see Fig. 4. The eigenvectors associated with the real eigenvalues on the wings are localized, and those on the wings are real. The plausibility argument for this assertion is that one can accumulate the h factors on any desired link (or set of links) through the gauge transformation noted above. For a localized eigenvector one can move all the h factors to a lattice location where the wave function is arbitrarily (exponentially) small. So those eigenvectors are governed by a piece of H which can be made Hermitian in the only part of the lattice that matters to them. Thus, they will have real eigenvalues. This doesn't work for extended eigenvectors, so they have complex eigenvalues.

The numerical results of Fig. 4 reveal some interesting general features of computational work on Hubbard models (and even more generally). Except for $h = 0.3$, $\Delta = 4.0$, $N = 1024$ is large enough that the results are 'self-averaging': The eigenspectra for different disorder realizations largely coincide. However, when h is small and the disorder is large enough, one begins to see significant variation from realization to realization (lower left panel of Fig. 4. The $N = 1024$ dimensional matrices can be diagonalized in about half a minute using the LAPACK routine *dgeevx*. Diagonalization scales as N^3 so $N = 4096$ would only take about a half-hour.

5 Perfect quantum state transfer

One of the most familiar and prominent aspects of quantum mechanics is the uncertainty principle. Our knowledge of the position and momentum of a quantum mechanical particle must obey $\Delta x \Delta p \geq \hbar/2$. Moreover, we expect uncertainties in position to grow in time ('spreading of the wave packet'). Consider a particle moving in d=1 with no potential $V(x)$=0. Contrast the motion of the 'slowest' part of the wave-packet at $x-\Delta x$ moving with momentum $p-\Delta p$, and the 'fastest' part of the wave-packet at $x+\Delta x$ moving with momentum $p+\Delta p$. The separation of the extremes grows as $2(\Delta x+t\Delta p)$. This provides a very crude picture for spreading, but this linear growth of uncertainty with time is not correct. Instead, $\Delta x \sim \sqrt{t}$ as can be seen by explicitly solving the free particle Schrödinger equation, or else simply by noting its similarity to the classical diffusion equation.

It is therefore remarkable that we can construct Hubbard models which exhibit 'perfect quantum state transfer' (QST). That is, a wavefunction perfectly localized at one end of a $d = 1$ chain will, at later times, be perfectly localized at the opposite end! Although spreading does occur at intermediate times, the wave function somehow re-coalesces to have zero position uncertainty. How is this (quantum mechanically) counter-intuitive result realized? We know that each eigenstate $|\phi_n\rangle$ of a quantum mechanical system evolves with a frequency ω_n=$E_n/\hbar$, where E_n is its energy. A generic (localized) wave function will be a linear combination of the $|\phi_n\rangle$ and it seems plausible that to get a different localized wavefunction at later time, the frequencies ω_n must somehow be such that the maxima of the different waves can come into alignment. An obvious way that could happen is if the ω_n were equally spaced. We are thus led to think about whether we can find a tridiagonal matrix whose eigenvalues have constant separation. Uniform hoppings $t_{l,l+1} = t$ will not work, since the resulting eigenvalues are $E(k)$=$-2t\cos(k)$.

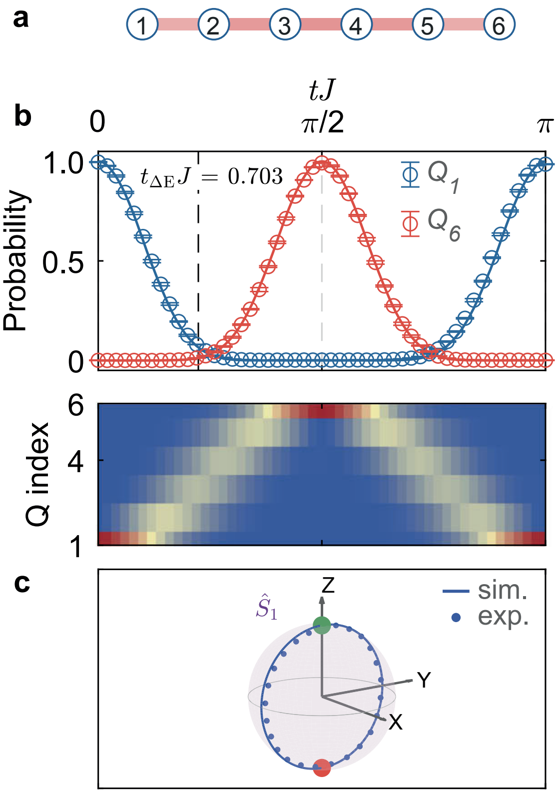

Fig. 5: (a,b): *Perfect quantum state transfer has been achieved experimentally in a collection of superconducting qubits with tunable couplings adjusted according to the prescription described in the text for a $N{=}6$ site chain. The system starts with qubit $Q{=}1$ excited, and the excitation is transferred to the other end of the chain $Q{=}6$ at a time $t = \pi/(2J)$ later.* **(c):** *A picture of the time evolution from the angular momentum perspective. Image taken from [16].*

A clever thought is this: The components of angular momentum operators have equally spaced levels. Consider $2\,\hat{S}_x = \hat{S}_+ {+} \hat{S}_-$ whose action on an eigenstate $|jm\rangle$ of $\hat{S}^2$ and $\hat{S}_z$ is $2\,\hat{S}_x|j,m\rangle = \sqrt{j(j{+}1) - m(m{+}1)}|j,m{+}1\rangle + \sqrt{j(j{+}1) - m(m{-}1)}|j,m{-}1\rangle$. Taking $j = 5/2$, there are six states with eigenvalues $2m\hbar = \big\{-5,-3,-1,+1,+3,+5\big\}\hbar$. Using the expression above, the state $|j,m\rangle$ is connected to its neighbors $|j,m{+}1\rangle$ and $|j,m{-}1\rangle$ with coefficients $\sqrt{5}$, $\sqrt{8}$, $\sqrt{9}$, $\sqrt{8}$, $\sqrt{5}$. (We have now set $\hbar = 1$.)

We also know the time evolution. A spin starting with z component of angular momentum $m = +5/2$, under the influence of $\hat{\mathcal{H}} = 2J\,\hat{S}_x$ will rotate to $m = -5/2$ in a time $t = \pi/(2J)$. A picture of this is provided in panel (c) of Fig. 5.

We now note that this mathematical structure of an operator connecting adjacent states (a tridiagonal matrix) is precisely that of the near-neighbor Hubbard kinetic energy operator in 1D. Translating the angular momentum formalism to this language, we see that if we had a six site chain with $\hat{\mathcal{H}} = -\sum_l t_{l,l+1}\big(\hat{c}^\dagger_{l+1}\hat{c}_l + \hat{c}^\dagger_l\hat{c}_{l+1}\big)$ and $t_{1,2} = \sqrt{5}J,\ t_{2,3} = \sqrt{8}J,\ t_{3,4} = \sqrt{9}J,\ t_{4,5} = \sqrt{8}J,$ and $t_{5,6} = \sqrt{5}J$, the eigenenergies would be $\{-5,-3,-1,+1,+3,+5\}\ J$. The time evolution would be such that an electron beginning with $\big|\psi(t{=}0)\big\rangle = \hat{c}^\dagger_1\,|\text{vac}\rangle$ will evolve *perfectly* into $\big|\psi(t{=}\pi/(2J))\big\rangle = \hat{c}^\dagger_6\,|\text{vac}\rangle$.

We have thus constructed a hopping Hamiltonian which exhibits perfect Quantum State Transfer. The general rule for a chain of arbitrary length N is $t_{l,l+1} = \sqrt{l(N{-}l)}$ [17]. This prescription was first noted by Christandl [18] and later generalized by Kay [19].

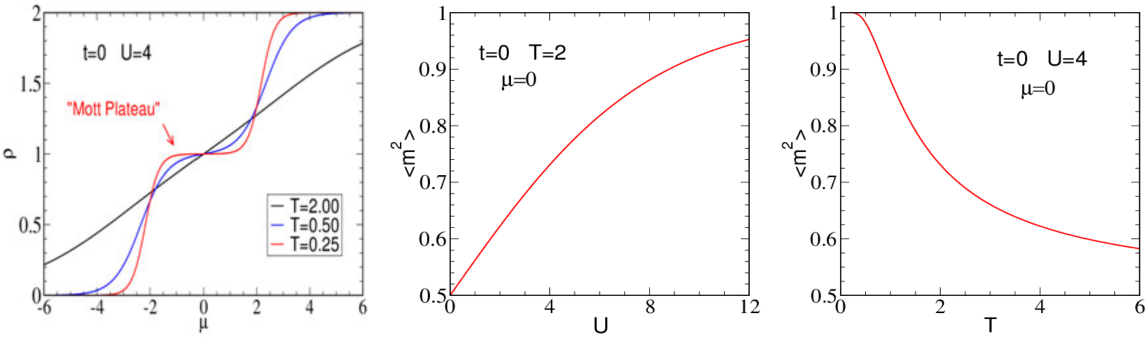

Fig. 6: *Left: The density ρ as a function of chemical potential for a single site with $U = 4$. As the temperature T is lowered, a Mott plateau develops. Center: The local moment $\langle \hat{m}^2 \rangle$ as a function of U at fixed temperature $T = 2$. Right: The local moment $\langle \hat{m}^2 \rangle$ as a function of T at fixed temperature $U = 4$. Local moments develop as either T is reduced or U is increased. Chemical potential $\mu = 0$ in the middle and right panels, so the site is half-filled.*

6 The strong coupling limit

We invested a lot of time on the non-interacting Hubbard model. It was time well-spent, since we saw there is a lot of very interesting physics, from nesting, to localization, to perfect Quantum State Transfer. But, of course we should not be satisfied with this $U = 0$ limit. In this section, we will consider the opposite extreme of strong coupling, $t = 0$, for which the Hubbard model becomes a collection of single sites

$$\hat{\mathcal{H}} = U \sum_{\mathbf{j}} \Big(\hat{n}_{\mathbf{j}\uparrow} - \frac{1}{2}\Big)\Big(\hat{n}_{\mathbf{j}\downarrow} - \frac{1}{2}\Big) - \mu \sum_{\mathbf{j}} \big(\hat{n}_{\mathbf{j}\uparrow} + \hat{n}_{\mathbf{j}\downarrow}\big) \tag{24}$$

which can be considered independently.

Each site has four possible configurations: empty, having a single electron (either spin up or spin down) or doubly occupied. The states $|0\rangle, |\uparrow\rangle, |\downarrow\rangle, |\uparrow\downarrow\rangle$ are eigenstates of $\hat{\mathcal{H}}$ with eigenvalues $+U/4$, $-\mu - U/4$, $-\mu - U/4$, $+U/4 - 2\mu$ respectively. At this point we can see the meaning of the interaction term being 'particle-hole symmetric': the contribution of the interaction term in Eq. (24) to the state $|0\rangle$ with two *holes* is identical to that of the state with two *particles* $|\uparrow\downarrow\rangle$. An important consequence of this convention is that half-filling conveniently occurs always at $\mu = 0$ for any value of temperature T and interaction strength U. Indeed, if we are on a bipartite lattice, this is true even if the hopping t is non-zero, as we shall see in the subsequent section. The $t = 0$ partition function then consists of a term

$$Z = \sum_{\alpha} \langle \alpha | e^{-\beta \hat{\mathcal{H}}} | \alpha \rangle = e^{-\beta U/4} + 2 e^{\beta\mu + \beta U/4} + e^{2\beta\mu - \beta U/4}, \tag{25}$$

for every site of the lattice. The energy per site is,

$$E = Z^{-1} \sum_{\alpha} \langle \alpha | \hat{\mathcal{H}} e^{-\beta \hat{\mathcal{H}}} | \alpha \rangle = \frac{1}{Z} \bigg(\frac{U}{4} e^{-\beta U/4} + 2\Big(-\frac{U}{4} - \mu\Big) e^{\beta\mu + \beta U/4} + \Big(\frac{U}{4} - 2\mu\Big) e^{2\beta\mu - \beta U/4} \bigg). \tag{26}$$

Meanwhile, the occupation is

$$\rho = \langle \hat{n} \rangle = Z^{-1} \sum_{\alpha} \big\langle \alpha \big| \, \hat{n} e^{-\beta \hat{\mathcal{H}}} \big| \alpha \big\rangle = \frac{1}{Z} \big(2e^{\beta\mu + \beta U/4} + 2e^{2\beta\mu - \beta U/4} \big). \tag{27}$$

A plot of the density ρ versus chemical potential μ, Fig. 6 (left), exhibits one of the most fundamental features of the Hubbard model, namely the "Mott insulating gap". As μ increases the density increases, but, at sufficiently low temperature, gets stuck at half-filling, $\rho{=}1$, for a range $-U/2{<}\mu{<}{+}U/2$. This jump in μ reflects the fact that once there is one electron on the site, the cost to add a second electron requires an additional energy cost U. It is important to emphasize that this is an entirely different type of gap than that which occurs in a band insulator when a band is completely filled with two electrons per state and there is a range of energy in which there are no states before the bottom of the next band begins. The Mott gap occurs for an odd number of electrons per site, a situation which band theory would insist on resulting in a metal.
In addition to the Mott insulating gap, one of the central features of the Hubbard model is the presence of magnetism. As noted earlier, the energy of the empty and doubly occupied states is $+U/4$, while that of the singly occupied states is $-U/4$. Thus the formation of 'local moments' (sites with non-zero spin) is energetically favored. The local moment $\langle \hat{m}^2 \rangle = \big\langle (\hat{n}_\uparrow {-} \hat{n}_\downarrow)^2 \big\rangle$ is a good measure of this tendency: it takes on the value 0 for empty and doubly occupied sites and is 1 for single occupation. Plots of $\langle \hat{m}^2 \rangle$ versus U at fixed temperature T and versus temperature T at fixed U are shown in 6 (center) and 6 (right) respectively. Large U and low T result in perfect moment formation $\langle \hat{m}^2 \rangle \to 1$. A nonzero hopping t introduces additional quantum fluctuations. For finite U, $\langle \hat{m}^2 \rangle$ will not go to 1 even at $T = 0$.
Moment formation, such as we are observing in the single site limit, is a pre-requisite for magnetism, but one also needs the magnetic moments on different sites to align (ferromagnetism) or antialign (anti-ferromagnetism) to speak of long range order. The physical picture for antiferromagnetism is that electrons on neighboring sites with spins which are antiparallel can hop onto each other, resulting in a second order lowering of energy proportional to t^2/U. This hopping is forbidden for electrons of parallel spin. Hence antiferromagnetism is favored. Ferromagnetism can also occur in the Hubbard model, but is much harder to achieve (in the single band case we are considering here). It is not too difficult to do a mean field calculation, and this will reveal magnetic behavior. However, we will not describe that here. Instead, we will note that one can easily compute the Green function in the $t{=}0$ limit (and also, actually, in the $U{=}0$ limit). Much of the initial progress in many-body physics rested upon diagrammatic perturbation theory, where the central quantity is the Green function. Understanding that technology is a long slog, so it is pleasant to be able to do a simple calculation of this somewhat mysterious object. Consider

$$G_\uparrow(\tau) \equiv \big\langle \hat{c}_\uparrow(\tau) \hat{c}_\uparrow^\dagger(0) \big\rangle$$

in this single-site limit. Only two of the states, those with the up spin occupied, contribute. For simplicity we will focus on the case $\mu = 0$. It is straightforward to show that,

$$G_\uparrow(\tau) = \frac{e^{+\beta U/4} e^{-\tau U/2} + e^{-\beta U/4} e^{\tau U/2}}{2\, e^{\beta U/4} + 2\, e^{-\beta U/4}}.$$

The Green's function is related to the spectral density $A(\omega)$ by the relation,

$$G(\tau) = \int_{-\infty}^{+\infty} A(\omega) \frac{e^{-\omega\tau}}{e^{-\beta\omega}+1}\, d\omega\,.$$

If you plug in

$$A(\omega) = \frac{1}{2}\left(\delta\Big(\omega - \frac{U}{2}\Big) + \delta\Big(\omega + \frac{U}{2}\Big)\right)$$

and do the integral you get precisely the $G_\uparrow(\tau)$ we computed. The spectral function of the $t=0$ Hubbard model consists of two delta function peaks separated by U. $A(\omega)$ is the many-body counterpart of the single particle density of states in the non-interacting limit. The separation of the peaks in $A(\omega)$ by U is then akin to a band gap which would occur in $N(\omega)$, and is thus sensibly referred to as the Mott gap.

7 Particle-hole transformations

Our final topic focuses on the implications of certain canonical transformations on the low temperature properties of the Hubbard model and its generalizations. We will assume here a familiarity with the ground state phase diagram of the repulsive Hubbard model, especially that it exhibits long range AF order at half-filling with the long range spin ordering being degenerate along any of S_x, S_y or S_z directions (Heisenberg universality class).
Let us begin by considering a 'partial' particle-hole transformation (PHT),

$$\hat{c}_{\mathbf{j}\downarrow} \rightarrow (-1)^{\mathbf{j}}\, \hat{c}^{\dagger}_{\mathbf{j}\downarrow} \tag{28}$$

in which only the down spin operators are affected. In writing Eq. (28) we assume we are on a bipartite lattice (see Sec. 3.3) so that the symbol $(-1)^{\mathbf{j}}$ takes on the value $+1$ for $\mathbf{j} \in \mathcal{A}$ and -1 of $\mathbf{j} \in \mathcal{B}$. Under this transformation, the kinetic energy remains unchanged because, although it interchanges the order of the creation and destruction operators in the hopping, that reversal can be undone by invoking the anticommutation relations. The resulting minus sign is precisely canceled by the signs from the $(-1)^{\mathbf{j}}$ terms, as long as only near neighbor hopping occurs (so that one site is in $\mathcal{A}$ and the other is in $\mathcal{B}$). What does the PHT do to the potential energy? The down spin density $\hat{n}_{\mathbf{j}\downarrow} \leftrightarrow 1 - \hat{n}_{\mathbf{j}\downarrow}$ and, as a consequence the sign of U is reversed, mapping attraction to repulsion and vice-versa. Notice that writing the interaction in particle-hole symmetric form makes this observation especially easy to discern.
Finally, consider the chemical potential term. As noted immediately above, the down spin density (but not the up spin density) picks up a minus sign. The roles of charge and spin operators are interchanged $\hat{n}_{\mathbf{j}\uparrow} + \hat{n}_{\mathbf{j}\downarrow} \leftrightarrow \hat{n}_{\mathbf{j}\uparrow}\hat{n}_{\mathbf{j}\downarrow}$. Thus the chemical potential term in $\hat{\mathcal{H}}$, $-\mu(\hat{n}_{\mathbf{j}\uparrow} + \hat{n}_{\mathbf{j}\downarrow})$, becomes $-\mu(\hat{n}_{\mathbf{j}\uparrow} - \hat{n}_{\mathbf{j}\downarrow})$ which is a Zeeman energy. Thus, $\mu \leftrightarrow B_z$ under this PHT.
To see how useful this mapping is, let's look at how physical observables are transformed. We note that because Eq. (28) applies only to the down spin operators, correlations of the Z component of spin map onto density correlations. On the other hand, the XY spin operators map onto s-wave pairing $\hat{c}^{\dagger}_{\mathbf{j}\uparrow}\, \hat{c}_{\mathbf{j}\downarrow} \leftrightarrow \hat{c}^{\dagger}_{\mathbf{j}\uparrow}\, \hat{c}^{\dagger}_{\mathbf{j}\downarrow}$.

With those mappings in place, the connections between the attractive and repulsive Hubbard models become clear. The fact that the square lattice repulsive Hubbard model has degenerate Z and XY antiferromagnetic spin order in its ground state at half-filling immediately implies the degeneracy of charge density wave and superconducting correlations in the attractive case. This is not at all an obvious thing if we just thought about the attractive model in isolation.

But there is even more to glean here: In a repulsive Hubbard model with antiferromagnetic order, a Zeeman field B_z causes AF Heisenberg spins to 'lie down' and order in the XY plane, perpendicular to the field. This is so because spins in the XY plane can tilt upwards into the Z direction and lower their energy linearly in the out of plane angle, whereas the disruption to the AF results in an energy cost which is quadratic in the angle. If the AF order were in the Z direction, tilting the spins would pick up only a quadratic field energy. The key observation is then to note that when we do the PHT such a Zeeman term in the $+U$ model becomes a chemical potential in the $-U$ model. The doped attractive Hubbard model is thus seen to have a tendency for s-wave superconducting order. Indeed, because the field in the z direction reduces the universality class from Heisenberg to XY, the transition to s-wave SC order can occur at finite temperature. This mapping and its consequences for *conventional* superconductivity have been known for nearly four decades. We will now show how an alternate canonical transformation lends similar insight into *exotic* superconductivity, something only realized recently [20].

To see this, let's consider a canonical transformation,

$$\hat{c}_{\mathbf{j}\downarrow} \rightarrow (-1)^{\mathbf{j}}\, \hat{c}_{\mathbf{j}\downarrow} \tag{29}$$

which is similar to that of Eq. (28) in having the staggered phase factor $(-1)^{\mathbf{j}}$, and acting only on the down spins, but lacks the transformation from particle to holes. Applying this to the attractive Hubbard model results in

$$\hat{\mathcal{H}}_{\sigma_z} = -t \sum_{\langle \mathbf{ij} \rangle} \sum_{\alpha\beta} \hat{c}^{\dagger}_{\mathbf{i}\alpha}\, \sigma_z^{\alpha\beta}\, \hat{c}_{\mathbf{j}\beta} - \mu \sum_{i,\alpha} \hat{n}_{\mathbf{i}\alpha} + U \sum_{\mathbf{i}} \Big(\hat{n}_{\mathbf{i}\uparrow} - \frac{1}{2}\Big)\Big(\hat{n}_{\mathbf{i}\downarrow} - \frac{1}{2}\Big) \tag{30}$$

The Pauli matrix σ_z has spin indices α, β and results in hopping amplitudes for the spin-up and spin-down fermions differing in sign.

We can now infer the properties of this 'σ_z Hubbard model' from those of the attractive Hubbard model. While the CDW correlations map into themselves, the s-wave SC phase is altered. Specifically, the on-site pairing transforms as $\Delta_{\mathbf{j}} = c_{\mathbf{j}\downarrow} c_{\mathbf{j}\uparrow} \rightarrow \Delta_{\mathbf{j}} = (-1)^{\mathbf{j}} c_{\mathbf{j}\downarrow} c_{\mathbf{j}\uparrow}$. Therefore, the pairing remains on-site but with an alternating sign, indicating that the system displays s-wave pair density wave (PDW) superconductivity: The pairing function can be written as

$$\Delta^{\dagger} = \frac{1}{\sqrt{N}} \sum_{j} (-1)^{\mathbf{j}}\, c^{\dagger}_{\mathbf{j}\uparrow} c^{\dagger}_{\mathbf{j}\downarrow} = \frac{1}{\sqrt{N}} \sum_{\mathbf{k}} c^{\dagger}_{\mathbf{k}\uparrow} c^{\dagger}_{-\mathbf{k}+\mathbf{K}_0\downarrow}$$

with $\mathbf{K}_0 = (\pm\pi, \pm\pi)$. Since we know the attractive Hubbard model has s-wave pairing, the σ_z Hubbard model must necessarily have a low temperature s-wave (singlet) PDW phase, in which an electron at momentum $\mathbf{k}$ pairs up with another at momentum $-\mathbf{k}+\mathbf{K}_0$, resulting in a Cooper pair carrying non-zero momentum.

An analogous mapping of the magnetism in the repulsive Hubbard model shows that the repulsive σ_z Hubbard model has a d-wave (triplet) PDW low temperature phase. These observations are quite remarkable. A PHT transformation, combined with the known phase diagram of the conventional Hubbard model, has revealed a microscopic model, the σ_z Hubbard model, which rigorously possesses pairing with non-zero momentum.

8 Concluding remarks

The Hubbard model was developed to explain some most fundamental many-body phenomena in condensed matter physics: the mysterious Mott insulating behavior and magnetism in transition metal oxides. Several decades later, it emerged as one of the leading theories of d-wave superconductivity in the cuprates, and appears to hold insight into related stripe formation. After two further decades the Hubbard model re-invented itself yet again in AMO community. One might think such a powerful theory would also be inaccessible. We hope these notes have proven that is not the case. We also hope that they suggest the Hubbard model is not yet finished having something to say about new condensed matter problems, including non-Hermitian physics, quantum state transfer, and pair density wave phases.

References

[1] Patrik Fazekas: *Lecture Notes on Electron Correlation and Magnetism* (World Scientific, Singapore, 1999)

[2] T. Esslinger, Annu. Rev. Cond. Matt. Phys. **1**, 129 (2010)

[3] L. Tarruell and L. Sanchez-Palencia, C. R. Acad. Phys. **19**, 365 (2018)

[4] J. Zaanen and O. Gunnarsson, Phys. Rev. B **40**, 7391, (1989)

[5] J.P.F. LeBlanc *et al.*, Phys. Rev. X **5**, 041041 (2015)

[6] S.R. White and D.J. Scalapino, Phys. Rev. Lett. **91**, 136403, (2003)

[7] K.Ch. Ńg, J. Carrasquilla, R.G. Melko, and E. Khatami, Phys. Rev. X **7**, 031038, (2017)

[8] D.P. Arovas, E. Berg, S.A. Kivelson, and S. Raghu, Annu. Rev. Cond. Matt. Phys. **13**, 239 (2022)

[9] E. Abrahams, P.W. Anderson, D.C. Licciardello, and T.V. Ramakrishnan, Phys. Rev. Lett. **42**, 673 (1979)

[10] F. Evers and A.D. Mirlin, Rev. Mod. Phys. **80**, 1355 (2008)

[11] A.A. Maradudin, P. Mazur, E.W. Montroll, and G.H. Weiss, Rev. Mod. Phys. **30**, 175, (1958)

[12] E. Abrahams, S.V. Kravchenko, and M.P. Sarachik Rev. Mod. Phys. **73**, 251 (2001)

[13] J. Feinberg and A. Zee, Nucl. Phys. B **504**, 579 (1997)

[14] C.M. Bender, Rep. Prog. Phys. **70**, 947 (2007)

[15] Y. Ashida, Z. Gong, and M. Ueda, Adv. Phys. **69**, 249 (2020)

[16] L. Xiang *et al.*, Nat. Commun. **15**, 4918 (2024)

[17] Indeed, by making the identification of the number of sites N to $2j{+}1$ and the site index n to $m{+}j{+}1$ it is simple to show $n = 1, 2, \ldots N$ and $\sqrt{j(j{+}1) - m(m{+}1)} = \sqrt{n(N{-}n)}$.

[18] M. Christandl, N. Datta, A. Ekert, and A.J. Landahl, Phys. Rev. Lett. **92**, 187902 (2004)

[19] A. Kay, Int. J. Quant. Inf. **08**, 641 (2010)

[20] A demonstration of exotic η-pairing from such canonical transformations also has a long history. See C.N. Yang, Phys. Rev. Lett. **63**, 2144 (1989). However the remarks which follow are first described in X. Zhu, J. Sun, S.-S. Gong, W. Huang, S. Feng, R.T. Scalettar, and H. Guo, arXiv:2404.11043 (2024).

4 The Physics of Doped Mott Insulators

Robert Eder
Karlsruhe Institute of Technology
Institute for Quantum Materials and Technologies

Contents

E. Pavarini and E. Koch (eds.)
Correlations and Phase Transitions
Modeling and Simulation Vol. 14
Forschungszentrum Jülich, 2024, ISBN 978-3-95806-751-6
http://www.cond-mat.de/events/correl24

1 Introduction

Following the discovery of copper oxide superconductors with their spectacularly high superconducting transition temperatures by Bednorz and Müller [1], the problem of the doped Mott insulator has become a central issue in solid state physics. Still, after more than 30 years of research and thousands of papers devoted to this subject, there is no generally accepted theory for this problem. So what exactly do we mean by 'doped Mott insulator' and why is this problem so hard to solve?

Let us consider a two-dimensional square lattice with lattice constant $a = 1$, which consists of $N = L^2$ sites and impose periodic boundary conditions with period L along both the x- and y-direction. We denote the number of electrons with spin σ by N_σ, the total number of electrons by $N_e = N_\uparrow + N_\downarrow$. Also, we denote densities per site by n, for example $n_e = N_e/N$. To explain the idea of a Mott-insulator it would be neither necessary that the system is two-dimensional, nor that we have a square lattice, but this is the suitable geometry to describe the CuO$_2$ planes in copper oxide superconductors. We assume that there is one s-like atomic orbital $|\phi_i\rangle$ centered at each lattice site i. Orbitals on different sites are assumed to be orthogonal, $\langle\phi_i|\phi_j\rangle = \delta_{i,j}$, but there may be nonvanishing matrix elements of the Hamiltonian – that means the kinetic and potential energy – between them, $\langle\phi_i|H|\phi_j\rangle = -t_{i,j}$. We assume that the orbital $|\phi\rangle$ is the same for each lattice site, whence the matrix element $\langle\phi_i|\phi_j\rangle$ depends only on the distance between i and j, $t_{i,j} = t_{\mathbf{R}_i-\mathbf{R}_j}$. We also assume that the atomic orbital $|\phi_i\rangle$ decays exponentially, $\langle\mathbf{r}|\phi_i\rangle \propto e^{-|\mathbf{r}-\mathbf{R}_i|/\zeta}$, so we expect $t_\mathbf{R} \propto e^{-|\mathbf{R}|/\zeta}$ and $t_{i,j}$ will differ appreciably from zero only for close neighbors. Introducing operators $c_{i,\sigma}^\dagger$ which create an electron of z-spin σ in the orbital $|\phi_i\rangle$ the Hamiltonian therefore reads

$$H_0 = -\sum_{i,j} t_{i,j} \sum_\sigma c_{i,\sigma}^\dagger c_{j,\sigma} = \sum_\mathbf{k} \sum_\sigma \varepsilon_\mathbf{k}\, c_{\mathbf{k},\sigma}^\dagger c_{\mathbf{k},\sigma}.$$

The second expression for H_0 is obtained by Fourier transformation

$$c_{\mathbf{k},\sigma}^\dagger = \frac{1}{\sqrt{N}} \sum_j e^{i\mathbf{k}\cdot\mathbf{R}_j}\, c_{j,\sigma}^\dagger \quad\Rightarrow\quad \varepsilon_\mathbf{k} = -\frac{1}{N}\sum_{i,j} t_{i,j}\, e^{i\mathbf{k}\cdot(\mathbf{R}_i-\mathbf{R}_j)} = -\sum_\mathbf{R} t_\mathbf{R}\, e^{i\mathbf{k}\cdot\mathbf{R}}. \tag{1}$$

Here $\mathbf{k} = \big(2n\pi/L, 2m\pi/L\big)$ with integer m and n such that $-L/2 < m, n \leq L/2$ is a wave vector in the first Brillouin zone. Unless otherwise stated we will from now on assume that $t_{i,j}$ is different from zero only for nearest neighbors i and j and denote its value by t, whence $\varepsilon_\mathbf{k} = -2t\big(\cos(k_x) + \cos(k_y)\big)$. The number of wave vectors $\mathbf{k}$ equals N and the ground state for N electrons is obtained by 'filling the band from below', that means occupying those $N/2$ wave vectors $\mathbf{k}$ which minimize the sum $\sum_\mathbf{k} \varepsilon_\mathbf{k}$ with two electrons of opposite spin. The band therefore is half-filled, the Fermi surface covers precisely half of the Brillouin zone and we have a metal.

In the discussion so far we have ignored the Coulomb interaction between the electrons. Recalling that the atomic orbital $\langle\mathbf{r}|\phi_i\rangle \propto e^{-|\mathbf{r}-\mathbf{R}_i|/\zeta}$, we expect that if the orbital is occupied by two electrons of opposite spin, the electrostatic energy is $U \propto e^2/\zeta$, whereas it is $V \propto e^2/a$ if the electrons are in orbitals on different sites. If we take the limit of a 'small atomic orbital', $\zeta \rightarrow 0$, we find $U/t \rightarrow \infty$ and $V/U \rightarrow 0$ whence we neglect the Coulomb repulsion between electrons in different orbitals. Taking the extreme limit $U \rightarrow \infty$ while t being fixed, and returning to the problem of finding the ground state with N electrons we find that there is precisely one electron in each of the N orbitals (putting two electrons into the same orbital increases the energy by the large amount U). The electrons thus are 'frozen in' and cannot react to an applied electric field, so that the system is an insulator. This is the prototype of a *Mott insulator*: a system which would be a metal in the band picture, but is an insulator due to the strong Coulomb repulsion between electrons in 'small' atomic orbitals. It should be noted that for noninteracting electrons ($U = 0$) and $t = 0$ the electrons would be unable to move as well and the system would be an insulator. However, any arbitrarily small value of t would immediately lead to the formation of a band and a Fermi surface, whereas in the presence of a large U switching on $t \ll U$ still would not change the insulating nature of the ground state. Let us now try to put these qualitative considerations into a more quantitative form – the famous Hubbard-I approximation.

2 The basic concept: Hubbard-I approximation

This is the 'defining approximation' of the Mott-insulator by which Hubbard for the first time introduced central concepts of strongly correlated electron systems such as the two Hubbard bands [2]. In the following we give a somewhat sloppy re-derivation of Hubbard's theory which is meant to clarify its the physical content.

We consider the of infinite U and $N_\uparrow = N_\downarrow = N/2$ so that $N_e = N$. The ground state has one electron per lattice site and the energy is $E = 0$. The way in which the spins are distributed over the sites is not determined, however, rather the number of ways to distribute the $\uparrow$-spins (which automatically fixes the $\downarrow$-spins) is

$$n_d = \binom{N}{N_\uparrow} \approx \sqrt{\frac{2}{\pi N}}\, 2^N, \tag{2}$$

where the Stirling formula has been used. This shows the enormous degree of degeneracy. We ignore this degeneracy, however, and assume that there is a unique state $|\Psi_0\rangle$ which may be thought of as a suitable superposition of all these n_d degenerate states and which we assume to be 'disordered' — it will become clear in a moment what this means.

Next we assume that U is gradually reduced from infinity. Then, a term in the kinetic energy such as $t_{i,j}\ c^\dagger_{i,\sigma} c_{j,\sigma}$ can transfer an electron of spin σ from site j to another site i resulting in an empty site at j and a double occupancy at site i, whereby the double occupancy increases the energy by U. The hopping process is possible only if the electron which was originally at the site i has the spin $-\sigma$ and since our initial state $|\Psi_0\rangle$ is 'disordered' the probability for this to be the case is $1/2$ — which is our definition of 'disordered'. We now interpret the original state $|\Psi_0\rangle$ as the vacuum state $|0\rangle$ of our theory and the state created by the hopping process as containing a fermionic hole-like particle at j and a fermionic double-occupancy-like particle at site i: $d^\dagger_{i,\sigma}\ h^\dagger_{j,-\sigma}|0\rangle$. The order of the fermionic operators in this state is due to the fact that in the original hopping term the annihilation operator $c_{j,\sigma}$ which creates the hole stands to the right of the creation operator $c^\dagger_{i,\sigma}$ which creates the double occupancy. Moreover we assign the negative spin to the operator which creates the hole because replacement of, e.g., an ↑-electron by a hole decreases the z-spin by $1/2$. We arrive at the following effective Hamiltonian to describe the holes and double occupancies

$$H_{\textit{eff},1} = \frac{1}{2}\sum_{i,j}\sum_{\sigma}\left(t_{i,j}\, d^\dagger_{i,\sigma}h^\dagger_{j,-\sigma} + H.c.\right) + U\sum_{i,\sigma} d^\dagger_{i,\sigma}d_{i,\sigma}\,. \tag{3}$$

Once a hole and a double occupancy have been created, each of these particles may be transported further by the hopping term. If we assume that the surplus or missing electron retains its spin, which means that the double occupancies and holes propagate without 'leaving a trace' of inverted spins, for example a surplus ↑-electron can hop from site i to site j only if the spin at site j is ↓ — again we assume that the probability for this is $1/2$. We therefore can write down the missing terms for the effective Hamiltonian

$$H_{\textit{eff},2} = \frac{1}{2}\sum_{i,j}\sum_{\sigma} t_{i,j}\ \left(d^\dagger_{i,\sigma}d_{j,\sigma} - h^\dagger_{i,-\sigma}h_{j,-\sigma}\right). \tag{4}$$

The negative sign of the hopping term for holes is due to the fact that the original hopping term has to be rewritten as $-t_{i,j}c_{j,\sigma}c^\dagger_{i,\sigma}$ to describe the propagation of a hole. Addition of (3) and (4) and Fourier transformation gives

$$H_{\textit{eff}} = \sum_{\mathbf{k},\sigma}\left(\left(\frac{\varepsilon_{\mathbf{k}}}{2}+U\right)d^\dagger_{\mathbf{k},\sigma}d_{\mathbf{k},\sigma} - \frac{\varepsilon_{\mathbf{k}}}{2}\ h^\dagger_{\mathbf{k},\sigma}h_{\mathbf{k},\sigma}\right) + \sum_{\mathbf{k},\sigma}\frac{\varepsilon_{\mathbf{k}}}{2}\left(d^\dagger_{\mathbf{k},\sigma}h^\dagger_{-\mathbf{k},-\sigma} + H.c.\right), \tag{5}$$

with $\varepsilon_{\mathbf{k}}$ given in Eq. (1). Note that this now is a quadratic form where the Coulomb interaction is described by the extra energy of U for the double-occupancy-like fermion. We make the *ansatz*

$$\begin{aligned} \gamma^\dagger_{\mathbf{k},+,\sigma} &= u_{\mathbf{k}}d^\dagger_{\mathbf{k},\sigma} + v_{\mathbf{k}}h_{-\mathbf{k},-\sigma}, \\ \gamma^\dagger_{\mathbf{k},-,\sigma} &= -v_{\mathbf{k}}d^\dagger_{\mathbf{k},\sigma} + u_{\mathbf{k}}h_{-\mathbf{k},-\sigma}, \end{aligned} \tag{6}$$

and demand that the Hamiltonian takes the form

$$H_{\textit{eff}} = \sum_{\mathbf{k},\sigma}\left(E_{\mathbf{k},+}\gamma^\dagger_{\mathbf{k},+,\sigma}\gamma_{\mathbf{k},+,\sigma} + E_{\mathbf{k},-}\gamma^\dagger_{\mathbf{k},-,\sigma}\gamma_{\mathbf{k},-,\sigma}\right). \tag{7}$$

We find $\left(\text{with } W_{\mathbf{k}} = \sqrt{\varepsilon^2_{\mathbf{k}}+U^2}\right)$

$$E_{\mathbf{k},\pm} = \frac{1}{2}\left(\varepsilon_{\mathbf{k}} + U \pm W_{\mathbf{k}}\right), \qquad u_{\mathbf{k}} = \sqrt{\frac{W_{\mathbf{k}}+U}{2W_{\mathbf{k}}}}, \qquad v_{\mathbf{k}} = \frac{\varepsilon_{\mathbf{k}}}{\sqrt{2W_k(W_k+U)}}. \tag{8}$$

In the limit $U/t \gg 1$ this simplifies to $E_{\mathbf{k},-} = \varepsilon_{\mathbf{k}}/2$, $E_{\mathbf{k},+} = \varepsilon_{\mathbf{k}}/2 + U$ so that the original band with dispersion $\varepsilon_{\mathbf{k}}$ is split into two bands, separated by a gap of U and each having half of the original width. To find out the occupation of the bands, and hence the nature of the Fermi

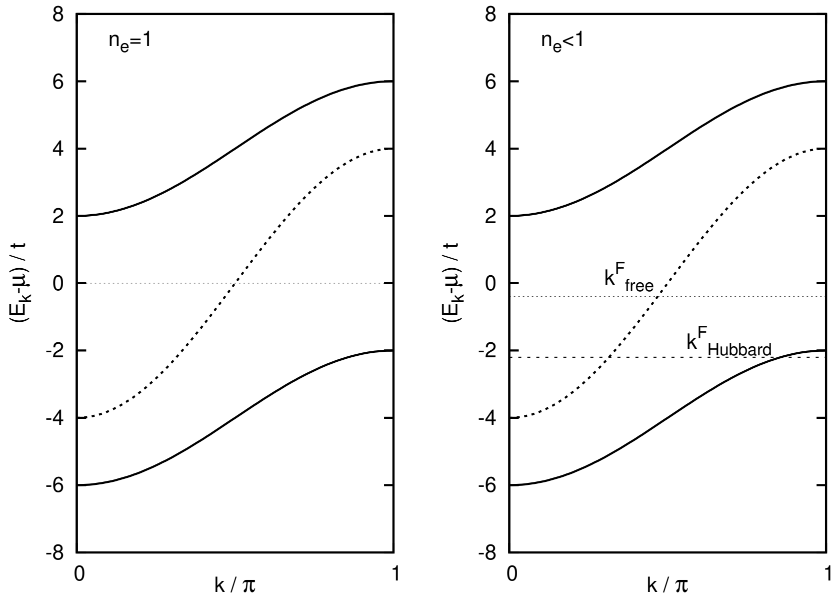

Fig. 1: *Band structures* $E_{\mathbf{k}}$ *for the noninteracting system (dashed line) and from the Hubbard-I approximation (*$U/t\,=\,8$*). The energies are plotted for* $\mathbf{k}\,=\,(k,k)$*, i.e., along the* $(1,1)$*-direction. For* $n_e=1$ *the half-filled noninteracting band is replaced by the two Hubbard bands, the chemical potential* μ *is in the center of the gap between the two Hubbard bands so that the lower one is completely filled, the upper empty.*
For $n_e<1$ *the noninteracting band becomes less than half-filled, the chemical potential cuts into the top of the lower Hubbard band, forming a hole pocket around* (π,π)*. Note the strong discrepancy of the Fermi wave vectors* $\mathbf{k}^F$*.*

surface, we need to count electrons. The vacuum state $|\Psi_0\rangle$ has one electron per site, i.e., a total of N electrons. Each double occupancy increases the electron number by one, each hole decreases it by one so that the operator of electron number becomes

$$N_e = N + \sum_{i,\sigma}\left(d^\dagger_{i,\sigma}d_{i,\sigma} - h^\dagger_{i,\sigma}h_{i,\sigma}\right) = \sum_{\mathbf{k},\sigma}\left(d^\dagger_{\mathbf{k},\sigma}d_{\mathbf{k},\sigma} + h_{-\mathbf{k},-\sigma}h^\dagger_{-\mathbf{k},-\sigma}\right) - N.$$

On going over to the expression on the extreme right we have switched to Fourier transforms and assumed fermion anticommutation relations to hold for the $h^\dagger_{\mathbf{k},\sigma}$. We note that in the basis $(d^\dagger_{\mathbf{k},\sigma}, h_{-\mathbf{k},-\sigma})$ the operator matrix for the expression in brackets is the unit matrix which is invariant under unitary transformations whence N_e also can be written as

$$N_e = \sum_{\mathbf{k},\sigma}\left(\gamma^\dagger_{\mathbf{k},-,\sigma}\gamma_{\mathbf{k},-,\sigma} + \gamma^\dagger_{\mathbf{k},+,\sigma}\gamma_{\mathbf{k},+,\sigma}\right) - N. \tag{9}$$

Demanding $\langle N_e\rangle = N$ the lower band $E_{\mathbf{k},-}$ must be completely filled whereas the upper band $E_{\mathbf{k},+}$ must be completely empty, i.e., the chemical potential must be in the center of the gap between lower and upper band see Figure 1. Namely in this case the expectation value of the term in brackets is $2N$. Rather than being a metal, as expected for the situation of a half-filled band, the presence of the Coulomb interaction turns the system into an insulator – and this is precisely the definition of the Mott-insulator.

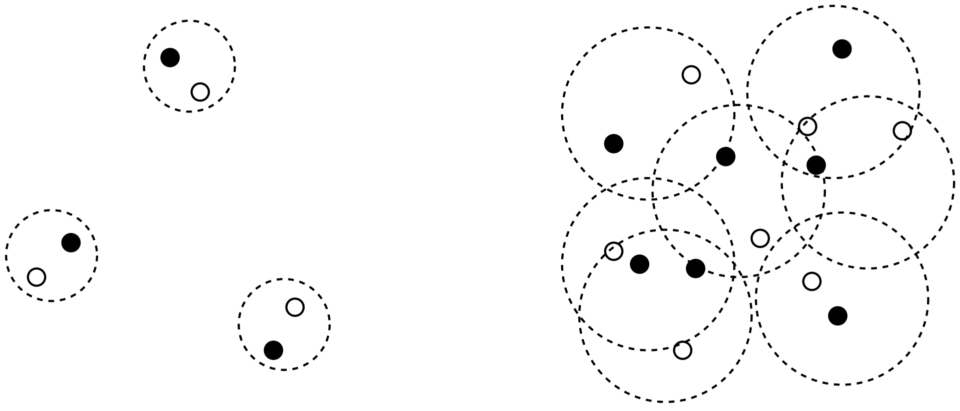

Fig. 2: *As the ratio U/t decreases more and more hole-double occupancy pairs are generated and the extent of the pairs increases. At a certain ratio of U/t the pairs overlap significantly and the phase transition to the metal occurs.*

It follows that the ground state wave function $|\Phi_0\rangle$ must obey $\gamma^\dagger_{\mathbf{k},-,\sigma}|\Phi_0\rangle = \gamma_{\mathbf{k},+,\sigma}|\Phi_0\rangle = 0$. This can be achieved by choosing

$$|\Phi_0\rangle = \prod_{\mathbf{k},\sigma}\left(u_{\mathbf{k}} + v_{\mathbf{k}}\, h^\dagger_{-\mathbf{k},-\sigma}\, d^\dagger_{\mathbf{k},\sigma}\right)|\Psi_0\rangle \propto e^{\sum_{\mathbf{k},\sigma}\frac{v_{\mathbf{k}}}{u_{\mathbf{k}}}h^\dagger_{-\mathbf{k},-\sigma}d^\dagger_{\mathbf{k},\sigma}}|\Psi_0\rangle.$$

The similarity with the BCS wave function shows that $|\Phi_0\rangle$ may be viewed as the original background $|\Psi_0\rangle$, which has one electron per site and is spin-disordered, populated by electron-hole pairs. The expression in the exponent is

$$\sum_{\mathbf{k},\sigma}\frac{v_{\mathbf{k}}}{u_{\mathbf{k}}}h^\dagger_{-\mathbf{k},-\sigma}d^\dagger_{\mathbf{k},\sigma} = \sum_{i,\mathbf{R}} f(\mathbf{R})\, h^\dagger_{\mathbf{R}_i,-\sigma}\, d^\dagger_{\mathbf{R}_i+\mathbf{R},\sigma} \quad \text{with} \quad f(\mathbf{R}) = \frac{1}{N}\sum_{\mathbf{k}}\frac{v_{\mathbf{k}}}{u_{\mathbf{k}}}\,e^{i\mathbf{k}\mathbf{R}} \underset{U\to\infty}{\longrightarrow} \frac{t}{U}\,\delta_{|\mathbf{R}|,1}.$$

This shows that for large U the density of pairs is $\propto (t/U)^2$ and the double-occupancy and the hole are almost exclusively on nearest neighbors.

If in a *gedankenexperiment* one would reduce the value of U starting from $U=\infty$, one would expect that, as U decreases, both the density of such pairs would increase and the diameter of a pair would increase, see Figure 2. If U becomes sufficiently low the pairs start to overlap and at that point the entire picture is likely to break down so we have the insulator-to-metal transition. Viewed that way one might conjecture that the order parameter for the insulator-to-metal transition is the double occupancy-hole pairing amplitude $\langle d^\dagger_{\mathbf{k},\sigma}\, h^\dagger_{-\mathbf{k},-\sigma}\rangle$. Does the Hubbard-I approximation describe such a transition to the metallic state? The simplest way to answer this question is to consider the gap between the upper and lower Hubbard band in the limit $U/t \to 0$. One finds

$$\Delta = E_{\mathbf{k}=(0,0),+} - E_{\mathbf{k}=(\pi,\pi),-} \quad \propto \quad \frac{U^2}{4t},$$

where the extreme right-hand-side holds for $U \to 0$. This shows that there is a gap even for arbitrarily small U, i.e., there is no insulator-to-metal transition with decreasing U in the Hubbard-I approximation.

Next, what would happen if we reduce the electron number N_e from $N \to (1-\delta)N$, i.e., we 'dope the Mott insulator'? First, one would assume that all the factors of $1/2$ in the above derivation should be replaced by $(1-\delta)/2$ because this is now the probability that on any given site there is an electron with a given spin σ. This will lead to only a slight modification of the quasiparticle dispersion. More importantly, however, the occupation of the lower Hubbard band will be reduced. Inspection of (9) shows that now

$$\left\langle \sum_{\mathbf{k},\sigma} \left(\gamma^{\dagger}_{\mathbf{k},-,\sigma}\gamma_{\mathbf{k},-,\sigma} + \gamma^{\dagger}_{\mathbf{k},+,\sigma}\gamma_{\mathbf{k},+,\sigma} \right) \right\rangle = (2-\delta)N,$$

so that the occupied part of the lower Hubbard band must now contain $N_{\mathit{Hubbard}} = (1-\delta/2)N$ momenta $\mathbf{k}$. This means that $N\delta/2$ $\mathbf{k}$-points must be unoccupied so that the Fermi surface is a small hole-pocket around the top of the lower Hubbard band at $\mathbf{k} = (\pi,\pi)$, see Figure 1. Compare this to the noninteracting case, $U = 0$ where the occupied part of the band contains $N_{\mathit{free}} = \big((1-\delta)/2\big)N$ momenta, whence the difference $N_{\mathit{Hubbard}} - N_{\mathit{free}} = N/2$. If we assume that the Hubbard-I approximation is at least qualitatively correct for the lightly doped Mott-insulator, i.e., small δ, this immediately leads to an interesting question: namely for low electron density $n_e \ll 1$ one recovers the noninteracting Fermi surface even for arbitrarily large U [3]. The reason is that for low electron density the probability for collisions between electrons is small and the interaction becomes largely irrelevant. Accordingly, if one gradually reduces the electron number starting from $n_e = 1$ one would expect that one first has the Fermi surface with a volume $\propto \delta/2$ as predicted by the Hubbard-I approximation but at a certain critical n_e the Fermi surface volume must change to the free-electron value of $(1-\delta)/2$, i.e., a phase transition between two phases with different Fermi surface volume with increasing doping. An obvious candidate for this phase transition would be the enigmatic quantum critical point in cuprate superconductors which gives rise to the superconducting dome in these compounds.

Finally let us address a subtle problem which actually is related to a very fundamental problem in strongly correlated electrons. In the above discussion we have assigned a spin to the holes and double occupancies: $d^{\dagger}_{i,\sigma}$ and $h^{\dagger}_{j,\sigma}$. However, both an empty site and a doubly occupied site are spinless objects! On the other hand, if the vacuum state $|\Psi_0\rangle$ has a definite z-spin S_z, the states $c_{i,\uparrow}|\Psi_0\rangle$ and $c_{i,\downarrow}|\Psi_0\rangle$ are orthogonal to each other because they have $S_z \mp 1/2$. This is despite the fact that the empty site at i is a spinless object. The information whether an $\uparrow$-electron or a $\downarrow$-electron has been removed from site i therefore must be 'stored' somewhere else in the resulting state. If one now were to remove an electron at site i and subsequently let the resulting state evolve under the action of the Hamiltonian one can take two different points of view: when the empty site propagates, the information about the spin of the removed electron may 'stay in the neighborhood' of the spinless vacancy, so that effectively there is a spin-1/2 particle propagating. Obviously, in the Hubbard-I approximation one is implicitly assuming just this. Alternatively one might assume that the spinless vacancy and the 'spin information' acquire an independent existence and separate from each other, a scenario often referred to as spin-charge separation.

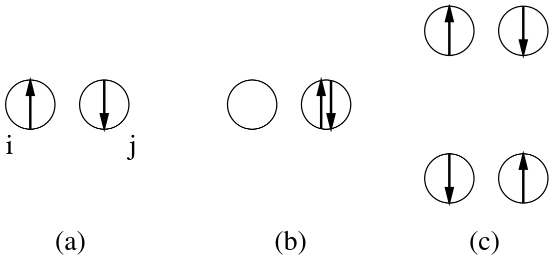

Fig. 3: *An exchange process in a Mott insulator.*

3 Antiferromagnets

3.1 Spin exchange

In the introduction we have already mentioned one of the reasons why the problem of the Mott-insulator is so difficult. Whereas the ground state for $N_e = N$ and $U = 0$ is unique and easy to write down – the half-filled Fermi sea – a well-defined ground state for $U/t = \infty$ does not even exist. Rather, the ground state is highly degenerate, see equation (2) above. In the Hubbard-I approximation we have bypassed this problem by assuming that there is a unique 'disordered' ground state of N electrons on N sites, and that the only active degrees of freedom are the double-occupancies and holes. This, however, ignores the possibility of *spin exchange*. If we reduce U/t from infinity to a large but finite value, the spins on the individual sites start to 'communicate' with each other via the process shown in Figure 3. An electron from site i may hop to a neighbor j and form an intermediate state with an empty orbital at i and a doubly occupied orbital at j, see Figure 3(b). Since the energy of this intermediate state is U, it will be short lived and one of the two electrons in j will hop to the empty site i, resulting in one of the two states in Figure 3(c). The upper state is identical to the initial state, Figure 3(a), but there is a gain in kinetic energy of order t^2/U due to the back-and-forth hopping of the electron. Since this back-and-forth hopping is possible only if the spins at i and j are antiparallel to each other, it is energetically favorable if spins on nearest neighbors are antiparallel. In the lower of the two states in Figure 3(c) both spins have flipped their direction as compared to Figure 3(a), so that the spins in the Mott insulator are not static, but have a dynamics of their own. A more quantitative treatment shows [4] that the 'virtual' hopping processes in Figure 3 can be described by the *Heisenberg antiferromagnet*

$$H_{HAF} = J \sum_{\langle i,j \rangle} \mathbf{S}_i \cdot \mathbf{S}_j = J \sum_{\langle i,j \rangle} \Big(S_i^z S_j^z + \frac{1}{2} \big(S_i^+ S_j^- + S_i^- S_j^+ \big) \Big). \tag{10}$$

Here $J = 4t^2/U$ while $\sum_{\langle i,j \rangle}$ denotes a sum over all $2N$ nearest neighbor pairs, and $\mathbf{S}_i$ is the operator of electron spin at site i and the spin raising and lowering operators $S^{\pm} = S_x \pm i S_y$ have been introduced to rewrite the term $S_{i,x} S_{j,x} + S_{i,y} S_{j,y}$. We see that although the electrons in a Mott insulator are localized, their spins acquire a 'life of their own', resulting in a magnetic ground state and a spectrum of *spin-excitations*.

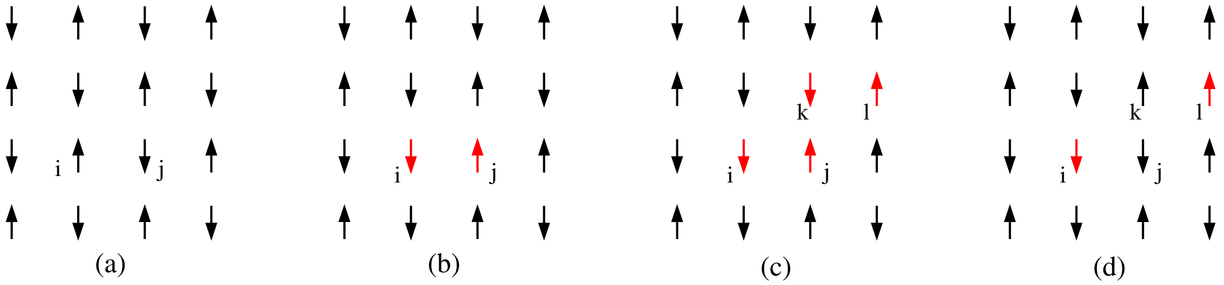

Fig. 4: *The Néel state (a) is* not *the ground state of the Heisenberg antiferromagnet. By acting, e.g., with the term* $\frac{J}{2}\ S_i^- S_j^+$ *in (10) the state (b) is generated, which is orthogonal to the Néel state. Acting further with* $\frac{J}{2}\ S_k^- S_l^+$ *produces (c) and then acting with* $\frac{J}{2}\ S_j^- S_k^+$ *gives (d).*

3.2 Magnons in an antiferromagnet

We consider the undoped Mott insulator, $N_e = N$, and assume that the spins degrees of freedom of the electrons are described by the Heisenberg antiferromagnet, Eq. (10). If only the terms $\propto S_i^z S_j^z$ were present, the ground state of (10) would be the *Néel state*, shown in Figure 4(a). In this state, the square lattice is divided into two *sublattices* whereby all sites of the A-sublattice are occupied by an $\uparrow$-electron, those of the B-sublattice by a $\downarrow$-electron (we assume that the A-sublattice is the one containing the site $(0,0)$). The energy of this state is $2N \cdot (-J/4) = -NJ/2$. The Néel state, however, is not an eigenstate of the full Hamiltonian (10): acting, e.g., with one of the products $\frac{J}{2} S_i^- S_j^+$ contained in the second term in (10), the spins at the sites i and j are inverted, resulting in the state shown in Figure 4(b) which is orthogonal to the Néel state. Interestingly, the inverted spins have very much the character of particles in that they can propagate: first, the term $\frac{J}{2} S_k^- S_l^+$ appends two additional inverted spins, see Figure 4(c), and then the term $\frac{J}{2} S_j^-\ S_k^+$ removes two inverted spins, to produce the state in Figure 4(d). The net result of this two-step process is that one of the inverted spins seems to have moved from site j to site l. The particle-like nature of the inverted spins has led to the name *magnons* for them. One can then envisage how this will go on: magnons are created in pairs at various places in the system, then separate and propagate independently by the append-and-remove process, but when two magnons meet they can also 'pair-annihilate' each other by the inverse process Figure 4(b) $\rightarrow$ (a). There are then two possible outcomes of this scenario: the density of magnons may reach an equilibrium value, where pair-creation and pair annihilations balance each other, so that the underlying antiferromagnetic order persists and we have a Néel state hosting a 'gas of magnons', or the process may go on until the ordered state is wiped out and we get an entirely new state without order. It turns out that in dimensions $D \geq 2$ the first scenario is realized, and the resulting gas of magnons in antiferromagnetic Mott insulators can be described very well by *linear spin wave theory*. This is frequently derived by means of the Holstein-Primakoff transformation [5] but for the extreme quantum limit of spin $^1/_2$, which we are considering here, a simpler and more transparent derivation is possible.

We interpret the Néel state in Figure 4(a) as the vacuum state $|0\rangle$ for magnons and model an inverted spin at the site i of the A sublattice by the presence of a boson, created by $a_i^\dagger$. Similarly, an inverted spin on the site j of the B sublattice is modeled by the presence of a boson created by $b_j^\dagger$. The state in Figure 4(b) thus would be represented as $a_i^\dagger b_j^\dagger|0\rangle$. We use bosons to represent the magnons because spin-flip operators such as S_i^+ and S_j^- commute for different sites i and j and these are the operators which create or annihilate the magnons. Since any given spin can be inverted only once, a state like $(a_i^\dagger)^2|0\rangle$ is meaningless. Accordingly, we have to impose the constraint that at most one boson can occupy a given site. This is equivalent to an infinitely strong on-site repulsion between the magnons and we call this the *hard-core constraint*. An inverted spin on either sublattice is parallel to its $z = 4$ nearest neighbors and the energy changes from $-J/4$ to $+J/4$ for each of these z bonds. Accordingly, we ascribe an energy of formation of $zJ/2$ to each boson. The spin-flip part creates or annihilates pairs of magnons on nearest neighbors, with the matrix element being $J/2$, so that the Hamiltonian for the magnons becomes

$$H_{SW} = \frac{zJ}{2}\Big(\sum_{i\in A} a_i^\dagger a_i + \sum_{i\in B} b_i^\dagger b_i\Big) + \frac{J}{2}\sum_{i\in A}\sum_{\mathbf{n}}\Big(a_i^\dagger b_{i+\mathbf{n}}^\dagger + b_{i+\mathbf{n}} a_i\Big). \tag{11}$$

Here $\mathbf{n}$ are the z vectors which connect a given site with its z nearest neighbors. Note that when two inverted spins reside on nearest neighbors, the number of frustrated bonds is $2(z-1)$ rather than $2z$. This could be incorporated into H_{SW} as an attractive interaction between magnons on nearest neighbors, but here we ignore this.

The Hamiltonian (11) is a quadratic form but we recall that the bosons are not free particles, but have to obey the hard-core constraint. However, for the moment we ignore this and treat the bosons as if they were noninteracting – we will return to this issue later on. Fourier transformation of (11) gives

$$\begin{aligned} H_{SW} &= \frac{zJ}{2}\sum_{\mathbf{k}}\Big(a_{\mathbf{k}}^\dagger a_{\mathbf{k}} + b_{\mathbf{k}}^\dagger b_{\mathbf{k}} + \gamma_{\mathbf{k}}\big(a_{\mathbf{k}}^\dagger b_{-\mathbf{k}}^\dagger + b_{-\mathbf{k}} a_{\mathbf{k}}\big)\Big), \\ a_{\mathbf{k}}^\dagger &= \sqrt{\frac{2}{N}}\sum_{j\in A} e^{i\boldsymbol{k}\cdot\boldsymbol{R}_j} a_j^\dagger, \\ \gamma_{\mathbf{k}} &= \frac{1}{z}\sum_{\mathbf{n}} e^{i\mathbf{k}\cdot\mathbf{n}} = \frac{1}{4}\big(2\cos(k_x) + 2\cos(k_y)\big), \end{aligned} \tag{12}$$

where $\mathbf{k}$ is a wave vector in the antiferromagnetic Brillouin zone (AFBZ), see Figure 5. We can diagonalize (12) by a *bosonic Bogoliubov transformation*, i.e., we make the ansatz

$$\begin{aligned} \alpha_{\mathbf{k}}^\dagger &= u_{\mathbf{k}}\ a_{\mathbf{k}}^\dagger + v_{\mathbf{k}}\, b_{-\mathbf{k}}, \\ \beta_{-\mathbf{k}}^\dagger &= u_{\mathbf{k}}\, b_{-\mathbf{k}}^\dagger + v_{\mathbf{k}}\ a_{\mathbf{k}}, \end{aligned} \qquad \Rightarrow \qquad \begin{aligned} a_{\mathbf{k}}^\dagger &= u_{\mathbf{k}}\,\alpha_{\mathbf{k}}^\dagger - v_{\mathbf{k}}\,\beta_{-\mathbf{k}}, \\ b_{-\mathbf{k}} &= -v_{\mathbf{k}}\ \alpha_{\mathbf{k}}^\dagger + u_{\mathbf{k}}\,\beta_{-\mathbf{k}}. \end{aligned} \tag{13}$$

Demanding that $\big[\alpha_{\mathbf{k}},\, \alpha_{\mathbf{k}}^\dagger\big] = \big[\beta_{\mathbf{k}},\, \beta_{\mathbf{k}}^\dagger\big] = 1$ gives the condition $u_{\mathbf{k}}^2 - v_{\mathbf{k}}^2 = 1$, which actually has been used to revert the equations on the left hand side of (13) to obtain the right hand side. Next, we demand that when expressed in terms of the $\alpha_{\mathbf{k}}^\dagger$ and $\beta_{\mathbf{k}}^\dagger$ the Hamiltonian takes the form

$$H = \sum_{\mathbf{k}} \omega_{\mathbf{k}}\big(\alpha_{\mathbf{k}}^\dagger \alpha_{\mathbf{k}} + \beta_{\mathbf{k}}^\dagger \beta_{\mathbf{k}}\big) + \mathit{const},$$

which implies that $\big[H,\, \alpha_{\mathbf{k}}^\dagger\big] = \omega_{\mathbf{k}}\alpha_{\mathbf{k}}^\dagger$. We now insert the *ansatz* (13) into this equation, use the bosonic commutation relations for $a^\dagger$ and $b^\dagger$, and equate the coefficients of $a_{\mathbf{k}}^\dagger$ and $b_{-\mathbf{k}}$ on both

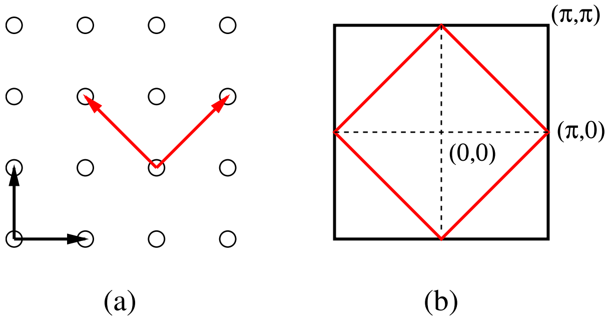

Fig. 5: *(a) The ordered moments in the Néel state make the two sublattices inequivalent, so that the new lattice vectors connect only the sites of one sublattice. The new unit cell is rotated by 45° and has twice the size of the original one. (b) Accordingly, the new Brillouin zone is rotated by 45° as well and has half the size of the original one.*

sides of the resulting equation. This leads to the following non-Hermitean eigenvalue problem:

$$\begin{pmatrix} zJ/2 & -\gamma_{\mathbf{k}} \\ \gamma^*_{\mathbf{k}} & -zJ/2 \end{pmatrix} \begin{pmatrix} u_{\mathbf{k}} \\ v_{\mathbf{k}} \end{pmatrix} = \omega_{\mathbf{k}} \begin{pmatrix} u_{\mathbf{k}} \\ v_{\mathbf{k}} \end{pmatrix}. \tag{14}$$

The eigenvalues and eigenvectors of (14) are easily calculated and one finds

$$\omega_{\mathbf{k}} = \frac{zJ}{2}\sqrt{1-\gamma^2_{\mathbf{k}}}, \qquad u_{\mathbf{k}} = \sqrt{\frac{1+\nu_{\mathbf{k}}}{2\nu_{\mathbf{k}}}}, \quad \text{and} \quad v_{\mathbf{k}} = \sqrt{\frac{1-\nu_{\mathbf{k}}}{2\nu_{\mathbf{k}}}}, \tag{15}$$

where $\nu_{\mathbf{k}} = \sqrt{1-\gamma^2_{\mathbf{k}}}$. In particular, for $\mathbf{k} \to 0$ we find $\gamma_{\mathbf{k}} \to 1 - (k_x^2 + k_y^2)/4 = 1-\mathbf{k}^2/4$ so that $\nu_{\mathbf{k}} \to |\mathbf{k}|/\sqrt{2}$ and $\omega_{\mathbf{k}} \to J\sqrt{2}|\mathbf{k}|$. This shows that the spin waves reach zero frequency at $\mathbf{k} = (0,0)$ and have a cone-shaped dispersion in the neighborhood.

Linear spin wave theory is extremely successful in describing many properties of antiferromagnetic Mott-insulators. An example for the experimental observation of magnons by inelastic neutron scattering and the excellent agreement of the experimental results with linear spin wave theory can be found in Ref. [6].

To conclude this section, we return to the issue of the hard-core constraint which the $a^\dagger$ and $b^\dagger$ bosons had to obey and which we had simply ignored. To address this question, we calculate the density of these bosons, i.e.

$$n_a = \frac{2}{N}\sum_{\mathbf{k}} \langle a^\dagger_{\mathbf{k}} a_{\mathbf{k}} \rangle = \frac{2}{N}\sum_{\mathbf{k}} v^2_{\mathbf{k}} = \frac{2}{N}\sum_{\mathbf{k}} \frac{1-\nu_{\mathbf{k}}}{2\nu_{\mathbf{k}}}.$$

Numerical evaluation for a 2D square lattice gives $n_a = 0.19$. The probability that two of the bosons occupy the same site and violate the constraint therefore is $\approx n_a^2 = 0.04 \ll 1$ and our assumption of relaxing the constraint is justified a posteriori.

Summarizing the discussion so far we have seen that in a Mott-insulator the sites carry a spin of $\pm 1/2$. These spins can communicate with each other by means of virtual charge fluctuations and this is described by the Heisenberg antiferromagnet. In dimensions $D \geq 2$ this leads to antiferromagnetic order in the ground state and a new type of excitations, magnons or spin waves, which correspond to spins standing opposite to the antiferromagnetic order and these inverted spins propagate through the lattice. In the next section we investigate how the doped holes interact with these spin excitations.

3.3 One hole in an antiferromagnet

We have seen that in a Mott insulator 'virtual' hopping processes lead to a coupling of spins which results in antiferromagnetic order and spin excitations. In this section we study the first step towards the 'doped' the Mott insulator and consider a single hole in an antiferromagnet. A single hole will not destroy the magnetic order due to the Heisenberg exchange between the remaining $N-1$ spins so we continue to assume antiferromagnetic order. The appropriate model to describe such a system is the famous t-J *model*

$$H_{t\text{-}J} = -t \sum_{\langle i,j \rangle} \sum_{\sigma} \left(\hat{c}^{\dagger}_{i,\sigma} \hat{c}_{j,\sigma} + H.c. \right) + J \sum_{\langle i,j \rangle} \mathbf{S}_i \cdot \mathbf{S}_j, \tag{16}$$

where the *Hubbard operator* $\hat{c}^{\dagger}_{i,\sigma} = c^{\dagger}_{i,\sigma}(1-n_{i,\bar{\sigma}})$ creates an electron only on an empty site. The t-J model was originally derived rigorously as the strong coupling version of the Hubbard model by Chao, Spałek, and Oleś [4]. The model describes the lower Hubbard band — note that the operator $\hat{c}_{i,\sigma}$ corresponds precisely to the operator $h^{\dagger}_{i,\bar{\sigma}}$ we used in the Hubbard-I approximation — but augments this by the effect of the Heisenberg exchange. Later it was shown by Zhang and Rice [7] that the t-J model is also the proper theoretical description of the CuO_2 planes in cuprate superconductors. For application to the CuO_2 planes, the appropriate parameter values are $t \approx 350$ meV and $J \approx 140$ meV, so $J/t = 0.4$. The Hilbert space of the t-J model consists of states where each site is occupied either by a vacancy or a spin. The first term $\propto -t$ exchanges a vacancy and a spin on nearest neighbors, the second term $\propto J$ is the Heisenberg exchange between spins. In order to study the motion of a single hole in an antiferromagnet we decompose the t-J Hamiltonian Eq. (16) as $H = H_t + H_I + H_\perp$ whereby

$$H_t = -t \sum_{\langle i,j \rangle} \sum_{\sigma} \left(\hat{c}^{\dagger}_{i,\sigma} \hat{c}_{j,\sigma} + H.c \right), \qquad H_I = J \sum_{\langle i,j \rangle} S^z_i S^z_j, \qquad H_\perp = \frac{J}{2} \sum_{\langle i,j \rangle} \left(S^+_i S^-_j + H.c. \right),$$

and choose $H_0 = H_t + H_I$ as our unperturbed Hamiltonian. As already stated, in the absence of any hole the ground state of H_0 is the Néel state with energy $E_N = -NJ/2$. Next assume that an electron is removed from site i belonging to the $\uparrow$-sublattice, see Figure 6(a). This raises the exchange energy by $zJ/4$, because z bonds change their energy from $-J/4$ to 0. We choose the exchange energy of the resulting state, $E_N + zJ/4$, as the zero of energy. Then, the hopping term in (16) can become active and the spin from a neighboring site i_1 is transferred to i, resulting in the state in Figure 6(b). Since the shifted spin has 'switched sublattices', however, it now is opposite to the antiferromagnetic order. In fact, this inverted spin at site i is nothing but a magnon as discussed in the preceding section, so that the hopping vacancy 'radiates off' magnons [8, 9]. Since the displaced spin at site i is parallel to $z-1$ neighbors, the exchange energy increases by $(z-1)J/2$. And this continues as the vacancy moves through the Néel state, see Figure 6(c): in each step another spin is shifted to the opposite sublattice, so that the vacancy leaves behind a trace of misaligned spins and the exchange energy increases roughly linearly with the distance travelled by the hole. We call a state which is created by the motion of a vacancy in the Néel state a 'string state' and denote it by $|i_0, i_1, \ldots, i_\nu\rangle$. Here i_0 is the site

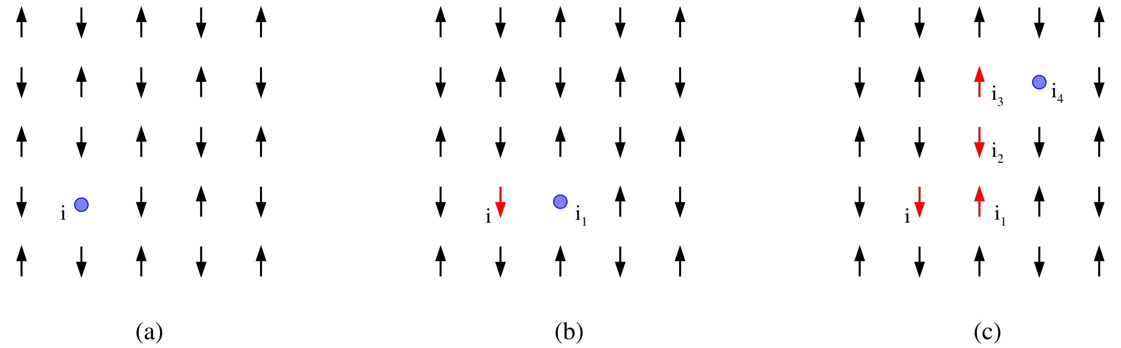

Fig. 6: *A hole hopping in the Néel state creates a 'string' of misaligned spins.*

where the hole was created, $i_1, i_2, i_{\nu-1}$ are the sites visited by the hole, whereas i_ν is the site where the vacancy is located. We call ν the length of the string, for example Figure 6(c) shows a string of length 4. There are z different string states with $\nu = 1$, whereas in any subsequent hop starting from a string state of length ν, $z-1$ new string states of length $\nu+1$ are generated. The number of different strings of length ν therefore is $n_\nu = z(z-1)^{\nu-1}$ for $\nu \geq 1$ whereas $n_0 = 1$. Since each displaced spin is parallel to $z-2$ neighbors, compare Figure 6, the magnetic energy increases by $J(z-2)/2$ per displaced spin, except for the first hop away from i where it increases by $J(z-1)/2$. Accordingly, the exchange energy for a string of length $\nu > 0$ his

$$I_\nu = \frac{(z-1)J}{2} + (\nu-1)\,\frac{(z-2)J}{2} = \frac{J}{2}\big((z-1) + (\nu-1)(z-2)\big), \tag{17}$$

and $I_0 = 0$. It may happen that the path which the hole has taken is folded or self-intersecting in which case (17) clearly is not correct. However it will be correct for 'most' possible paths of the hole, in particular it is correct for $\nu \leq 2$ so that we will use this expression. Neglecting the possibility of self-intersection or folding of the string is an approximation known as *Bethe-lattice*. Since the magnetic energy increases linearly with the number of hops the hole has taken we conclude that under the action of H_0 the hole is self-trapped. To describe the resulting localized state we make the *ansatz*

$$|\Phi_i\rangle = \sum_{\nu=0}^{\infty} \alpha_\nu \sum_{i_1,i_2,\ldots,i_\nu} |i, i_1, i_2, \ldots, i_\nu\rangle, \tag{18}$$

where it is understood that the second sum runs only over those ν-tuples of sites which correspond to a true string starting at i. Since we assume that the magnetic energy is the same for all strings of length ν, the coefficient α_ν also depends only on the length of the string. The coefficients α_ν in (18) are to be determined by minimizing the expectation value of H_0. The norm and magnetic energy are

$$\langle \Phi_i|\Phi_i\rangle = \sum_{\nu=0}^{\infty} n_\nu \alpha_\nu^2 = \sum_{\nu=0}^{\infty} \beta_\nu^2, \tag{19}$$

$$\langle \Phi_i|H_I|\Phi_i\rangle = \sum_{\nu=0}^{\infty} n_\nu I_\nu \alpha_\nu^2 = \sum_{\nu=0}^{\infty} I_\nu \beta_\nu^2\,, \tag{20}$$

where we have introduced $\beta_\nu = \alpha_\nu/\sqrt{n_\nu}$.

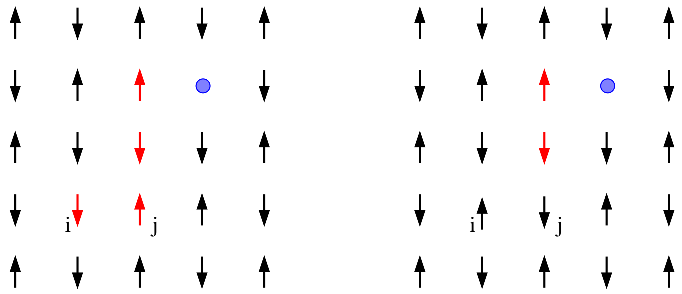

Fig. 7: *By acting with the term $\frac{J}{2}\,S_i^+S_j^-$ the first two defects created by the hole can be 'healed' and the starting point of the string be shifted to a neighbor.*

To obtain the expectation value of the kinetic energy we consider a string state of length $\nu \geq 1$ which has the coefficient α_ν. By acting with the hopping term we obtain $z-1$ strings of length $\nu+1$, with coefficient $\alpha_{\nu+1}$, and 1 string of length $\nu-1$, with coefficient $\alpha_{\nu-1}$. For $\nu = 0$ we obtain z strings of length 1. In this way we find

$$\langle \Phi_i | H_t | \Phi_i \rangle = t\Big(z\alpha_0\alpha_1 + \sum_{\nu=1}^{\infty} n_\nu \alpha_\nu \big(\alpha_{\nu-1} + (z-1)\alpha_{\nu+1}\big)\Big) = 2t\sum_{\nu=0}^{\infty} n_{\nu+1}\alpha_\nu\alpha_{\nu+1} = 2\sum_{\nu=0}^{\infty} \tilde{t}_\nu\ \beta_\nu\beta_{\nu+1}, \tag{21}$$

where $\tilde{t}_0 = \sqrt{z}\,t$ and $\tilde{t}_\nu = \sqrt{z-1}\,t$ for $\nu > 0$. The prefactor on the right hand side is t instead of $-t$ as one might have expected from (16) because the hopping term has to be rearranged as $-t\,\hat{c}_{i,\sigma}^\dagger \hat{c}_{j,\sigma} = t\,\hat{c}_{j,\sigma}\hat{c}_{i,\sigma}^\dagger$ to describe the hopping of a hole. As already stated, the β_ν now are determined from the requirement that the expectation value $E_{loc} = \langle \Phi_i | H_0 | \Phi_i \rangle / \langle \Phi_i | \Phi_i \rangle$ be stationary under variation of each β_ν

$$\begin{aligned} \frac{\partial E_{loc}}{\partial \beta_\nu} &= \frac{1}{\langle \Phi_i | \Phi_i \rangle^2} \left[\frac{\partial \langle \Phi_i | H_0 | \Phi_i \rangle}{\partial \beta_\nu} \langle \Phi_i | \Phi_i \rangle - \langle \Phi_i | H_0 | \Phi_i \rangle \frac{\partial \langle \Phi_i | \Phi_i \rangle}{\partial \beta_\nu} \right] \\ &= \frac{1}{\langle \Phi_i | \Phi_i \rangle} \left[\frac{\partial \langle \Phi_i | H_0 | \Phi_i \rangle}{\partial \beta_\nu} - E_{loc} \frac{\partial \langle \Phi_i | \Phi_i \rangle}{\partial \beta_\nu} \right] = 0. \end{aligned}$$

Setting the square bracket equal to zero and using Eqs. (19), (20) and (21) we obtain [10]

$$\left(\tilde{t}_\nu \beta_{\nu+1} + \tilde{t}_{\nu-1} \beta_{\nu-1} \right) + I_\nu \beta_\nu = E_{loc} \beta_\nu,$$

with the boundary condition $\beta_{-1} = 0$. This results in a tridiagonal Hamilton matrix for the β_ν and after cutting off at a sufficiently large ν, E_{loc} and the βs can be obtained by a simple numerical matrix diagonalization.

So far it seems that the hole in the Néel state is localized. It is easy to see, however, that the term $H_\perp$ which we have neglected so far can assist the trapped hole in escaping from the string potential, see Figure 7. Namely by acting on the first two sites of a string the spins which were inverted by the hole are inverted a second time and thus fit with the Néel order again: $H_\perp |i, i_1, i_2, i_3, \dots, i_\nu\rangle = J/2\ |i_2, i_3, \dots, i_\nu\rangle$. The initial site of the string thus is shifted to a $(2,0)$- or $(1,1)$-like neighbor while simultaneously the length ν is decreased by two. The term $H_\perp$ may also append two new defects to a string, $H_\perp |i_2, i_3, \dots, i_\nu\rangle = J/2\ |i, i_1, i_2, i_3, \dots, i_\nu\rangle$

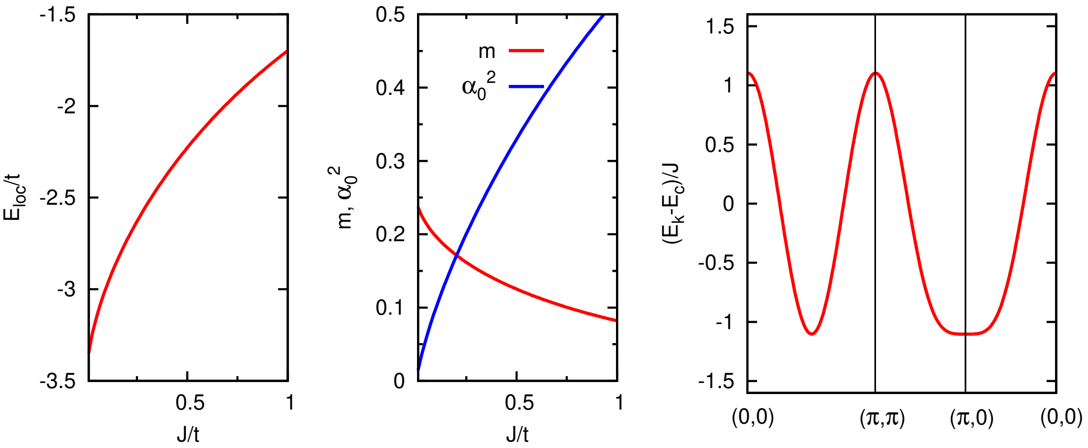

Fig. 8: *Left: Energy of the self-trapped state E_{loc} versus J/t. Center: Matrix element m due to string truncation and renormalization factor α_0^2 for the t' and t'' hopping terms versus J/t. Right: Band structure $E_{\mathbf{k}}$ for $J/t = 0.4$.*

thus increasing the length by 2 and again shifting the starting point to a $(2,0)$- or $(1,1)$-like neighbor. Using again the Bethe lattice approximation we find the matrix element

$$\langle \Phi_{i+2\hat{x}}|H_\perp|\Phi_i\rangle = J\sum_{\nu=0}^{\infty}(z-1)^\nu \alpha_\nu\alpha_{\nu+2} = \frac{J}{z}\left(\sqrt{\frac{z}{z-1}}\,\beta_0\beta_2 + \sum_{\nu=1}^{\infty}\beta_\nu\beta_{\nu+2}\right) = J\cdot m,$$

whereas $\langle \Phi_{i+\hat{x}+\hat{y}}|H_\perp|\Phi_i\rangle = 2J\cdot m$ because a string to a $(1,1)$-like neighbor can pass either trough $(1,0)$ or $(0,1)$ and the contributions from these two different paths are additive.
When the full Hamiltonian $H_0 + H_\perp$ is taken into account the hole therefore can propagate through the entire lattice and we describe this by the Bloch state

$$|\Phi_{\mathbf{k}}\rangle = \sqrt{\frac{2}{N}}\sum_{j\in A} e^{-i\mathbf{k}\cdot\mathbf{R}_j}\,|\Phi_i\rangle. \tag{22}$$

This is reminiscent of an LCAO wave function such as (1), but the role of the atomic orbital $|\phi_i\rangle$ here is played by the self-trapped function $|\Phi_i\rangle$. Since the matrix element of $H_\perp$ between $(1,1)$-like neighbors is twice that between $(2,0)$-like neighbors we obtain the dispersion

$$\begin{aligned} E_{\mathbf{k}} &= E_{loc} + 2Jm\cdot 4\cos(k_x)\cos(k_y) + Jm\cdot 2\big(\cos(2k_x)+\cos(2k_y)\big) \\ &= E_{loc} - 4Jm + 4Jm\big(\cos(k_x)+\cos(k_y)\big)^2 \end{aligned} \tag{23}$$

This expression shows several remarkable features which reflect the unusual nature of hole motion. First, there is the constant term $E_{loc} \propto t$. As we have seen, in the absence of the spin-flip term $H_\perp$ the hole is self-trapped in a linearly ascending 'effective potential' due to magnetic frustration. The hole executes a rapid zig-zag motion on a timescale $\tau_{loc} \propto t^{-1}$, and E_{loc} is the gain of kinetic energy due to this zig-zag motion. Figure 8 shows that $E_{loc} \approx -2.4\,t$ at $J/t = 0.4$, which is an appreciable fraction of $-4t$, the lowest possible kinetic energy which a freely propagating electron can have in an empty $2D$ lattice. On the longer time scale $\tau_{deloc} \propto J^{-1}$, the

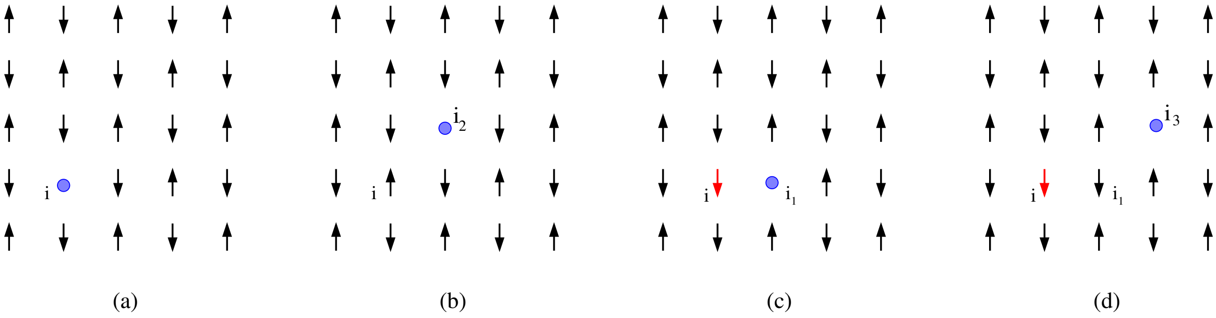

Fig. 9: *Hopping processes involving a term $\propto t'$ that connects $(1,1)$-like neighbors.*

spin-flip term shifts the center of the zig-zag motion to a 2^{nd} or 3^{rd} nearest neighbor, and the zig-zag motion starts anew. It follows that the bandwidth for coherent motion is *not* proportional to the hopping integral t, but to the smaller exchange constant J. The total bandwidth is $16Jm$ and since m is around 0.14 for $J/t = 0.4$, see Figure 8, the bandwidth is roughly $2J$. With $J = 140$ meV as appropriate for cuprates we expect $W \approx 300$ meV, almost a factor of 10 smaller than the width of the free tight-binding dispersion, which is $8t \approx 2.8$ eV. $E_{\mathbf{k}}$ has a degenerate minimum along $(\pi,0) \rightarrow (0,\pi)$ and symmetry equivalent lines, its maxima are at $(0,0)$ and (π,π). It has 'antiferromagnetic symmetry', $E_{\mathbf{k}+\mathbf{Q}} = E_{\mathbf{k}}$, which is to be expected since we are considering hole motion in an antiferromagnetic background.

In order to compare our theory to experiment we need to take into account that in the actual CuO$_2$-planes there are appreciable additional hopping integrals t' between $(1,1)$-like and t'' between $(2,0)$-like neighbors. Since these terms connect pairs of neighbors which are on the same sublattice, they do not create frustration and it might seem that they immediately dominate the hole motion. However, this is not the case and the reason can be seen in Figure 9. Fig. 9(a) shows a 'string of length 0', that means a hole at site i and the hopping term $\propto t'$ can transport the hole to the $(1,1)$-like neighbor i_2 without creating a magnon. On the other hand, 9(c) shows a 'string of length 1', that means a hole which has executed one nearest neighbor hopping process and is now at site i_1, with a single magnon at site i. Again, the t'-term can transport the hole to the $(1,1)$-like neighbor i_3, but it cannot transport the magnon along with the hole. Therefore, the hopping terms $\propto t', t''$ can transport only the 'bare hole', and since this has the coefficient α_0 in the self-trapped states $|\Phi_i\rangle$, these terms are renormalized by a factor α_0^2. Accordingly, they give the following contribution to the hole dispersion relation

$$E_{lr}(\mathbf{k}) = 4t'\alpha_0^2 \cos(k_x)\cos(k_y) + 2t''\alpha_0^2\big(\cos(2k_x) + \cos(2k_y)\big)$$

which has to be added to (23). Note again the opposite sign of the hopping terms as compared to the original Hamiltonian (16) because the fermion operators have to be exchanged to transport a hole. Figure 10 shows a comparison of the modified hole dispersion and the experimental band structure obtained by Angle Resolved Photoemission Spectroscopy (ARPES) on the insulating CuO-compound Sr$_2$CuO$_2$Cl$_2$ [11]. The band structure for a hole has to be turned upside down to compare to ARPES because the minimum of the hole-bandstructure is the maximum of the electron-band structure. The agreement is reasonable whereby it has to be kept in mind that in a

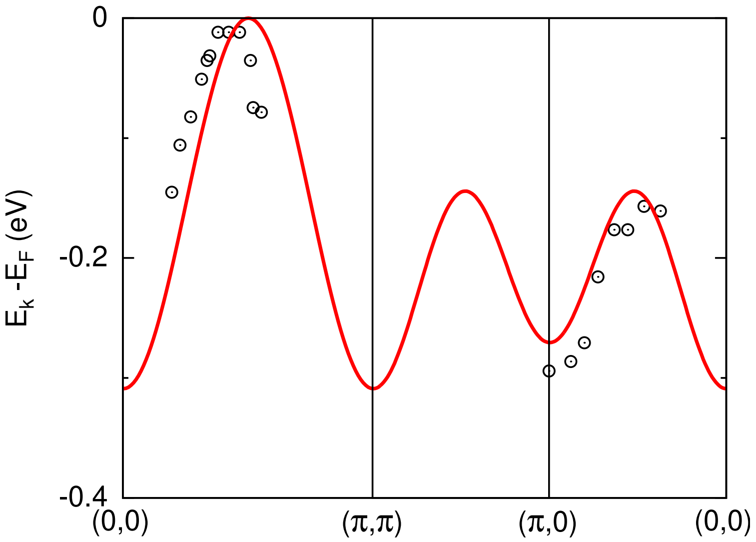

Fig. 10: *The band structure for the t-J model with additional hopping terms compared to the experimental valence band structure for the antiferromagnetic insulator* $Sr_2CuO_2Cl_2$ *[11]. Parameter values are* $t = 350$ *meV,* $J = 140$ *meV,* $t' = -120$ *meV,* $t'' = 60$ *meV.*

wide area around (π, π) and also close to $(0, 0)$ the band structure cannot be observed because the band has vanishing spectral weight in ARPES. In any way, the drastic reduction of the bandwidth can be seen clearly.

Looking back, the above discussion illustrates the general remarks in the introduction. In a Mott insulator each site carries a spin and spins on neighboring sites i and j are coupled by the exchange term $J\mathrm{S}_i \cdot \mathrm{S}_j$. This leads to a tendency for neighboring spins to be antiparallel and the appearance of *spin excitations*, which in the antiferromagnetic phase discussed above take the form of spin waves. Doped holes then have to move through this 'spin background' and by their very motion constantly interact with the spin excitations. As we have seen this leads to a drastic modification of the hole motion and band structure. And in fact, this also goes the other way round: since the holes are constantly 'stirring' the spins, these react and change their arrangement so as to make hole motion easier and allow for a gain of kinetic energy. In fact, in cuprate superconductors the antiferromagnetic order which was the basis of the above theory breaks down for hole concentrations of only a few per cent. Even in the resulting disordered state, the spin exchange term in the t-J Hamiltonian still favors antiparallel orientation of spins on nearest neighbors and in fact neutron scattering experiments show that there is still *short range antiferromagnetic order*, i.e., the spin correlation function $\langle \boldsymbol{S}_i \cdot \boldsymbol{S}_{i+\boldsymbol{R}} \rangle \propto e^{i\boldsymbol{Q}\cdot\boldsymbol{R}}\; e^{-|\boldsymbol{R}|/\zeta}$. This is reminiscent of the density correction function in a molten crystal, where locally the correlations between atoms resemble that of the original solid but there is no more long range crystalline order. Accordingly, such a state is called a 'spin liquid' and the description of such a spin liquid is the hardest part of the description of the doped Mott-insulator. The main difficulty is that so far nobody has been able to give a wave function for a Heisenberg antiferromagnet that has one electron/site and has no order of any kind. It will become clear in the next paragraph that this requires very drastic and questionable approximations.

4 Spin liquids

4.1 Dimer basis

As a prelude we follow Sachdev and Bhatt [12] as well as Gopalan, Rice, and Sigrist [13] and consider a *dimer* of two sites, labeled 1 and 2, and assume that both of them are occupied by one electron each, with their spins coupled by the exchange term $H = J\ \mathbf{S}_1 \cdot \mathbf{S}_2$. According to the rules for addition of angular momenta, the two spins of $1/2$ can be coupled to the total spin $S = 1$ (spin triplet) or $S = 0$ (spin singlet). The singlet and the three components of the triplet are eigenstates of the square of the operator of total spin $\mathbf{S} = \mathbf{S}_1 + \mathbf{S}_2$ with eigenvalue $S(S{+}1)$: $\mathbf{S}^2 = \mathbf{S}_1^2 + 2\mathbf{S}_1 \cdot \mathbf{S}_2 + \mathbf{S}_2^2 = S(S{+}1)$, and using that $\mathbf{S}_1^2 = \mathbf{S}_2^2 = \frac{1}{2}\left(\frac{1}{2}+1\right) = \frac{3}{4}$ we find $\mathbf{S}_1 \cdot \mathbf{S}_2 = \frac{1}{2}\big(S(S{+}1) - \frac{3}{2}\big)$. Accordingly, $\mathbf{S}_1 \cdot \mathbf{S}_2$ gives $-3/4$ when acting on the singlet and $1/4$ for a triplet. Due to the limited size of the Hilbert space of the dimer, constructing states with definite total spin thus is equivalent to diagonalizing the exchange term, and we find the eigenenergies $-3J/4$ for the singlet, and $J/4$ for the three components of the triplet. The eigenstates themselves are given by [12, 13]

$$\begin{aligned}
|\,s\,\rangle &= \frac{1}{\sqrt{2}}\,\left(\,c_{1,\uparrow}^\dagger c_{2,\downarrow}^\dagger - c_{1,\downarrow}^\dagger c_{2,\uparrow}^\dagger\,\right)|0\rangle,\\
|t_x\rangle &= \frac{1}{\sqrt{2}}\,\left(\,c_{1,\downarrow}^\dagger c_{2,\downarrow}^\dagger - c_{1,\uparrow}^\dagger c_{2,\uparrow}^\dagger\,\right)|0\rangle,\\
|t_y\rangle &= \frac{i}{\sqrt{2}}\,\left(\,c_{1,\uparrow}^\dagger c_{2,\uparrow}^\dagger + c_{1,\downarrow}^\dagger c_{2,\downarrow}^\dagger\,\right)|0\rangle,\\
|t_z\rangle &= \frac{1}{\sqrt{2}}\,\left(\,c_{1,\uparrow}^\dagger c_{2,\downarrow}^\dagger + c_{1,\downarrow}^\dagger c_{2,\uparrow}^\dagger\,\right)|0\rangle.
\end{aligned}\tag{24}$$

with $|s\rangle$ the singlet and $|t_x\rangle$, $|t_y\rangle$ and $|t_z\rangle$ the three components of the triplet. Note that the three $|t_\alpha\rangle$ in (24) are *not* eigenstates of the total z-spin, rather they are linear combinations of the states with fixed z-spin which obey $S_\alpha|t_\beta\rangle = i\varepsilon_{\alpha\beta\gamma}\ |t_\gamma\rangle$, for example

$$\begin{aligned}
S_x|t_y\rangle &= \frac{1}{2}\sum_{i=1}^{2}\left(S_i^-{+}S_i^+\right)\frac{i}{\sqrt{2}}\left(c_{1,\uparrow}^\dagger c_{2,\uparrow}^\dagger + c_{1,\downarrow}^\dagger c_{2,\downarrow}^\dagger\right)\\
&= \frac{i}{2\sqrt{2}}\left(c_{1,\downarrow}^\dagger c_{2,\uparrow}^\dagger + c_{1,\uparrow}^\dagger c_{2,\downarrow}^\dagger + c_{1,\uparrow}^\dagger c_{2,\downarrow}^\dagger + c_{1,\downarrow}^\dagger c_{2,\uparrow}^\dagger\right) = i|t_z\rangle.
\end{aligned}$$

This means that the three states $|t_\alpha\rangle$ transform like a vector under spin rotations which will be convenient later on. We also note that under the exchange of the two sites, $1 \leftrightarrow 2$, we have $|s\rangle \to |s\rangle$ but $|t_\alpha\rangle \to -|t_\alpha\rangle$.

We return to the undoped Heisenberg antiferromagnet on a 2D square lattice with N sites. A state which on the one hand is disordered and on the other hand is an exact spin singlet can be obtained in the following way: let the N sites be partitioned into $N/2$ dimers, whereby each dimer comprises two nearest neighbor sites, see Figure 11(a), and assume moreover that the two spins in each dimer are coupled to the singlet state. The resulting state of the plane is the

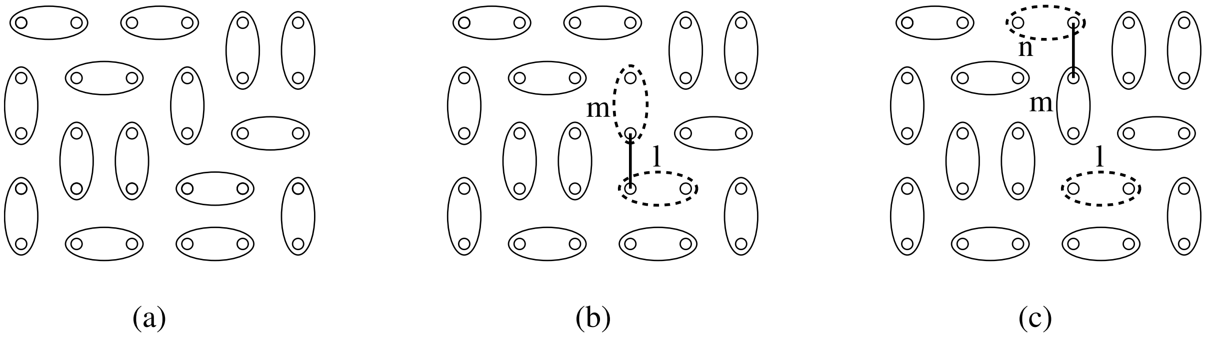

(a) (b) (c)

Fig. 11: *(a) A dimer covering of the plane: spins on sites covered by an ellipse are coupled to a singlet. (b) By acting with the exchange along the bond connecting the dimers l and m both dimers are excited into the triplet state. (c) By acting with the exchange along the bond connecting the dimers m and n bond m is de-excited to the singlet whereas dimer n is excited to the triplet — the triplet has propagated.*

product

$$|\Psi_0\rangle = \prod_{(i,j)\in D} \frac{1}{\sqrt{2}}\Big(c^\dagger_{i,\uparrow}c^\dagger_{j,\downarrow} - c^\dagger_{i,\downarrow}c^\dagger_{j,\uparrow}\Big)|0\rangle$$

where D is the set of $N/2$ pairs (i,j) of nearest neighbor sites corresponding to the given dimer covering. $|\Psi_0\rangle$ is an eigenstate of the 'depleted Hamiltonian' $H_d = J \sum_{(i,j)\in D} \mathbf{S}_i \cdot \mathbf{S}_j$ with eigenvalue $E_{d,0} = (N/2)\cdot(-3J/4)$. Since $\langle \mathbf{S}_i \cdot \mathbf{S}_j \rangle = 0$ if i and j belong to different dimers, as will be shown in a moment, this is also the expectation value of the full Hamiltonian in the state $|\Psi_0\rangle$. Next, let us consider what happens if we act onto $|\Psi_0\rangle$ with the exchange along a bond *not included* in the set D, that means a bond which connects spins in different dimers, such as the bond indicated in Figure 11(b). Due to the product nature of $|\Psi_0\rangle$ it is sufficient to discuss what happens when the spin operator acts on a singlet, e.g.

$$S_{1,x}|s\rangle = \frac{1}{2}\big(S_1^- + S_1^+\big)\frac{1}{\sqrt{2}}\left(c^\dagger_{1,\uparrow}c^\dagger_{2,\downarrow} - c^\dagger_{1,\downarrow}c^\dagger_{2,\uparrow}\right)|0\rangle = \frac{1}{2\sqrt{2}}\left(c^\dagger_{1,\downarrow}c^\dagger_{2,\downarrow} - c^\dagger_{1,\uparrow}c^\dagger_{2,\uparrow}\right)|0\rangle. \tag{25}$$

Comparing with (24), the expression on the right hand side is seen to be $\frac{1}{2}|t_x\rangle$. Next, we exchange $1 \leftrightarrow 2$ on both sides of (25), whence $S_{1,x} \to S_{2,x}$, $|s\rangle \to |s\rangle$, and $|t_x\rangle \to -|t_x\rangle$, and obtain $S_{2,x}|s\rangle = -\frac{1}{2}|t_x\rangle$. Since the triplets where constructed to transform like a vector, this holds true for the other Cartesian components as well: $S_{1,\alpha}|s\rangle = \frac{1}{2}|t_\alpha\rangle$, $S_{2,\alpha}|s\rangle = \frac{1}{2}|t_\alpha\rangle$ with $\alpha \in \{x,y,z\}$. Acting with the term $J\mathbf{S}_i \cdot \mathbf{S}_j$ along a bond which connects sites i and j in different dimers therefore simultaneously excites both dimers to the triplet state, with a prefactor of $\pm J/4$ (the prefactor will be discussed more precisely below). The new state again is an eigenstate of the 'depleted Hamiltonian' H_d, with eigenvalue $E_{d,0}{+}2J$ and obviously is orthogonal to $|\Psi_0\rangle$, which also proves that the expectation value $\langle \mathbf{S}_i \cdot \mathbf{S}_j \rangle$ vanishes if the sites i and j belong to different dimers. Next consider what happens when the exchange term acts along the bond indicated in Figure 11(c). We already know that bond n will be excited to the triplet state but we need to study what happens when the spin operator acts on the triplet in bond

m:

$$S_{1,x}|t_x\rangle = \frac{1}{2}\big(S_1^+ + S_1^-\big)\frac{1}{\sqrt{2}}\left(c^\dagger_{1,\downarrow}c^\dagger_{2,\downarrow} - c^\dagger_{1,\uparrow}c^\dagger_{2,\uparrow}\right)|0\rangle = \frac{1}{2\sqrt{2}}\left(c^\dagger_{1,\uparrow}c^\dagger_{2,\downarrow} - c^\dagger_{1,\downarrow}c^\dagger_{2,\uparrow}\right)|0\rangle, \tag{26}$$

which is nothing but $\frac{1}{2}|s\rangle$. Therefore, acting with the exchange term along the bond indicated in Figure 11(c), the dimer m is de-excited to the singlet state according to (26), whereas the dimer n is excited to the triplet state according to (25) or, put another way, the 'excited dimer' jumps from dimer m to dimer n. Comparing now with Figure 4 we see a quite analogous pattern arising: both, the Néel state and the dimer state $|\Psi_0\rangle$ are the ground state of a part of the Hamiltonian, namely the longitudinal part $J\sum_{\langle i,j\rangle} S_{i,z}S_{j,z}$ in the case of the Néel state and the depleted Hamiltonian H_d for the dimer state. Switching on the remainder of the Hamiltonian then creates 'fluctuations': these were the inverted spins or magnons in the case of the Néel state, and the excited dimers in the case of the singlet soup. The fluctuations increase the energy: by $zJ/2$ for a magnon, and by J for a triplet. After having been created these fluctuations then propagate through the lattice. This suggests that we proceed exactly as in the case of spin wave theory and interpret the triplets as effective bosonic particles (we use bosons because a triplet is composed of two electrons). To be more quantitative, we need to introduce some conventions: We assume that the bonds are labeled by a number $n \in \{1,\dots,N/2\}$. Since the triplet has negative parity under the exchange of sites, $1 \leftrightarrow 2$, we need to specify which of the sites i and j in a given dimer corresponds to the site 1 in Eq. (24) and which one to the site 2. We adopt the convention that for a bond in x-direction (y-direction) the left (lower) site always corresponds to the site 1. We call the site which corresponds to 1 the '1-site of the dimer' and the site which corresponds to 2 the '2-site of the dimer'. For each site i we define $\lambda_i = 1$ if it is the 1-site of its respective dimer, and -1 if it is the 2-site. Then, if a given dimer m is occupied by a singlet, we consider it as occupied by a bosonic particle, created by $s^\dagger_m$, whereas if the dimer is in one of the three triplet states we consider it as occupied by a boson, created by $t^\dagger_{m,\alpha}$ with $\alpha \in \{x,y,z\}$. We have already seen that the three triplet states transform like a vector under spin rotations and it follows that the corresponding creation operators form a *vector operator* $\left[S_\alpha,\, t^\dagger_\beta\right] = i\varepsilon_{\alpha\beta\gamma}t^\dagger_\gamma$, and Hermitean conjugation shows that the annihilation operator $\mathbf{t}_m$ is a vector operator as well. Calculating the action of the spin operator on triplet states gives the representation of the spin operator

$$\mathbf{S}_j \to \frac{\lambda_j}{2}\big(s^\dagger\mathbf{t} + \mathbf{t}^\dagger s\big) - \frac{i}{2}\,\mathbf{t}^\dagger\times\mathbf{t}. \tag{27}$$

The x-component of the correspondence $\mathbf{S}_j \to \frac{\lambda_j}{2}\big(s^\dagger\mathbf{t} + \mathbf{t}^\dagger s\big)$ was demonstrated in (25) and (26). We recall that we found $S_{1,x}|s\rangle = \frac{1}{2}|t_x\rangle$ whereas $S_{2,x}|s\rangle = -\frac{1}{2}|t_x\rangle$ and the factor of λ_i keeps track of this sign. From the discussion after (25) we see that such a sign, and hence a factor of λ_i, will occur whenever the Hamiltonian induces a transition between states which have opposite parity under $1 \leftrightarrow 2$. Next, The overall form of the terms on the right hand side follows from the fact that S is a Hermitean vector operator, so the right hand side has to be one as well. Then, the vector product $\mathbf{t}^\dagger\times\mathbf{t}$ is the only way to contract two vector operators into a single one, but since the vector product is anti-Hermitean it has to be multiplied by the factor of i to make it Hermitean. Next, by forming the scalar product, we can write down the exchange term $h_{m,n} = J\ \mathbf{S}_i \cdot \mathbf{S}_j$ along a bond connecting the sites i and j such that site i belongs to dimer m, site j to dimer n with $m \neq n$:

$$\begin{aligned} h_{m,n} \;\; = \;\; & \frac{J\lambda_i\lambda_j}{4}\Big(\mathbf{t}_n^\dagger\!\cdot \mathbf{t}_m\ s_n s_m^\dagger + \mathbf{t}_m^\dagger\!\cdot \mathbf{t}_n\ s_m s_n^\dagger + \mathbf{t}_m^\dagger\!\cdot \mathbf{t}_n^\dagger\ s_n s_m + \mathbf{t}_m\!\cdot \mathbf{t}_n\ s_m^\dagger s_n^\dagger\Big) \\ & -\frac{iJ}{4}\Big(\lambda_i\big(s_m^\dagger \mathbf{t}_m + \mathbf{t}_m^\dagger s_m\big)\!\cdot\!\big(\mathbf{t}_n^\dagger\!\times\!\mathbf{t}_n\big) + \lambda_j\big(s_n^\dagger \mathbf{t}_n + \mathbf{t}_n^\dagger s_n\big)\!\cdot\!\big(\mathbf{t}_m^\dagger \times \mathbf{t}_m\big)\Big) \\ & -\frac{J}{4}\big(\mathbf{t}_n^\dagger\!\times\!\mathbf{t}_n\big)\!\cdot\!\big(\mathbf{t}_m^\dagger\!\times\!\mathbf{t}_m\big). \end{aligned} \tag{28}$$

As expected the right hand side comprises all possible ways to construct a spin scalar from the vectors $\mathbf{t}$ and $\mathbf{t}^\dagger$ and only the numerical prefactors needed to be determined.

4.2 Spin excitations

While the representation of the Heisenberg antiferromagnet derived in the preceding section is exact for any given dimer covering of the plane, we have not gained very much because even writing down a dimer covering for a macroscopic system is not feasible, let alone solve the corresponding Hamiltonian. One might consider choosing a particularly 'simple' dimer covering such as columns of dimers in, say, x-direction. However, since one is forced to make approximations, the special symmetry of the covering will make itself felt in the approximate solutions as an artificial supercell structure, leading to a reduction of the Brillouin zone and an unphysical backfolding of bands.

On the other hand, rewriting the Heisenberg Hamiltonian in terms of the singlet and triplet bosons provides an exact representation of the Heisenberg model for *any* dimer covering of the plane. This means that for example the result for the spin correlation function $\big\langle \mathbf{S}_j(t)\!\cdot\!\mathbf{S}_i\big\rangle$ cannot depend on the specific dimer covering in which the calculation is carried out. Put another way, the way in which a spin excitation propagates through the network of dimers from site $i \to j$ during the time t does not depend at all on the geometry of the particular dimer covering. This suggests to construct a translationally invariant approximate Hamiltonian by *averaging* the dimer Hamiltonian over all possible coverings. We find

$$H_{av} = J\sum_m \mathbf{t}_m^\dagger\!\cdot \mathbf{t}_m + \sum_{m,n}\sum_{\substack{i\in m\\ j\in n}}\ \zeta_{m,n} h_{m,n}\,. \tag{29}$$

Here we have chosen the energy of the state where all bonds are occupied by triplets as the zero of energy, the first term then adds an energy of J for every bond occupied by a triplet. The sum $\sum_{m,n}$ runs over all pairs of bonds connected by an exchange term $J\ \mathbf{S}_i \cdot \mathbf{S}_j$ with $i \in m$ and $j \in n$ and $h_{m,n}$ is given in (28). The renormalization factor $\zeta_{m,n}$ is defined as

$$\zeta_{m,n} = \frac{N_{m,n}}{N_d}\,, \tag{30}$$

where $N_{m,n}$ is the number of dimer coverings which contain the bonds n and m whereas N_d is the total number of dimer coverings. The resulting Hamiltonian is translationally invariant and

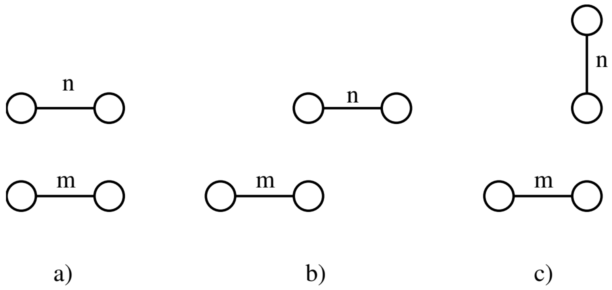

Fig. 12: *Estimation of the renormalization factor ζ.*

isotropic. We estimate ζ by a crude approximation: consider two adjacent bonds as in Figure 12. By symmetry the bond m is covered by a dimer in exactly $1/4$ of all dimer coverings and we restrict ourselves to these. Assuming for simplicity that the number of coverings containing one of the three possible orientations of the adjacent bond n are equal, we estimate $\zeta = 1/12$.

Using the averaging procedure we have circumvented the problem of having to consider a fixed dimer covering, but inspection of (28) shows that $h_{m,n}$ still is a sum of quartic terms and thus impossible to solve. In the next step of approximation therefore assume that the singlet bosons are condensed and replace the corresponding *operators* $s_n^\dagger$ and s_n in (28) by the real *condensation amplitude* s. This is equivalent to assuming that the singlets form an inert background and the only active degrees of freedom are the triplets. Further inspection of (28) shows that after singlet condensation it contains terms of second, third and fourth order in the triplet operators. As the final approximation we discard the terms of third and fourth order, which describe scattering processes between the triplets, whence the Hamiltonian finally becomes

$$H_{av} = \tilde{J} \sum_m \mathbf{t}_m^\dagger \cdot \mathbf{t}_m + \frac{\zeta s^2}{4} \sum_{m,n} \sum_{\substack{i\in m \\ j\in n}} J_{i,j} \lambda_i \lambda_j \left(\mathbf{t}_n^\dagger \cdot \mathbf{t}_m + \mathbf{t}_m^\dagger \cdot \mathbf{t}_n + \mathbf{t}_m^\dagger \cdot \mathbf{t}_n^\dagger + \mathbf{t}_n \cdot \mathbf{t}_m \right). \tag{31}$$

The sums over m, n run over all $2N$ bonds of the plane, $J_{i,j} = J$ if i and j are nearest neighbors and zero otherwise.

From this point on we can proceed exactly in the same way as we did for the antiferromagnetic magnons. Being a quadratic form (31) is readily diagonalized by Fourier transform, we only need to specify a convention for the position of a bond: if bond m connects the sites i and j we define $\mathbf{R}_m = (\mathbf{R}_i + \mathbf{R}_j)/2$. Moreover we have two species of bonds: bonds in x-directions and bonds in y-direction. We specify this by an additional subscript for the Fourier transformed operators, e.g. $\mathbf{t}_{\mathbf{k},\mu}^\dagger$ with $\mu \in \{x, y\}$. The products $\lambda_i \lambda_j$ are given in Figure 13 from which we readily can read off

$$H = \sum_{\mathbf{k}} \sum_{\mu,\mu' \in \{x,y\}} \left(\mathbf{t}_{\mathbf{k},\mu}^\dagger \left(\tilde{J} \delta_{\mu\mu'} + \varepsilon_{\mu,\mu'}(\mathbf{k}) \right) \mathbf{t}_{\mathbf{k},\mu'} + \frac{1}{2} \left(\mathbf{t}_{\mathbf{k},\mu}^\dagger \varepsilon_{\mu,\mu'}(\mathbf{k})\ \mathbf{t}_{-\mathbf{k},\mu'}^\dagger + H.c. \right) \right)$$

$$\begin{aligned}
\varepsilon_{\,x,x}(\mathbf{k}) &= \zeta s^2 J \Big(\cos(k_y) - \frac{1}{2} \cos(2k_x) - \cos(k_x)\cos(k_y) \Big), \\
\varepsilon_{\,x,y}(\mathbf{k}) &= \zeta s^2 J \Big(\sin\Big(\frac{3k_x}{2}\Big) \sin\Big(\frac{k_y}{2}\Big) + \sin\Big(\frac{k_x}{2}\Big) \sin\Big(\frac{3k_y}{2}\Big) \Big),
\end{aligned}$$

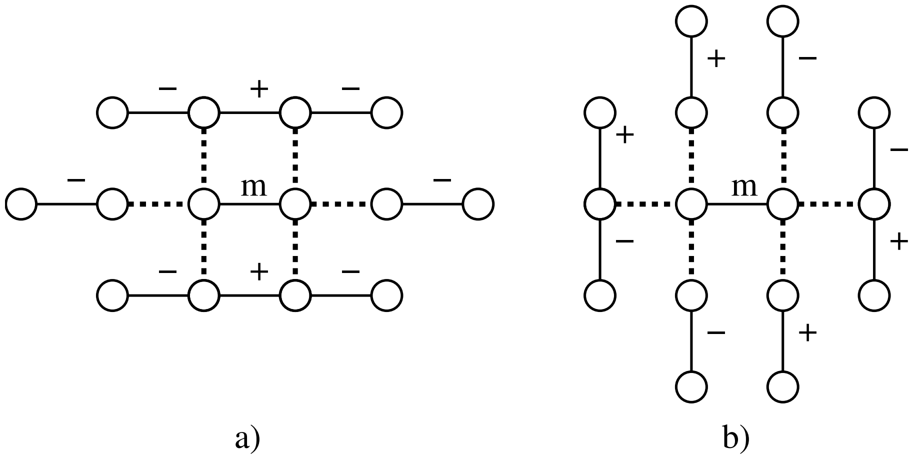

Fig. 13: *The factors of $\lambda_i\lambda_j$ for all bonds connected to the bond m by a nearest neighbor bond. In a) both bonds are along the x-direction so that these pairs contribute to $\varepsilon_{x,x}$ whereas in b) one bond is along the y-direction so that these pairs contribute to $\varepsilon_{x,y}$. In a) both bonds connecting parallel bonds have $\lambda_i\lambda_j = 1$.*

$\varepsilon_{\,y,x} = \varepsilon_{\,x,y}$, and $\varepsilon_{\,y,y}$ is obtained from $\varepsilon_{\,x,x}$ by $k_x \leftrightarrow k_y$. To diagonalize H we proceed as for antiferromagnetic magnons and make the *ansatz* $\big($with $\nu \in \{1,2\}\big)$

$$\begin{aligned}
\boldsymbol{\tau}^\dagger_{\nu,\mathbf{k}} &= \sum_{\mu\in\{x,y\}} \big(u_{\nu,\mathbf{k},\mu}\,\mathbf{t}^\dagger_{\mathbf{k},\mu} + v_{\nu,\mathbf{k},\mu}\,\mathbf{t}_{-\mathbf{k},\mu}\big),\\
\boldsymbol{\tau}_{\nu,-\mathbf{k}} &= \sum_{\mu\in\{x,y\}} \big(v^*_{\nu,\mathbf{k},\mu}\,\mathbf{t}^\dagger_{\mathbf{k},\mu} + u^*_{\nu,\mathbf{k},\mu}\,\mathbf{t}_{-\mathbf{k},\mu}\big).
\end{aligned} \tag{32}$$

Demanding $\big[H,\,\boldsymbol{\tau}^\dagger_{\nu,\mathbf{k}}\big] = \omega_{\nu,\mathbf{k}}\boldsymbol{\tau}^\dagger_{\nu,\mathbf{k}}$ gives the $4{\times}4$ eigenvalue problem

$$\begin{pmatrix} \tilde{J}{+}\varepsilon_{\mathbf{k}} & -\varepsilon_{\mathbf{k}} \\ \varepsilon^*_{-\mathbf{k}} & -\tilde{J}{-}\varepsilon^*_{-\mathbf{k}} \end{pmatrix} \begin{pmatrix} u_{\nu,\boldsymbol{k}} \\ v_{\nu,\boldsymbol{k}} \end{pmatrix} = \omega_{\nu,\mathbf{k}} \begin{pmatrix} u_{\nu,\boldsymbol{k}} \\ v_{\nu,\boldsymbol{k}} \end{pmatrix}. \tag{33}$$

For a matrix like the one on the left hand side it is easy to show that if (u,v) is an eigenvector with eigenvalue ω, then (v^*,u^*) is an eigenvector with eigenvalue $-\omega$ so that the eigenvalues come in pairs of $\pm\omega$. We multiply (33) by $\omega_{\nu,\mathbf{k}}$ and replace products such as $\omega_{\nu,\mathbf{k}}u_{\nu,\boldsymbol{k}}$ or $\omega_{\nu,\mathbf{k}}v_{\nu,\boldsymbol{k}}$ on the left hand side of the resulting equations by the expressions given by the original version of (33). Since the commutator $\big[\tilde{J}{+}\varepsilon_{\mathbf{k}},\,\varepsilon_{\mathbf{k}}\big] = 0$ we obtain

$$\big(\tilde{J}^2 + 2\tilde{J}\varepsilon_{\mathbf{k}}\big)u_{\nu,\boldsymbol{k}} = \omega^2_{\nu,\mathbf{k}}u_{\nu,\boldsymbol{k}},$$

and the same equation for $v_{\nu,\boldsymbol{k}}$. It follows that $\omega_{\nu,\mathbf{k}} = \sqrt{\tilde{J}^2 + 2\tilde{J}\lambda_{\nu,\mathbf{k}}}$, where $\lambda_{\nu,\mathbf{k}}$ are the eigenvalues of the Hermitean $2{\times}2$ matrix $\varepsilon_{\mathbf{k}}$, and both, $u_{\nu,\boldsymbol{k}}$ and $v_{\nu,\boldsymbol{k}}$, must be the corresponding eigenvector, albeit multiplied by different prefactors. The eigenvalues of $\varepsilon_{\mathbf{k}}$ are easily shown to be $\lambda_{1,\mathbf{k}} = -\zeta s^2 J/2$ and $\lambda_{2,\mathbf{k}} = \zeta s^2 J\big(3/2 + 2\gamma_{\mathbf{k}} - 4\gamma^2_{\mathbf{k}}\big)$, with $\gamma_{\mathbf{k}}$ given in (12).

In principle the singlet condensation amplitude s and the renormalized triplet energy $\tilde{J}$ should now be calculated self-consistently, but for the sake of simplicity we here switch to a more

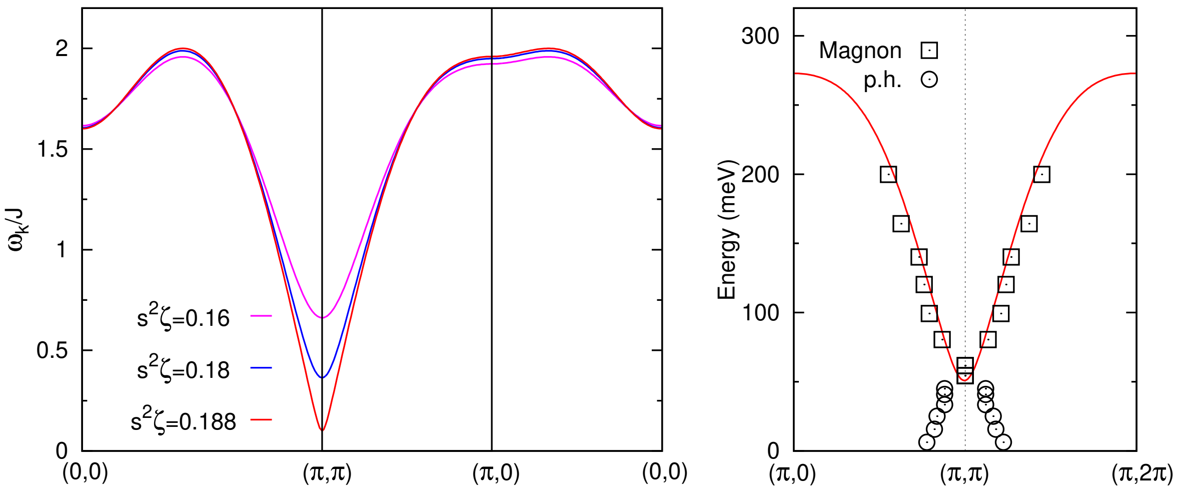

Fig. 14: *Left: Spin excitation dispersion relation* $\omega_{\mathbf{k}}$ *using the parameter values* $\tilde{J} = 1.7\ J$ *and different* $s^2\zeta$*. Right:* $\omega_{\mathbf{k}}$ *calculated for* $\tilde{J} = 1.7\ J$*,* $s^2\zeta = 0.16$ *and* $J = 140$ *meV compared to the hourglass dispersion measured in La*$_{1.875}$*Ba*$_{0.125}$*CuO*$_4$ *[14]. The data points labeled 'Magnon' correspond to the triplet dispersion, the points labeled 'p.h.' correspond to particle-hole excitations which are absent in our theory.*

phenomenological description and consider $s^2\zeta$ and $\tilde{J}$ as adjustable parameters. Regarding $s^2\zeta$ we recall that ζ was determined somewhat vaguely anyway. Regarding $\tilde{J}$ we expect $\tilde{J} > J$ because $\tilde{J}$ gives the cost in energy needed to create a triplet. This is of course J itself, but should be augmented by a loss of kinetic energy that is incurred because a triplet on, say, dimer m blocks pair creation and hopping processes on all dimers that share a site with m. Our theory thus has two adjustable parameters, which we use to fix two physical quantities, the total bandwidth of the spin excitations, and the spin gap (to be explained below). Lastly, we recall that we have two eigenvalues $\lambda_{\nu,\mathbf{k}}$ for each wave vector $\mathbf{k}$, whereby $\lambda_{1,\mathbf{k}}$ has the peculiar feature of being independent of $\mathbf{k}$. A more detailed analysis shows [15], that the band derived from the dispersionless eigenvalue also has zero spectral weight in the spin correlation function. This suggests, that this band is an artifact of the enlargement of the basis by doubling the number of bonds. We therefore drop this dispersionless band and retain only the band of spin excitations resulting from $\lambda_{2,\mathbf{k}}$. Figure 14 shows the resulting triplet dispersion $\omega_{\mathbf{k}}$. The parameter $\tilde{J}$ has been adjusted to set the total bandwidth to $2J$, the bandwidth for antiferromagnetic spin waves. $\omega_{\mathbf{k}}$ has a minimum at (π, π) and the energy at this wave vector is frequently called the spin gap, Δ_S. With increasing value of $s^2\zeta$, Δ_S closes rapidly and one can envisage how for $\Delta_S \to 0$ the cone-shaped dispersion of antiferromagnetic spin waves at (π, π) is recovered. Experimentally, inelastic neutron scattering on many cuprate compounds shows an 'hourglass' dispersion around (π, π), an example is also shown in Figure 14. This is frequently interpreted [16] as a magnon-like collective mode above the neck of the hour-glass co-existing with particle-hole excitations of the Fermi gas of free carriers below the neck. The part above the neck of the hourglass thus should correspond to our triplet band and the comparison in Figure 14 shows indeed reasonable agreement.

4.3 Doped holes

Next, we extend the theory for the spin liquid to include doped holes. As the first step we introduce dimers which contain a single electron or no electron at all. We again consider a dimer with sites 1 and 2, but now assume that the dimer contains one electron with spin σ. Instead of the exchange term, it is now the hopping term which is active: $H_t = -t\sum_\sigma \big(\hat{c}^\dagger_{1,\sigma}\hat{c}_{2,\sigma} + H.c.\big)$ and there are two eigenstates of H_t

$$|f_{\pm,\sigma}\rangle = \frac{1}{\sqrt{2}}\big(\hat{c}^\dagger_{1,\sigma} \pm \hat{c}^\dagger_{2,\sigma}\big)|0\rangle. \tag{34}$$

These obey $H_t|f_{\pm,\sigma}\rangle = \mp t|f_{\pm,\sigma}\rangle$. We introduce a new type of effective particle to represent dimers occupied by one electron. If the dimer m is in one of the states $|f_{\pm,\sigma}\rangle$ we consider it as occupied by a fermion, created by $f^\dagger_{m,\pm,\sigma}$. We choose a fermion, because the number of electrons in such a dimer is one. We also introduce an additional boson, created by $e^\dagger$, to represent an empty dimer. In order to include these particles we need to transcribe the electron creation and annihilation operators $\hat{c}^\dagger_{i,\sigma}$ and $\hat{c}_{i,\sigma}$. The two spin components of a fermion creation operator can be combined to a two-component vector, a covariant spinor [17], $\mathbf{c}^\dagger = (c^\dagger_\uparrow,\, c^\dagger_\downarrow)^T$. Similarly the spin components of the annihilation operator for a so-called contravariant spinor $\mathbf{c} = (c_\uparrow,\, c_\downarrow)^T$. Proceeding in an analogous way as in the derivation of (27) for the spin operator we find $\big($with $j \in \{1,2\}\big)$

$$\mathbf{c}_j \rightarrow\, : \frac{1}{2}\big(s\, i\tau_y + \lambda_j \mathbf{t}\cdot\boldsymbol{\tau}\, i\tau_y\big)\big(\mathbf{f}^\dagger_+ - \lambda_j \mathbf{f}^\dagger_-\big) + \frac{1}{\sqrt{2}} e^\dagger\big(\mathbf{f}_+ + \lambda_j \mathbf{f}_-\big) : \tag{35}$$

where $: \cdots :$ denotes normal ordering. The first term on the right hand side describes a singlet or triplet state on a given bond being converted into a single-electron state, the second term describes a single-hole state being converted into the empty bond. As was the case for the triplets, the overall form of the terms on the right hand side can be guessed by making use of the transformation properties under spin rotations. The so-called metric spinor $i\tau_y$ converts the covariant spinors $\mathbf{f}^\dagger_\pm$ into contravariant ones [17] and the 'spinor product' $\mathbf{t}\cdot\boldsymbol{\tau}\mathbf{c}$ is the only way to construct a contravariant spinor from the vector operator $\mathbf{t}$ and another contravariant spinor $\mathbf{c}$. The factors of λ_j again are associated with states of opposite parity under $1 \leftrightarrow 2$. Using (35) we can rewrite the hopping term, along a bond connecting the sites i and j such that site i belongs to dimer m, site j to dimer n

$$\begin{aligned} -t\sum_\sigma \hat{c}^\dagger_{i,\sigma}\hat{c}_{j,\sigma} \;\;\rightarrow\;\; & \frac{t}{4}\Big(\big(s^\dagger_m s_n \; + \lambda_i\lambda_j \mathbf{t}^\dagger_m \cdot \mathbf{t}_n\big)\big(\sum_\sigma f^\dagger_{n,j,\sigma} f_{m,i,\sigma}\big) \\ & \qquad - \big(\lambda_i \mathbf{t}^\dagger_m s_n + \lambda_j s^\dagger_m \mathbf{t}_n\big)\cdot \mathbf{v}_{(n,j),(m,i)} - i\lambda_i\lambda_j\big(\mathbf{t}^\dagger_m \times \mathbf{t}_n\big)\cdot \mathbf{v}_{(n,j),(m,i)}\Big), \end{aligned} \tag{36}$$

where the combination $f_{m,i,\sigma} = f_{m,+,\sigma} - \lambda_i\, f_{m,-,\sigma}$ and the vector

$$\mathbf{v}_{(n,j),(m,i)} = \sum_{\sigma,\sigma'} f^\dagger_{n,j,\sigma}\, \boldsymbol{\tau}_{\sigma,\sigma'}\, f_{m,i,\sigma'}$$

obeys $\big[S_\alpha,\, v_\beta\big] = i\varepsilon_{\alpha\beta\gamma} v_\gamma$. Again, the right hand side in (36) is a linear combination of all possible ways to construct a spin scalar from two spinors and zero, one, or two vector operators.

Next, we proceed as in the case of the triplet Hamiltonian. We again average the Hamiltonian over dimer coverings, again introducing the factors of ζ, and replace the singlet operators $s_m^\dagger$, s_m by the real singlet condensation amplitude s. Lastly we discard all terms which describe the emission/absorption of a triplet by a fermion or the scattering of a fermion from a triplet. With these simplifications we obtain the fermionic Hamiltonian

$$H_F = -t \sum_{m,\sigma} \left(f_{m,+,\sigma}^\dagger f_{m,+,\sigma} - f_{m,-,\sigma}^\dagger f_{m,-,\sigma} \right) + \frac{s^2\zeta}{4} \sum_{m,n} \sum_{\substack{i\in m \\ j\in n}} t_{i,j} \sum_{\sigma} f_{n,j,\sigma}^\dagger f_{m,i,\sigma}, \tag{37}$$

where the sum over m, n run over all $2N$ bonds in the system and $t_{i,j} = t$ if i and j are nearest neighbors and zero otherwise.

Next, we switch to the question about how to count electrons. Obviously, each $f_{m,\pm,\sigma}^\dagger$-fermion contains one hole and has a z-spin of σ. Accordingly, in a given dimer covering the number of fermions must be equal to the number of doped holes, which is $N-N_e$

$$N-N_e = \sum_{m,\sigma} \left(f_{m,+,\sigma}^\dagger f_{m,+,\sigma} + f_{m,-,\sigma}^\dagger f_{m,-,\sigma} \right), \tag{38}$$

where the sum over m runs over the $N/2$ dimers. We have obtained an approximate theory by averaging over dimer coverings, so that each of the $2N$ bonds in the plane can be occupied by a boson or fermion. The physically relevant quantity, however, is the *density of holes per site*, whereas the number of dimers loses its significance due to the averaging approximation. Accordingly, we retain the condition (38), but the sum over m now runes over all $2N$ bonds in the system. This condition implies, that the bands obtained by diagonalizing (37) have to be filled from below with $N-N_e = N\delta$ *holes*, and since the $f_{m,\pm,\sigma}^\dagger$-fermions have a spin of $1/2$ the Fermi surface covers a fraction of $\delta/2$ of the Brillouin zone. We recall that this is precisely what we found in the framework of the Hubbard-I approximation. This is no surprise if we recall our discussion of spin-charge-separation in the context of the Hubbard-I approximation. There we noted that while a vacancy is a spinless object, the Hubbard-I approximation implicitly assumes that the information about the spin of the missing electron is 'stored' in the neighborhood of the vacancy and moves along with the vacancy. This is precisely the case in the dimer theory, where remaining electron in the dimer has opposite spin to the missing electron whence the dimers containing holes in fact are spin-$1/2$ particles.

We continue with the discussion of the band structure. We are interested mainly in the lowermost bands, these are the ones which will accommodate the doped holes, so for simplicity we drop the $f_{m,-,\sigma}^\dagger$-fermions, because their energy is $2t$ above that of the $f_{m,+,\sigma}^\dagger$-fermions, whereas the dispersive terms are $\propto s^2\zeta t \approx 0.2\ t$. With this last approximation Fourier transformation gives $H_F = \sum_{\mathbf{k},\sigma} v_{\mathbf{k},\sigma}^\dagger \tilde{H}_{\mathbf{k}} v_{\mathbf{k},\sigma}$ with the vector $v_{\mathbf{k},\sigma} = (f_{\boldsymbol{k},x,+,\sigma},\ f_{\boldsymbol{k},y,+,\sigma})^T$. The $\mathbf{k}$-dependence of the 2×2 matrix $\tilde{H}_{\mathbf{k}}$ can again be read off from Figure 13, but with all $\lambda = 1$. We obtain

$$\begin{aligned} \tilde{H}_{x,x} &= -t + s^2\zeta t\Big(\cos(k_y) + \cos(k_x)\cos(k_y) + \frac{1}{2}\cos(2k_x)\Big) \\ \tilde{H}_{x,y} &= s^2\zeta t\Big(\cos\Big(\frac{3k_x}{2}\Big)\cos\Big(\frac{k_y}{2}\Big) + \cos\Big(\frac{k_x}{2}\Big)\cos\Big(\frac{3k_y}{2}\Big)\Big). \end{aligned}$$

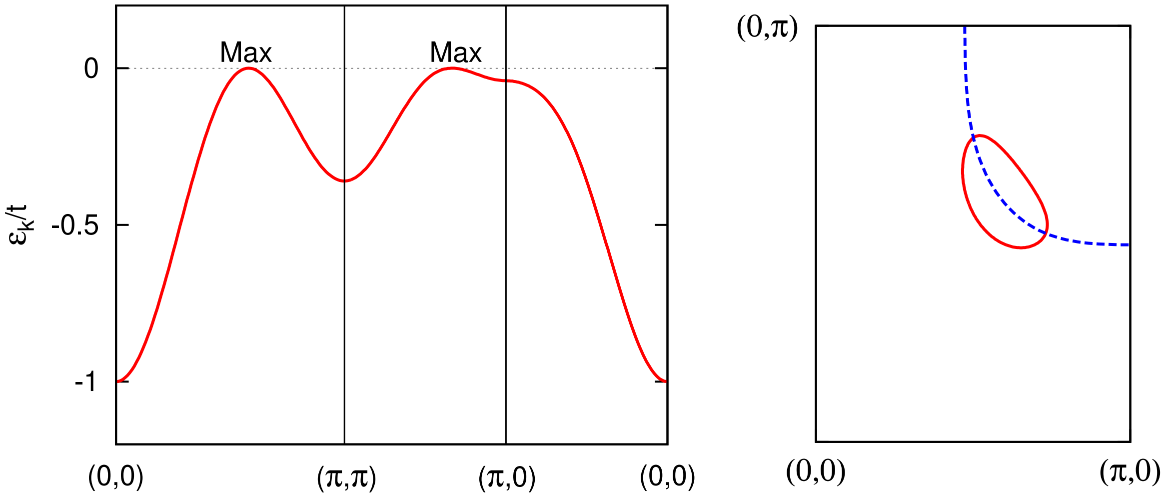

Fig. 15: *Left: Dispersion dispersion relation* $-\varepsilon_{2,\boldsymbol{k}}$ *for* $s^2\zeta = 0.16$*. Holes would occupy the maxima of this band as indicated in the Figure, so that the zero of energy corresponds roughly to the Fermi energy for small doping. Right: Adding additional hopping terms between* $(1,1)$ *and* $(2,0)$*-like neighbors lifts the degeneracy of the band maximum (indicated in blue) and the Fermi surface takes the form of a hole pocket (indicated in red) [15]. The values* $t' = -0.2t$*,* $t'' = 0.1t$ *and the hole concentration* $\delta = 1-n_e = 0.1$*.*

$\tilde{H}_{y,x} = \tilde{H}_{x,y}$ and $\tilde{H}_{y,y}$ is obtained from $\tilde{H}_{x,x}$ by $k_x \leftrightarrow k_y$. The eigenvalues of $\tilde{H}_{\mathbf{k}}$ are $\varepsilon_{1,\mathbf{k}} = -t + s^2\zeta t/2$ and $\varepsilon_{2,\mathbf{k}} = -t + s^2\zeta t\big(-3/2+2\gamma_{\mathbf{k}}+4\gamma_{\mathbf{k}}^2\big)$. More detailed investigation again shows [15] that the dispersionless band $\varepsilon_{1,\mathbf{k}}$ has zero weight in the electron spectral function, so again we interpret this as an artifact of the enlargement of the basis states and discard it. As we have seen above the band structure resulting from (37) has to be filled with holes from below, that means at $T = 0$ the condition for the Fermi energy E_F is

$$\delta = \frac{2}{N}\sum_{\boldsymbol{k}} \Theta(\varepsilon_{2,\mathbf{k}} - E_F).$$

Figure 15 shows $-\varepsilon_{2,\mathbf{k}}$, that means the band is again turned upside down as it would be seen in ARPES. The maxima therefore correspond to the minima of $\varepsilon_{2,\mathbf{k}}$, and this is the location in $\mathbf{k}$-space where the doped holes would accumulate. $\varepsilon_{2,\mathbf{k}}$ depends on $\mathbf{k}$ only via $\gamma_{\mathbf{k}}$, so that lines of constant $\gamma_{\mathbf{k}}$ automatically are lines of constant $\varepsilon_{2,\mathbf{k}}$, in particular the maximum of the inverted dispersion is a roughly circular contour around (π,π). The Fermi surface therefore would be a ring with a width $\propto \delta$, which does not agree with ARPES results. However, we recall that in the actual CuO$_2$ planes there are the additional hopping terms $\propto t', t''$ discussed above and inclusion of the terms indeed lifts the degeneracy and leads to a Fermi surface which takes the form of a hole pocket centered along the $(1,1)$ direction, see Figure 15. Compared to experiment, the pocket is shifted towards (π,π), but it should be noted that we have made many simplifications and a qualitative agreement with experiment is already a reasonable result.

5 Summary and Outlook

As explained in the introduction, the hallmark of a Mott insulator is the breakdown of the Fermi surface due to the effectively enhanced Coulomb repulsion in 'small' atomic orbitals: if the number of electrons is equal to the number of sites, $N,$ the electrons are caught in a 'traffic jam' and form a spin system instead of a half-filled band with a Fermi surface. The spins interact via virtual hopping processes of electrons as described by the Heisenberg exchange, which leads to antiferromagnetic correlations and spin excitations.

In the description of the *doped* Mott insulator given in the preceding sections, the electrons continue to form a mere spin system: the majority of electrons are coupled to inert ('condensed') singlets, a few singlets are excited to the triplet state, so that most electrons still contribute only their spin degrees of freedom. This is not surprising, because for a low density of vacancies, most electrons still are completely surrounded by other electrons and thus 'stuck'. Instead, the true mobile fermions in the system are the $f^\dagger$-particles, which may be viewed as tightly bound states of a spinless hole and one spin, and their number equals the doped holes. Since the $f^\dagger$-particles have a spin of $1/2$, their Fermi surface covers a fraction $\delta/2$ of the Brillouin zone, where $\delta = 1-n_e$ is the concentration of *holes*. We recall that for free electrons the fraction of the Brillouin zone covered by the Fermi surface is $n_e/2$, which differs drastically from $\delta/2$.

On the other hand, we expect that the state where the electrons are 'jammed' and form an inert background can persist only over a limited range of the hole concentration δ. A crude estimate for the range of stability of this phase can be obtained by noting that once δ reaches $1/z = 0.25$, on average each electron will find an empty site on one of its z neighbors to which it can hop without creating a double occupancy. With increasing δ it therefore will become energetically favorable for the electrons to form the all-electron Fermi surface of the free electron gas, although the strong scattering will lead to correlation narrowing of the quasiparticle band and strong incoherent weight in the single-particle spectral function. In fact, in the limit $n_e \to 0$ it is known [3] that one recovers a Fermi surface with volume $n_e/2$ but enhanced effective mass.

Accordingly, at some critical δ_c we expect a phase transition from the doped Mott-insulator with a hole-like Fermi surface of fractional volume $\delta/2$ described by the above theory, to a renormalized all-electron Fermi liquid with an electron-like Fermi surface of fractional volume $n_e/2$. And in fact the experimental situation has pretty much converged to this scenario: a transition between two nonmagnetic Fermi liquids of spin-$1/2$ particles without any obvious order but different Fermi surface volume, which occurs at a hole concentration $n_{h,c} \approx 0.22$. This is discussed in detail in Ref. [15]. Assuming that this $T = 0$ phase transition 'shrouds itself in superconductivity' as quantum phase transitions often do, one arrives at the well-known phase diagram of cuprate superconductors. In fact, unlike many other quantum phase transitions, the transition in the cuprates appears to be between two phases which are homogeneous, isotropic and nonmagnetic and differ only in the Fermi surface volume, so that there is no obvious order parameter. This would be consistent with the above scenario. The detailed description of this transition and how it can give rise to the spectacularly high superconducting transition temperatures is probably the key problem in understanding cuprate superconductors.

References

[1] J.G. Bednorz and K.A. Müller, Z. Phys. B **64**, 189 (1986)

[2] J. Hubbard, Proc. Roy. Soc. London A **276** 238 (1963)

[3] A.L. Fetter and J.D. Walecka, *Quantum Theory of Many-Particle Systems* (McGraw-Hill, San Francisco, 1971)

[4] K.A. Chao, J. Spałek, A.M. Oleś, J. Phys. C **10**, L 271 (1977)

[5] P.W. Anderson, Phys. Rev. **86**, 694 (1952)

[6] R. Coldea, S.M. Hayden, G. Aeppli, T.G. Perring, C.D. Frost, T.E. Mason, S.-W. Cheong, and Z. Fisk, Phys. Rev. Lett. **86**, 5377 (2001)

[7] F.C. Zhang, T.M. Rice, Phys. Rev. B **37**, 3759 (1988)

[8] L.N. Bulaevskii, E.L. Nagaev, and D.L. Khomskii, Sov. Phys. JETP. **27**, 836 (1968)

[9] S.A. Trugman, Phys. Rev. B **37**, 1597 (1988); *ibid* **41**, 892 (1990)

[10] R. Eder and K.W. Becker, Z. Phys. B **78**, 219 (1990)

[11] S. LaRosa, I. Vobornik, F. Zwick, H. Berger, M. Grioni, G. Margaritondo, R.J. Kelley, M. Onellion, and A. Chubukov Phys. Rev. B **56**, R525 (1997)

[12] S. Sachdev and R.N. Bhatt, Phys. Rev. B **41**, 9323 (1990)

[13] S. Gopalan, T.M. Rice, and M. Sigrist, Phys. Rev. B **49**, 8901 (1994)

[14] J.M. Tranquada, H. Woo, T.G. Perring, H. Goka, G.D. Gu, G. Xu, M. Fujita, and K. Yamada, Nature **429** 534 (2004)

[15] R. Eder, Phys. Rev. B **100**, 085133 (2019)

[16] M. Fujita, H. Hiraka, M. Matsuda, M. Matsuura, J.M. Tranquada, S. Wakimoto, G. Xu, and K. Yamada, J. Phys. Soc. Jpn. **81**, 011007 (2012)

[17] L.D. Landau and E.M. Lifshitz: *Lehrbuch der Theoretischen Physik* (Akademie Verlag, Berlin, 1988)

5 Orbital Ordering in Materials

Eva Pavarini
Institute for Advanced Simulation
Forschungszentrum Jülich GmbH

Contents

E. Pavarini and E. Koch (eds.)
Correlations and Phase Transitions
Modeling and Simulation Vol. 14
Forschungszentrum Jülich, 2024, ISBN 978-3-95806-751-6
http://www.cond-mat.de/events/correl24

1 Introduction

The term *orbital ordering* (OO) indicates the emergence of a broken symmetry state in which localized occupied orbitals form a regular pattern, in a similar way as spins do in magnetically ordered structures. Orbital ordering phenomena typically occur in Mott insulators with *orbital degrees of freedom*; for transition-metal compounds, the main focus of this lecture, the latter stem from the partially filled d shells of the transition metal. The perhaps most representative case is the perovskites $\mathrm{KCuF_3}$, shown in Fig. 1. In first approximation $\mathrm{KCuF_3}$ is cubic (O_h point group) with Cu^{2+} at the center of a regular octahedron of F^- ions (anions), enclosed in a cage of K^+ (cations). Due to O_h symmetry at the Cu site, the d manifold, 5-fold degenerate for free Cu^{2+}, splits into a t_{2g} triplet (xz, yz, xy), lower in energy, and a e_g doublet ($x^2{-}y^2$ and $3z^2{-}r^2$); the electronic configuration of the Cu^{2+} ion is thus $t_{2g}^6 e_g^3$ (one $3d$ hole). The t_{2g} states are completely filled and do not play any active role in OO; instead, electrons in the e_g^3 configuration have orbital degeneracy $d{=}2$. Making an analogy with spin degrees of freedom, they behave as an effective $\tau{=}1/2$ *pseudospin*; in this view, one of the two e_g states, say $|x^2{-}y^2\rangle$, plays the role of the pseudospin up, $|\nearrow\rangle$, and the other one, $|3z^2{-}r^2\rangle$, of the pseudospin down, $|\searrow\rangle$. The two pseudospin states are degenerate and, by symmetry, one could expect them to be equally occupied. In reality the symmetry is broken and $\mathrm{KCuF_3}$ is orbitally ordered with the orbital structure shown in Fig. 1; depicted are the empty (hole) e_g states at each Cu site. Furthermore, the system exhibits a *co-operative Jahn-Teller (JT) distortion*, also shown in Fig. 1, with long and short Cu-F bonds alternating in the $\boldsymbol{ab}$ plane. Indeed, the two phenomena – electronic OO and structural JT distortion – are concurrent; it is therefore difficult to say which one is the cause and which one is, instead, the effect. This is a classical case of a chicken-and-egg problem. The second paradigmatic system showing OO is $\mathrm{LaMnO_3}$ $\big($ion Mn^{3+}, configuration $3d^4\big)$, the mother compound of colossal magnetoresistance manganites, also a perovskite. Due to the Hund's rule coupling J, the actual electronic configuration of Mn^{3+} is $t_{2g}^3 e_g^1$. The half-filled t_{2g}^3 state has no orbital degeneracy; the only orbital degrees of freedom are, as for $\mathrm{KCuF_3}$, those associated with e_g electrons. Again, the system is orbitally ordered and OO goes hand in hand with the co-operative JT distortion. Among t_{2g} systems, i.e., materials with partially filled t_{2g} shells, classical examples of orbitally-ordered crystals are the perovskites $\mathrm{LaTiO_3}$ and $\mathrm{YTiO_3}$ $\big($configuration $t_{2g}^1\big)$, $\mathrm{LaVO_3}$ and $\mathrm{YVO_3}$ $\big(t_{2g}^2\big)$, and $\mathrm{Ca_2RuO_4}$ $\big(t_{2g}^4\big)$; in these cases the t_{2g} electrons behave as an orbital pseudospin $\tau{=}1$. Although this is not a prerequisite for orbital ordering, as we have seen, many orbitally-ordered materials are perovskites; for this reason in the present lecture we will use the perovskite structure as representative.

The origin of orbital ordering has been investigated for decades. One of the problems in clarifying its nature is that, while magnetic order can be directly probed, e.g., via neutron scattering experiments, orbital ordering is typically only indirectly observed. Indeed, its principal hallmark is the presence of the co-operative Jahn-Teller distortion itself. Identifying the origin of orbital ordering is thus intimately related to finding the cause of the co-operative Jahn-Teller distortion. In this lecture I will first illustrate the two main mechanisms [1,2] which have been proposed as possible explanation for OO phenomena, the classical Jahn-Teller effect [1], perhaps

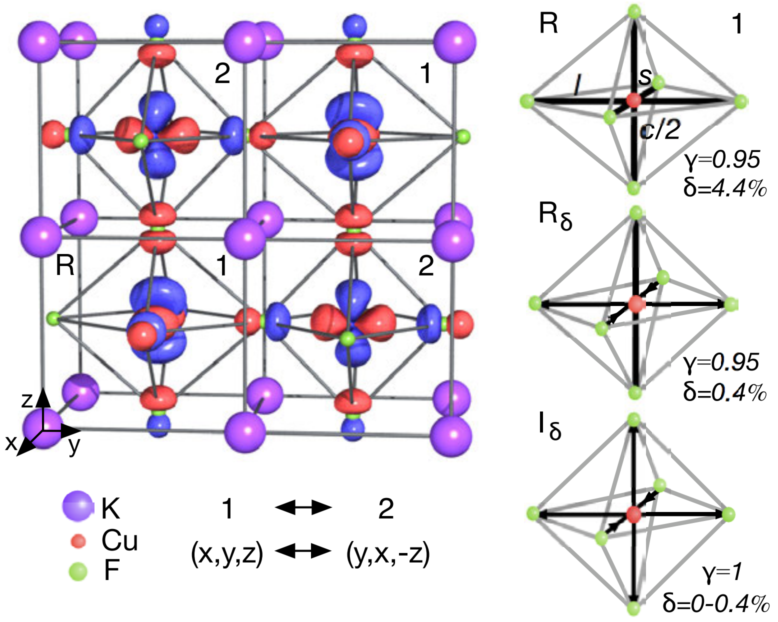

Fig. 1: *Crystal structure, distortions, and orbital ordering in KCuF*$_3$*. Cu is at the center of F octahedra enclosed in a K cage. The conventional cell is tetragonal with axes* **a**, **b**, **c**. *The pseudocubic axes* **x**, **y**, **z** *pointing towards neighboring Cu, are shown in the corner. Short* (s) *and long* (l) *CuF bonds alternate between* **x** *and* **y** *along all pseudocubic axes (co-operative Jahn-Teller distortion). The distortions are measured by* $\delta=(l-s)/(l+s)/2$ *and* $\gamma=c/a\sqrt{2}$. R *is the experimental structure* (γ=0.95, δ=4.4%), R_δ (γ=0.95) *and* I_δ (γ=1) *two ideal structures with reduced distortions. In the* I_0 *structure the cubic crystal-field at the Cu site splits the 3d manifold into a* t_{2g} *triplet and a* e_g *doublet. In the* R *structure, site symmetry is lowered further by the tetragonal compression* (γ<1) *and the Jahn-Teller distortion* ($\delta \neq 0$). *The figure shows the highest-energy* 3d *orbital. From Ref. [3].*

enhanced by Coulomb repulsion [4], and Kugel-Khomskii (KK) superexchange [2]. Kanamori well illustrated the first mechanism in an influential work [1] in 1960; the main idea is that electron-phonon coupling yields a static Jahn-Teller distortion, which lowers the symmetry of the system and produces a crystal-field splitting. As a consequence, electrons preferably occupy the lower energy states, giving rise to a periodic pattern of occupied orbitals. This is self-evident in the limit in which the crystal-field splitting is very large, let us say, larger than the bandwidth; the lower-energy states at each site will be clearly the first ones to be occupied. If, however, the bandwidth is large in comparison with the crystal-field splitting, the hopping integrals can strongly reduce such a tendency to orbital ordering. A natural question thus arises at this point. How large should the crystal-field splitting be to give rise to an orbitally-ordered state? To answer this question we have to remind ourselves that transition-metal systems with partially filled d shells are also typical examples of strongly-correlated materials. Their low-energy properties are believed to be well described by a generalized multi-band *Hubbard model*,

$$\hat{H} = \hat{H}_0 + \hat{H}_U,$$

the sum of a one-electron term, $\hat{H}_0$, describing the transition-metal d bands and a Coulomb electron-electron repulsion term, $\hat{H}_U$. The first is given by

$$\hat{H}_0 = -\sum_{ii'}\sum_{\sigma}\sum_{mm'} t^{i,i'}_{mm'}\, c^\dagger_{im\sigma} c_{im'\sigma} \,,$$

where $c^\dagger_{im\sigma}$ creates an electron at site i with spin σ and orbital quantum number m, and the parameter $t^{i,i'}_{mm'}$ are the hopping integrals ($i{\neq}i'$) or the crystal-field splittings ($i{=}i'$). The Coulomb repulsion can be written as

$$\hat{H}_U = \frac{1}{2}\sum_{i}\sum_{\sigma\sigma'}\sum_{m_\alpha m'_\alpha}\sum_{m_\beta m'_\beta} U_{m_\alpha m_\beta m'_\alpha m'_\beta}\, c^\dagger_{im_\alpha\sigma} c^\dagger_{im_\beta\sigma'} c_{im'_\beta\sigma'} c_{im'_\alpha\sigma} \,.$$

The elements the Coulomb interaction tensor, $U_{m_\alpha m_\beta m'_\alpha m'_\beta}$, can be expressed in terms of the Slater integrals.[1] Here we will restrict the discussion to the e_g or t_{2g} manifolds only. In this case, in the basis of real harmonics, the Hubbard model takes the form

$$\begin{aligned}
\hat{H} = & -\sum_{ii'}\sum_{\sigma}\sum_{mm'} t^{i,i'}_{mm'}\, c^\dagger_{im\sigma} c_{im'\sigma} + U\sum_{i}\sum_{m} \hat{n}_{im\uparrow}\hat{n}_{im\downarrow} \\
& + \frac{1}{2}\sum_{i}\sum_{\sigma\sigma'}\sum_{m\neq m'} (U{-}2J{-}J\delta_{\sigma,\sigma'})\, \hat{n}_{im\sigma}\hat{n}_{im'\sigma'} \\
& - J\sum_{i}\sum_{m\neq m'} \left(c^\dagger_{im\uparrow} c^\dagger_{im\downarrow} c_{im'\uparrow} c_{im'\downarrow} + c^\dagger_{im\uparrow} c_{im\downarrow} c^\dagger_{im'\downarrow} c_{im'\uparrow} \right) ,
\end{aligned} \tag{1}$$

where m, m' are here either t_{2g} or e_g states, $U_{mm'mm'}{=}U_{m,m'}{=}U{-}2J(1{-}\delta_{m,m'})$ and, for $m{\neq}m'$, $U_{mm'm'm}{=}J_{m,m'}{=}J$. The last two terms describe the pair-hopping and spin-flip processes ($U_{mmm'm'}{=}J_{m,m'}$ if we use a basis of real harmonics, while for spherical harmonics $U_{mmm'm'}{=}0$). Finally, $U{=}U_0$ and $J{=}J_1$ (t_{2g} electrons) or $J{=}J_2$ (e_g electrons), with

$$\begin{aligned}
U_0 &= F_0 + \frac{8}{5}\mathcal{J}_{\text{avg}}, & \mathcal{J}_{\text{avg}} &= \frac{5}{7}\frac{1}{14}(F_2+F_4) \\
J_1 &= \frac{3}{49}F_2 + \frac{20}{9}\frac{1}{49}F_4, & J_2 &= -2\mathcal{J}_{\text{avg}} + 3J_1 \,.
\end{aligned}$$

In strongly correlated systems described by a Hamiltonian of type (1), it turns out that a small crystal-field splitting, a fraction of the bandwidth, is sufficient to produce orbital order even at high temperature. This happens because the Coulomb repulsion effectively enhances it, while suppressing orbital fluctuations [4]. Hence, the mechanism illustrated by Kanamori becomes very efficient in the presence of strong correlations (small t/U limit, the typical limit for Mott insulators; here t is an average hopping integral). This is, however, not the end of the story: Coulomb electron-electron interaction provides, in addition, an alternative explanation of the origin of orbital ordering. In a seminal work, Kugel and Khomskii [2] have shown in 1973 that, in the presence of orbital degeneracy, many-body effects can produce orbital ordering even in the absence of a static distortion, i.e., of a crystal-field splitting. This happens via

---

[1] For a pedagogical introduction see, e.g, Ref. [5].

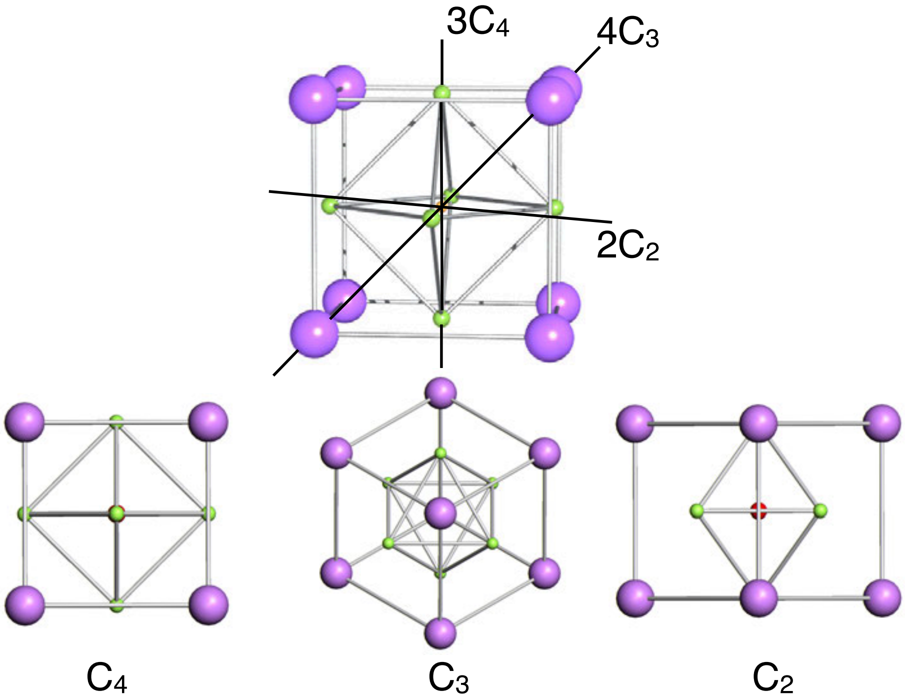

Fig. 2: *The unit cell of a cubic perovskite ABC*$_3$ *and its symmetry axes; the lattice constant is* a. *The transition metal B (red) is at* $(0,0,0)$*; the ligands C (green) are located at* $(\pm a/2,0,0)$, $(0,\pm a/2,0)$,$(0,0,\pm a/2)$ *and form an octahedron; the cations A are located at* $(\pm a/2,\pm a/2,\pm a/2)$, $(\pm a/2,\mp a/2,\pm a/2)$, $(\mp a/2,\pm a/2,\pm a/2)$, $(\pm a/2,\pm a/2,\mp a/2)$ *and form a cube. The bottom figures illustrate the rotational symmetries of the cell.*

electronic spin-orbital superexchange, the effective low-energy interaction which emerges, in the small t/U limit, from the orbitally-degenerate Hubbard model. In this picture, the cooperative Jahn-Teller distortion is rather the consequence than the cause of orbital order. As I already mentioned, the predictions of the two theories for the final broken-symmetry structure are basically identical for most systems; thus it is very hard to determine which of the two mechanisms, Jahn-Teller effect or Kugel-Khomskii superexchange, dominates. In the last part of the lecture we will see how the problem was recently solved in representative cases [3,6] by using a new theoretical approach based on the local-density-approximation + dynamical mean-field theory (LDA+DMFT) [7–10] method. For the paradigmatic systems $\mathrm{KCuF_3}$ and $\mathrm{LaMnO_3}$, it was shown that Kugel-Khomskii superexchange alone, although strong, cannot explain the presence of the Jahn-Teller distortion above 350 K ($\mathrm{KCuF_3}$) [3] and 650 K ($\mathrm{LaMnO_3}$) [6]; experimentally, however, the distortion persists in both systems basically up to the melting temperature. This leads to the conclusion that a mechanism directly generating a static crystal-field splitting, such as the standard Jahn-Teller effect, is necessary to explain the experimental findings. In fact, for $\mathrm{KCuF_3}$ and other ionic systems, it turns out that even the classical JT picture fails. A new mechanism, based on Born-Mayer repulsion, has to be invoked to describe the actual experimental structure and the associated ordering at high temperature [11]. A true Kugel-Khomskii system was instead recently identified in the t_{2g}^2 system $\mathrm{LaVO_3}$ [12].

2 Cubic crystal-field splitting

Let us consider a system with the ideal cubic perovskite structure ABC$_3$, shown in Fig. 2. In this structure, B is the transition metal with partially filled d shell. The site symmetry at site B is cubic; thus, as we mentioned before, d states split into e_g and t_{2g}. Let us understand how exactly this happens. For a free ion, the potential $v_{\rm R}(\boldsymbol{r})$ which determines the single-electron energies is rotationally invariant, i.e., it has symmetry $O(3)$. This means that all single-electron states within a given l shell are degenerate, as it happens in the case of hydrogen-like atoms. When the same ion is inside a molecule or a solid, $v_{\rm R}(\boldsymbol{r})$ has in general lower symmetry, corresponding to a finite point group.[2] Thus one-electron states within a given shell l, degenerate for the free atom, can split. The symmetry reduction arises from the *crystal field*; the latter has two components, the Coulomb potential generated by the surrounding charged ions, dominant in ionic crystals, and the *ligand field* due to the bonding neighbors. In this section we will analyze the first contribution; the covalent contribution to the crystal-field splitting is discussed in the next section. Both effects give rise to a similar splitting of levels; which contribution dominates depends on the system.

Let us thus assume that the crystal is perfectly ionic and that the ions can be treated as point charges q_α (point-charge model). Then, the one-electron potential can be written as

$$v_{\rm R}(\boldsymbol{r}) = \sum_\alpha \frac{q_\alpha}{|\boldsymbol{R}_\alpha - \boldsymbol{r}|} = v_0(r) + \sum_{\alpha\neq 0} \frac{q_\alpha}{|\boldsymbol{R}_\alpha - \boldsymbol{r}|} = v_0(r) + v_c(\boldsymbol{r}), \tag{2}$$

where $\boldsymbol{R}_\alpha$ are the positions of the ions and q_α their charges. The term $v_0(r)$ is the ionic central potential at site $\boldsymbol{R}_0$, with spherical symmetry. The term $v_c(\boldsymbol{r})$ is the electric field generated at a given site $\boldsymbol{R}_0$ by all the surrounding ions in the crystal and it is called *crystal-field potential.*

For the perovskite structure ABC$_3$ we are interested in the crystal-field potential at the site of the transition metal, B. Let us first assume that only the contribution of nearest neighbors (the negative C ions, typically oxygens or fluorines) is relevant. The six C ions are located at positions $(\pm d_C, 0, 0)$, $(0, \pm d_C, 0)$, $(0, 0, \pm d_C)$ and have all the same charge q_C, while the B ion is at $(0, 0, 0)$; in terms of a, the cubic lattice constant, $d_C{=}a/2$. Then we can write the potential around ion B as

$$v_{\rm R}(\boldsymbol{r}) = \frac{q_B}{r} + \frac{q_C}{d_C}\left[\Delta v\left(\frac{x}{d_C}; \frac{r}{d_C}\right) + \Delta v\left(\frac{y}{d_C}; \frac{r}{d_C}\right) + \Delta v\left(\frac{z}{d_C}; \frac{r}{d_C}\right)\right]$$

where

$$\Delta v(\xi;\rho) = \frac{1}{\sqrt{1+\rho^2}}\left(\frac{1}{\sqrt{1+\frac{2\xi}{1+\rho^2}}} + \frac{1}{\sqrt{1-\frac{2\xi}{1+\rho^2}}}\right).$$

Via the Taylor expansion

$$\frac{1}{\sqrt{1+\eta}} \sim 1 - \frac{1}{2}\eta + \frac{3}{8}\eta^2 - \frac{5}{16}\eta^3 + \frac{35}{128}\eta^4 + \dots$$

---

[2] For a concise introduction to group theory see, e.g., Ref. [13], chapter 6.

we can find an approximate expression of $\varDelta v(\xi;\rho)$ for small ξ, i.e., close to ion B; the first contribution with less than spherical symmetry is

$$v_{\text{oct}}(\boldsymbol{r}) = \frac{35}{4}\frac{q_C}{d_C^5}\left(x^4+y^4+z^4-\frac{3}{5}r^4\right) = D\left(x^4+y^4+z^4-\frac{3}{5}r^4\right).$$

We can rewrite this potential as

$$v_{\text{oct}}(\boldsymbol{r}) = \frac{7\sqrt{\pi}}{3}\frac{q_C}{d_C^5}r^4\left[Y_0^4(\vartheta,\varphi)+\sqrt{\frac{5}{14}}\left(Y_4^4(\vartheta,\varphi)+Y_{-4}^4(\vartheta,\varphi)\right)\right], \qquad (3)$$

where

$$\begin{aligned} Y_0^4(\vartheta,\varphi) &= \frac{3}{16}\frac{1}{\sqrt{\pi}}\left(35\cos^4\vartheta-30\cos^2\vartheta+3\right) = \frac{3}{16}\frac{1}{\sqrt{\pi}}\frac{35z^4-30z^2r^2+3r^4}{r^4}, \\ Y_{\pm4}^4(\vartheta,\varphi) &= \frac{3}{16}\sqrt{\frac{35}{2\pi}}\sin^4\vartheta e^{\pm 4i\varphi} = \frac{3}{16}\sqrt{\frac{35}{2\pi}}\frac{(x\pm iy)^4}{r^4}. \end{aligned}$$

To obtain the crystal field due to the cubic cage of cations A (with charge q_A), shown in Fig. 2 we repeat the same calculation; the main difference is that there are eight A ions, located at positions $(\pm d_C,\pm d_C,\pm d_C)$,$(\mp d_C,\pm d_C,\pm d_C)$, $(\pm d_C,\mp d_C,\pm d_C)$, $(\pm d_C,\pm d_C,\mp d_C)$, with the distance from the origin being $d_A{=}\sqrt{3}a/2$. By following the same procedure that we used for B octahedron, one can show that

$$v_{\text{cube}}(\boldsymbol{r}) = -\frac{8}{9}\frac{q_A}{q_C}\left(\frac{d_C}{d_A}\right)^5 v_{\text{oct}}(\boldsymbol{r}),$$

i.e., $v_{\text{cube}}(\boldsymbol{r})$ has the same form as $v_{\text{oct}}(\boldsymbol{r})$; this happens because a cube and an octahedron are dual polyhedra[3] and have therefore the same symmetry properties. If $q_A/q_C>0$, $v_{\text{cube}}(\boldsymbol{r})$ has opposite sign than $v_{\text{oct}}(\boldsymbol{r})$; in the case of a perovskite, however, A positions are occupied by cations, i.e., positive ions; thus the crystal field due to the A cage has the same sign of the crystal field generated by the B octahedron.

The crystal-field potential $v_{\text{c}}(\boldsymbol{r})$ lowers the site symmetry and can therefore split the $(2l{+}1)$-fold degeneracy of the atomic levels. To calculate how the l manifold splits, we use two approaches. The first is exact and based on group theory. We assume for simplicity that the symmetry is only O (group of the proper rotations which leave a cube invariant); using the full symmetry group of the cube, $O_h = O\otimes C_i$ (where C_i is the group made by the identity and the inversion) does not change the result, because the spherical harmonics are all either even or odd. The character table of group O is given by

partner	functions	O	E	$8C_3$	$3C_2$	$6C_2'$	$6C_4$
	$(x^2+y^2+z^2)$	A_1	1	1	1	1	1
		A_2	1	1	1	−1	−1
	$(x^2-y^2, 3z^2-r^2)$	E	2	−1	2	0	0
(R_x,R_y,R_z)	(x,y,z)	T_1	3	0	−1	−1	1
	(xy,xz,yz)	T_2	3	0	−1	1	−1

(4)

---

[3] Every polyhedron has a dual which can be obtained by exchanging the location of faces and vertices.

Let us explain this table. The first line yields the group, here O, and the symmetry operations of the group, collected in classes $\mathcal{C}_k$, here $\{E\}, \{C_3\}, \{C_2\}, \{C_2'\}, \{C_4\}$. For each class only a representative element is given and the number N_k in front of this element yields the number of operations in the class; for example $8C_3$ indicates 8 symmetry operations in class $\{C_3\}$. The symmetry operation C_n is an anticlockwise rotation of an angle $\alpha = 2\pi/n$. For a finite group with h elements, the h group operations $\big\{O(g)\big\}$ can be expressed as h matrices $\big\{\varGamma(g)\big\}$ acting on an invariant linear space; the basis of this space, $\{|m\rangle\}$, can be, for example, a finite set of linearly independent functions, such as the spherical harmonics with angular quantum number l. The collection of matrices $\big\{\varGamma(g)\big\}$ is a *representation* of the group; the dimension of the invariant linear space yields also the dimension of the matrices, i.e., the *dimensionality* of the representation. Each group has infinitely many possible representations, but some sets are special and play the role of an orthonormal basis in a space of vectors; they are called *irreducible*. If G is the group of operations which leave the Hamiltonian invariant, the irreducible representations of G can be used to classify all eigenstates of the Hamiltonian; eigenstates which build a basis for different irreducible representations are mutually orthogonal and have typically (leaving the cases of accidental degeneracy and hidden symmetry aside) different energies. The (non-equivalent) irreducible representations $\varGamma_i$ of group O are listed in the first column of Table 4, below the group name; they are A_1 (trivial representation, made of 1-dimensional identity matrices), A_2, also 1-dimensional, E, two-dimensional, and T_1 and T_2, both three-dimensional. The numbers appearing in Table 4 are the characters $\chi_i(g)$, defined as

$$\chi_i(g) = \mathrm{Tr}\ \varGamma_i(g) = \sum_m \big\langle m\big|\varGamma_i(g)\big|m\big\rangle = \sum_m \varGamma_i^{mm}(g)\,.$$

For a given representation (corresponding to a line of Table 4) the character for a specific element can be found below the corresponding class label (columns of Table 4); all elements in the same class have the same character. Thus the second column of the character table, showing the character of the identity, yields also the dimensionality d_i of the representation itself. Next we calculate the characters of the matrix representation $\varGamma^l$ constructed using spherical harmonics with angular quantum number l as a basis. An easy way to do this is to assume that the rotation axis is also the quantization axis, i.e., $\hat{z}$; in fact, the characters do not depend on the direction of the quantization axis, but only on the angle α of rotation. Thus for $O(g){=}C_\alpha$ we have

$$\begin{aligned} C_\alpha\, Y_m^l(\vartheta,\varphi) &= Y_m^l(\vartheta,\varphi{-}\alpha) = e^{-im\alpha}\, Y_m^l(\vartheta,\varphi) \\ \varGamma^l_{mm'}(C_\alpha) &= \delta_{mm'}e^{-im\alpha}. \end{aligned}$$

This yields the following expression for the character

$$\chi^l(C_\alpha) = \sum_{m=-l}^{l} e^{-im\alpha} = \frac{\sin\big(l{+}\frac{1}{2}\big)\alpha}{\sin\frac{\alpha}{2}}\,.$$

The characters for representations $\mathit{\Gamma}^l$ are therefore

O	E	$8C_3$	$3C_2$	$6C_2$	$6C_4$
$\mathit{\Gamma}^0 = \mathit{\Gamma}^s$	1	1	1	1	1
$\mathit{\Gamma}^1 = \mathit{\Gamma}^p$	3	0	-1	-1	1
$\mathit{\Gamma}^2 = \mathit{\Gamma}^d$	5	-1	1	1	-1
$\mathit{\Gamma}^3 = \mathit{\Gamma}^f$	7	1	-1	-1	-1

In spherical symmetry $\big($group $O(3)\big)$ representations $\mathit{\Gamma}^l$ are irreducible. In cubic symmetry (group O), instead, the $\mathit{\Gamma}^l$ can be reducible, i.e., they can be written as the tensorial sum $\oplus$ of irreducible representations of the group O. The various components can be found by using the orthogonality properties of irreducible representations, which lead to the decomposition formula

$$\mathit{\Gamma}^l = \bigoplus_i a_i \mathit{\Gamma}_i \qquad \text{with} \quad a_i = \langle \mathit{\Gamma}_i | \mathit{\Gamma}^l \rangle = \frac{1}{h} \sum_g \, \big[\chi_i(g)\big]^* \chi^l(g)\,, \tag{5}$$

where h, the number of elements in the group, is 24 for group O. Hereafter the symmetry representations of electronic states are written in lower case to distinguish them from capital letters which we will use later for labeling vibrational modes. We find

$$\begin{aligned} \mathit{\Gamma}^s &= a_1 \\ \mathit{\Gamma}^p &= t_1 \\ \mathit{\Gamma}^d &= e \oplus t_2 \\ \mathit{\Gamma}^f &= a_2 \oplus t_1 \oplus t_2\,. \end{aligned}$$

Thus, in cubic symmetry, the s- and the p-functions do not split, because the a_1 irreducible representation is one-dimensional and the t_1 irreducible representation is 3-dimensional. Instead, d-functions split into a doublet and a triplet, and f-functions into a singlet and two triplets. To determine which functions $\big\{|m\rangle_i\big\}$ form a basis (a so-called set of *partner functions*) for a specific irreducible representation $\mathit{\Gamma}_i$ we can, e.g., use the projector for that representation

$$\hat{\mathcal{P}}_i = \frac{d_i}{h} \sum_g \big[\chi_i(g)\big]^* O(g). \tag{6}$$

In our case, we can read directly the partner functions $\big\{|m\rangle_i\big\}$ for a given irreducible representation of the group O in the first column of Table 4, on the left. In short, for representation e possible partner functions are $\big(x^2{-}y^2,\, 3z^2{-}r^2\big)$ and for representation t_2 we can instead use $\big(xy,\, xz,\, yz\big)$. A small step is still missing: As we already mentioned, the full symmetry of the B site is O_h, and the group O_h can be obtained as direct product, $O_h = O \otimes C_i$; with respect to O, group O_h has twice the number of elements and classes, and thus twice the number of irreducible representations. The latter split into even $\big(a_{1g}, a_{2g}, e_g, t_{1g}, t_{2g}\big)$ and odd $\big(a_{1u}, a_{2u}, e_u, t_{1u}, t_{2u}\big)$. All d-functions are even, and therefore $x^2{-}y^2$ and $3z^2{-}r^2$ are partners functions for the e_g irreducible representation, while xy, xz, yz are partner functions for the

t_{2g} irreducible representation. Summarizing, t_{2g} states $(xy, xz,$ and $yz)$ and e_g states $(x^2{-}y^2$ and $3z^2{-}r^2)$ have in general (again excluding the cases of accidental degeneracy and hidden symmetry) different energy.

Group theory tells us *if* the degenerate $2l{+}1$ levels split at a given site in a lattice, but not by *how much* they do split, and which orbitals are higher in energy. We can, however, calculate the crystal-field splitting approximately using the potential (3) as a perturbation. This is the second approach previously mentioned; differently from group theory, it is not exact, but it gives us an estimate of the size of the effect and the sign of the splitting. For d states we can calculate the elements of the octahedral potential $v_{\text{oct}}(\boldsymbol{r})$ in the basis of atomic functions $\psi_{nlm}(\rho,\vartheta,\varphi){=}R_{nl}(\rho)\,Y^l_m(\vartheta,\varphi)$, where $R_{nl}(\rho)$ is the radial part, $\rho{=}Zr$, Z is the atomic number, $Y_l^m(\vartheta,\varphi)$ a spherical harmonic, and n the principal quantum number (Appendix B). We obtain

$$\begin{aligned} \langle\psi_{n20}\;\,|\hat{v}_{\text{oct}}\,|\psi_{n20}\;\,\rangle &= +6Dq & \qquad \langle\psi_{n2\pm1}|\hat{v}_{\text{oct}}\,|\psi_{n2\pm1}\rangle &= -4Dq \\ \langle\psi_{n2\pm2}|\hat{v}_{\text{oct}}\,|\psi_{n2\pm2}\rangle &= +\;\,Dq & \qquad \langle\psi_{n2\pm2}|\hat{v}_{\text{oct}}\,|\psi_{n2\mp2}\rangle &= +5Dq \end{aligned}$$

where $Dq{=}q_C\langle r^4\rangle/6d_C^5$ and $\langle r^k\rangle{=}\int r^2dr\,r^k\,R^2_{n2}(Zr)$. The crystal-field splitting between e_g and t_{2g}-states can be then obtained by diagonalizing the crystal-field matrix

$$H_{\text{CF}} = \left(\begin{array}{lllll} Dq & 0 & 0 & 0 & 5Dq \\ 0 & -4Dq & 0 & 0 & 0 \\ 0 & 0 & 6Dq & 0 & 0 \\ 0 & 0 & 0 & -4Dq & 0 \\ 5Dq & 0 & 0 & 0 & Dq \end{array}\right).$$

We find two degenerate e_g eigenvectors with energy $6Dq$

$$\begin{aligned} |\psi_{n20}\rangle &= |3z^2{-}r^2\rangle, \\ \frac{1}{\sqrt{2}}\big(|\psi_{n2-2}\rangle{+}|\psi_{n22}\rangle\big) &= |x^2{-}y^2\rangle, \end{aligned}$$

and three degenerate t_{2g} eigenvectors with energy $-4Dq$

$$\begin{aligned} \frac{i}{\sqrt{2}}\big(|\psi_{n2-2}\rangle{-}|\psi_{n22}\rangle\big) &= |xy\rangle, \\ \frac{1}{\sqrt{2}}\big(|\psi_{n2-1}\rangle{-}|\psi_{n21}\rangle\big) &= |xz\rangle, \\ \frac{i}{\sqrt{2}}\big(|\psi_{n2-1}\rangle{+}|\psi_{n21}\rangle\big) &= |yz\rangle. \end{aligned}$$

The total splitting is

$$\varDelta_{\text{CF}} = E_{e_g}{-}E_{t_{2g}} = 10Dq.$$

Thus the e_g-states are actually higher in energy than the t_{2g}-states. This happens because e_g electrons point towards the negative C ions (see Fig. 3), and will therefore feel a larger Coulomb repulsion than t_{2g} electrons, which have the lobes directed between two negative C ions.

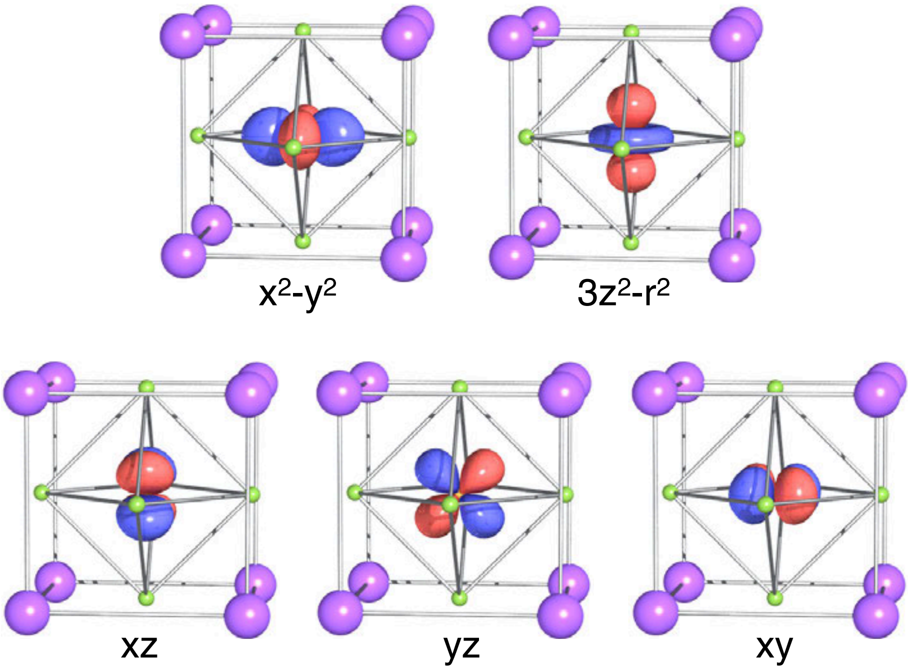

Fig. 3: *The Cu e_g and t_{2g} Wannier orbitals for the cubic perovskite KCuF$_3$, obtained from first principles calculations, using a Wannier basis that spans all bands.*

How general is, however, this result? We obtained it via a truncated Taylor expansion of the potential close to the nucleus. Does this mean that we have perhaps neglected important higher-order terms? For a generic lattice, we can expand the crystal-field potential (2) in spherical harmonics using the exact formula

$$\frac{1}{|\boldsymbol{r}_1-\boldsymbol{r}_2|}=\sum_{k=0}^{\infty}\frac{r_<^k}{r_>^{k+1}}\,\frac{4\pi}{2k+1}\sum_{q=-k}^{k}Y_q^k(\vartheta_2,\varphi_2)\overline{Y}_q^k(\vartheta_1,\varphi_1),$$

where $r_<$ ($r_>$) is the smaller (larger) of r_1 and r_2. The crystal-field potential takes the form

$$v_c(\boldsymbol{r})=\sum_{k=0}^{\infty}\sum_{q=-k}^{k}B_q^k\,Y_q^k, \tag{7}$$

where $B_q^k=(-1)^q\bar{B}_{-q}^k$. Although the series in (7) is in principle infinite, one can terminate it by specifying the wavefunctions, since

$$\langle Y_m^l|Y_q^k|Y_{m'}^l\rangle=0 \quad \text{if} \quad k>2l.$$

For example, for p electrons $k\leq 2$, for d-electrons, $k\leq 4$, and f electrons $k\leq 6$. Thus, for d-electrons and O_h symmetry, the terms that appear in the potential (3) are actually also the only ones to be taken into account, because all other terms yield an expectation value equal to zero. Finally, the derivation of both equations (3) and (7) presented here might let us think that the first-nearest neighbors are those that determine the crystal field. This is, however, not always the case, because Coulomb repulsion is a long-range interaction; for example, in some systems

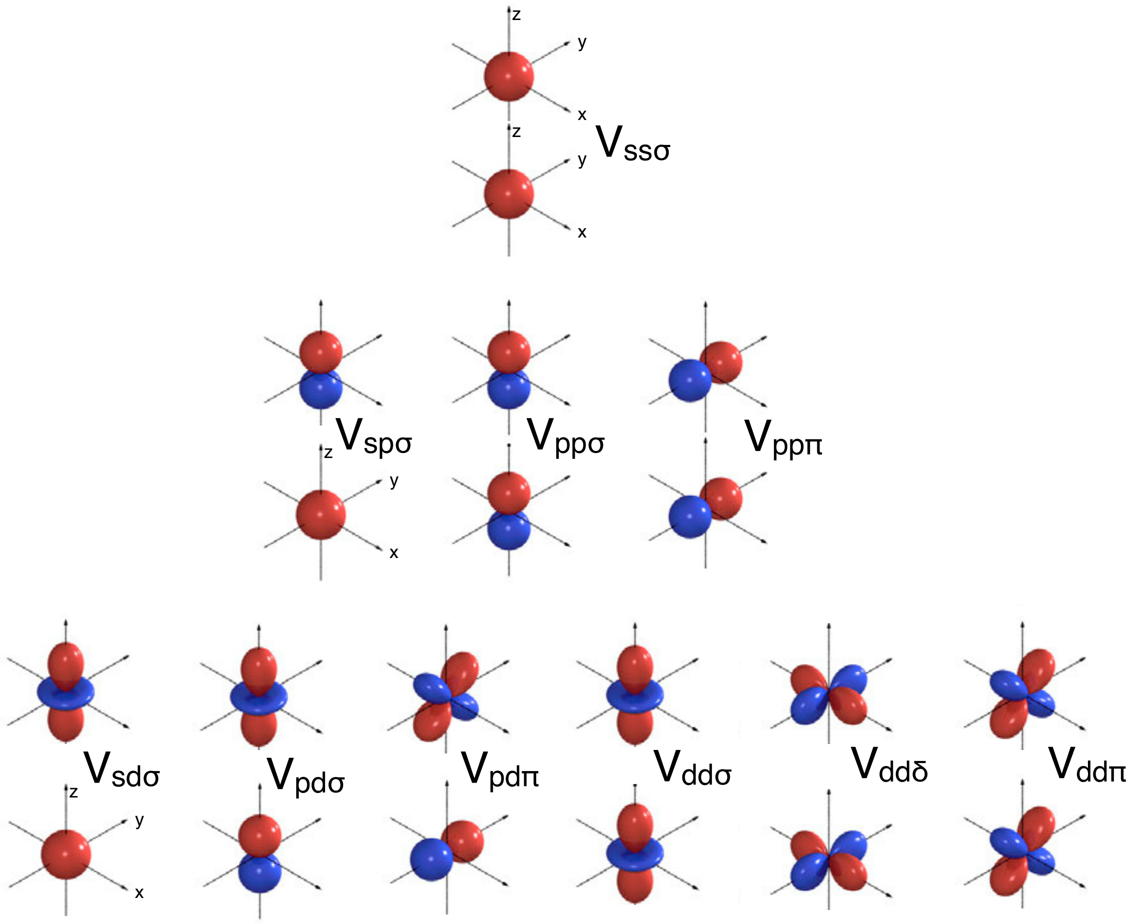

Fig. 4: *Independent Slater-Koster two-center integrals for s, p, and d atomic orbitals (Appendix B). The label σ indicates that the bonding state is symmetrical with respect to rotations about the bond axis; the label π that the bond axis lies in a nodal plane; the label δ that the bond axis lies in two nodal planes.*

the first-nearest neighbors yield cubic symmetry at a given site but further neighbors lower the symmetry.[4] Furthermore, the point-charge model discussed in this section is useful to explain the relation between crystal field and site symmetry, however yields unsatisfactory results for the crystal-field splitting in real materials. Corrections beyond the point-charge approximation turn out to be important. In addition, as we will see in the next section, in many systems the crystal field has a large, sometimes dominant, covalent contribution, the ligand field. The modern approach to calculate crystal-field splittings including the ligand-field contribution is based on material-specific potentials obtained *ab-initio* via density-functional-theory (DFT) and the associated DFT localized Wannier functions. Nevertheless, it is worth to point out the remarkable success of the point-charge model in giving qualitatively correct d crystal-field states in cubic perovskites; such a success relies on the fact that this approach, even if approximate, yields the exact symmetry of final states, i.e., the same obtained via group theory, and does not neglect any relevant (e.g., high-order) term.

---

[4] This means that, of course, O_h is not the actual symmetry of the site.

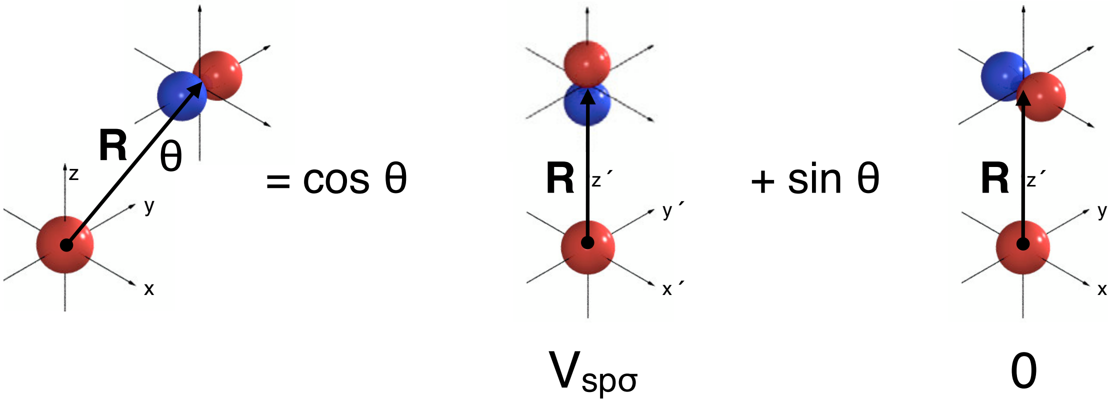

Fig. 5: *Illustration of the decomposition of a general s-p two-center integral in terms of* $V_{sp\sigma}$.

3 Tight-binding e_g and t_{2g} bands of cubic perovskites

In this section we will construct the bands of KCuF$_3$ in the cubic limit using tight-binding theory. Let us first remind ourselves of the crucial steps of this approach. The one-electron Hamiltonian can be written as

$$\hat{h}_e(\boldsymbol{r}) = -\frac{1}{2}\nabla^2 + \sum_{i\alpha} v(\boldsymbol{r}-\boldsymbol{T}_i-\boldsymbol{R}_\alpha) = -\frac{1}{2}\nabla^2 + v_R(\boldsymbol{r}),$$

where $\boldsymbol{R}_\alpha$ is the positions of basis atom α in the unit cell and $\boldsymbol{T}_i$ the lattice vectors. We take as a basis atomic orbitals with quantum numbers lm (we drop here the principal quantum number for convenience). For each atomic orbital we construct a Bloch state

$$\psi^\alpha_{lm}(\boldsymbol{k},\boldsymbol{r}) = \frac{1}{\sqrt{N}} \sum_i e^{i\boldsymbol{T}_i\cdot\boldsymbol{k}}\, \psi_{lm}(\boldsymbol{r}-\boldsymbol{T}_i-\boldsymbol{R}_\alpha), \tag{8}$$

where N is the number of lattice sites. In the Bloch basis (8), the Hamiltonian and the overlap matrix are given by

$$H^{\alpha,\alpha'}_{lm,l'm'}(\boldsymbol{k}) = \left\langle \psi^\alpha_{lm}(\boldsymbol{k}) \middle| \hat{h}_e \middle| \psi^{\alpha'}_{l'm'}(\boldsymbol{k}) \right\rangle,$$
$$O^{\alpha,\alpha'}_{lm,l'm'}(\boldsymbol{k}) = \left\langle \psi^\alpha_{lm}(\boldsymbol{k}) \middle| \psi^{\alpha'}_{l'm'}(\boldsymbol{k}) \right\rangle.$$

These matrices define a generalized eigenvalue problem, the solution of which yields the band structure. The Hamiltonian matrix is given by

$$H^{\alpha,\alpha'}_{lm,l'm'}(\boldsymbol{k}) = \varepsilon^0_{l'\alpha'}\, O^{\alpha,\alpha'}_{lm,l'm'}(\boldsymbol{k}) + \Delta\varepsilon^\alpha_{lm,l'm'}\,\delta_{\alpha,\alpha'} - \frac{1}{N}\sum_{i\alpha\neq i'\alpha'} e^{i(\boldsymbol{T}_{i'}-\boldsymbol{T}_i)\cdot\boldsymbol{k}}\, t^{i\alpha,i'\alpha'}_{lm,l'm'}\,.$$

Here $\varepsilon^0_{l\alpha}$ are the atomic levels, and $\Delta\varepsilon^\alpha_{lm,l'm'}$ the crystal-field matrix elements

$$\Delta\varepsilon^\alpha_{lm,l'm'} = \int d\boldsymbol{r}\; \overline{\psi_{lm}}(\boldsymbol{r}-\boldsymbol{R}_\alpha)\Big(v_R(\boldsymbol{r})-v(\boldsymbol{r}-\boldsymbol{R}_\alpha)\Big)\psi_{l'm'}(\boldsymbol{r}-\boldsymbol{R}_\alpha)\,, \tag{9}$$

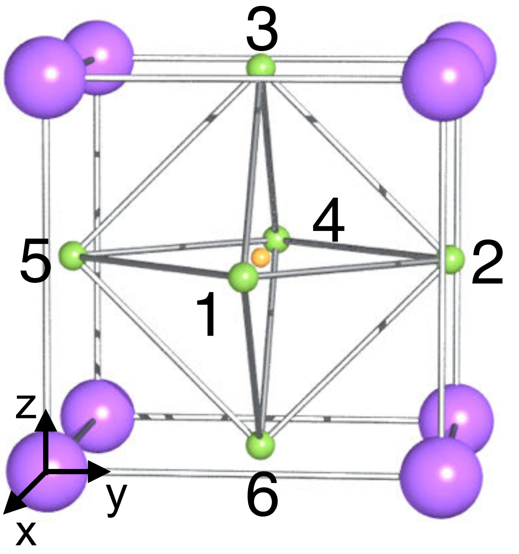

Fig. 6: *Unit cell of idealized cubic KCuF$_3$ with cubic axes in the left corner.*

which are two-center integrals. Finally,

$$t^{i\alpha,i'\alpha'}_{lm,l'm'} = -\int d\boldsymbol{r}\;\overline{\psi_{lm}}(\boldsymbol{r}-\boldsymbol{R}_\alpha-\boldsymbol{T}_i)\Big(v_R(\boldsymbol{r})-v(\boldsymbol{r}-\boldsymbol{R}_{\alpha'}-\boldsymbol{T}_{i'})\Big)\psi_{l'm'}(\boldsymbol{r}-\boldsymbol{R}_{\alpha'}-\boldsymbol{T}_{i'}). \tag{10}$$

The hopping integrals (10) contain two- and three-center terms; if the basis is sufficiently localized we can, however, neglect the three-center contributions and assume $t^{i\alpha,i'\alpha'}_{lm,l'm'} \sim -V^{i\alpha,i'\alpha'}_{lm,l'm'}$, where

$$V^{i\alpha,i'\alpha'}_{lm,l'm'} = \int d\boldsymbol{r}\;\overline{\psi_{lm}}(\boldsymbol{r}-\boldsymbol{R}_\alpha-\boldsymbol{T}_i)\,v(\boldsymbol{r}-\boldsymbol{R}_\alpha-\boldsymbol{T}_i)\,\psi_{l'm'}(\boldsymbol{r}-\boldsymbol{R}_{\alpha'}-\boldsymbol{T}_{i'})$$

is a Slater-Koster two-center integral (Appendix B). A generic Slater-Koster two-center integral can be expressed as a function of a few independent two-center integrals, shown in Fig. 4 for s, p, and d-functions. Apart from the σ bond, which is the strongest, other bonds are possible; the π bonds are made of orbitals which share a nodal plane to which the bond axis belongs, and the δ bond, for which two nodal planes intersect in the bond axis connecting the two ions. Fig. 5 shows how to obtain a generic two-center integral involving p and s orbitals.[5] Let us now consider the case of the e_g and t_{2g} bands of KCuF$_3$; here we assume for simplicity that the system is an ideal cubic perovskite, shown in Fig. 6. The primitive cell contains one formula unit (a single K cube in Fig. 1). The cubic axes are $\boldsymbol{x}$, $\boldsymbol{y}$, $\boldsymbol{z}$, and the lattice constant is a. A Cu atom at site $\boldsymbol{R}_i$ is surrounded by two apical F atoms, F$_3$ at $\boldsymbol{R}_i+\frac{1}{2}\boldsymbol{z}$ and F$_6$ at $\boldsymbol{R}_i-\frac{1}{2}\boldsymbol{z}$, and four planar F atoms, F$_1$ and F$_4$ at $\boldsymbol{R}_i \pm \frac{1}{2}\boldsymbol{x}$ and F$_2$ and F$_5$ at $\boldsymbol{R}_i \pm \frac{1}{2}\boldsymbol{y}$. In Fig. 7 one can see the effects of the cubic approximation on the e_g bands: the crystal-field splitting of the e_g states is zero, the band width slightly reduced, gaps disappear, and the dispersion relations is sizably modified. The cubic band structure in Fig. 7 was obtained with a unit cell containing two formula units, in order to compare it with the band structure of the experimental (Jahn-Teller distorted) structure

---

[5] More details on the tight-binding approach can be found in Ref. [13].

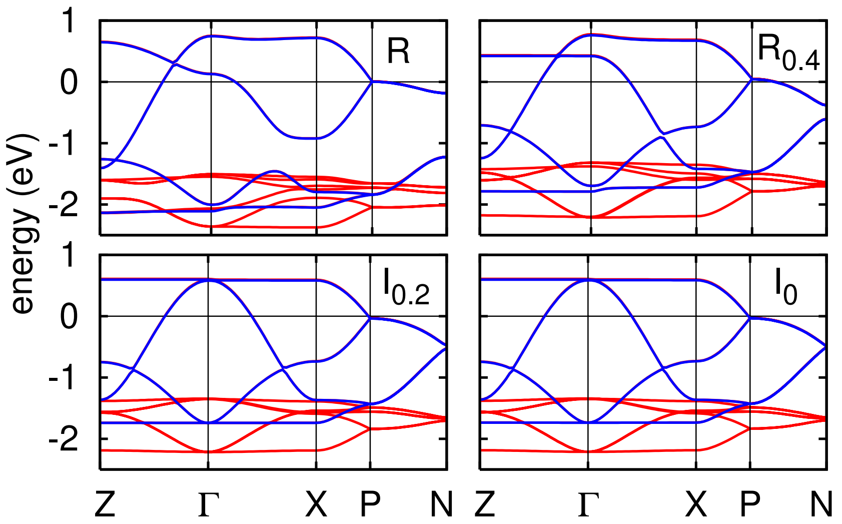

Fig. 7: *LDA e_g (blue) and t_{2g}(red) band structure of KCuF$_3$ for the experimental structure (R) and ideal structures with progressively reduced distortions (see Fig. 1). I_0: simple cubic. The unit cell used in this calculation contains two formula units. The figure is from Ref. [3].*

of KCuF$_3$; hence we see four (instead of two) e_g bands. The band-structure of cubic KCuF$_3$ for a cell with one formula unit is shown in Fig. 8; in the following we will refer for comparison to that figure only. Let us take as tight-binding basis the atomic $3d$ e_g orbitals for Cu and the $2p$ orbitals for F; we neglect for convenience the overlap integrals (i.e., we assume that our atomic functions are, approximately, localized *Wannier functions*). For such a tight-binding basis the only relevant Slater-Koster parameter is $V_{pd\sigma}$. The $|3z^2-r^2\rangle_i$ and $|x^2-y^2\rangle_i$ states of the Cu at $\boldsymbol{R}_i$ can couple via $V_{pd\sigma}$ to $|z^c\rangle_i$, the p_z orbitals of F$_3$ and F$_6$, to $|x^a\rangle_i$, the p_x orbitals of F$_1$ and F$_4$ and to $|y^b\rangle_i$, the p_y orbitals of F$_2$ and F$_5$. From the basis $|\alpha\rangle_i$ of localized atomic functions we construct the Bloch states $|\boldsymbol{k}\alpha\rangle = \frac{1}{\sqrt{N}}\sum_i e^{i\boldsymbol{k}\cdot\boldsymbol{R}_i}|\alpha\rangle_i$, and obtain the tight-binding Hamiltonian

$$\begin{array}{l|ccccc}
H^{\mathrm{TB}}_{e_g} & |\boldsymbol{k}\; z^c\rangle & |\boldsymbol{k}\; x^a\rangle & |\boldsymbol{k}\; y^b\rangle & |\boldsymbol{k}\; 3z^2-r^2\rangle & |\boldsymbol{k}\; x^2-y^2\rangle \\
\hline
|\boldsymbol{k}\; z^c\rangle & \varepsilon_p & 0 & 0 & -2V_{pd\sigma}s_z & 0 \\
|\boldsymbol{k}\; x^a\rangle & 0 & \varepsilon_p & 0 & V_{pd\sigma}s_x & -\sqrt{3}V_{pd\sigma}s_x \\
|\boldsymbol{k}\; y^b\rangle & 0 & 0 & \varepsilon_p & V_{pd\sigma}s_y & \sqrt{3}V_{pd\sigma}s_y \\
|\boldsymbol{k}\; 3z^2-r^2\rangle & -2V_{pd\sigma}\overline{s}_z & V_{pd\sigma}\overline{s}_x & V_{pd\sigma}\overline{s}_y & \varepsilon_d & 0 \\
|\boldsymbol{k}\; x^2-y^2\rangle & 0 & -\sqrt{3}V_{pd\sigma}\overline{s}_x & \sqrt{3}V_{pd\sigma}\overline{s}_y & 0 & \varepsilon_d
\end{array} \qquad (11)$$

where $s_\alpha = ie^{-ik_\alpha a/2}\sin k_\alpha a/2$, $\alpha = x, y, z$, $\varepsilon_p < \varepsilon_d = \varepsilon_p + \Delta_{pd}$, and $V_{pd\sigma} < 0$. If $|V_{pd\sigma}|/\Delta_{pd}$ is small, the occupied bands are F p-like, while the partially filled bands Cu e_g-like. We now calculate the bands along high-symmetry lines.[6] Along Γ-Z, the eigenvalues ε_i ($\varepsilon_i \le \varepsilon_{i+1}$) of

---

[6] Special points: $\Gamma = (0,0,0)$, Z$= (0,0,\pi/a)$, X$= (\pi/a,0,0)$, M$= (\pi/a,\pi/a,0)$, R$= (\pi/a,\pi/a,\pi/a)$.

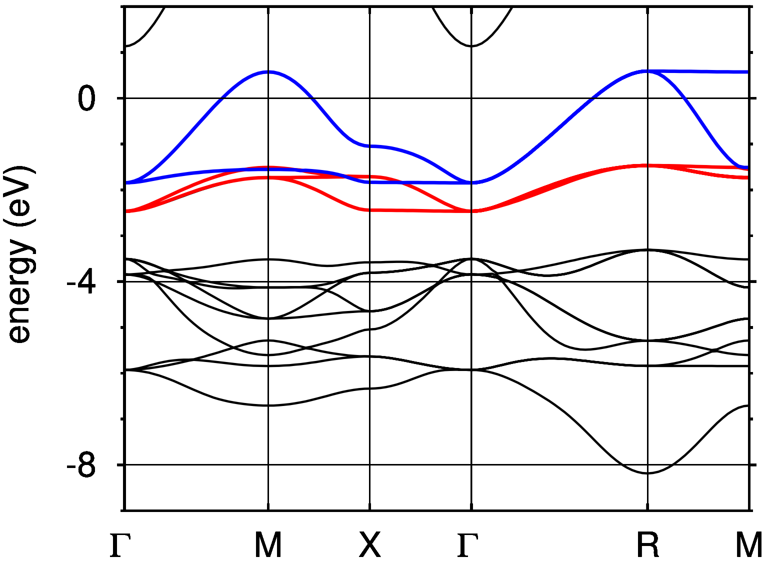

Fig. 8: *LDA band structure of cubic KCuF$_3$. The t_{2g} bands are in red and the e_g bands in blue.*

$H^{\rm TB}_{e_g}$ are

$$\begin{aligned}
\varepsilon_2 &= \varepsilon_p\\
\varepsilon_3 &= \varepsilon_p\\
\varepsilon_4 &= \varepsilon_d\\
\varepsilon_{1,5} &= \varepsilon_p + \tfrac{1}{2}\Delta_{pd} \pm \tfrac{1}{2}\sqrt{\Delta_{pd}^2 + 16V_{pd\sigma}^2|s_z|^2}
\end{aligned}$$

where ε_1 (sign $-$) is bonding and F z-like, while ε_5 (sign $+$) anti-bonding and Cu $3z^2{-}r^2$-like. Along Γ-X, we have instead the dispersion relations

$$\begin{aligned}
\varepsilon_2 &= \varepsilon_p\\
\varepsilon_3 &= \varepsilon_p\\
\varepsilon_4 &= \varepsilon_d\\
\varepsilon_{1,5} &= \varepsilon_p + \tfrac{1}{2}\Delta_{pd} \pm \tfrac{1}{2}\sqrt{\Delta_{pd}^2 + 16V_{pd\sigma}^2|s_x|^2}
\end{aligned}$$

where ε_1 is bonding and F x-like, while ε_5 anti-bonding and Cu $x^2{-}y^2$-like. To obtain the e_g-like bands, instead of diagonalizing $H^{\rm TB}_{e_g}$ as we have done above, we can also use the *downfolding* procedure, which, for non-interacting electrons, can be carried out exactly. This method works as follows. We divide the orbitals in passive (F p) and active (Cu d), and write the eigenvalues equation as

$$\begin{pmatrix} H_{pp} & H_{pd} \\ H_{dp} & H_{dd} \end{pmatrix} \begin{pmatrix} |\boldsymbol{k}\, p\rangle \\ |\boldsymbol{k}\, d\rangle \end{pmatrix} = \varepsilon \begin{pmatrix} I_{pp} & 0 \\ 0 & I_{dd} \end{pmatrix} \begin{pmatrix} |\boldsymbol{k}\, p\rangle \\ |\boldsymbol{k}\, d\rangle \end{pmatrix},$$

where H_{pp} (I_{pp}) is the Hamiltonian (identity matrix) in the p-electron space (3×3), and H_{dd} (I_{dd}) the Hamiltonian (identity matrix) in the d-electron space (2×2). By downfolding to the d sector we obtain the energy-dependent operator H^{ε}_{dd}, which acts in the d space only

$$H^{\varepsilon}_{dd} = H_{dd} - H_{dp}(H_{pp}{-}\varepsilon I_{pp})^{-1}H_{pd},$$

and a correspondingly transformed and energy-dependent basis set for the active space, $|\mathbf{k}\, d\rangle_\varepsilon$. The operator H^ε_{dd} has the same eigenvalues and eigenvectors as the original Hamiltonian. In the case of the e_g bands ($H^\varepsilon_{dd} = H^\varepsilon_{e_g}$) of KCuF$_3$

$$\begin{array}{c|cc}
H^\varepsilon_{e_g} & |\boldsymbol{k}\; 3z^2{-}r^2\rangle_\varepsilon & |\boldsymbol{k}\; x^2{-}y^2\rangle_\varepsilon \\
\hline
|\boldsymbol{k}\; 3z^2{-}r^2\rangle_\varepsilon & \varepsilon_d^\prime{-}2t^\sigma_\varepsilon[\frac{1}{4}(\cos k_x a{+}\cos k_y a){+}\cos k_z a] & 2t^\sigma_\varepsilon[\frac{\sqrt{3}}{4}(\cos k_x a{-}\cos k_y a)] \\
|\boldsymbol{k}\; x^2{-}y^2\rangle_\varepsilon & 2t^\sigma_\varepsilon[\frac{\sqrt{3}}{4}(\cos k_x a{-}\cos k_y a)] & \varepsilon_d^\prime{-}2t^\sigma_\varepsilon[\frac{3}{4}(\cos k_x a{+}\cos k_y a)]
\end{array} \tag{12}$$

where the effective parameters are

$$t^\sigma_\varepsilon = \frac{V^2_{pd\sigma}}{\varepsilon - \varepsilon_p}, \quad \varepsilon_d^\prime = \varepsilon_d + 3t^\sigma_\varepsilon .$$

The downfolding procedure has *renormalized* the parameters ε_d of the original model (11), but also introduced a new interaction: inter-orbital coupling. Furthermore, H^ε_{dd} and the Bloch basis are now energy dependent. Along Γ-Z, the eigenvalues of (12) are given implicitly by the equations $\varepsilon{=}\varepsilon_d{+}2t^\sigma_\varepsilon{-}2t_\varepsilon \cos k_z a$ (band ε_5) and $\varepsilon{=}\varepsilon_d$ (band ε_4); in second-order perturbation theory we find

$$t^\sigma_\varepsilon \sim t^\sigma_{\varepsilon_d} = \frac{V^2_{pd\sigma}}{\Delta_{pd}},$$

$$\varepsilon_5 \sim \varepsilon_d + 2t^\sigma_{\varepsilon_d} - 2t^\sigma_{\varepsilon_d} \cos k_z a\, .$$

From Hamiltonian (12) it is relatively easy to see that the e_g bands are 2-fold degenerate along direction Γ-R, to find the dispersion along Γ-M and R-M, and to obtain the e_g-like bands in Fig. 8. By Fourier transforming the Bloch states $|\boldsymbol{k}\;\, 3z^2{-}r^2\rangle_\varepsilon$ and $|\boldsymbol{k}\;\, x^2{-}y^2\rangle_\varepsilon$ we can build a set of Wannier functions. They have $3z^2{-}r^2$ or $x^2{-}y^2$ symmetry as the atomic orbitals, and, additionally, they span, to arbitrary accuracy, the e_g bands. These Wannier functions are by construction longer range than atomic orbitals, since they have p tails on the downfolded neighboring F sites.

We can now repeat the same calculation for the t_{2g} bands. The minimal tight-binding basis is of course different with respect to the case of e_g bands. The states $|xy\rangle_i$ of the Cu ion located at $\boldsymbol{R}_i$ are coupled via $V_{pd\pi}$ to the $|y^a\rangle_i$, the p_y orbitals of F$_1$ and F$_4$ and to $|x^b\rangle_i$, the p_x orbitals of F$_2$ and F$_5$; in a similar way, $|xz\rangle_i$ is coupled via $V_{pd\pi}$ to the $|z^a\rangle_i$, the p_z orbitals of F$_1$ and F$_4$, and to the $|x^c\rangle_i$, the p_x orbitals of F$_3$ and F$_6$; finally $|yz\rangle_i$ is coupled via $V_{pd\pi}$ to the $|z^b\rangle_i$, the p_z orbitals of F$_2$ and F$_5$, and to the $|y^c\rangle_i$, the p_y orbitals of F$_3$ and F$_6$. After constructing for each $|\alpha\rangle_i$ the corresponding Bloch state, we obtain the tight-binding Hamiltonian. The latter splits into three decoupled blocks,

$$\begin{array}{c|ccc}
H^{\mathrm{TB}}_{t_{2g}} & |\boldsymbol{k}\; y^a\rangle & |\boldsymbol{k}\; x^b\rangle & |\boldsymbol{k}\; xy\rangle \\
\hline
|\boldsymbol{k}\; y^a\rangle & \varepsilon_p & 0 & 2V_{pd\pi} s_x \\
|\boldsymbol{k}\; x^b\rangle & 0 & \varepsilon_p & 2V_{pd\pi} s_y \\
|\boldsymbol{k}\; xy\rangle & 2V_{pd\pi} \overline{s}_x & 2V_{pd\pi} \overline{s}_y & \varepsilon_d
\end{array}$$

and cyclic permutations of x, y, and z (and, correspondingly, of a, b, and c). In the Γ-X direction we thus find

$$\begin{aligned}\varepsilon_{2'}(\boldsymbol{k}) =& \varepsilon_d \\ \varepsilon_5(\boldsymbol{k}) =& \varepsilon_p + \frac{\Delta_{pd}}{2} + \frac{\sqrt{\Delta_{pd}^2 + 16V_{pd\pi}^2|s_x|^2}}{2} \\ \sim& \varepsilon_d + 2t^{\pi}_{\varepsilon_d} - 2t^{\pi}_{\varepsilon_d}\cos k_x a\end{aligned}$$

where $t^{\pi}_{\varepsilon_d} = V_{pd\pi}^2/\Delta_{pd}$. By downfolding the oxygen states we obtain

$H^{\varepsilon}_{t_{2g}}$	$\lvert\boldsymbol{k}\ yz\rangle_{\varepsilon}$	$\lvert\boldsymbol{k}\ xz\rangle_{\varepsilon}$	$\lvert\boldsymbol{k}\ xy\rangle_{\varepsilon}$
$\lvert\boldsymbol{k}\ yz\rangle_{\varepsilon}$	$\varepsilon_d'' - 2t^{\pi}_{\varepsilon}\,(\cos k_x a + \cos k_y a)$	0	0
$\lvert\boldsymbol{k}\ xz\rangle_{\varepsilon}$	0	$\varepsilon_d'' - 2t^{\pi}_{\varepsilon}\,(\cos k_x a + \cos k_z a)$	0
$\lvert\boldsymbol{k}\ yz\rangle_{\varepsilon}$	0	0	$\varepsilon_d'' - 2t^{\pi}_{\varepsilon}\,(\cos k_y a + \cos k_z a)$

where the parameters in the matrix are

$$\begin{aligned}\varepsilon_d'' =& \varepsilon_d + 4t^{\pi}_{\varepsilon}, \\ t^{\pi}_{\varepsilon} =& \frac{|V_{pd\pi}|^2}{\varepsilon - \varepsilon_p}.\end{aligned}$$

As in the case of the e_g bands, we find renormalized energy levels and effective band dispersions; since different Cu t_{2g} states couple to different F p states, and we neglected hopping integrals between the ligands, the xy, xz, and yz bands are totally decoupled in our model. We are now in the position of calculating the (approximate) expression of the covalent contribution to the e_g-t_{2g} crystal-field splitting, i.e., the energy difference

$$\Delta_{\mathrm{CF}} \sim \varepsilon_d' - \varepsilon_d'' = 3\frac{|V_{pd\sigma}|^2}{\Delta_{pd}} - 4\frac{|V_{pd\pi}|^2}{\Delta_{pd}} > 0. \tag{13}$$

As we can see, the sign of the covalent crystal-field splitting is the same as that of the ionic contribution. This happens for two reasons. First, the so-called d bands are the anti-bonding states of the p-d Hamiltonian, hence both the energy of the e_g and t_{2g} states moves upwards due to the interaction with the p orbitals. Second, σ bonds are stronger than π bonds, hence e_g states shift to sizably higher energy than t_{2g} states.

The tight-binding model we have used so far is oversimplified, but it already qualitatively well describes the e_g and t_{2g} bands in Fig. 8. A more accurate description can be obtained including other Slater-Koster integrals, such as the hopping to apical F s states, or between neighboring F p states. With increasing number of parameters, it becomes progressively harder to estimate them, e.g., from comparison with experiments; furthermore a large number of fitting parameters makes it impossible to put a theory to a test. Modern techniques allow us, however, to calculate hopping integrals and crystal-field splittings *ab-initio*, using localized Wannier functions as the basis and the Kohn-Sham potential $v_R(\boldsymbol{r})$ as the one-electron potential; because Wannier functions are orthogonal, the corresponding overlap matrix is by construction diagonal.

4 Jahn-Teller effect

In order to introduce the Jahn-Teller effect we have to take a step back and start from the central equation of solid-state physics, the eigenvalue problem $\hat{H}\Psi = E\Psi$, defined (in the non-relativistic limit) by the many-body Hamiltonian

$$\hat{H} = \underbrace{-\frac{1}{2}\sum_i \nabla_i^2}_{\hat{T}_e} + \underbrace{\frac{1}{2}\sum_{i\neq i'} \frac{1}{|\boldsymbol{r}_i - \boldsymbol{r}_{i'}|}}_{\hat{V}_{ee}} \underbrace{-\sum_{i\alpha} \frac{Z_\alpha}{|\boldsymbol{r}_i - \boldsymbol{R}_\alpha|}}_{\hat{V}_{en}} \underbrace{-\sum_\alpha \frac{1}{2M_\alpha}\nabla_\alpha^2}_{\hat{T}_n} + \underbrace{\frac{1}{2}\sum_{\alpha\neq\alpha'} \frac{Z_\alpha Z_{\alpha'}}{|\boldsymbol{R}_\alpha - \boldsymbol{R}_{\alpha'}|}}_{\hat{V}_{nn}}.$$

Here $\{\boldsymbol{r}_i\}$ are the coordinates of the N_e electrons, $\{\boldsymbol{R}_\alpha\}$ those of the N_n nuclei, Z_α the atomic numbers, and M_α the nuclear masses. The Born-Oppenheimer Ansatz

$$\Psi(\{\boldsymbol{r}_i\},\{\boldsymbol{R}_\alpha\}) = \psi\big(\{\boldsymbol{r}_i\};\{\boldsymbol{R}_\alpha\}\big)\ \Phi\big(\{\boldsymbol{R}_\alpha\}\big)\,, \tag{14}$$

splits the Schrödinger equation $\hat{H}\Psi = E\Psi$ into the system

$$\begin{cases} \hat{H}_e\psi\big(\{\boldsymbol{r}_i\};\{\boldsymbol{R}_\alpha\}\big) = & \varepsilon(\{\boldsymbol{R}_\alpha\})\psi\big(\{\boldsymbol{r}_i\};\{\boldsymbol{R}_\alpha\}\big), \\ \hat{H}_n\Phi\big(\{\boldsymbol{R}_\alpha\}\big) = & E\Phi\big(\{\boldsymbol{R}_\alpha\}\big), \end{cases} \tag{15}$$

where the Hamilton operators for the electrons ($\hat{H}_e$) and that for the lattice ($\hat{H}_n$) are

$$\hat{H}_e = \hat{T}_e + \hat{V}_{ee} + \hat{V}_{en} + \hat{V}_{nn}, \tag{16}$$

$$\hat{H}_n = \hat{T}_n + \varepsilon\big(\{\boldsymbol{R}_\alpha\}\big) = \hat{T}_n + \hat{U}_n, \tag{17}$$

and where in (17) we neglect non-adiabatic corrections.[7] In the electronic Hamiltonian (16) the atomic positions $\{\boldsymbol{R}_\alpha\}$ are simple parameters. The electronic eigenvalue $\varepsilon\big(\{\boldsymbol{R}_\alpha\}\big)$ acts as potential for the nuclei and defines a Born-Oppenheimer (BO) energy surface. While (16) describes the electronic structure, (17) yields the equilibrium crystal structure and the vibrational modes. These equations are impossible to solve in the general case. The first difficulty is that Hamiltonian (16) describes the electronic quantum many-body problem. The latter can be solved only approximately, for example the energy of the ground state can be obtained via density-functional theory using one of the known approximations to the universal functional. For strongly-correlated systems, advanced methods combine density-functional theory with many-body approaches such as the dynamical mean-field theory [7, 8]. The second issue is the very high number of atoms, and therefore of $\{\boldsymbol{R}_\alpha\}$ parameters to explore; finally, even if we solve the electronic many-body problem exactly, we still have to deal with the nuclear many-body problem, Hamiltonian (17). Despite all these obstacles, let us assume for a moment that, for a given system, we did solve the electronic problem for general values of $\{\boldsymbol{R}_\alpha\}$. Let us also assume that the set of positions $\{\boldsymbol{R}_\alpha\} = \{\boldsymbol{R}_\alpha^0\}$ defines a specific crystal structure, whose electronic ground state (i.e., the lower energy BO surface) has degeneracy $d > 1$. We can at this point ask ourself the question: Is structure $\{\boldsymbol{R}_\alpha^0\}$ actually stable?

---

[7] We neglect the operator $\hat{\Lambda}_n$, with elements $\langle m|\hat{\Lambda}_n|m'\rangle = -\sum_\alpha \frac{1}{M_\alpha}\left[\frac{1}{2}\langle\psi_m|\nabla_\alpha^2\psi_{m'}\rangle + \langle\psi_m|\nabla_\alpha\psi_{m'}\rangle\cdot\nabla_\alpha\right]$

The Jahn-Teller theorem states that any electronically degenerate system can lower its energy by undergoing some structural distortions, and therefore is unstable.[8] This is due to the coupling between electrons and lattice. In order to better understand the microscopic origin of this phenomenon, let us consider a system in a high-symmetry structure, $\{\boldsymbol{R}^0_\alpha\}$, for which the electronic ground state has energy $\varepsilon\big(\{\boldsymbol{R}^0_\alpha\}\big)$ with degeneracy $d > 1$. This means that there are d Born-Oppenheimer surfaces degenerate for $\{\boldsymbol{R}_\alpha\} = \{\boldsymbol{R}^0_\alpha\}$,

$$\varepsilon_m\big(\{\boldsymbol{R}^0_\alpha\}\big) = \varepsilon\big(\{\boldsymbol{R}^0_\alpha\}\big).$$

In the rest of the chapter we will take $\varepsilon\big(\{\boldsymbol{R}^0_\alpha\}\big)$ as the energy zero. The corresponding degenerate electronic wavefunctions are $\psi_m\big(\{\boldsymbol{r}_i\};\{\boldsymbol{R}^0_\alpha\}\big)$. Let us expand the nuclear potential $\hat{U}_n$ for one of these surfaces around the symmetric structure $\{\boldsymbol{R}^0_\alpha\}$. This leads to the Taylor series

$$\hat{H}_n = \hat{T}_n + \sum_{\alpha\mu}\left[\frac{\partial \hat{U}_n}{\partial u_{\alpha\mu}}\right]_{\{\boldsymbol{R}^0_\alpha\}} u_{\alpha\mu} + \frac{1}{2}\sum_{\alpha\mu}\sum_{\alpha'\mu'}\left[\frac{\partial^2 \hat{U}_n}{\partial_{\alpha\mu}\partial_{\alpha'\mu'}}\right]_{\{\boldsymbol{R}^0_\alpha\}} u_{\alpha\mu}\, u_{\alpha'\mu'} + \ldots,$$

where $\boldsymbol{u}_\alpha = \boldsymbol{R}_\alpha - \boldsymbol{R}^0_\alpha$ are displacement vectors with respect to the equilibrium position, and $\mu = x, y, z$. If $\{\boldsymbol{R}^0_\alpha\}$ is an equilibrium structure, the gradient is zero and

$$\hat{H}_n \sim \hat{T}_n + \frac{1}{2}\sum_{\alpha\mu}\sum_{\alpha'\mu'}\left[\frac{\partial^2 \hat{U}_n}{\partial_{\alpha\mu}\partial_{\alpha'\mu'}}\right]_{\{\boldsymbol{R}^0_\alpha\}} u_{\alpha\mu}u_{\alpha'\mu'} + \ldots \;=\; \hat{T}_n + \hat{U}_n^{\mathrm{PH}}(\{\boldsymbol{R}^0_\alpha\}) + \ldots, \tag{18}$$

The standard procedure to diagonalize (18) consists of two steps. First we change coordinates

$$\tilde{u}_{\alpha\mu} = u_{\alpha\mu}\sqrt{M_\alpha}.$$

Second we introduce the dynamical matrix

$$D_{\alpha\mu,\alpha\mu'} = \frac{1}{\sqrt{M_\alpha}}\frac{1}{\sqrt{M_{\alpha'}}}\left[\frac{\partial^2 \hat{U}_n}{\partial_{\alpha\mu}\partial_{\alpha'\mu'}}\right]_{\{\boldsymbol{R}^0_\alpha\}},$$

and diagonalize it. Its N_m eigenvectors are the normal modes $\boldsymbol{Q}_\eta$,

$$D\boldsymbol{Q}_\eta = \omega_\eta^2\boldsymbol{Q}_\eta,$$

$$Q_{\eta\nu} = \sum_{\alpha=1}^{N_n}\sum_{\mu=x,y,z} a_{\eta\nu,\alpha\mu}u_{\alpha\mu},$$

with $\eta = 1, \ldots N_m$, and $\nu = x, y, z$. The *normal coordinates* $\{Q_{n\nu}\}$, together with the associated canonically-conjugated momenta $\{P_{n\nu}\}$, bring (18) in the form

$$\hat{H}_n \sim \frac{1}{2}\sum_{\eta\nu}\left(P^2_{\eta\nu} + \omega^2_\eta Q^2_{\eta\nu}\right). \tag{19}$$

---

[8] The only exceptions are linear molecules and Kramers degeneracy.

In a crystal, this Hamiltonian yields the phononic energy levels. Let us now determine the possible N_m normal modes for a cubic perovskite. For simplicity we consider here only a single octahedron and the modes associated with the vibrations of its atoms. Given that each atom can move in three directions, and there are 6 atoms of type C and 1 atom of type B, in principle such a system has 21 degrees of freedom; eliminating global translations (3 degrees of freedom) and global rotations (3 degrees of freedom), i.e., displacements which are not vibrations, 15 degrees of freedom are left, hence the system has 15 possible normal modes. In group theory language, assuming again for simplicity that the group is O instead of O_h, one can show that these modes can be labeled as belonging to irreducible representations A_1, E, T_1 or T_2. To obtain this result we first build a matrix representation of the group in the linear space of all possible displacements; this space is 21-dimensional, and so is the associated matrix representation Γ_{tot}. The latter can be expressed as the direct product $\Gamma_{\text{tot}} = \Gamma_{\text{a.s.}} \otimes \Gamma_{\text{vector}}$, where $\Gamma_{\text{a.s.}}$ is the so-called atomic-site representation. $\Gamma_{\text{a.s.}}$ has as a basis the original atomic positions (without displacements); in our case it is has therefore dimensionality 7. The character of $\Gamma_{\text{a.s.}}$ for a given operation is simply the number of sites left invariant by that operation. Finally, in group O the irreducible representation for a vector is $\Gamma_{\text{vector}} = T_1$; this can be seen from the partner functions (x, y, z) in Table 4. Summarizing all this in a character table, we have

O	E	$8C_3$	$3C_2$	$6C_2$	$6C_4$
$\Gamma^{\text{a.s.}}$	7	1	3	1	3
$\Gamma^{\text{tot}} = \Gamma^{\text{a.s.}} \otimes \Gamma_{\text{vector}}$	21	0	-3	-1	3

Once we know the characters for representation Γ_{tot}, we can split the latter into irreducible representations of group O via the decomposition formula Eq. (5). After subtracting (tensor subtraction $\ominus$) the representations for mere translations (T_1) and mere rotations (T_1) of the octahedron,[9] we arrive at the final decomposition of the vibrational-modes representation $\Gamma_{\text{vibrations}} = \Gamma_{\text{tot}} \ominus \Gamma_{\text{vector}} \ominus \Gamma_{\text{rotation}} = A_1 \oplus E \oplus 2T_1 \oplus 2T_2$. Normal modes which are a basis for different irreducible representations have in general different energies. Let us focus on modes A_1 and E. We can obtain mode A_1 by using the projector, Eq. (6), for irreducible representation A_1. As a matter of fact, if we assume that atom F_1 (Fig. 9) is displaced by $\boldsymbol{u}_1$, by applying the projector $\hat{P}^{A_1}$ to $\boldsymbol{u}_1$ we generate automatically the linear combination of atomic displacements (all having the same length) forming the mode of symmetry A_1. This leads to

$$\boldsymbol{Q}_0 = \boldsymbol{u}_1(q_0) + \boldsymbol{u}_2(q_0) + \boldsymbol{u}_3(q_0) + \boldsymbol{u}_4(q_0) + \boldsymbol{u}_5(q_0) + \boldsymbol{u}_6(q_0).$$

---

[9] The representation for an improper vector (rotation) is $\Gamma_{\text{rotation}} = T_1$, as can be seen from the corresponding partner functions (R_x, R_y, R_z) in Table 4.

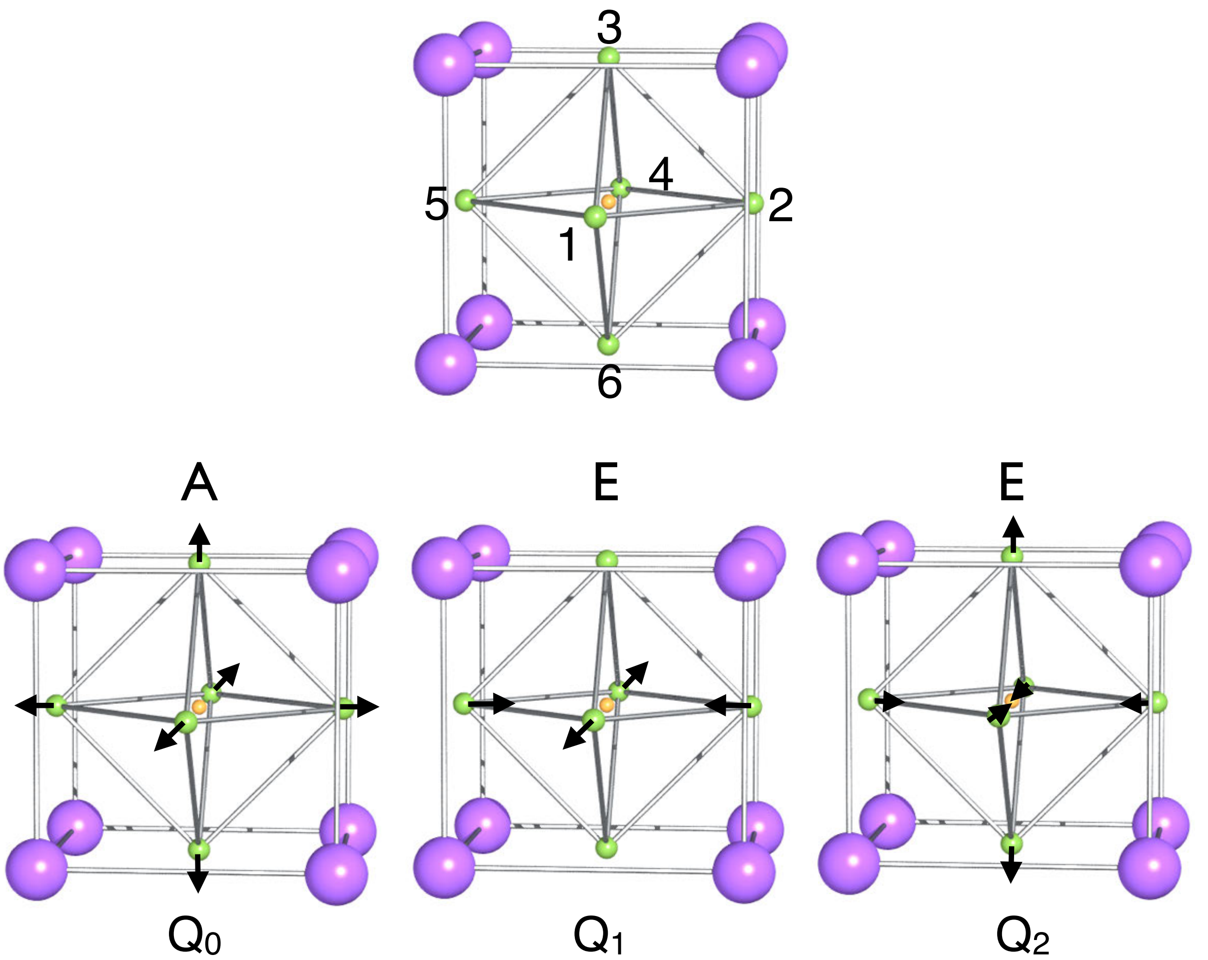

Fig. 9: *Unit cell (top) and vibrational modes Q_0, Q_1, and Q_2 of cubic KCuF$_3$.*

Here $\boldsymbol{u}_i$ are the (normalized) displacements for the C_i atom (see Fig. 9) which we rewrite as

$$\begin{aligned}
\boldsymbol{u}_1(q_0) &= \tfrac{1}{\sqrt{6}}\, q_0(1,0,0)\\
\boldsymbol{u}_2(q_0) &= \tfrac{1}{\sqrt{6}}\, q_0(0,1,0)\\
\boldsymbol{u}_3(q_0) &= \tfrac{1}{\sqrt{6}}\, q_0(0,0,1)\\
\boldsymbol{u}_4(q_0) &= -\tfrac{1}{\sqrt{6}}\, q_0(1,0,0)\\
\boldsymbol{u}_5(q_0) &= -\tfrac{1}{\sqrt{6}}\, q_0(0,1,0)\\
\boldsymbol{u}_6(q_0) &= -\tfrac{1}{\sqrt{6}}\, q_0(0,0,1)
\end{aligned}$$

The potential energy of such a *breathing mode* is

$$U_n^{\mathrm{PH}} = \frac{1}{2} C_{A_1} q_0^2 \,.$$

The $\boldsymbol{Q}_0$ mode expands or compresses the unit cell, but does not change its symmetry which remains cubic. Hence, this mode has no influence on the stability of the structure, at most it can affect the actual value of the lattice constant. More interesting are the two degenerate modes of type E. These modes can be obtained in a similar way as we have done for $\boldsymbol{Q}_0$, this time using the projector for irreducible representation E; within the resulting 2-dimensional space, we choose as basis the mutually orthogonal modes that transform as the $l = 2$ partner functions of E, x^2-y^2 and $3z^2-r^2$. These are $\boldsymbol{Q}_1$ and $\boldsymbol{Q}_2$, shown in Fig. 9. They are defined as

$$\begin{aligned}
\boldsymbol{Q}_1 &= \boldsymbol{u}_1(q_1) + \boldsymbol{u}_2(q_1) + \boldsymbol{u}_4(q_1) + \boldsymbol{u}_5(q_1),\\
\boldsymbol{Q}_2 &= \boldsymbol{u}_1(q_2) + \boldsymbol{u}_2(q_2) + \boldsymbol{u}_3(q_2) + \boldsymbol{u}_4(q_2) + \boldsymbol{u}_5(q_2) + \boldsymbol{u}_6(q_2),
\end{aligned}$$

where the displacements are

$$\begin{array}{rcrrcr}
\boldsymbol{u}_1(q_1) &=& \frac{1}{\sqrt{4}}\, q_1(1,0,0) & \quad \boldsymbol{u}_1(q_2) &=& -\frac{1}{\sqrt{12}}\, q_2(1,0,0)\\
\boldsymbol{u}_2(q_1) &=& -\frac{1}{\sqrt{4}}\, q_1(0,1,0) & \quad \boldsymbol{u}_2(q_2) &=& -\frac{1}{\sqrt{12}}\, q_2(0,1,0)\\
\boldsymbol{u}_3(q_1) &=& (0,0,0) & \quad \boldsymbol{u}_3(q_2) &=& \frac{2}{\sqrt{12}}\, q_2(0,0,1)\\
\boldsymbol{u}_4(q_1) &=& -\frac{1}{\sqrt{4}}\, q_1(1,0,0) & \quad \boldsymbol{u}_4(q_2) &=& \frac{1}{\sqrt{12}}\, q_2(1,0,0)\\
\boldsymbol{u}_5(q_1) &=& \frac{1}{\sqrt{4}}\, q_1(0,1,0) & \quad \boldsymbol{u}_5(q_2) &=& \frac{1}{\sqrt{12}}\, q_2(0,1,0)\\
\boldsymbol{u}_6(q_1) &=& (0,0,0) & \quad \boldsymbol{u}_6(q_2) &=& -\frac{2}{\sqrt{12}}\, q_2(0,0,1)
\end{array}$$

The corresponding quadratic potential has the form

$$\hat{U}_n^{\mathrm{PH}} = \frac{1}{2} C_E \big(q_1^2 + q_2^2\big).$$

The normal modes T_1 and T_2 can be obtained in a similar way; since they are not relevant for structure stability in the example considered here we do not provide their form explicitly.

Up to now we have assumed that the hypothetical high-symmetry structure $\{\boldsymbol{R}_\alpha^0\}$ is a stationary point. In general, however, this might or might not be true. The behavior of the BO energy surfaces close to the point in which they are degenerate allows us to separate them into two classes, the first one in which $\{\boldsymbol{R}_\alpha^0\}$ is a stationary point for all degenerate electronic states m (Renner-Teller intersection), and the second in which the surface is not a stationary point at least for some of the surfaces (Jahn-Teller intersection). The classical Jahn-Teller systems are those for which $\nabla \hat{U}_n\big(\{\boldsymbol{R}_\alpha^0\}\big) \neq 0$ at least in some direction (see, e.g., Fig. 10). Let us now calculate the first-order correction to the m degenerate eigenvalues due to a small distortion around $\{\boldsymbol{R}_\alpha^0\}$. The electronic Hamiltonian (16) has matrix elements

$$\big\langle \psi_m \big| \hat{H}_e(\{\boldsymbol{R}_\alpha\}) \big| \psi_{m'} \big\rangle = \underbrace{\sum_{\alpha\mu} \langle \psi_m | \left[\frac{\partial \hat{H}_e}{\partial u_{\alpha\mu}} \right]_{\{\boldsymbol{R}_\alpha^0\}} | \psi_{m'} \rangle u_{\alpha\mu}}_{\hat{U}^{\mathrm{JT}}_{m,m'}} + \dots \;=\; \hat{U}^{\mathrm{JT}}_{m,m'} + \dots .$$

The perturbation $\hat{U}^{\mathrm{JT}}$, the Jahn-Teller potential, couples the degenerate BO energy surfaces; it also couples electrons and lattice vibrations, as we can see from the coordinates $u_{\alpha\mu}$ appearing in the expression above. Thus, if there are modes for which $\hat{U}^{\mathrm{JT}} \neq C\, \hat{I}$ where $\hat{I}$ is the identity matrix and C a constant, the system gains energy at linear order via a distortion which lowers the symmetry; the Jahn-Teller theorem states that such modes always exist for electronically degenerate systems (with the exceptions of Kramers degeneracy and linear molecules).

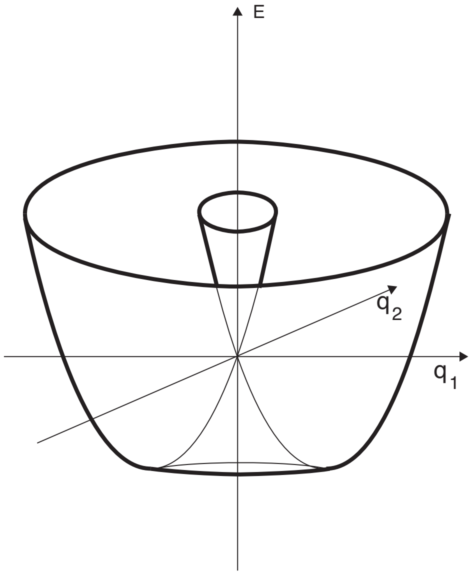

Fig. 10: *Born-Oppenheimer potential-energy surface exhibiting the form of a mexican hat. The slope of the curve at small distortions* q_1*,* q_2 *yields the Jahn-Teller coupling constant* λ*.*

In order to better understand the effect of the electron-lattice coupling, we generalize the Born-Oppenheimer Ansatz as follows

$$\Psi\big(\{\boldsymbol{r}_i\},\{\boldsymbol{R}_\alpha\}\big)=\sum_m \psi_m\big(\{\boldsymbol{r}_i\};\{\boldsymbol{R}_\alpha\}\big)\,\Phi_m\big(\{\boldsymbol{R}_\alpha\}\big).$$

To find the equations for the functions $\{\Phi_m\}$, we write the Schrödinger equation $H\Psi = E\Psi$, multiply on the left by $\overline{\psi_m}$, and integrate over the coordinates of the electrons. We obtain

$$\hat{H}_n\Phi_m\big(\{\boldsymbol{R}_\alpha\}\big)=\Big[\hat{T}_n+\hat{U}_n^{\mathrm{PH}}\Big]\,\Phi_m\big(\{\boldsymbol{R}_\alpha\}\big)+\sum_{m'}\hat{U}^{\mathrm{JT}}_{m,m'}\Phi_{m'}\big(\{\boldsymbol{R}_\alpha\}\big)=E\Phi_m\big(\{\boldsymbol{R}_\alpha\}\big). \quad (20)$$

The dynamics of the system close to the degeneracy point is determined by all degenerate sheets. The minimization of the new potential energy yields a new structure $\{\tilde{\boldsymbol{R}}^0_\alpha\}$ in which the electronic states are not any more degenerate. The modes that can produce such an instability should satisfy the condition

$$A_1 \in \Big\{[\Gamma_m\otimes\Gamma_m]\otimes(\Gamma_{\text{vibrations}}\neq A_1)\Big\},$$

where Γ_m is the irreducible representation to which the electronic degenerate states belong, and $[\Gamma_m\otimes\Gamma_m]$ is the symmetric direct product; for e_g states, $[e_g\otimes e_g]{=}a_1\oplus e_g$. The trivial representation A_1 has to be excluded from $\Gamma_{\text{vibrations}}$ because, as already discussed, it does not lower the symmetry. In the case cubic KCuF$_3$, the relevant normal modes coupling to the degenerate e_g electronic states are thus the E modes; as for the electronic states, if the group $O\to O_h$, then $E\to E_g$. Thus we can say that KCuF$_3$ is an example of a $e_g\otimes E_g$ Jahn-Teller system, a system in which an electronic doublet (e_g) is coupled to a doublet of normal modes (E_g). The form of the Jahn-Teller potential $\hat{U}^{\mathrm{JT}}$ can be obtained from the effect of perturbations of type $\boldsymbol{Q}_1$ and $\boldsymbol{Q}_2$ on the crystal-field matrix. As for the crystal field, there are both a ionic and a covalent contribution. For the ionic contribution, we can use once more perturbation theory. In this case, we have to take into account that the Cu-F distance d_C depends on the direction, i.e,

$$d_C \to d_C + \delta d_C^{\mu},$$

where $\mu = x, y, z$; the specific δd_C^{μ} values for each atom are given by the specific vibrational mode. After summing up all contribution, the first non-cubic correction due to E_g modes is

$$\varDelta v_{\mathrm{JT}} = \lambda \begin{pmatrix} q_2 & q_1 \\ q_1 & -q_2 \end{pmatrix}.$$

It is, at this point, useful to introduce pseudo-spin operators acting on the e_g states, i.e., operators $\hat{\tau}_\mu$ with $\mu = x, y, z$ and

$$\begin{array}{lll} \hat{\tau}_z | \searrow\rangle = -| \searrow\rangle, & \hat{\tau}_x | \searrow\rangle = +| \nearrow\rangle, & \hat{\tau}_y | \searrow\rangle = -i| \nearrow\rangle \\ \hat{\tau}_z | \nearrow\rangle = +| \nearrow\rangle, & \hat{\tau}_x | \nearrow\rangle = +| \searrow\rangle, & \hat{\tau}_y | \nearrow\rangle = +i| \searrow\rangle \end{array}$$

where $| \nearrow\rangle = |x^2{-}y^2\rangle$ and $| \searrow\rangle = |3z^2{-}r^2\rangle$. In matrix form these operators can be written as pseudo-Pauli matrices

$$\hat{\tau}_z = \begin{pmatrix} 1 & 0 \\ 0 & -1 \end{pmatrix} \quad \hat{\tau}_x = \begin{pmatrix} 0 & 1 \\ 1 & 0 \end{pmatrix} \quad \hat{\tau}_y = \begin{pmatrix} 0 & -i \\ i & 0 \end{pmatrix}. \tag{21}$$

We can then rewrite the Jahn-Teller potential as

$$\varDelta v_{\mathrm{JT}} = \lambda \Big(q_1 \hat{\tau}_x + q_2 \hat{\tau}_z \Big),$$

where $\lambda \sim (q_C/d_C^4)\ (36/7\sqrt{3}) > 0$. This potential expresses both the essence of the Jahn-Teller theorem and its relation with orbital order; the systems gains energy at linear order by making a distortion; the latter produces a crystal-field splitting, which leads to preferential occupation of the lower energy level. For example, if $q_1 = 0$ and $q_2 < 0$ (tetragonal compression) the $3z^2{-}r^2$ state is higher in energy. Let us now calculate the covalent contribution to the Jahn-Teller potential. In this case the linear-order correction is

$$\varDelta\varepsilon_{lm,l'm'}(\mathbf{0}, \boldsymbol{R}_\alpha{+}\boldsymbol{u}) - \varDelta\varepsilon_{lm,l'm'}(\mathbf{0}, \boldsymbol{R}_\alpha) \sim \nabla \varDelta\varepsilon_{lm,l'm'}(\mathbf{0}, \boldsymbol{R}_\alpha) \cdot \boldsymbol{u}$$

For e_g-states we use for simplicity the following approximations[10]

$$\begin{aligned} \varDelta\varepsilon_{3z^2-r^2,3z^2-r^2} &\sim \left[n^2 - \frac{1}{2}\big(l^2{+}m^2\big) \right]^2 \tilde{V}_{dd\sigma}, \\ \varDelta\varepsilon_{3z^2-r^2,x^2-y^2} &\sim \frac{\sqrt{3}}{2}\big(l^2{-}m^2\big) \left[n^2 - \frac{1}{2}\big(l^2{+}m^2\big) \right] \tilde{V}_{dd\sigma}, \\ \varDelta\varepsilon_{x^2-y^2,x^2-y^2} &\sim \frac{3}{4}\big(l^2{-}m^2\big)^2 \tilde{V}_{dd\sigma}. \end{aligned}$$

---

[10] The crystal-field integrals are also two-center integrals; the table of Slater-Koster integrals in Appendix B is thus still valid, provided that $V_{ll'\alpha}$ are replaced by the corresponding crystal-field terms, which we indicate as $\tilde{V}_{ll'\alpha}$.

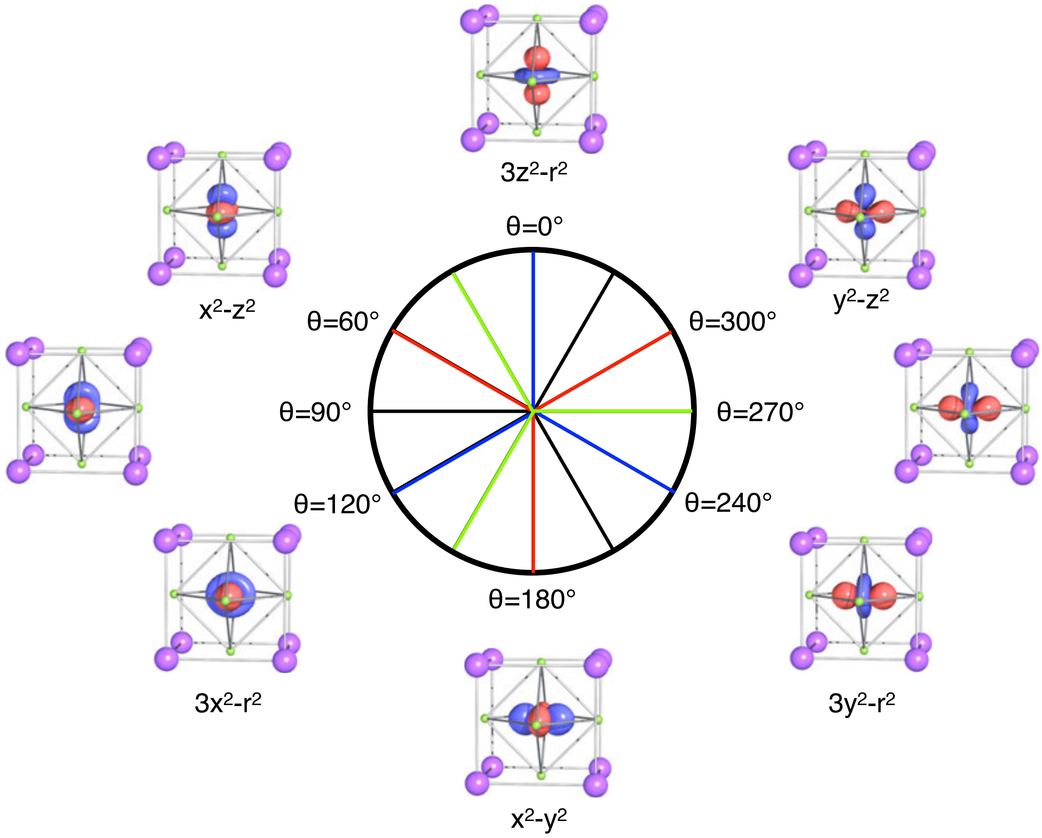

Fig. 11: *Linear combinations of e_g-states, $|\vartheta\rangle = -\sin\frac{\vartheta}{2}|x^2{-}y^2\rangle + \cos\frac{\vartheta}{2}|3z^2{-}r^2\rangle$. The $\vartheta = 0°$ orbital is the excited state in the presence of a tetragonal compression along the z axis, while $\vartheta = \pm 2\pi/3$ are excited states for a tetragonal compression along x or y. This three-fold degeneracy (rotation by $\pm 2\pi/3$) is due to cubic symmetry.*

By summing up the contributions from all C ions for each mode, we obtain

$$\Delta\varepsilon_{\rm JT}(q_1,q_2) = \lambda\begin{pmatrix} q_2 & q_1 \\ q_1 & -q_2 \end{pmatrix} = \lambda\Big(q_1\hat{\tau}_x + q_2\hat{\tau}_z\Big),$$

where $\lambda \sim -\frac{\sqrt{3}}{2}\tilde{V}'_{dd\sigma} > 0$. This is the same form of potential that we have obtained for the ionic contribution. Again, if $q_1 = 0$ and $q_2 < 0$ (tetragonal compression) $3z^2{-}r^2$ is higher in energy. In conclusion, if we neglect the kinetic energy of the nuclei (limit $M_\alpha/m_e \to \infty$), the ground state of the system can be calculated by minimizing a potential energy of the form

$$\hat{U}(q_1,q_2) = \hat{U}^{\rm JT} + \hat{U}^{\rm PH}_n = \lambda\begin{pmatrix} q_2 & q_1 \\ q_1 & -q_2 \end{pmatrix} + \frac{1}{2}C_E\left(q_1^2+q_2^2\right)\hat{I}, \tag{22}$$

where $\hat{I}$ is the $2{\times}2$ identity matrix. To find the minimum of (22), it is convenient to introduce polar coordinates, which we define as $q_2 = -q\cos\vartheta, q_1 = -q\sin\vartheta$, so that for $0 < \vartheta < \pi/2$ we have $q_1 \leq 0$ (compression of $\hat{x}$ axis) and $q_2 \leq 0$ (compression of $\hat{z}$ axis); this corresponds to the distortion of the octahedron labeled with number 1 in Fig. 1. In these coordinates

$$\hat{U}^{\text{JT}} = -\lambda q \begin{pmatrix} \cos\vartheta & \sin\vartheta \\ \sin\vartheta & -\cos\vartheta \end{pmatrix}.$$

The diagonalization of matrix (22) yields two eigenvalues; the lower energy branch

$$E_-(q) = -\lambda q + \frac{C_E}{2} q^2$$

takes the form of a mexican hat, shown in Fig. 10. The minimum of $E_-(q)$ is obtained for $q = q_0 = \lambda/C$ and has value

$$E_{\text{JT}} = -\lambda^2/2C_E;$$

the quantity E_{JT} is defined as the Jahn-Teller energy of the system. The electronic ground state can be written as

$$|\vartheta\rangle_G = -\sin\frac{\vartheta-\pi}{2}|x^2-y^2\rangle + \cos\frac{\vartheta-\pi}{2}|3z^2-r^2\rangle.$$

The excited state (hole orbital), with energy

$$E_+(q) = \lambda q + \frac{C_E}{2} q^2,$$

is then given by

$$|\vartheta\rangle_E = -\sin\frac{\vartheta}{2}\,|x^2-y^2\rangle + \cos\frac{\vartheta}{2}\,|3z^2-r^2\rangle.$$

The states $|\vartheta\rangle_E$ with different ϑ are shown in Fig. 11. In the simple model discussed so far, all states $|\vartheta\rangle_G$ have the same Jahn-Teller energy. Cubic symmetry, however, only requires states

$$|\vartheta\rangle,\ |\vartheta{+}2\pi/3\rangle,\ |\vartheta{-}2\pi/3\rangle$$

to be degenerate. The additional (accidental) degeneracy is removed when we take into account anharmonic terms, the lowest order of which has the form

$$U^{\text{anh}}(q_1, q_2) = A\big(q_2^3 - 3q_2q_1^2\big) = Aq^3\big(\cos^3\vartheta - 3\cos\vartheta\sin^2\vartheta\big) = -Aq^3\cos 3\vartheta$$

and yields the tetragonal distortion as a ground state, with $\vartheta = 0,\ \pm 2\pi/3$ for positive A and with $\vartheta = \pi,\ \pi{\pm}2\pi/3$ for negative A. Higher-order terms can make the $\boldsymbol{Q}_1$ Jahn-Teller distortion ($\vartheta = \pi/2, \pi/2 \pm 2\pi/3$) more stable [1]. For a periodic lattice, mode $\boldsymbol{Q}_1$ leads to a co-operative distortion where long and short bonds alternate in the x and y direction; in such a case, the hole orbital rotates by $\pi/2$ if we move from a Cu site to its Cu first-nearest neighbors in the $\boldsymbol{ab}$ plane. Let us now analyze the different electronic configurations that can occur in perovskites. For the electronic configuration $3d^1{=}3t_{2g}^1$, the procedure is as the one illustrated above, except that t_{2g} states are 3-fold degenerate and form π bonds, which are weaker, therefore the splitting introduced by the Jahn-Teller effect is smaller than for e_g states. In the case of electronic configurations $3d^n$ with $n > 1$, to determine if the ion is Jahn-Teller active, one has to consider the degeneracies of the many-body state, including Coulomb repulsion. Weak Jahn-Teller states are $3d^1$ (Ti^{3+} in $LaTiO_3$) and $3d^2$ (V^{3+} in $LaVO_3$), as also $3t_{2g}^4$, $3t_{2g}^5$, $3t_{2g}^4e_g^2$, $3t_{2g}^5e_g^2$; strong Jahn-Teller configurations are, e.g., $3d^9$ (Cu^{2+} in $KCuF_3$) and $3t_{2g}^3e_g^1$ (Mn^{3+} in $LaMnO_3$); the configurations $3t_{2g}^3$ and $3t_{2g}^3e_g^2$ are not degenerate and therefore usually not Jahn-Teller active.

5 Kugel-Khomskii superexchange

Let us now start from a totally different perspective, from the Hubbard model for a cubic perovskite with partially filled e_g or t_{2g} shell. The Hamiltonian takes the form $\hat{H} = \hat{H}_0 + \hat{H}_T + \hat{H}_U$ where

$$\begin{aligned}
\hat{H}_0 &= \varepsilon_d \sum_i \sum_\sigma \sum_m \hat{n}_{im\sigma} \\
\hat{H}_T &= -\sum_{i \neq i'} \sum_\sigma \sum_{mm'} t^{i,i'}_{mm'}\, c^\dagger_{im\sigma} c_{im'\sigma} \\
\hat{H}_U &= U \sum_i \sum_m \hat{n}_{im\uparrow} \hat{n}_{im\downarrow} + \frac{1}{2} \sum_i \sum_{\sigma\sigma'} \sum_{m \neq m'} \left(U - 2J - J\delta_{\sigma,\sigma'}\right) \hat{n}_{im\sigma} \hat{n}_{im'\sigma'} \\
&\quad - J \sum_i \sum_{m \neq m'} \left(c^\dagger_{im\uparrow} c^\dagger_{im\downarrow} c_{im'\uparrow} c_{im'\downarrow} + c^\dagger_{im\uparrow} c_{im\downarrow} c^\dagger_{im'\downarrow} c_{im'\uparrow} \right),
\end{aligned}$$

and where m labels either the e_g or the t_{2g} orbitals. Kugel and Khomskii have shown that, in the large t/U limit, this Hamiltonian can be mapped onto an effective generalized superexchange Hamiltonian with an orbitally-ordered ground state. The actual general super-exchange Hamiltonian can be found in Ref. [14], for all possible e_g^n and t_{2g}^n configurations.

Here, to understand the origin of the orbital super-exchange interaction, let us simplify the problem and consider first a system with only two atoms ($i = A, B$) and two orbitals ($\varepsilon_d = \varepsilon_{e_g}$), and for which the hopping matrix is diagonal in the orbitals

$$\hat{H}_T = -t \sum_\sigma \sum_m \left(c^\dagger_{Am} c_{Bm} + c^\dagger_{Bm} c_{Am} \right).$$

Furthermore, let us simplify the Coulomb interaction and neglect the spin-flip and pair-hopping terms, so that

$$\hat{H}_U \longrightarrow \hat{H}'_U = U \sum_{i=AB} \sum_m \hat{n}_{im\uparrow} \hat{n}_{im\downarrow} + \frac{1}{2} \sum_{i=AB} \sum_{\sigma\sigma'} \sum_{m \neq m'} \left(U - 2J - J\delta_{\sigma,\sigma'}\right) \hat{n}_{im\sigma} \hat{n}_{im'\sigma'}.$$

Finally, we assume that the systems has one electron per atom (quarter filling, e_g^1 configuration). In the $t = 0$ or atomic limit there are two types of possible states for this system, those in which each atom is occupied by one electron, $|1,1\rangle_\alpha$, and those in which one atom has two electrons and the other zero, $|2,0\rangle_{\alpha'}$. The 16 states of type $|1,1\rangle_\alpha$, all degenerate with energy $E_\alpha(1,1) = 2\varepsilon_{e_g}$, can be written as $c^\dagger_{Am_A\sigma_A} c^\dagger_{Bm_B\sigma_B} |0\rangle$ with $\alpha = (m_A\sigma_A, m_B\sigma_B)$; here $m_i\sigma_i$ are the quantum numbers for the electron at site $i = A, B$. There are 12 states $|2,0\rangle_\alpha$ with one atom occupied by two electrons; they are listed below together with their energies

$\|2,0\rangle_{\alpha'}$	$E_{\alpha'}(2,0)$	
$\|2,0\rangle_{i1m} = c^\dagger_{im\uparrow} c^\dagger_{im\,\downarrow} \|0\rangle$	$2\varepsilon_{e_g} + U$	
$\|2,0\rangle_{i2m} = c^\dagger_{im\uparrow} c^\dagger_{im'\downarrow} \|0\rangle$	$2\varepsilon_{e_g} + U - 2J$	$m' \neq m$
$\|2,0\rangle_{i3\sigma} = c^\dagger_{im\sigma} c^\dagger_{im'\sigma} \|0\rangle$	$2\varepsilon_{e_g} + U - 3J$	$m' \neq m$

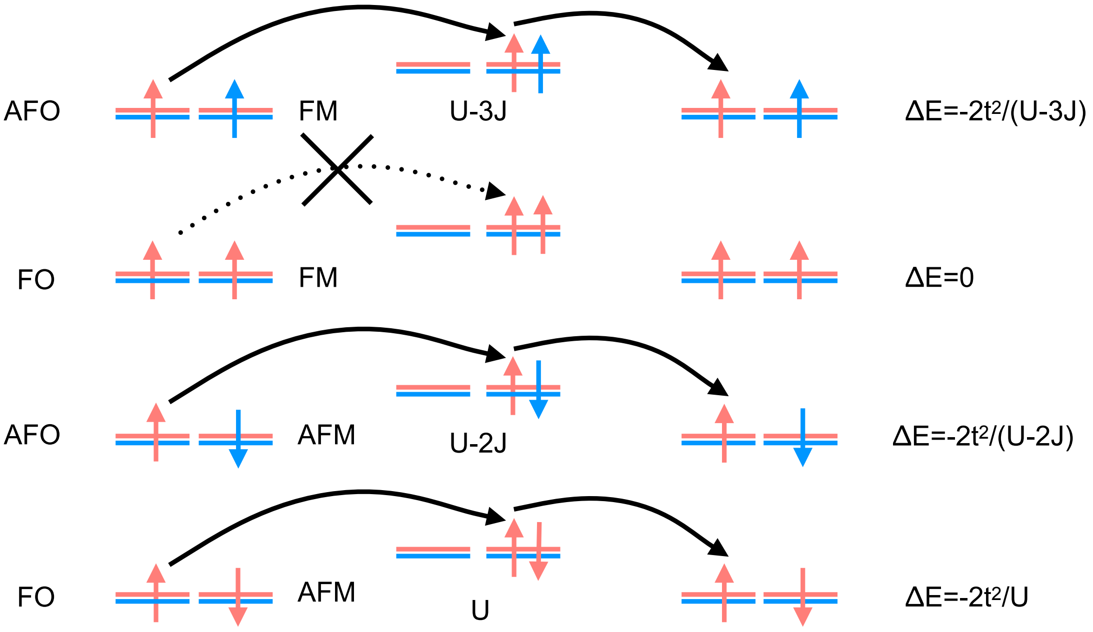

Fig. 12: *Superexchange energy gain for possible quarter-filling ground states of a two-site 2-fold degenerate Hubbard model with orbital- and spin-diagonal hopping matrices.*

The Coulomb repulsion U is positive and J is small with respect to U; therefore the $|1,1\rangle_\alpha$ states define the ground-state manifold. If t is finite but small ($t/U \ll 1$), we can treat $\hat{H}_T$ as a perturbation, and calculate the second-order correction to the energy of states $|1,1\rangle_\alpha$. This correction is always negative (energy gain) and it is given by the matrix

$$\Delta E_{\alpha_1,\alpha_2}(1,1) = -\sum_{\alpha'} {}_{\alpha_1}\langle 1,1|\hat{H}_T|2,0\rangle_{\alpha'} \frac{1}{E_{\alpha'}(2,0) - E_\alpha(1,1)} {}_{\alpha'}\langle 2,0|\hat{H}_T|1,1\rangle_{\alpha_2}$$

There are four interesting cases, depicted in Fig. 12. The first is the ferro-magnetic (same spin) and antiferro-orbital (different orbitals) state, first line of the figure. The corresponding second order energy gain ($\alpha_1 = \alpha_2 = m\sigma, m'\sigma$) is

$$\Delta E_{\alpha_1,\alpha_1}(1,1) = -\frac{2t^2}{U-3J}.$$

For the ferro-magnetic (same spin) and ferro-orbital (same orbital) state (second line in the figure, $\alpha_1 = \alpha_2 = m\sigma, m\sigma$) the energy gain is, instead, zero

$$\Delta E_{\alpha_1,\alpha_1}(1,1) = 0.$$

The reason is that no hopping is possible due to the Pauli principle. For the antiferro-magnetic antiferro-orbital state (third line, $\alpha_1 = \alpha_2 = m\sigma, m' - \sigma$), we have

$$\Delta E_{\alpha_1,\alpha_1}(1,1) = -\frac{2t^2}{U-2J},$$

and finally for the antiferro-magnetic ferro-orbital state ($\alpha_1 = \alpha_2 = m\sigma, m-\sigma$) we find

$$\varDelta E_{\alpha_1,\alpha_1}(1,1) = -\frac{2t^2}{U}.$$

Among these four states, the ferro-magnetic antiferro-orbital state is thus the lowest in energy. The main message is that the system gains superexchange energy by occupying preferentially different orbitals with the same spin, although the orbitals are by themselves degenerate. The $16{\times}16$ matrix of the second-order energy corrections $\varDelta E_{\alpha_1,\alpha_2}(1,1)$ can be rewritten as the effective superexchange Hamiltonian

$$\begin{aligned}\hat{H}_{\rm SE} =& 2\varGamma_{-+}\left[\boldsymbol{S}^A\cdot\boldsymbol{S}^B-\frac{1}{4}\right]\left[O_z^A\,O_z^B+\frac{1}{4}\right]+2\varGamma_{+-}\left[\frac{1}{4}+S_z^A\,S_z^B\right]\left[\boldsymbol{O}^A\cdot\boldsymbol{O}^B-\frac{1}{4}\right]\\ &+2\varGamma_{--}\left[\left(\boldsymbol{S}^A\cdot\boldsymbol{S}^B-S_z^A\,S_z^B\right)\left(\boldsymbol{O}^A\cdot\boldsymbol{O}^B-O_z^A\,O_z^B\right)-\left(S_z^A\,S_z^B-\frac{1}{4}\right)\left(O_z^A\,O_z^B-\frac{1}{4}\right)\right]\end{aligned}$$

where $\mathbf{O}_i = \boldsymbol{\tau}_i/2$ are operators acting only on orbital degrees of freedom, $\boldsymbol{\tau}$ are the pseudo-spin operators introduced in the previous section, Eq. (21), and

$$\varGamma_{-+} = \frac{4t^2}{U} \qquad \varGamma_{+-} = \frac{4t^2}{U-3J} \qquad \varGamma_{--} = -\frac{4t^2}{U-2J}\,.$$

When the second-order Hamiltonian is written in this form it is immediately clear that, among the four states we considered, the ferro-magnetic antiferro-orbital state is the lowest in energy. This happens because the superexchange coupling $\varGamma_{+-}$ is the largest. If the orbital degeneracy is one, we can replace the terms $\boldsymbol{O}^A\cdot\boldsymbol{O}^B$ and $O_z^A\,O_z^B$ with the ferro-orbital value 1/4; then, the terms proportional to $\varGamma_{+-}$ and $\varGamma_{--}$ drop out and we recover the Heisenberg superexchange Hamiltonian, as expected for the one-band Hubbard model.

What about $\mathrm{KCuF_3}$ and $\mathrm{LaMnO_3}$? If we consider only hopping integrals between neighboring B sites in the cubic perovskite structure, the hopping integral matrices take the simple form

$$t_{mm'}^{i,i\pm\hat{z}} = t_\varepsilon\begin{pmatrix}0 & 0\\ 0 & 1\end{pmatrix} \quad t_{mm'}^{i,i\pm\hat{x}} = \frac{t_\varepsilon}{4}\begin{pmatrix}3 & \sqrt{3}\\ \sqrt{3} & 1\end{pmatrix} \quad t_{mm'}^{i,i\pm\hat{y}} = \frac{t_\varepsilon}{4}\begin{pmatrix}3 & -\sqrt{3}\\ -\sqrt{3} & 1\end{pmatrix}. \qquad (23)$$

The structure of these matrices can be obtained by using Slater-Koster two-center integrals. The only non-zero hopping integral in the $\hat{z}$ direction is the one between $|3z^2{-}r^2\rangle$ states. As we have previously seen by using the downfolding approach, it is given by $t_\varepsilon = V_{pd\sigma}^2/(\varepsilon{-}\varepsilon_p)$. As in the case of the two-site molecule, for integer filling (n electrons per atom) and in the large t_ε/U limit the lattice Hubbard model can be mapped onto an effective superexchange Hamiltonian by downfolding high-energy states in which some of the atoms have an electron number larger than n. Only two electronic configurations are relevant for orbital ordering, e_g^1 ($\mathrm{LaMnO_3}$) and e_g^3 ($\mathrm{KCuF_3}$). The remaining partially filled state, e_g^2, is magnetic with $S=1$ but, due to Hund's rule coupling J, it exhibits no orbital degeneracy ($L=0$). After excluding e_g^2 we can, for simplicity, set $J=0$. Let us now construct all atomic states $|N_e\rangle_\alpha$ with N_e electrons.

For a single atom they are

$\|N_e\rangle_\alpha$	$E_{\alpha'}(N_e)$	$d(N_e)$
$\|0\rangle$	$E(0) = \ 0$	$d(0) = 1$
$\|1\rangle = c^\dagger_{m\sigma}\|0\rangle$	$E(1) = \ \varepsilon_{e_g}$	$d(0) = 4$
$\|2\rangle = c^\dagger_{m\sigma}c^\dagger_{m'\sigma'}\|0\rangle$	$E(2) = 2\varepsilon_{e_g} + \ U$	$d(0) = 6$
$\|3\rangle = c^\dagger_{m\sigma}c^\dagger_{m'\uparrow}c^\dagger_{m'\downarrow}\|0\rangle$	$E(3) = 3\varepsilon_{e_g} + 3U$	$d(0) = 4$
$\|4\rangle = c^\dagger_{m\uparrow}c^\dagger_{m\downarrow}c^\dagger_{m'\uparrow}c^\dagger_{m'\downarrow}\|0\rangle$	$E(4) = 4\varepsilon_{e_g} + 6U$	$d(0) = 1$

The total (spin and orbital) degeneracy of the n-electron sector, $d(N_e)$, is given in the third column. Let us consider two neighboring sites i and i' and their states $|N_e\rangle^i_\alpha$ and $|N'_e\rangle^{i'}_{\alpha'}$, where α and α' run over all degenerate states in the N_e-electron sector. We define the collective state of such a two-site system as $|N_e\rangle^i_\alpha|N'_e\rangle^{i'}_{\alpha'}$. Let us start from an e_g^1 configuration. In the large-U limit, at quarter filling (n=1) the ground state will be within the N_e=N'_e=1 manifold, $|\mathrm{G}\rangle$=$\big\{|1\rangle^i_\alpha|1\rangle^{i'}_{\alpha'}\big\}$. The latter has a degeneracy 4^N, where N is the number of sites, here N=2; this degeneracy can be partially lifted via virtual excitations to the doubly occupied states $|\mathrm{E}\rangle$=$\big\{|2\rangle^i_\alpha|0\rangle^{i'}\big\}$, $\big\{|0\rangle^i|2\rangle^{i'}_{\alpha'}\big\}$, which in turn generate an effective low-energy Hamiltonian $\hat{H}_{\mathrm{SE}}$. We can again calculate $\hat{H}_{\mathrm{SE}}$ by treating $\hat{H}_T$ as a perturbation.

Let us consider at first only pairs of sites along the $\hat{z}$ axis. In second-order perturbation theory in $\hat{H}_T$, we obtain for the lattice the following effective Hamiltonian

$$\begin{aligned}
\hat{H}^{\hat{z}}_{\mathrm{SE}} &\sim -\frac{1}{U}\sum_E \hat{H}_T|E\rangle\langle E|\hat{H}^\dagger_T \\
&= -\frac{t^2}{U}\frac{1}{2}\sum_{ii'}\sum_{\sigma\sigma'}\sum_{\alpha}\Big\{c^\dagger_{i\tau\sigma}|0\rangle^{i\,i}\langle 0|c_{i\tau\sigma'}\left(c_{i'\tau\sigma}|2\rangle^{i'\,i'}_{\alpha\,\alpha}\langle 2|c^\dagger_{i'\tau\sigma'}\right) + (i \longleftrightarrow i')\Big\}\,\delta_{\tau,\searrow} \\
&= -\frac{2t^2}{U}\frac{1}{2}\sum_{ii'}\sum_{\sigma\sigma'}\Big\{(-1)^{-\sigma'-\sigma}P^i_{\tau\sigma-\sigma'}P^{i'}_{\tau\sigma'-\sigma} + \frac{1}{2}\left(P^i_{\tau\sigma\sigma}P^{i'}_{-\tau\sigma'\sigma'} + P^i_{-\tau\sigma\sigma}P^{i'}_{\tau\sigma'\sigma'}\right)\Big\}\,\delta_{\tau,\searrow},
\end{aligned}$$

where we already replaced in the denominator $\Delta E = E(2) + E(0) - 2E(1)$ with its value, U, and where, once more, $|\searrow\rangle = |3z^2{-}r^2\rangle$, $|\nearrow\rangle = |x^2{-}y^2\rangle$. In Hamiltonian $\hat{H}^{\hat{z}}_{\mathrm{SE}}$ we introduced the operators $P^i_{\tau\sigma\sigma'}$, which are given by

$$P^i_{\tau\sigma\sigma'} = c^\dagger_{i\tau\sigma}|0\rangle\langle 0|c_{i\tau\sigma'} = \hat{o}^z_{\tau\tau}\ \left(\hat{s}^z_{\sigma\sigma'} + \hat{s}^+_{\sigma\sigma'} + \hat{s}^-_{\sigma\sigma'}\right).$$

In this expression on the right-hand side we rewrote $P^i_{\tau\sigma\sigma'}$ as product of an orbital and a spin term, defined as follows:

$$\begin{aligned}
\hat{o}^z_{\tau\tau'} &= \left(\frac{n_i}{2}\,\hat{I} + (-1)^\tau O^i_z\right)\delta_{\tau\tau'} & \hat{s}^z_{\sigma\sigma} &= \left(\frac{n_i}{2}\,\hat{I} + (-1)^\sigma S^i_z\right)\delta_{\sigma\sigma'} \\
\hat{o}^+_{\tau\tau'} &= O^i_+(1-\delta_{\tau\tau'}) & \hat{s}^+_{\sigma\sigma'} &= S^i_+(1-\delta_{\sigma\sigma'}) \\
\hat{o}^-_{\tau\tau'} &= O^i_-(1-\delta_{\tau\tau'}) & \hat{s}^-_{\sigma\sigma'} &= S^i_-(1-\delta_{\sigma\sigma'})\,,
\end{aligned}$$

where $(-1)^\sigma = +1$ for spin (pseudospin) up and -1 otherwise; the operator $\hat{I}$ is the identity matrix. Hence, we can express the effective Hamiltonian as

$$\hat{H}^{\hat{z}}_{\rm SE} = \frac{\varGamma}{2}\sum_{ii'}\left[\boldsymbol{S}^i\cdot\boldsymbol{S}^{i'} - \frac{n_i n_{i'}}{4}\right]\left[O^i_z - \frac{n_i}{2}\right]\left[O^{i'}_z - \frac{n_{i'}}{2}\right] + \frac{1}{2}\left[O^i_z O^{i'}_z - \frac{n_i n_{i'}}{4}\right],$$

where $\varGamma = 4t^2/U > 0$. If we drop all processes involving orbital $|\nearrow\rangle$ we recover the usual superexchange Heisenberg Hamiltonian for the one-band Hubbard model

$$\hat{H}^{\hat{z}}_{\rm SE} = \frac{\varGamma}{2}\sum_{ii'}\left[\boldsymbol{S}^i\cdot\boldsymbol{S}^{i'} - \frac{n_i n_{i'}}{4}\right].$$

Let us now consider two neighboring sites and the energy of some possible states $|\mathrm{G}\rangle = \left\{|1\rangle^i_\alpha |1\rangle^{i'}_{\alpha'}\right\}$. A ferro-magnetic spin configuration has energy

$$\varDelta E_{\tau\uparrow,\tau'\uparrow} = -\frac{\varGamma}{4}\big(1-\delta_{\tau,\tau'}\big),$$

hence, there is an energy gain if the electrons occupy different orbitals, i.e., if the systems has antiferro-orbital arrangement. Let us consider now a antiferro-magnetic spin arrangement. The corresponding energy is

$$\varDelta E_{\tau\uparrow,\tau'\downarrow} = -\frac{\varGamma}{2}\delta_{\tau,\tau'}\delta_{\tau,\searrow} - \frac{\varGamma}{4}(1-\delta_{\tau,\tau'}).$$

The expression above shows that in the antiferro-magnetic case the system gains more energy if the occupied state is $|\searrow\rangle$ at both sites. Up to now we considered magnetically ordered states. In LaMnO$_3$ and KCuF$_3$, however, orbital order takes place well above the magnetic transition. Let us then assume that the system is orbitally ordered but paramagnetic, with occupied state

$$|\vartheta\rangle_i = -\sin\frac{\vartheta-\pi}{2}\,|x^2-y^2\rangle + \cos\frac{\vartheta-\pi}{2}\,|3z^2-r^2\rangle$$

at site i and $|\vartheta\rangle_{i\pm\hat{z}} = |\vartheta\rangle_i$ at the neighboring site $i' = i \pm \hat{z}$. This choice corresponds to ferro-orbital order along $\hat{z}$, the type of stacking realized in LaMnO$_3$ (see Fig. 13). What is the value of ϑ than minimizes the energy? We can calculate it using the variational method. The superexchange energy gain with respect to a paramagnetic paraorbital state is given by

$$\varDelta E(\vartheta) = \frac{\varGamma}{16}\bigg(\cos^2(\vartheta-\pi) + 2\cos(\vartheta-\pi)\bigg).$$

This function is minimized for $\vartheta = 0$, an angle corresponding to a tetragonal compression. To determine the optimal angle for the three-dimensional system we have in addition to take into account the effective Hamiltonian stemming from virtual hoppings in the remaining directions. Due to cubic symmetry, if we rotate the quantization axis, the superexchange Hamiltonian has the same form in all cubic directions; to sum up all terms we have merely to rotate back the quantization axis to $\hat{z}$. Hence, we have to make the replacements

$$O^i_z \underbrace{\rightarrow}_{\hat{z}\to\hat{x}} -\frac{1}{2}O^i_z - \frac{\sqrt{3}}{2}O^i_x$$

$$O^i_z \underbrace{\rightarrow}_{\hat{z}\to\hat{y}} -\frac{1}{2}O^i_z + \frac{\sqrt{3}}{2}O^i_x$$

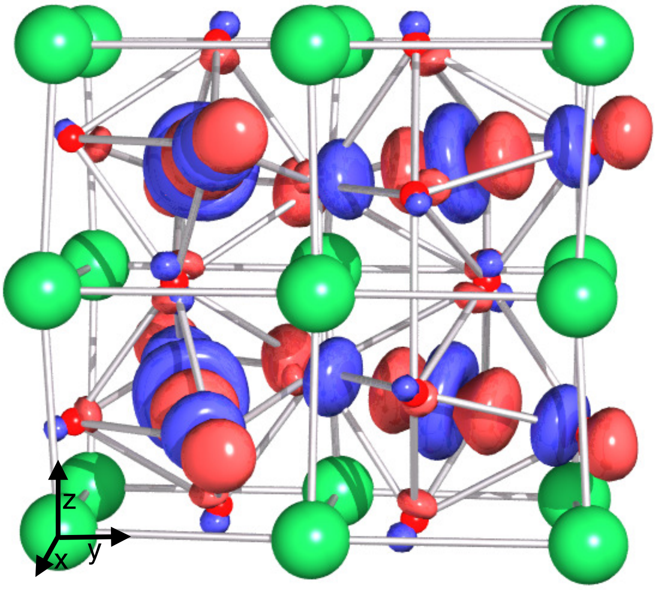

Fig. 13: *Orbital order (LDA+DMFT calculations) in the rare-earth perovskite TbMnO*$_3$ *with the GdFeO*$_3$*-type structure. From Ref. [6]. This system has the same structure of LaMnO*$_3$.

Let us assume antiferro-orbital order in the plane, again as in the case of LaMnO$_3$, shown in Fig. 13. This means that, for $i' = i \pm \hat{x}$ or $i' = i \pm \hat{y}$, the occupied state is

$$|\vartheta\rangle_{i'} = + \sin\frac{\vartheta-\pi}{2}\,|x^2-y^2\rangle + \cos\frac{\vartheta-\pi}{2}\,|3z^2-r^2\rangle.$$

We can easily verify that $|\vartheta\rangle_{i'}{=}|-\vartheta+2\pi\rangle_i$. This is state $|\vartheta\rangle_i$ rotated by $\pi/2$ ($x \to y$, $y \to -x$). The total superexchange energy gain with respect to a paramagnetic paraorbital state is then given by[11]

$$\varDelta E(\vartheta) = \frac{\varGamma}{16}\left(3\cos^2(\vartheta-\pi)-\frac{3}{2}\right).$$

This expression has a minimum for $\vartheta = \pi/2$ (Jahn-Teller-like $\boldsymbol{Q}_1$ distortion). For the e_g^3 configuration (KCuF$_3$), due to particle-hole symmetry, we obtain the same result. This can be verified by observing, first of all, that the e_g bands obtained from the hopping-integrals matrices (23), the bands which we have discussed in detail in Sec. 3, are symmetric with respect to the Fermi level for half filling. In addition, the energy difference entering in the denominator of the superexchange Hamiltonian for an e_g^3 ground state, $\varDelta E = E(4) + E(2) - 2E(3)$, has the same value ($\varDelta E = U$) as in the case of an e_g^1 ground state. The main difference between LaMnO$_3$ (e_g^1) and KCuF$_3$ (e_g^3), for what concerns the results presented in this section, is that the stacking along $\hat{z}$, ferro-orbital for LaMnO$_3$, can be either antiferro- or ferro-orbital for KCuF$_3$; Fig. 1 shows the case of antiferro-orbital arrangement. Remarkably, the variational energy gain $\varDelta E(\vartheta)$ is the same for both types of stacking along $\hat{z}$, i.e., for $|\vartheta\rangle_{i\pm\hat{z}} = |\vartheta\rangle_i$ and for $|\vartheta\rangle_{i\pm\hat{z}} = |-\vartheta+2\pi\rangle_i$. The conclusions of this section are thus identical for LaMnO$_3$ and KCuF$_3$.

---

[11] For the application of this approach to the general super-exchange Hamiltonian see Ref. [14].

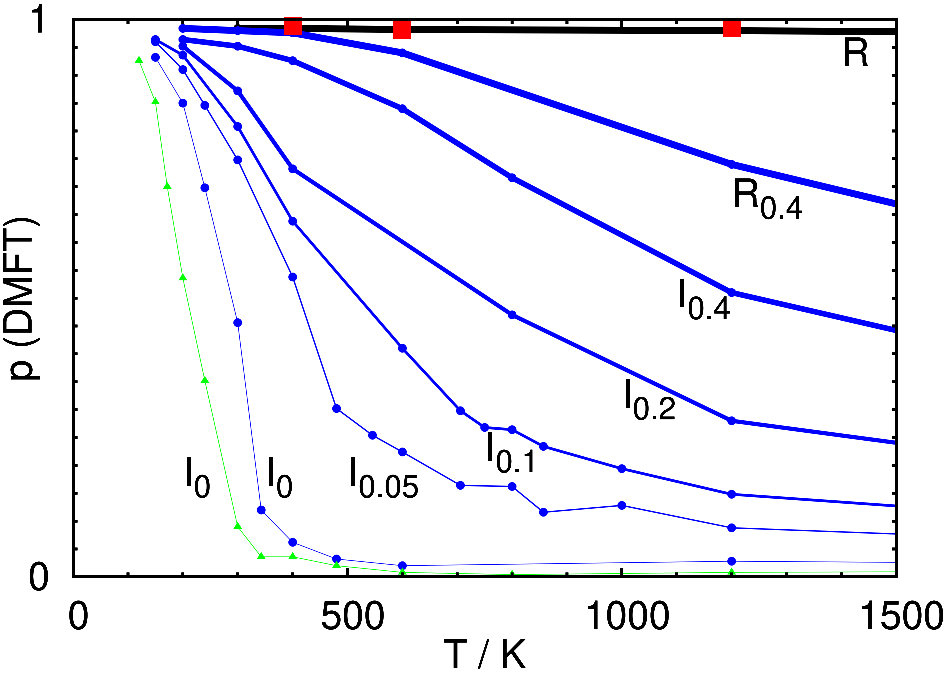

Fig. 14: *Orbital order transition in KCuF*$_3$*. Orbital polarization* p *as a function of temperature calculated in LDA+DMFT. R: experimental structure. Circles: idealized structures* R_δ *and* I_δ *with decreasing crystal-field and* U=7 *eV. Green/Triangles:* U= 9 *eV,* I_0 *only. Red/Squares: two-sites CDMFT. From Ref. [3].*

6 The origin of orbital ordering in materials

As we discussed in the introduction, the hallmark of orbital order is the co-operative Jahn-Teller distortion. This static distortion gives rise to a crystal field, which splits the otherwise degenerate e_g doublet or t_{2g} triplet. Due to Coulomb repulsion, it turns out that even a crystal-field splitting much smaller than the band width can lead to orbital ordering. The importance of this effect for real materials has been realized first for LaTiO$_3$ and YTiO$_3$ [4]. This reduction of orbital fluctuation is dynamical, but it can be already understood from the static Hartree-Fock contribution to the self-energy; the latter yields an effective enhancement of the crystal-field proportional to orbital polarization p. For an e_g system p is defined as the difference in occupation between the most and the least occupied orbital, $|1\rangle$ and $|2\rangle$, the so-called natural orbitals. Thus $p{=}n_1{-}n_2$, and the Hartree-Fock self-energy correction to the crystal-field splitting is

$$\Delta\varepsilon_{\rm CF} = \Sigma_2(\omega_n{\to}\infty) - \Sigma_1(\omega_n{\to}\infty) \sim \frac{1}{2}(U{-}5J)p\,.$$

If $p > 0$, as it happens in the presence of a crystal-field $\varepsilon_{\rm CF}{=}\varepsilon_2{-}\varepsilon_1{>}0$, this term effectively increases the crystal-field splitting. This effect is at work not only in LaTiO$_3$ and YTiO$_3$, but also in several other systems with different electronic structure and even smaller crystal-field splittings. The case of $3d^9$ KCuF$_3$ and $3d^4$ LaMnO$_3$ is extreme: the e_g crystal-field splitting is $\sim 0.5{-}1$ eV; with such a large splitting, orbital fluctuations are suppressed up to the melting temperature. Thus, Coulomb repulsion makes the Jahn-Teller mechanism discussed in the article of Kanamori very efficient. This result, however, does not clarify which of the two mech-

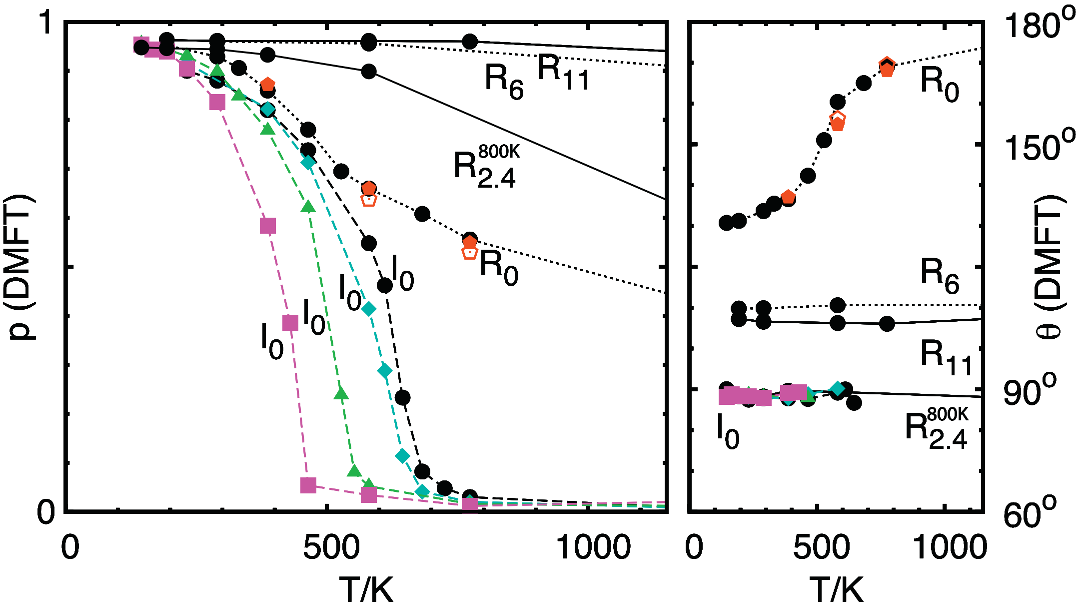

Fig. 15: *Orbital-ordering transition in LaMnO*$_3$*. Orbital polarization* p *(left) and (right) occupied state* $|\vartheta\rangle = \cos\frac{\vartheta}{2}|3z^2-r^2\rangle + \sin\frac{\vartheta}{2}|x^2-y^2\rangle$ *as a function of temperature. Solid lines: 300 K experimental structure (*R_{11}*) and 800 K experimental structure. Dots: orthorhombic structures with half (*R_6*) or no (*R_0*) Jahn-Teller distortion. Pentagons: 2 (full) and 4 (empty) site CDMFT. Dashes: ideal cubic structure (*I_0*). Circles:* $U = 5$ *eV. Diamonds:* $U{=}5.5$ *eV. Triangles:* $U = 6$ *eV. Squares:* $U{=}7$ *eV. Crystal field splittings (meV): 840 (*R_{11}*), 495 (*R_6*), 168 (*$R_{2.4}^{800\ K}$*), and 0 (*I_0*). From Ref. [6].*

anisms, Kugel-Khomskii superexchange or conventional electron-phonon coupling, plays the major role in causing orbital order and stabilizing the distortion. Remarkably, in fact, Coulomb repulsion has also an important effect on structure stabilization. LDA+U total energy calculations have early on shown that the co-operative Jahn-Teller distortion is stabilized by U [15,16], a result confirmed recently by LDA+DMFT [17]. This could be—and initially was—taken as an indication that superexchange is the driving mechanism. If this is the case, it is, however, hard to explain why the magnetic transition temperature ($T_N{\sim}40$ K for KCuF$_3$ and $T_N{\sim}140$ K for LaMnO$_3$), also determined by superexchange, is relatively low while the co-operative Jahn-Teller distortion persists up to the melting temperature. On the other hand, if Kugel-Khomskii superexchange is not the driving mechanism, the associated energy gain should be small with respect to the total energy gain due to the Jahn-Teller distortion.

To clarify the nature of the dominant mechanism, we disentangled electron-phonon and superexchange effects. To this end we performed LDA+DMFT (single-site and cluster) calculations for a series of hypothetical structures, in which the distortions (and thus the crystal-field splitting) are progressively reduced. In the case of KCuF$_3$, these hypothetical structures are shown in Fig. 1, and the corresponding e_g bands are shown in Fig. 7. For each structure we calculate the order parameter, the orbital polarization p. In Fig. 14 we show p as a function of temperature. For the experimental structure (R in the figure), we find that $p{\sim}1$ up to the melting temperature. The empty orbitals on different sites make the pattern shown in Fig. 1.

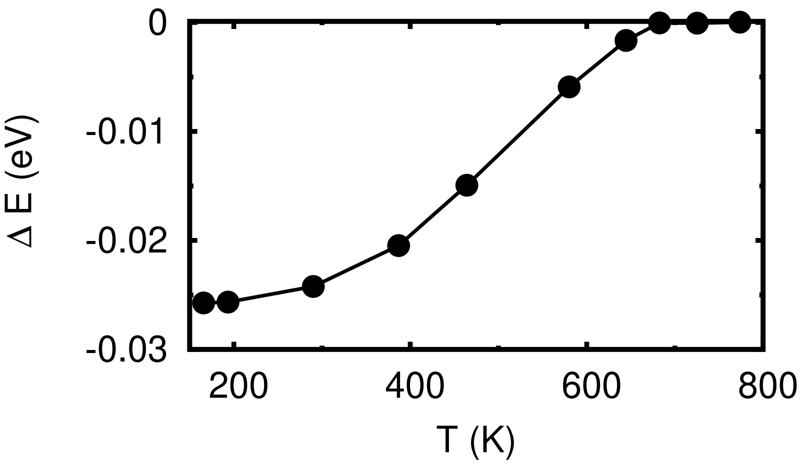

Fig. 16: *Superexchange energy gain for LaMnO*$_3$, $\Delta E \sim -T_{KK}/2$. *From Ref. [6].*

For the ideal cubic structure I_0, we find that $p{=}0$ at high temperature, but a transition occurs at $T_{\rm KK} \sim 350$ K. This $T_{\rm KK}$ is the critical temperature in the absence of electron-phonon coupling, i.e., the superexchange critical temperature. Our results show that around 350 K superexchange alone could indeed drive the co-operative Jahn-Teller distortion; it cannot, however, explain the presence of a co-operative Jahn-Teller distortion above 350 K. We performed a similar study for LaMnO$_3$. For this $t_{2g}^3 e_g^1$ system we have to take into account the Hund's rule coupling between e_g electrons and t_{2g} spins, $\boldsymbol{S}_{t_{2g}}$. Thus the minimal model to understand orbital order is the modified Hubbard model [18]

$$\begin{aligned} H = &-\sum_{ii'}\sum_{\sigma\sigma'}\sum_{mm'} t^{i,i'}_{m,m'}\, u^{i,i'}_{\sigma,\sigma'}\, c^\dagger_{im\sigma} c_{i'm'\sigma'} - h\sum_{im}(\hat{n}_{im\uparrow} - \hat{n}_{im\downarrow}) \\ &+U\sum_{im}\hat{n}_{im\uparrow}\hat{n}_{im\downarrow} + \frac{1}{2}\sum_{i}\sum_{\sigma\sigma'}\sum_{m(\neq m')}\left(U{-}2J{-}J\delta_{\sigma,\sigma'}\right)\hat{n}_{im\sigma}\hat{n}_{im'\sigma'}, \\ &-J\sum_{i}\sum_{m\neq m'}\left(c^\dagger_{im\uparrow}c^\dagger_{im\downarrow}c_{im'\uparrow}c_{im'\downarrow} + c^\dagger_{im\uparrow}c_{im\downarrow}c^\dagger_{im'\downarrow}c_{im'\uparrow}\right). \end{aligned}$$

Here the local magnetic field $h{=}JS_{t_{2g}}$ describes the Hund's rule coupling to t_{2g} electrons, and $u_{i\sigma,i'\sigma'}{=}2/3(1{-}\delta_{i,i'})$ accounts for the disorder in orientation of the t_{2g} spins. By performing the same type of analysis as for KCuF$_3$, we find the impressively large $T_{\rm KK}{\sim}700$ K (Fig. 15). There is a small point neglected so far; besides the co-operative Jahn-Teller distortion and tetragonal compression, LaMnO$_3$ exhibits a GdFeO$_3$-type distortion (Fig. 13), which tends to reduce the e_g band width [4]. To account for this we studied the orbital-order transition for the ideal structure R_0, which retains all distortions except for the Jahn-Teller one. For structure R_0 we cannot obtain $T_{\rm KK}$ from $p(T)$, because, due to the ${\sim}200$ meV crystal-field splitting, Coulomb repulsion strongly suppress orbital fluctuations even at 1500 K. We can, however, study the evolution with temperature of the occupied orbital, here defined as $|\vartheta\rangle{=}\cos\frac{\vartheta}{2}\,|3z^2{-}r^2\rangle + \sin\frac{\vartheta}{2}\,|x^2{-}y^2\rangle$. For the experimental structure (R_{11}) we find $\vartheta \sim 108°$, in agreement with experiments, while for the I_0 structure we obtain $\vartheta = 90°$. For the R_0 structure we find two regimes: At high temper-

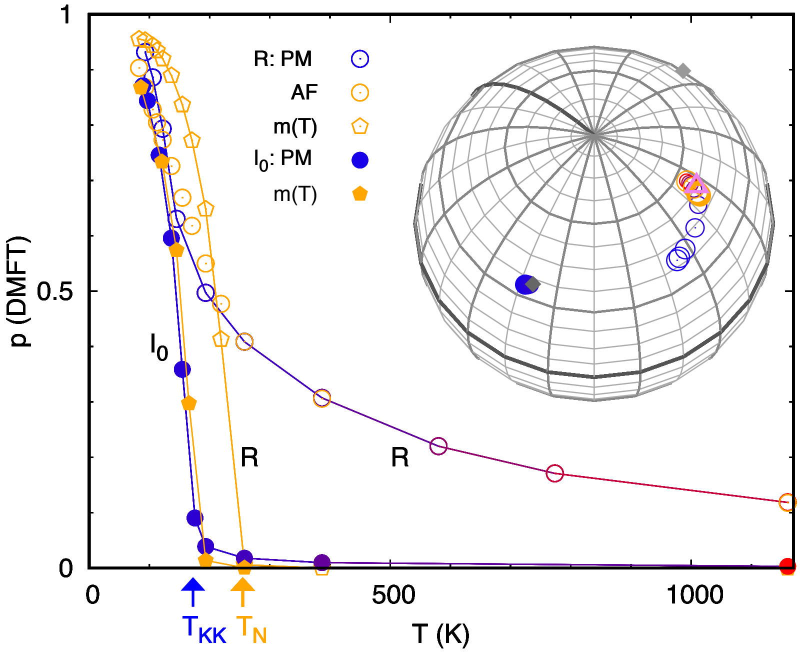

Fig. 17: *Orbital ordering in the t_{2g}^2 system LaVO$_3$. Filled circles: ideal case without crystal-field splitting. Empty circles: experimental structure. For each temperature, the associated hole orbital is shown on the Bloch sphere. At high temperature it coincides with the predictions of crystal-field theory (triangle). At the Kugel-Khomskii transition temperature, T_{KK}, it starts to move towards the ideal Kugel-Khomskii result (filled blue circle). From Ref. [12].*

ature the occupied orbital is the lower-energy crystal-field orbital (ϑ=180°). At $T_{\text{KK}} \sim 550$ K superexchange rotates this ϑ towards 90°, reaching 130° in the zero-temperature limit; this is the actual superexchange transition temperature for LaMnO$_3$. Such T_{KK} is still remarkably large, however not sufficient to explain the persistence of the Jahn-Teller distortion in nanoclusters up to basically melting temperature [19]. Furthermore, the superexchange energy gain associated with orbital order (Fig. 16) is small compared to the total energy gain due to the Jahn-Teller distortion, calculated via LDA+U [15, 16] or LDA+DMFT [17]. Thus, as in the case of KCuF$_3$, the conclusion is that a static crystal-field splitting, as the one generated by the electron-lattice coupling, is essential to explain orbital ordering at high temperature. We obtained a similar conclusion for various families of compounds, including t_{2g} systems, an indication that pure Kugel-Khomskii materials are actually rare. The first clear-cut case in which the super-exchange interaction controls orbital ordering, turning the hole orbital away from the state expected from crystal-field theory, was recently identified in the t_{2g}^2 system LaVO$_3$ [12]. This is shown in Fig. 17, where the changes in the hole orbital on lowering the temperature can be followed on the Bloch sphere (empty circles). Decreasing the temperature the color of the empty circles changes from red to blue, while the associated polarization increases towards its maximum vale. One may see that at high temperature they overlap with the pink triangle, representing the state expected from crystal-field theory. Decreasing the temperature they move towards the filled blue circle, representing the Kugel-Khomskii ideal value.

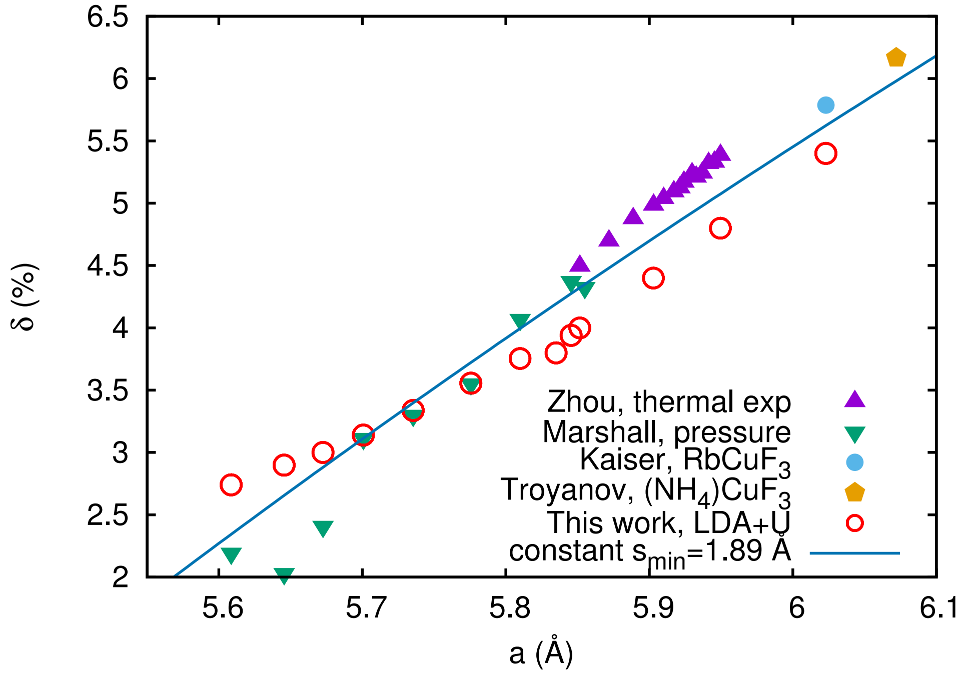

Fig. 18: *Distortion parameter δ as a function of lattice constant a in thermally expanding KCuF$_3$ [20], under hydrostatic pressure [21], for RbCuF$_3$ [22] and (NH$_4$)CuF$_3$ [23], compared to our calculations and the values obtained assuming a constant short Cu-F distance (s_{min}). From Ref. [11].*

Let us now return to KCuF$_3$, the case we have examined in greatest detail. The main conclusion we had reached is that a static distortion is necessary to explain the presence of orbital ordering at high temperature. Based on the discussion so far, one could at this point conclude that the latter is determined by the Jahn-Teller effect. However, it turns out that the reality is even more complex. Indeed, in a second-order transition one would expect that the order parameter goes to zero at the transition temperature, $T_{\rm OO}$. In the case of electron-phonon-coupling driven orbital ordering, the order parameter is the Jahn-Teller distortion. If $T_{\rm OO}$ is not yet reached at the melting temperature, the order parameter should at least decrease with temperature. In KCuF$_3$, however, it has been found that this simple picture fails to describe experiments. This is shown in Fig. 18. Increasing the temperature the lattice constant increases by thermal expansion. At the same time the (dimensionless) Jahn-Teller distortion parameter δ also increases. This surprising behavior is due to the fact that the short Cu-F bond remains almost constant while the long Cu-F bond becomes longer [11], instead of the two changing coherently together as expected via the Jahn-Teller Q_1 mode. Going to the microscopical origin of this behavior, it turns out that the Jahn-Teller mode is so soft that the distortion is actually determined by the Born-Mayer repulsion of the ions. Thus the distortion increases with the lattice constant, and, via thermal expansion, the order parameter increases with temperature. This new ordering mechanism was identified in Ref. [11] for the first time. It can operate even in closed-shell systems and would result in an inverted Landau transition, with symmetry breaking *above* a critical temperature.

7 Conclusion

In this lecture we have studied two mechanisms that can lead to orbital ordering phenomena in Mott insulators. The first is well illustrated in the influential paper of Kanamori, Ref. [1]. In this picture, a co-operative Jahn-Teller distortion generates a static crystal-field, which in turn splits orbitals otherwise degenerate. This mechanism is made more efficient by Coulomb repulsion; the latter enhances the orbital polarization, leading to an orbitally-ordered state even if the crystal-field splitting is a mere fraction of the bandwidth [4]. The second mechanism, proposed by Kugel and Khomskii [2] in 1973, predicts orbital ordering even in the absence of a static crystal field; in this picture, orbital ordering is due to the superexchange interaction, the effective interaction emerging from the orbitally-degenerate Hubbard model in the large U limit. The general super-exchange Hamiltonians for e_g and t_{2g} systems can be found in Ref. [14], where the interaction is decomposed in its irreducible tensor components. In paradigmatic materials, both the Jahn-Teller and super-exchange coupling predict a similar type of order. Thus identifying which interaction dominates is very difficult. For this reason, the riddle of the origin of orbital ordering in materials can be viewed an example of a chicken-and-egg problem – and has been accordingly a matter of debate for decades.

In the last section we saw how this problem was solved in representative cases. This was done by disentangling the superexchange Kugel-Khomskii interaction from the rest. For the two classical text-book examples of orbitally-ordered systems, $KCuF_3$ and $LaMnO_3$, it was shown via this approach that, although Kugel-Khomskii superexchange is very efficient, it cannot alone explain the presence of a co-operative Jahn-Teller distortion up to the melting temperature. The conclusion is that an interaction giving directly rise to a static crystal-field splitting, e.g., electron-phonon coupling, is necessary to explain experimental findings [3,6]. The same result was obtained for many other materials, with either e_g or t_{2g} partially filled shells. This shows that purely super-exchange driven ordering is rare in nature. A clear cut case of Kugel-Khomskii material was nevertheless recently identified, $LaVO_3$ [12]. Finally, to complicate the matter, for $KCuF_3$ it was shown that not even the Jahn-Teller effect alone does explain the evolution of distortions with temperature. A new ordering mechanism in which the Born-Mayer repulsion of the ions plays a key role had to be identified [11]. Only then it could be understood why the order parameter experimentally increases (instead of decreasing) with temperature.

Appendices

A Constants and units

In this lecture, formulas are given in atomic units. The unit of mass m_0 is the electron mass ($m_0 = m_e$), the unit of charge e_0 is the electron charge ($e_0 = e$), the unit of length a_0 is the Bohr radius ($a_0 = a_B \sim 0.52918$ Å), and the unit of time is $t_0 = 4\pi\varepsilon_0\hbar a_0/e^2$. In these units, m_e, a_B, e and $1/4\pi\varepsilon_0$ have the numerical value 1, the speed of light is $c = 1/\alpha \sim 137$, and the unit of energy is $1\mathrm{Ha} = e^2/4\pi\varepsilon_0 a_0 \sim 27.211$ eV.

B Atomic orbitals

B.1 Radial functions

The nlm hydrogen-like atomic orbital is given by

$$\psi_{nlm}(\rho,\vartheta,\varphi) = R_{nl}(\rho)Y_m^l(\vartheta,\varphi),$$

where $R_{nl}(\rho)$ is the radial function and $Y_m^l(\vartheta,\varphi)$ a spherical harmonic, $\rho = Zr$ and Z the atomic number. In atomic units, the radial functions are

$$R_{nl}(\rho) = \sqrt{\left(\frac{2Z}{n}\right)^3 \frac{(n-l-1)!}{2n[(n+l)!]^3}}\, e^{-\rho/n} \left(\frac{2\rho}{n}\right)^l L_{n-l-1}^{2l+1}\left(\frac{2\rho}{n}\right),$$

where L_{n-l-1}^{2l+1} are generalized Laguerre polynomials of degree $n-l-1$.
The radial function for $n = 1, 2, 3$ are

$$\begin{array}{lcll}
R_{1s}(\rho) = & 2 & Z^{3/2} & e^{-\rho} \\
R_{2s}(\rho) = & \frac{1}{2\sqrt{2}} & Z^{3/2} & (2-\rho)\, e^{-\rho/2} \\
R_{2p}(\rho) = & \frac{1}{2\sqrt{6}} & Z^{3/2} & \rho\, e^{-\rho/2} \\
R_{3s}(\rho) = & \frac{2}{3\sqrt{3}} & Z^{3/2} & (1 - 2\rho/3 + 2\rho^2/27)\, e^{-\rho/3} \\
R_{3p}(\rho) = & \frac{4\sqrt{2}}{9\sqrt{3}} & Z^{3/2} & \rho(1-\rho/6)\, e^{-\rho/3} \\
R_{3d}(\rho) = & \frac{2\sqrt{2}}{81\sqrt{15}} & Z^{3/2} & \rho^2\, e^{-\rho/3}
\end{array}$$

where we used the standard notation s for l=0, p for l=1 and d for l=2. The spherical Harmonics, using the Condon-Shortley convention, are given by

$$Y_m^\ell(\vartheta,\varphi) = (-1)^m \sqrt{\frac{(2\ell+1)}{4\pi}\frac{(\ell-m)!}{(\ell+m)!}}\, P_m^\ell(\cos\vartheta)\, e^{im\varphi} \tag{24}$$

where $P_m^\ell(\cos\vartheta)$ in an associated Legendre polynomial.

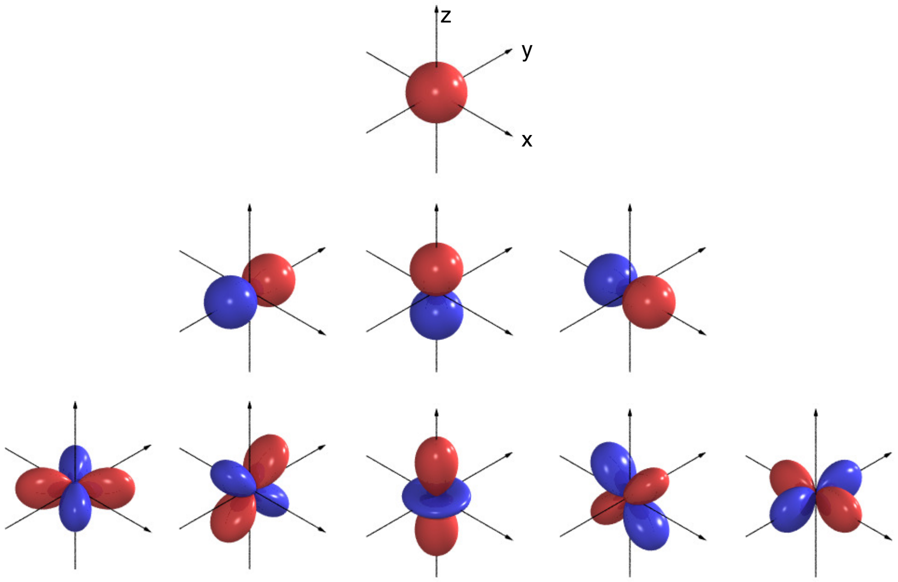

Fig. 19: *The* s *(first row),* p_y*,* p_z*,* p_x *(second row), and* d_{xy}*,* d_{yz}*,* $d_{3z^2-r^2}$*,* d_{xz}*,* $d_{x^2-y^2}$ *(last row) real harmonics.*

B.2 Real harmonics

To study solids, it is usually convenient to work in the basis of real harmonics. The latter are defined in terms of the spherical harmonics as follows:

$$y_{l0} = Y_0^l, \quad y_{lm} = \frac{1}{\sqrt{2}}\big(Y_{-m}^l + (-1)^m Y_m^l\big), \quad y_{l-m} = \frac{i}{\sqrt{2}}\big(Y_{-m}^l - (-1)^m Y_m^l\big), \quad m > 0.$$

Using the definitions $x = r\sin\vartheta\cos\varphi$, $y = r\sin\vartheta\sin\varphi$, $z = r\cos\vartheta$, so that

$$\cos\vartheta = \frac{z}{r}, \qquad e^{\pm i\varphi}\sin\vartheta = \frac{(x \pm iy)}{r}, \tag{25}$$

we can express the $l = 0, 1, 2$ real harmonics (Fig. 19) as

$$\begin{aligned}
s &= y_{00} &&= Y_0^0 &&= \sqrt{\tfrac{1}{4\pi}} && \\
p_y &= y_{1-1} &&= \tfrac{i}{\sqrt{2}}\big(Y_{-1}^1 + Y_1^1\big) &&= \sqrt{\tfrac{3}{4\pi}} && y/r \\
p_z &= y_{10} &&= Y_2^0 &&= \sqrt{\tfrac{3}{4\pi}} && z/r \\
p_x &= y_{11} &&= \tfrac{1}{\sqrt{2}}\big(Y_{-1}^1 - Y_1^1\big) &&= \sqrt{\tfrac{3}{4\pi}} && x/r \\
d_{xy} &= y_{2-2} &&= \tfrac{i}{\sqrt{2}}\big(Y_{-2}^2 - Y_2^2\big) &&= \sqrt{\tfrac{15}{4\pi}} && xy/r^2 \\
d_{yz} &= y_{2-1} &&= \tfrac{i}{\sqrt{2}}\big(Y_{-1}^2 + Y_1^2\big) &&= \sqrt{\tfrac{15}{4\pi}} && yz/r^2 \\
d_{3z^2-r^2} &= y_{20} &&= Y_2^0 &&= \sqrt{\tfrac{15}{4\pi}}\tfrac{1}{2\sqrt{3}} && (3z^2-r^2)/r^2 \\
d_{xz} &= y_{21} &&= \tfrac{1}{\sqrt{2}}\big(Y_{-1}^2 - Y_1^2\big) &&= \sqrt{\tfrac{15}{4\pi}} && xz/r^2 \\
d_{x^2-y^2} &= y_{22} &&= \tfrac{1}{\sqrt{2}}\big(Y_{-2}^2 + Y_2^2\big) &&= \sqrt{\tfrac{15}{4\pi}}\tfrac{1}{2} && (x^2-y^2)/r^2
\end{aligned}$$

B.3 Slater-Koster integrals

The interatomic Slater-Koster two-center integrals are defined as

$$E_{lm,l'm'} = \int d\boldsymbol{r}\ \overline{\psi_{lm}}(\boldsymbol{r}-\boldsymbol{d})V(\boldsymbol{r}-\boldsymbol{d})\psi_{l'm'}(\boldsymbol{r}).$$

They can be expressed as a function of radial integrals $V_{ll'\alpha}$, which scale with the distance d roughly as $d^{-(l+l'+1)}$ [24], and direction cosines, defined as

$$l{=}\boldsymbol{d}\cdot\hat{x}/d, \quad m{=}\boldsymbol{d}\cdot\hat{y}/d, \quad n{=}\boldsymbol{d}\cdot\hat{z}/d.$$

The Slater-Koster integrals for s-, p-, and d-orbitals [24] are listed below.

$$\begin{array}{lcrrr}
E_{s,s} & = & V_{ss\sigma} & & \\
E_{s,x} & = & lV_{sp\sigma} & & \\
E_{x,x} & = & l^2V_{pp\sigma} & +(1-l^2)V_{pp\pi} & \\
E_{x,y} & = & lmV_{pp\sigma} & -lmV_{pp\pi} & \\
E_{x,z} & = & lnV_{pp\sigma} & -lnV_{pp\pi} & \\
E_{s,xy} & = & \sqrt{3}lmV_{sd\sigma} & & \\
E_{s,x^2-y^2} & = & \frac{1}{2}\sqrt{3}(l^2-m^2)V_{sd\sigma} & & \\
E_{s,3z^2-r^2} & = & [n^2-\frac{1}{2}(l^2+m^2)]V_{sd\sigma} & & \\
E_{x,xy} & = & \sqrt{3}l^2mV_{pd\sigma} & +m(1-2l^2)V_{pd\pi} & \\
E_{x,yz} & = & \sqrt{3}lmnV_{pd\sigma} & -2lmnV_{pd\pi} & \\
E_{x,zx} & = & \sqrt{3}l^2nV_{pd\sigma} & +n(1-2l^2)V_{pd\pi} & \\
E_{x,x^2-y^2} & = & \frac{\sqrt{3}}{2}l[(l^2-m^2)]V_{pd\sigma} & +l(1-l^2+m^2)V_{pd\pi} & \\
E_{y,x^2-y^2} & = & \frac{\sqrt{3}}{2}m[(l^2-m^2)]V_{pd\sigma} & -m(1+l^2-m^2)V_{pd\pi} & \\
E_{z,x^2-y^2} & = & \frac{\sqrt{3}}{2}n[(l^2-m^2)]V_{pd\sigma} & -n(l^2-m^2)V_{pd\pi} & \\
E_{x,3z^2-r^2} & = & l[n^2-\frac{1}{2}(l^2+m^2)]V_{pd\sigma} & -\sqrt{3}ln^2V_{pd\pi} & \\
E_{y,3z^2-r^2} & = & m[n^2-\frac{1}{2}(l^2+m^2)]V_{pd\sigma} & -\sqrt{3}mn^2V_{pd\pi} & \\
E_{z,3z^2-r^2} & = & n[n^2-\frac{1}{2}(l^2+m^2)]V_{pd\sigma} & +\sqrt{3}n(l^2+m^2)V_{pd\pi} & \\
E_{xy,xy} & = & 3l^2m^2V_{dd\sigma} & +(l^2+m^2-4l^2m^2)V_{dd\pi} & +(n^2+l^2m^2)V_{dd\delta} \\
E_{xy,yz} & = & 3lm^2nV_{dd\sigma} & +ln(1-4m^2)V_{dd\pi} & +ln(m^2-1)V_{dd\delta} \\
E_{xy,zx} & = & 3l^2mnV_{dd\sigma} & +mn(1-4l^2)V_{dd\pi} & +mn(l^2-1)V_{dd\delta} \\
E_{xy,x^2-y^2} & = & \frac{3}{2}lm(l^2-m^2)V_{dd\sigma} & 2lm(m^2-l^2)V_{dd\pi} & \frac{1}{2}lm(l^2-m^2)V_{dd\delta} \\
E_{yz,x^2-y^2} & = & \frac{3}{2}mn(l^2-m^2)V_{dd\sigma} & -mn[1+2(l^2-m^2)]V_{dd\pi} & +mn[1+\frac{1}{2}(l^2-m^2)]V_{dd\delta} \\
E_{zx,x^2-y^2} & = & \frac{3}{2}nl(l^2-m^2)V_{dd\sigma} & +nl[1-2(l^2-m^2)]V_{dd\pi} & -nl[1-\frac{1}{2}(l^2-m^2)]V_{dd\delta} \\
E_{xy,3z^2-r^2} & = & \sqrt{3}lm[n^2-\frac{1}{2}(l^2+m^2)]V_{dd\sigma} & -2\sqrt{3}lmn^2V_{dd\pi} & \frac{\sqrt{3}}{2}lm(1+n^2)V_{dd\delta} \\
E_{yz,3z^2-r^2} & = & \sqrt{3}mn[n^2-\frac{1}{2}(l^2+m^2)]V_{dd\sigma} & +\sqrt{3}mn(l^2+m^2-n^2)V_{dd\pi} & -\frac{\sqrt{3}}{2}mn(l^2+m^2)V_{dd\delta} \\
E_{zx,3z^2-r^2} & = & \sqrt{3}ln[n^2-\frac{1}{2}(l^2+m^2)]V_{dd\sigma} & +\sqrt{3}ln(l^2+m^2-n^2)V_{dd\pi} & -\frac{\sqrt{3}}{2}ln(l^2+m^2)V_{dd\delta} \\
E_{x^2-y^2,x^2-y^2} & = & \frac{3}{4}(l^2-m^2)^2V_{dd\sigma} & +[l^2+m^2-(l^2-m^2)^2]V_{dd\pi} & +[n^2+\frac{1}{4}(l^2-m^2)^2]V_{dd\delta} \\
E_{x^2-y^2,3z^2-r^2} & = & \frac{\sqrt{3}}{2}(l^2-m^2)[n^2-\frac{1}{2}(l^2+m^2)]V_{dd\sigma} & +\sqrt{3}n^2(m^2-l^2)V_{dd\pi} & +\frac{\sqrt{3}}{4}(1+n^2)(l^2-m^2)V_{dd\delta} \\
E_{3z^2-r^2,3z^2-r^2} & = & [n^2-\frac{1}{2}(l^2+m^2)]^2V_{dd\sigma} & +3n^2(l^2+m^2)V_{dd\pi} & \frac{3}{4}(l^2+m^2)^2V_{dd\delta}
\end{array}$$

References

[1] J. Kanamori, J. Appl. Phys. **31**, S14 (1960)

[2] K.I. Kugel and D.I. Khomskii, Zh. Eksp. Teor. Fiz. **64**, 1429 (1973)

[3] E. Pavarini, E. Koch, and A.I. Lichtenstein, Phys. Rev. Lett. **101**, 266405 (2008)

[4] E. Pavarini, S. Biermann, A. Poteryaev, A.I. Lichtenstein, A. Georges, O.K. Andersen, Phys. Rev. Lett. **92**, 176403 (2004)
E. Pavarini A. Yamasaki, J. Nuss and O.K. Andersen, New J. Phys. **7**, 188 (2005)

[5] E. Pavarini: *The LDA+DMFT Approach*, in [7]

[6] E. Pavarini and E. Koch, Phys. Rev. Lett. **104**, 086402 (2010)
A. Flesch, G. Zhang, E. Koch, and E. Pavarini, Phys. Rev. B **85**, 035124 (2012)

[7] E. Pavarini, E. Koch, A. Lichtenstein, D. Vollhardt (eds.):
The LDA+DMFT approach to strongly correlated materials,
Reihe Modeling and Simulation, Vol. 1 (Forschungszentrum Jülich, 2011)
`http://www.cond-mat.de/events/correl11`

[8] E. Pavarini, E. Koch, A. Lichtenstein, D. Vollhardt (eds.):
DMFT at 25: Infinite Dimensions,
Reihe Modeling and Simulation, Vol. 4 (Forschungszentrum Jülich, 2014)
`http://www.cond-mat.de/events/correl14`

[9] E. Pavarini, E. Koch, A. Lichtenstein, D. Vollhardt (eds.):
DMFT: From Infinite Dimensions to Real Materials,
Reihe Modeling and Simulation, Vol. 8 (Forschungszentrum Jülich, 2018)
`http://www.cond-mat.de/events/correl18`

[10] E. Pavarini, E. Koch, A. Lichtenstein, D. Vollhardt (eds.):
Dynamical Mean-Field Theory of Correlated Electrons,
Reihe Modeling and Simulation, Vol. 12 (Forschungszentrum Jülich, 2022)
`http://www.cond-mat.de/events/correl22`

[11] H. Sims, E. Pavarini, and E. Koch, Phys. Rev. B **96**, 054107 (2017)

[12] X.-J. Zhang, E. Koch and E. Pavarini, Phys. Rev. B **106**, 115110 (2022)

[13] E. Pavarini, E. Koch, F. Anders, M. Jarrell (eds.):
Correlated Electrons: From Models to Materials,
Reihe Modeling and Simulation, Vol. 2 (Forschungszentrum Jülich, 2012)
`http://www.cond-mat.de/events/correl12`

[14] X.-J. Zhang, E. Koch and E. Pavarini, Phys. Rev. B **105**, 115104 (2022)

[15] V.I. Anisimov, F. Aryasetiawan and A.I. Lichtenstein,
J. Phys. Condens. Matter **9**, 767 (1997)

[16] W.G. Yin, D. Volja, and W. Ku, Phys. Rev. Lett. **96**, 116405 (2006)

[17] I. Leonov, N. Binggeli, Dm. Korotin, V.I. Anisimov, and D. Vollhardt,
Phys. Rev. Lett. **101**, 096405 (2008)
I. Leonov, Dm. Korotin, N. Binggeli, V.I. Anisimov, and D. Vollhardt,
Phys. Rev. B **81**, 075109 (2010)

[18] K.H. Ahn, and A.J. Millis, Phys. Rev. B **61**, 13545 (2000)

[19] M.C. Sánchez, G. Subías, J. García, and J. Blasco, Phys. Rev. Lett. **90**, 045503 (2003)

[20] L.G. Marshall, J. Zhou, J. Zhang, J. Han, S.C. Vogel, X.Yu, Y. Zhao, M. Fernández-Díaz,
J. Cheng, and J.B. Goodenough, Phys. Rev. B **87**, 014109 (2013)

[21] J.-S. Zhou, J.A. Alonso, J.T. Han, M.T. Fernández-Díaz, J.-G. Cheng, and
J.B. Goodenough, J. Fluorine Chem. **132**, 1117 (2011)

[22] V. Kaiser, M. Otto, F. Binder, and D. Babel, Z. Anorg. Allg. Chem. **585**, 93 (1990)

[23] S.I. Troyanov, I.V. Morozov, and Y.M. Korenev,
Zhurnal Neorganicheskoi Khimii **38**, 984 (1993) [Russian J. Inorg. Chem. **38**, 909 (1993)]

[24] W.A. Harrison: *Electronic Structure and The Properties of Solids* (Dover, 1989)

6 Electron-Phonon Coupling

Rolf Heid
Institute for Quantum Materials and Technologies
Karlsruhe Institute of Technology

Contents

E. Pavarini and E. Koch (eds.)
Correlations and Phase Transitions
Modeling and Simulation Vol. 14
Forschungszentrum Jülich, 2024, ISBN 978-3-95806-751-6
http://www.cond-mat.de/events/correl24

1 Introduction

The electron-phonon interaction is, besides the Coulomb interaction, one of the fundamental interactions of quasiparticles in solids. It plays an important role for a variety of physical phenomena. In particular, in metals, low-energy electronic excitations are strongly modified by the coupling to lattice vibrations, which influences, e.g., transport and thermodynamical properties. Electron-phonon coupling (EPC) also provides in a fundamental way an attractive electron-electron interaction, which is always present and, in many metals, is the origin of electron pairing underlying the macroscopic quantum phenomenon of superconductivity.

This lecture addresses the consequences of electron-phonon coupling in both the normal and superconducting state of metals. In Section 2, the basic Hamiltonian describing the coupled electron-phonon system is introduced. In Section 3, a closer look onto normal state effects in a metal is taken, focusing on the renormalization of quasiparticles, which allows to experimentally quantify the strength of the interaction. Section 4 is devoted to phonon-mediated superconductivity. First a derivation of the effective attractive interaction among electrons mediated by phonon exchange is given. Then we analyze the role of electron-phonon coupling for superconductivity in the context of the strong-coupling Migdal-Eliashberg theory in some detail. In Section 5, we introduce an approach based on density-functional theory to calculate electron-phonon coupling quantities and present two examples to illustrate its predictive power. Throughout this Chapter, only nonmagnetic states are considered and atomic units $\hbar = 2m_e = e^2/2 = 1$ as well as $k_B = 1$ are used.

2 Electron-phonon Hamiltonian

2.1 Electron-phonon vertex

The lowest-order process involving the electron-phonon interaction is the scattering of a single electron by a simultaneous creation or annihilation of a single phonon, as diagrammatically shown in Fig. 1. The probability for the scattering process is called the electron-phonon vertex g. We will briefly sketch its derivation starting from rather general grounds. For more details one can refer to the book of Grimvall [1].

Due to the large ratio of the ionic and electronic mass, the dynamics of the ions and the electrons can be systematically expanded in terms of the small parameter $\kappa = (m/M)^{1/4}$, which results in a partial decoupling [2, 3]. To lowest order in κ, called the adiabatic or Born-Oppenheimer approximation, the total wavefunction of the coupled electron-ion system can be written as a product $\Psi(\underline{\mathbf{r}}, \underline{\mathbf{R}}) = \chi(\underline{\mathbf{R}})\psi(\underline{\mathbf{r}}; \underline{\mathbf{R}})$, where $\underline{\mathbf{r}}$ and $\underline{\mathbf{R}}$ denote the sets of electron and ion coordinates, respectively. The electronic wavefunction obeys the equation

$$\big(T_e + V_{ee} + H_{e\text{-}i}(\underline{\mathbf{R}})\big)\psi_n(\underline{\mathbf{r}}; \underline{\mathbf{R}}) = E_n(\underline{\mathbf{R}})\psi_n(\underline{\mathbf{r}}; \underline{\mathbf{R}}) , \tag{1}$$

where T_e and V_{ee} denote the kinetic energy and Coulomb interaction of the electron system, respectively. Eq. (1) depends parametrically on the ionic positions $\underline{\mathbf{R}}$ via the electron-ion interaction $H_{e\text{-}i}$.

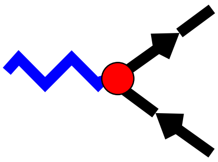

Fig. 1: *Diagrammatic representation of the basic electron-phonon scattering process. Black lines represent electrons, the blue zigzag line a phonon, and the red circle the screened vertex.*

The electron-phonon vertex appears in first order beyond the adiabatic approximation. One can show that it induces off-diagonal matrix elements among the electronic eigenstates ψ_n and has the form

$$\langle n|\, \delta_{\mathbf{R}} V |n'\rangle. \tag{2}$$

The operator $\delta_{\mathbf{R}} V$ stands for the linear change of the potential felt by the electrons under a displacement of an atom from its rest position: $\mathbf{R} = \mathbf{R}_0 + \mathbf{u}$. If the potential V is the bare electron-ion potential V^0, then $\delta_{\mathbf{R}} V = \mathbf{u} \cdot \nabla V^0\big|_{\mathbf{R}_0}$. Eq. (2) represents the bare vertex. However, in solids, and in particular in metals, the bare electron-ion potential is screened by the other electrons. Screening also alters the vertex significantly. Within linear response theory this operator takes the form

$$\delta_{\mathbf{R}} V = \mathbf{u} \cdot \varepsilon^{-1} \nabla V^0\big|_{\mathbf{R}_0}, \tag{3}$$

where ε^{-1} is the inverse dielectric matrix [4], which is a measure of the screening. Note that in Eq. (3), the screening operator does not commute with the gradient operation, and thus can not be written in terms of the gradient of a screened potential.

2.2 Fröhlich Hamiltonian

We now aim to develop a systematic perturbative treatment of the mutual influence of the electronic and phononic subsystems in a solid. Thereby the question arises, what are the proper noninteracting quasiparticles to start with. The correct answer requires to know the solution to some extent. As we will see, electronic states are significantly influenced by lattice vibrations mostly in close vicinity of the Fermi energy. It is therefore appropriate to start with electrons moving in a static potential of a rigid ion lattice, without any renormalization by the lattice vibrations. In contrast, the bare vibrations of the ion lattice would be a bad starting point, because they are strongly altered by the screening of the electrons. This screening must be built into the description of the harmonic lattice vibrations which defines the noninteracting phonons.

For the discussion of electron-phonon coupling effects in periodic solids, a good starting point is the *Fröhlich Hamiltonian*, which reads in second quantization

$$H = H_e + H_{ph} + H_{e\text{-}ph} \tag{4}$$

Here the electron system is described by noninteracting quasi-particles with dispersion ε_k. These quasiparticles are considered to be the stationary solutions of band electrons in a perfect periodic lattice, and include already the renormalization from Coulomb interaction

$$H_e = \sum_{\mathbf{k}\nu\sigma} \varepsilon_{\mathbf{k}\nu}\, c^\dagger_{\mathbf{k}\nu\sigma} c_{\mathbf{k}\nu\sigma} \,. \tag{5}$$

Here $c_{\mathbf{k}\nu\sigma}$ $\left(c^\dagger_{\mathbf{k}\nu\sigma}\right)$ are the annihilation (creation) operators for an electronic state with momentum $\mathbf{k}$, band index ν, spin σ, and band energy $\varepsilon_{\mathbf{k}\nu}$.

The lattice Hamiltonian is expressed in terms of quantized harmonic vibrations, and represents noninteracting phonons

$$H_{ph} = \sum_{\mathbf{q}j} \omega_{\mathbf{q}j} \left(b^\dagger_{\mathbf{q}j} b_{\mathbf{q}j} + \frac{1}{2} \right), \tag{6}$$

where $b_{\mathbf{q}j}$ $\left(b^\dagger_{\mathbf{q}j}\right)$ are the annihilation (creation) operators for a phonon with momentum $\mathbf{q}$, branch index j, and energy $\omega_{\mathbf{q}j}$. Phonons are the quanta of the normal mode vibrations (for more details see Appendix A). The operator of atom displacements is expressed in terms of the phonon operators by

$$u_{ls\alpha} = \frac{1}{\sqrt{N_q}} \sum_{\mathbf{q}j} e^{i\mathbf{q}\mathbf{R}^0_{ls}} A^{\mathbf{q}j}_{s\alpha} \left(b_{\mathbf{q}j} + b^\dagger_{-\mathbf{q}j} \right) \qquad \text{with} \qquad A^{\mathbf{q}j}_{s\alpha} = \frac{\eta_{s\alpha}(\mathbf{q}j)}{\sqrt{2M_s\omega_{\mathbf{q}j}}} \,. \tag{7}$$

Atoms are characterized by two indices denoting the unit cell (l) and the atoms inside a unit cell (s), respectively, with M_s the corresponding atom mass. α denotes Cartesian indices, and $\eta_{s\alpha}(\mathbf{q}j)$ is the eigenvector of the normal mode $\mathbf{q}j$. The number of points in the summation over $\mathbf{q}$ is N_q.

The third term describes the lowest-order coupling between electrons and phonons derived from Eq. (3). Using the relationship Eq. (7) it has the form

$$H_{e\text{-}ph} = \sum_{\mathbf{k}\nu\nu'\sigma} \sum_{\mathbf{q}j} g^{\mathbf{q}j}_{\mathbf{k}+\mathbf{q}\nu',\mathbf{k}\nu}\, c^\dagger_{\mathbf{k}+\mathbf{q}\nu'\sigma} c_{\mathbf{k}\nu\sigma} \left(b_{\mathbf{q}j} + b^\dagger_{-\mathbf{q}j} \right) . \tag{8}$$

$g^{\mathbf{q}j}_{\mathbf{k}+\mathbf{q}\nu',\mathbf{k}\nu}$ is the electron-phonon matrix element and describes the probability amplitude for scattering an electron with momentum $\mathbf{k}$ from band ν to a state with momentum $\mathbf{k}+\mathbf{q}$ in band ν' under the simultaneous absorption (emission) of a phonon with momentum $\mathbf{q}$ ($-\mathbf{q}$) and branch index j

$$g^{\mathbf{q}j}_{\mathbf{k}+\mathbf{q}\nu',\mathbf{k}\nu} = \sum_{s\alpha} A^{\mathbf{q}j}_{s\alpha} \left\langle \mathbf{k}+\mathbf{q}\nu'\sigma \right| \delta^{\mathbf{q}}_{s\alpha} V \left| \mathbf{k}\nu\sigma \right\rangle . \tag{9}$$

Here again the screened first-order change of the potential enters the matrix elements. They are independent of spin for nonmagnetic ground states.

This general form of the Fröhlich Hamiltonian will be the starting point for the many-body perturbation outlined in the next sections. To simplify the treatment, we will use a compact notation combining momentum and band/branch index into a single symbol: $k = (\mathbf{k}\nu)$, $k' = (\mathbf{k}'\nu')$, and $q = (\mathbf{q}j)$. The EPC matrix elements are then denoted as

$$g^{q}_{k',k} = g^{\mathbf{q}j}_{\mathbf{k}'\nu',\mathbf{k}\nu}\, \delta_{\mathbf{k}',\mathbf{k}+\mathbf{q}} \,, \tag{10}$$

which implicitly takes into account momentum conservation.

3 Normal-state effects

3.1 Green functions and perturbation

In this section we will discuss the effects of electron-phonon interaction in the normal state of a metal. This will be done using many-body perturbation techniques [5–7]. The focus will be on the renormalization of electronic and phononic quasiparticles, which provides ways to experimentally gain information about the coupling strength. This will set the stage for the discussion of phonon-mediated superconductivity in the next section.

The following treatment is based on the Fröhlich Hamiltonian Eq. (4), where $H_0 = H_e + H_{ph}$ denotes the Hamiltonian of the unperturbed quasiparticles, and $H_{e\text{-}ph}$ is a perturbation linear in the electron-phonon coupling. We will work with the imaginary-time Green functions

$$G(k,\tau) = -\big\langle T_\tau c_{k\sigma}(\tau) c^\dagger_{k\sigma}(0)\big\rangle \tag{11}$$

for the fermionic quasiparticles, where the field operators are given in a Heisenberg picture using an imaginary time $-i\tau$, $c_{k\sigma}(\tau) = e^{H\tau} c_{k\sigma} e^{-H\tau}$ with $-\beta < \tau < \beta$, $\beta = 1/T$. The Wick operator T_τ reorders operators to increasing τ from right to left.

For the bosonic quasiparticles, the Green function of the displacement operators is defined as

$$U_{s\alpha,s'\alpha'}(\mathbf{q},\tau) = -\big\langle T_\tau u_{\mathbf{q}s\alpha}(\tau) u_{-\mathbf{q}s'\alpha'}(0)\big\rangle = \sum_j A^{\mathbf{q}j}_{s\alpha} A^{-\mathbf{q}j}_{s'\alpha'} D(\mathbf{q}j,\tau)\,, \tag{12}$$

where D denotes the phonon Green function $\big(q = (\mathbf{q}j)\big)$

$$D(q,\tau) = -\big\langle T_\tau \big(b_q(\tau) + b^\dagger_{-q}(\tau)\big)\big(b_{-q}(0) + b^\dagger_q(0)\big)\big\rangle \tag{13}$$

$G(k,\tau)$ and $D(q,\tau)$ can be defined as periodic functions in τ with the symmetry properties $G(k,\tau{+}\beta) = -G(k,\tau)$ and $D(k,\tau{+}\beta) = D(k,\tau)$, respectively. Their Fourier transforms are given by

$$G(k,i\omega_n) = \frac{1}{2}\int_{-\beta}^{\beta} d\tau e^{i\omega_n\tau} G(k,\tau) \tag{14}$$

$$D(q,i\nu_m) = \frac{1}{2}\int_{-\beta}^{\beta} d\tau e^{i\nu_m\tau} D(q,\tau)\,, \tag{15}$$

where $\omega_n = (2n{+}1)\pi T$ and $\nu_m = 2m\pi T$, with integer values n, m, denote fermionic and bosonic Matsubara frequencies, respectively.

Two further simplifications have been assumed: (i) because we are dealing with nonmagnetic states only, the spin index in the electronic Green function can be suppressed; (ii) the perturbation $H_{e\text{-}ph}$ does not mix different electronic bands or phononic modes, such that the interacting Green functions can still be represented by a single band/mode index.

The bare Green functions of the unperturbed Hamiltonian $H_0 = H_e + H_{ph}$ are

$$G_0(k,i\omega_n) = \frac{1}{i\omega_n - \varepsilon_k} \tag{16}$$

$$D_0(q,i\nu_m) = \frac{1}{i\nu_m - \omega_q} - \frac{1}{i\nu_m + \omega_q}\,. \tag{17}$$

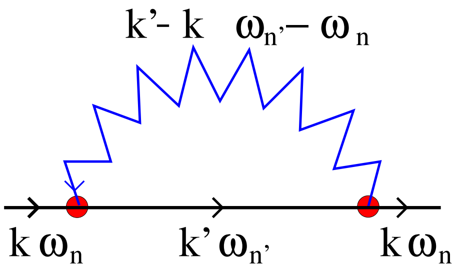

Fig. 2: *Diagrammatic representation of the lowest-order contribution to the electron self-energy from the electron-phonon coupling. Blue zigzag and black lines represent phonon and electron propagators, respectively.*

Electronic energies are measured with respect to the chemical potential. By applying many-body perturbation theory to the Fröhlich Hamiltonian, the interacting Green functions are expressed by an infinite series of Feynman diagrams containing the bare Green functions and an increasing number of electron-phonon vertices.

Partial resummation leads to the Dyson equations

$$G(k, i\omega_n)^{-1} = G_0(k, i\omega_n)^{-1} - \Sigma(k, i\omega_n) \tag{18}$$

$$D(q, i\nu_m)^{-1} = G_0(q, i\nu_m)^{-1} - \Pi(q, i\nu_m)\,, \tag{19}$$

which connects bare and renormalized Green functions via the electron and phonon self-energy, Σ and Π, respectively. The self-energies are defined as the sum of all one-particle irreducible Feynman diagrams, i.e., as the sum of all Feynman diagrams, which cannot be separated into two distinct graphs by cutting a single electron or phonon line.

In the following we will discuss the most important contributions to the self-energies in more detail.

3.2 Electron self-energy

The lowest-order diagram of the electron self-energy represents a virtual exchange of a phonon as shown in Fig. 2

$$\Sigma_{ep}(k, i\omega_n) = -\frac{1}{\beta}\sum_{n'}\frac{1}{N_q}\sum_{k',q} g^q_{k',k} G_0(k', i\omega_{n'})(g^q_{k',k})^* D_0(q, i\omega_{n'} - i\omega_n)\,. \tag{20}$$

With Eqs. (16) and (17), and after performing the Matsubara sum over $\omega_{n'}$ one obtains

$$\Sigma_{ep}(k, i\omega_n) = \frac{1}{N_q}\sum_{k',q} |g^q_{k',k}|^2 \left(\frac{b(\omega_q) + f(\varepsilon_{k'})}{i\omega_n + \omega_q - \varepsilon_{k'}} + \frac{b(\omega_q) + 1 - f(\varepsilon_{k'})}{i\omega_n - \omega_q - \varepsilon_{k'}} \right). \tag{21}$$

Σ_{ep} depends on temperature T via the Fermi and Bose distribution functions, $f(\varepsilon) = \left(e^{\varepsilon/T} + 1\right)^{-1}$ and $b(\omega) = \left(e^{\omega/T} - 1\right)^{-1}$, respectively.

To discuss the quasiparticle renormalization, we consider the retarded Green function, which is obtained by analytic continuation to the real axis via $i\omega_n \to \varepsilon{+}i\delta$ with an infinitesimal positive δ. It is connected to the analytic continuation of the self-energy via the Dyson equation

$$G(k,\varepsilon) = \big(\varepsilon - \varepsilon_k - \varSigma(k,\varepsilon)\big)^{-1}. \tag{22}$$

If the self-energy is small enough, the spectral function $A_k(\varepsilon) = -\operatorname{Im} G(k,\varepsilon{+}i\delta)$ consists of a well defined peak at a shifted quasiparticle energy determined by the real part of $\varSigma$

$$\bar{\varepsilon}_k = \varepsilon_k + \operatorname{Re}\varSigma(k,\bar{\varepsilon}_k)\,. \tag{23}$$

The quasiparticle acquires a finite lifetime leading to a linewidth (full width at half maximum)

$$\varGamma_k = -2\operatorname{Im}\varSigma(k,\bar{\varepsilon}_k), \tag{24}$$

which is determined by the imaginary part.

It is straightforward to perform the analytic continuation of $\varSigma_{ep}(k, i\omega_n \to \varepsilon{+}i\delta)$ in the form given in Eq. (21) and to derive the expression for the imaginary part

$$\operatorname{Im}\varSigma_{ep}(k,\varepsilon){=}{-}\frac{\pi}{N_q}\sum_{k',q}|g^q_{k',k}|^2\Big[\delta(\varepsilon{-}\varepsilon_{k'}{+}\omega_q)\big(b(\omega_{\mathbf{q}j}){+}f(\varepsilon_{k'})\big){+}\delta(\varepsilon{-}\varepsilon_{k'}{-}\omega_q)\big(b(\omega_q){+}1{-}f(\varepsilon_{k'})\big)\Big]. \tag{25}$$

This can be rewritten by introducing two spectral functions

$$\alpha^2F^{\pm}_k(\varepsilon,\omega) = \frac{1}{N_q}\sum_q \delta(\omega{-}\omega_q)\sum_{k'}|g^q_{k',k}|^2\,\delta(\varepsilon{-}\varepsilon_{k'}{\pm}\omega)\,. \tag{26}$$

They depend on the electronic state k via the EPC vertex. The imaginary part can then be cast in the form

$$\operatorname{Im}\varSigma_{ep}(k,\varepsilon) = -\pi\int_0^\infty\! d\omega\Big(\alpha^2F^+_k(\varepsilon,\omega)\big[b(\omega){+}f(\omega{+}\varepsilon)\big]{+}\alpha^2F^-_k(\varepsilon,\omega)\big[b(\omega){+}f(\omega{-}\varepsilon)\big]\Big)\,. \tag{27}$$

The physical interpretation of this expression is as follows. When a quasiparticle hole is created at a state k ($\varepsilon < \varepsilon_F$), electrons can scatter from states with higher or lower energies, respectively (see Fig. 3). By conservation of energy, the first process involves a simultaneous emission of a phonon, while the second one is related to the absorption of a phonon. The probability is described by $\alpha^2F^-_k$ and $\alpha^2F^+_k$, respectively, weighted with the appropriate bosonic and fermionic distribution functions. Both processes provide decay channels contributing additively to the linewidth (inverse lifetime) of the quasiparticle. A similar description holds when a quasiparticle (electron) is created at energies above the Fermi level.

Very often, a simplification is made which is called quasielastic approximation. Because the electronic energy scale is typically much larger than the phonon energies, differences between emission and absorption spectra are rather small, and it is well justified to ignore the phonon energy ω_q in the δ-function of (26), such that $\alpha^2F^{\pm}_k \approx \alpha^2F_k$ with

$$\alpha^2F_k(\varepsilon,\omega) = \frac{1}{N_q}\sum_q \delta(\omega{-}\omega_q)\sum_{k'}|g^q_{k',k}|^2\,\delta(\varepsilon{-}\varepsilon_{k'})\,. \tag{28}$$

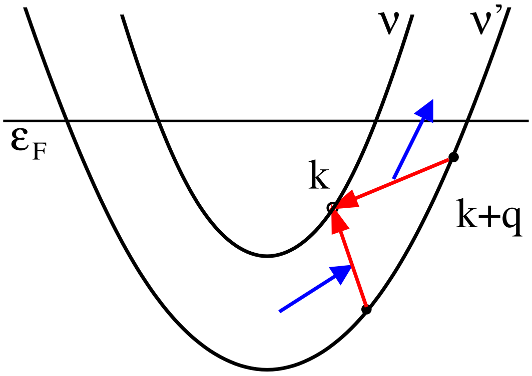

Fig. 3: *Illustration of the scattering processes contributing to the self-energy of a hole quasi-particle with momentum* $\mathbf{k}$ *and band index* ν*. Electrons (red lines) can scatter virtually from states with higher or lower energies under simultaneous emission or absorption of a phonon (blue lines), respectively.*

The self-energy then simplifies to

$$\mathrm{Im}\,\Sigma_{ep}(k,\varepsilon) = -\pi \int_0^\infty d\omega \left(\alpha^2 F_k(\varepsilon,\omega) \big[2b(\omega) + f(\omega{+}\varepsilon) + f(\omega{-}\varepsilon) \big] \right) . \tag{29}$$

It is instructive to evaluate this expression for the simple Einstein model, where only a single dispersionless phonon mode with energy Ω couples to the electrons. In the limit $T \to 0$ one finds

$$\mathrm{Im}\,\Sigma_{ep}(k,\varepsilon) \to -\pi A(\varepsilon) \big(2 - \Theta(\Omega{-}\varepsilon) - \Theta(\Omega{+}\varepsilon) \big) , \tag{30}$$

where $\Theta(x)$ denotes the Heaviside step function, and $A(\varepsilon) = 1/N_k \sum_{k',q} |g^q_{k',k}|^2 \, \delta(\varepsilon{-}\varepsilon_{k'})$ represents the density of states at energy ε weighted by scattering matrix elements. Typically $A(\varepsilon)$ is slowly varying on the scale of phonon energies. In contrast, $\Sigma_{ep}(\varepsilon)$ vanishes for energies $|\varepsilon| < \Omega$ and shows a step at Ω, because of the presence of the step functions. This reflects the fact that no phonon modes are available for decay when $|\varepsilon| < \Omega$. $\mathrm{Re}\,\Sigma_{ep}$ can be obtained via the Kramers-Kronig relation

$$\mathrm{Re}\,\Sigma_{ep}(k,\varepsilon) = \frac{1}{\pi} \int d\varepsilon' \, \frac{\mathrm{Im}\,\Sigma_{ep}(k,\varepsilon')}{\varepsilon - \varepsilon'} . \tag{31}$$

As shown in Fig. 4(a) it contains a maximum at $\varepsilon = \Omega$ and has a finite slope at $\varepsilon \to 0$. The resulting dispersion for the renormalized quasiparticle is sketched in Fig. 4(b). It shows two characteristics: (i) the dispersion is strongly modified in the vicinity of ε_F in the range of phonon energies, altering the Fermi velocity related to the slope of $\mathrm{Re}\,\Sigma_{ep}(\varepsilon \to 0)$. (ii) A cusp appears at $\varepsilon = \pm\Omega$.

For a more realistic phonon spectrum which covers continuously an energy range $0 \le \omega \le \omega_{\max}$, the step-like feature in $\mathrm{Im}\,\Sigma_{ep}(\varepsilon)$ is washed out, but $\Sigma_{ep}(\varepsilon)$ still varies rapidly in the energy range of the phonons. The cut in the renormalized dispersion is then replaced by a kink. An example of an experimentally determined self-energy is given in Fig. 4(c) and (d).

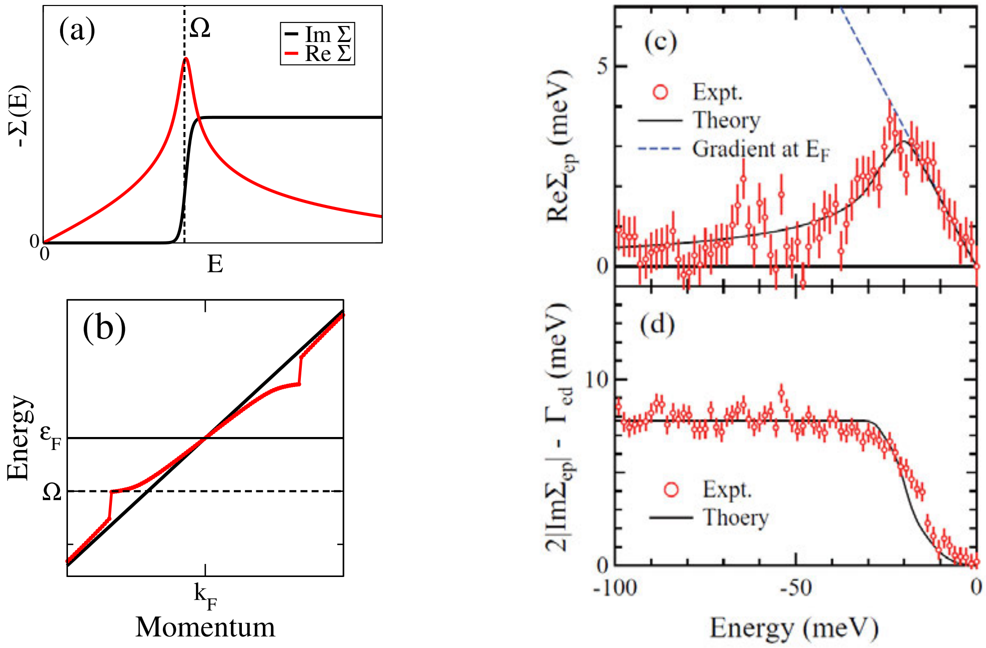

Fig. 4: *Illustration of the renormalization of an electronic band coupling to an Einstein-type phonon branch with energy Ω. (a) Real and imaginary part of the electron self-energy. (b) Renormalized quasiparticle dispersion, showing a kink at the phonon frequency. (c) Real and (d) imaginary part of the electron self-energy extracted from angle-resolved photoemission spectroscopy measurements taken for an electronic surface band of the Cu(110) surface. After Jiang* et al. *[8]*

The spectral function $\alpha^2 F_k$ contains the essential information related to the electron-phonon coupling of the specific electronic state $k = (\mathbf{k}\nu)$. A convenient measure for the strength of the EPC is the dimensionless coupling parameter

$$\lambda_k = 2 \int d\omega \, \frac{\alpha^2 F_k(\bar{\varepsilon}_k, \omega)}{\omega} \, . \tag{32}$$

It characterizes the strength of the coupling of a specific electronic state to the whole phonon spectrum, and depends both on the momentum and band character of the electronic state.

There are two relations which connect this parameter to experimentally accessible quantities. The first is related to the real part of the self-energy for an electronic band crossing the Fermi level:

$$\lambda_k = \left. \frac{\partial \, \mathrm{Re}\, \Sigma_{ep}(k, \varepsilon)}{\partial \varepsilon} \right|_{\varepsilon=0, T=0} \, . \tag{33}$$

Thus the coupling constant is given by the slope of $\mathrm{Re}\, \Sigma_{ep}$ right at the Fermi energy in the limit $T \to 0$. λ_k is also called the mass-enhancement parameter, because the quasiparticle velocity is changed to $v_F^* = v_F/(1+\lambda_k)$ and can be interpreted as an enhanced effective mass $m_k^* = m_k(1+\lambda_k)$, where m_k denotes the unrenormalized mass. Eq. (33) is often utilized in ARPES measurements of bands crossing the Fermi level, which attempt to extract the energy dependence of the real part of the self-energy.

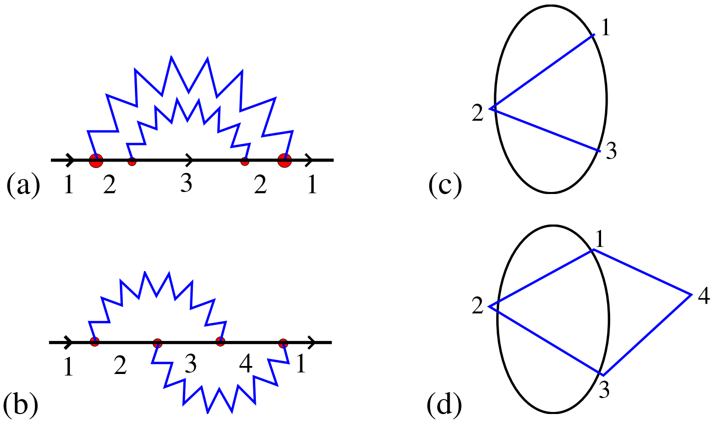

Fig. 5: *(a) and (b) Diagrammatic representation of the two second-order contributions to the electron self-energy. Blue zigzag lines represent phonons and black lines electron propagators. (c) and (d) Schematic drawing of Fermi surface and states contributing to the graphs (a) and (b), respectively.*

A second route to determine the coupling constant of an electronic state is via the temperature dependence of the linewidth

$$\varGamma_k(T) = \pi \int_0^\infty d\omega \Big(\alpha^2 F_k(\bar{\varepsilon}_k, \omega) \big(2b(\omega) + f(\omega + \bar{\varepsilon}_k) + f(\omega - \bar{\varepsilon}_k) \big) \Big) . \tag{34}$$

In Eq. (34), the T-dependence it contained solely in the Bose and Fermi distribution functions. For $T \to 0$, it approaches a finite value given by

$$\varGamma_k(T) \to 2\pi \int_0^{\omega_{\max}} d\omega \, \alpha^2 F_k(\bar{\varepsilon}_k, \omega) \, . \tag{35}$$

With increasing T, the linewidth increases monotonously. For temperatures larger than the maximum phonon frequencies, this T-dependence becomes almost linear, and its slope is determined by the average coupling parameter defined above

$$\varGamma_k(T) \approx 2\pi \lambda_k T \, . \tag{36}$$

This relationship has been widely used to extract λ_k from measurements of $\varGamma_k(T)$, in particular for surface electronic states.

3.3 Migdal's theorem

So far we have discussed the influence of phonons on the electronic properties in lowest order of the electron-phonon coupling. What about higher-order corrections? A very important answer is given by the *Migdal's theorem*, which is relevant for both the normal-state properties discussed here and the Eliashberg theory of superconductivity presented in the next section. We give only a very brief qualitative discussion here, more details can be found in literature [9,10,7].

Fig. 6: *(a) Diagrammatic representation of the imaginary part of the phonon self-energy up to second order in the electron-phonon vertex. Blue zigzag lines represent phonons, black lines electron propagators.*

Fig. 5 (a) and (b) show two next-order corrections to Σ_{ep}. The first is a self-energy contribution to an inner line and can be taken into account by using the full Green function G for the intermediate state instead of G_0. In contrast, the graph in Fig. 5(b) is a *vertex correction*. Migdal's theorem now states that vertex corrections are small and can be neglected. More precisely, this is true for those parts of the renormalized Green function which are sensitive to the phonons. Such contributions involve intermediate states whose energies are close to each other.

Fig. 5(c) and (d) show schematically the Fermi surfaces and states which make a contribution to the graphs in Fig. 5 (a) and (b), respectively. The first case contains only small energy differences $\varepsilon_{12} = \varepsilon_1 - \varepsilon_2$ and ε_{13}. In the second case, momentum conservation leads to a large difference ε_{14}. This unfavorable situation can only be avoided when one of the intermediate phonon momenta becomes small. Migdal showed, that for normal metals the phase space for such processes is very small, and the contribution from graph Fig. 5(d) is by a factor ω_D/ε_F smaller than that from graph (a), where ω_D denotes the Debye frequency and ε_F the Fermi energy. ω_D/ε_F is of the order of 0.1 for typical phononic and electronic energy scales.

The phase space argument of Migdal's theorem breaks down in two circumstances: (i) For a significant part of processes both phonons have small q (both $k_2 - k_1$ and $k_3 - k_2$ are small). This can happen in metals with very small Fermi surfaces, for example in low-doped semiconductors. (ii) Metals with a one-dimensional Fermi surface topology (quasi-1D). In addition, Migdal's theorem becomes questionable in the case of metals with very small band widths, where the ratio ω_D/ε_F is not small any more.

According to Migdal's theorem, Σ_{ep} is well represented by the single graph shown in Fig. 2, except that G_0 is replaced by G, and other contributions can be neglected. According to arguments given by Migdal and Holstein, this replacement again gives small corrections of the order of ω_D/ε_F. [9, 11]. Thus to a good approximation it is justified to use G_0, so the previous formulas still hold. This approximation does not work anymore for the superconducting state, as discussed in the next section.

However, the analysis given above rests on a simplified solution of the Dyson equation which can break down for larger coupling. Then the renormalization becomes much more involved and requires the solution of the Dyson equation in the complex plane [12]. The spectral function develops a complex structure, which indicates the break-down of the quasiparticle picture.

3.4 Phonon self-energy and linewidth

The EPC also renormalizes the phononic quasiparticles. The measurement of the phonon linewidth actually provides another way to gain experimental information about the coupling strength. We will briefly sketch this approach here.

The finite linewidth or inverse lifetime of a phonon mode is connected to the imaginary part of the phonon self-energy by $\gamma_q = -2\,\mathrm{Im}\,\mathit{\Pi}_q(\omega)$. The lowest-order contribution to $\mathrm{Im}\,\mathit{\Pi}_q(\omega)$ is derived from the diagram shown in Fig. 6

$$\mathit{\Pi}_q(i\nu_m) = \frac{1}{\beta}\sum_n \frac{1}{N_k}\sum_{k,k'} \left|g^q_{k',k}\right|^2 G_0(k,i\omega_n)\, G_0(k'\nu', i\omega_n{+}i\nu_m) = \frac{1}{N_k}\sum_{k',k} \left|g^q_{k',k}\right|^2 \frac{f(\varepsilon_k)-f(\varepsilon_{k'})}{i\nu_m{+}\varepsilon_k{-}\varepsilon_{k'}}, \tag{37}$$

leading after analytic continuation to the following expression for the linewidth (half-width at half maximum)

$$\gamma_q = -2\,\mathrm{Im}\,\mathit{\Pi}_q(\omega_q) = 2\pi\frac{1}{N_k}\sum_{k',k} \left|g^q_{k',k}\right|^2 \big(f(\varepsilon_k) - f(\varepsilon_{k'})\big)\, \delta\big(\omega_q + (\varepsilon_k{-}\varepsilon_{k'})\big)\,. \tag{38}$$

This expression contains the T-dependence via the Fermi distribution function f. Because phonon energies are typically small compared to electronic energies, the energy difference $\varepsilon_k{-}\varepsilon_{k'}$ is also small, and one can approximate

$$f(\varepsilon_k) - f(\varepsilon_{k'}) \approx f'(\varepsilon_k)(\varepsilon_k{-}\varepsilon_{k'}) \to -f'(\varepsilon_k)\omega_q \tag{39}$$

with $f' = df/d\varepsilon$. For $T \to 0$, $f'(\varepsilon_k) \to -\delta(\varepsilon_k)$, and by neglecting ω_q inside the δ-function, the expression further simplifies to

$$\gamma_q = 2\pi\omega_q\frac{1}{N_k}\sum_{k',k} \left|g^q_{k',k}\right|^2 \delta(\varepsilon_k)\,\delta(\varepsilon_{k'})\,. \tag{40}$$

This approximate expression for the linewidth, first derived by Allen [13], is widely used in numerical calculations. As will be discussed in the next section, γ_q in the form of Eq. (40) enters directly the expression for the coupling strength of a phonon mode relevant for superconductivity. Thus measurements of the phonon linewidths, for example by inelastic neutron or X-ray scattering experiments, provide information about the importance of a phonon mode for the pairing. One has to keep in mind, however, that γ_q only represents the contribution from EPC, while the experimental linewidth also contains other contributions like those from anharmonic decay processes. Furthermore, approximation (40) does not hold in the limit $\mathbf{q} \to 0$ for metals, because the phonon frequency in Eq. (38) cannot be neglected anymore for intraband contributions, which involve arbitrarily small energy differences $\varepsilon_k{-}\varepsilon_{k'}$.

4 Phonon-mediated superconductivity

Superconductivity is a macroscopic quantum phenomenon of the electron system. Its origin lies in an instability of the Fermi liquid state that leads to a new ground state of correlated paired electrons (Cooper pairs). In their seminal paper, Bardeen, Cooper, and Schrieffer (BCS) [14] have shown that this state is stabilized, whenever there exists an attractive interaction among two electrons. Such an attractive interaction is always provided by the electron-phonon coupling, which thus represents a natural source for pairing in any metal. EPC is known to be the pairing mechanism in most superconductors, which are commonly termed classical superconductors to distinguish them from more exotic materials where other types of pairing mechanism are suspected.

The BCS theory treated the EPC only in a simplified form appropriate for the weak coupling limit. A more complete theory has been soon after worked out applying many-body techniques (for reviews see, e.g., Refs. [15–17, 10]). The resulting Eliashberg theory [18] extends the framework of BCS into the strong coupling regime and allows a quantitative prediction of many properties of the superconducting state. An important property of the superconducting state is that the quasiparticle spectrum is gaped. The size of the gap plays the role of an order parameter. In the following, we discuss the essential ingredients of the theory of strong-coupling phonon-mediated superconductivity, also known as the Migdal-Eliashberg theory. First, we give a simple derivation of an effective electron-electron interaction mediated by phonons. Using many-body techniques we then derive the superconducting gap equations and identify the important quantities related to the electron-phonon coupling, which determine the superconducting properties.

4.1 Effective electron-electron interaction

The coupling of the electrons to the phonon system does introduce an effective electron-electron interaction, which can act as a pairing interaction evoking the superconducting state. The general approach using many-body techniques will be discussed below. Here a simple but instructive derivation of the effective interaction is given with the help of a properly chosen canonical transformation. To simplify the discussion, we will consider the case of a single, spinless quasiparticle band coupled to a single phonon (boson) mode. The Fröhlich Hamiltonian then reads ($g_{\mathbf{k},\mathbf{q}} \equiv g^{\mathbf{q}}_{\mathbf{k}+\mathbf{q},\mathbf{k}}$)

$$H = \sum_{\mathbf{k}} \varepsilon_{\mathbf{k}}\, c^{\dagger}_{\mathbf{k}} c_{\mathbf{k}} + \sum_{\mathbf{q}} \omega_{\mathbf{q}} \left(b^{\dagger}_{\mathbf{q}} b_{\mathbf{q}} + \frac{1}{2} \right) + \sum_{\mathbf{k}\mathbf{q}} g_{\mathbf{k},\mathbf{q}}\, c^{\dagger}_{\mathbf{k}+\mathbf{q}} c_{\mathbf{k}} \left(b_{\mathbf{q}} + b^{\dagger}_{-\mathbf{q}} \right) . \tag{41}$$

Let us consider the Hamiltonian

$$H = H_0 + \eta H_1 , \tag{42}$$

where H_0 is the unperturbed Hamiltonian, H_1 the perturbation, and η represents an expansion coefficient, which is considered to be small. The idea is to perform a canonical transformation

$$H' = e^{-\eta S} H e^{\eta S} \tag{43}$$

and eliminate the first-order term in η by choosing the operator S appropriately. Expanding Eq. (43) in a power series in η gives

$$\begin{aligned} H' &= H + \eta[H,\, S] + \frac{\eta^2}{2}\big[[H,\, S], S\big] + \mathcal{O}(\eta^3) && (44) \\ &= H_0 + \eta\big(H_1 + [H_0,\, S]\big) + \eta^2[H_1,\, S] + \frac{\eta^2}{2}\big[[H_0,\, S],\, S\big] + \mathcal{O}(\eta^3) . && (45) \end{aligned}$$

To eliminate the term linear in η one has to find an S which fulfills the condition

$$H_1 + [H_0,\, S] = 0\,. \tag{46}$$

Then the transformed Hamiltonian can be written as

$$H' = H_0 + H_{\text{eff}} + O(\eta^3) \qquad \text{with} \qquad H_{\text{eff}} = \frac{\eta^2}{2}[H_1, S]\,. \tag{47}$$

This general approach is now applied to the Fröhlich Hamiltonian (41) with $H_0 = H_e + H_{ph}$ and $\eta H_1 = H_{e\text{-}ph}$. For the canonical operator we make the ansatz

$$S = \sum_{\mathbf{kq}} g_{\mathbf{k},\mathbf{q}}\, c^\dagger_{\mathbf{k}+\mathbf{q}} c_{\mathbf{k}} \left(x_{\mathbf{k},\mathbf{q}} b_{\mathbf{q}} + y_{\mathbf{k},\mathbf{q}} b^\dagger_{-\mathbf{q}} \right)\,. \tag{48}$$

The parameters $x_{\mathbf{k},\mathbf{q}}$ and $y_{\mathbf{k},\mathbf{q}}$ will be determined in order to fulfill Eq. (46). Evaluating the commutators gives

$$[H_e,\, S] \;=\; \sum_{\mathbf{kq}} g_{\mathbf{k},\mathbf{q}} \left(\varepsilon_{\mathbf{k}+\mathbf{q}} - \varepsilon_{\mathbf{k}}\right) c^\dagger_{\mathbf{k}+\mathbf{q}} c_{\mathbf{k}} \left(x_{\mathbf{k},\mathbf{q}} b_{\mathbf{q}} + y_{\mathbf{k},\mathbf{q}} b^\dagger_{-\mathbf{q}} \right) \tag{49}$$

$$[H_{ph},\, S] \;=\; \sum_{\mathbf{kq}} g_{\mathbf{k},\mathbf{q}} c^\dagger_{\mathbf{k}+\mathbf{q}} c_{\mathbf{k}} \left(-x_{\mathbf{k},\mathbf{q}} \omega_{\mathbf{q}} b_{\mathbf{q}} + y_{\mathbf{k},\mathbf{q}} \omega_{-\mathbf{q}} b^\dagger_{-\mathbf{q}} \right)\,. \tag{50}$$

Using the relation $\omega_{\mathbf{q}} = \omega_{-\mathbf{q}}$ this combines to

$$H_1 + [H_0,\, S] = \sum_{\mathbf{kq}} g_{\mathbf{k},\mathbf{q}}\, c^\dagger_{\mathbf{k}+\mathbf{q}} c_{\mathbf{k}} \Big(\big(1 + (\varepsilon_{\mathbf{k}+\mathbf{q}} - \varepsilon_{\mathbf{k}} - \omega_{\mathbf{q}}) x_{\mathbf{k},\mathbf{q}}\big) b_{\mathbf{q}} + \big(1 + (\varepsilon_{\mathbf{k}+\mathbf{q}} - \varepsilon_{\mathbf{k}} + \omega_{\mathbf{q}}) y_{\mathbf{k},\mathbf{q}}\big) b^\dagger_{-\mathbf{q}} \Big). \tag{51}$$

This expression vanishes when

$$x_{\mathbf{k},\mathbf{q}} = \left(\varepsilon_{\mathbf{k}} - \varepsilon_{\mathbf{k}+\mathbf{q}} + \omega_{\mathbf{q}}\right)^{-1} \quad \text{and} \quad y_{\mathbf{k},\mathbf{q}} = \left(\varepsilon_{\mathbf{k}} - \varepsilon_{\mathbf{k}+\mathbf{q}} - \omega_{\mathbf{q}}\right)^{-1}. \tag{52}$$

The last step is to evaluate the effective interaction Eq. (47). The commutator $[H_1,\, S]$ has the form $[Aa,\, Bb]$ with $A, B \propto c^\dagger c$ containing products of fermion operators, and $a, b \propto xb + yb^\dagger$ containing sums of boson operators. From the general relationship $[Aa,\, Bb] = AB[a,\, b] + [A,\, B]ab - [A,\, B][a,\, b]$ it is easy to see that there are three types of contributions. Keeping in mind that $[A,\, B]$ is again a product of the form $c^\dagger c$ and $[a,\, b]$ a c-number, the last term represents a one-body electron operator, which actually can be shown to vanish. The second term describes an effective coupling of an electron to two phonons, also called a non-linear coupling term.

We are interested in the first term, which is proportional to the product of two fermionic creation and two annihilation operators, $c^\dagger c c^\dagger c$, and thus represents an effective electron-electron interaction. Explicitly it has the form

$$H_{\text{eff}} \;=\; \frac{\eta^2}{2} \sum_{\mathbf{kk'q}} g_{\mathbf{k},\mathbf{q}}\, g_{\mathbf{k'},-\mathbf{q}} \big(y_{\mathbf{k'},-\mathbf{q}} - x_{\mathbf{k'},-\mathbf{q}} \big)\, c^\dagger_{\mathbf{k}+\mathbf{q}} c_{\mathbf{k}} c^\dagger_{\mathbf{k'}-\mathbf{q}} c_{\mathbf{k'}} \tag{53}$$

$$\;=\; \eta^2 \sum_{\mathbf{kk'q}} V_{\text{eff}}(\mathbf{k}, \mathbf{k'}, \mathbf{q})\, c^\dagger_{\mathbf{k}+\mathbf{q}} c_{\mathbf{k}} c^\dagger_{\mathbf{k'}-\mathbf{q}} c_{\mathbf{k'}} \tag{54}$$

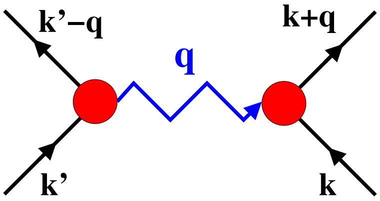

Fig. 7: *Diagrammatic representation of the effective electron-electron interaction mediated by the exchange of a phonon (blue zigzag line). Black lines indicate electronic states.*

with

$$V_{\text{eff}}(\mathbf{k},\mathbf{k}',\mathbf{q}) = g_{\mathbf{k},\mathbf{q}}g_{\mathbf{k}',-\mathbf{q}}\frac{\omega_{\mathbf{q}}}{(\varepsilon_{\mathbf{k}'}-\varepsilon_{\mathbf{k}'-\mathbf{q}})^2-\omega_{\mathbf{q}}^2}\,. \tag{55}$$

H_{eff} describes the scattering of two electrons with momenta $\mathbf{k}$ and $\mathbf{k}'$ into states with momenta $\mathbf{k}+\mathbf{q}$ and $\mathbf{k}'-\mathbf{q}$ by the exchange of a virtual boson with momentum $\mathbf{q}$. This process is sketched in Fig. 7.

In the context of pairing in superconductors, the effective interaction between electrons with momenta $\mathbf{k}$ and $-\mathbf{k}$ is of special importance. Using $\varepsilon_{-\mathbf{k}}=\varepsilon_{\mathbf{k}}$ and $g_{-\mathbf{k},-\mathbf{q}}=g^*_{\mathbf{k},\mathbf{q}}$ one obtains

$$V_{\text{eff}}(\mathbf{k},-\mathbf{k},\mathbf{q}) = |g_{\mathbf{k},\mathbf{q}}|^2\frac{\omega_{\mathbf{q}}}{(\varepsilon_{\mathbf{k}}-\varepsilon_{\mathbf{k}+\mathbf{q}})^2-\omega_{\mathbf{q}}^2}\,. \tag{56}$$

This effective interaction is attractive (negative) for $|\varepsilon_{\mathbf{k}}-\varepsilon_{\mathbf{k}+\mathbf{q}}| < \omega_{\mathbf{q}}$ and repulsive (positive) for $|\varepsilon_{\mathbf{k}}-\varepsilon_{\mathbf{k}+\mathbf{q}}| > \omega_{\mathbf{q}}$. Eq. (56) shows that the electron-phonon coupling always introduces an attractive interaction for electronic scattering processes involving small energies of the order of phonon energies.

4.2 Strong-coupling theory

4.2.1 Nambu formalism

The superconducting state is a macroscopic quantum state, which is characterized by a coherent occupation of Cooper pairs, i.e., states with $(k\uparrow,-k\downarrow)$. In a many-body description, it is related to the appearance of anomalous Green functions

$$F(k,\tau) = -\big\langle T_\tau c_{k\uparrow}(\tau)c_{-k\downarrow}(0)\big\rangle \quad \text{and} \quad F^*(k,\tau) = -\big\langle T_\tau c^\dagger_{-k\downarrow}(\tau)c^\dagger_{k\uparrow}(0)\big\rangle \tag{57}$$

originally introduced by Gor'kov [19]. In the normal state these anomalous Green functions vanish. Starting from the Fröhlich Hamiltonian, one can set up a systematic perturbation expansion of the normal and anomalous Green functions, with the goal to obtain a set of self-consistent equations. A necessary step is a partial resummation of an infinite number of diagrams, because the superconducting state can not be reached in any finite order of the perturbation.

A very convenient way to organize this algebra of diagrams has been introduced by Nambu [20]. One starts by defining the two-component operators

$$\Psi_k = \begin{pmatrix} c_{k\uparrow} \\ c^\dagger_{-k\downarrow} \end{pmatrix} \qquad \Psi^\dagger_k = \begin{pmatrix} c^\dagger_{k\uparrow}, & c_{-k\downarrow} \end{pmatrix} \tag{58}$$

and a 2×2 Green function

$$\begin{aligned} \underline{G}(k,\tau) &= -\big\langle T_\tau \Psi_k(\tau)\Psi^\dagger_k(0)\big\rangle = -\begin{pmatrix} \big\langle T_\tau c_{k\uparrow}(\tau)c^\dagger_{k\uparrow}(0)\big\rangle & \big\langle T_\tau c_{k\uparrow}(\tau)c_{-k\downarrow}(0)\big\rangle \\ \big\langle T_\tau c^\dagger_{-k\downarrow}(\tau)c^\dagger_{k\uparrow}(0)\big\rangle & \big\langle T_\tau c^\dagger_{-k\downarrow}(\tau)c_{-k\downarrow}(0)\big\rangle \end{pmatrix} \\ &= \begin{pmatrix} G(k,\tau) & F(k,\tau) \\ F^*(k,\tau) & -G(-k,-\tau) \end{pmatrix} . \end{aligned} \tag{59}$$

In the following, underlined symbols indicate 2×2 matrices in spin space. Switching to the Fourier transform gives

$$\underline{G}(k,i\omega_n) = \frac{1}{2}\int_{-\beta}^{\beta} d\tau\, e^{i\omega_n\tau}\underline{G}(k,\tau) = \begin{pmatrix} G(k,i\omega_n) & F(k,i\omega_n) \\ F^*(k,-i\omega_n) & -G(-k,-i\omega_n) \end{pmatrix} . \tag{60}$$

The next step is to rewrite the Fröhlich Hamiltonian in terms of $\Psi, \Psi^\dagger$. This is most easily done by using the Pauli matrices

$$\underline{\tau}_0 = \begin{pmatrix} 1 & 0 \\ 0 & 1 \end{pmatrix}, \ \underline{\tau}_1 = \begin{pmatrix} 0 & 1 \\ 1 & 0 \end{pmatrix}, \ \underline{\tau}_2 = \begin{pmatrix} 0 & -i \\ i & 0 \end{pmatrix}, \ \underline{\tau}_3 = \begin{pmatrix} 1 & 0 \\ 0 & -1 \end{pmatrix} . \tag{61}$$

The non-interacting electronic part is rewritten as

$$H_e = \sum_{k\sigma} \varepsilon_k\, c^\dagger_{k\sigma}c_{k\sigma} \to \sum_k \varepsilon_k\, \Psi^\dagger_k \underline{\tau}_3 \Psi_k \tag{62}$$

and the interaction part as

$$H_{e\text{-}ph} = \sum_{k\sigma}\sum_{\mathbf{q}j} g^q_{k'k}\, c^\dagger_{k'\sigma}c_{k\sigma}\left(b_q + b^\dagger_{-q}\right) \to \sum_k g^q_{k'k}\, \Psi^\dagger_{k'}\underline{\tau}_3\Psi_k \left(b_q + b^\dagger_{-q}\right) . \tag{63}$$

The bare Green function (related to H_e) takes the form

$$\underline{G}_0(k,i\omega_n) = \begin{pmatrix} G_0(k,i\omega_n) & 0 \\ 0 & -G_0(-k,-i\omega_n) \end{pmatrix} = \begin{pmatrix} (i\omega_n - \varepsilon_k)^{-1} & 0 \\ 0 & (i\omega_n + \varepsilon_k)^{-1} \end{pmatrix} = \left(i\omega_n\underline{\tau}_0 - \varepsilon_k\underline{\tau}_3\right)^{-1} . \tag{64}$$

One can show that the Dyson equation retains its usual form

$$\underline{G}^{-1}(k,i\omega_n) = \underline{G}_0^{-1}(k,i\omega_n) - \underline{\Sigma}(k,i\omega_n) \tag{65}$$

with the inversion performed in the 2-dimensional spin space, where the self-energy $\underline{\Sigma}$ is now a 2×2 matrix.

The diagrammatic expansion of the self-energy contains the same diagrams as in the normal state, with the difference that Green functions and vertices are now represented by 2×2 matrices. In particular $g^q_{k'k}$ is replaced by $g^q_{k'k}\,\underline{\tau}_3$.

4.2.2 Eliashberg theory

The Eliashberg theory is in essence the extension of the normal-state Migdal theory to the superconducting state. Using Migdal's theorem, the only important self-energy diagram is again given by Fig. 2. Within the Nambu formulation this gives

$$\underline{\Sigma}(k,i\omega_n) = -\frac{1}{\beta}\sum_{n'}\frac{1}{N_q}\sum_{k',q} g^q_{k'k}\,\underline{\tau}_3\,\underline{G}(k',i\omega_{n'})\,\underline{\tau}_3\,g^{-q}_{kk'}\,D(q,i\omega_{n'}{-}i\omega_n)\,. \tag{66}$$

Using the Pauli matrices, $\underline{\Sigma}$ can be written in the general form

$$\underline{\Sigma}(k,i\omega_n) = i\omega_n\big(1{-}Z(k,i\omega_n)\big)\underline{\tau}_0 + \chi(k,i\omega_n)\underline{\tau}_3 + \Phi(k,i\omega_n)\underline{\tau}_1 + \overline{\Phi}(k,i\omega_n)\underline{\tau}_2 \tag{67}$$

with as yet unknown and independent real functions Z,χ,Φ, and $\overline{\Phi}$. From the Dyson equation one finds

$$\underline{G}^{-1}(k,i\omega_n) = i\omega_n Z(k,i\omega_n)\underline{\tau}_0 - \big(\varepsilon_k{+}\chi(k,i\omega_n)\big)\underline{\tau}_3 - \Phi(k,i\omega_n)\underline{\tau}_1 - \overline{\Phi}(k,i\omega_n)\underline{\tau}_2\,. \tag{68}$$

The inverted Green function is then, using $\big(a_0\underline{\tau}_0 + \vec{a}\cdot\vec{\underline{\tau}}\big)\big(a_0\underline{\tau}_0 - \vec{a}\cdot\vec{\underline{\tau}}\big) = (a_0^2{-}\vec{a}^2)\underline{\tau}_0$

$$\underline{G}(k,i\omega_n) = \Big(i\omega_n Z(k,i\omega_n)\underline{\tau}_0 + \big(\varepsilon_k{+}\chi(k,i\omega_n)\big)\underline{\tau}_3 + \Phi(k,i\omega_n)\underline{\tau}_1 + \overline{\Phi}(k,i\omega_n)\underline{\tau}_2\Big)/\mathcal{D} \tag{69}$$

with $\mathcal{D} := \det \underline{G}^{-1} = (i\omega_n Z)^2 - (\varepsilon_k{+}\chi)^2 - \Phi^2 - \overline{\Phi}^2$. If one uses this expression for Eq. (66) and separates it into the τ-components, one arrives at four self-consistent equations for the four unknown functions Z, χ, Φ, and $\overline{\Phi}$

$$\begin{aligned}
i\omega_n\big(1{-}Z(k,i\omega_n)\big) &= -\frac{1}{\beta}\sum_{n'}\frac{1}{N_q}\sum_{k',q}\big|g^q_{k'k}\big|^2 D(q,i\omega_{n'}{-}i\omega_n)\,\frac{i\omega_{n'}Z(k',i\omega_{n'})}{\mathcal{D}(k',i\omega_{n'})}\\
\chi(k,i\omega_n) &= -\frac{1}{\beta}\sum_{n'}\frac{1}{N_q}\sum_{k',q}\big|g^q_{k'k}\big|^2 D(q,i\omega_{n'}{-}i\omega_n)\,\frac{\varepsilon_{k'}+\chi(k',i\omega_{n'})}{\mathcal{D}(k',i\omega_{n'})}\\
\Phi(k,i\omega_n) &= \frac{1}{\beta}\sum_{n'}\frac{1}{N_q}\sum_{k',q}\big|g^q_{k'k}\big|^2 D(q,i\omega_{n'}{-}i\omega_n)\,\frac{\Phi(k',i\omega_{n'})}{\mathcal{D}(k',i\omega_{n'})}\\
\overline{\Phi}(k,i\omega_n) &= \frac{1}{\beta}\sum_{n'}\frac{1}{N_q}\sum_{k',q}\big|g^q_{k'k}\big|^2 D(q,i\omega_{n'}{-}i\omega_n)\,\frac{\overline{\Phi}(k',i\omega_{n'})}{\mathcal{D}(k',i\omega_{n'})}\,.
\end{aligned} \tag{70}$$

We note that because momentum conservation determines the phonon momentum, $\mathbf{q} = \mathbf{k}'{-}\mathbf{k}$, the sum over q is actually only a sum over different phonon branches (j).
Quasiparticle properties are determined by the poles of the Green function after analytic continuation, i.e., from $\mathcal{D}(k,i\omega_n \to \varepsilon{+}i\delta) = 0$. This gives

$$E_k = \sqrt{\frac{(\varepsilon_k+\chi)^2}{Z^2} + \frac{\Phi^2+\overline{\Phi}^2}{Z^2}}\,. \tag{71}$$

The normal state corresponds to a solution $\Phi = \overline{\Phi} = 0$. Z is the quasiparticle renormalization factor, and χ describes shifts in the electron energies. The superconducting state is characterized by a non-zero Φ or $\overline{\Phi}$. From Eq. (71) one can see that the gap function is given by

$$\varDelta(k,i\omega_n)=\frac{\varPhi(k,i\omega_n)-i\overline{\varPhi}(k,i\omega_n)}{Z(k,i\omega_n)} \tag{72}$$

and describes the energy gap in the quasiparticle spectrum. $\varPhi$ and $\overline{\varPhi}$ obey the same equations and are expected to have the same functional form up to a common phase factor. This phase factor becomes important in the description of Josephson junctions, but is irrelevant for the thermodynamic properties of a homogeneous superconductor. In the following, we choose the simple gauge $\overline{\varPhi}=0$.

4.2.3 Isotropic gap equations

The Eliashberg equations (70) represent a complicated non-linear set of equations which couple all momenta k with each other. We will now simplify them and derive the so-called isotropic equations where only the frequency dependence remains. A very detailed derivation was given by Allen and Mitrović [10]. Here we only briefly sketch the main steps. (i) We ignore changes of the phonon quasiparticles and replace D by the unrenormalized Green function

$$D(q,i\nu_m)\rightarrow D_0(q,i\nu_m)=\int d\omega\;\delta(\omega-\omega_q)\,\frac{2\omega}{(i\nu_m)^2-\omega^2}\,. \tag{73}$$

(ii) Similar to the normal state, the electron-phonon self-energy evokes a significant renormalization of quasiparticles only in an energy range $\pm\omega_D$ around the Fermi energy. It is therefore appropriate to consider the quantities Z and ϕ only at the Fermi energy. (iii) We consider only Fermi-surface averages of these quantities. The justification comes from the observation that the superconducting gaps are often very isotropic. Moreover, in real materials, defects are always present which tend to average anisotropic gaps [21].

Under these conditions we can replace the quantities Z and ϕ by their Fermi surface averages, e.g.,

$$Z(i\omega_n)=\frac{1}{N_k}\sum_k w_k Z(k,i\omega_n) \tag{74}$$

with weights $w_k=\delta(\varepsilon_k)/N(0)$, where $N(0)=\frac{1}{N_k}\sum_k\delta(\varepsilon_k)$ denotes the electronic density of states per spin at the Fermi energy. To simplify the following discussion, we will drop the equation for χ thus ignoring the related, often small, shift in the electronic energies. Indeed $\chi=0$ holds exactly in the limit of infinite band width [17].

Finally, after performing the internal momentum summation in Eqs. (70) one obtains the *isotropic gap equations*

$$\begin{aligned}\omega_n\bigl(1-Z(i\omega_n)\bigr) &= -\pi\frac{1}{\beta}\sum_{n'}\varLambda(\omega_n-\omega_{n'})\,\frac{\omega_{n'}}{\sqrt{\omega_{n'}^2+\varDelta(i\omega_{n'})^2}}\\ \varDelta(\omega_n)Z(i\omega_n) &= \pi\frac{1}{\beta}\sum_{n'}\varLambda(\omega_n-\omega_{n'})\,\frac{\varDelta(i\omega_{n'})}{\sqrt{\omega_{n'}^2+\varDelta(i\omega_{n'})^2}}\,,\end{aligned} \tag{75}$$

where $\varDelta(i\omega_n)=\varPhi(i\omega_n)/Z(i\omega_n)$. The interaction kernel

$$\varLambda(\nu_m)=\int d\omega\frac{2\omega\alpha^2F(\omega)}{(\nu_m)^2+\omega^2} \tag{76}$$

contains the electron-phonon coupling via the *isotropic Eliashberg function*

$$\alpha^2F(\omega) = \frac{1}{N(0)}\frac{1}{N_k^2}\sum_{kk'}|g^q_{k'k}|^2\delta(\varepsilon_k)\,\delta(\varepsilon_{k'})\,\delta(\omega-\omega_q). \tag{77}$$

The set of non-linear equations (75) must be solved self-consistently for a given temperature T and pairing function α^2F. The kernel entering both equations is an even function of ν_m. It takes its largest value at $\nu_m = 0$

$$\lambda = \Lambda(0) = 2\int d\omega\,\frac{\alpha^2F(\omega)}{\omega}\,. \tag{78}$$

λ is called the (isotropic) coupling constant and is a dimensionless measure of the average strength of the electron-phonon coupling. Depending on its value, materials are characterized as strong ($\lambda > 1$) or weak coupling ($\lambda < 1$) . Due to the factor $1/\omega$ in the integral, low-energy modes contribute more to the coupling strength than high-energy modes.

The superconducting state is characterized by a solution with $\Delta(i\omega_n) \neq 0$. The largest T which still allows such a solution defines the critical temperature T_c. Because $\alpha^2F(\omega)$ as defined in Eq. (77) is a positive function, (75) always possess such a superconducting solution for low enough temperatures, i.e., a finite T_c.

An important feature of the Eliashberg gap equations is that they only depend on normal-state properties, which specify a particular material. These comprise the electronic band structure, phonons, and the EPC vertex, quantities which are accessible to *first principles* techniques as discussed in the next section.

At this stage it is useful to make the connection to some normal-state quantities introduced in the previous section. The isotropic Eliashberg function is related to the state-dependent spectral function (28) via appropriate momentum averages at the Fermi energy

$$\alpha^2F(\omega) = \sum_k w_k\alpha^2F_k(\varepsilon=0,\omega)\,, \tag{79}$$

while the isotropic coupling constant is given by

$$\lambda = \sum_k w_k\lambda_k\,. \tag{80}$$

Similarly, α^2F can be expressed in terms of the phonon linewidths derived in the limit $T \to 0$, Eq. (40), as

$$\alpha^2F(\omega) = \frac{1}{2\pi N(0)}\frac{1}{N_q}\sum_q\frac{\gamma_q}{\omega_q}\,\delta(\omega-\omega_q)\,, \tag{81}$$

which leads to the formula for the isotropic coupling constant

$$\lambda = \frac{1}{\pi N(0)}\frac{1}{N_q}\sum_q\frac{\gamma_q}{\omega_q^2}\,. \tag{82}$$

The dimensionless prefactor γ_q/ω_q in (81) can be interpreted as a measure of the coupling due to an individual phonon mode. The Eliashberg function is then given as a sum over all phonon branches and averaged over phonon momentum.

4.2.4 Coulomb effects

Our derivation up to now was based on the Fröhlich Hamiltonian, where the electronic subsystem is approximated by bands of noninteracting quasiparticles ignoring any Coulomb interaction. The largest consequences of the Coulomb interaction are supposed to be build into the quantities ε_k (and similarly into ω_q). The residual Coulomb interaction among the quasiparticles can, however, not be completely neglected in the discussion of phonon-mediated superconductivity. It has a repulsive character and tends to reduce or completely suppress the pairing. The quantity analogous to the electron-phonon coupling constant λ is the Coulomb parameter

$$\mu = N(0)\, \langle\langle V_C(k,k') \rangle\rangle_{FS} \,, \tag{83}$$

which is a Fermi surface average of the effective screened Coulomb interaction $V_C(k,k')$. μ is of the order of 1 and thus not a small parameter. But because the electronic timescale is usually much smaller than the vibrational one, or equivalently electronic energies are much larger than phononic ones, only a significantly reduced Coulomb parameter enters the Eliashberg equations. It was shown by Morel and Anderson [22], that the Coulomb repulsion can be taken into account by replacing the kernel in the equation for the gap function by

$$\Lambda(i\omega_n - i\omega_{n'}) \to \big(\Lambda(i\omega_n - i\omega_{n'}) - \mu^*(\omega_c)\big)\, \Theta(\omega_c - |\omega_{n'}|) \,. \tag{84}$$

A cutoff ω_c is introduced which must be chosen to be much larger than phononic energies. The effective Coulomb parameter or *Morel-Anderson Coulomb pseudopotential* obeys a scaling relation

$$\mu^*(\omega_c) = \frac{\mu}{1 + \mu \ln(\varepsilon_0/\omega_c)} \,. \tag{85}$$

ε_0 denotes a characteristic energy scale of the electronic system, where the average matrix elements of the Coulomb interaction become small ($\varepsilon_0 \approx$ few ε_F). In practice, μ^* is commonly treated as a phenomenological parameter of the order of ≈ 0.1 for normal metals. A more satisfactory approach, which actually allows to incorporate Coulomb effects from *first principles*, is the density-functional theory of superconductors [23].

4.2.5 Transition temperature T_c

The transition temperature T_c is solely determined by the material-dependent quantities $\alpha^2 F(\omega)$ and μ^*. A thorough numerical analysis of the isotropic gap equations was carried out by Allen and Dynes [24], who used a standard spectrum for $\alpha^2 F$ but varied λ and μ^* over a large parameter range. Their study revealed two important aspects. Firstly, they found that in a reduced parameter space ($\lambda < 2$ and $\mu^* < 0.15$) T_c can be well approximated by a T_c formula proposed originally by McMillan [25], but with a modified prefactor

$$T_c = \frac{\omega_{\log}}{1.2} \exp\left[-\frac{1.04(1+\lambda)}{\lambda - \mu^*(1+0.62\lambda)} \right] \,. \tag{86}$$

The prefactor contains a properly defined average frequency of the phonon spectrum weighted with the coupling strength

$$\omega_{\log} = \exp\left[\int d\omega \; \log(\omega) W(\omega)\right], \tag{87}$$

with the normalized weight function

$$W(\omega) = \frac{2}{\lambda} \frac{\alpha^2 F(\omega)}{\omega}. \tag{88}$$

This T_c formula is a significant refinement of the BCS formula $T_c = 1.13\,\omega_D \exp(-1/\lambda)$ derived for the weak-coupling limit. Secondly, while the T_c formula suggests that T_c approaches a finite value in the limit $\lambda \to \infty$, the isotropic gap equations do not possess an intrinsic upper bound for T_c. Instead the asymptotic relationship

$$T_c \propto \sqrt{\lambda \langle \omega^2 \rangle} \tag{89}$$

holds, where $\langle \omega^2 \rangle$ is the second moment of $W(\omega)$.

5 Density functional theory approach

In the previous sections we have outlined the basic theory for the effects of EPC in the normal and superconducting state. Central quantities are the screened EPC matrix elements, which are not directly accessible from experiment. Thus it is desirable to have a computational scheme which allows materials-dependent predictions. The most common approach is based on density functional theory, which is briefly described in the following.

5.1 Density functional perturbation theory

5.1.1 Basics of density functional theory

The foundations of density functional theory (DFT) have been laid down in the seminal works by Hohenberg, Kohn, and Sham [26, 27] in the mid 60's, and are outlined in numerous reviews [28–30]. It provides a framework to map the complex many-body problem of interacting electrons moving in an external potential $v_{\text{ext}}(\mathbf{r})$ onto a fictitious system of noninteracting electrons. Their wavefunctions obey a single-particle equation (Kohn-Sham equation) [27]

$$\Big(-\nabla^2 + v_{\text{eff}}(\mathbf{r})\Big)\psi_i(\mathbf{r}) = \varepsilon_i \psi_i(\mathbf{r}). \tag{90}$$

Here, ε_i denotes the energy of the single-particle state ψ_i. The effective potential $v_{\text{eff}}(\mathbf{r})$ is a functional of the density given as the sum of the external potential and a screening potential

$$v_{\text{eff}}[n] = v_{\text{ext}} + v_{\text{scr}}[n] = v_{\text{ext}} + v_H[n] + v_{XC}[n]. \tag{91}$$

The Hartree and exchange-correlation potentials v_H and v_{XC} are functionals of the density defined as the functional derivative of the Hartree and exchange-correlation energies, $E_H[n] = \int d^3r \int d^3r'\, n(\mathbf{r})n(\mathbf{r}')/|\mathbf{r}-\mathbf{r}'|$ and E_{XC}. The density is determined by the wavefunctions via

$$n(\mathbf{r}) = \sum_i f_i |\psi_i(\mathbf{r})|^2 \tag{92}$$

with f_i the occupation number of the single-particle state ψ_i. Eqs. (90) and (92) have to be solved self-consistently.

5.1.2 Linear response within the Kohn-Sham scheme

In the following we will sketch how one can calculate the linear response to an external perturbation within the Kohn-Sham scheme. As the Kohn-Sham equations describe non-interacting electrons, standard perturbation techniques can be applied. Let us now consider a small perturbation of the effective potential, δv_{eff}. This gives rise to a first-order variation of the single-particle wave functions

$$\delta\psi_i(\mathbf{r}) = \sum_{j(\neq i)} \frac{\langle j|\, \delta v_{\text{eff}} |i\rangle}{\varepsilon_i - \varepsilon_j}\, \psi_j(\mathbf{r})\,. \tag{93}$$

Using a similar expression for $\delta\psi_i^*(\mathbf{r})$ gives

$$\delta n(\mathbf{r}) = \sum_i f_i \big(\psi_i^*(\mathbf{r})\delta\psi_i(\mathbf{r}) + \delta\psi_i^*(\mathbf{r})\psi_i(\mathbf{r})\big) = \sum_{i\neq j} \frac{f_i - f_j}{\varepsilon_i - \varepsilon_j} \langle j|\, \delta v_{\text{eff}} |i\rangle\, \psi_i^*(\mathbf{r})\psi_j(\mathbf{r})\,. \tag{94}$$

Keeping in mind, that the effective potential depends on the density, on obtains

$$\begin{aligned} \delta v_{\text{eff}}(\mathbf{r}) &= \delta v_{\text{ext}}(\mathbf{r}) + \delta v_{\text{scr}}(\mathbf{r}) = \delta v_{\text{ext}}(\mathbf{r}) + \int d^3r'\, I(\mathbf{r},\mathbf{r}')\, \delta n(\mathbf{r}') \\ I(\mathbf{r},\mathbf{r}') &\equiv \frac{\delta v_{\text{scr}}(\mathbf{r})}{\delta n(\mathbf{r}')} = \frac{\delta v_{\text{H}}(\mathbf{r})}{\delta n(\mathbf{r}')} + \frac{\delta v_{\text{XC}}(\mathbf{r})}{\delta n(\mathbf{r}')} = \frac{2}{|\mathbf{r}-\mathbf{r}'|} + \frac{\delta^2 E_{XC}}{\delta n(\mathbf{r})\, \delta n(\mathbf{r}')}\,. \end{aligned} \tag{95}$$

Eqs. (94) and (95) must be solved self-consistently to obtain the first-order variation of the density. Direct evaluation of Eq. (94) is, however, numerically inefficient, because the sum i, j runs over all occupied and unoccupied states and converges very slowly with the number of unoccupied states included.

5.1.3 Modern formulation: Density functional perturbation theory

An important progress has been achieved by a new formulation of the linear-response approach, which avoids some of the aforementioned problems. It is called density functional perturbation theory (DFPT). We will give a brief outline for the case of a non-metallic system, while a concise description can be found in [31].

In the expression (94) for the first-order density variation, the prefactor $(f_i - f_j)/(\varepsilon_i - \varepsilon_j)$ restricts the sum to combinations where one state comes from the valence space and the other from the conduction space. Using time-reversal symmetry, this can be rewritten as

$$\delta n(\mathbf{r}) = 2 \sum_{vc} \frac{1}{\varepsilon_v - \varepsilon_c} \langle c|\, \delta v_{\text{eff}} |v\rangle\, \psi_v^*(\mathbf{r})\psi_c(\mathbf{r})\,. \tag{96}$$

Now one defines the quantity

$$|\varDelta_v\rangle = \sum_c \frac{1}{\varepsilon_v - \varepsilon_c} |c\rangle\langle c|\, \delta v_{\text{eff}}|v\rangle \,, \tag{97}$$

which collects the summation over the conduction bands. The linear response of the density is rewritten as

$$\delta n(\mathbf{r}) = 2\sum_v \psi_v^*(\mathbf{r})\varDelta_v(\mathbf{r})\,. \tag{98}$$

To avoid an explicit evaluation of the sum in the definition of $\varDelta_v$, one makes use of the following property

$$(H_{KS} - \varepsilon_v)|\varDelta_v\rangle = -\sum_c |c\rangle\langle c|\, \delta v_{\text{eff}}|v\rangle = -P_c\, \delta v_{\text{eff}}|v\rangle = (P_v{-}1)\, \delta v_{\text{eff}}|v\rangle\,. \tag{99}$$

Here, $H_{KS} = -\nabla^2 + v_{\text{eff}}$ is the Kohn-Sham Hamiltonian. $P_c = \sum_c |c\rangle\langle c|$ denotes the projector onto the conduction space, and $P_v = 1{-}P_c$ the projector onto the valence space. Eq. (99) represents a linear equation for $\varDelta_v$, where only valence-state quantities enter. Solution of this linear equation turns out to be numerically much more efficient than the expensive summation over conduction states. In practice, Eqs. (98), (99) together with (95) define a set of self-consistent equations which is typically solved in an iterative manner.

We now apply this scheme to the case of a solid, where ions in their rest positions are sitting on a periodic lattice. Kohn-Sham eigenstates are Bloch states $|\mathbf{k}\nu\rangle$ characterized by momentum $\mathbf{k}$ and band index ν, respectively, and are solutions of $H_{KS}|\mathbf{k}\nu\rangle = \varepsilon_{\mathbf{k}\nu}|\mathbf{k}\nu\rangle$. In a periodic crystal, ions are characterized by two indices l and s, which denote the unit cell and the ions inside a unit cell, respectively. We consider periodic displacements of the ions from their equilibrium positions, $\mathbf{R}_{ls} = \mathbf{R}^0_{ls} + \mathbf{u}_{ls}$, of the form

$$u_{ls\alpha} = d_{s\alpha}e^{i\mathbf{q}\mathbf{R}^0_{ls}} + d^*_{s\alpha}e^{-i\mathbf{q}\mathbf{R}^0_{ls}}\,, \tag{100}$$

where α indicates Cartesian coordinates. The complex amplitudes $d_{s\alpha}$ allow to vary the relative phase of the displacement. It is convenient to denote the corresponding derivatives by $\delta^{\mathbf{q}}_{s\alpha} \equiv \frac{\partial}{\partial d_{s\alpha}}$ and $\delta^{-\mathbf{q}}_{s\alpha} \equiv \frac{\partial}{\partial d^*_{s\alpha}}$.

It is instructive to look at the effect of such a perturbation on the external potential, which is commonly expressed as a superposition of atomic potentials v_s centered at the instantaneous positions of the ions

$$v_{\text{ext}}(\mathbf{r}) = \sum_{ls} v_s(\mathbf{r}{-}\mathbf{R}_{ls})\,. \tag{101}$$

Then its first-order variation, evaluated at the equilibrium positions, is given by

$$\delta^{\mathbf{q}}_{s\alpha}v_{\text{ext}}(\mathbf{r}) = -\sum_l \nabla^{\mathbf{r}}_\alpha v_s(\mathbf{r}{-}\mathbf{R}^0_{ls})e^{i\mathbf{q}\mathbf{R}^0_{ls}} = -e^{i\mathbf{q}\mathbf{r}}\sum_l e^{i\mathbf{q}(\mathbf{R}^0_{ls}-\mathbf{r})}\nabla^{\mathbf{r}}_\alpha v_s(\mathbf{r}{-}\mathbf{R}^0_{ls})\,. \tag{102}$$

The quantity defined by the lattice sum has the periodicity of the original lattice. Thus the derivative $\delta^{\mathbf{q}}_{s\alpha}$ can be considered to carry a momentum $\mathbf{q}$.

When using a Bloch representation for the electronic eigenstates, the variation of the effective potential, $\delta^{\mathbf{q}}_{s\alpha} v_{\text{eff}}$, connects states of momentum $\mathbf{k}$ with those of momentum $\mathbf{k}{+}\mathbf{q}$. The Fourier transform of the first order density variation takes the form (see Eq. (98))

$$\delta^{\mathbf{q}}_{s\alpha} n(\mathbf{q}{+}\mathbf{G}) = -\frac{4}{V} \sum_{\mathbf{k}v} \big\langle \mathbf{k}v \big| e^{-i(\mathbf{q}+\mathbf{G})\mathbf{r}} \big| \Delta^{\mathbf{q}}_{s\alpha}(\mathbf{k}v) \big\rangle, \tag{103}$$

where V denotes the crystal volume. The quantity appearing on the right hand side is closely related to the first-order variation of the valence state $|\mathbf{k}v\rangle$ and is defined by (see Eq. (97))

$$|\Delta^{\mathbf{q}}_{s\alpha}(\mathbf{k}v)\rangle = \sum_{c} \frac{|\mathbf{k}{+}\mathbf{q}c\rangle\langle\mathbf{k}{+}\mathbf{q}c|\, \delta^{\mathbf{q}}_{s\alpha} v_{\text{eff}} |\mathbf{k}v\rangle}{\varepsilon_{\mathbf{k}+\mathbf{q}c} - \varepsilon_{\mathbf{k}v}} \,. \tag{104}$$

It is obtained by solving the inhomogeneous linear equations (see Eq. (99))

$$\big(H_{KS} - \varepsilon_{\mathbf{k}v}\big) |\Delta^{\mathbf{q}}_{s\alpha}(\mathbf{k}v)\rangle = \big(P^{\mathbf{k}+\mathbf{q}}_{v} {-} 1\big)\, \delta^{\mathbf{q}}_{s\alpha} v_{\text{eff}} |\mathbf{k}v\rangle \,. \tag{105}$$

Eqs. (103) and (105) together with (95) constitute a set of equations, which is solved self-consistently for a fixed $\mathbf{q}$ to obtain $\delta^{\mathbf{q}}_{s\alpha} n$. As a by-product, also $\delta^{\mathbf{q}}_{s\alpha} v_{\text{eff}}$ is calculated.
An important application of the linear response scheme is the calculation of lattice dynamical properties. The electronic contribution to the dynamical matrix (see Appendix A), which determines the normal modes or phonons, is proportional to a mixed second derivative of the total energy

$$D_{s\alpha s'\beta}(\mathbf{q}) = \frac{1}{\sqrt{M_s M_{s'}}}\, \delta^{\mathbf{q}}_{s\alpha} \delta^{-\mathbf{q}}_{s'\beta} E \Big|_{\mathbf{u}=0} \,, \tag{106}$$

which can be expressed as

$$\delta^{\mathbf{q}}_{s\alpha} \delta^{-\mathbf{q}}_{s'\beta} E = \sum_{\mathbf{G}} \Big(\delta^{\mathbf{q}}_{s\alpha} n(\mathbf{G}{+}\mathbf{q}) \delta^{-\mathbf{q}}_{s'\beta} v_{\text{ext}}(\mathbf{G}{+}\mathbf{q}) + \delta^{\mathbf{q}}_{s\alpha} \delta^{-\mathbf{q}}_{s'\beta} v_{\text{ext}}(\mathbf{G}) \Big). \tag{107}$$

The fact that this second derivative of the energy only requires the knowledge of the first-order derivative of the density is a specific case of the so-called $(2n{+}1)$ theorem, which states that all derivatives of the total energy up to $(2n{+}1)$-th order with respect to an adiabatic perturbation can be calculated from the knowledge of all derivatives of the Kohn-Sham eigenstates and density up to n-th order. The proof given by Gonze *et al.* [32, 33] essentially rests on the variational property of the energy functional.

5.2 Electron-phonon vertex from DFPT

We have seen that the lowest-order electron-ion interaction describes scattering of electronic states via the operator $\delta_{\mathbf{R}} V$ which denotes the change of the potential felt by the electrons due to an ionic displacement. If the potential V is the bare electron-ion potential V^0, then $\delta_{\mathbf{R}} V = \nabla V^0 \big|_{\mathbf{R}_0} \mathbf{u}$. In the context of DFPT, Eq. (2) would then be identified with

$$g^{\mathbf{q}j}_{\mathbf{k}+\mathbf{q}\nu',\mathbf{k}\nu} = \sum_{s\alpha} A^{\mathbf{q}j}_{s\alpha} \big\langle \mathbf{k}{+}\mathbf{q}\nu' \big|\, \delta^{\mathbf{q}}_{s\alpha} v_{\text{ext}} \big| \mathbf{k}\nu \big\rangle \qquad \text{with} \qquad A^{\mathbf{q}j}_{s\alpha} = \frac{\eta_{s\alpha}(\mathbf{q}j)}{\sqrt{2M_s\omega_{\mathbf{q}j}}} \,, \tag{108}$$

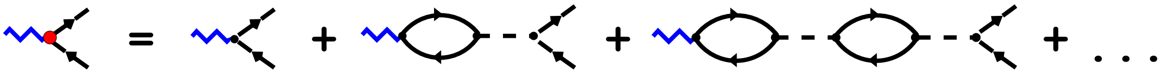

Fig. 8: *Diagrammatic representation of the screened electron-phonon vertex within the DFT framework. Blue zigzag lines represent phonons, black lines electron propagators, and the dashed lines the effective electron-electron interaction.*

where a transformation to the normal-mode coordinates is performed. Physically, g represents the probability amplitude of scattering a single electron by a simultaneous creation or annihilation of a single phonon. In the form given above is called the bare vertex.
However, in solids, and in particular in metals, the bare electron-ion potential is screened by the other electrons. Screening also alters the vertex significantly. It is instructive to look at it from a many-body perturbation perspective. Fig. 8 shows a diagrammatic representation of the screened vertex. The bare vertex is given by the first graph on the right hand side, and is screened by virtual electron-hole excitations coupled via an effective interaction. In the context of DFT, the electron-hole bubble represents the charge susceptibility of the non-interaction Kohn-Sham system. The effective interaction is given by the kernel I defined in Eq. (95) and incorporates besides the Coulomb interaction also contributions from exchange and correlation.
In essence this leads to a replacement of the external potential by the screened or effective one

$$g^{\mathbf{q}j}_{\mathbf{k}+\mathbf{q}\nu',\mathbf{k}\nu} = \sum_{s\alpha} A^{\mathbf{q}j}_{s\alpha} \left\langle \mathbf{k}+\mathbf{q}\nu' \middle| \, \delta^{\mathbf{q}}_{s\alpha} v_{\text{eff}} \middle| \mathbf{k}\nu \right\rangle . \tag{109}$$

DFPT allows direct access to this screened electron-phonon vertex, because the effective potential $\delta^{\mathbf{q}}_{s\alpha} v_{\text{eff}}$ is calculated within the self-consistent procedure outlined above, which automatically takes into account the important screening effects. Evaluation of Eq. (109), which is a numerically rather inexpensive task, provides the screened EPC matrix elements on a microscopic level, including their full momentum dependence and resolving the contributions from different electronic bands and phononic modes.
DFPT has been widely used to predict lattice dynamical and EPC properties from *first principles* for a large variety of materials, and has proven to be quite accurate in predicting the pairing strength in phonon-mediated superconductors. This is briefly demonstrated by two examples.
The first one is a combined study of EPC by DFPT and neutron-scattering experiments shown in Fig. 9 for $\text{YNi}_2\text{B}_2\text{C}$ [34, 35]. This member of the nickelborocarbide family is a strong coupling superconductor ($T_C = 15.2$ K), and exhibits pronounced phonon anomalies related to large and momentum dependent EPC. Good agreement for both renormalized phonon frequencies and linewidths as a function of momentum indicates a good predictive power of DFPT for this compound.
The second example, shown in Fig. 10, addresses the non-centrosymmetric, strong-coupling superconductor SrPt_3P ($T_C = 8.4$ K). DFPT predicts that the pairing is driven mainly by a low-frequency mode, which carries more than 80% of the coupling. The existence of the low-frequency mode was subsequently confirmed by high-resolution inelastic X-ray experiments [36].

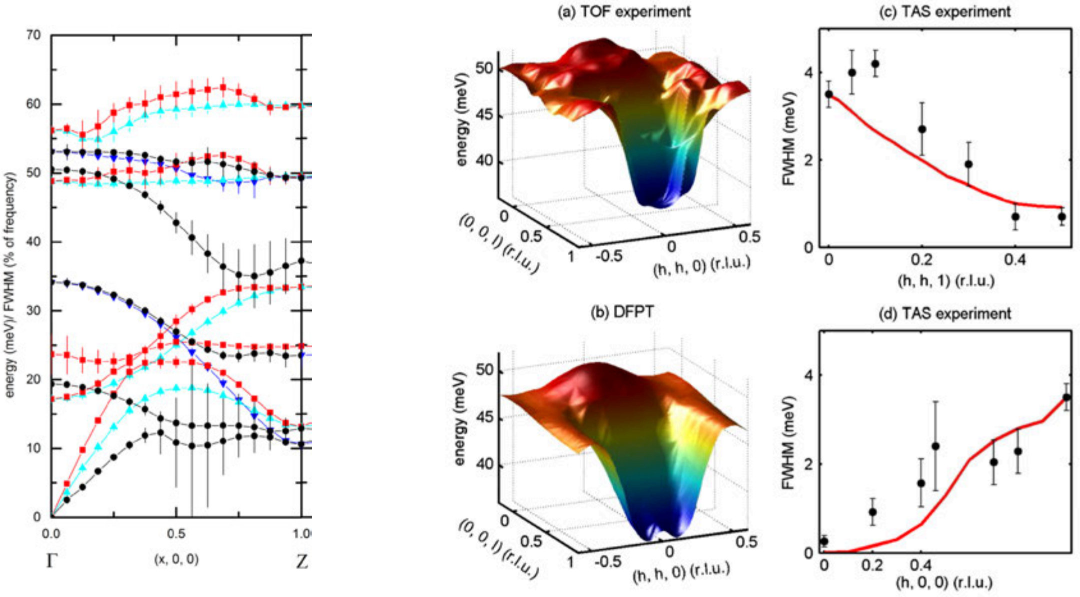

Fig. 9: *Lattice dynamics of* YNi_2B_2C*. Left panel: theoretical phonon dispersion and linewidths (vertical bars) from DFPT. Right panel: time-of-flight neutron scattering results for the dispersion (a) and linewidth (c) of a prominent phonon branch compared with predictions from DPFT in (b) and (d), respectively. After [34, 35].*

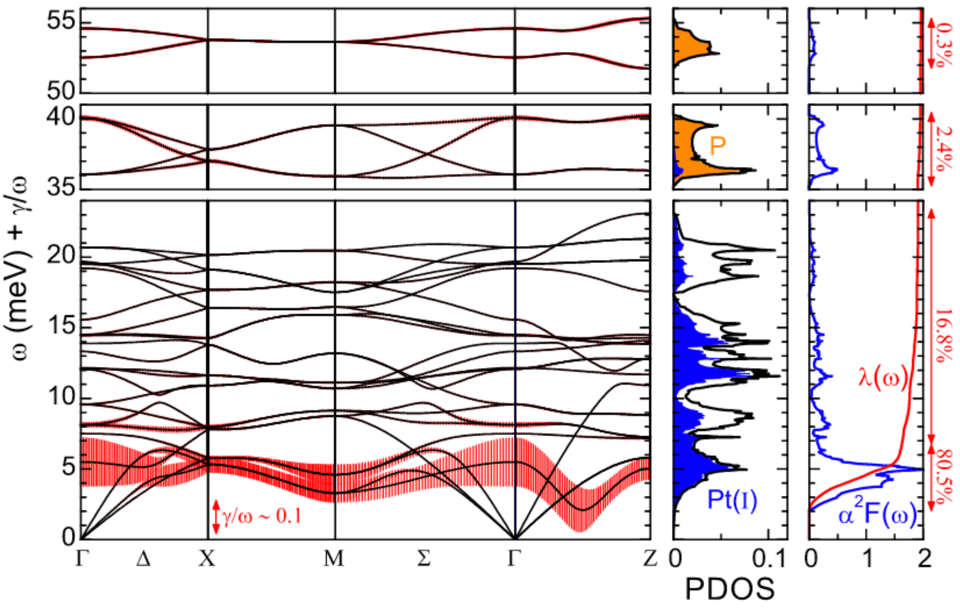

Fig. 10: *DFPT results for the superconductor* $SrPt_3P$*. Left: phonon dispersion and relative linewidths (vertical red bars); middle: phonon density of states; right: calculated isotropic* α^2F*. DFPT predicts a soft, but strong-coupling phonon branch, which is the origin of the large peak in* α^2F *at low energies, and of a large coupling constant of* $\lambda \approx 2$*. After [36].*

6 Summary

In this tutorial, an introduction to the theory of the electron-phonon interaction in metals was given. Focus was put on the renormalization properties of electronic and vibronic quasiparticles in the normal state, and on its role for the pairing interaction relevant for the superconducting state. This strong-coupling or Eliashberg theory has been tremendously successful in predicting material-dependent properties of various superconductors in great detail. Density functional theory provides a rather accurate *first principles* computational scheme to calculate the relevant electron-phonon vertex, which is one of the central quantities determining physical observables like electron renormalization, phonon linewidth, or phonon-mediated pairing interaction. Yet one has to keep in mind that the Eliashberg theory incorporates a variety of approximations. The current theoretical challenge is to extend its framework to include usually neglected aspects of anharmonicity [37], and to quantify electron-phonon coupling effects in materials which are characterized by small electronic energy scales [38] and/or strong electron correlations [39].

Appendix

A Phonon quantization

Within the adiabatic approximation, statics and dynamics of the ions are governed by an effective potential

$$\Omega(\underline{\mathbf{R}}) = V_{ii}(\underline{\mathbf{R}}) + E_0(\underline{\mathbf{R}})\,, \tag{110}$$

where $E_0(\underline{\mathbf{R}})$ denotes the electronic ground-state energy for a given ion configuration $\underline{\mathbf{R}}$. The effective potential Ω builds the starting point of the microscopic theory of lattice dynamics, which has been outlined in a number of review articles [40–42].

Dynamical properties are derived by a systematic expansion of Ω for atom displacements $\mathbf{u}$ around a chosen reference configuration, $\mathbf{R}_i = \mathbf{R}_i^0 + \mathbf{u}_i$, leading to

$$\Omega(\underline{\mathbf{R}}) = \Omega(\underline{\mathbf{R}}^0) + \sum_{i\alpha} \Phi_a(i)\, u_{i\alpha} + \frac{1}{2}\sum_{i\alpha j\beta} \Phi_{\alpha\beta}(i,j)\, u_{i\alpha} u_{j\beta} + \cdots \tag{111}$$

Greek indices α and β denote Cartesian coordinates, while i and j are atom indices. The term of first order is the negative of the force acting on an atom in the reference configuration

$$F_{i\alpha} = -\left.\frac{\partial\Omega}{\partial R_{i\alpha}}\right|_0 = -\Phi_\alpha(i)\,. \tag{112}$$

It vanishes if one chooses as reference the equilibrium configuration, which minimizes Ω. The second-order coefficients are given by

$$\Phi_{\alpha\beta}(i,j) = \left.\frac{\partial^2\Omega}{\partial R_{i\alpha}\partial R_{j\beta}}\right|_0 . \tag{113}$$

In periodic crystals, the atoms are characterized by two indices $i = (ls)$, which denote the unit cell (l) and the atoms inside a unit cell (s), respectively. For periodic boundary conditions, the Fourier transform of the force constant matrix is related to the dynamical matrix

$$D_{s\alpha s'\beta}(\mathbf{q}) = \frac{1}{\sqrt{M_s M_{s'}}} \sum_l \Phi_{\alpha\beta}(ls, 0s') e^{-i\mathbf{q}(\mathbf{R}^0_{ls} - \mathbf{R}^0_{0s'})}\,, \tag{114}$$

which determines the equation for the normal modes or phonons,

$$\sum_{s'\beta} D_{s\alpha s'\beta}(\mathbf{q})\, \eta_{s'\beta}(\mathbf{q}j) = \omega^2_{\mathbf{q}j} \eta_{s\alpha}(\mathbf{q}j)\,. \tag{115}$$

$\omega_{\mathbf{q}j}$ and $\eta_{s\alpha}(\mathbf{q}j)$ denote the energy and polarization of the normal mode determined by the wavevector $\mathbf{q}$ and branch index j.

These quantities enter into the relationship between the atom displacements and the usual phonon annihilation and creation operators, $b_{\mathbf{q}j}$ and $b^\dagger_{\mathbf{q}j}$, describing quantized normal modes, as given in Eq. (7).

References

[1] G. Grimvall: *The Electron–Phonon Interaction in Metals* (Selected Topics in Solid State Physics, edited by E. Wohlfarth, North-Holland, New York, 1981)

[2] M. Born and J.R. Oppenheimer, Ann. Phys. **84**, 457 (1927)

[3] G.V. Chester and A. Houghton, Proc. Phys. Soc. **73**, 609 (1959)

[4] S.K. Sinha, Phys. Rev. **169**, 477 (1968)

[5] A.A. Abrikosov, L.P. Gorkov, and I.E. Dzyaloshinski: *Methods of Quantum Field Theory in Statistical Physics* (Prentice-Hall, New Jersey, 1964)

[6] A.L. Fetter and J.D. Walecka: *Quantum Theory of Many-Particle Systems* (McGraw-Hill, San Francisco, 1971)

[7] G.D. Mahan: *Many-Particle Physics*, (Plenum Press, New York, 1990)

[8] J. Jiang, S.S. Tsirkin, K. Shimada, H. Iwasawa, M. Arita, H. Anzai, H. Namatame, M. Taniguchi, I.Yu. Sklyadneva, R. Heid, K.-P. Bohnen, P.M. Echenique, and E.V. Chulkov, Phys. Rev. B **89**, 085404 (2014)

[9] A.B. Migdal, Sov. Phys. JETP **34**, 996 (1958)

[10] P.B. Allen and B. Mitrović, Solid State Physics **37**, 1 (1982)

[11] T. Holstein, Ann. Phys. **29**, 410 (1964)

[12] A. Eiguren, C. Ambrosch-Draxl, and P.M. Echenique, Phys. Rev. B **79**, 245103 (2009)

[13] P.B. Allen, Phys. Rev. B **6**, 2577 (1972)

[14] J. Bardeen, L.N. Cooper, and J.R. Schrieffer, Phys. Rev. **108**, 1175 (1957)

[15] D.J. Scalapino: *Superconductivity, Vol. 1* (R.D. Parks, ed., Dekker, New York, 1969)

[16] J.P. Carbotte, Rev. Mod. Phys. **62**, 1027 (1990)

[17] J.P. Carbotte and F. Marsiglio: *Electron-Phonon Superconductivity* in K.H. Bennemann and J.B. Ketterson (eds.): *The Physics of Superconductors* (Springer, 2003)

[18] G.M. Eliashberg, Zh. Eksp. Fiz. **38**, 966 (1960) [Sov. Phys. JETP **11**, 696 (1960)]

[19] L.P. Gor'kov, Zh. Eksp. Teor. Fiz. **34** (1958) [Sov. Phys. JETP **7**, 505 (1958)]

[20] Y. Nambu, Phys. Rev. **117**, 648 (1960)

[21] P.W. Anderson, J. Phys. Chem. Solids **11**, 26 (1959)

[22] P. Morel and P.W. Anderson, Phys. Rev. **125**, 1263 (1962)

[23] L.N. Oliveira, E.K.U. Gross, and W. Kohn, Phys. Rev. Lett. **50**, 2430 (1988)

[24] P.B. Allen and R.C. Dynes, Phys. Rev. B**12**, 905 (1975)

[25] W.L. McMillan, Phys. Rev. **176**, 331 (1968)

[26] P. Hohenberg and W. Kohn, Phys. Rev. B**136**, 864 (1964)

[27] W. Kohn and L.J. Sham, Phys. Rev. A**140**, 1133 (1965)

[28] R.M. Dreizler and E.K.U. Gross: *Density Functional Theory: An Approach to the Quantum Many-Body Problem* (Springer, Berlin, 1990)

[29] R.O. Jones and O. Gunnarsson, Rev. Mod. Phys. **61**, 689 (1989)

[30] R.G. Parr and W. Yang: *Density-Functional Theory of Atoms and Molecules* (Oxford University Press, New York, 1989)

[31] S. Baroni, S. de Gironcoli, A. Dal Corso, and P. Giannozzi, Rev. Mod. Phys. **73**, 515 (2001)

[32] X. Gonze and J.-P. Vigneron, Phys. Rev. B **39**, 13120 (1989)

[33] X. Gonze, Phys. Rev. A **52**, 1086 (1995); *ibid* **52**, 1096 (1995)

[34] F. Weber, S. Rosenkranz, L. Pintschovius, J.-P. Castellan, R. Osborn, W. Reichardt, R. Heid, K.-P. Bohnen, E.A. Goremychkin, A. Kreyssig, K. Hradil, and D. Abernathy, Phys. Rev. Lett. **109**, 057001 (2012)

[35] F. Weber, L. Pintschovius, W. Reichardt, R. Heid, K.-P. Bohnen, A. Kreyssig, D. Reznik, and K. Hradi, Phys. Rev. B **89**, 104503 (2014)

[36] D.A. Zocco, S. Krannich, R. Heid, K.-P. Bohnen, T. Wolf, T. Forrest, A. Bosak, and F. Weber, Phys. Rev. B **92**, 220504 (2015)

[37] I. Errea, M. Calandra, and F. Mauri, Phys. Rev. Lett. **111**, 177002 (2013)

[38] L.P. Gor'kov. Phys. Rev. B **93**, 054517 (2016)

[39] Z.P. Yin, A. Kutepov, and G. Kotliar, Phys. Rev. X**3**, 021011 (2013)

[40] M. Born and K. Huang: *Dynamical Theory of Crystal Lattices* (Clarendon Press, Oxford, 1954)

[41] A.A. Maradudin, E.W. Montroll, G.H. Weiss, and I.P. Ipatova: *Solid State Physics, Supplement 3* (Academic Press, New York, 1971), p. 1

[42] H. Boettger: *Principles of the Theory of Lattice Dynamics* (Physik Verlag, Weinheim, 1983)

7 Hole Superconductivity

Jorge E. Hirsch
Department of Physics
University of California San Diego
La Jolla, CA, USA

Contents

E. Pavarini and E. Koch (eds.)
Correlations and Phase Transitions
Modeling and Simulation Vol. 14
Forschungszentrum Jülich, 2024, ISBN 978-3-95806-751-6
http://www.cond-mat.de/events/correl24

1 Introduction: Overview of superconductivity

That some metals, called "supraconductors" in the old days [1], make a transition to a state with zero electrical resistance below a critical temperature T_c was discovered experimentally by Kamerlingh Onnes in 1911 [2]. That if a magnetic field is present in the interior of a superconductor for $T > T_c$, it gets expelled when the temperature is lowered to $T < T_c$ was discovered experimentally by Meissner and Ochsenfeld in 1933 [3] and is called the Meissner effect. The Meissner effect was a great surprise: before 1933 it was expected that superconductors would *exclude* magnetic fields but not that they would *expel* magnetic fields. This follows from Faraday's law, and was known as "Lippmann's theorem" [4] back in the days [5]: if a magnetic field is applied to a zero resistance material, the material will react by generating a surface current that does not let the field penetrate, thus excluding the magnetic field from its interior. However, Faraday's law / Lippmann's theorem would predict that if a material with finite resistance has a magnetic field in its interior, when it is cooled into the superconducting state with zero resistance no current would flow and the magnetic field would remain in the interior, even if the external source of magnetic field is removed. That is *not* what superconductors do: metals going superconducting spontaneously generate a surface current that *expels* magnetic fields from their interior [3]. This appears to violate Faraday's law.

The London equation proposed in 1935 by the London brothers [1, 6] provided a phenomenological description of the magnetic behavior of superconductors, but did not explain how superconductors manage to violate Faraday's law. Neither did the BCS theory, proposed in 1957 by Bardeen, Cooper and Schrieffer [7], based on the electron-phonon interaction. BCS theory provided a microscopic description of superconductors that describes many of their properties accurately, it is generally believed to apply to materials called "conventional superconductors", that include all superconducting elements and many compounds. There are around 30 different classes of superconducting materials [8], only about a third of them are generally agreed to be "conventional superconductors". For the remaining two thirds, there is no generally accepted theory. The field is wide open for further progress.

1.1 The known knowns: London equation, Cooper pairs, BCS theory

The known knowns are what ***we know we know*** about superconductivity.

It took 22 years, from the discovery of zero resistance by Kamerlingh Onnes in 1911, to experimentally discover the Meissner effect in 1933. The London brothers embodied this experimental fact in the London equation [1, 6]

$$\vec{\nabla} \times \vec{J} = -\frac{ne^2}{m_e c}\vec{B} \tag{1}$$

where $\vec{J}$ is the current density, e and m_e are the electron's charge and mass, n is the carrier density and $\vec{B}$ is an applied magnetic field. Eq. (1), together with Ampere's law

$$\vec{\nabla} \times \vec{B} = \frac{4\pi}{c}\vec{J} \tag{2}$$

lead to

$$\nabla^2\vec{B} = \frac{4\pi ne^2}{m_e c^2}\vec{B} \equiv \frac{1}{\lambda_L^2}\vec{B} \tag{3}$$

which says that an external magnetic field decays exponentially to zero in going from the surface to the interior of the superconductor, over a length given by the London penetration depth λ_L. The London Eq. (1) was *derived* by the Londons for the situation where a magnetic field is applied to a material that is already superconducting, i.e., describing *exclusion* of an applied magnetic field. They *postulated* without derivation that it also applies to situations where a normal metal with a magnetic field in its interior is cooled into the superconducting state. *If* that postulate is valid, the material will *expel* the magnetic field to reach the state described by Eq. (3), which is what is observed experimentally [3]. But no theoretical proof that this should happen was provided by the London brothers nor anybody else.

In 1956, Leon Cooper pointed out [9] that if electrons in a Fermi gas interact through a small net *attractive* interaction resulting from the electron-phonon interaction, they would form a bound pair with binding energy Δ, and suggested that a system of such bound pairs may Bose-condense into a superconducting state. In 1957 Bardeen, Cooper and Schrieffer formulated a theory of superconductivity [7] describing the many-body state of such Cooper pairs. They showed that the ground state wavefunction of the "reduced Hamiltonian"

$$H_{red} = \sum_{k\sigma}(\varepsilon_k - \mu)\, c^\dagger_{k\sigma}c_{k\sigma} + \sum_{kk'} V_{kk'}\, c^\dagger_{k\uparrow}c^\dagger_{-k\downarrow}c_{-k'\downarrow}c_{k'\uparrow} \tag{4}$$

with μ the chemical potential (that determines the band filling) is of the form

$$\big|\Psi_{BCS}\big\rangle = \prod_k \left(u_k^2 + v_k^2\, c^\dagger_{k\uparrow}c^\dagger_{-k\downarrow}\right)\big|\,0\big\rangle. \tag{5}$$

where $c^\dagger_{k\sigma}$ creates an electron of spin σ in the single particle state of crystal momentum k, and u_k and v_k are complex amplitudes determined by minimization of the energy. BCS showed that if the net interaction between electrons is attractive, the state Eq. (5) has a lower energy than the normal metal Fermi sea. At finite temperatures, the system has quasiparticle excitations with minimum energy $\Delta(T)$, the superconducting energy gap, which is a decreasing function of temperature. At a critical temperature T_c, $\Delta(T)$ reaches zero and the system transitions into the normal state. They furthermore showed that below T_c the system has many properties that resemble what is experimentally found for superconductors.

BCS formulated their theory under the assumption that the attractive interaction between electrons resulted from the electron-phonon interaction. Under that assumption, a simplified expression for the critical temperature is

$$T_c = \hbar\omega_D e^{-1/\lambda} \tag{6}$$

where λ is the dimensionless electron-phonon coupling and ω_D is the Debye temperature, inversely proportional to the square root of the ionic mass M. Hence Eq. (6) predicts the isotope effect, namely that

$$\frac{\partial \ln T_c}{\partial \ln M} = -\alpha \tag{7}$$

with $\alpha = 1/2$.

Finally, we should include among the *"known knowns"* the understanding intuited by London [10], implicit in BCS theory, anticipated by Ginzburg and Landau [11], and demonstrated by the physical effects predicted by Brian Josephson [12], that the superconducting condensate can be represented by a macroscopic quantum wavefunction $\psi(\vec{r}) = |\psi(\vec{r})|e^{i\theta(\vec{r})}$ with a unique phase $\theta(\vec{r})$ common to all electrons in the superfluid, and an amplitude $|\psi(\vec{r})|$ whose square gives the density of superfluid electrons.
All of the above, we all agree we know. Hence they are ***known knowns***. Good references for the above are the books by Tinkham [13] and by de Gennes [14].

1.2 The known unknowns: Mechanisms of unconventional superconductivity

The known unknowns are what ***we know that we don't know*** about superconductivity.

We know (meaning everybody agrees) that for materials that conduct electricity at ambient pressure, hence can potentially be superconductors, the electron-phonon interaction is not strong enough to overcome the Coulomb repulsion between electrons and give rise to superconductivity at temperatures above liquid nitrogen temperature, 77 K [15]. Some cuprate superconductors [16], a class of materials discovered in 1986, superconduct up to much higher temperatures, up to 140 K. Therefore, we know that there has to be at least one other mechanism that gives rise to superconductivity that is not the electron-phonon interaction. Superconducting materials not driven by the electron-phonon interaction are called "unconventional superconductors".
For a variety of reasons, many classes of materials, even if they have critical temperatures much lower than 77 K, are believed to be "unconventional superconductors", as surveyed in Ref. [8]. There are a large number of unconventional theories of superconductivity proposed to describe the cuprates and other unconventional superconductors (see introduction in Ref. [17] for many references), but there is no general agreement on which (if any) of the theories is correct for any materials. These theories are generally proposed to apply to one or more classes of unconventional superconductors but not to all.
Since it is known that there are superconducting materials not described by BCS electron-phonon theory, and there is no general agreement on which mechanisms give rise to superconductivity in the so-called unconventional superconductors, the mechanism(s) that give rise to unconventional superconductivity are ***known unknowns***.

1.3 The unknown unknowns: Does BCS theory explain the Meissner effect?

The unknown unknowns are what ***we don't know that we don't know*** about superconductivity.

It is universally believed that BCS theory explains the Meissner effect. I disagree, I believe this has not been carefully considered. BCS showed that the BCS state with magnetic field excluded has lower free energy than the normal state with magnetic field in the interior. However, BCS theory has not explained the *process* by which a normal metal becoming superconducting *expels* the magnetic field to reach the BCS state. I have argued [18] that BCS superconductors (meaning superconductors described by BCS theory) do not have the physical elements necessary to give rise to a Meissner effect, and that as a consequence, if cooled from above T_c to below T_c in the presence of a magnetic field, they would not make a transition to the superconducting state that excludes the magnetic field but would instead remain in a metastable normal state with the magnetic field remaining in the interior, contrary to what is seen experimentally. This implies, since real superconductors do exhibit a Meissner effect, that real superconductors cannot be described by BCS theory. Since the Meissner effect is not generally considered to be an unexplained phenomenon, I call this an ***unknown unknown***.

Moreover, I believe there is a single theory to describe all superconductors, i.e., the so-called conventional and unconventional superconductors, that also explains the Meissner effect. A survey of the theory in its present state is given in my book [19]. A substantial part of the theory was developed in collaboration with Frank Marsiglio, papers are listed in Ref. [20].

1.4 The unknown knowns: Are there *any* electron-phonon superconductors?

An unknown known is something ***we think we know but in reality we don't know***.

There is essentially universal agreement that the electron-phonon interaction gives rise to superconductivity in conventional materials, including the hydrides under high pressure [21]. Hence, that electron-phonon superconductors exist in nature. For the hydrides, transition temperatures are claimed to approach room temperature, in drastic violation of what was expected [15]. This is argued to come about due to the light mass of hydrogen and the strong electron-phonon coupling in such materials [21], as originally predicted by Ashcroft [22].

There is however no rigorous proof that the electron-phonon interaction gives rise to superconductivity in any material. The direct Coulomb repulsion between electrons is a first order effect, generally much stronger than the second-order frequency-dependent electron-electron interaction mediated by phonons that can be attractive under certain conditions. In calculations that claim to predict superconductivity driven by the electron-phonon interaction, the effect of the Coulomb repulsion is generally lumped into a phenomenological parameter μ^* [23], the "Coulomb pseudopotential", assumed to be of order 0.1, which allows for superconductivity driven by the attractive electron-phonon interaction. However there is no reliable way to calculate μ^* [24]. At the time when no other mechanisms for attractive interactions were known, i.e., in the 1960's, this might have been a tenable scenario, it was adopted then and is firmly believed to be valid to this date. I believe this is wrong, that in fact the electron-phonon interaction is irrelevant to superconductivity in all materials. Since everybody believes the opposite, that there are electron-phonon superconductors in nature, I say that this is an ***unknown known***.

2 Correlated electron models for superconductivity

So-called Hubbard models are widely used to describe correlated electrons in solids. Various incarnations of these models have been used to describe essential aspects of superconductivity within a variety of different theories.

2.1 Attractive and repulsive Hubbard models

The simplest Hubbard model is given by the tight binding Hamiltonian

$$H = -\sum_{i,j,\sigma} t_{ij}\big(c^\dagger_{i\sigma}c_{j\sigma} + h.c.\big) + U\sum_i n_{i\uparrow}n_{i\downarrow}. \tag{8}$$

describing electrons in a single orbital at each site in a lattice of N sites, with on-site interactions only. In momentum space the Hamiltonian is

$$H = \sum_{k\sigma} \varepsilon_k\, c^\dagger_{k\sigma}c_{k\sigma} + \frac{U}{N}\sum_{kk'q} c^\dagger_{k+q\uparrow}c^\dagger_{k'-q\downarrow}c_{k'\downarrow}c_{k\uparrow} \tag{9}$$

For an attractive interaction $U < 0$, the ground state of its “reduced Hamiltonian”, of the form Eq. (4), is of the form Eq. (5). This follows from the fact that the BCS gap equation [13]

$$\varDelta_k = -\frac{1}{N}\sum_{k'} V_{kk'}\varDelta_{k'}\frac{1-2f(E_{k'})}{2E_{k'}} \tag{10}$$

with f the Fermi distribution function, $V_{kk'} = U$, $\varDelta_k = \varDelta$, and

$$E_k = \sqrt{(\varepsilon_k - \mu)^2 + \varDelta^2} \tag{11}$$

has a solution $\varDelta \neq 0$ at sufficiently low temperatures for any $U < 0$.
For a repulsive interaction $U > 0$, the gap equation (10) has no solution. However, it has been argued [25] that more elaborate treatments of the repulsive Hubbard model Eq. (8) do give rise to a superconducting state induced by spin fluctuations in that model as well as the related t-J model [26], with the gap function having d-wave symmetry

$$\varDelta_k = \varDelta_0\big(\cos(k_x a) - \cos(k_y a)\big). \tag{12}$$

There is however no rigorous proof that I know of that the repulsive Hubbard model has a superconducting ground state. The t-J model does have a superconducting ground state, and it is argued that the model results from the repulsive Hubbard model in the limit of strong coupling, $U \gg t$ [26]. However I have shown [27] that to the same order in t/U the Hamiltonian resulting from the Hubbard model has, in addition to the t-J terms, three-site terms that exactly cancel the attractive interaction resulting from the two-site terms.
There are no good reasons why the *attractive* Hubbard model should describe the essential physics of interacting electrons in real materials. And whether the *repulsive* Hubbard model exhibits superconductivity for any value of $U > 0$ is certainly not established [28, 29]. Thus, the question whether the Hubbard model Eq. (8) has *any* relevance to the superconductivity of real materials is not a settled question, despite the enormous amounts of research efforts that has been devoted to that hypothesis [30, 31] during the last 40 years [32].

2.2 Electron-phonon attraction versus electron-electron attraction

The interaction between electrons and phonons (lattice vibrations) is typically described by the Hamiltonian

$$H_{e\text{-}ph} = \frac{1}{\sqrt{N}} \sum_{k,q,\sigma} g_{kq}\big(b_q + b^\dagger_{-q}\big)c^\dagger_{k+q\sigma}c_{k\sigma} \tag{13}$$

where the operators b_q and $b^\dagger_{-q}$ destroy and create phonons with wavevector q and $-q$ respectively, and frequency $\omega_q = \omega_{-q}$. Eliminating the phonons in second order perturbation theory leads to the effective electron-electron interaction [33]

$$H^{ph}_{e\text{-}e} = \frac{1}{N} \sum_{k,q,\sigma\sigma'} |g_{kq}|^2 \, \frac{2\hbar\omega_q}{(\varepsilon_{k+q}-\varepsilon_k)^2 - (\hbar\omega_q)^2} \, c^\dagger_{k+q\sigma}c^\dagger_{k'-q\sigma'}c_{k'\sigma'}c_{k\sigma} \tag{14}$$

which is attractive for $|\varepsilon_{k+q}-\varepsilon_k| < \hbar\omega_q$. It is argued that this frequency-dependent ("retarded") attractive interaction between electrons near the Fermi surface can overcome the much larger instantaneous repulsive interaction between electrons, given in its simplest form by the Hubbard repulsion Eq. (9), through what is called the "Coulomb pseudopotential" effect [23, 24] that we will not go into here.

The electron-electron attraction mediated by phonons Eq. (14), identified in the 1950's [33], arises from *second-order* processes. In the 1960's, it was pointed out that another source of electron-electron attraction could be second order 'excitonic' processes, where the excitations are electronic rather than phononic giving rise to interactions of the form Eq. (14) where the phonon energy $\hbar\omega_q$ is replaced by an electronic excitation. However those proposals did not gain much traction.

It turns out, however, that a *first order* attractive interaction between electrons exists, originating in the Coulomb interaction between electrons in the presence of the periodic ionic lattice potential [34]. In a tight binding formulation, the Hamiltonian containing diagonal as well as off-diagonal matrix elements resulting from the Coulomb interaction is a 'generalized Hubbard model' [35, 36] given in real space by

$$H_{gen} = -\sum_{i,j,\sigma} t_{ij}\big(c^\dagger_{i\sigma}c_{j\sigma} + h.c.\big) + \sum_{ijkl}(ij/kl)c^\dagger_{i\sigma}c^\dagger_{j\sigma'}c_{l\sigma'}c_{k\sigma} \tag{15}$$

with

$$(ij/kl) = \int d^3r d^3r' \, \varphi^*_i(r)\varphi^*_j(r') \, \frac{e^2}{|r-r'|} \, \varphi_l(r')\varphi_k(r) \tag{16}$$

where φ_i is the atomic orbital associated with site i, $U = (ii/ii) > 0$ is the on-site repulsion, and the repulsion between electrons on different sites i and j is $V_{ij} = (ij/ij) > 0$. Here we want to focus on the two-center off-diagonal matrix element of the Coulomb interaction (ii/ij) given by

$$(ii/ij) \equiv \Delta t_{ij} = \int d^3r d^3r' \varphi^*_i(r)\varphi_j(r)\frac{e^2}{|r-r'|}|\varphi^*_i(r')|^2. \tag{17}$$

The sign of the interaction Eq. (17) depends on the orbitals involved, in particular it is positive for s-orbitals and negative for p-orbitals oriented along the i-j direction. The important point however is that Eq. (17) is *of the same sign* as the single electron hopping matrix element t_{ij} arising from the electron-ion interaction, given approximately by [37]

$$t_{ij} = -\int d^3r\varphi_i^*(r)\Big(-\frac{Ze^2}{|r-R_i|}\Big)\varphi_j(r) \tag{18}$$

where $Z|e|$ is the ionic charge, that we can rewrite as

$$t_{ij} = -\int d^3rd^3r'\,\varphi_i^*(r)\varphi_j(r)\Big(-\frac{Ze^2}{|r-r'|}\Big)\big|\chi_i(r')\big|^2 \tag{19}$$

with $\chi_i(r')$ the 'ionic wave function' such that $|\chi_i(r')|^2 = \delta(r'-R_i)$, to make its close relationship with Eq. (17) apparent [34]. Thus, it is reasonable to assume that $\Delta t_{ij} = \alpha t_{ij}$ with α a *positive* constant. The Hamiltonian that results then including this interaction and the Hubbard on-site repulsion U is

$$H = -\sum_{i,j,\sigma}\big(t_{ij} - \Delta t_{ij}(n_{i,-\sigma}+n_{j,-\sigma})\big)\big(c_{i\sigma}^\dagger c_{j\sigma} + h.c.\big) + U\sum_i n_{i\uparrow}n_{i\downarrow}. \tag{20}$$

The interaction Δt_{ij} is called "correlated hopping". In momentum space the Hamiltonian is

$$H = \sum_{k\sigma}\varepsilon_k\, c_{k\sigma}^\dagger c_{k\sigma} + \frac{1}{N}\sum_{kk'q}\big(U - \alpha(\varepsilon_k+\varepsilon_{k+q}+\varepsilon_{k'}+\varepsilon_{k'-q})\big)c_{k+q\uparrow}^\dagger c_{k'-q\downarrow}^\dagger c_{k'\downarrow}c_{k\uparrow} \tag{21}$$

with $\varepsilon_k = \sum_j t_{0j}e^{ikR_j}$, where $\sum_k \varepsilon_k = 0$ since we are defining $t_{ii} = 0$. It can be seen from Eq. (21) that this interaction *increases* the Hubbard repulsion near the bottom of the band, where $\varepsilon_k < 0$, and *decreases* it near the top of the band where $\varepsilon_k > 0$. It is the only interaction of the form Eq. (16) involving two centers that breaks electron-hole symmetry.

The reduced Hamiltonian for Eq. (21) is

$$H_{red} = \sum_{k\sigma}(\varepsilon_k-\mu)c_{k\sigma}^\dagger c_{k\sigma} + \frac{1}{N}\sum_{kk'}V_{kk'}\,c_{k\uparrow}^\dagger c_{-k\downarrow}^\dagger c_{-k'\downarrow}c_{k'\uparrow} \tag{22a}$$

$$V_{kk'} = U - 2\alpha(\varepsilon_k+\varepsilon_{k'}) \tag{22b}$$

with $-D/2 \leq \varepsilon_k \leq D/2$, where D is the bandwidth. For a system with only nearest neighbor hopping with $t_{ij} = t$, $\Delta t_{ij} = \Delta t$, and z nearest neighbors to each atom, the bandwidth is $D = 2zt$ and

$$U-4z\Delta t < V_{kk'} < U+4z\Delta t \tag{23}$$

so the reduction of the on-site repulsion U increases with the coordination number of the lattice. Even for parameter values such that $V_{kk'}$ is always repulsive, i.e., $U > 4z\Delta t$, the BCS gap equation Eq. (10) will have solutions [38]. This happens because Δ_k changes sign and becomes negative far from the Fermi energy when the interaction is most repulsive. We have called this a "spatial pseudopotential effect" [38], since it is analogous to what occurs for the electron-phonon interaction due to its frequency dependence [23].

We can also write the Hamiltonian Eq. (20), assuming we are dealing with a bipartite lattice, in terms of hole operators, by performing the transformation

$$c^\dagger_{i\sigma} \to (-1)^i c_{i\sigma} \tag{24}$$

and it becomes

$$H = -\sum_{i,j,\sigma} \big(\bar{t}_{ij} + \Delta t_{ij}(n_{i,-\sigma}{+}n_{j,-\sigma})\big)\big(c^\dagger_{i\sigma}c_{j\sigma} + h.c.\big) + U\sum_i n_{i\uparrow}n_{i\downarrow}. \tag{25}$$

with $\bar{t}_{ij} = t_{ij}{-}2\Delta t_{ij}$. It will be more useful in this form for further developments.

There is a caveat, however, associated with the derivation given here. In the computation of the Coulomb matrix elements Eq. (16) we have assumed that the orbitals are atomic orbitals, which are not orthogonal at neighboring sites. Instead, the Hamiltonian Eq. (15) implicitly assumes that the fermion operators create electrons in orthogonal orbitals. If we use orthogonal orbitals instead to compute the matrix elements of the Coulomb interaction, it is found that the off-diagonal element given by Eq. (17) is nearly zero [39,40]. However, we will show in the next section that there are other physical reasons for why the Hamiltonian Eq. (20) with appreciable values of Δt_{ij} is relevant.

Thus, both the electron-phonon Hamiltonian Eq. (13) and the purely electronic Hamiltonian without electron-phonon interaction Eq. (21) can give rise to superconductivity in model systems. Whether or not both or one of them or neither of them gives rise to superconductivity in real materials is a question for which there is no universally agreed answer.

2.3 Electron-hole asymmetry, correlated hopping and dynamic Hubbard models

After having been a devoted fan of the Hubbard model in the early stages of my physics career [41], I came to the conclusion 35 years ago that the Hubbard model Eq. (8) has a fundamental flaw: it is *electron-hole symmetric*. By that I mean, the properties of a system with n *electrons* per site are identical to those of a system with n *holes* per site, or equivalently $2{-}n$ electrons per site. Around the same time, I came to the conclusion that electron-hole asymmetry is the key to superconductivity [42]. That moment marked my definitive divorce from the Hubbard model Eq. (8). Years later I attempted reconciliation with electron-hole *asymmetric* versions of the Hubbard model, namely *dynamic* Hubbard models [43], discussed later in this paper.

The fundamental electron-hole *asymmetry* of condensed matter systems follows from the basic fact that the mass of the electron is 2000 smaller than the mass of the proton. It manifests itself for example in the fact that the mean inner potential of solids is necessarily positive [44,45]. It renders the repulsive Hubbard model Eq. (8) irrelevant for the description of real systems [46]. Let us see why: Eq. (8) contains two energy scales, the hopping parameter t and the on-site repulsion U. But it excludes a third energy scale ε that is always in-between t and U, namely the spacing between atomic energy levels. When a second electron comes to occupy the orbital already occupied by the first electron, the first electron does not sit idle to pay the very large

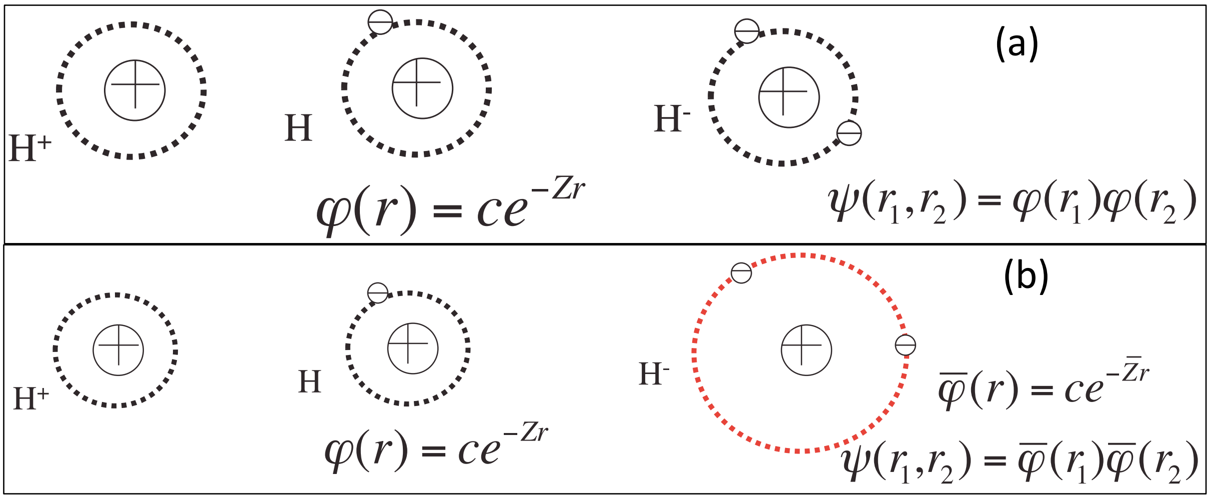

Fig. 1: *The top panel shows the atomic physics assumed in most models of interacting electrons such as the Hubbard model: the atomic orbital does not change with electron occupancy. The bottom panel shows the real physics: the atomic orbital expands when it is doubly occupied.*

Coulomb repulsion that would result from the second electron invading its turf. Instead, it (as well as the second electron) will expand their wavefunction, partially occupying higher energy single-particle states, thus reducing their Coulomb repulsion. This is shown schematically in Fig. 1. For electrons in the ground state of hydrogen-like ions of charge Z, the radius of the expanded orbital, or equivalently the value of $\bar{Z}$ is, within the Hartree approximation,

$$\bar{Z} = Z - 5/16. \tag{26}$$

This reduces the Coulomb repulsion between electrons, from $U = 17$ eV $\times Z = (5/4)\varepsilon_0 Z$, with $\varepsilon_0 = 13.6$ eV, to

$$\bar{U} = \frac{5}{4}\bar{Z} = U - \frac{25}{64}\varepsilon_0 = U - 5.31 \text{ eV} \tag{27}$$

and reduces the kinetic energy of each electron, because of the orbital expansion, from $K = \varepsilon_0 Z^2$ to $K = \varepsilon_0 \bar{Z}^2$, while it increases the potential energy of each electron, because they are further away from the nucleus, from $-2\varepsilon_0 Z^2$ to $-2\varepsilon_0 Z\bar{Z}$, for a net energy reduction of

$$E(\bar{Z}) - E(Z) = -\frac{25}{128}\varepsilon_0 = -2.66 \text{ eV} \tag{28}$$

so that the effective repulsion between electrons, defined as $U_{\mathit{eff}} = E(2) + E(0) - 2E(1)$, with $E(n)$ the energy of the ion with n electrons, is [43]

$$U_{\mathit{eff}} = U - \frac{25}{128}\varepsilon_0 = U - 2.66 \text{ eV}. \tag{29}$$

From experimental values of ionization energies of hydrogen-like ions we find that

$$U_{\mathit{eff}} \sim U - 4.1 \text{ eV}, \tag{30}$$

the reduction is greater than Eq. (29) because of radial and angular correlations for electrons in the doubly occupied orbital that we did not take into account.

The Hubbard model ignores the fundamental fact that the orbitals are modified upon double occupancy. In the Hubbard model, both the singly and the doubly occupied atomic orbitals are assumed to be single Slater determinants with the same single particle wavefunctions

$$|\uparrow\rangle = c_\uparrow^\dagger|0\rangle \tag{31a}$$

$$|\uparrow\downarrow\rangle = c_\uparrow^\dagger c_\downarrow^\dagger|0\rangle \tag{31b}$$

so that

$$\langle 0|c_\uparrow|\uparrow\rangle = \langle\downarrow|c_\uparrow|\uparrow\downarrow\rangle = 1 \tag{31c}$$

which embodies the fundamental electron-hole *symmetry* of the Hubbard Hamiltonian. However, this is qualitatively incorrect because the doubly occupied state is never a single Slater determinant but rather a linear combination of Slater determinants involving higher single electron states

$$|\uparrow\downarrow\rangle = \sum_{m,n} A_{mn}\, c_{m\uparrow}^\dagger c_{n\downarrow}^\dagger|0\rangle \tag{32a}$$

$$\sum_{m,n} |A_{mn}|^2 = 1 \tag{32b}$$

where the sum runs over a complete set of atomic orbitals with the lowest single particle orbital denoted by $m = 0$, i.e. $c_{0\sigma} = c_\sigma$, as well as over continuum states [47]. Eq. (32b) implies of course that $A_{mn} < 1$ for any m, n. Hence we have

$$c_\uparrow|\uparrow\downarrow\rangle = \sum_n A_{0n}\, c_{n\downarrow}^\dagger|0\rangle = A_{00}|\downarrow\rangle + \sum_{n\neq 0} A_{0n}\, c_{n\downarrow}^\dagger|0\rangle \tag{33}$$

and

$$1 = \langle 0|c_\uparrow|\uparrow\rangle \neq \langle\downarrow|c_\uparrow|\uparrow\downarrow\rangle = A_{00} < 1. \tag{34}$$

In other words, creating an electron into an empty orbital (or destroying an electron in the singly occupied orbital) is qualitatively different from creating a hole in the doubly occupied orbital (or creating an electron in the single occupied orbital).

For an electronic energy band that is close to empty, when electrons hop between sites transitions occur mostly between empty and singly occupied orbitals, so no other states are involved and the spectral function $A(k,\omega)$ will be a δ-function with quasiparticle weight $z = 1$, $A(k,w) = \delta(\omega - \varepsilon_k)$. Instead, for a band that is close to full, when a hole hops from a site to a neighboring site with no hole (i.e. doubly occupied), the final state can involve any of the atomic excited states at the two sites. The spectral function will have a quasiparticle part with quasiparticle weight $z < 1$, representing ground state to ground state transitions, and a broad incoherent part, as shown schematically in Fig. 2. We can describe this physics by writing the electron creation operator at site i as [48,49]

$$c_{i\sigma}^\dagger = \big(1 + (S-1)\tilde{n}_{i,-\sigma}\big)\tilde{c}_{i\sigma}^\dagger \tag{35}$$

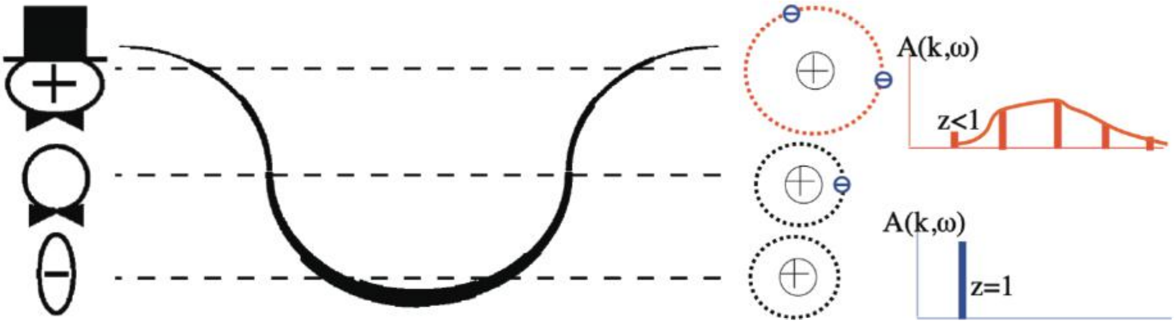

Fig. 2: *Electronic energy band ε_k versus k. Near the top of the band, most orbitals are doubly occupied and hence expanded. As the Fermi level moves up in the band, quasiparticles at the Fermi energy become increasingly dressed by the atomic electron-electron interaction, and increasingly heavier, and turn from electrons to holes. On the right we show schematically the spectral function evolving from a δ-function near the bottom of the band with quasiparticle weight z=1 to one with small quasiparticle weight $z < 1$ near the top of the band, with the rest of the spectral weight spread out in incoherent processes. The thickness of the curve giving the ε_k versus k relation indicates schematically the magnitude of the quasiparticle weight, which can be vanishingly small near the top of the band when the effective ionic charge is small.*

where $\tilde{c}^{\dagger}_{i\sigma}$ creates a quasielectron at site i, and $S = \langle \bar{\varphi}(r) | \varphi(r) \rangle$ is the overlap matrix element between expanded and unexpanded orbitals shown in Fig. 1. The quasiparticle spectral weight as a function of band filling $0 < n_e < 2$ is

$$z(n_e) = \Big(1 + (S{-}1)\frac{n_e}{2}\Big)^2 \tag{36}$$

and goes from $z = 1$ for an almost empty band to $z = S^2$ for an almost full band. Alternatively, in terms of hole operators (denoted by the same symbols to avoid proliferation of symbols)

$$c^{\dagger}_{i\sigma} = \big(S + (1{-}S)\tilde{n}_{i,-\sigma}\big)\tilde{c}^{\dagger}_{i\sigma} \tag{37}$$

and the quasiparticle weight as function of hole concentration $n_h = 2{-}n_e$ is

$$z(n_h) = \Big(S + (1{-}S)\frac{n_h}{2}\Big)^2. \tag{38}$$

The kinetic energy part of the Hamiltonian is

$$H_{kin} = -\sum_{ij,\sigma} t^{\sigma}_{ij}\big(c^{\dagger}_{i\sigma}c_{j\sigma} + h.c.\big) \tag{39}$$

and replacing the electron operators by their expression in terms of quasiparticle operators Eq. (35) we obtain

$$H_{kin} = -\sum_{ij,\sigma} t^{\sigma}_{ij}\big(\tilde{c}^{\dagger}_{i\sigma}\tilde{c}_{j\sigma} + h.c.\big) \tag{40}$$

with correlated hopping

$$t^{\sigma}_{ij} = t_{ij}\big(1 + (S{-}1)(\tilde{n}_{i,-\sigma}{+}\tilde{n}_{j,-\sigma}) + (S{-}1)^2\tilde{n}_{i,-\sigma}\tilde{n}_{j,-\sigma}\big). \tag{41}$$

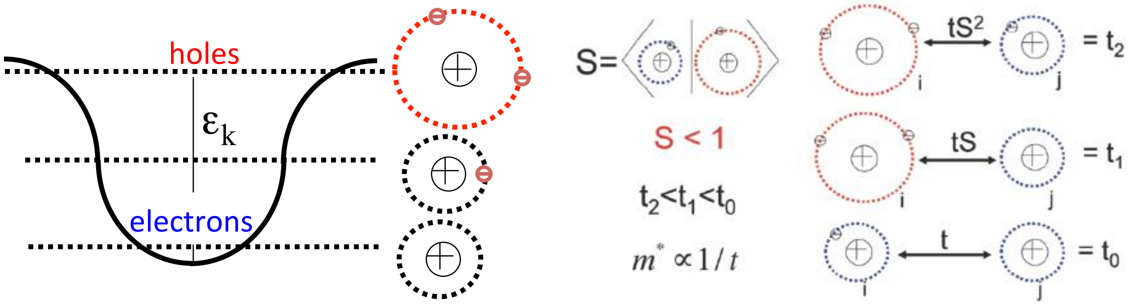

Fig. 3: *Hopping amplitudes for electrons at the Fermi energy as function of band occupation. As the number of electrons increases, hopping amplitudes are suppressed due to the modulation of the hopping by the overlap matrix element S of expanded and unexpanded orbitals.*

Alternatively, in terms of hole operators, we have the same Eq. (40), with the hopping amplitudes given by

$$t_{ij}^{\sigma} = t_{ij}S^2\Big(1+\Big(\frac{1}{S}-1\Big)\big(\tilde{n}_{i,-\sigma}+\tilde{n}_{j,-\sigma}\big)+\Big(\frac{1}{S}-1\Big)^2\tilde{n}_{i,-\sigma}\tilde{n}_{j,-\sigma}\Big). \tag{42}$$

Fig. 3 shows the hopping amplitudes resulting from these equations.

The hopping amplitudes Eqs. (41) or (42) give rise to four-fermion and six-fermion terms in the Hamiltonian. In the presence of on-site repulsion, the six-fermion term will be irrelevant for the form Eq. (41) (Eq. (42)) when the Fermi level is close to the bottom (top) of the band. For the latter case, the Hamiltonian for hole operators is then

$$H = -\sum_{\langle ij\rangle,\sigma}\big(\bar{t}_{ij}+\Delta t_{ij}(n_{i,-\sigma}+n_{j,-\sigma})\big)\big(c_{i\sigma}^{\dagger}c_{j\sigma}+h.c.\big)+U\sum_i n_{i\uparrow}n_{i\downarrow} \tag{43}$$

of the same form as Eq. (25), with $\bar{t}_{ij} = t_{ij}S^2$ and $\Delta t_{ij} = t_{ij}S(1-S)$.

For small S, $\bar{t}_{ij}$ will be very small, giving rise to a narrow energy band, of width D that grows as the number of holes in the band increases. For a hypercubic lattice with nearest neighbor hopping only $\bar{t}_{ij} = \bar{t}$ the bandwidth is

$$D(n_h) = 2z\bar{t}\big(1+n_h\Delta t\big) \tag{44}$$

with z the number of nearest neighbors to a site.

The physics discussed above is not present in the conventional Hubbard model. For those that cannot renounce the credo that the Hubbard model describes the essential physics of electron correlation in solids I offer “dynamic Hubbard models” [43] that embody the essential ubiquitous presence of electron-hole asymmetry. The physics is schematically shown in Fig. 4. We introduce a fictitious local boson displacement coordinate q_i for atom i that modulates the Hubbard U

$$U(q_i) = U + \alpha q_i \tag{45}$$

that will relax when double occupancy occurs. As the simplest model we describe the boson dynamics by a harmonic oscillator of frequency $\omega_0 = \sqrt{K/M}$

$$H_i = \frac{p_i^2}{2M}+\frac{1}{2}Kq_i^2+\big(U+\alpha q_i\big)n_{i\uparrow}n_{i\downarrow}\,. \tag{46}$$

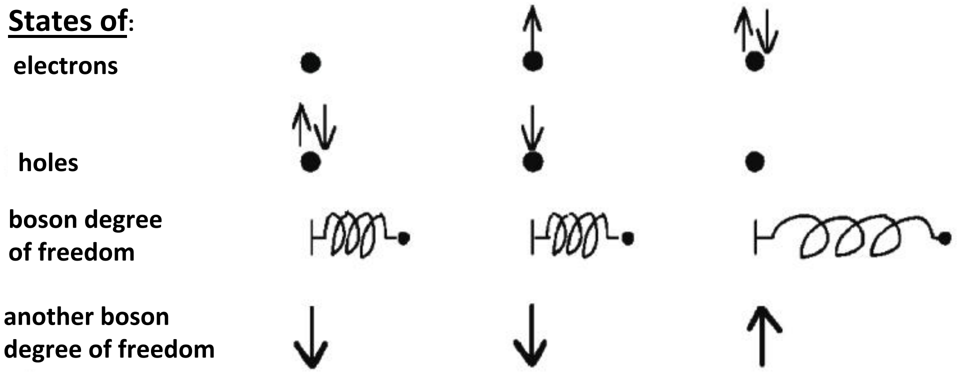

Fig. 4: *Dynamic Hubbard models, or electron-hole asymmetric polarons: a boson degree of freedom is associated with each site. The first electron at the site causes no change or a small change in the ground state of this degree of freedom, and the second electron causes a large change. For holes, the situation is reversed. Two examples of the boson degree of freedom are shown, an oscillator and a spin 1/2.*

The equilibrium position of the boson is $q_i = 0$ for the site empty or singly occupied and $q_i = -\alpha/K$ for the site doubly occupied. This embodies the physics of orbital expansion of the doubly occupied sites discussed above, and increasingly "dresses" the quasiparticles as the Fermi level goes up in the band. In terms of boson creation and annihilation operators $a_i^\dagger$, a_i the site Hamiltonian and the effective Coulomb repulsion between electrons are

$$H_i = \omega_0 \, a_i^\dagger a_i + \big(U + g\omega_0(a_i^\dagger + a_i)\big) n_{i\uparrow} n_{i\downarrow} \tag{47a}$$

$$U_{\mathit{eff}} = U - \frac{\alpha^2}{2K} = U - \omega_0 g^2 \tag{47b}$$

with $g = \alpha/(2K\omega_0)^{1/2}$. The boson degree of freedom describes the electronic excitation of an electron when a second electron is added to the orbital. Hence the frequency ω_0 is related to the excitation energies of the atom, and we expect

$$\omega_0 = cZ^2 \tag{48}$$

where c is a constant of order eV, since the excitation energies in an atom scale with the square of the nuclear charge. From Eqs. (29), (47b) and (48) we conclude that

$$g^2 = \frac{c'}{Z^2}. \tag{49}$$

For a lattice system with hopping amplitude t_{ij} the Hamiltonian is then

$$H = -\sum_{ij,\sigma} t_{ij} \big(c_{i\sigma}^\dagger c_{j\sigma} + h.c.\big) + \sum_i \big(U + g\omega_0(a_i^\dagger + a_i)\big) n_{i\uparrow} n_{i\downarrow} + \sum_i \omega_0 a_i^\dagger a_i \tag{50}$$

Treating the four-fermion term in mean field, the electron-boson part of the Hamiltonian Eq. (50) is

$$H_{\mathit{el\text{-}b}} = g(n)\omega_0 \big(a_i^\dagger + a_i\big) \big(n_{i\uparrow} + n_{i\downarrow}\big) \tag{51a}$$

with

$$g(n) = \frac{n}{2} g \tag{51b}$$

that is, an ordinary electron-boson coupling with a coupling constant that increases with band filling. Hence as in the usual electron-phonon interaction it will give rise to an effective mass enhancement and a quasiparticle weight reduction which increases as the band filling increases. Performing a generalized Lang-Firsov transformation on the fermion and boson operators [48] we obtain

$$c_{i\sigma} = e^{g(a_i^\dagger - a_i)\tilde{n}_{i,-\sigma}} \tilde{c}_{i\sigma} \equiv X_{i\sigma} \tilde{c}_{i\sigma} \tag{52a}$$

$$a_i = \tilde{a}_i - g \tilde{n}_{i\uparrow} \tilde{n}_{i\downarrow} \tag{52b}$$

and the Hamiltonian Eq. (50) becomes

$$H = -\sum_{ij,\sigma} t_{ij} \big(X_{i\sigma}^\dagger X_{j\sigma} \tilde{c}_{i\sigma}^\dagger \tilde{c}_{j\sigma} + h.c. \big) + \sum_i U_{\mathit{eff}} \tilde{n}_{i\uparrow} \tilde{n}_{i\downarrow} + \sum_i \omega_0 \tilde{a}_i^\dagger \tilde{a}_i \tag{53}$$

with U_{eff} given by Eq. (47b). The ground state expectation value of the $X_{i\sigma}$ operator is

$$\langle X_{i\sigma} \rangle_0 = e^{-(g^2/2)\tilde{n}_{i,-\sigma}} = 1 + (S-1) \tilde{n}_{i,-\sigma} \tag{54a}$$

$$S = e^{-g^2/2} \tag{54b}$$

The part of the fermion operator Eq. (52a) associated with ground state to ground state transitions of the boson field is the coherent part of the operator, the quasiparticle. We have then

$$c_{i\sigma} = |0\rangle\langle 0| \big(1 + (S-1) \tilde{n}_{i,-\sigma} \big) \tilde{c}_{i\sigma} + c_{i\sigma}^{\mathit{incoh}} \tag{55}$$

where the coherent part was given in Eq. (35). $|0\rangle$ denotes the ground state of the auxiliary boson. The incoherent part of the operator

$$c_{i\sigma}^{\mathit{incoh}} = \Bigg(\tilde{n}_{i,-\sigma} \sum_{(l,l') \neq (0,0)} |l\rangle\langle l| e^{g(a_i^\dagger - a_i)} |l'\rangle\langle l'| + \sum_{l \neq 0} |l\rangle\langle l| \Bigg) \tilde{c}_{i\sigma} \tag{56}$$

describes processes where the boson field makes transitions to and from excited states $|l\rangle$, $l \neq 0$, which only take place if $\tilde{n}_{i,-\sigma} = 1$, that is if the orbital is occupied by another electron of opposite spin.

Replacing the ground state expectation values of the $X_{i\sigma}$ operators in the Hamiltonian Eq. (53), gives rise to the hopping amplitudes discussed earlier, Eq. (41). This will be accurate for $\omega \gg t_{ij}$. The quasiparticle weight in this model is, from Eq. (55)

$$z(n) = \Big(1 + \frac{n}{2} (S-1) \Big)^2 \tag{57}$$

as was already given in Eq. (36), it decreases monotonically with electronic band filling n_e, $0 \leq n_e \leq 2$, so that quasiparticles become increasingly dressed as the band filling increases. The factor S is the overlap matrix element of the oscillator ground states with and without site double occupancy [48], and S^2 gives the quasiparticle weight for a hole in the filled band (n=2

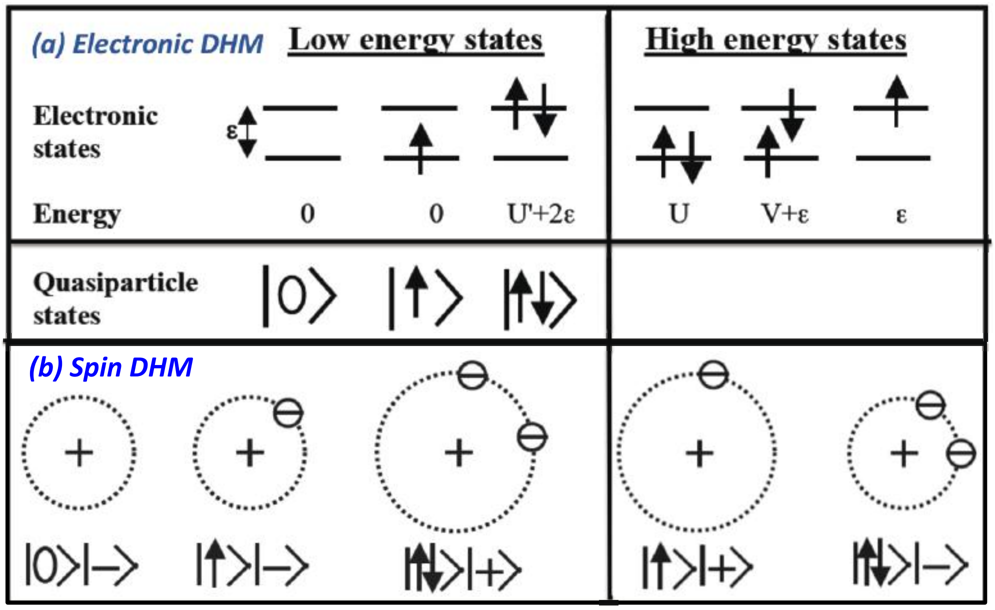

Fig. 5: *(a) Site states of an electronic dynamic Hubbard model (DHM) with two orbitals per site. (b) Site states of a dynamic Hubbard model with an auxiliary spin degree of freedom denoted by states $|+\rangle, |-\rangle$. For both cases, as indicated in the center panel, the left three states are lowest in energy and are the quasiparticle states in the low energy effective Hamiltonian with the correlated hopping term Eq. (43).*

in Eq. (57)). According to Eqs. (49) and (54b), as the ionic charge Z decreases S decreases rapidly, implying that hole quasiparticles become increasingly incoherent.

We can estimate S from first principles for a hydrogen-like ion. In the Hartree approximation, S will be given by the overlap matrix element of the electron wave function in the presence and in the absence of another electron in the orbital

$$S = |\langle \varphi_{1s} | \bar{\varphi}_{1s} \rangle| = \frac{(1 - \frac{5}{16Z})^{3/2}}{(1 - \frac{5}{32Z})^3} \tag{58}$$

with $\bar{\varphi}_{1s}$ the $1s$ orbital with Z replaced by $\bar{Z} = Z - 5/16$, as appropriate for the Hartree wavefunction [43]. Better estimates can be obtained with other more accurate approximations to the two-electron wavefunction [50].

Other forms of dynamic Hubbard models have also been proposed and studied, where the auxiliary boson degree of freedom is a spin 1/2 instead of an oscillator, as well as one with purely electronic degrees of freedom involving two orbitals per site [50, 51]. The low and high energy states in these models are shown in Fig. 5. The essential physics is always the same and leads to the correlated hopping Hamiltonian Eq. (43) in the limit where the boson excitation energies are large. Dynamic Hubbard models have been studied numerically using exact diagonalization [51–53], quantum Monte Carlo [52, 54] and dynamical mean-field theory [55]. The effect of finite boson frequency was studied analytically in Ref. [56] using Eliashberg theory. Both from exact diagonalization for small clusters [52] and analytically [56] it was found that finite frequencies enlarge the parameter regime that gives rise to pairing and superconductivity relative to that in the antiadiabatic limit.

2.4 Superconductivity in dynamic Hubbard models

The dynamic Hubbard models discussed in the previous section describe increased dressing of the quasiparticles when the Fermi level goes up in the band. When the Fermi level is close to the top of the band, and carriers pair, it means that locally the band filling decreases, hence carriers partially undress. This provides a mechanism for superconductivity [57,58], driven by lowering of kinetic energy [59]. The undressing gives rise to experimental signatures, in particular transfer of spectral weight from high to low frequencies in both the single and two-particle spectral function [49,53,60], that can be detected experimentally in photoemission [61] and optical [62] experiments respectively. This physics leads to an apparent violation of the conductivity sum rule, that was predicted theoretically in 1992 [63,60] and first observed experimentally 10 years later [62]. The fact that the superconductivity mechanism is tied to electron-hole asymmetry also gives rise to experimental signatures, in particular a tunneling asymmetry of universal sign, predicted theoretically in 1989 [64] and first observed experimentally around 1995 and thereafter [65].

We focus on the low energy physics that results from the correlated hopping Hamiltonian Eq. (21), with the addition of off-site Coulomb repulsion $V_{ij}n_in_j$. In momentum space the Hamiltonian is, in hole representation

$$H=\sum_{k\sigma}\big(\varepsilon_k-\mu\big)c^\dagger_{k\sigma}c_{k\sigma}+\frac{1}{N}\sum_{kk'q}\big(V(q)+\alpha(\varepsilon_k+\varepsilon_{k+q}+\varepsilon_{k'}+\varepsilon_{k'-q})\big)c^\dagger_{k+q\uparrow}c^\dagger_{k'-q\downarrow}c_{k'\downarrow}c_{k\uparrow} \tag{59a}$$

$$V(q)=\sum_j e^{iqR_j}V_{0j} \tag{59b}$$

with $V_{00}=U$, and $\alpha=\Delta t_{ij}/\bar{t}_{ij}$. Assuming only nearest neighbor hopping and only on-site and nearest-neighbor repulsion, we write the pair interaction in the BCS reduced Hamiltonian Eq. (4) as

$$V_{kk'}=V(\varepsilon_k,\varepsilon_{k'})=U+\frac{K}{D/2}(\varepsilon_k+\varepsilon_{k'})+\frac{W}{D/2}\varepsilon_k\varepsilon_{k'} \tag{59c}$$

with the bandwidth $D=2z\bar{t}$, z the number of nearest neighbors to a site, $K=2z\Delta t$ and $W=zV$. We have left out some terms in $V(k-k')$ that are odd under $k\to-k$ or $k'\to-k'$ that drop out in the subsequent development. Note that everything depends on kinetic energy rather than momentum, hence the resulting gap function will obey $\Delta_k=\Delta(\varepsilon_k)$, and in particular will be constant over the Fermi surface. The usual BCS gap equation is

$$\Delta_k=-\frac{1}{N}\sum_{k'}V(\varepsilon_k,\varepsilon_{k'})\Delta_{k'}\frac{\tanh(\beta E_{k'}/2)}{2E_{k'}}\,. \tag{60}$$

with

$$E_k=\sqrt{(\varepsilon_k-\mu)^2+\Delta_k^2}. \tag{61}$$

From the form of $V(\varepsilon_k,\varepsilon_{k'})$ it follows that $\Delta_k=\Delta(\varepsilon_k)$ is a linear function of ε_k, which we parametrize as

$$\Delta(\varepsilon_k)=\Delta_m\Big(-\frac{\varepsilon_k}{D/2}+c\Big) \tag{62}$$

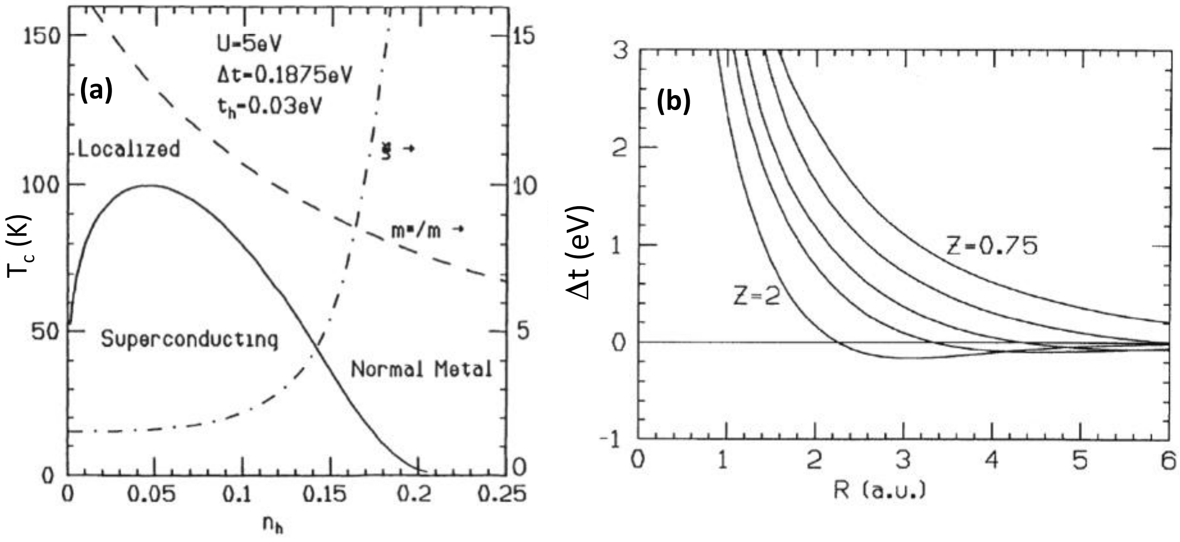

Fig. 6: *The left panel shows the typical behavior of critical temperature versus hole concentration in this model for one set of parameters appropriate for high T_c cuprates; the behavior of the coherence length versus hole concentration in units of lattice spacing and of the ratio of effective mass to band mass is shown on the right-hand scale $\big(m^*/m = (\bar{t}+2\Delta t)/(\bar{t}+n_h\Delta t)\big)$. The right panel shows the behavior of the parameter Δt as function of interatomic distance and various values of the effective ionic charge Z ($Z = 0.75$, 1, 1.25, 1.5, 2).*

and replacement of Eq. (62) in Eq. (60) yields the following two equations [57,58]

$$1 = K(I_1+cI_0) - W(I_2+cI_1) \tag{63a}$$

$$c = K(I_2+cI_1) - U(I_1+cI_0) \tag{63b}$$

with

$$I_\ell = \frac{1}{N}\sum_k \Big(-\frac{\varepsilon_k}{D/2}\Big)^\ell \, \frac{\tanh(\beta E_{k'}/2)}{2E_{k'}} \, . \tag{64}$$

These equations are solved numerically for Δ_m and c as function of temperature and band filling determined by μ. To obtain the critical temperature, a single equation needs to be solved, obtained by combining Eqs. (63a) and (63b)

$$1 = 2KI_1 - WI_2 - UI_0 + \big(K^2-WU\big)\big(I_0I_2-I_1^2\big) \tag{65}$$

with $E_k = |\varepsilon_k-\mu|$ in the formulas for I_ℓ. Eq. (65) will have a solution, i.e. give rise to superconductivity, when the parameters in the Hamiltonian Eq. (59) satisfy the condition [36]

$$k > \sqrt{(1+u)(1+w)} - 1 \tag{66}$$

with $u = gU, w = gW, k = gK$, and g the density of states at the Fermi energy.

Fig. 6(a) shows the typical behavior for critical temperature versus hole concentration resulting from this model for a set of parameters appropriate to describe cuprate superconductors. In Fig. 6(b) we show the results for the parameter Δt versus interatomic distance for various values

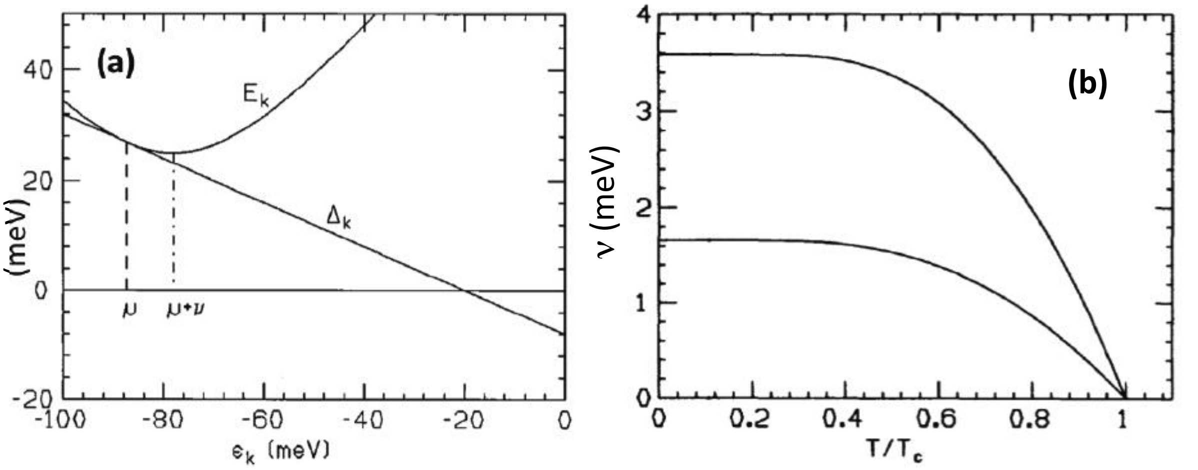

Fig. 7: *(a) shows the gap function and the quasiparticle energy as function of kinetic energy in a hole representation. Note that the gap function changes sign as* ε_k *increases. The minimum in the quasiparticle energy is shifted from the chemical potential* μ *by the asymmetry parameter* ν*. (b) shows the temperature dependence of* ν *for two sets of parameter values. Lower curve:* $U = 5$ *eV,* $K = 3.61$ *eV,* $W = 2.24$ *eV,* $D_h = 0.24$ *eV. Upper curve:* $U = 5$ *eV,* $K = 3.78$ *eV,* $W = 2.60$ *eV,* D_h=0. K=$2z\Delta t$*,* W=zV*, and* z=4*,* z *the number of nearest neighbors to a site.*

of the effective ionic charge Z, obtained from an approximate first-principles calculation for a diatomic molecule [66]. It can be seen that Δt is larger for negatively charged ions ($Z < 2$) in close proximity.

The parameters for Fig. 6(a) are $U = 5$ eV, $\bar{t} = 0.03$ eV, $\Delta t = 0.1875$ eV. The bare bandwidth is 3.24 eV when the Fermi level is near the bottom of the band, but when it is near the top it is narrowed to 0.24 eV since $\bar{t} = t - 2\Delta t$. Superconductivity only occurs near the top of the band, with the characteristic dome-type structure seen in the cuprates as well as in other materials like in the transition metal series [67]. The figure also shows that the effective mass decreases as the Fermi level moves down in the band, and the superconducting coherence length increases. There is a cross-over between strong and weak coupling regimes as the hole concentration increases, as seen in the cuprate superconductors.

From Eqs. (62) and (63), we find that the quasiparticle excitation energy in the superconducting state is given by

$$E_k = \sqrt{a^2(\varepsilon_k - \mu - \nu)^2 + \Delta_0^2} \tag{67a}$$

with

$$a = \sqrt{1 + \left(\frac{\Delta_m}{D/2}\right)^2}\,, \quad \Delta_0 = \frac{\Delta(\mu)}{a} \quad \text{and} \quad \nu = \frac{1}{a}\frac{\Delta_m}{D/2}\,\Delta_0\,. \tag{67b}$$

This is shown in Fig. 7(a). It can be seen that the minimum in the E_k versus ε_k relation is not at the chemical potential, as in usual BCS, because of the energy dependence of the gap. Instead, it is shifted to $\mu+\nu$. Thus, the quasiparticle excitations are not charge-neutral as in usual BCS, they are positively charged. The behavior of the asymmetry parameter ν versus temperature is shown in Fig. 7(b). Both the gap slope $\Delta_m/(D/2)$ and the gap Δ_0 vanish at T_c as the square root of $T_c - T$, hence ν goes linearly to zero at T_c.

The parameter ν gives rise to the asymmetry of universal sign in S-I-N tunneling mentioned earlier. It also gives rise to *positive* thermoelectric power of tunnel junctions: under open-circuit conditions, the thermoelectric voltage is predicted to be [68]

$$V_t = \frac{\nu}{e}\frac{T_s - T_n}{T_n} \tag{68}$$

with T_s and T_n the temperatures in the normal and superconducting sides of the junction respectively. Thus, this effect provides a direct measure of the fundamental asymmetry parameter ν, or equivalently of the gap function slope $\Delta_m/(D/2)$, given an independent estimate of the gap Δ_0. The parameter ν is expected to be of order meV for cuprate superconductors and µeV for conventional superconductors. For quasiparticle tunneling between two superconductors A and B the thermoelectric voltage under open-circuit conditions is

$$V_{AB} = \frac{\nu_A + \nu_B}{e}\frac{T_B - T_A}{(T_A + T_B)/2} \tag{69}$$

neglecting a small correction of order $\nu_A \nu_B / \Delta_{0A}\Delta_{0B}$. These predictions have not been experimentally tested.

3 Charge expulsion and alternative London electrodynamics

In the models discussed in the previous section, charge asymmetry plays an essential role. Superconductivity only occurs when the band is almost full, i.e., a lot of *negative* electrons are present. The essential physics at the atomic level is that the doubly occupied orbital expands, hence negative charge moves outward, driven by both lowering of Coulomb repulsion and lowering of quantum kinetic energy. The pairing interaction Δt is larger when the atoms involved are *negatively* charged anions, i.e., the effective nuclear charge Z is small (Fig. 6b), in which case the atomic orbital expansion is larger. Having fewer electrons in the vicinity of a given electron allows it to hop with larger hopping amplitude, hence its kinetic energy decreases. All of this suggests that systems governed by this physics will have a tendency to *expel* electrons from their interior [69]. That is indeed what they do, and it has fundamental consequences.

3.1 Charge expulsion in dynamic Hubbard models

As was shown in Fig. 7(a), the quasiparticle excitation energy E_k is not symmetric around the chemical potential due to the energy dependence of the gap. The BCS coherence factors are given by the usual form

$$u_k^2 = \frac{1}{2}\Big(1 + \frac{\varepsilon_k - \mu}{E_k}\Big) = \frac{1}{2}\Big(1 + \frac{\varepsilon_k - \mu - \nu}{E_k}\Big) + \frac{\nu}{2E_k} \tag{70a}$$

$$v_k^2 = \frac{1}{2}\Big(1 - \frac{\varepsilon_k - \mu}{E_k}\Big) = \frac{1}{2}\Big(1 - \frac{\varepsilon_k - \mu - \nu}{E_k}\Big) - \frac{\nu}{2E_k} \tag{70b}$$

and as a consequence quasiparticles are positively charged on average. The net quasiparticle charge per site is given by

$$Q^* = \frac{2}{N}\sum_k \left(u_k^2 - v_k^2\right) f(E_k) = 2\nu \frac{1}{N}\sum_k \frac{1}{E_k}\,. \tag{71}$$

As a consequence of quasiparticles being positively charged, the condensate will acquire an extra negative charge.

Hence the superconductor is characterized by having two different ‘chemical potentials’. The chemical potential μ corresponds to the condensate, and $\mu' = \mu + \nu$ to the quasiparticle excitations. In a hole representation, $\mu' > \mu$, in an electron representation $\mu' < \mu$. The negatively charged condensate, by virtue of being a superfluid as well as because of the effective mass reduction that occurs due to pairing and undressing, is highly mobile, in contrast to the quasiparticles which experience normal scattering and have the higher effective mass characteristic of the normal-state dressed carriers. As a consequence, one expects that the negative condensate will have a tendency to move out of the bulk of the superconductor, so as to tend to equate the chemical potentials μ and μ' in the bulk. Because of overall charge neutrality, the negative charge will accumulate near the surface of the superconductor.

An estimate of the maximum amount of charge that will be expelled from the bulk of the superconductor is given by the ratio of the difference in chemical potentials to the bandwidth D:

$$n_{max} = \frac{2(\mu' - \mu)}{D} = \frac{2\nu}{D} \tag{72}$$

carriers per site, so it is very small. However, the tendency to charge expulsion will be counteracted by Coulomb charging energy.

That this physics takes place is confirmed by numerical analysis of the underlying Hamiltonian [70]. We consider the Hamiltonian in the hole representation

$$H = -\sum_{ij\sigma} t_{ij}^{\sigma}\left(c_{i\sigma}^{\dagger} c_{j\sigma} + h.c.\right) + U \sum_i n_{i\uparrow} n_{i\downarrow} \tag{73a}$$

$$t_{ij}^{\sigma} = t_h + \Delta t\left(n_{i,-\sigma} + n_{j,-\sigma}\right) + \Delta t_2 n_{i,-\sigma} n_{j,-\sigma} \tag{73b}$$

with $t_h = tS^2$ $\Delta t = tS(1-S)$, $\Delta t_2 = t(1-S)^2 = (\Delta t)^2/t_h$. The fact that the hopping amplitudes Eq. (73b) increase with hole occupation suggests that the system will have a tendency to *expel electrons* from its interior to the surface, because the coordination of sites in the interior is larger than of sites at the surface. This is indeed what we find numerically. We assume a cylindrical geometry of radius R and infinite length in the z-direction, and decouple the interaction terms within a simple mean field approximation assuming $\langle n_{i\sigma}\rangle = n_i/2$ with n_i the hole occupation at site i, yielding the mean field Hamiltonian

$$H_{mf} = -\sum_{\langle ij\rangle,\sigma} \left(t_h + \Delta t n_i + \Delta t_2 \frac{n_i^2}{4}\right)\left(c_{i\sigma}^{\dagger} c_{j\sigma} + h.c.\right) + \frac{U}{4}\sum_i n_i^2 - \sum_{\langle ij\rangle} n_i \left(\Delta t + \frac{n_j}{2}\Delta t_2\right) \sum_\sigma \langle c_{i\sigma}^{\dagger} c_{j\sigma}\rangle \tag{74}$$

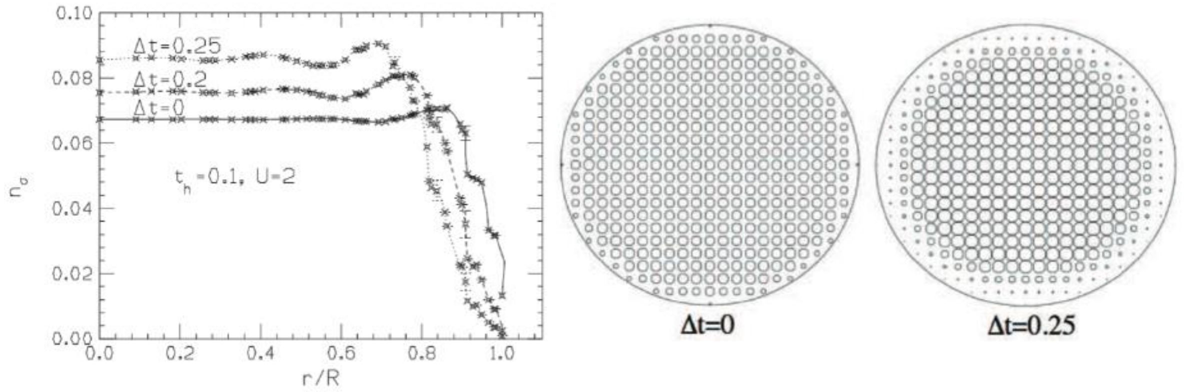

Fig. 8: *Left panel: hole site occupation per spin n_σ for a cylinder of radius R=11 as a function of r/R, with r the distance to the center, for a cubic lattice of side length 1. There are 377 sites in a cross-sectional area ($\pi R^2 = 380.1$). The average occupation for both spins is $n = 0.126$ holes per site. Parameters in the Hamiltonian are shown on the left panel. $\Delta t_2 = 0$. On the right panel we show the results for two cases from the left panel, representing the hole occupation at the site with circles of diameter proportional to it. Note that for finite Δt the hole occupation increases in the interior and is depleted near the surface, leading to charge inhomogeneity with excess negative charge near the surface and excess positive charge in the interior, relative to a neutralizing background of charge density n.*

Note that the local average bond occupation modifies the local chemical potential. Assuming a band filling of n holes per site, we diagonalize the Hamiltonian Eq. (74) on a finite lattice with initial values $n_i = n$ and fill the lowest energy levels until the occupation n is achieved. From the Slater determinant of that state we obtain new values of n_i for each site and for the local bond occupation, and iterate this procedure until self-consistently is achieved. We then examine the resulting occupation of the sites as function of the distance r to the center of the cylinder. Fig. 8 shows a typical example of the behavior found. Here we assumed $\Delta t_2 = 0$, corresponding to the simpler Hubbard model with correlated hopping and no six-fermion operator term. Even for $\Delta t = 0$ the hole occupation is somewhat larger in the interior than near the surface. When the interaction Δt is turned on, the hole occupation increases in the interior and decreases near the surface. This indicates that the system expels electrons from the interior to the surface. The effect becomes more pronounced when Δt is increased or t_h is decreased. Finite Δt_2 enhances the effect. For larger values of the parameters the system develops a tendency to phase separation, where holes condense in the interior and the outer region of the cylinder has no holes. The instability condition for phase separation can be found analytically.

Of course in a real material this tendency to charge segregation will be countered by longer range Coulomb repulsion. But it is clear that this physics will cause a tendency to develop local charge inhomogeneity: because kinetic energy dominates the physics of the dynamic Hubbard model, the system will develop charge inhomogeneity at a cost in potential energy if it can thereby lower its kinetic energy more, unlike systems where the dominant physics is potential-energy driven like the conventional Hubbard model. High T_c cuprates, for which Δt should be large, show a strong tendency to charge inhomogeneity.

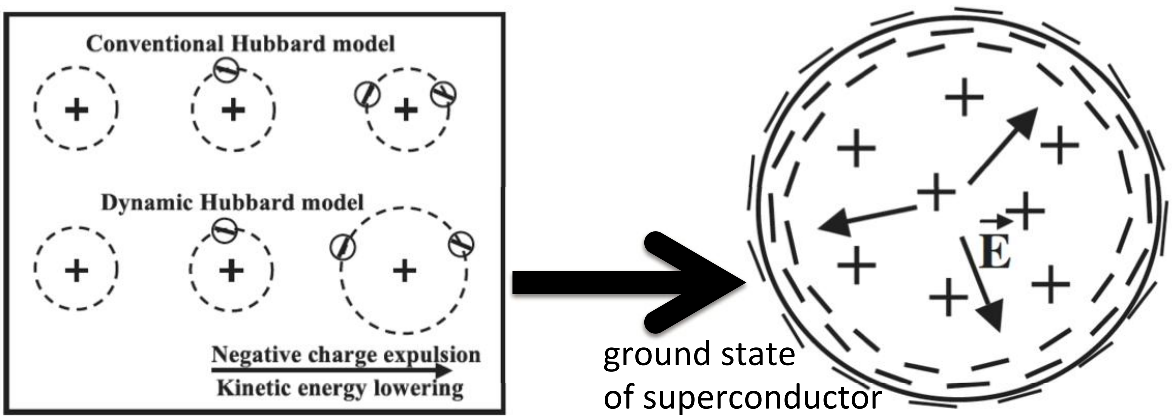

Fig. 9: *The dynamic Hubbard model describes negative charge expulsion and kinetic energy lowering at the atomic level, due to orbital expansion (left panel). In a lattice system it leads to expulsion of negative charge from the interior to the surface. In the superconducting state, a macroscopic charge inhomogeneity develops as shown on the right panel, with an electric field* $\vec{E}(\vec{r})$ *in the interior that points towards the surface.*

3.2 Electric fields in superconductors and alternative London charge electrodynamics

The physics discussed in the previous sections leads to the prediction that when a system goes superconducting it will expel electrons from the interior to the surface, resulting in macroscopic charge inhomogeneity, as shown on the right panel of Fig. 9. In the normal state this cannot occur, the tendency to charge expulsion is countered by the Coulomb repulsion and no electric field can exist in the interior of a normal metal. That minimizes the potential energy. However the superconducting state is a macroscopic quantum state, where the sum of potential and quantum kinetic energy need to be minimized. Just like in the microscopic atom the charge distribution is inhomogeneous, with the negative charge more "spread out" than the positive charge to lower its quantum kinetic energy, the same will be true in the superconductor, which is in some sense a "giant atom". This is also suggested by the fact that the superfluid condensate is described by a macroscopic quantum wavefunction $\psi(\vec{r})=|\psi(\vec{r})|e^{i\theta(\vec{r})}$ [11, 12], just like the single electron in the hydrogen atom. This results in the existence of an electric field in the interior of superconductors, just like in the hydrogen atom, as shown on the right panel of Fig. 9.

The conventional London equations do not allow for electric fields inside superconductors. However a simple modification of them does [1, 71, 72]. The London equation is derived as:

$$\frac{\partial \vec{J}}{\partial t} = \frac{n_s e^2}{m_e}\vec{E} \to \vec{\nabla}\times\vec{J} = -\frac{n_s e^2}{m_e c}\vec{B} = -\frac{c}{4\pi\lambda_L^2}\vec{B}, \quad \frac{1}{\lambda_L^2} = \frac{4\pi n_s e^2}{m_e c^2} \to \nabla^2\vec{B} = \frac{1}{\lambda_L^2}\vec{B} \tag{75}$$

The equation on the left describes the collisionless response of a conducting fluid of density n_s to an applied electric field $\vec{E}$, i.e., free acceleration of superfluid carriers of charge e and mass m_e, giving rise to the supercurrent $\vec{J} = n_s e\vec{v}$, with $\vec{v}$ the carrier velocity. Upon application of the curl on both sides, using Faraday's law and integrating over the time derivatives, the second equation results, called the London equation. From applying the curl to both sides of Ampere's law $\vec{\nabla}\times\vec{B} = (4\pi/c)\vec{J}$ and replacing $\vec{\nabla}\times\vec{J}$ in Eq. (75), the right-hand side expression results, that predicts that the magnetic field decays exponentially over a distance λ_L in going from the surface towards the interior of the superconductor.

We note however that the London equation can be written as

$$\vec{\nabla}\times\vec{J} = -\frac{c}{4\pi\lambda_L^2}\vec{B} \rightarrow \vec{J} = -\frac{c}{4\pi\lambda_L^2}\vec{A} \tag{76}$$

with $\vec{A}$ the magnetic vector potential, $\vec{\nabla}\times\vec{A} = \vec{B}$. Faraday's law, upon integration, leads to

$$\vec{\nabla}\times\vec{E} = -\frac{1}{c}\frac{\partial\vec{B}}{\partial t} \rightarrow \vec{E} = -\vec{\nabla}\phi - \frac{1}{c}\frac{\partial\vec{A}}{\partial t} \tag{77}$$

where ϕ is the electric potential. Taking the time derivative of the right hand side of Eq. (76) and using Eq. (77) leads to

$$\frac{\partial\vec{J}}{\partial t} = \frac{n_s e^2}{m_e}\big(\vec{E}+\vec{\nabla}\phi\big) \tag{78}$$

which, unlike the left-hand-side of Eq. (75), allows for the presence of an electric field that derives from a potential that will not give rise to an infinite current. Note that the left-hand-side of Eq. (75) is derived from Newton's equation by replacing the total time derivative by the partial time derivative, which is not correct.

Note that the right-hand-side of Eq. (76) relates the electric current density, a physical quantity, to the magnetic vector potential, that is gauge-dependent. Assuming different gauges for $\vec{A}$ in Eq. (76) leads to different physics. The London brothers assumed that $\vec{\nabla}\cdot\vec{A} = 0$, the "London gauge", which has as a consequence that no electric fields can exist in the interior of superconductors. But that was just an unproven assumption. Instead, we will assume that $\vec{A}$ obeys the Lorentz gauge, as was also done in the first London paper [1]

$$\vec{\nabla}\cdot\vec{A} = -\frac{1}{c}\frac{\partial\phi}{\partial t}. \tag{79}$$

Upon taking the divergence of both sides of the right-hand-side of Eq. (76), and using the continuity equation $\vec{\nabla}\cdot\vec{J} = -\partial\rho/\partial t$ with ρ the charge density and the gauge condition Eq. (79) we obtain

$$\vec{J} = -\frac{c}{4\pi\lambda_L^2}\vec{A} \rightarrow \frac{\partial\rho}{\partial t} = -\frac{1}{4\pi\lambda_L^2}\frac{\partial\phi}{\partial t} \tag{80}$$

and integrating with respect to time to

$$\phi(\vec{r},t)-\phi_0(\vec{r}) = -4\pi\lambda_L^2\big(\rho(\vec{r},t)-\rho_0(\vec{r})\big) \tag{81}$$

where $\phi_0(\vec{r})$ and $\rho_0(\vec{r})$ are constants of integration. A possible choice would be $\phi_0 = \rho_0 = 0$ [1]. Instead, motivated by the physics discussed in the previous sections, we choose $\rho(\vec{r}) = \rho_0 > 0$, that is, a uniform positive charge density in the interior of the superconductor. This then implies that the electrostatic potential $\phi(\vec{r},t)$ equals $\phi_0(\vec{r})$ when the charge density in the interior of the superconductor is constant, uniform, and equal to ρ_0. From Maxwell's equations we deduce that $\phi_0(\vec{r})$ is given by

$$\phi_0(\vec{r}) = \int_V d^3r'\,\frac{\rho_0}{|\vec{r}-\vec{r}'|} \tag{82}$$

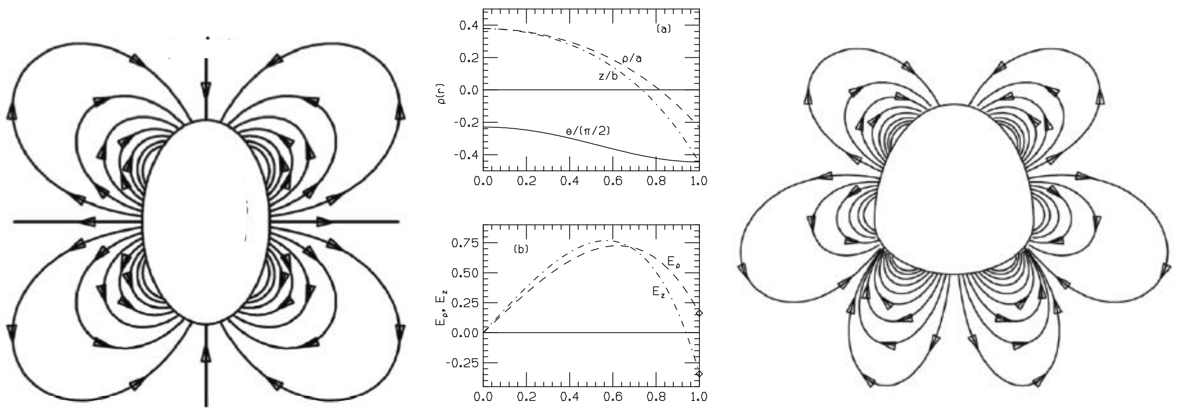

Fig. 10: *Results from numerical solution of the electrostatic equations. Left panel: electric field lines in the exterior of a sample of ellipsoidal shape, of dimensions* $a = 1, b = 1.5$. *London penetration depth is* $\lambda_L = 0.5$ *and* $\rho_0 = 0.1$. *Middle panel top: Charge density in the interior of the superconductor along the horizontal axis plotted versus* ρ/a *(curve labeled* ρ/a *and along the vertical axis plotted versus* z/b *(curve labeled* z/b*) and on the boundary plotted versus* $\theta/(\pi/2)$*, with* $\theta = \tan^{-1}(z/b)/(\rho/a)$*; note that the negative charge density near the surface is larger in magnitude along the* z*-direction. Middle panel bottom: Electric fields in the interior along the* ρ/a *and* z/b *(dot-dashed) directions. Note that the electric field along the* z*-direction changes sign near the surface, and that the electric fields are finite at the surface. Right panel: Electric field lines in the exterior of a sample of egg-like shape*

where the integral is over the volume of the superconducting body. ρ_0 is a function of the material, the temperature, and the volume and shape of the superconducting body. Before discussing its value, we discuss some consequences of these equations.

In the absence of time dependence, the electrostatic equations can be solved analytically for simple geometries (sphere, cylinder, plane) and numerically for other geometries. For example, for a sphere of radius R we obtain for the charge density and electric field

$$\rho(r) = \rho_0 \left(1 - \frac{1}{3} \frac{R^3}{\lambda_L^2 r} \frac{\sinh(r/\lambda_L)}{f(R/\lambda_L)} \right); \quad \vec{E}(r) = \frac{4}{3} \pi \rho_0 \vec{r} \left(1 - \frac{R^3}{r^3} \frac{f(r/\lambda_L)}{f(R/\lambda_L)} \right) \tag{83}$$

with $f(x) = x \cosh x - \sinh x$. Within a layer of thickness λ_L from the surface there is excess negative charge density $\rho_- = -R/(3\lambda_L)\rho_0$. The electric field grows linearly with distance from the center of the sphere, peaks at distance λ_L from the surface, with peak value $E_m = -4\pi\lambda_L\rho_-$, decays to zero at $r = R$, and is of course zero for $r > R$. For a long cylinder of radius R, the peak value of the electric field E_m at distance λ_L from the surface is given by the same expression in terms of ρ_-, and $\rho_- = -R/(2\lambda_L)\rho_0$. The expressions for the charge density and electric field as function of r involve Bessel functions of imaginary argument.

For more general geometries, the electric field will "leak out" from the interior and be non-zero outside the superconducting sample. In particular, ellipsoidal samples give rise to quadrupolar electric fields in the exterior [73, 74]. Figure 10 shows examples of field lines and position dependence of charge density and electric field in the interior of an ellipsoidal sample. Note that the electric field lines outside the samples go out from regions of lower surface curvature and go into regions of higher surface curvature. This is easy to understand qualitatively. As we will discuss later, there are spin currents flowing near the surface of the superconducting body. In the regions of high curvature (low curvature) electrons slow down (speed up), just like racing cars would, so their kinetic energy decreases (increases) and consequently their potential energy increases (decreases), to keep the total energy constant. Higher (lower) potential energy for the electron means lower (higher) electric potential, and electric field lines go from high potential to low potential.

From Eq. (81) and Maxwell's equations, we deduce that electric and magnetic fields, charges and currents in superconductors, obey the following equations:

$$\nabla^2 \vec{B} = \frac{1}{\lambda_L^2}\vec{B} + \frac{1}{c^2}\frac{\partial^2 \vec{B}}{\partial t^2} \tag{84a}$$

$$\nabla^2 \big(\vec{E} - \vec{E}_0\big) = \frac{1}{\lambda_L^2}(\vec{E} - \vec{E}_0) + \frac{1}{c^2}\frac{\partial^2 (\vec{E} - \vec{E}_0)}{\partial t^2} \tag{84b}$$

$$\nabla^2 \vec{J} = \frac{1}{\lambda_L^2}\vec{J} + \frac{1}{c^2}\frac{\partial^2 \vec{J}}{\partial t^2} \tag{84c}$$

$$\nabla^2 \big(\rho - \rho_0\big) = \frac{1}{\lambda_L^2}(\rho - \rho_0) + \frac{1}{c^2}\frac{\partial^2 (\rho - \rho_0)}{\partial t^2} \tag{84d}$$

so that all quantities obey exactly the same equation.

The simplicity of eqs. (84) derives from the fact that the theory is relativistically covariant. We define the current four-vector and the four-vector potential in the usual way

$$J = \big(\vec{J}(\vec{r},t),\, ic\rho(\vec{r},t)\big) \quad \text{and} \qquad A = \big(\vec{A}(\vec{r},t),\, i\phi(\vec{r},t)\big). \tag{85}$$

The continuity equation sets the four-dimensional divergence of the four-vector J equal to zero, where the fourth derivative is $\partial/\partial(ict)$, and the Lorenz gauge condition sets the divergence of the four-vector A to zero

$$\mathrm{Div}\, J = 0 \quad \text{and} \qquad \mathrm{Div}\, A = 0. \tag{86}$$

Furthermore we define the four-vectors associated with the positive uniform charge density ρ_0 and its associated current $\vec{J}_0$, denoted by J_0, and the associated four-vector potential A_0. In the frame of reference where the superconducting body is at rest the spatial part of these four-vectors is zero, hence

$$J_0 = \big(0, ic\rho_0\big) \quad \text{and} \qquad A_0 = \big(0, i\phi_0(\vec{r})\big) \tag{87}$$

in that reference frame. In any inertial reference frame, A_0 and J_0, as well the four-vectors J and A obey

$$\Box^2 A_0 = -\frac{4\pi}{c} J_0 \quad \text{and} \qquad \Box^2 A = -\frac{4\pi}{c} J \tag{88}$$

with the d'Alembertian operator

$$\Box^2 = \nabla^2 - \frac{1}{c^2}\frac{\partial^2}{\partial t^2}. \tag{89}$$

Our fundamental equation is then either of the following relations between four-vectors

$$\Box^2(A-A_0)=\frac{1}{\lambda_L^2}(A-A_0) \quad \text{and} \qquad J-J_0=-\frac{c}{4\pi\lambda_L^2}(A-A_0) \tag{90}$$

valid in any inertial reference frame. In the frame of reference at rest with respect to the superconducting body, J_0 and A_0 have only time-like components, in another reference frame they will also have space-like components. Eq. (84) for the fields, current and charge density can be written in covariant form as

$$\Box^2(J-J_0)=\frac{1}{\lambda_L^2}(J-J_0) \quad \text{and} \qquad \Box^2(F-F_0)=\frac{1}{\lambda_L^2}(F-F_0) \tag{91}$$

where F is the usual electromagnetic field tensor and F_0 is the field tensor with entries $\vec{E}_0$ and 0 for $\vec{E}$ and $\vec{B}$ respectively when expressed in the reference frame at rest with respect to the ions. An important consequence of these equations is that they predict that externally applied electrostatic fields should be screened over a distance λ_L, the London penetration depth [75, 76], rather than over the much shorter Thomas-Fermi screening length, as the conventional theory predicts. This should be so at zero temperature. At finite temperatures, the effective screening length decreases since excited quasiparticles screen with the much shorter Thomas Fermi screening length.

3.3 Spin electrodynamics and the Spin-Meissner effect

The canonical momentum of an electron with superfluid velocity $\vec{v}_s$ is $\vec{p}=m_e\vec{v}_s+\frac{e}{c}\vec{A}$, with $\vec{A}$ the magnetic vector potential. In the BCS ground state the expectation value $\langle\vec{p}\rangle=0$, hence the superfluid velocity is given by $\vec{v}_s=-\frac{e}{m_ec}\vec{A}=-\frac{e\lambda_L}{m_ec}\vec{B}\times\hat{n}$. The second equality applies to a cylindrical geometry, where $\hat{n}$ is the outward pointing normal of the lateral surface of the cylinder and $\vec{B}$ is the magnetic field along the axis of the cylinder.

Consider an electron that moves radially outward from the axis of a cylinder in the presence of a magnetic field $\vec{B}$ parallel to the cylinder. The equation of motion is

$$m_e\frac{d\vec{v}}{dt}=\frac{e}{c}\vec{v}\times\vec{B}+\vec{F}_r \tag{92}$$

where the first term is the magnetic Lorentz force and the second term is a radial force arising from “quantum pressure” that drives the electron outward. From it we infer

$$\vec{r}\times\frac{d\vec{v}}{dt}=\frac{e}{m_ec}\vec{r}\times(\vec{v}\times\vec{B}) \tag{93}$$

where $\vec{r}$ is in the plane perpendicular to the axis of the cylinder. Hence $\vec{r}\cdot\vec{B}=0$ and $\vec{r}\times(\vec{v}\times\vec{B})=-(\vec{r}\cdot\vec{v})\vec{B}$, and

$$\frac{d}{dt}(\vec{r}\times\vec{v})=-\frac{e}{m_ec}(\vec{r}\cdot\vec{v})\vec{B}=-\frac{e}{2m_ec}\left(\frac{d}{dt}r^2\right)\vec{B} \tag{94}$$

so that $\vec{r}\times\vec{v}=-\frac{e}{2m_ec}r^2\vec{B}$, and the acquired azimuthal velocity in moving out a distance r is

$$v_\phi=-\frac{e}{2m_ec}rB \tag{95}$$

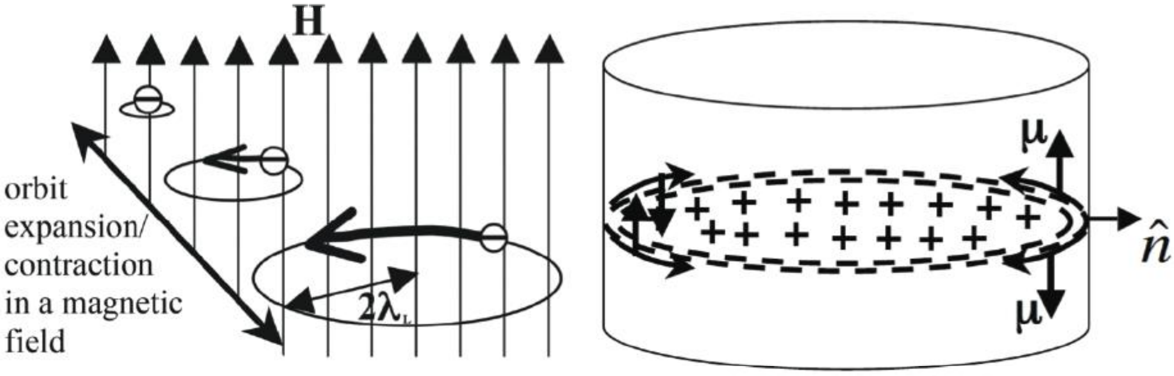

Fig. 11: *Left panel: when electrons forming a Cooper pair enlarge their orbits from a microscopic radius to radius $2\lambda_L$, they acquire the azimuthal velocity required for the Meissner current. The interior currents cancel out, and a charge current circulating in the surface layer of thickness λ_L results, the Meissner current. Right panel: electrons in expanding orbits acquire also azimuthal velocity through the spin-orbit interaction of their magnetic moment $\mu_z = -2\mu_B S_z$, with μ_B the Bohr magneton, leading to a spin current circulating in the surface layer of thickness λ_L, that adds to the charge current (if any), or is a pure spin current in the absence of applied magnetic field.*

Thus, to acquire the azimuthal speed needed for the Meissner current, $v_s = -e\lambda_L/(m_e c)B$, requires the action of the Lorentz force *over a radially outgoing motion to radius* $r = 2\lambda_L$. This is shown schematically in Fig. 11 left panel.
Consider next a magnetic moment $\vec{\mu}$ along the z direction that moves radially outward with velocity $\vec{v}$. It is equivalent to an electric dipole moment $\vec{p} = \frac{\vec{v}}{c} \times \vec{\mu}$. The radial electric field of the cylinder that results from the positive charge that compensates the superfluid negative charge density en_s is $\vec{E} = 2\pi\rho\vec{r} = 2\pi|e|n_s\vec{r}$. The electric dipole experiences a torque

$$\vec{\tau} = \vec{p} \times \vec{E} = \left(\frac{\vec{v}}{c} \times \vec{\mu}\right) \times \vec{E} = -2\pi\,|e\,n_s \vec{r} \times \left(\frac{\vec{v}}{c} \times \vec{\mu}\right) \tag{96}$$

which causes a change in its angular momentum

$$\frac{d\vec{L}}{dt} = m_e \frac{d}{dt}\left(\vec{r} \times \vec{v}\right) = \vec{\tau} \tag{97}$$

hence

$$\vec{r} \times \frac{d\vec{v}}{dt} = \frac{2\pi e n_s}{m_e} \vec{r} \times \left(\frac{\vec{v}}{c} \times \vec{\mu}\right). \tag{98}$$

Eq. (98) is identical to Eq. (93) if we define the 'effective' magnetic field

$$\vec{B}_\sigma = 2\pi n_s \vec{\mu} \tag{99}$$

and hence leads to the azimuthal velocity as derived earlier, $v_s = -e\lambda_L/(m_e c)B$, with B_σ replacing B and $|\vec{\mu}| = \mu_B$ the intrinsic magnetic moment of the electron

$$v_\phi = -\frac{\pi e n_s}{m_e c} r \mu_B \quad \text{and} \qquad v_\phi = \frac{\pi n_s e^2 \hbar r}{2m_e^2 c^2} = \frac{\hbar r}{8 m_e \lambda_L^2} \tag{100}$$

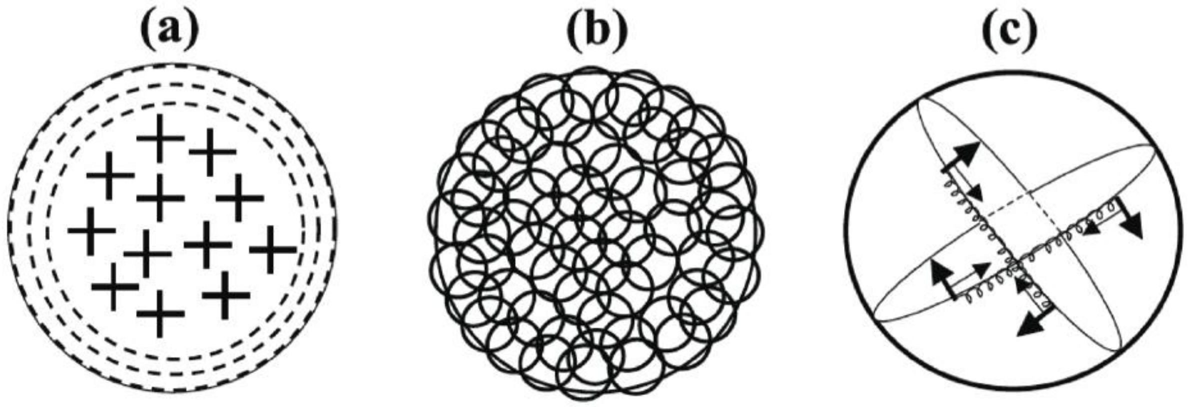

Fig. 12: *Illustration of the three key aspects of the physics of superconductors discussed here. (a) : Superconductors expel negative charge from their interior to the region near the surface. (b) : Carriers reside in mesoscopic overlapping orbits of radius $2\lambda_L$. (c) : A spin current flows near the surface of superconductors (the arrow perpendicular to the orbit denotes the direction of the electron magnetic moment).*

with $\mu_B = |e|\hbar/2m_e c$ the Bohr magneton. The two electrons in a Cooper pair have opposite spin and orbit in opposite directions. The orbital angular momentum of each electron is $l = m_e r v_\phi = \hbar r^2/(8\lambda_L^2)$.

Remarkably, for $r = 2\lambda_L$, the size of the orbit required to explain the Meissner effect, the orbital angular momentum is $\boxed{l = \hbar/2}$.

The azimuthal velocity has magnitude $v_\phi \equiv v_\sigma^0 = \hbar/(4m_e\lambda_L)$. In the interior, the azimuthal velocities cancel out. Within a layer of thickness λ_L from the surface, they give rise to a spin current, where electrons of opposite spin flow in opposite directions, as shown schematically in Fig. 11 right panel [77,78].

Figure 12 shows the three key aspects of the physics of superconductors within the theory discussed here. (a) The charge distribution in the superconductor is macroscopically inhomogeneous, with excess negative charge near the surface and excess positive charge in the interior. (b) Superfluid carriers reside in overlapping mesoscopic orbits of radius $2\lambda_L$. (c) A macroscopic spin current flows near the surface of superconductors in the absence of applied external fields. Macroscopic phase coherence results from the fact that the $2\lambda_L$ orbits are strongly overlapping.

The fact that superfluid electrons reside in mesoscopic orbits of radius $2\lambda_L$ can be seen from the equivalence of the following two expressions for the total angular momentum L of n_s electrons per unit volume flowing with velocity v along the lateral surface of a cylinder of radius R and height h carrying the Meissner current within a distance λ_L from the surface:

$$L = \big(2\pi R\lambda_L h n_s\big)\big(m_e v R\big) = \big(\pi R^2 h n_s\big)\big(m_e v(2\lambda_L)\big). \tag{101}$$

When spin is taken into account, the four-vector current is $J = J_\uparrow + J_\downarrow$ and the electrodynamic equation (88) becomes [78]

$$J_\sigma - J_{\sigma 0} = -\frac{c}{8\pi\lambda_L^2}\big(A_\sigma - A_{\sigma 0}\big) \quad \text{and} \quad J_\sigma = \big(\vec{J}_\sigma,\, ic\rho_\sigma\big)\ , \quad A_\sigma = \big(\vec{A}_\sigma,\, i\phi_\sigma\big)\,. \tag{102}$$

$\vec{J}_\sigma = e(n_s/2)\vec{v}_\sigma$ is the component of the current of spin σ and ρ_σ is the charge density with spin σ. The spin potentials are given by [78]

$$\vec{A}_\sigma = \lambda_L \vec{\sigma} \times \vec{E}(\vec{r},t) + \vec{A}(\vec{r},t) \quad \text{and} \qquad \phi_\sigma(\vec{r},t) = -\lambda_L \vec{\sigma}\cdot\vec{B}(\vec{r},t) + \phi(\vec{r},t) \tag{103}$$

Finally, the quantities with subindex 0 are

$$J_{\sigma 0} = \left(\vec{J}_{\sigma 0}(\vec{r}), ic\rho_{\sigma 0}\right) , \quad \vec{J}_{\sigma 0}(\vec{r}) = -\frac{c\rho_0}{2}\vec{\sigma} \times \hat{r} , \quad \rho_{\sigma 0} = \frac{\rho_0}{2} \tag{104}$$

and

$$A_{\sigma 0} = \left(\vec{A}_{\sigma 0}(\vec{r}),\, i\phi_{\sigma 0}(\vec{r})\right) , \quad \vec{A}_{\sigma 0}(\vec{r}) = \lambda_L \vec{\sigma} \times \vec{E}_0(\vec{r}) , \quad \phi_{\sigma 0}(\vec{r}) = \phi_0(\vec{r}) . \tag{105}$$

These equations predict the existence of a spontaneous spin current flowing within a London penetration depth of the surface of the superconductor in the absence of applied fields, with carrier densities $(n_s/2)$ and opposite spin electrons flowing in opposite direction with speed $v^0_\sigma = \hbar/(4m_e\lambda_L)$, and a spontaneous electric field throughout the interior of the superconductor. Remarkably, the formalism uniquely determines the value of the expelled charge and maximum electric field in the interior [78], as

$$E_m = -\frac{\hbar c}{4e\lambda_L^2} , \quad \rho_- = -\frac{E_m}{4\pi\lambda_L} , \quad \rho_- = en_s\frac{v_{\sigma_0}}{c} , \quad v^0_\sigma = \frac{\hbar}{4m_e\lambda_L} . \tag{106}$$

Note that E_m is the same as the lower critical magnetic field of a BCS superconductor H_{c1}. In the absence of an applied magnetic field, electrons near the surface move in opposite direction with speed v^0_σ, as shown in Fig. 12. When a magnetic field is applied, electrons of one spin speed up and those of opposite spin slow down, according to $v_\sigma = v_s + \sigma v^0_\sigma$. The total excess negative charge density $\rho_- = \rho_\uparrow + \rho_\downarrow$ does not change, but it has different magnitudes for spin up and down, according to

$$\rho_\sigma = \frac{n_s e}{2}\Big(\frac{v^0_\sigma + \sigma v_s}{c}\Big) , \quad v_s = -\frac{e\lambda_L}{m_e c}B ; \quad \frac{1}{\lambda_L^2} = \frac{4\pi n_s e^2}{m_e c^2} . \tag{107}$$

These equations imply that for applied magnetic field $H_{c1} = E_m$ one of the components of the spin current stops, at which point the magnetic field penetrates the sample [78].

The value of the interior positive charge density ρ_0 is determined by charge neutrality. For a cylinder and a sphere, it is $\rho_0 = -2\lambda_L/R\rho_-$ and $\rho_0 = -3\lambda_L/R\rho_-$ respectively.

4 How the Meissner effect works

We next will show that the physics discussed in the previous sections leads to a dynamical explanation of the Meissner effect. Contrary to what is generally believed, BCS theory has not provided a dynamical explanation of the Meissner effect. Why is it that it is generally believed that BCS theory explains the Meissner effect?

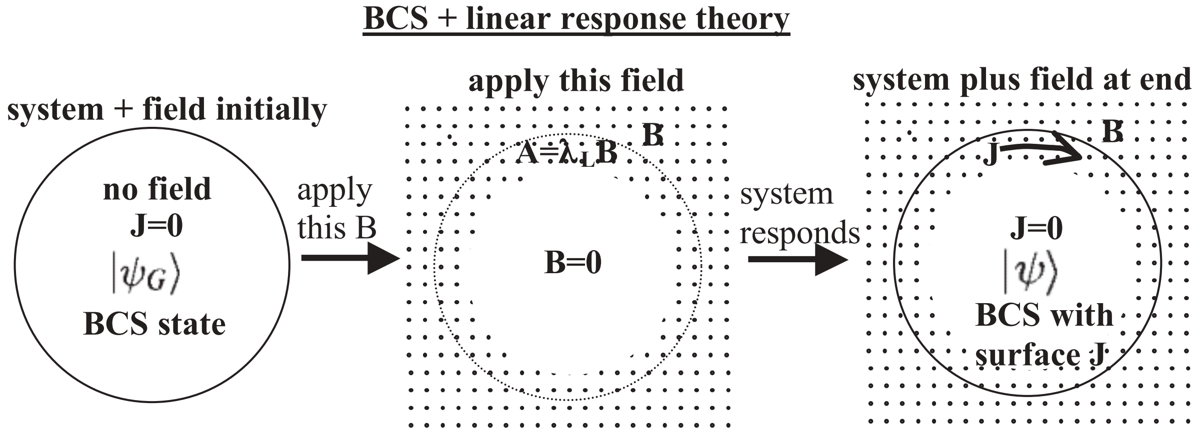

Fig. 13: *The BCS explanation of the Meissner effect. The system (cylinder, top view) is initially in the BCS state (left panel) with no magnetic field. Its linear response to the magnetic field shown in the middle panel (dots) is computed to first order in the magnetic field. The result is the state shown in the right panel, with a surface current J circulating.*

4.1 BCS theory *does not explain* the Meissner effect

Within BCS theory, the Meissner effect is explained as follows [7]. One considers the linear response of a system *in the BCS state* Eq. (5) to the perturbation created by a magnetic field, as shown in Fig. 13. The perturbing Hamiltonian H_1 is the linear term in the magnetic vector potential $\vec{A}$ that results from the kinetic energy $\left(\vec{p}-(e/c)\vec{A}\right)^2/2m$, and it causes a change in the BCS ground state $|\Psi_{BCS}\rangle$ to first order in $\vec{A}$

$$H_1=\frac{ie\hbar}{2mc}\sum_i\left(\vec{\nabla}_i\cdot A+\vec{A}\cdot\vec{\nabla}\right)\;,\quad |\Psi\rangle=|\Psi_{BCS}\rangle-\sum_n\frac{\langle\Psi_n|H_1|\Psi_{BCS}\rangle}{E_n}|\Psi_n\rangle \tag{108}$$

where $|\Psi_n\rangle$ are states obtained from the BCS state $|\Psi_{BCS}\rangle$ by exciting 2 quasiparticles, and E_n is the excitation energy. The expectation value of the current operator $\vec{J}_{op}$ with this wave function gives the electric current $\vec{J}$, and hence the "London Kernel" K [13]. In the long wavelength limit this calculation yields

$$\vec{J}=\langle\Psi|\vec{J}_{op}|\Psi\rangle=-\frac{c}{4\pi}K\vec{A}\quad\text{with}\quad K=\frac{1}{\lambda_L^2} \tag{109}$$

where λ_L is the London penetration depth. Eq. (109) is the (second) London equation Eq. (76). In combination with Ampere's law, Eq. (109) predicts that the magnetic field does not penetrate the superconductor beyond a distance λ_L from the surface, where the current $\vec{J}$ circulates, as shown schematically in Fig. 13 right panel.

However, note that this calculation *uses only the BCS wavefunction in and around the BCS state*, namely the ground state wavefunction $|\Psi_{BCS}\rangle$ and the wavefunctions $|\Psi_n\rangle$ that result from breaking one Cooper pair at a time. The wavefunction of the normal metal never appears. This is *not* explaining the Meissner effect. The Meissner effect is what is shown in Fig. 14: the *process* by which a system starting in the normal metallic state expels a magnetic field in the process of becoming a superconductor. It cannot be explained by starting from the assumption that the

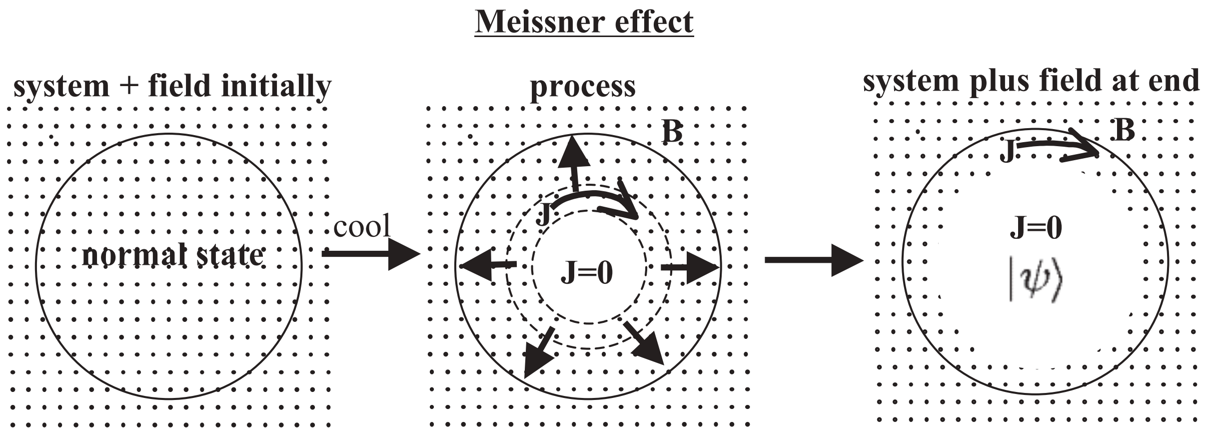

Fig. 14: *What the Meissner effect really is: the* process *by which a normal metal becomes superconducting in the presence of a magnetic field throughout its interior initially. The simplest route in this process (not the only one) is depicted in the figure. The superconducting region (white region) expands gradually from the center to fill the entire volume, expelling the magnetic field in the process.*

system is in the final BCS state and gets perturbed by H_1. Explaining this process requires explaining how the interface between normal and superconducting regions moves (center panel in Fig. 14). Because calculations of the sort described in Eqs. (108) and (109) contain no information about what is the nature of the initial state when the Meissner effect starts, namely the normal metal, they cannot be a microscopic derivation of the Meissner effect.

During the process of field expulsion, as well as its reverse, the process where a superconductor with a magnetic field excluded turns normal and the field penetrates, a Faraday electric field is generated that opposes the process. This electric field drives current in direction opposite to the current that develops. So it is necessary to explain: (i) How can a Meissner current start to flow in direction opposite to the Faraday electric force resisting magnetic flux change (Lenz's law)? (ii) How is the angular momentum of the developing supercurrent compensated so that momentum conservation is not violated? (iii) When a supercurrent stops, what happens to the angular momentum that the supercurrent had? (iv) How can a supercurrent stop without generation of Joule heat and associated with it an irreversible increase in the entropy of the universe that is known not to occur? None of these questions are addressed in the BCS literature.

4.2 The Meissner effect *necessitates* charge expulsion

That the London derivation of the London equation does not account for the Meissner effect is clear. To get from the first to the second equality in Eq. (75), a time integration was performed after taking the curl and using Faraday's law. More explicitly,

$$\frac{\partial \vec{J}}{\partial t}=\frac{n_s e^2}{m_e}\vec{E} \rightarrow \frac{\partial}{\partial t}\big(\vec{\nabla}\times\vec{J}\big)=-\frac{n_s e^2}{m_e c}\frac{\partial \vec{B}}{\partial t} \rightarrow \vec{\nabla}\times\big(\vec{J}(\vec{r},t)-\vec{J}(\vec{r},0)\big)=-\frac{n_s e^2}{m_e c}\big(\vec{B}(\vec{r},t)-\vec{B}(\vec{r},0)\big). \tag{110}$$

The last equality in Eq. (110) leads to the London equation Eq. (75) if $\vec{B}(\vec{r},0)=\vec{J}(\vec{r},0)=0$. However, under the initial conditions appropriate to the Meissner effect, namely $\vec{B}(\vec{r},0)=\vec{B}_0$,

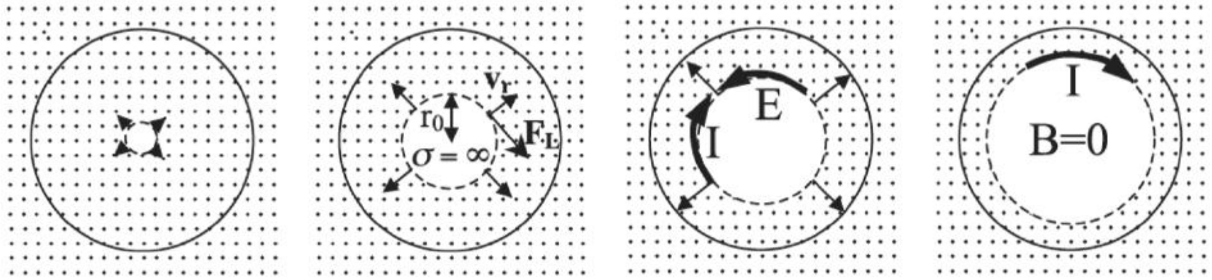

Fig. 15: *Schematic depiction of a perfectly conducting fluid (σ=∞) that flows radially outward with radial velocity v_r in a uniform magnetic field perpendicular to the plane of the paper. The carriers at the boundary experience a Lorentz force F_L. Assuming the sign of the charge q is positive for definiteness the Lorentz force $F_L = (q/c)v_rB$ points in the clockwise direction. The resulting electric current I at the boundary flows clockwise (for negative charge carriers the Lorentz force would be in the opposite direction, the current in the same direction), generating a magnetic field opposite to the external field so that no magnetic field lines can penetrate the fluid. During this process, a Faraday electric field E is generated that opposes the current flow.*

$\vec{J}(\vec{r},0) = 0$ it leads instead to the solution $\vec{B}(\vec{r},t) = \vec{B}_0$, $\vec{J}(\vec{r},t) = 0$. No current is generated, and the magnetic field is not expelled, contrary to what experiment tells us.

To understand what is needed to expel the magnetic field, let us consider more carefully the equation of motion for an electron of charge e and mass m_e in the presence of electric and magnetic fields

$$\frac{d\mathbf{v}}{dt} = \frac{e}{m_e}\mathbf{E} + \frac{e}{m_e c}\mathbf{v} \times \mathbf{B}\,. \tag{111}$$

The left-hand side of Eq. (111) is the total (convective) time derivative, which is related to the local (partial) time derivative by

$$\frac{d\mathbf{v}}{dt} = \frac{\partial \mathbf{v}}{\partial t} + \big(\mathbf{v}\cdot\nabla\big)\mathbf{v} = \frac{\partial \mathbf{v}}{\partial t} + \nabla\Big(\frac{\mathbf{v}^2}{2}\Big) - \mathbf{v}\times\big(\nabla\times\mathbf{v}\big). \tag{112}$$

Defining the ‘generalized vorticity’

$$\mathbf{w} = \nabla\times\mathbf{v} + \frac{e}{m_e c}\mathbf{B}, \tag{113}$$

taking the curl of Eq. (111) and using Eq. (112) and Faraday’s law $\nabla\times\mathbf{E} = -(1/c)\partial\mathbf{B}/\partial t$ leads to the following equation of motion for $\mathbf{w}$

$$\frac{\partial \mathbf{w}}{\partial t} = \nabla\times\big(\mathbf{v}\times\mathbf{w}\big). \tag{114}$$

Note that $\mathbf{w}$ is essentially the curl of the canonical momentum $\mathbf{p} = m_e\mathbf{v} + (e/c)\mathbf{A}$, with $\mathbf{A}$ the magnetic vector potential. In the Meissner process we have at time $t = 0$: $\mathbf{w}(\mathbf{r}, t{=}0) = \frac{e}{m_e c}\mathbf{B}(t{=}0) \equiv \mathbf{w}_0$ independent of position $\mathbf{r}$. We set $\nabla\times\mathbf{v} = 0$ because in the normal state there is no net macroscopic charge flow. Hence the canonical momentum $\mathbf{p}$ is nonzero throughout the interior of the superconductor in the initial state. In the superconducting state, the superfluid velocity $\mathbf{v}$ obeys the London equation $\nabla \times \mathbf{v} = -\frac{e}{m_e c}\mathbf{B}$. Therefore, $\mathbf{w}(\mathbf{r}, t{=}\infty) = 0$ everywhere

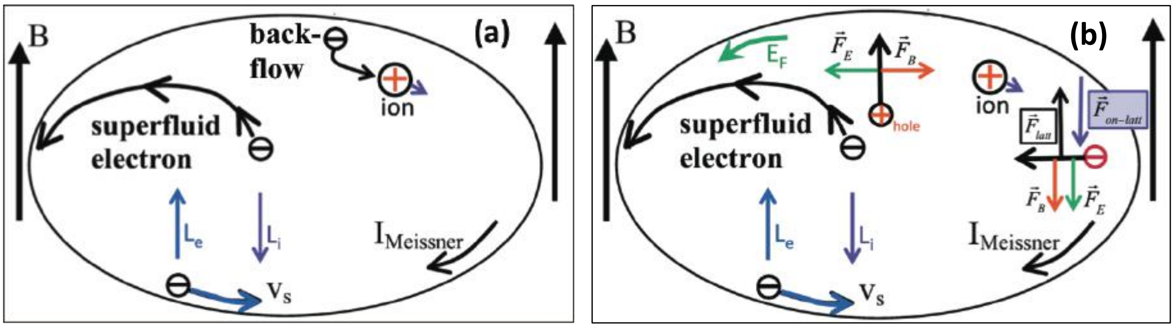

Fig. 16: *Left panel: electrons becoming superconducting move out, and are deflected by the Lorentz force in counterclockwise direction, generating the clockwise Meissner current $I_{Meissner}$. A backflow of normal electrons gets deflected clockwise and transmit their azimuthal momentum to the ions, hence to the body as a whole. Right panel: explains how the backflowing electrons transmit their azimuthal momentum to the ions without scattering processes, that would generate Joule heat in contradiction with the observation that the transition is reversible (see text).*

in the superconducting body. Equivalently, the canonical momentum $\mathbf{p} = 0$ throughout the interior of the (simply connected) superconductor. In a cylindrical geometry, assuming azimuthal symmetry as well as translational symmetry along the cylinder axis (z-direction, infinitely long cylinder) $\mathbf{w}(\mathbf{r}, t) = w(r, t)\hat{z}$ and Eq. (114) takes the form

$$\frac{\partial w}{\partial t} = -\frac{1}{r}\frac{\partial}{\partial r}(rwv_r) \tag{115}$$

with r the radius in cylindrical coordinates. Eq. (115) implies that w *can only change if there a is radial flow of charge* ($v_r \neq 0$). Moreover, for w to evolve towards its final value 0 requires $v_r > 0$, i.e., a radial *outflow* of electrons. This is a particular case of what is called Alfven's theorem [79], that says that in a perfectly conducting fluid magnetic field lines are frozen into the fluid and move with the fluid. It predicts what is shown in Fig. 15: if a perfectly conducting fluid expands from the center in the presence of magnetic field, it will push the magnetic field lines out as it expands, since otherwise Alfven's theorem would be violated.

4.3 Why holes are indispensable to understand the Meissner effect

The left panel of Fig. 16 shows qualitatively how the Meissner effect works [18]. Electrons condensing into the superconducting state move radially outward, and in the presence of a magnetic field B acquire counterclockwise azimuthal velocity, giving rise to the Meissner current $I_{Meissner}$ flowing near the surface that generates a magnetic field in opposite direction to the applied field and cancels it in the interior. There is also a backflow of normal electrons to preserve near charge neutrality, that acquire through the Lorentz force an azimuthal velocity in opposite direction. The backflowing electrons do not cancel the Meissner current because they transmit their azimuthal momentum to the ions, i.e., to the body as a whole. The body rotates very slowly in clockwise direction, compensating the counterclockwise motion of superfluid electrons in the Meissner current, so that momentum conservation is maintained.

However, the question arises: how do the backflowing electrons transmit their azimuthal momentum to the body? It cannot happen through collisions with impurities or phonons, because

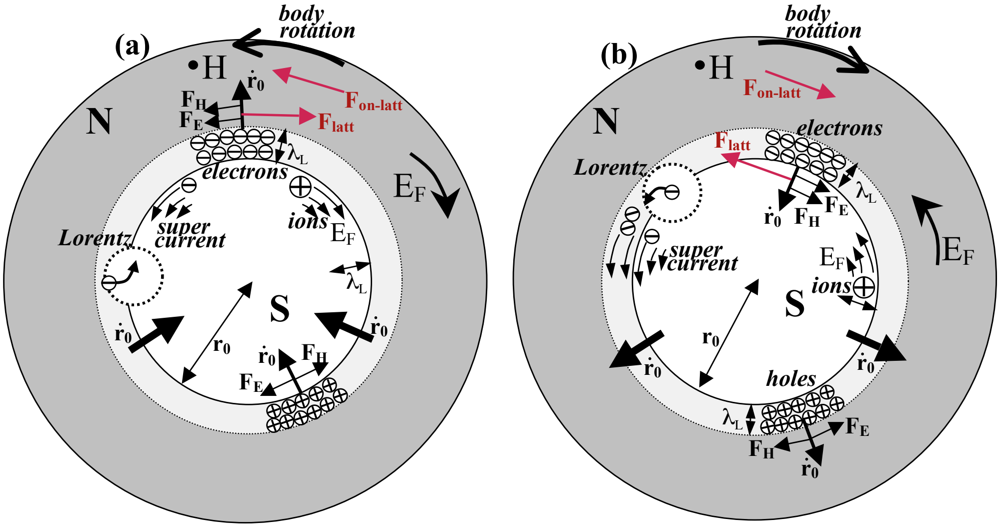

Fig. 17: *Transition from the normal into the superconducting state (left panel) and from the superconducting into the normal state (right panel) in the presence of a magnetic field. The processes are discussed in the text.*

such collisions would generate Joule heat. However it is known that the transition is thermodynamically reversible, this has been carefully tested experimentally [80] and is also implicit in BCS theory, allowing the understanding of the transition as a thermodynamic phase transition, of second order without a magnetic field and first order in the presence of a magnetic field.

The answer to this question requires *holes*, or equivalently antibonding electrons. *The backflowing electrons need to have negative effective mass.* If so, their motion is purely radial, as Fig. 16(b) shows: they experience magnetic and electric forces in the same direction, clockwise, and the lattice exerts a counterclockwise force F_{latt} that exactly cancels the electromagnetic forces. By Newton's third law, a force on the ions $F_{on\text{-}latt} = -F_{latt}$ is exerted by the electrons, transferring their azimuthal momentum to the body without any dissipation. If we prefer to describe the backflowing normal electrons equivalently as outflowing normal holes we can also do that. In that case, electric and magnetic forces are exactly cancelled, as Fig. 16(b) shows.

The electric force discussed above arises from the Faraday electric field that exists during the process of flux expulsion. If the phase boundary is moving at speed v_r, the Faraday electric field at the boundary is $E_F = (v_r/c)B$, and the magnetic force on normal carriers moving radially with the boundary, $F_B = e(v_r/c)B$, is of the same magnitude as the electric force exerted by the Faraday field $F_E = eE_F$, in opposite direction for holes and in the same direction for electrons, as shown in Fig. 16(b).

Fig. 17 illustrates the processes in more detail. Starting with the left panel, that describes the Meissner effect, the phase boundary is moving outward with speed $\dot{r}_0$. Normal electrons at the boundary expand their orbits to radius $2\lambda_L$, as discussed earlier, and this expansion imparts them the azimuthal speed of carriers in the Meissner current, as was shown in Eqs. (92)–(93). The resulting outward motion of negative charge gives rise to an inflow of normal electrons just outside the boundary, moving inward with speed $\dot{r}_0$. They experience a Lorentz force pointing clockwise, and are also subject to the clockwise electric force resulting from Faraday's electric field pointing counterclockwise that originates in the outward motion of magnetic flux. The

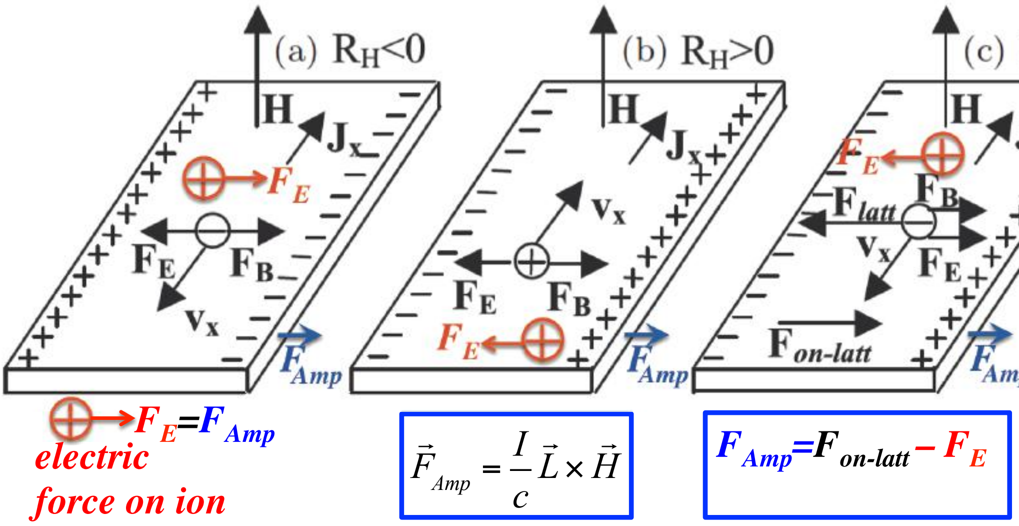

Fig. 18: *Illustration of momentum transfer without energy dissipation in a Hall bar. The Ampere force points to the right independently of whether the material has negative or positive Hall coefficient. For the material with negative Hall coefficient (left panel) the Ampere force results from the electric force resulting from the electric field created by the charge imbalance on the positive ions (in red). For the material with positive Hall coefficient (middle and right panels) the force from the electric field acting on positive ions is opposite to the Ampere force.*

forces are balanced by a force exerted by the lattice on the backflowing electron that has negative effective mass, F_{latt}, as discussed earlier, pointing in counterclockwise direction, so that the backflow is radial. In turn the backflowing electron exerts an equal and opposite force on the lattice, $F_{on\text{-}latt}$, thus transmitting azimuthal momentum to the body without dissipation, compensating for the counterclockwise momentum acquired by electrons expanding their orbits and joining the Meissner current. Instead of backflowing electrons we can understand the process with outward moving normal holes, as shown on the lower part of the left panel. As the phase boundary moves further out, the superelectrons at its boundary that acquired azimuthal velocity through orbit expansion get slowed down by the Faraday electric field and stop contributing to the supercurrent when the phase boundary has moved beyond them a distance λ_L. All this is discussed quantitatively in Refs. [81, 82]. The same momentum transfer without energy dissipation explains the origin of the Ampere force on conductors with positive Hall coefficient, as illustrated in Fig. 18.

Switching the sign of all the processes we can understand the right panel of Fig. 17, namely the process by which a superconductor in a magnetic field carrying a Meissner current near its surface, turns normal and the supercurrent stops [83]. As the phase boundary moves in, electrons that are in the superconducting region at distance λ_L from it get accelerated by the Faraday electric field in counterclockwise direction, reaching maximum velocity when the phase boundary reaches them, at which point their orbits shrink and they are stopped by the action of the Lorentz force on the shrinking orbit pushing in clockwise direction. This explains how the supercurrent stops when the system becomes normal, without collisions and hence no dissipation. Momentum conservation results from the compensating backflow of normal electrons of negative effective mass as discussed earlier.

Finally, the same physics that explain how the Meissner effect works explains how magnetic fields are generated in rotating superconductors [84], and how charge flows in a superconducting wire connected to normal metal leads [85]. BCS theory does not have the physical elements necessary to describe any of these processes.

5 Theory of hole superconductivity versus the conventional theory

In the conventional understanding of superconductivity, there is a large set of materials considered to be "conventional superconductors", for which the pairing mechanism is believed to be the electron-phonon interaction. There is another large set of materials considered to be "unconventional superconductors", for which the pairing interaction is believed *not* to be the electron-phonon interaction. There is no general agreement on how many other pairing mechanisms exist, nor what is their nature, although most physicists believe that magnetic interactions of some kind are responsible for pairing in various unconventional superconductors such as the cuprates. A survey of 32 classes of superconducting materials is given in Ref. [8].

Instead, within the theory of hole superconductivity discussed here, there is a single mechanism of superconductivity for all materials, that originates in the fundamental charge asymmetry of matter, namely the fact that the proton is 2000 times heavier than the electron, leading to electron-hole asymmetry in condensed matter, essential to understand both the pairing mechanism of charge carriers near the top of electronic energy bands, as well as their ability to interchange momentum with the body as a whole without dissipation due to their negative effective mass, which is necessary to understand how electric currents start and stop in superconductors without dissipating Joule heat. Both points of view could be wrong, but not both can be right. What do we learn from superconducting materials? We discuss this in the next section.

5.1 Superconducting materials: judge and jury of theories of superconductivity

It is difficult to prove theories wrong in condensed matter physics, because they are based on model Hamiltonians whose connection with real materials is difficult to ascertain. It is especially difficult for the case of BCS theory, because it is generally assumed that if a material does not conform to it this does not indicate that the theory is wrong but rather that the material is "wrong", i.e. non-conventional.

Here we have argued that Hamiltonians such as dynamic Hubbard models contain the essential physics necessary to describe superconductivity, and Hamiltonians describing the electron-phonon interaction do not. How do we decide which is right and which is wrong? One way is to consider what real material tell us [17].

The highest T_c unconventional superconductors are cuprates. The highest T_c *proven* conventional superconductor is magnesium diboride (we exclude the hydrides for reasons discussed later). What do MgB_2 and cuprates have in common?

According to the conventional view, nothing. MgB_2 becomes superconducting because of a strong electron-phonon interaction, and cuprates become superconducting because of magnetic fluctuations. MgB_2 does not have magnetic fluctuations, and cuprates do not have strong electron-phonon interaction.

Instead, according to the theory of hole superconductivity, what they have in common is that in both materials holes conduct through negatively charged anions in close proximity: B^- ions in MgB_2, O^{2-} ions in cuprates. That is what makes them high temperature superconductors.

The conventional theory predicts that light atoms should give rise to high critical temperatures, because the lattice vibration frequencies are high. But there is no evidence from materials for that, as illustrated in Fig. 19. For example, Pb, a very heavy element, has the third highest T_c among the elements. Li, a very light element, has the lowest T_c among the elements. On the other hand, there is a very strong correlation between positive sign of the Hall coefficient and the element being a superconductor, as the right panel of Fig. 19 shows, and as the theory of hole superconductivity predicts. Correlations between superconductivity and a variety of normal state properties of elements are analyzed in Ref. [86]. The same non-correlation with ionic mass and strong correlation with sign of the Hall coefficient is seen in compounds [17, 67, 87].

5.2 Experimental tests and open questions

Of course the ultimate test of theories is experiments. It is generally believed that BCS theory has been proven right by experiments. However, many of the predictions of BCS theory are common to other theories including the theory of hole superconductivity. The role of the electron-phonon interaction in causing superconductivity has not been proven experimentally. The isotope effect is not a proof, since many materials considered to be conventional do not obey the BCS prediction, including several elements and the compound PdH, where the mass of H can be increased by a factor of 2 by substitution with the isotope deuterium, and T_c goes up rather than down [88]. Small wiggles in tunneling characteristics [89], attributed to electron-phonon coupling and generally believed to prove that superconductivity is caused by it [90], may also result from modulation of the pairing interaction Δt discussed here by phonons [91], implying that pairing would persist even if the ionic mass is infinite, i.e., if the lattice does not vibrate. It has been claimed that hydrogen-rich materials at high pressures superconduct at temperatures close to room temperature, proving the importance of the electron phonon interaction, that is predicted to give highest T_c for light ions such as hydrogen [92]. We have analyzed multiple experiments reporting such claims and in every case concluded that the experimental observations are incompatible with superconductivity [93].

There are several predictions of the theory of hole superconductivity that are specific to it, but most have not been tested experimentally to date. Some of the predictions are: (i) tunneling asymmetry of universal sign [64], (ii) positive thermoelectric power of superconductive tunnel junctions [68], (iii) apparent violation of the conductivity sum rule [63], (iv) electric screening length in the superconducting state much larger than in the normal metallic state [75, 76], (v) electric fields in the interior and in the vicinity of superconducting samples [73], (vi) in-

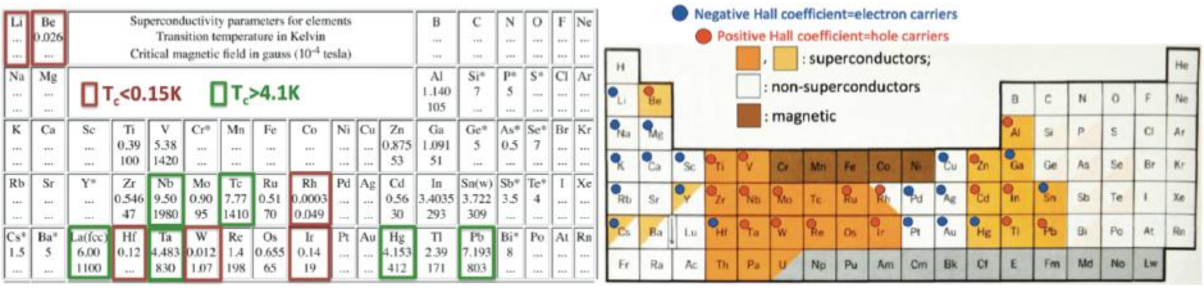

Fig. 19: *Two images of superconductors in the periodic table. The left image highlights the superconducting elements with highest T_c in green and those with lowest T_c in brown. The ionic mass* increases *as we move down and to the right in the table, and T_c should* decrease *as the ionic mass increases according to the conventional theory. It does not. The right image shows which elements among superconducting and non-superconducting ones have positive and negative Hall coefficients. It is clear that positive Hall coefficients are predominant in superconducting elements, and negative Hall coefficients are predominant in non-superconducting elements.*

crease in the mean inner potential in the superconducting state [45], (vii) charge imbalance in the absence of applied fields [94], (viii) radial electric fields during the normal-superconductor transition [95], (ix) Alfven-like waves along superconductor-normal phase boundaries [96], (x) absence of superconductivity in any material that does not have hole carriers [67].

Why is it important and urgent to decide which theory of superconductivity describes real materials? One important reason is that it would allow to make real progress in the theoretical search for new materials, to guide experimental search and discovery of superconductors that work at room temperature. Room temperature superconductors will change the world. Imagine how different our lives would be today if semiconductors only worked at temperatures below 150K. The current theoretical guidance based on BCS theory, that focuses on light elements [97], has *not* led to progress.

In conclusion, I would like to stress that the understanding of superconductivity based on the principles discussed in this paper is far from complete. There are many opportunities for further advances through theoretical and experimental research. Furthermore, a full understanding of how quantum mechanics operates on a macroscopic scale in superconductors may well lead to new insights on how it operates on the microscopic scale [98].

Acknowledgments

The author is grateful to Frank Marsiglio for collaboration in substantial parts of this work.

References

[1] F. London and H. London, Proc.Roy.Soc. A **149**, 71 (1935)

[2] H. Kamerlingh Onnes, Comm. Leiden 1911, Nr I22b, I24C; 1913, Nr 133a, I33C.

[3] W. Meissner and R. Ochsenfeld, Naturwissenschaften **21**, 787 (1933)

[4] G. Lippmann, Comptes Rendus de l' Academie des Sciences, **168**, **73** (1919)

[5] T. Sauer, Arch. Hist. Exact Sci. **61**, 159 (2007)

[6] F. London and H. London, Physica **2**, 341 (1935)

[7] J. Bardeen, L.N. Cooper, and J.R. Schrieffer, Phys. Rev. **108**, 1175 (1957)

[8] Physica C **514**, 1–444 (2015), Special Issue: *Superconducting Materials: Conventional, Unconventional and Undetermined. Dedicated to Theodore H. Geballe on the year of his 95th birthday*, ed. by J.E. Hirsch, M.B. Maple, and F. Marsiglio,

[9] L.N. Cooper, Phys. Rev. **104**, 1189 (1956)

[10] F. London: *Superfluids, Vol. I* (Dover, New York, 1961)

[11] V.L. Ginzburg and L.D. Landau, Zh. Eksp. Teor. Fiz. **20**, 1064 (1950)

[12] B.D. Josephson, Phys. Lett. **1**, 251 (1962)

[13] M. Tinkham: *Introduction to superconductivity, 2nd Ed.* (McGraw Hill, New York, 1996)

[14] P.G. de Gennes: *Superconductivity of Metals and Alloys* (Benjamin, New York, 1966)

[15] M.L. Cohen and P.W. Anderson, AIP Conf. Proc. **4**, 17 (1972)

[16] C.W. Chu, L.Z. Deng and B. Lv, Physica C **514**, 290 (2015)

[17] J.E. Hirsch, Appl. Phys. Lett. **121**, 080501 (2022)

[18] J.E. Hirsch, Phys. Scr. **91**, 035801 (2016)

[19] J.E. Hirsch: *Superconductivity begins with H* (World Scientific, Singapore, 2020)

[20] See https://jorge.physics.ucsd.edu/hole.html for a list of references.

[21] W.E. Pickett, Rev. Mod. Phys. **95**, 021001 (2023)

[22] N.W. Ashcroft, Phys. Rev. Lett. **92**, 187002 (2004)

[23] P. Morel and P.W. Anderson, Phys. Rev. **125**, 1263 (1962)

[24] J.S. Bauer, J.E. Han and O. Gunnarsson, J. Phys.: Condens. Matter **24**, 492202 (2012)

[25] D.J. Scalapino, J. Low Temp. Phys. **117**, 179 (1999) and references therein.

[26] E. Dagotto and J. Riera, Phys. Rev. B **46**, 12084(R) (1992)

[27] J.E. Hirsch, Phys. Lett. A **136**, 163 (1989)

[28] J.E. Hirsch, E. Loh, D.J. Scalapino and S. Tang, Physica C **153–155**, 549 (1988)

[29] M. Qin, Chia-Min Chung, H. Shi, E. Vitali, C. Hubig, U. Schollwöck, S.R. White, and S. Zhang, Phys. Rev. X **10**, 031016 (2020)

[30] J.E. Hirsch, Phys. Rev. Lett. **54**, 1317 (1985)

[31] D.J. Scalapino, E. Loh, Jr., and J.E. Hirsch, Phys. Rev. B **34**, 8190(R) 1986)

[32] Nat. Phys. **9**, 523 (2013): *The Hubbard model at half a century*

[33] J. Bardeen and D. Pines, Phys. Rev. **99**, 1140 (1955)

[34] J.E. Hirsch, Phys. Lett. A **138**, 83 (1989)

[35] S. Kivelson, W.-P. Su, J.R. Schrieffer, and A.J. Heeger, Phys. Rev. Lett. **58**, 1899 (1987)

[36] J.E. Hirsch, Physica C **158**, 326 (1989)

[37] N.W. Ashcroft and N.D. Mermin: *Solid State Physics* (Cengage, Boston, 1976) Eq. (10.18)

[38] J.E. Hirsch and F. Marsiglio, Phys. Rev. B **39**, 11515 (1989)

[39] A. Painelli and A. Girlando, Synthetic Metals **27**, A15 (1988)

[40] J.E. Hirsch, Chem. Phys. Lett. **171**, 161 (1990)

[41] J.E. Hirsch *et al.*, in A. Montorsi (ed.): *The Hubbard Model: A Reprint Volume* (World Scientific, Singapore, 1992) p. 123–126, 206–213, 217–233, 274–282

[42] J.E. Hirsch, in J. Ashkenazi *et al.* (eds.): *High-Temperature Superconductivity* (Springer, 1991) p. 295

[43] J.E. Hirsch, Phys.Rev. Lett. **87**, 206402 (2001)

[44] H. Bethe, Ann. Phys. **392**, 55 (1928)

[45] J.E. Hirsch, Ann. Phys. **526**, 63 (2013)

[46] J.E. Hirsch, Physica B **199–200**, 366 (1994)

[47] J. Hutchinson, M. Baker and F. Marsiglio, Europ. J. Phys. **34**, 111 (2013)

[48] J.E. Hirsch, Phys. Rev. B **62**, 14487 (2000)

[49] J.E. Hirsch, Phys. Rev. B **62**, 14998 (2000)

[50] J.E. Hirsch, Phys.Rev.B **65**, 184502 (2002)

[51] J.E. Hirsch, Phys. Rev. B **67**, 035103 (2003)

[52] J.E. Hirsch, Phys. Rev. B **65**, 214510 (2002)

[53] J.E. Hirsch, Phys. Rev. B **66**, 064507 (2002)

[54] K. Bouadim *et al.*, Phys. Rev. B **77**, 014516 (2008)

[55] G.H. Bach, J.E. Hirsch, and F. Marsiglio, Phys. Rev. B **82**, 155122 (2010)

[56] F. Marsiglio, R. Teshima and J.E. Hirsch, Phys. Rev. B **68**, 224507 (2003)

[57] J.E. Hirsch and F. Marsiglio, Phys. Rev. B **39**, 11515 (1989)

[58] F. Marsiglio and J.E. Hirsch, Phys. Rev. B **41**, 6435 (1990)

[59] J.E. Hirsch, Int. J. Mod. Phys. B **225**, 1173 (2011)

[60] J.E. Hirsch, Physica C **201**, 347 (1992)

[61] H. Ding *et al.*, Phys. Rev. Lett. **87**, 227001 (2001)

[62] H.J.A. Molegraaf, C. Presura, D. van der Marel, P.H. Kes, and M. Li, Science **295**, 2239 (2002)

[63] J.E. Hirsch, Physica C **199**, 305 (1992)

[64] F. Marsiglio and J.E. Hirsch, Physica C **159**, 157 (1989)

[65] Ch. Renner and O. Fischer, Phys. Rev. B **51**, 9208 (1995)

[66] J.E. Hirsch, Phys.Rev.B **48**, 3327 (1993)

[67] J.E. Hirsch, Physica C **472**, 78 (2012) and references therein.

[68] J.E. Hirsch, Phys. Rev. Lett. **72**, 558 (1994)

[69] J.E. Hirsch, Phys. Lett. A **281**, 44 (2001)

[70] J.E. Hirsch, Phys. Rev. B **87**, 184506 (2013)

[71] J.E. Hirsch, Phys. Rev. B **68**, 184502 (2003)

[72] J.E. Hirsch, Phys. Rev. B **69**, 214515 (2004)

[73] J.E. Hirsch, Phys. Rev. Lett. **92**, 016402 (2004)

[74] J.E. Hirsch, Jour. Supercond. Novel Mag. **25**, 1357 (2012)

[75] J.E. Hirsch, Physica C: **478**, A42 (2012)

[76] J.E. Hirsch, Elsevier Physica C **508**, 21 (2015)

[77] J.E. Hirsch, Europhys. Lett. **81**, 67003 (2008)

[78] J.E. Hirsch, Ann. Phys. (Berlin) **17**, 380 (2008)

[79] H. Alfven, Nature **150**, 405 (1942); Ark. Mat. Astron. Fys. **39**, 2 (1943)

[80] P.H. van Laer and W.H. Keesom, Physica **5**, 993 (1938)

[81] J.E. Hirsch, Phys. Rev. B **95**, 014503 (2017)

[82] J.E. Hirsch, Ann. Phys. **373**, 230 (2016)

[83] J.E. Hirsch, Europhys. Lett. **114**, 57001 (2016)

[84] J.E. Hirsch, Ann. Phys. (Berlin) **531**, 1900212 (2019)

[85] J.E. Hirsch, Phys. Lett. A **413**, 127592 (2021)

[86] J.E. Hirsch, Phys. Rev. B **55**, 9007 (1997)

[87] J.E. Hirsch, J. Supercond. Nov. Mag. **33**, 61 (2019)

[88] T. Skoskiewicz, A.W. Szafranski, W. Bujnowski, and B. Baranowski, J. Phys. C: Solid State Phys. **7**, 2670 (1974)

[89] I. Giaever, H.R. Hart Jr., and K. Megerle, Phys. Rev. **126**, 941 (1962)

[90] D.J. Scalapino, J.R. Schrieffer, and J.W. Wilkins, Phys. Rev. **148**, 263 (1966)

[91] F. Marsiglio and J.E. Hirsch, (unpublished)

[92] W. Pickett and M.I. Eremets, Physics Today **72**, 52 (May 2019)

[93] J.E. Hirsch, Nat. Sci. Rev. **11**, nwad174 (2023) and references therein.

[94] J.E. Hirsch, Phys. Rev. B **58**, 8727 (1998)

[95] J.E. Hirsch, Physica C 544, 54 (2018)

[96] J.E. Hirsch, Physica C **564**, 42 (2019)

[97] L. Boeri and G.B. Bachelet, J. Phys.: Condens. Matter **31**, 234002 (2019)

[98] J.E. Hirsch, Phys. Lett. A **374**, 3777 (2010); Mod. Phys. Lett. B **24**, 2201 (2010)

8 Unconventional Superconductivity: Overview and Planar Tunneling into a Kondo Lattice

Laura H. Greene
National MagLab and Florida State University
Tallahassee, Florida

Contents

E. Pavarini and E. Koch (eds.)
Correlations and Phase Transitions
Modeling and Simulation Vol. 14
Forschungszentrum Jülich, 2024, ISBN 978-3-95806-751-6
http://www.cond-mat.de/events/correl24

1 Overview

Unconventional superconductors differ from conventional superconductors in that they typically exhibit a ubiquitous phase diagram with intriguing, correlated electron phases that break the symmetry of the underlying lattice at temperatures well above T_c. These non-Fermi liquid phases remain some of the greatest unsolved problems in physics. After this overview, I will present some of our recent work on planar tunneling into Kondo insulators, and a possible new paring mechanism in the heavy-fermion superconductor $\mathrm{CeCoIn_5}$.

2 Introduction

The past several years, I have been giving colloquia and public lectures with the title "The Dark Energy of Quantum Materials." Why this title? One reason is that we all were enthralled with the LIGO successful of detection of gravity waves – measuring a motion of less than the width of a proton, and astoundingly, for a power of $3.6{\cdot}10^{49}$ Watts, which is more than the combined power of all light radiated by all the stars in the observable universe. That LIGO detected gravity waves signified that for the first time, we could look at the universe in a new way, without using light or matter.

The LIGO observatory was invented to find gravity waves, as it did, but the larger question is: Will this new observatory help us to understand dark matter or other phenomena we have not previously been able to explain. In quantum materials, there is not a single phenomenon to explain but a host of correlated electron states. We in condensed matter have developed a wide host of observatories, i.e., measurement techniques (e.g., ARPES, STM, EXAFS, ...); have significantly improved our crystal growth techniques; and have developed a host of computational techniques. All of these new and improved observatories: measurement, growth, and computational techniques are addressing correlated electrons with more and more success. The larger question here is: Will these hosts of quantum matter observatories help us to understand the many non-Fermi liquid phases. In the longer term, can we learn to predictively design correlated functional materials such as superconductors and thermoelectrics?

My many years in studying superconductivity have led me to adopt a general overview that understanding unconventional superconductivity is no less fundamental than cosmology, and no less fascinating, with one important complication: There are many families of unconventional superconductors, and thus, many fundamental questions to be addressed, making this a multi-modal complex problem. Here, I give my personal overview of the fundamental questions, with the apology that I will not have all the scholarship in time for this publication.

The BCS electron-phonon coupled theory of conventional superconductivity is considered by most to be one of the few solved problems in quantum materials. Conventional superconductivity is typically characterized by materials that exhibit Fermi liquid behavior above T_c, while below T_c, the superconducting order parameter is of the same symmetry as the underlying lattice. This contrasts with unconventional superconductivity, which often reveals non-Fermi liquid (NFL) behavior above T_c, and where the T_c as a function of some variable such as pressure or doping, varies as a dome across that phase diagram. Unconventional superconductivity was discovered in 1979 by Steglich and co-workers in heavy Fermions [1], and in 2001, Lonzarich and co-workers discovered the first domed phase diagram in a heavy fermion superconductor as a function of applied pressure in $\mathrm{CePd_2Si_2}$ [2]. At the time, it was surprising that superconductivity could appear associated with a magnetic state, and the electron-phonon theory of Cooper pairing was questioned. Since then, many families of unconventional superconductors have been discovered that exhibit a domed phase diagram, typically with NFL at temperatures above the dome.

We can describe the electronic properties of Fermi liquids with general electronic structure calculations: Simply put, the electronic, thermodynamic, and optical properties are explained by the lattice structure and the atoms that make up the lattice. We are also able to describe the electronic, thermodynamic, and optical properties of the superconducting state, both conventional and unconventional, because, as to date, all superconductors we know of are composed of Cooper pairs, so can be described with the Bogoliubov-de Gennes equations. Conventional metallic superconductors are easy to model, and there is more of a challenge in unconventional superconductors where you need to take the symmetry of the superconducting order parameter and the possibility of more than one band in to account. So even if you do not know the microscopic mechanism of the Cooper pairing, the superconducting state can be modeled.

The larger question is that the NFL states above the dome typically cannot be described by simple Fermi liquid theory due to electron-electron correlations. And these correlations are quite varied: In the heavy fermions the electronic mass measured thermodynamically is larger than can be described by Fermi liquid theory; in the cuprates there is the enigmatic pseudogap where electronic stripes can be found; in the di-chalcogenides the T-dependent charge-density wave behavior cannot be accounted for [3]; there are quantum-critical fluctuations above quantum critical points; and in the Fe-based superconductors there exists electronic nematic phases where the electrons can form elongated clusters even at temperatures in the tetragonal phase.

Before the discovery of the Fe-based superconductors, unconventional superconductivity was defined as having a superconducting order parameter of a lower symmetry than the underlying lattice. Since the proposed symmetry of their superconducting state, $s_{\pm}$, is of the same symmetry as the underlying lattice, a more general and accurate definition is that the symmetry of the electron fluid above the dome breaks the symmetry of the underlying lattice – most clearly demonstrated in the nematic phase of the Fe-based superconductors.

3 Planar Tunneling

The work in my laboratory primarily involves electron transport, with a focus on planar tunneling spectroscopy (PTS). In this technique, electrons are injected from one electrode to another across a thin, insulating barrier. It was PTS that showed phonons were responsible for the Cooper pairing: that the Pb phonons that were observed by neutron scattering, were observed in the Pb tunneling density of states [4].

In normal-insulating-normal (NIN) junctions, single-step elastic tunneling will reveal Ohm's law because in the tunneling equation, the conductance is calculated from the energy integral over the Fermi velocity times the density of states, which divide out for Fermi liquids, as dictated by Harrison's theorem [5]. This theorem was derived for one-dimensional elastic tunneling between simple metals. If one of the electrodes is replaced with a superconductor (S), the SIS tunneling conductance reveals the quasiparticle superconducting density of states, including the energy gap and the coherence peaks at the gap edge, precisely because a superconductor is not a Fermi liquid. In fact, planar tunneling, with the proper diagnostics, is a direct probe of NFL behavior. The same arguments can be made for point contact spectroscopy. Some of our examples include mapping out the nematic phases in several families of Fe-based superconductors [6] and detecting the hybridization gap as a Fano line shape in background conductance of the heavy fermion $\mathrm{CeCoIn_5}$ [7].

In planar tunneling spectroscopy, diagnostics are required to determine the quality of the junctions, in particular, to see if the predominant transport across the junction is single-step elastic tunneling. In studying new materials, it is important to start with a well-known superconductor as the counter-electrode, such a Pb (which is also easy to grow) to determine the quality of the junction from the quality of the measured Pb tunneling density of states. Then you can easily drive the Pb normal ($H_c \sim 0.1$ T; $T_c \sim 7.2$ K) so the Pb becomes a Fermi liquid and the resulting non-ohmic conductance arises from any NFL behavior of the new material. Another important diagnostic is reproducibility: Once the growth of the planar junction is worked out (includes growing or polishing one electrode, growing or forming a thin insulating tunnel barrier, then depositing the counter-electrode) the PTS conductance must be of good quality and reproducible. After experience with the new material is acquired, non-superconducting counter-electrodes can be used because the quality of the now-known, reproducible, tunneling density of states of the new material becomes an important diagnostic.

4 Planar Tunneling into the Heavy Fermion $\mathrm{CeCoIn_5}$

In the case of PTS into $\mathrm{CeCoIn_5}$, we created reproducible, high-quality planar tunnel junctions on three major crystallographic orientations: [001], [100], and [110] [8]. As described in general, above, using Pb counter electrodes, we establish the quality of the junctions from the measured Pb tunneling density of states at low temperature and zero applied magnetic field, where the expected Pb superconducting gap and coherence peaks are clearly observed. Once the junction quality is established, the Pb is driven normal with the applied field of 0.2 T, and since the H_{c_2} of $\mathrm{CeCoIn_5}$ is 4.95 T for [001] and 11.8 T for [100] and [110] that applied field is a tiny perturbation. Our earlier work on $\mathrm{CeCoIn_5}$ showed that the superconducting order parameter symmetry was $d_{x^2-y^2}$ [7], which has been verified since. Our PTS verified that symmetry, and that there were preformed pairs above T_c [9, 10].

The compelling findings are these. First, at temperatures below T_c (2.3 K), with applied magnetic field, the $\mathrm{CeCoIn_5}$ tunneling density of state for [001] and [100] shows a suppression of the d-wave gap with increasing field, as expected, and surprisingly, this gap evolves slowly into a splitting, or field-induced gap, that grows linearly with applied field up to the highest fields

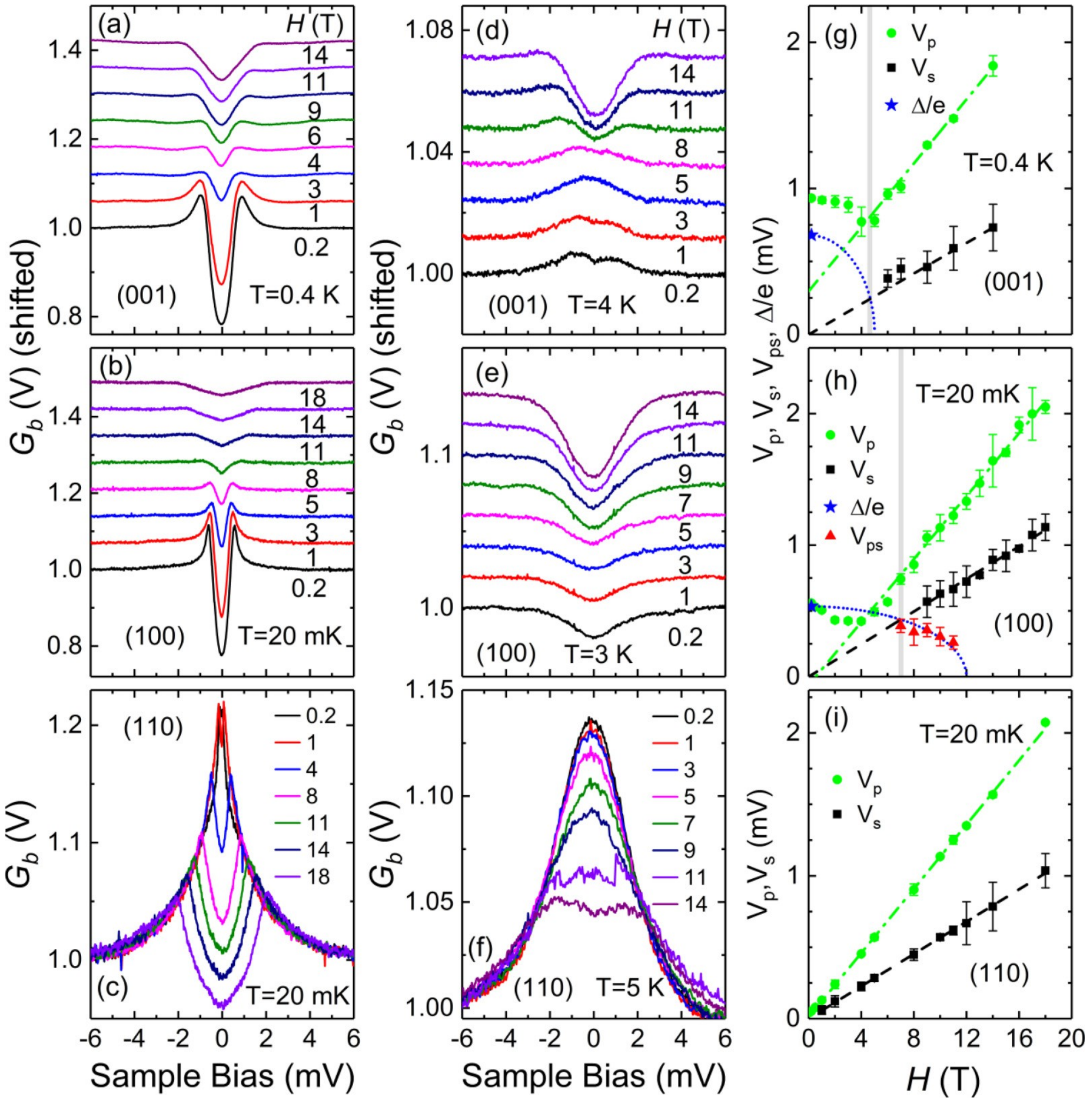

Fig. 1: *Magnetic evolution of the planar tunneling conductance for* CeCoIn_5 *in the [001] (top), [100] (middle), and [110] (bottom) orientations for* $T < T_c$. *The first column shows the conductance for* $T < T_c = 1.3$ *K and the center column in the temperature range of the preformed pairs (*$T = 3$*–*5 *K), where curves are shifted vertically for the [001] and [100] orientations. The right column plots the magnetic evolution of the superconducting gap and the field splitting at low temperature. Note the superconducting gap evolves into a splitting well above* H_{c_2}. *Not shown here, at higher temperatures (*> 10 *K), there is no observable superconducting gap feature, as expected, and no subsequent field dependence (after [8]).*

measured (18 T). The same behavior occurs in the temperature regime between T_c and that of the preformed pairs (∼5 K), a gap is seen that evolves into a high-field splitting. At temperatures above that of the pre-formed pairs, there is almost no field dependence.

We find that the high field splitting *only* appears when there are Cooper pairs, or preformed pairs. We note that the 40 meV spin-correlation resonance observed by inelastic neutron scattering (INS) is seen in the tunneling in the cuprate and Fe-based superconductors but is not seen in CeCoIn_5 tunneling. In INS, there is a 0.6 meV resonance, but it is robust to doping [11] and this feature is not seen in tunneling spectroscopy. We conclude then that the spin-spin correlations that play a role in the pairing of the high-Tc superconductors do not play a role in $\mathrm{CeCoIn_5}$. Instead, this heavy-Fermion material has f-level magnetic scattering. Therefore, in comparison with the planar tunneling models of Anderson and Applebaum, where the tunneling conductance exhibits a linear splitting with applied magnetic field due to Kondo scattering by magnetic impurities in the tunneling barrier [12], we surmise that the pairing in $\mathrm{CeCoIn_5}$ may arise, at least in part, from f-level scattering.

5 Conclusion

In conclusion, unconventional superconductivity is a complex subject with many important problems to be solved. It is clear to me that there is not only one solution for the pairing mechanism in all superconductors [13], which makes these problems daunting. Just as the new LIGO observatories have promise for understanding fundamental questions of our cosmological makeup, I believe that our myriad or new and novel measurement, growth, and computation techniques will help us understand the many questions of non-Fermi liquid behavior and unconventional superconductivity.

References

[1] F. Steglich, J. Aarts, C.D. Bredl, W. Lieke, D. Meschede, W. Franz, and H. Schäfer, Phys. Rev. Lett. **43**, 1892 (1979)

[2] F.M. Grosche, I.R. Walker, S.R. Julian, N.D. Mathur, D.M. Freye, M.J. Steiner, and G.G. Lonzarich, J. Phys.: Condens. Matter **13** 2845 (2001)

[3] E. Morosan, H.W. Zandbergen, B.S. Dennis, J.W.G. Bos, Y. Onose, T. Klimczuk, A.P. Ramirez, N.P. Ong, and R.J. Cava, Nat. Phys. **2**, 544 (2006)

[4] W.L. McMillan and J.M. Rowell, Phys. Rev Lett **14**, 108 (1964)

[5] W.A. Harrison, Phys. Rev. **123**, 85 (1961)

[6] H.Z. Arham, C.R. Hunt, W.K. Park, J. Gillett, S.D. Das, S.E. Sebastian, Z. J. Xu, J.S. Wen, Z.W. Lin, Q. Li, G. Gu, A. Thaler, S. Ran, S. L. Bud'ko, P.C. Canfield, D. Y. Chung, M.G. Kanatzidis, and L.H. Greene, Phys. Rev. B **85**, 214515 (2012)

[7] W.K. Park, J.L. Sarrao, J.D. Thompson, and L.H. Greene, Phys. Rev. Lett. **100**, 177001 (2008)

[8] K. Shrestha, S. Zhang, L.H. Greene, Y. Lai, R.E. Baumbach, K. Sasmal, M.B. Maple, and W.K. Park, Phys. Rev. B **103**, 224515 (2021)

[9] S. Ernst, S. Wirth, F. Steglich, Z. Fisk, J.L. Sarrao, and J.D. Thomson, Phys. Stat. Sol. B **247**, 624 (2010)

[10] Y. Fasano, P. Szabo, J. Kacmarcik, Z. Pribulova, P. Pedrazzini, P. Samuely, and V.F. Correa, Physica B **536**, 798 (2018)

[11] Y. Song, J. Van Dyke, I.K. Lum, B.D. White, S. Jang, D. Yazici, L. Shu, A. Schneidewind, P. Čermák, Y. Qiu, M.B. Maple, D.K. Morr, and P. Dai, Nat. Commun. **7**, 12774 (2016)

[12] L.Y.L. Shen and J.M. Rowell, Phys. Rev. **165**, 566 (1968);
P.W. Anderson Phys. Rev. Lett. **17**, 95 (1966);
J. Applebaum Phys. Rev. Lett. **17**, 91 (1966)

[13] J. Levallois, M.K. Tran, D. Pouliot, C. N. Presura, L.H. Greene, J. Eckstein, J. Uccelli, E. Giannini, G.D. Gu, A.J. Leggett, and D. van der Marel, Phys. Rev. X **6**, 031027 (2016)

9 Unconventional Superconductivity: Mechanisms and Experimental Probes

Andreas Kreisel
Niels Bohr Institute
Jagtvej 155, 2100 Copenhagen

Contents

E. Pavarini and E. Koch (eds.)
Correlations and Phase Transitions
Modeling and Simulation Vol. 14
Forschungszentrum Jülich, 2024, ISBN 978-3-95806-751-6
http://www.cond-mat.de/events/correl24

1 Introduction

The superconducting state for conventional and unconventional superconductivity exhibits four unusual behaviors which are (i) zero resistance below a characteristic critical temperature T_c of the material (ii) persistent currents in superconductors of ring shape where currents have been observed to flow for time scales of several years, (iii) perfect diamagnetism as expulsion of a weak magnetic field from the interior of the superconductor and (iv) an energy gap $|\Delta|$ that opens up in the superconducting state. The last phenomenon is used to characterize the superconducting state in spectroscopic experiments, but has many imprints on thermodynamic and transport properties as at finite temperatures thermal excitations are present. For a full energy gap $|\Delta|$, these are an exponentially small number while for superconductors with nodal gaps, the number of excitations exhibit a power law which is inherited to the low temperature specific heat and thermal conductivity as these are governed by the low energy density of states. For conventional superconductors where the superconducting pairing is mediated by electron-phonon interaction, the energy gap turns out to be constant for all momentum states on the Fermi surface of the normal state metal, $|\Delta_{\mathbf{k}}| = \Delta_0$. The research field of unconventional superconductivity started with the discovery of superconductivity in the heavy-fermion material $CeCu_2Si_2$ in 1979 [1]. Until then, superconductivity was thought to be restricted to metallic elements and simple compounds and characterized by a superconducting gap Δ_0 that does not show momentum dependence. Since then many unconventional superconductors were identified experimentally (some example materials are shown in Fig. 1), prominent classes listed according to the time of discovery are (i) heavy-fermion materials where electrons with f-orbital character are at the Fermi level [1] (ii) 1D organic Bechgaard salts [2], (iii) copper-oxide materials (cuprates) where record high critical temperatures were observed [3] (iv) Fullerenes based on C_{60} molecules [4] (v) Sr_2RuO_4 as material similar to the cuprates [5] and (vi) iron-based superconductors [6]. Other interesting superconductors where pairing was or is still debated are (a) MgB_2 with a relatively high T_c and multiband character [7] (b) H_3S as possible high-temperature superconductor [8] (whereas only under extreme pressure conditions) and (c) Kagome superconductors for example the materials AV_3Sb_5 A=K, Rb, Cs [9].

2 Superconducting pairing

The starting point of the theoretical analysis of superconducting pairing in BCS theory is usually the presence of a metallic normal state described by a Fermi sea and the assumption of an attractive interaction of strength g_0 in a shell around the Fermi level of ω_D. From this, one can show that there exists a bound state irrespective of the value of g_0 (Cooper problem) or the Fermi sea has an instability towards a superconducting state (BCS theory). The assumption however does not consider the Coulomb interaction between the electrons which is repulsive in nature. Here, we will sketch two mechanisms to still overcome the Coulomb interaction and discuss consequences of this for the order parameter characterizing the superconducting phase. The two possible mechanisms can be summarized by the picture that the electrons avoid each

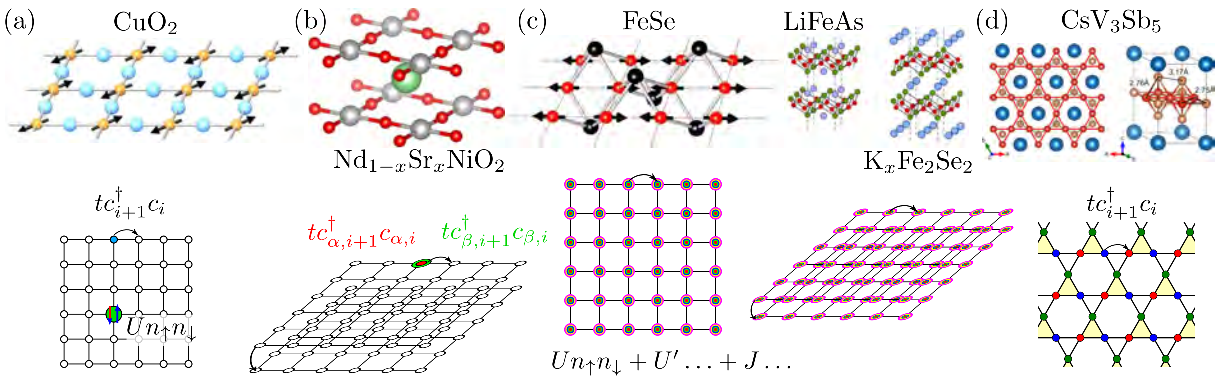

Fig. 1: *Examples of (potentially) unconventional superconductors: Crystal structure and sketch of models of the electronic structure. (a) Cuprates are often discussed by using a single band Hubbard model on a square lattice [10]. (b) The nickelates might need a multiple orbitals (red/green dot) and three dimensional electronic structure [11]. (c) Fe-based superconductors where all 5 d-orbitals are close to the Fermi level (colored dots) and dispersion in the third direction might play a role (especially for the 122 systems) [10, 12]. Interactions can be parametrized by the parameters U, U' and J. (d) Kagome superconductors require at least a three band model due to the three different sublattices (red/green/blue) in the unit cell [9].*

other in (i) time (retardation) for a conventional pairing mechanism and (ii) in space (momentum-dependent pairing) for unconventional pairing. The first case is realized from the conventional electron-phonon interaction where in a simple picture, one (negatively charged) electron moving through the lattice of atomic cores deforms the lattice. Since the atomic cores are much heavier than the electron, this deformation happens retarded such that a second electron will effectively feel a positive charge that is left "behind" by the first moving electron and therefore yields an effective attractive interaction, see Fig. 2. A detailed analysis of the (dynamic) order parameter $\Delta(\omega)$ yields that it acquires a sign change in energy in this case. We are not further discussing this mechanism in this lecture and refer to textbooks on this topic [13, 12].

2.1 Momentum-dependent paring and anisotropic superconducting order parameter

The electrons can also overcome the Coulomb interaction by another mechanism which we now illustrate by starting from a Hamiltonian of an electron gas together with a momentum-dependent interaction described by $V(\mathbf{k},\mathbf{k}')$; its origin will be discussed later. The Hamiltonian is given by

$$H = \sum_{\mathbf{k},\sigma} \varepsilon_{\mathbf{k}}\, c^\dagger_{\mathbf{k}'\uparrow} c_{\mathbf{k}\downarrow} + \frac{1}{2N} \sum_{\mathbf{k},\mathbf{k}'} \Big(V(\mathbf{k},\mathbf{k}')\, c^\dagger_{\mathbf{k}'\uparrow} c^\dagger_{-\mathbf{k}'\downarrow} c_{-\mathbf{k}\downarrow} c_{\mathbf{k}\uparrow} + \text{H.c.} \Big), \tag{1}$$

where $\varepsilon_{\mathbf{k}}$ is the energy dispersion and $c^\dagger_{\mathbf{k}\sigma}$, $c_{\mathbf{k}\sigma}$ are fermionic creation/annihilation operators of electrons at momentum $\mathbf{k}$ and spin σ.

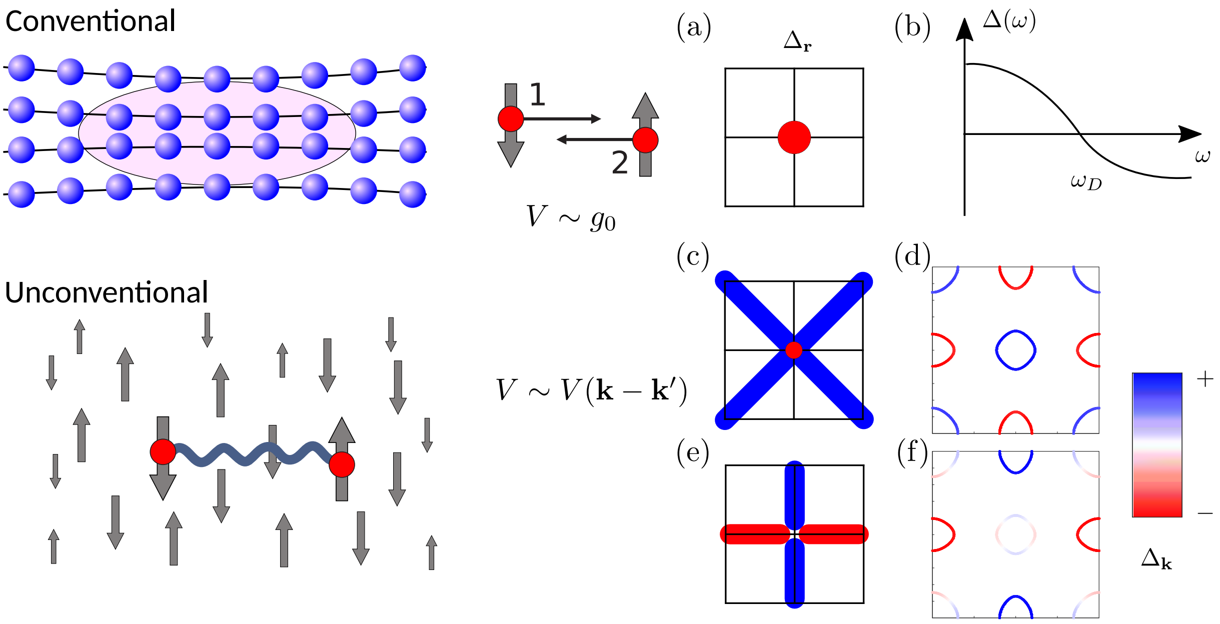

Fig. 2: *Conventional pairing: Two electrons (red dots) attract each other when the first deforms the lattice of positively charged atomic cores (light red region) the second is attracted to that region. The order parameter $\Delta_{\mathbf{r}}$ is just onsite $\mathbf{r} = 0$ (a). For the retarded interaction, it changes sign in frequency at the characteristic frequency of the attractive interaction ω_D(b) [10, 13]. Unconventional pairing: Electrons interact effectively with each other by polarizing the other conduction electrons by the Coulomb interaction. For the antiferromagnetic polarization ("neighbored" electrons tend to have the opposite spin direction), the second electron can lower its energy in the polarized region of the first electron, leading to an effective interaction (wiggly line) [12, 10] which is momentum dependent. Multiple order parameters can be realized; here two examples are shown: The $s_\pm$ state has the full symmetry of the lattice (c), but exhibits pairing to the next nearest neighbors. A sign change of the order parameter $\Delta_{\mathbf{k}}$ on the Fermi surface occurs (d). The $d_{x^2-y^2}$ order parameter has lower symmetry than the lattice since the horizontal bond orders have opposite sign from the vertical ones (e). Similar reduced symmetry of the order parameter in momentum space is given, where the order parameter has symmetry enforced nodes on the Fermi surface and very small gap on the Γ and M pockets (f) [14].*

Single band model on the square lattice In view of an example, we are later considering the single band model with nearest neighbor hopping t and next nearest neighbor hopping t',

$$\varepsilon_{\mathbf{k}} = -2t\big(\cos k_x + \cos k_y\big) - 4t' \cos k_x \cos k_y - \mu, \tag{2}$$

where we set the lattice constant $a = 1$ in the following and use $t = 1$ as energy unit. This simple model is flexible enough to discuss a number of Fermi surface topologies and stabilize a number different symmetries of the superconducting order parameter. In Fig. 3, we show the band structure and the density of states for variations of $t' < 0$. It turns out that one can tune several Lifshitz transitions which are marked as red, blue and green line in the phase diagram in Fig. 4 (left panel) to yield four representative Fermi surface topologies: (1) at large $|t'|$ the model exhibits electronlike pockets at the X and Y point. Crossing the blue line, these pockets touch and eventually lead to (2) a Fermi surface with electronlike and holelike Fermi pockets.

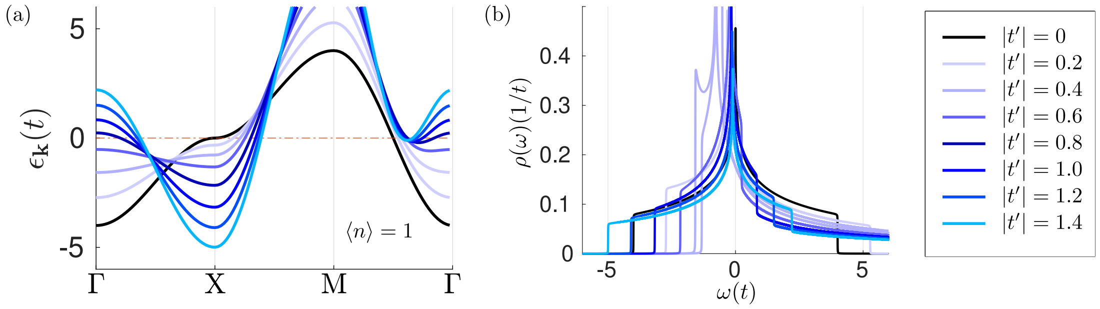

Fig. 3: *Single band model (a) dispersion along high symmetry path for different choices of* $t'\!<0$, *but the chemical potential tuned to stay at half filling* $\langle n\rangle\!=\!1$. *(b) Corresponding density of states* $\rho(\omega)$ *exhibiting van Hove singularities from band maxima/minima and saddle points.*

Reducing $|t'|$, the Γ pocket disappears and a Fermi surface reminiscent for cuprate materials is realized. Crossing the red line of a van Hove singularity with diverging density of states, one reaches (4) a single electronlike pocket around the Γ point, see Fig. 4.

Mean-field theory To map the Hamiltonian in Eq. (1) onto a formally non-interacting problem, we use the mean-field approximation. Starting from an interacting Hamiltonian $H = AB$ containing the product of two operators A and B we rewrite the operators as their mean value and a deviation from it, $A = \langle A\rangle + \delta A$, $B = \langle B\rangle + \delta B$ and ignore the term $\delta A \delta B$ of second order in the deviations from the mean such that we can replace $H \to H_{MF} = \langle A\rangle B + A\langle B\rangle - \langle A\rangle\langle B\rangle$. This amounts to rewriting the Hamiltonian in a simpler form that can be solved exactly, but depends on the mean values of the two operators as parameters. Next, we need to find a self-consistent solution in which the mean values $\langle A\rangle$ and $\langle B\rangle$ are calculated using the eigenvalues and eigenstates of H_{MF}.

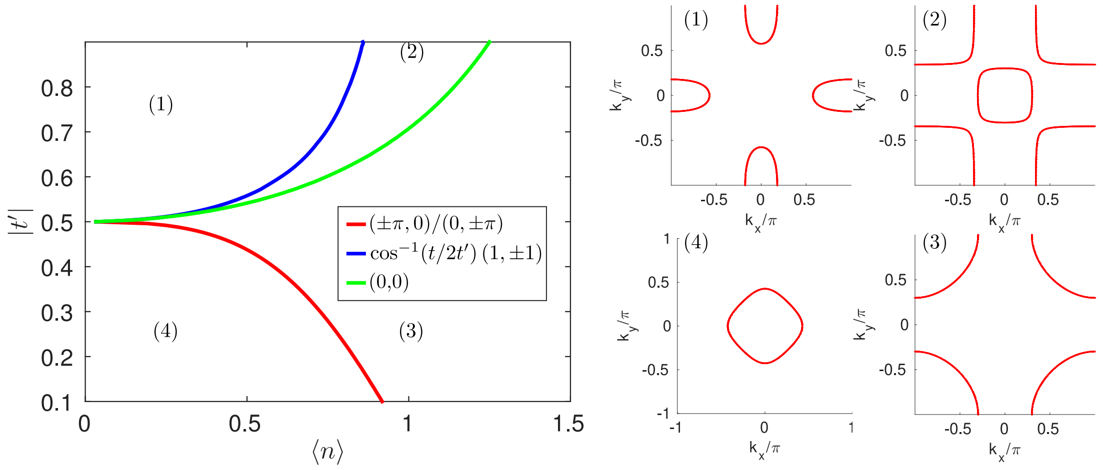

Fig. 4: *Single band model and Lifshitz transitions: Lines indicate where a point with vanishing Fermi velocity crosses the Fermi level. green: a local band maximum crosses at the* Γ *point, removing a hole pocket. red: A saddle point crosses and turns electronlike sheets into holelike sheets. blue: Touching of pockets at the zone diagonals. In total four different Fermi surface topologies are possible (1)–(4).*

BCS theory With the choice of $A = c^\dagger_{\mathbf{k}'\uparrow} c^\dagger_{-\mathbf{k}'\downarrow}$ and $B = c_{-\mathbf{k}\downarrow} c_{\mathbf{k}\uparrow}$, we obtain the mean-field Hamiltonian

$$\begin{aligned} H_{MF} = \sum_{\mathbf{k},\sigma} \varepsilon_{\mathbf{k}}\, c^\dagger_{\mathbf{k}\sigma} c_{\mathbf{k}\sigma} + \\ \frac{1}{N} \sum_{\mathbf{k},\mathbf{k}'} V(\mathbf{k},\mathbf{k}') \Big(\big\langle c^\dagger_{\mathbf{k}'\uparrow} c^\dagger_{-\mathbf{k}'\downarrow} \big\rangle c_{-\mathbf{k}\downarrow} c_{\mathbf{k}\uparrow} + c^\dagger_{\mathbf{k}'\uparrow} c^\dagger_{-\mathbf{k}'\downarrow} \big\langle c_{-\mathbf{k}\downarrow} c_{\mathbf{k}\uparrow} \big\rangle - \big\langle c^\dagger_{\mathbf{k}'\uparrow} c^\dagger_{-\mathbf{k}'\downarrow} \big\rangle \big\langle c_{-\mathbf{k}\downarrow} c_{\mathbf{k}\uparrow} \big\rangle + \text{H.c.} \Big). \end{aligned} \tag{3}$$

Note that the expectation values $\langle A \rangle = \big\langle c^\dagger_{\mathbf{k}'\uparrow} c^\dagger_{-\mathbf{k}'\downarrow} \big\rangle$ and $\langle B \rangle = \big\langle c_{-\mathbf{k}\downarrow} c_{\mathbf{k}\uparrow} \big\rangle$ are neither singlet nor triplet order parameters at this point. Defining the mean-fields in the singlet (s) and triplet (t) channel,

$$\varDelta^{s/t}_{\mathbf{k}} = -\frac{1}{N} \sum_{\mathbf{k}'} V^{s/t}(\mathbf{k},\mathbf{k}') \big\langle c^\dagger_{\mathbf{k}'\uparrow} c^\dagger_{-\mathbf{k}'\downarrow} \big\rangle, \tag{4}$$

where we also have projected to the symmetric (singlet) and antisymmetric (triplet) interactions

$$V^{s/t}(\mathbf{k},\mathbf{k}') = \frac{1}{2} \big(V(\mathbf{k},\mathbf{k}') \pm V(-\mathbf{k},\mathbf{k}') \big), \tag{5}$$

we can rewrite the Hamiltonian as

$$H_{MF} = \sum_{\mathbf{k},\sigma} \varepsilon_{\mathbf{k}}\, c^\dagger_{\mathbf{k}\sigma} c_{\mathbf{k}\sigma} - \sum_{\mathbf{k}} \varDelta^{s/t*}_{\mathbf{k}}\, c_{-\mathbf{k}\downarrow} c_{\mathbf{k}\uparrow} \mp \sum_{\mathbf{k}} \varDelta^{s/t}_{\mathbf{k}}\, c^\dagger_{\mathbf{k}\uparrow} c^\dagger_{-\mathbf{k}\downarrow} + \text{const.} \tag{6}$$

For the mean-field Hamiltonian to obey the Pauli principle, the order parameter has to be even parity in the momentum $\mathbf{k}$ for the upper sign of $\mp$, i.e., the singlet order parameter ($\varDelta^s_{\mathbf{k}} = \varDelta^s_{-\mathbf{k}}$) and odd parity in the momentum $\mathbf{k}$ for the lower sign for the triplet order parameter ($\varDelta^t_{\mathbf{k}} = -\varDelta^t_{-\mathbf{k}}$). Note that one can also assign two spin indices to the order parameter (and consider other quantum numbers such as orbitals or sublattice degrees of freedom). In this case, the order parameter has to be overall odd if all quantum numbers are exchanged. Since our interaction was spin-independent, we can use another spin-quantization axis in the original Hamiltonian and transform the triplet order parameter $\varDelta^t_{\mathbf{k}} = \varDelta_{\mathbf{k}\uparrow\downarrow} + \varDelta_{\mathbf{k}\downarrow\uparrow}$ into triplet order parameters that formally are in the $\uparrow\uparrow$ and $\downarrow\downarrow$ channel while the singlet order parameter remains invariant under such a basis transformation. More generally, the superconducting order parameter matrix can be described by a singlet term and a $\vec{d}$ vector to parametrize the three components of the triplet order parameter [15].

The mean-field Hamiltonian (with either $\varDelta^s_{\mathbf{k}}$ or $\varDelta^t_{\mathbf{k}}$) is now quadratic in the fermionic operators, i.e., describes a non-interacting system and can be diagonalized by a Bogoliubov transformation

$$\begin{pmatrix} \gamma_{\mathbf{k}\uparrow} \\ \gamma^\dagger_{-\mathbf{k}\downarrow} \end{pmatrix} = \begin{pmatrix} u^*_{\mathbf{k}} & -v_{\mathbf{k}} \\ v^*_{\mathbf{k}} & u_{\mathbf{k}} \end{pmatrix} \begin{pmatrix} c_{\mathbf{k}\uparrow} \\ c^\dagger_{-\mathbf{k}\downarrow} \end{pmatrix} \tag{7}$$

which defines new quasiparticle operators $\gamma_{\mathbf{k}\uparrow}$ that are linear combinations of electron creation and annihilation operators. For this transformation to preserve the anticommutation relations $\big\{\gamma_{\mathbf{k}\sigma}, \gamma^\dagger_{\mathbf{k}'\sigma'}\big\} = \delta_{\mathbf{k},\mathbf{k}'}\delta_{\sigma,\sigma'}$, we require $|u_{\mathbf{k}}|^2 + |v_{\mathbf{k}}|^2 = 1$ and can finally fix the value of the coefficients by first inverting the transformation and inserting it into the mean-field Hamiltonian and then requiring that the terms containing only quasiparticle annihilation operator to vanish. Dropping again constant terms, we can rewrite the Hamiltonian as

$$H_{BCS} = \sum_{\mathbf{k}\sigma} E_{\mathbf{k}}\, \gamma^{\dagger}_{\mathbf{k}\sigma}\gamma_{\mathbf{k}\sigma} \tag{8}$$

with the quasiparticle dispersion

$$E_{\mathbf{k}} = \sqrt{\varepsilon_{\mathbf{k}}^2 + |\Delta_{\mathbf{k}}^{s/t}|^2}. \tag{9}$$

Having the quasiparticle dispersion and the transformation at hand, we can evaluate the expectation value in Eq. (4) to obtain the self-consistency condition

$$\Delta_{\mathbf{k}}^{s/t} = -\frac{1}{N}\sum_{\mathbf{k}'} V^{s/t}(\mathbf{k},\mathbf{k}')\,\frac{\Delta_{\mathbf{k}'}^{s/t}}{2E_{\mathbf{k}'}}\,\tanh\Big(\frac{\beta E_{\mathbf{k}'}}{2}\Big), \tag{10}$$

evaluated at finite temperature. As a side remark, we note that this value of the order parameter indeed minimizes the free energy F, i.e., the equation above can also be derived from finding a stationary point via $\frac{\delta F}{\delta \Delta_{\mathbf{k}}} = 0$ [13]. In this case, also the constant terms need to be kept in the Hamiltonian and one sees that the superconducting state indeed has a lower energy than the state of a normal metal once the temperature is low enough that Eq. (10) has a nontrivial solution.

Linearized gap equation For a practical discussion of superconducting instabilities given a pairing interaction $V^{s/t}(\mathbf{k},\mathbf{k}')$, it is convenient to linearize this equation by setting $E_{\mathbf{k}'} = \varepsilon_{\mathbf{k}}$ on the r.h.s. Observing that the energy gain in the limit of $\Delta_{\mathbf{k}} \to 0$, i.e., at $T \to T_c$ has only contributions from states at the Fermi level, the integral over the Brillouin zone becomes a Fermi surface average in the linearized gap equation

$$-\frac{1}{V_G}\int_{FS} dS'\, V^{s/t}(\mathbf{k},\mathbf{k}')\frac{g_i(\mathbf{k}')}{|v_F(\mathbf{k}')|} = \lambda_i g_i(\mathbf{k}')\,. \tag{11}$$

Here V_G is the volume of the Brillouin zone, the integral $\int_{FS} dS'$ is over the Fermi surface evaluated at the points $\mathbf{k}'$, $g_i(\mathbf{k})$ is the gap symmetry function which contains the momentum dependence of the superconducting instability with eigenvalue λ_i where the instability with largest eigenvalue is realized at T_c. Formally, one can calculate the critical temperature from the eigenvalue by $T_c = \omega_0 e^{-1/\lambda_i}$, but the energy scale ω_0 from the effective pairing interaction is usually not known. In practice the linearized gap equation is solved by discretizing the Fermi surface into a set of Fermi points $\mathbf{k}'$ with associated area $l_{\mathbf{k}'}$ and finding the eigenvalues and eigenvectors of the matrix

$$M^{s/t}_{\mathbf{k},\mathbf{k}'} = -\frac{1}{V_G}\frac{l_{\mathbf{k}'}}{|v_F(\mathbf{k}')|}\, V^{s/t}(\mathbf{k},\mathbf{k}'). \tag{12}$$

We note that this matrix is not symmetric since on the r.h.s. the weight $l_{\mathbf{k}'}/|v_F(\mathbf{k}')|$ appears only in $\mathbf{k}'$ and not in $\mathbf{k}$, but the problem can be cast into the problem of diagonalizing a symmetric real-valued matrix that guarantees real eigenvalues and eigenvectors as follows: We define a matrix with diagonal elements of the weights $\Lambda_{\mathbf{k}} = \mathrm{diag}(l_{\mathbf{k}'}/|v_F(\mathbf{k}')|)/V_G$ such that one can trivially obtain $\sqrt{\Lambda}$ and $\sqrt{\Lambda}^{-1}$ as diagonal matrices as well. Dropping the s/t label and the labels $\mathbf{k}$ and $\mathbf{k}'$, one can write Eq. (12) as matrix multiplication, $M = V\Lambda_{\mathbf{k}'}$. We multiply this equation with $\sqrt{\Lambda_{\mathbf{k}}}$ and $\sqrt{\Lambda_{\mathbf{k}'}}^{-1}$ from left and right to obtain $\sqrt{\Lambda_{\mathbf{k}}}M\sqrt{\Lambda_{\mathbf{k}'}}^{-1} = \sqrt{\Lambda_{\mathbf{k}}}V\sqrt{\Lambda_{\mathbf{k}'}} \equiv \tilde{M}$, i.e., a symmetric (real-valued) matrix $\tilde{M}$. This matrix now has real eigenvalues λ_i and eigenvectors $\tilde{g}_i$ obeying $\tilde{M}\tilde{g}_i = \lambda_i\tilde{g}_i$. Substituting back the definition of $\tilde{M}$ and multiplication with $\sqrt{\Lambda_{\mathbf{k}}}^{-1}$ yields $M\sqrt{\Lambda_{\mathbf{k}'}}^{-1}\tilde{g}_i = \lambda_i\sqrt{\Lambda_{\mathbf{k}'}}^{-1}\tilde{g}_i$, in other words $g_i \equiv \sqrt{\Lambda_{\mathbf{k}'}}^{-1}\tilde{g}_i$ is eigenvector to the original matrix in Eq. (12) to the eigenvalue λ_i.

To evaluate whether the self-consistency equation and/or the linearized gap equation has a nontrivial solution and understand the momentum-dependence of the solution, we now discuss a number of special cases. First, we note that for an attractive interaction (within some energy range ω_D) as obtained from the electron-phonon interaction, it is clear that the minus sign is cancelled by $V(\mathbf{k},\mathbf{k}') = g_0$ with $g_0 < 0$ and we can infer that there exists a solution of the type $\Delta^s_{\mathbf{k}} = \Delta_0$ because the order parameter can be factored out of the momentum sum and divided out. Transforming now the integral into an energy integral by introduction of the density of states $\rho(\omega) = \frac{1}{N}\sum_{\mathbf{k}}\delta(\varepsilon_{\mathbf{k}}-\omega)$, we find the self-consistency equation

$$1 = g_0\int_{-\omega_D}^{\omega_D} d\omega\,\rho(\omega)\frac{\tanh\left(\frac{\beta}{2}\sqrt{\omega^2+|\Delta_0|^2}\right)}{2\sqrt{\omega^2+|\Delta_0|^2}} \tag{13}$$

leading to the known mean-field temperature dependence of the order parameter that can simply be calculated by a root-finding if the density of states is assumed to be constant close to the Fermi level $\rho(\omega) \approx \rho(0)$, see Fig. 5(a).

A calculation of the order parameter at zero temperature in the weak coupling limit yields $\Delta_0(T{=}0) = 2\omega_D\exp\left(-1/(g_0\rho(0))\right)$ and the critical temperature can be obtained from solving the linearized gap equation by an energy integral. The result $k_BT_c = \frac{2e^\gamma}{\pi}\omega_0\exp\left(-1/(g_0\rho(0))\right)$ is expressed with the Euler constant γ. The universal ratio between critical temperature and order parameter is given by $2\Delta_0(T=0)/k_BT_c = 2\pi/e^\gamma \approx 3.53$. Experimental deviations from this ratio are sometimes associated with the superconductor being in the strong coupling regime although unconventional pairing, i.e., sign-changing order parameter or anisotropic order parameter can give rise to modifications even in weak coupling BCS theory [16].

Momentum dependent pairing For momentum-dependent interactions, we want to give two perspectives. In the first perspective, we expand the interaction $V^{s/t}(\mathbf{k},\mathbf{k}')$ close to the Fermi surface in lattice harmonics which are a set of orthogonal functions in the Brillouin zone (similar to the spherical harmonics to expand a function on a sphere). Because of orthogonality and the parity constraints of the order parameter, the dependence on $\mathbf{k}$ and $\mathbf{k}'$ can be expanded separately and factorized. For illustration, let us take the pairing interaction

$$V(\mathbf{k},\mathbf{k}') = U - \frac{3J}{2}\left(\cos(k_x{-}k_x') + \cos(k_y{-}k_y')\right) \tag{14}$$

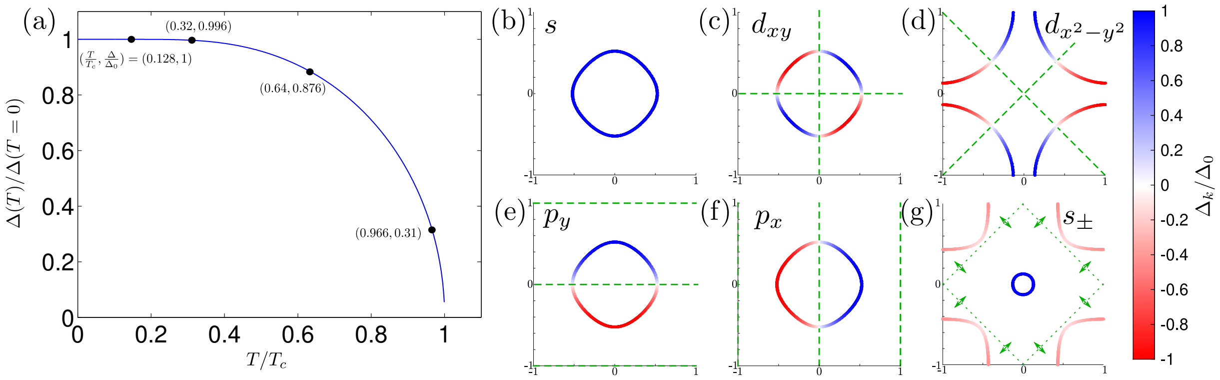

Fig. 5: *(a) Temperature dependence of the order parameter from self-consistency equation Eq. (13). (b)–(g) Examples of order parameters on a Fermi surface with only electron pocket* $\big(t'=0,\ n=0.25$ *(b), (c), (e), (f)*$\big)$ *and* $\big(t'=-0.35,\ n=0.85$ *(d)*$\big)$*,* $\big(t'=-1.2,\ n=0.75$ *(g)*$\big)$*. Symmetry enforced nodal lines are marked by green dashed lines, accidental nodal lines in panel (g) are marked with dotted lines and can move according to the arrows. Red/blue: sign of order parameter see colorbar.*

as it can be derived from rewriting the Hubbard model with nearest neighbor Heisenberg Hamiltonian $H_{\text{int}} = J\sum_{\langle i,j\rangle}\vec{S}_i\cdot\vec{S}_j$ in the form of Eq. (1) [13]. The singlet interaction is then obtained from the symmetrization, Eq. (5), $V^s(\mathbf{k},\mathbf{k}') = U - (3J/2)\big(\cos k_x \cos k'_x + \cos k_y \cos k'_y\big)$ which we can rewrite as $V^s(\mathbf{k},\mathbf{k}') = V_s + V_d$ with the s-wave term consisting in a repulsive part and the extended s-wave interaction $V_s = U - (3J/4)(\cos k_x + \cos k_y)(\cos k'_x + \cos k'_y)$ and the d-wave interaction $V_d = -(3J/4)(\cos k_x - \cos k_y)(\cos k'_x - \cos k'_y)$. These interactions are now written as products of the lowest harmonics for the respective order parameters, i.e., a constant for a s-wave order parameter, the function $f_s(\mathbf{k}) = \cos k_x + \cos k_y$ that is invariant under C_4 rotations of the momentum and the function $f_d(\mathbf{k}) = \cos k_x - \cos k_y$ that changes sign under a C_4 rotation. When doing a mean-field decoupling in the two channels, i.e., by choosing $A = f_{s/d}(\mathbf{k}')\, c^\dagger_{\mathbf{k}'\uparrow} c^\dagger_{-\mathbf{k}'\downarrow}$ and $B = f_{s/d}(\mathbf{k})\, c_{-\mathbf{k}\downarrow} c_{\mathbf{k}\uparrow}$, we obtain mean-field equations where the form factor from right and left side drops out. In summary, we obtain for the d-wave channel the same gap equation as Eq. (13), but with $g_0 = 3J\rho(0)/8$, i.e., there is an effective attraction in the d-wave channel and the on-site Hubbard repulsion is orthogonal (i.e., the product of U and the function $f_d(\mathbf{k})$ exactly averages to zero under a BZ integral). The the sign-changing d-wave pair condensate realizes an order parameter of the form $\Delta_{\mathbf{k}} = \Delta_0(\cos k_x - \cos k_y)$. This order parameter $\Delta_{\mathbf{k}}$ exhibits sign changes (by symmetry) and has nodal lines along the diagonals of the Brillouin zone. If these hit the Fermi surface, it has implications for the low-energy properties of the superconductor, see Fig. 5(d).

The second perspective is guided by knowledge of how typical spin-fluctuation pairing interactions behave: Usually, the interaction is repulsive everywhere, i.e., $V(\mathbf{k},\mathbf{k}') > 0$ for all combinations of $\mathbf{k}$ and $\mathbf{k}'$. This property is also inherited to the singlet interaction, $V^s(\mathbf{k},\mathbf{k}') > 0$, see Eq. (5). Looking now at the mean-field self-consistency equation, Eq. (10), one sees that for an order parameter $\Delta_{\mathbf{k}}$ that has the same sign everywhere, let us choose it positive $\Delta_{\mathbf{k}} > 0$, there is mathematically no solution possible because the l.h.s. is positive for all $\mathbf{k}$ and the r.h.s. is a sum of negative terms since $\tanh(x) > 0$ for $x > 0$ and $E_{\mathbf{k}'} > 0$. Allowing for a sign changing order parameter, there is however the possibility of finding a self-consistent solution if the order parameter $\Delta^s_{\mathbf{k}'}$ has a different sign than the order parameter $\Delta^s_{\mathbf{k}}$ for pairs of $\mathbf{k}$ and $\mathbf{k}'$ where the pairing interaction $V^s(\mathbf{k},\mathbf{k}')$ is largest. Indeed, the order parameter needs to be a smooth function of $\mathbf{k}$ and satisfy the condition $\Delta^s_{\mathbf{k}} = \Delta^s_{-\mathbf{k}}$ (even parity) such that the momentum sum $\sum_{\mathbf{k}'}$ sums up positive and negative contributions but still can compensate for the overall minus sign on the r.h.s.

Finally, a remark for the case of triplet superconductivity: Even with a repulsive bare interaction $V(\mathbf{k},\mathbf{k}') > 0$, one sees that the anti-symmetrization in Eq. (5) yields a pairing interaction $V^{s/t}(\mathbf{k},\mathbf{k}')$ that is positive for some $\mathbf{k}$ and $\mathbf{k}'$ and negative for others (simply from the fact that there is a momentum dependence). However, the order parameter needs to be of odd parity $\Delta^t_{\mathbf{k}} = -\Delta^t_{-\mathbf{k}}$ so that the order parameter must exhibit a sign change if becoming nonzero.

3 Spin fluctuation pairing

3.1 Spin susceptibility

Many unconventional superconducting materials have similar phenomenology in the overall phase diagram, namely that there is a magnetic state close to the superconducting phase, thus suggesting that fluctuations in the vicinity of the magnetic phase can provide the necessary effective pairing interaction because near the magnetic phase boundary the magnetic susceptibility $\chi(\mathbf{q},\omega)$ is enhanced [10]. The magnetic susceptibility as quantum mechanical response function is given by the spin-spin correlator $\langle T_\tau \vec{S}(\mathbf{r},\tau)\cdot \vec{S}(0,0)\rangle$ with the spin-operator $\vec{S}(\mathbf{r},\tau) = \frac{1}{2}c^\dagger_{\mathbf{r},\alpha}(\tau)\vec{\sigma}_{\alpha\beta}c_{\mathbf{r},\beta}(\tau)$ and the time ordering operator T_τ [13]. Parametrizing the components of the spin operator in terms of the raising and lowering operators $S^\pm = S^x \pm iS^y$, one can discuss the spin-spin correlator (and therefore the spin susceptibility) in terms of transverse $\langle S^+S^-\rangle$ and longitudinal $\langle S^zS^z\rangle$ parts. Starting from the paramagnetic phase (without spin-orbit coupling), these are identical such that we focus on the transverse part only.

Fourier transformation to momentum space yields

$$\begin{aligned}\chi_0^{+-}(\mathbf{q},\tau) &= \frac{1}{N}\sum_{\mathbf{k},\mathbf{k}'}\big\langle T_\tau S^+(\mathbf{q},\tau)S^-(-\mathbf{q},0)\big\rangle\\ &= \frac{1}{N}\sum_{\mathbf{k},\mathbf{k}'}\big\langle T_\tau c^\dagger_{\mathbf{k}+\mathbf{q},\uparrow}(\tau)c_{\mathbf{k},\downarrow}(\tau)c^\dagger_{\mathbf{k}'-\mathbf{q},\downarrow}(0)c_{\mathbf{k}',\uparrow}(0)\big\rangle.\end{aligned} \tag{15}$$

The correlator can be calculated using Wick's theorem (note the Fermionic statistics) and expressed in terms of the free Green function $G_0^\sigma(\mathbf{k},\tau) = \big\langle T_\tau c_{\mathbf{k},\sigma}(\tau)c^\dagger_{\mathbf{k},\sigma}(0)\big\rangle$ (for an introduction to the Green function formalism, see for example Ref. [17]). with the result

$$\begin{aligned}\chi_0^{+-}(\mathbf{q},\tau) &= -\frac{1}{N}\sum_{\mathbf{k},\mathbf{k}'}\big\langle T_\tau c_{\mathbf{k}',\uparrow}(0)c^\dagger_{\mathbf{k}+\mathbf{q},\uparrow}(\tau)\big\rangle\big\langle T_\tau c_{\mathbf{k},\downarrow}(\tau)c^\dagger_{\mathbf{k}'-\mathbf{q},\downarrow}(0)\big\rangle\\ &= -\frac{1}{N}\sum_{\mathbf{k}} G_0^\uparrow(\mathbf{k}{+}\mathbf{q},-\tau)\,G_0^\downarrow(\mathbf{k},\tau).\end{aligned} \tag{16}$$

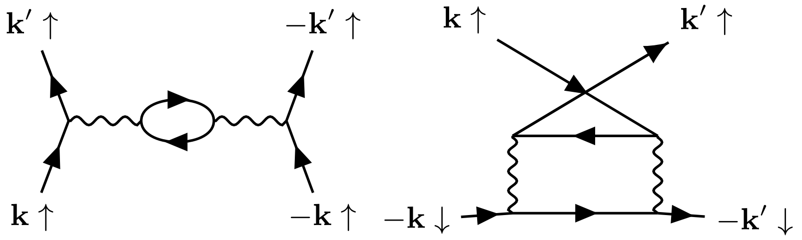

Fig. 6: *Second order screening (bubble) and exchange (ladder) diagrams. Note that each interaction line U depicted by a wiggly line connects opposite spins only.*

To evaluate the susceptibility, we transform from imaginary time τ to Matsubara frequency and introduce the Green functions $G_0^\sigma(\mathbf{k},\tau) = \frac{1}{\beta}\sum_{i\omega_n} e^{-i\omega_n} G_0^\sigma(\mathbf{k}, i\omega_n)$ to obtain

$$\chi_0^{+-}(\mathbf{q}, i\nu_n) = \int_0^\beta d\tau \, e^{i\nu_n\tau}\chi_0^{+-}(\mathbf{q},\tau) = -\frac{1}{\beta N}\sum_{\mathbf{k},i\omega_m} G_0^\uparrow(\mathbf{k}{+}\mathbf{q}, i\omega_m{+}i\nu_n)\, G_0^\downarrow(\mathbf{k}, i\omega_m) \tag{17}$$

The Matsubara Green functions of a free electron gas with energy dispersion $\varepsilon_\mathbf{k}$ are given by $G_0^\sigma(\mathbf{k}, i\omega_m) = 1/(i\omega_n - \varepsilon_\mathbf{k})$, i.e., have poles at $i\omega_n = \varepsilon_\mathbf{k}$ and are independent of spin for the paramagnetic case. Finally, we can evaluate the Matsubara sum over the fermionic frequency $i\omega_m$ to yield the susceptibility at the bosonic frequency $i\nu_n$,

$$\chi_0^{+-}(\mathbf{q}, i\nu_n) = -\frac{1}{N}\sum_\mathbf{k} \frac{n_F(\varepsilon_{\mathbf{k}+\mathbf{q}}) - n_F(\varepsilon_\mathbf{k})}{i\nu_n + \varepsilon_{\mathbf{k}+\mathbf{q}} - \varepsilon_\mathbf{k}}\,, \tag{18}$$

that for a paramagnetic metal is identical to the longitudinal one $\chi_0^{+-}(\mathbf{q}, i\nu_n) = \chi_0^{zz}(\mathbf{q}, i\nu_n)$. At zero frequency $i\nu_n = 0$, one can analyze the conditions for sizeable contributions in the momentum sum: The numerator generates a singularity for the same values of the energy dispersion $\varepsilon_{\mathbf{k}+\mathbf{q}} = \varepsilon_\mathbf{k}$, but the difference of the Fermi functions n_F for these arguments are only sizeable if the eigenenergies are close to zero energy (within a window of several k_BT), thus there are only contributions from k and $\mathbf{k}{+}\mathbf{q}$ close to the Fermi surface. Phase space is large if additionally, the respective Fermi velocities $v_F(\mathbf{k})$ and $v_F(\mathbf{k}{+}\mathbf{q})$ are (small and opposite to each other) yielding the argument about Fermi surface nesting for large contributions to the (static) susceptibility/Lindhard function.

3.2 Pairing interaction

The interaction from a Hubbard model

$$H_{\text{int}} = U\sum_\mathbf{r} c^\dagger_{\mathbf{r},\uparrow}c_{\mathbf{r},\uparrow}c^\dagger_{\mathbf{r},\downarrow}c_{\mathbf{r},\downarrow} = U\sum_\mathbf{r} n_{\mathbf{r},\uparrow}n_{\mathbf{r},\downarrow}\,, \tag{19}$$

can be taken into account in perturbation theory [18] (see Fig. 6) by considering the screening effect due to all other electrons (bubble diagrams, longitudinal) and the exchange of electrons (ladder diagrams, transverse). The effective interaction as already postulated in Eq. (1) is given by

$$V(\mathbf{k},\mathbf{k}') = U + V_{\text{lo}}^{\text{RPA}}(\mathbf{k}{-}\mathbf{k}') + V_{\text{tr}}^{\text{RPA}}(\mathbf{k}{+}\mathbf{k}'). \tag{20}$$

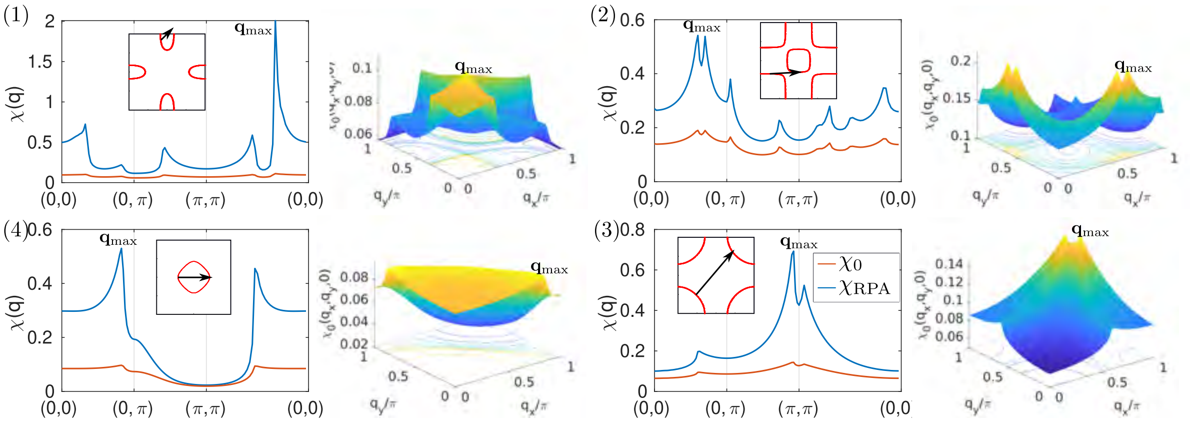

Fig. 7: *Single band model: susceptibility (red: bare, blue: RPA) at a choice of Hubbard interactions yielding a fixed eigenvalue $\lambda_1 = 0.1$ for the pairing. (1)–(4) The four representative single band models have quite different structure of the susceptibility with peak structures that are localized (2), (3) or ridges of large susceptibility (1), (4). The maximum of the susceptibility a momentum transfer $\mathbf{q}_{max}$ is given by a combination of Fermi surface nesting, density of states properties and available phase space for scattering processes indicated by the black arrow in the inset with the Fermi surface.*

The longitudinal contribution is restricted to an even number of bubbles, thus the series only has even powers of U and can be rewritten in terms of the spin (s) and charge (c) susceptibility,

$$V_{\text{lo}}^{\text{RPA}}(\mathbf{k}-\mathbf{k}') = \frac{U^3\chi_0^{zz}(\mathbf{k}-\mathbf{k}')^2}{1-U^2\chi_0^{zz}(\mathbf{k}-\mathbf{k}')^2} = \frac{U^2}{2}\left(\frac{\chi_0^{zz}(\mathbf{k}-\mathbf{k}')}{1-U\chi_0^{zz}(\mathbf{k}-\mathbf{k}')} - \frac{\chi_0^{zz}(\mathbf{k}-\mathbf{k}')}{1+U\chi_0^{zz}(\mathbf{k}-\mathbf{k}')}\right)$$
$$= \frac{U^2}{2}\big(\chi_{\text{s}}(\mathbf{k}-\mathbf{k}') - \chi_{\text{c}}(\mathbf{k}-\mathbf{k}')\big). \tag{21}$$

The transverse part is formally given by a geometric series with the transverse susceptibility,

$$V_{\text{tr}}^{\text{RPA}}(\mathbf{k}+\mathbf{k}') = \frac{U^2\chi_0^{+-}(\mathbf{k}+\mathbf{k}')}{1-U\chi_0^{+-}(\mathbf{k}+\mathbf{k}')}\,. \tag{22}$$

Since we are only discussing the paramagnetic case, from now on the difference between transverse and longitudinal susceptibility is dropped. First, we observe that the spin susceptibility exhibits a singularity if $1-U\chi_0^{zz}(\mathbf{q}) = 0$, which signals an instability towards a spin-density wave state if it occurs at finite $\mathbf{q}$. It is the usual Stoner instability for an itinerant ferromagnet if it occurs at $\mathbf{q} = 0$ since the (bare) susceptibility at $T=0$ and $\mathbf{q}=0$ is just the density of states at the Fermi level $\chi_0^{zz}(0) = \rho(0)$. Second, close to such a magnetic phase, the spin fluctuations are strong and the effective pairing interaction becomes large as well. Ignoring the charge fluctuations (which in this approximation do not become dominant because of the $1+U\chi_0^{zz}(\mathbf{q})$ denominator), one sees that the spin susceptibility (and consequently the pairing interaction) is a monotonous function of U, i.e., large values of $\chi_0^{zz}(\mathbf{q})$ lead to large values of $\chi_s(\mathbf{q})$. Consequently, to identify dominant contributions for pairing and qualitatively understand the solutions $\varDelta_{\mathbf{k}}$ of the self-consistence equation Eq. (10), it is sufficient to look for peaks in the bare susceptibility (Lindhard function).

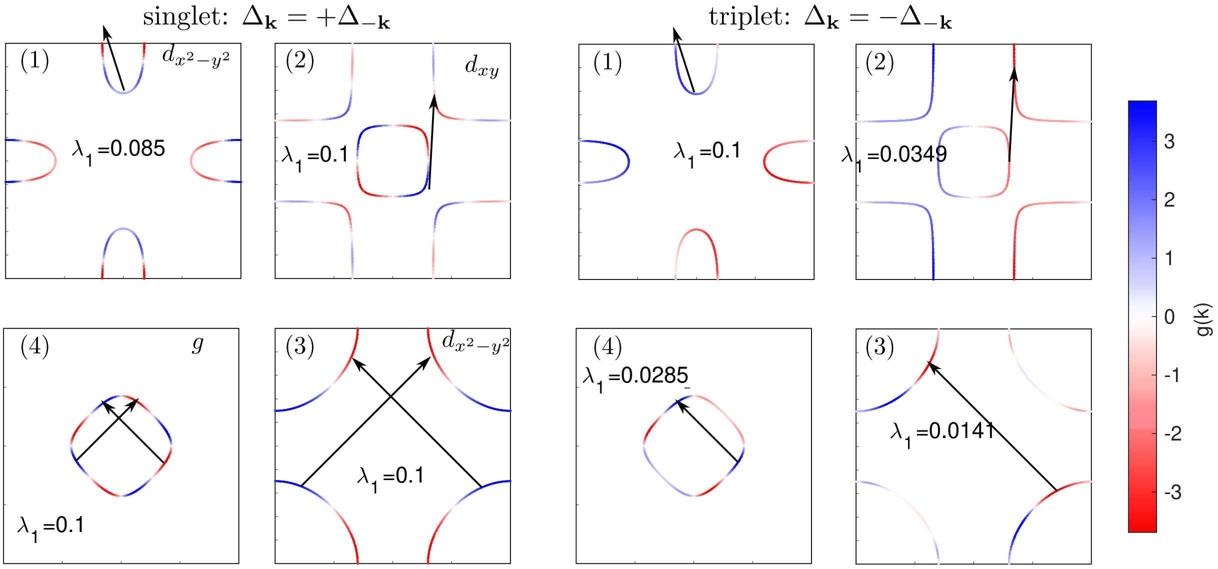

Fig. 8: *Single band model: superconducting order parameter calculated using Eq. (11) from the spin-fluctuation paring interaction in Eq. (20). Solutions of the linearized gap equation for the four representative models (1)–(4), compare Fig. 4 with bare interaction U tuned such that the leading instability has $\lambda = 0.1$. Arrows indicate dominant peaks in the bare susceptibility as shown in Fig. 7. For singlet states, these connect order parameters of different sign while for the triplet states, the dominant pair scattering connects between parts where the order parameter has the same sign.*

3.3 Single band model

In the following, we discuss a couple of examples of simple band structures, the properties of the susceptibility and expected superconducting pairing states. The starting point is a single-band model with one $d_{x^2-y^2}$ orbital as discussed in view of the cuprate superconductors. The model is given already in Eq. (2) and is parametrized by the nearest neighbor hopping t, the next-nearest-neighbor hopping t' and the chemical potential μ. In the following we assume the chemical potential to be tuned such that a given (spin-summed) density $\langle n \rangle$ is achieved. This model allows four different Fermi surface topologies, see Fig. 4 and therefore also different nesting conditions with differences in the Lindhard function (susceptibility), see Fig. 7. The dominant peaks in the susceptibility are then responsible for the momentum structure of the superconducting order parameter. For singlet pairing $\mathbf{q}_{\text{max}}$ connects Fermi surface points where the order parameter is maximum and has opposite sign, while for solutions in the triplet channel, the pairing interaction is negative and largest for this momentum transfer and consequently $\mathbf{q}_{\text{max}}$ connects order parameter of the same sign as illustrated in Fig. 8.

Given the three Lifshitz transition lines for the single band model, the Fermi surface topology is already very different in each regime and allows for pairing states of all possible symmetries, see Fig. 9. Indeed, there are also triplet instabilities either close to the van Hove filling where the density of states is large or in the regime of small Fermi energy where the band structure

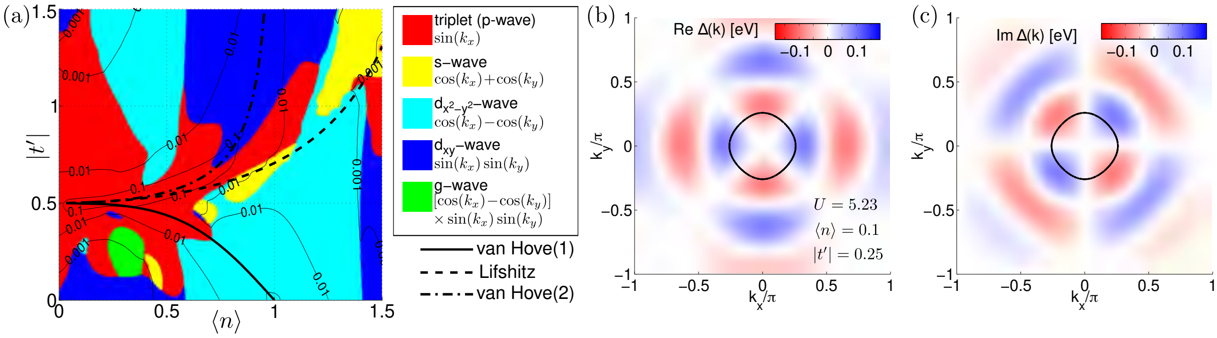

Fig. 9: *(a) Superconducting phase diagram from spin-fluctuations showing the superconducting instabilities of the one band model in the limit of small interactions* $U = 0.08$. *Lines indicate eigenvalue* λ *of the leading instability. (b) At small filling (Fermi surface indicated by black circle), spin-fluctuation theory predicts a time-reversal symmetry breaking* $d_{x^2-y^2}+id_{xy}$ *superconducting instability as worked out by a self-consistent Bogoliubov-de-Gennes calculation based on Eq. (10) [21].*

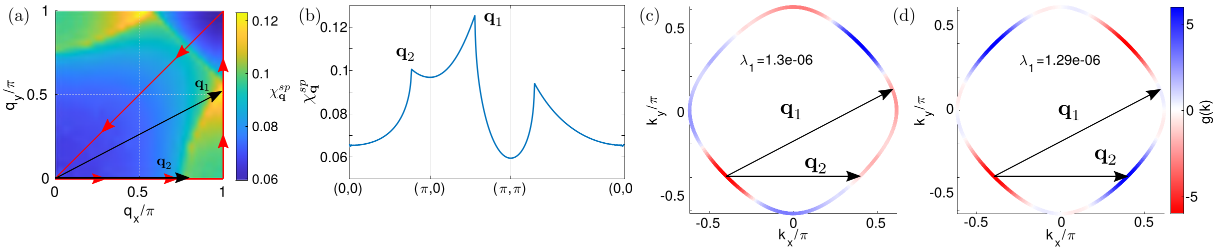

Fig. 10: *Triplet pairing from spin fluctuations at finite momentum in the single band Hubbard model: (a) The spin susceptibility* $\big(U{=}0.05,\ t{=}1,\ t'{=}0,\ n{=}0.54,\ T{=}0.0001\big)$ *exhibits two dominant peaks at* $\mathbf{q}_1$ *and* $\mathbf{q}_2$. *(b) Linear plot along a high symmetry path. Gap symmetry function* $g(\mathbf{k})$ *of the leading triplet instability (c) and leading singlet instability (d) showing that the dominant scattering vectors connect parts where the order parameter is large [19].*

resembles a parabolic band which has been discussed to exhibit an instability in the triplet channel (at weak coupling). In this case, the pairing state is a $p_{x,y}$ state with momentum dependence $\propto \sin k_x$ or $\propto \sin k_y$. If the susceptibility is peaked at a finite $\mathbf{q}_{\text{max}}$, the pairing instabilities tend to be dominated by singlet states, but there is the possibility to take advantage of the spin fluctuations even in the triplet channel if $\mathbf{q}_{\text{max}}$ spans multiple nodes and the Fermi surface topology is susceptible for those pairing states with higher order harmonics, see Fig. 10 [19].

To conclude this section on spin-fluctuations in a single band Hubbard model, we want to stress that the approach presented here is based on a perturbative expansion of the pairing interaction in powers of U. It is strictly correct only in the weak coupling regime and to order U^3 since in the RPA approach, only certain types of diagrams are summed over. Still it seems to connect smoothly to numerically exact and unbiased calculations in the strong coupling regime for the mentioned single band model [20].

3.4 Multiband generalization

A number of unconventional superconductors cannot be described by a single band model because of multiple atoms in the elementary cell and/or a crystal field splitting such that multiple orbital degrees of freedom have to be considered for the relevant low-energy electronic structure. Prominent material examples are the Fe-based superconductors where all five Fe-d states contribute to the electronic structure [22, 12], in $\mathrm{Sr_2RuO_4}$ three orbital degrees of freedom are important [23], the nickelate systems (with one or more layers) [11,24] and the kagome systems where three sublattice degrees of freedom are in the elementary cell [9].

In the case of multiorbital systems, the normal state Hamiltonian can be written in a tight-binding model as

$$H_0 = \sum_{\mathbf{k}\sigma\ell\ell'} t_{\mathbf{k}}^{\ell\ell'} \, c_{\ell\sigma}^{\dagger}(\mathbf{k}) c_{\ell'\sigma}(\mathbf{k}), \tag{23}$$

where $t_{\mathbf{k}}^{\ell\ell'} = \sum_\delta t_\delta^{\ell\ell'} \exp(i\mathbf{k}\cdot\delta)$ is the Fourier transform of the hopping elements connecting orbital ℓ with orbital ℓ' at distance δ.

A unitary transformation with the matrix elements $a_\mu^\ell(\mathbf{k})$ diagonalizes the Bloch Hamiltonian such that it becomes

$$H_0 = \sum_{\mathbf{k}\sigma\mu} \varepsilon_{\mu,\mathbf{k}} \, c_{\mu\sigma}^{\dagger}(\mathbf{k}) c_{\mu\sigma}(\mathbf{k}) \tag{24}$$

with eigenenergies $\varepsilon_{\mu,\mathbf{k}}$ and $c_{\mu\sigma}^{\dagger}(\mathbf{k})$ is the operator creating an electron in Bloch state of band μ at momentum $\mathbf{k}$. In Fig. 11(e,f) the electronic structure of such a five band model is illustrated for the example of LiFeAs. This model has been derived from an ab-initio calculation in Ref. [26] by restricting to the $k_z = 0$ plane. The model of $\mathrm{K}_x\mathrm{Fe_2Se_2}$ (g,h) only has electronlike pockets. For completeness and later reference, we also cite the generalization of the Hubbard interaction Eq. (19) to multiple orbitals as usually discussed in terms of a Hubbard-Kanamori form,

$$H_{\text{int}} = U\sum_{i,\ell} n_{i\ell\uparrow}n_{i\ell\downarrow} + U'\sum_{i,\ell'<\ell} n_{i\ell}n_{i\ell'} + J\sum_{i,\ell'<\ell}\sum_{\sigma,\sigma'} c_{i\ell\sigma}^{\dagger}c_{i\ell'\sigma'}^{\dagger}c_{i\ell\sigma'}c_{i\ell'\sigma} + J'\sum_{i,\ell'\neq\ell} c_{i\ell\uparrow}^{\dagger}c_{i\ell\downarrow}^{\dagger}c_{i\ell'\downarrow}c_{i\ell'\uparrow}, \tag{25}$$

where the parameters $U,\ U',\ J,\ J'$ are related by $U' = U - 2J$, and $J = J'$ in the spin-rotational invariant case, i.e., two parameters U and J/U parametrize the interactions [28, 29].

If the additional degree of freedom is a sublattice, the interaction might need to be complemented by nearest neighbor Coulomb interactions (for a single orbital model)

$$H_{\mathrm{V}} = V \sum_{\substack{ij\\ \mu\sigma\sigma'}} n_{\alpha,i,\sigma} n_{\overline{\alpha},j,\sigma'} \, , \tag{26}$$

where α denotes a sublattice and $\overline{\alpha}$ is a sublattice distinct from α. We are not elaborating on this further here, more details can be found for example in Ref. [30].

For a multiband model, the analog of the paramagnetic susceptibility, Eq. (17) is given by

$$\chi^0_{\ell_1\ell_2\ell_3\ell_4}(\mathbf{q}, i\nu_n) = -\sum_{\mathbf{k}, i\omega_n} G^{\ell_1\ell_3}(\mathbf{k}+\mathbf{q}, i\omega_n + i\nu_n)\, G^{\ell_2\ell_4}(\mathbf{k}, i\omega_n) \tag{27}$$

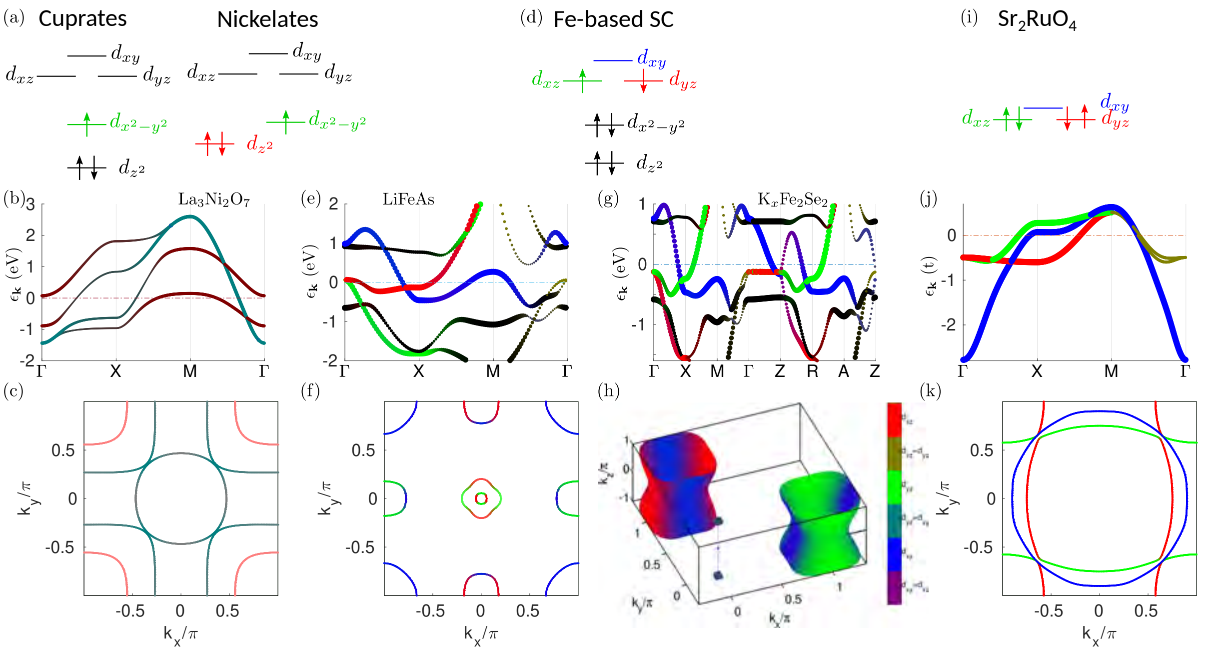

Fig. 11: *Examples of electronic structure of multiband superconductors (a) Sketch of crystal field splitting for cuprate and nickelate systems (b) Band structure of a bilayer nickelate [25] (c) corresponding Fermi surface with d_{z^2} and $d_{x^2-y^2}$ orbital character. (d) Fe-based systems exhibiting the three t_{2g} orbitals at the Fermi level. (e) Band structure of a model for LiFeAs [26] and (f) corresponding Fermi surface with electron pockets at X and Y point and holelike pockets at the Γ point and M point. (g) Electronic structure of a 122 system with sizeable dispersion along k_z exhibiting only electronlike pockets at the X and Y point for $K_xFe_2Se_2$ [27]. (i) Three relevant orbital states in Sr_2RuO_4 yield three bands (j) and three Fermi sheets (k).*

where the Green functions can be expressed in spectral representation

$$G^{\ell_1\ell_2}(\mathbf{k}, i\omega_n) = \sum_{\mu} \frac{a_\nu^{\ell_1}(\mathbf{k}) a_\nu^{\ell_2,*}}{i\omega_n - \varepsilon_{\mu,\mathbf{k}}} \,. \tag{28}$$

Again, we can perform the frequency sum analytically and obtain the generalized Lindhard function

$$\chi^0_{\ell_1\ell_2\ell_3\ell_4}(\mathbf{q}, i\nu_n) = -\sum_{\mathbf{k},\mu,\nu,i\omega_n} \frac{a_\nu^{\ell_4}(\mathbf{k}) a_\nu^{\ell_2,*}(\mathbf{k}) a_\mu^{\ell_1}(\mathbf{k}{+}\mathbf{q}) a_\mu^{\ell_3,*}(\mathbf{k}{+}\mathbf{q}) \big(n_F(\varepsilon_{\mu,\mathbf{k}+\mathbf{q}}) - n_F(\varepsilon_{\nu,\mathbf{k}})\big)}{i\nu_n + \varepsilon_{\mu,\mathbf{k}+\mathbf{q}} - \varepsilon_{\nu,\mathbf{k}}} \,. \tag{29}$$

To calculate the effective pairing interaction from a spin-fluctuation mechanism, the RPA approach needs to be generalized to a matrix expression [22, 29]

$$\chi^{\mathrm{RPA}}_{\mathrm{s/c}\,\ell_1\ell_2\ell_3\ell_4}(\mathbf{q}, \omega) = \Big(\chi^0(\mathbf{q}, \omega)\big(1 \mp \bar{U}^{\mathrm{s/c}}\chi^0(\mathbf{q}, \omega)\big)^{-1}\Big)_{\ell_1\ell_2\ell_3\ell_4} , \tag{30}$$

where the interaction matrices $\bar{U}^{s,c}$ contain the bare interactions parametrized by U, U', J and J' and become momentum dependent in the presence of nearest-neighbor Coulomb interactions, Eq. (26).

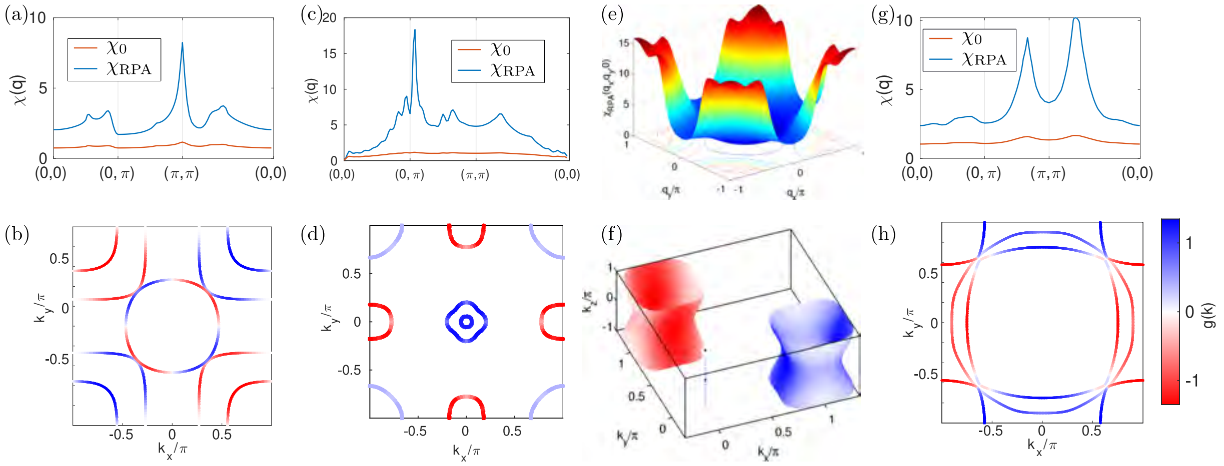

Fig. 12: *Examples of superconducting pairing in multiband systems. (a) Susceptibility and (b) pairing state of a bilayer nickelate exhibiting a* d*-wave state. (c) Susceptibility for LiFeAs and (d) corresponding leading* $s_\pm$ *pairing state with full gap. (e) Susceptibility as calculated from a model of* $K_xFe_2Se_2$ *that only exhibits electronlike pockets and has a* d*-wave instability (f). The susceptibility of* Sr_2RuO_4 *using a band structure from a plain DFT calculation sustains a* d*-wave instability (h).*

The generalization of the pairing interaction (in orbital representation) is then given by

$$\Gamma_{\ell_1\ell_2\ell_3\ell_4}(\mathbf{k},\mathbf{k}')=\frac{1}{2}\Big(3\bar{U}^{\mathrm{s}}\chi_{\mathrm{s}}^{\mathrm{RPA}}(\mathbf{k}-\mathbf{k}')\bar{U}^{\mathrm{s}}+\bar{U}^{\mathrm{s}}-\bar{U}^{\mathrm{c}}\chi_{\mathrm{c}}^{\mathrm{RPA}}(\mathbf{k}-\mathbf{k}')\bar{U}^{\mathrm{c}}+\bar{U}^{\mathrm{c}}\Big)_{\ell_1\ell_2\ell_3\ell_4} \tag{31}$$

and enters the self-consistent equation (analogous to Eq. (10)) with a symmetrized and antisymmetrized pairing interaction.

Taking the limit $T\to T_{\mathrm{c}}$, only the states on the Fermi surface become relevant. In that process, the pairing interaction is projected to band space such that the pairing vertex in band space

$$\Gamma_{\nu\mu}(\mathbf{k},\mathbf{k}')=\mathrm{Re}\sum_{\ell_1\ell_2\ell_3\ell_4}a_{\nu}^{\ell_1,*}(\mathbf{k})\,a_{\nu}^{\ell_4,*}(-\mathbf{k})\,\Gamma_{\ell_1\ell_2\ell_3\ell_4}(\mathbf{k},\mathbf{k}')\,a_{\mu}^{\ell_2}(\mathbf{k}')\,a_{\mu}^{\ell_3}(-\mathbf{k}') \tag{32}$$

enters the linearized gap equation, Eq. (11). Note that the band index on the r.h.s. is formally a dummy index since the knowledge of $\mathbf{k}$ and $\mathbf{k}'$ on the Fermi surface automatically fixes the band indices μ and ν. We note that the pairing interaction in Eq. (31) is dominated by momentum transfer $\mathbf{k}\pm\mathbf{k}'$ where the susceptibility is peaked and is dominated by inter-orbital contributions since for those the susceptibility tends to be large and the bare interaction $\bar{U}^{\mathrm{s,c}}$ is larger for these processes as well. Still, we note that dominant Hund's pairing [31, 32], i.e., when $U'=U-2J$ becomes negative can induce large inter-orbital pairing and some combinations of the pairing interaction can become negative as discussed in Ref. [29] to drive inter-orbital pairing together with intra-orbital pairing. In Fig. 12 some examples of pairing in multiband models are shown where the dominant mechanism can be understood from the structure of the spin susceptibility

$$\chi_{\mathrm{phys}}(\mathbf{q})=\frac{1}{2}\sum_{\ell\ell'}\chi_{\ell\ell'\ell'\ell}(\mathbf{q}). \tag{33}$$

Interplay of Fermi surface geometry and nesting We now discuss some representative example materials; the choice is done for illustration purposes only and does not claim to be complete in any way. The nickelate superconductors have been proposed as a sister compound to the cuprates [24], but only recently, it was possible to actually obtain superconducting infinite layer nickelates in thin films or bilayer nickelates that are found to be superconducting under moderate pressure [33]. The common theme for the superconducting mechanism is thought to be similar to the cuprates. However, there are several differences such as the different crystal field splitting (see Fig. 11(a)), i.e., multiple orbitals are relevant for the low energy electronic structure or the question of dispersion in the third direction as evidenced from a smaller anisotropy in transport. For the superconducting instability, some investigations point towards a d-wave state in analogy to single band cuprates. Taking into account correlations, there might be a competing s-wave instability; the same trend is also found in models for bilayer nickelates; depending on the details either a sign-changing s-wave or d-wave instability seems favorable (see Fig. 11(b)) [25, 34]. For the Fe-based superconductors, calculations using the spin-fluctuation pairing mechanism find competing $s_\pm$ states for the prototype Fermi surface (see Fig. 11(d)) [26], but different Fermi surface topologies as found in strongly doped $\mathrm{K}_x\mathrm{Fe}_2\mathrm{Se}_2$ [27] of the monolayer FeSe with large T_c would favor a d-wave instability with sign change between the electronlike Fermi surfaces. The case of $\mathrm{Sr}_2\mathrm{RuO}_4$ has been under intense investigation in the last two decades. Early evidence for spin triplet superconductivity from NMR Knight shifts sparked large interest in the compound and led to theoretical investigations of how to stabilize such an instability. More experimental efforts using NMR revealed that there was a technical challenge that was overcome in a later experiment finding a suppression of the spin susceptibility in the superconducting state, a clear evidence for spin singlet superconductivity; the same conclusions were also drawn from data for the specific heat in a magnetic field. The exact nature of the superconducting order parameter is still under debate, both experimentally and theoretically [23]. Reconciling all experimental data with one single proposal for the superconducting state seems not possible, but a plain calculation for spin-fluctuation driven superconductivity starting from an ab-initio band structure points to a d-wave instability, see Fig. 12(h).

3.5 Sublattice degree of freedom and kagome systems

The calculation of the susceptibility and consequently also the pairing interaction for systems with multiple lattice points per elementary cell needs some additional care. Relevant examples in view of unconventional superconductors are Fe-based systems of the 122 structure, where no exact downfolding to a five band model with only one Fe per elementary cell exists (more reading on this in Chapter 6 in Ref. [35]) or the kagome systems where three sublattices are needed, see Fig. 1.

The underlying concept can be understood by examining electrons on a one dimensional chain. For calculating the (bare) susceptibility in this system, we start with the dispersion

$$\varepsilon_k = -2t \cos ka \,, \tag{34}$$

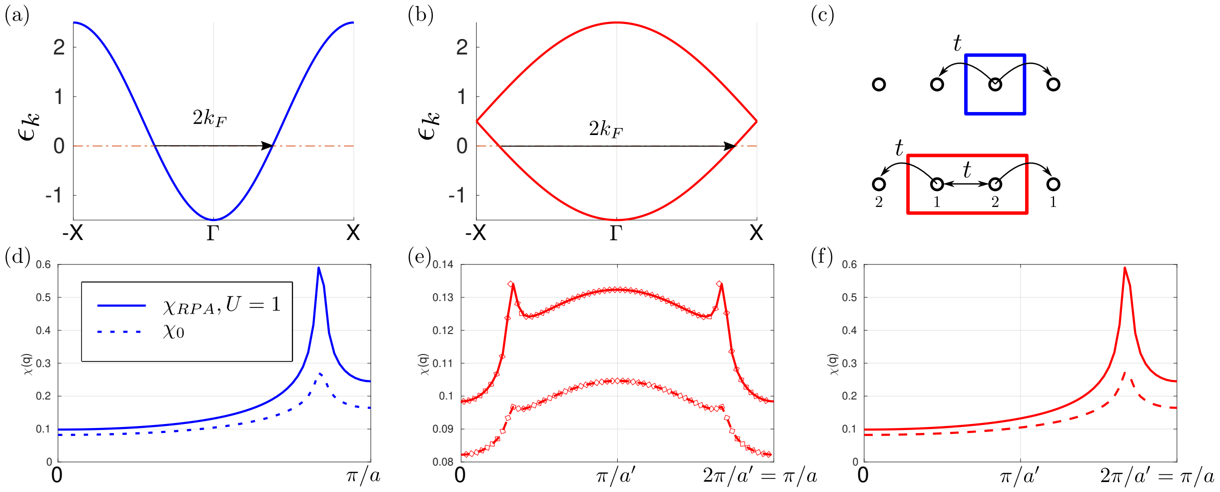

Fig. 13: *Susceptibility and sublattice degree of freedom: (a) Bandstructure of a 1d nearest neighbor tight-binding model (b) same model, but described with two identical sublattices. (c) Description of the same physical system with one lattice point per elementary cell (blue) and two lattice points per elementary cell (red) where intra-unit cell hoppings (straight lines) and inter-unit cell hoppings (curved lines) are present. (d) Paramagnetic susceptibility at* $\mu = -0.5t$*. (e) Paramagnetic susceptibility from Eq. (27) calculated in the basis where the Hamiltonian is periodic in the BZ, (f) same, but including the effect of the unitary transformation, Eq. (35).*

and use Eq. (18). Indeed, the Bloch Hamiltonian is just ε_k and periodic in the Brillouin zone $\varepsilon_k = \varepsilon_{k+2\pi/a}$ and it becomes obvious that the susceptibility $\chi_0^{+-}(\mathbf{q}, i\nu_n)$ is also periodic with the reciprocal lattice vector $\chi_0^{+-}(q, i\nu_n) = \chi_0^{+-}(q{+}2\pi/a, i\nu_n)$. To illustrate the effect of a sublattice, we now use a different elementary cell (that is not a primitive elementary cell) to perform the same calculation. Defining a two sublattice system, the Bloch Hamiltonian becomes a $2{\times}2$ matrix as

$$\tilde{H}(k) = -t \begin{pmatrix} 0 & 1 + \exp(ik/a') \\ 1 + \exp(-ik/a') & 0 \end{pmatrix} . \tag{35}$$

Now, the lattice constant is $a' = 2a$ and there are intra unit cell hopping processes that do not acquire a momentum dependence, see Fig. 13(c). We note that the Brillouin zone is now smaller $(-\pi/a' \cdot \pi/a']$, still the Hamiltonian is periodic with a reciprocal vector $\tilde{H}_k = \tilde{H}_{k+\pi/a'}$ and so is the susceptibility $\chi^{+-}_{\ell_1\ell_2\ell_3\ell_4}(q, i\nu_n) = \chi^{+-}_{\ell_1\ell_2\ell_3\ell_4}(q{+}2\pi/a, i\nu_n)$. However, this result does not agree with the susceptibility as calculated using the primitive elementary cell, see Fig. 13(e). The reason is because the Bloch Hamiltonian does not "know" anything about the internal position of the two sublattice states. A way out is to work in a different basis that is connected to the current one by the unitary transformation

$$U = \begin{pmatrix} 1 & 0 \\ 0 & \exp(ika'/2) \end{pmatrix} \tag{36}$$

such that the Bloch Hamiltonian is now

$$H(k) = -t \begin{pmatrix} 0 & 2\cos(ka'/2) \\ 2\cos(ka'/2) & 0 \end{pmatrix} , \tag{37}$$

which has the same eigenvalues as $\tilde{H}_k$, but the eigenvectors are different and are not periodic with a reciprocal lattice vector since also the Hamiltonian is not $H_k \neq H_{k+2\pi/a'}$. The susceptibility calculated following Eq. (27) using this Hamiltonian is periodic with two reciprocal lattice vectors, $\chi^{+-}_{\ell_1\ell_2\ell_3\ell_4}(q, i\nu_n) = \chi^{+-}_{\ell_1\ell_2\ell_3\ell_4}(q{+}4\pi/a', i\nu_n) = \chi^{+-}_{\ell_1\ell_2\ell_3\ell_4}(q{+}2\pi/a, i\nu_n)$ which is the reciprocal lattice vector of the original (primitive) setting. Thus, calculating the physical susceptibility using Eq. (33) one indeed obtains the same result as in the primitive setting. Note that the susceptibilities in the two basis settings of the Hamiltonian are related by just the multiplication of a phase factor $\exp(\pm i\mathbf{q}/2)$ for the off-diagonal elements that connect the two sublattices as one can easily show from the relation of the eigenvectors in the two settings and the possibility to factor these from the momentum sum in Eq. (27).

Kagome lattice For a concrete example where the sublattice degree qualitatively enters the susceptibility calculation and therefore is important for calculations of superconducting paring, we consider a model on the kagome lattice. This is motivated by the recent discovery of superconductivity in kagome materials [9] where the nature of the superconducting order parameter is currently under debate.

We start from a minimal tight-binding model with only nearest neighbor hoppings such that the Hamiltonian is given by

$$\mathcal{H}_0 = \sum_{\mathbf{k},\sigma} \psi^\dagger_{\mathbf{k}\sigma} H_0(\mathbf{k}) \psi_{\mathbf{k}\sigma}, \tag{38}$$

where $\psi_{\mathbf{k}\sigma} = \big(c_{\mathbf{k}\sigma A},\, c_{\mathbf{k}\sigma B},\, c_{\mathbf{k}\sigma C}\big)^T$ is a vector containing fermionic operators for the three sublattices and the Bloch Hamiltonian

$$H_0(\mathbf{k}) = -\begin{pmatrix} \mu & t\cos k_3 & t\cos k_1 \\ t\cos k_3 & \mu & t\cos k_2 \\ t\cos k_1 & t\cos k_2 & \mu \end{pmatrix}. \tag{39}$$

The momenta $k_n = \mathbf{k}\cdot\mathbf{a}_n$ are parametrized with help of the vectors $\mathbf{a}_1 = \big(1,\, 0\big)/2$, $\mathbf{a}_2 = \big(1,\, \sqrt{3}\big)/4$ and $\mathbf{a}_3 = \big(-1,\, \sqrt{3}\big)/4$ connecting to the nearest neighbors. μ is the chemical potential and t the NN hopping integral. The Hamiltonian is diagonalized by a unitary transformation, $u^*_{n\alpha}(\mathbf{k}) H_{0,\alpha\beta}(\mathbf{k}) u_{\beta m}(\mathbf{k}) = \varepsilon_{n,\mathbf{k}}\delta_{nm}$ yielding the band energies $\varepsilon_{n,\mathbf{k}}$ and the eigenstates $u_{n\alpha}(\mathbf{k})$ of band n. The unitary transformation

$$T(\mathbf{k}) = \begin{pmatrix} e^{-ik_1} & 0 & 0 \\ 0 & e^{-ik_2} & 0 \\ 0 & 0 & 1 \end{pmatrix} \tag{40}$$

transforms the Hamiltonian into a basis which is periodic in the first BZ,

$$\tilde{H}_0(\mathbf{k}) = -\begin{pmatrix} \mu & t\big(1{+}e^{2ik_3}\big) & t\big(1{+}e^{-2ik_1}\big) \\ t\big(1{+}e^{-2ik_3}\big) & \mu & t\big(1{+}e^{-2ik_2}\big) \\ t\big(1{+}e^{2ik_1}\big) & t\big(1{+}e^{2ik_2}\big) & \mu \end{pmatrix} \tag{41}$$

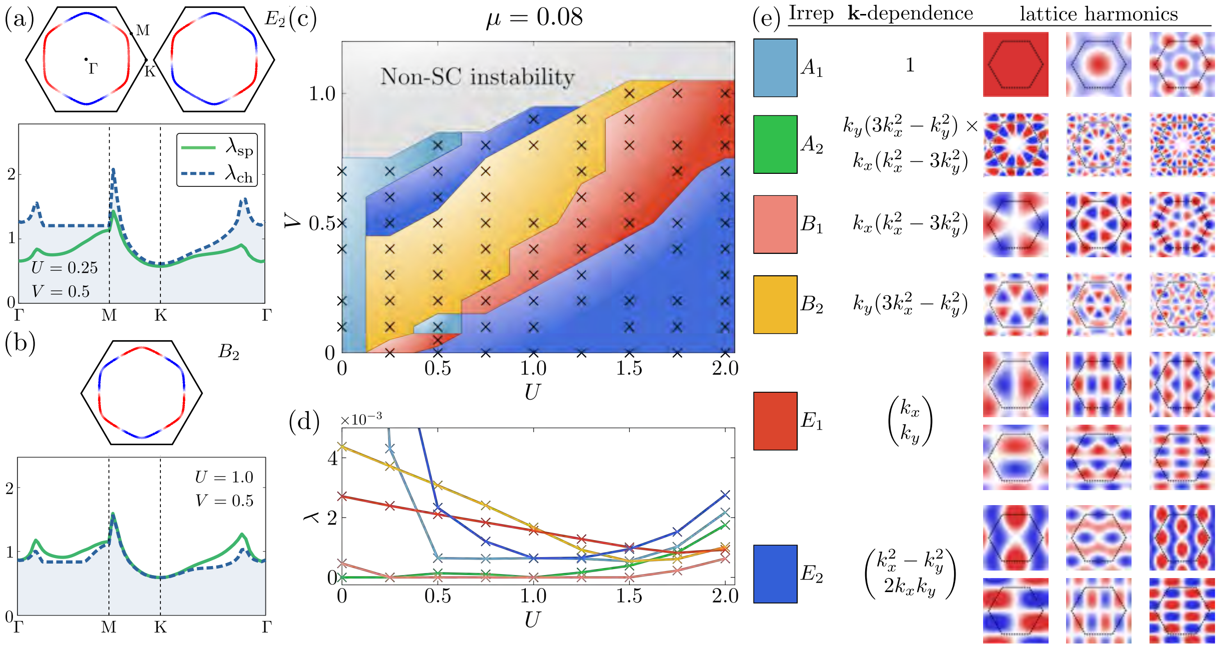

Fig. 14: *Superconducting instabilities in a kagome system from spin fluctuations including NN Coulomb interactions. Leading superconducting instability driven by spin (a) and charge (b) fluctuations (plotted along high symmetry path). (c) Phase diagram exhibiting many competing superconducting instabilities as revealed from the calculation of the eigenvalue of the linearized gap equation Eq. (11). (e) Labeling for the phase diagram and momentum structure of the SC instabilities [30].*

to be used to evaluate the momentum integral in Eq. (29) and the elements of the unitary transformation $T(\mathbf{k})$ to be used for calculating the susceptibility in the other basis setting,

$$\chi^{+-}_{0,\alpha\beta}(\mathbf{q},\omega) = \begin{pmatrix} \tilde{\chi}^{+-}_{0,AA} & e^{i(q_2-q_1)}\tilde{\chi}^{+-}_{0,AB} & e^{-iq_1}\,\tilde{\chi}^{+-}_{0,AC} \\ e^{i(q_1-q_2)}\tilde{\chi}^{+-}_{0,BA} & \tilde{\chi}^{+-}_{0,BB} & e^{-iq_2}\,\tilde{\chi}^{+-}_{0,BC} \\ e^{iq_1}\,\tilde{\chi}^{+-}_{0,CA} & e^{iq_2}\,\tilde{\chi}^{+-}_{0,CB} & \tilde{\chi}^{+-}_{0,CC} \end{pmatrix}, \tag{42}$$

where $\tilde{\chi}^{+-}_{0,\alpha\beta}(\mathbf{q},\omega)$ is the spin susceptibility evaluated using $\tilde{H}_0(\mathbf{k})$, and $q_n = \mathbf{q}\cdot\mathbf{a}_n$.

Superconductivity from spin fluctuations on the kagome lattice Fig. 14(a,b) show the (eigenvalues of the) susceptibility for the kagome lattice at $\mu = 0.08$. Nearest neighbor interactions according to Eq. (26) are taken into account making the charge fluctuations sizeable. Consequently, superconducting instabilities of many symmetries are expected as shown in the phase diagram (c). Looking at the phase diagram, one finds a significant parameter space at sizeable U, but moderate V where the E_2, i.e., a d-wave type solution is favorable. Generically, the two orthogonal solutions exhibit the same T_c and therefore condense at the same temperature with two possible settings: Either a real combination of the order parameter is stable, i.e., $d{+}d$ where an additional crystal symmetry is broken when entering the superconducting state, or the order parameters form a complex linear combination $d{+}id$. For an extended discussion on time reversal symmetry breaking in superconductors, see the reviews in Refs. [36, 37]. In the latter case, the time reversal symmetry is broken in the superconducting state and for the given Fermi surface, the quasiparticle spectrum becomes fully gapped since the nodes of the two states do not coincide. The second case usually lowers the condensation energy and is generically favored see appendix in Ref. [38]. This state would also be consistent with some observations in the kagome materials, namely the full gap as seen in tunneling spectra [39] and evidence for time reversal symmetry breaking in the superconducting state [40]. The latter could also arise from other mechanisms such as loop currents in a complex charge density wave, indicated by the presence of other instabilities in these materials occurring at higher transition temperatures.

4 Spectroscopic probes

In this section, we will theoretically analyze properties of unconventional superconductors and point out qualitative differences in a set of spectroscopic probes that can be used to experimentally distinguish between conventional and unconventional superconductors and deduce possible gap symmetries.

To accomplish this task, we first formulate BCS theory in terms of Green functions and then derive physical observables. For a mean-field Hamiltonian of the form of Eq. (6), we can rewrite it in the form

$$H_{\mathrm{MF}} = \sum_{\mathbf{k}} \Psi^\dagger_{\mathbf{k}} \widehat{H}_{\mathrm{BdG}}(\mathbf{k}) \Psi_{\mathbf{k}} \,, \tag{43}$$

where we introduced the matrix of the Bogoliubov de Gennes Hamiltonian (BdG)

$$\widehat{H}_{\mathrm{BdG}}(\mathbf{k}) = \begin{pmatrix} h(\mathbf{k}) & \Delta^{s/t}(\mathbf{k}) \\ \Delta(\mathbf{k})^{s/t\,\dagger} & -h(-\mathbf{k})^T \end{pmatrix} , \tag{44}$$

and $\Psi^\dagger_{\mathbf{k}} = \big(c^\dagger_{\mathbf{k}\uparrow},\, c_{-\mathbf{k}\downarrow}\big)$. For a single band model, we have $h(\mathbf{k}) = \varepsilon_{\mathbf{k}}$ and $\Delta^{s/t}(\mathbf{k}) = \Delta^{s/t}_{\mathbf{k}}$, while for the multiband case, the operator runs over all auxiliary quantum numbers that can be orbital or sublattice $c^\dagger_{\mathbf{k},\sigma} = \big(c^\dagger_{\mathbf{k}\sigma 1},\, c^\dagger_{\mathbf{k}\sigma 2},\, \dots\big)$. The retarded Green function that formally solves the Schrödinger equation is given by

$$\widehat{G}^{(0)}(\mathbf{k},\omega) = \Big((\omega{+}i\eta)\mathbb{1} - \widehat{H}_{\mathrm{BdG}}(\mathbf{k})\Big)^{-1} = \begin{pmatrix} G^{(0)}_{11}(\mathbf{k},\omega) & G^{(0)}_{1\bar{1}}(\mathbf{k},\omega) \\ G^{(0)}_{\bar{1}1}(\mathbf{k},\omega) & G^{(0)}_{\bar{1}\bar{1}}(\mathbf{k},\omega) \end{pmatrix}, \tag{45}$$

where we introduced the normal or anomalous parts of the Green function with the notation of 11 and $1\bar{1}$. For the single band case, the matrix inversion can be done analytically giving the $2{\times}2$ matrix

$$\widehat{G}^{(0)}(\mathbf{k},\omega) = \frac{(\omega{+}i\eta)\tau_0 + \varepsilon_{\mathbf{k}}\tau_3 + \Delta^{s/t}_{\mathbf{k}}\tau_1}{(\omega{+}i\eta)^2 - \varepsilon^2_{\mathbf{k}} - \big(\Delta^{s/t}_{\mathbf{k}}\big)^2} \tag{46}$$

with the usual Pauli matrices τ_i and the unit matrix τ_0.

4.1 Density of states

The quasiparticle density of states is then given by

$$\rho_s(\omega) = -\frac{1}{\pi}\,\mathrm{Tr}\,\mathrm{Im}\,\widehat{G}^{(0)}(\mathbf{k},\omega)\,, \tag{47}$$

and the electronic density of states relevant for tunneling is given by

$$\rho(\omega) = -\frac{1}{\pi}\,\mathrm{Tr}\,\mathrm{Im}\,G^{(0)}_{11}(\mathbf{k},\omega) = -\frac{1}{2\pi}\,\mathrm{Tr}\,\mathrm{Im}\,\big(G^{(0)}_{11}(\mathbf{k},\omega) + G^{(0)}_{\bar{1}\bar{1}}(\mathbf{k},-\omega)\big), \tag{48}$$

where the trace is over the auxiliary degrees of freedom (orbital, sublattice) and a sum over momentum $\mathbf{k}$. With the help of the unitary transformation in Eq. (7), one can obtain the spectral representation of the Green function that contains products of the matrix elements of the Bogoliubov transformation and finally yields for the density of states (in the one band case) the expression

$$\rho(\omega) = \sum_{\mathbf{k}} \Big(|u_{\mathbf{k}}|^2\, \delta(\omega{-}E_{\mathbf{k}}) + |v_{\mathbf{k}}|^2\, \delta(\omega{+}E_{\mathbf{k}}) \Big), \tag{49}$$

which weights the positive and negative eigenvalues according to the composition of the quasiparticle states in terms of the original electrons and holes. For a superconductor with a constant order parameter Δ_0, there are no states at $\omega < \Delta_0$, and a singularity $\propto |\omega|/\sqrt{\omega^2{-}\Delta_0^2}$ above that energy. For momentum-dependent order parameters, there are no states below the minimum of the order parameter $\Delta_- = \min_{\mathbf{k}_F} \Delta_{\mathbf{k}_F}$ (at the Fermi surface). Because of the form of the quasiparticle energies $E_{\mathbf{k}} = \sqrt{\varepsilon_{\mathbf{k}}^2 + |\Delta_{\mathbf{k}}^{s/t}|^2}$, there appear van Hove singularities in the density of states whenever the order parameter has a minimum or maximum. We note that these singularities arise from minima (Δ_-) or saddle points $\big($at $\Delta_+ = \max_{\mathbf{k}_F} \Delta_{\mathbf{k}_F}\big)$ of the quasiparticle dispersion $E_{\mathbf{k}}$. In two dimensions, these lead to steps at $\omega = \Delta_-$ or logarithmically diverging density of states at the respective energies $\omega = \Delta_+$ (where also local maxima contribute).

For nodal superconductors, the low-energy density of states is given by the low energy expansion of $E_{\mathbf{k}}$. If the order parameter exhibits a (simple) sign-change this leads to a linear quasiparticle dispersion (Dirac-cone) close the node and therefore in the simplest case to a linear density of states close to $\omega = 0$. This behavior is identical for nodes dictated by symmetry (for example d-wave order parameter) as well as accidental nodes (for example $s_\pm$ order parameter). Low temperature expansions of thermodynamic properties such as specific heat, penetration depth (superfluid density) and thermal transport can be calculated from the low energy expansion of the density of states. Thus, these quantities have imprints of the order parameter, and corresponding power law dependencies in the experimental data are used to examine the superconducting order parameter.

The electronic density of states itself can be measured in (scanning) tunneling experiments where the differential conductance is to a good approximation given by $dI/dV \propto \rho(\omega)$ [41], while there might be corrections from tunneling processes through the surface layers [42,43]. Some examples of densities of states for unconventional superconducting states in single and multiband systems are shown in Fig. 15 where it becomes obvious that the symmetry of the

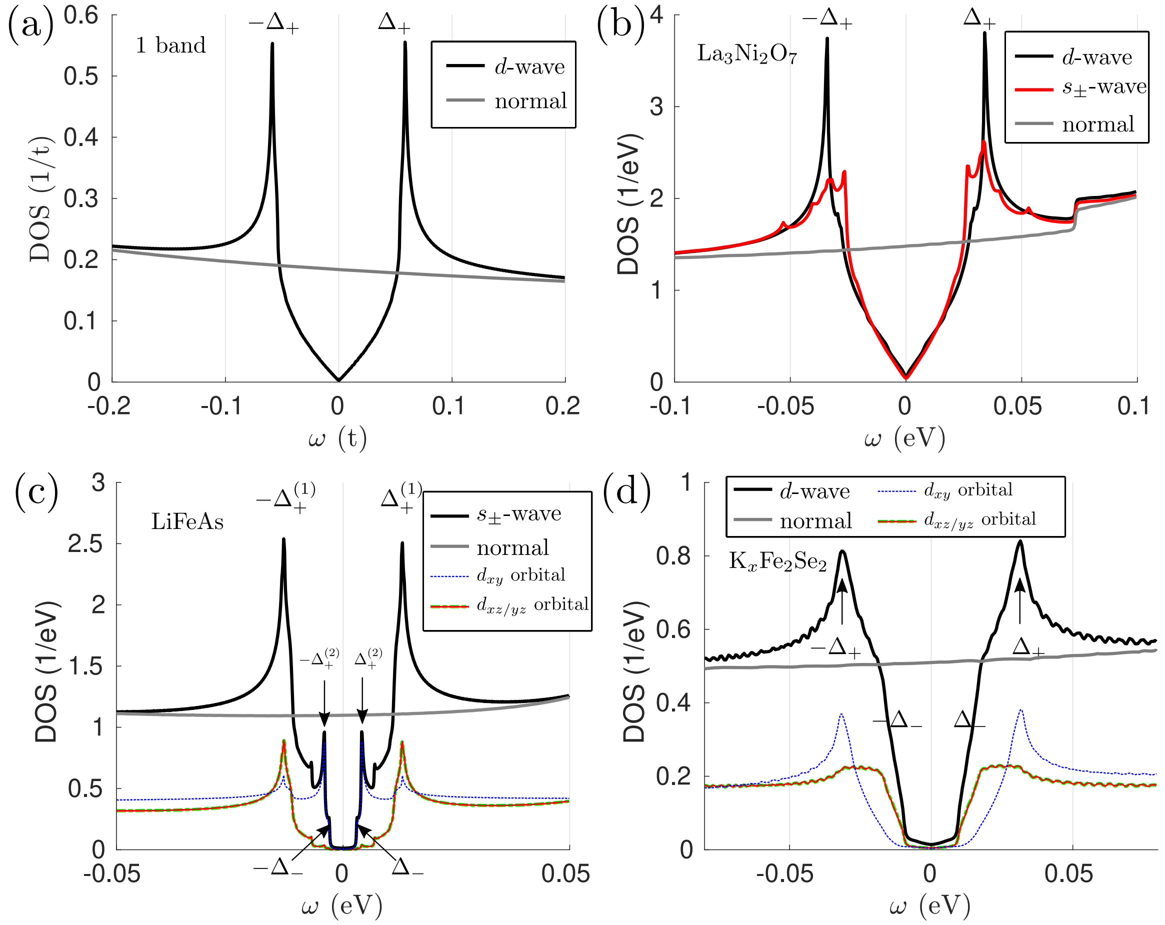

Fig. 15: *Examples of densities of states for unconventional superconductors: (a) single band model with d-wave order parameter (see Fig. 8, panel (3) left) exhibiting logarithmically divergent coherence peaks and a linear DOS as low energies from the Dirac-like dispersion close to the nodal points (in two dimensions). (b) Multiband result for bilayer nickelate system where the leading d-wave instability (see Fig. 12(a)) shows the characteristic behavior known from the single band case, but also a sub-leading $s_\pm$ state has almost identical spectral signatures. (c) DOS for sign changing $s_\pm$ state without nodes. Multiple coherence peaks for gap maxima on the pockets (see Fig. 12(b)) appear. (d) The nodeless d-wave solution for the system with only electronlike pockets shows coherence peaks and a step at the minimum of the order parameter on the Fermi surface, compare Fig. 12(c).*

order parameter cannot always be deduced from the spectrum. There are cases where sign-changing s-wave and d-wave states are almost identical (panel b) for the nodal case. Also the fully gapped situation can occur from different symmetries of the order parameter (panels c,d).

4.2 Bound states from impurities

The effect of disorder can be used to distinguish conventional from unconventional superconductors and eventually also differentiate between different symmetries of unconventional superconductivity. Here, we will concentrate on the effect of a single impurity in a superconductor [44].

In order to investigate the response of the Cooper pair wavefunction of different pairing candidates to single impurities, we introduce a nonmagnetic impurity or a (classical) magnetic impurity as a variation of the onsite potential via the matrix

$$\widehat{H}_{\text{imp}} = V\tau^z \otimes M \tag{50}$$

for a potential scatterer, and

$$\widehat{H}_{\text{imp}} = S_z\tau^0 \otimes M \tag{51}$$

for a magnetic impurity, where the matrix M contains the structure of the impurity in the auxiliary quantum numbers, i.e., $M = 1$ for a single band model. The basis is again as for Eq. (44). The effect of disorder on the superconducting order parameter itself will be neglected in this section; on the mean-field level one can however treat it self-consistently by solving the BCS equation, Eq. (4), in real space. For some physical observables (especially if states from multiple impurities overlap), this might be important. However for the presence and properties of bound states on single impurities as discussed here, there is no qualitative difference.

Assuming no effect on the order parameter itself as mentioned above, the full Green function in real space can be calculated within the T-matrix approximation as

$$\widehat{G}(\mathbf{r},\mathbf{r}',\omega) = \widehat{G}^{(0)}(\mathbf{r}-\mathbf{r}',\omega) + \widehat{G}^{(0)}(\mathbf{r},\omega)\,\widehat{T}(\omega)\,\widehat{G}^{(0)}(-\mathbf{r}',\omega), \tag{52}$$

with the T-matrix given by

$$\widehat{T}(\omega) \equiv \left(\mathbb{1} - \widehat{H}_{\text{imp}}\widehat{G}^{(0)}(\mathbf{0},\omega)\right)^{-1}\widehat{H}_{\text{imp}}\,. \tag{53}$$

Here, the free real-space Green function is calculated by the Fourier transform from Eq. (45),

$$\widehat{G}^{(0)}(\mathbf{r},\omega) = \frac{1}{N}\sum_{\mathbf{k}}\widehat{G}^{(0)}(\mathbf{k},\omega)\,e^{i\mathbf{k}\cdot\mathbf{r}}. \tag{54}$$

Having the real space Green function at hand, we can calculate the spin-summed electronic local density of states (LDOS) at auxiliary quantum number α

$$\rho_\alpha(\mathbf{r},\omega) = -\frac{1}{\pi}\,\text{Im}\left(G_{\alpha\alpha}(\mathbf{r},\mathbf{r},\omega) + G_{\bar{\alpha}\bar{\alpha}}(\mathbf{r},\mathbf{r},-\omega)\right). \tag{55}$$

Conventional and unconventional single band superconductors For the single band case in a conventional superconductor ($\varDelta_{\mathbf{k}} = \varDelta$), the calculation of the effect of a single (non)magnetic impurity can be done analytically. Using Eq. (46), we can calculate the local Green functions with the result for the diagonal part

$$G^{(0)}_{11}(\omega) = -\frac{\pi\rho(0)\omega}{\sqrt{|\varDelta|^2 - \omega^2}} \tag{56}$$

and the off-diagonal part

$$G^{(0)}_{1\bar{1}}(\omega) = \frac{\pi\rho(0)\,\varDelta}{\sqrt{|\varDelta|^2 - \omega^2}}\,. \tag{57}$$

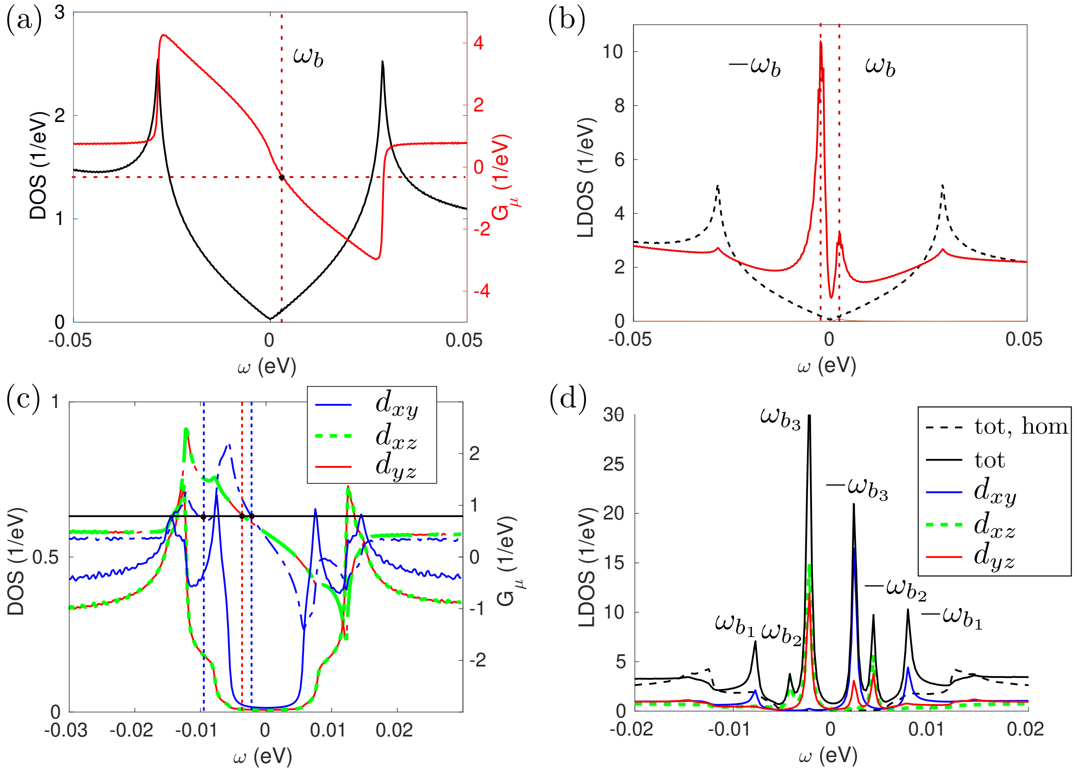

Fig. 16: *Impurity bound states in unconventional superconductors (a) In a d-wave superconductor, the real part of the local green function matches the inverse of the impurity potential (black dot), $1/V = \mathrm{Re}\, G_{1\bar{1}}(\omega_b)$. At the bound state energy, the density of states is nonzero, but small. The different weights of the peaks are due to the properties of the free Green function in Eq. (52). (b) Corresponding LDOS exhibiting two impurity peaks from $\pm\omega_b$ with small broadening. (c) For a multiband system, the analysis is a bit more complicated, but matching $1/V = \mathrm{Re}\, G^{\mu}_{1\bar{1}}(\omega_{b_i})$ for each orbital component yields the correct number of impurity resonances that occur in the LDOS (d). Note that the weight in the individual orbitals is again due to the free Green function $\widehat{G}^{(0)}(\mathbf{r}-\mathbf{r}', \omega)$, here with $\mathbf{r} = [1, 0]$, i.e., spectra next to the impurity.*

Finding solutions for ω where the T-matrix diverges is only possible for a magnetic impurity, but not for a non-magnetic impurity in this case. This is just the finding that there are bound states within the gap [45–47] for magnetic impurities, while non-magnetic potentials do not lead to those (Anderson's theorem) [48]. For a d-wave superconductor (and other order parameters that average to zero over the Brillouin zone) $\sum_{\mathbf{k}} \Delta_{\mathbf{k}} = 0$, also the anomalous Green function vanishes, $G^{(0)}_{1\bar{1}}(\omega) = 0$, such that bound state solutions exist for magnetic and nonmagnetic impurities. Since the density of states for nodal superconductors is finite, these bound states have a finite lifetime [44]. Examples of impurity bound states are shown in Fig. 16 for a single band d-wave superconductor and the multiband system LiFeAs which exhibits multiple bound states for each orbital channel that can become sharp because of the vanishing DOS at low energies of this fully gapped superconductor (compare Fig. 15(c)).

Introducing non-magnetic disorder into superconductors and the measurements of the LDOS close to these impurities can be used to identify unconventional superconductors: If there is a bound state, the superconductor has to be unconventional. The opposite conclusion is however not true in general as it is discussed in the following for the kagome lattice.

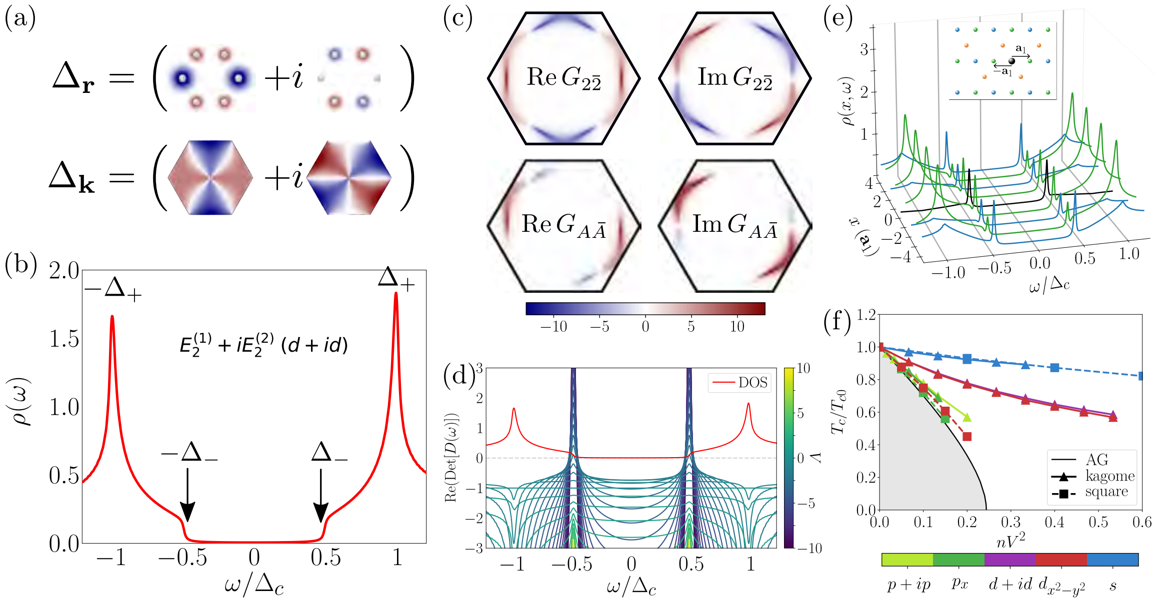

Fig. 17: *Absence of pair breaking in unconventional superconductors on the kagome lattice: (a) $d{+}id$ order parameter in real space $\Delta_{\mathbf{r}}$ with onsite pairing on the three sublattices and in momentum space ($\Delta_{\mathbf{k}}$) with characteristic sign-changing structure. (b) Density of states yielding a fully gapped system. (c) The Green function in band space $G_{2\bar{2}}$ averages to zero as in usual d-wave superconductors, but the sublattice interference makes the Green function in sublattice space $G_{A\bar{A}}$ not to vanish and protects superconductivity from pairbreaking. (d) No resonances in the T-matrix within the fully gapped energy such that (e) no impurity bound states from potential scatterers exist. (f) Also T_c is protected from a fast suppression in d wave superconductors on the kagome lattice (triangles) [49].*

The case of the kagome lattice As discussed above, the kagome lattice exhibits three sublattices and generically, single pointlike impurities are located either on the A, B, or C sublattice. To be concrete, we assume a single nonmagnetic impurity on the A sublattice. Following the outline above, the T-matrix calculation can be used with the choice $M_{ij} = \delta_{1i}\delta_{1j}$ in Eq. (50). Choosing an order parameter of the type $d{+}id$ which might be a candidate order parameter because of (i) indications of time reversal symmetry breaking in the superconducting state [40] and (ii) suggestions of this order parameter from spin-fluctuation pairing calculations [30], the T-matrix calculation is done. The BdG Hamiltonian is set up from the normal state Hamiltonian, Eq. (41), and the order parameter that is onsite in the elementary cell $\big($but exhibits sign change between the sublattices, see Fig. 17(a)$\big)$ [49]

$$\Delta_{d+id} = \Delta_0\Big(f^S_{\mathrm{OS},E_2^{(1)}} + i f^S_{\mathrm{OS},E_2^{(2)}}\Big), \tag{58}$$

with the matrices

$$f^S_{\mathrm{OS},E_2^{(1)}} = \frac{1}{\sqrt{6}}\begin{pmatrix} +1 & 0 & 0 \\ 0 & -2 & 0 \\ 0 & 0 & +1 \end{pmatrix} \quad \text{and} \quad f^S_{\mathrm{OS},E_2^{(2)}} = \frac{1}{\sqrt{2}}\begin{pmatrix} +1 & 0 & 0 \\ 0 & 0 & 0 \\ 0 & 0 & -1 \end{pmatrix}. \tag{59}$$

While the individual order parameters (in band space) have symmetry-imposed nodes (see Fig. 17(a)), we obtain a fully gapped density of states of the homogeneous system because of

the complex linear combination of the two order parameters. There are steps from the minima of $|\Delta_{\mathbf{k}}|$ at Δ_- in band space and coherence peaks at the maximum gap Δ_+ (Fig. 17(b)).
Considering single impurity disorder on the sublattice positions, it turns out that the important quantity entering the T-matrix calculation is the Green function in sublattice space where the momentum dependence is basically a product of the order parameter in band space with the matrix elements $\big($as also evident when looking at the spectral representation of the Green function, Eq. (28)$\big)$. Unlike the Green function in band space $G_{2\bar{2}}(\mathbf{k},\omega)$, the one in sublattice space $G_{A\bar{A}}(\mathbf{k},\omega)$ does not average to zero when calculating the local Green function according to Eq. (54), see (Fig. 17(c)). This means that there is no root of the denominator in Eq. (53) (panel (d)) and no in-gap bound state exists as shown in panel (e) where LDOS spectra at the impurity (black) and along a path to and away from the impurity are shown. From the same physical mechanism d-wave superconductivity remains robust under presence of pointlike disorder. The suppression of the critical temperature T_c follows rather the trend for a conventional superconductor than the Abrikosov-Gorkov (AG) [50] law, see Fig. 17 (f)) [49].

4.3 Dynamical susceptibility and neutron resonance

In section 3, we have discussed the behavior of the (static, $\omega = 0$) susceptibility from a perspective of Fermi surface nesting and deduced the expected superconducting pair states in a spin-fluctuation pairing mechanism. The spin susceptibility can be accessed experimentally in inelastic neutron scattering experiments. This information can be used to either verify whether the theoretical framework for obtaining the spin susceptibility works for the material under consideration, or in a more bottom up approach, one can directly use the measured spin susceptibility as input for calculations of the superconducting pairing.
Once it is established that there are strong spin fluctuations in a superconductive material, more can be learned from the change of the spin fluctuations in the superconducting state. The first observation is a reduction of the spin-response at energies $\omega \leq 2\Delta_-$ $\big(\omega \leq 2\Delta_0\big)$ because for gapped superconductors, there are no quasiparticles (less quasiparticles) within this energy range. Second, for unconventional superconductors (with sign change), an enhancement of the spin-fluctuations for momenta $\mathbf{q}$ connecting parts of the Fermi surface with opposite sign, $\Delta_{\mathbf{k}} = -\Delta_{\mathbf{k}+\mathbf{q}}$, is achieved; the so-called neutron resonance as observed in cuprate materials and Fe-based systems. From the energy of the resonance obtained by subtracting intensities above T_c from the intensities measured below T_c, one can draw conclusions about the Δ/T_c ratio and connect the superconducting material to the weak or strong coupling regime.
The starting point of the calculation of the susceptibility in the superconducting state is Eq. (15), but now, we need to take into account the anomalous Green functions as well, i.e., obtain

$$\begin{aligned}\chi_0^{+-}(\mathbf{q},\tau) = &-\frac{1}{N}\sum_{\mathbf{k},\mathbf{k}'}\Big(\big\langle T_\tau c_{\mathbf{k}',\uparrow}(0)c^\dagger_{\mathbf{k}+\mathbf{q},\uparrow}(\tau)\big\rangle\big\langle T_\tau c_{\mathbf{k},\downarrow}(\tau)c^\dagger_{\mathbf{k}'-\mathbf{q},\downarrow}(0)\big\rangle \\ &\qquad + \big\langle T_\tau c^\dagger_{\mathbf{k}'-\mathbf{q},\downarrow}(0)c^\dagger_{\mathbf{k}+\mathbf{q},\uparrow}(\tau)\big\rangle\big\langle T_\tau c_{\mathbf{k},\downarrow}(\tau)c_{\mathbf{k}',\uparrow}(0)\big\rangle\Big) \\ = &-\frac{1}{N}\sum_{\mathbf{k}}\Big(G^0_{11}(\mathbf{k}{+}\mathbf{q},-\tau)\,G^0_{\bar{1}\bar{1}}(\mathbf{k},\tau) + G^0_{\bar{1}1}(\mathbf{k}{+}\mathbf{q},-\tau)\,G^0_{1\bar{1}}(\mathbf{k},\tau)\Big),\end{aligned} \tag{60}$$

where we used a similar notation as in Eq. (45) for the anomalous Green function. Again, for the single band case, we can use the analytical result for the Green function in frequency space, Eq. (46) to obtain a closed expression of the susceptibility

$$\begin{aligned}\chi_0^{+-}(\mathbf{q},\omega) = \frac{1}{\mathcal{N}} \sum_{\mathbf{k},E>0} \Bigg[&\left(1 - \frac{\varepsilon_{\mathbf{k}}\varepsilon_{\mathbf{k+q}} + \Delta^*_{\mathbf{k+q}}\Delta_{\mathbf{k}}}{E_{\mathbf{k}}E_{\mathbf{k+q}}}\right) \frac{1 - f(E_{\mathbf{k}}) - f(E_{\mathbf{k+q}})}{\omega + E_{\mathbf{k+q}} + E_{\mathbf{k}} + i\eta} \\ + &\left(1 - \frac{\varepsilon_{\mathbf{k}}\varepsilon_{\mathbf{k+q}} + \Delta^*_{\mathbf{k+q}}\Delta_{\mathbf{k}}}{E_{\mathbf{k}}E_{\mathbf{k+q}}}\right) \frac{f(E_{\mathbf{k}}) + f(E_{\mathbf{k+q}}) - 1}{\omega - E_{\mathbf{k+q}} - E_{\mathbf{k}} + i\eta} \\ + &\left(1 + \frac{\varepsilon_{\mathbf{k}}\varepsilon_{\mathbf{k+q}} + \Delta^*_{\mathbf{k+q}}\Delta_{\mathbf{k}}}{E_{\mathbf{k}}E_{\mathbf{k+q}}}\right) \frac{f(E_{\mathbf{k}}) - f(E_{\mathbf{k+q}})}{\omega + E_{\mathbf{k+q}} - E_{\mathbf{k}} + i\eta} \\ + &\left(1 + \frac{\varepsilon_{\mathbf{k}}\varepsilon_{\mathbf{k+q}} + \Delta^*_{\mathbf{k+q}}\Delta_{\mathbf{k}}}{E_{\mathbf{k}}E_{\mathbf{k+q}}}\right) \frac{f(E_{\mathbf{k+q}}) - f(E_{\mathbf{k}})}{\omega + E_{\mathbf{k}} - E_{\mathbf{k+q}} + i\eta} \Bigg], \end{aligned} \tag{61}$$

where we have performed the Matsubara summation analytically, done the analytical continuation $i\nu_n \to \omega{+}i\eta$ and used the particle-hole symmetry of the BdG Hamiltonian to rewrite the summation in terms of positive energies only. The Hubbard interactions can be taken into account in an RPA approach similar to Eq. (30). Resonances are now divergences in the imaginary part of the susceptibility at the respective frequency ω_0. Splitting the susceptibility in real and imaginary part, $\chi^{+-}(\mathbf{q},\omega) = \chi^{+-\prime} + i\chi^{+-\prime\prime}$, we can calculate the imaginary part of the susceptibility as follows (dropping the arguments and the transverse label $+-$),

$$\chi^{+-\prime\prime} = \mathrm{Im}\, \frac{\chi^{+-\prime} + i\chi^{+-\prime\prime}}{1 - U(\chi^{+-\prime} + i\chi^{+-\prime\prime})} = \mathrm{Im}\, \frac{\chi_0}{1 - U\chi_0} = \frac{\chi_0''}{(1{-}U\chi_0')^2 + (U\chi_0'')^2}\,. \tag{62}$$

This diverges if the numerator vanishes which requires $1{-}U\chi_0' = 0$ (similar as the criterion for the magnetic instability) and $\chi_0'' \to 0$ (gapped spectrum). The second is exactly fulfilled for a full gap superconductor because of missing excitations at this energy, the first can be fulfilled in the superconducting state if there is a sign-change in the order parameter as we discuss in the following. The first observation is that the first two terms in Eq. (61) vanish in the normal state when $\varepsilon_{\mathbf{k}} = E_{\mathbf{k}}$ and $\Delta_{\mathbf{k}} = 0$. For states close to the Fermi level, where there is an effect from the superconducting state, we can set $\varepsilon_{\mathbf{k}} \approx 0$ and obtain $E_{\mathbf{k}} = |\Delta_{\mathbf{k}}|$ because of the sqrt in the quasiparticle dispersion, Eq. (9). Looking at the coherence factor,

$$\left(1 - \frac{\Delta_{\mathbf{k+q}}\Delta_{\mathbf{k}}}{|\Delta_{\mathbf{k}}||\Delta_{\mathbf{k+q}}|}\right) \approx \left\{ \begin{array}{l} 0 \\ 2 \end{array} \right. \tag{63}$$

it exhibits two values depending on the order parameter: For momenta $\mathbf{k}$ and $\mathbf{k}{+}\mathbf{q}$ with the same sign of the order parameter it vanishes, and for momenta with $\operatorname{sign} \Delta^*_{\mathbf{k+q}} = -\operatorname{sign} \Delta_{\mathbf{k}}$ it reaches the value 2. Sign-changing order parameters therefore increase the real susceptibility and lead to the mentioned spin-resonance (when taking into account interactions at least within RPA), while conventional superconductivity (without sign-change) yields just a suppressed susceptibility. Some examples of theoretical investigations in multiband settings on this topic can be found in Refs. [51, 27].

4.4 Spin relaxation rate and Hebel-Slichter peak

As a second example of a spectroscopic probe related to the spin susceptibility, we want to discuss the spin relaxation rate in nuclear magnetoresonance (NMR) experiments. In a typical NMR experiment, the nuclear spins are polarized by an external field and then tilted from the equilibrium position by a radio frequency pulse. Left in this state, the spins precess around the external field and eventually relax to the polarized state because of scattering events from the (conduction) electrons in the system with a relaxation time T_1. Solving the Bloch equations for the dynamics of the magnetization in presence of electron spins and the hyperfine coupling, leads to the following relation for the longitudinal relaxation due to spin fluctuations [13]

$$\alpha \equiv \frac{1}{T_1 T} \propto \lim_{\omega \to 0} \frac{1}{\mathcal{N}} \sum_{\mathbf{q}} \mathrm{Im} \frac{\chi_0^{+-}(\mathbf{q}, \omega)}{\omega}. \tag{64}$$

The relevant energy scale is the Larmor frequency ω_L that is practically very small, $\hbar\omega_L \approx 10^{-7}$ eV, so it is considered as the smallest energy scale in the problem, which is the meaning of the limit $\omega \to 0$ in the equation above.

The spin susceptibility can now be calculated using Eq. (61) where it turns out that now, the first two terms do not contribute because the energy of the quasiparticles are (almost) always much larger than the very small ω in the denominator, so these terms do not contribute to the imaginary part of the susceptibility at low frequencies. Different for the last two terms with the opposite sign of $E_{\mathbf{k}}$ and $E_{\mathbf{k}+\mathbf{q}}$ which gives a contribution even in the limit $\omega \to 0$. Close to T_c where the order parameter is very small, there is an enhancement of the density of states (coherence peak) close to zero energy. This leads to an increase of the integrated spin susceptibility (compared to the normal state) just below T_c. For a superconductor with a constant gap, the density of states diverges as $1/\sqrt{\omega^2 - \Delta_0(T)^2}$ while for an anisotropic superconductor with a maximum gap Δ_+, there is only a weaker divergence such that there is still a weak enhancement. In this case, the relevant prefactor behaves as

$$\left(1 + \frac{\Delta_{\mathbf{k}+\mathbf{q}} \Delta_{\mathbf{k}}}{|\Delta_{\mathbf{k}}||\Delta_{\mathbf{k}+\mathbf{q}}|}\right) \approx \begin{cases} 2 & \text{same sign} \\ 0 & \text{different sign} \end{cases} \tag{65}$$

at low ω. To understand this in more detail, it is instructive to examine the factor

$$B(\mathbf{q}, \mathbf{k}_n) = \frac{\Delta^*_{\mathbf{k}_n+\mathbf{q}} \Delta_{\mathbf{k}_n}}{E_{\mathbf{k}_n} E_{\mathbf{k}_n+\mathbf{q}}}, \tag{66}$$

which for a conventional superconductor (without sign-change) remains finite while for a d-wave oder parameter it averages to zero when integrated over $\mathbf{k}$ for a fixed $\mathbf{q}$ as illustrated in Fig. 18(a). This leads to an additional enhancement of the spin relaxation rate α below T_c for an s-wave order parameter while for a sign-changing order parameter only the enhancement from the (weak) peak in the density of states contributes. Experimentally, the absence of a (visible) Hebel-Slichter peak is interpreted as an indication of unconventional superconductivity, while its presence is an indication for a non-sign changing order parameter. See however Ref. [52] for more subtle behavior in unconventional superconductors close to T_c.

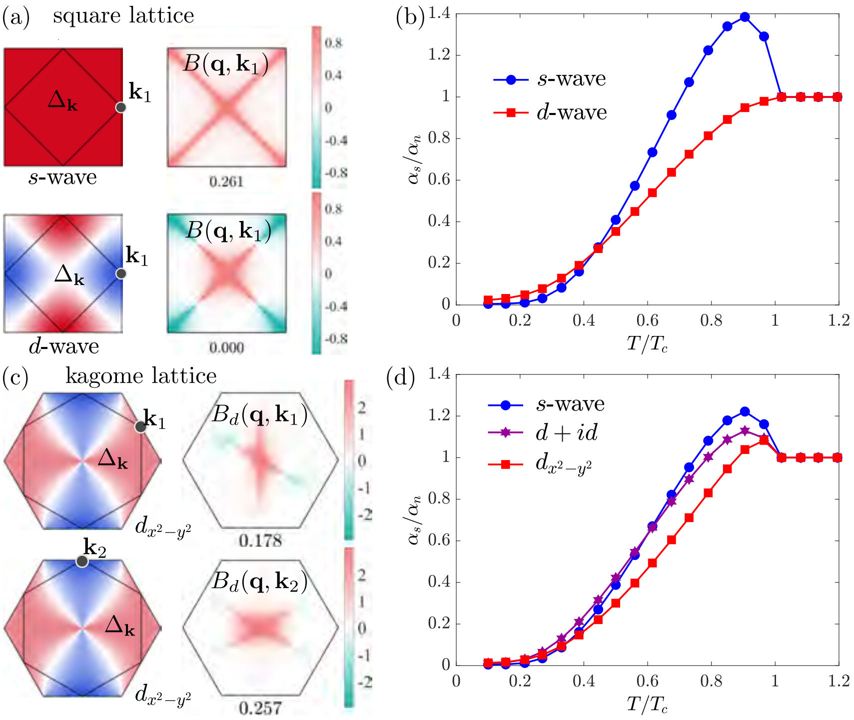

Fig. 18: *Hebel-Slichter peak for different lattices (a) In the square lattice, the constant order parameter yields a (positive) value of $B(\mathbf{q},\mathbf{k}_n)$ everywhere in the Brillouin zone (and independent of the choice of $\mathbf{k}_n$). Yielding a positive integral (0.261 in this case), enhances the spin relaxation rate compared to its normal state value (b). For the d-wave order parameter (lower panels in (a)), the factor $B(\mathbf{q},\mathbf{k}_n)$ is always equally positive and negative, such that the integral over it vanishes and no Hebel-Slichter peak is visible. (c) For the kagome lattice, there are positive and negative regions of $B_d(\mathbf{q},\mathbf{k}_n)$, however the negative regions are suppressed because of the different sublattice weight for $\mathbf{k}$ points far away from $\mathbf{k}_n$. In summary, the integral does not average to zero and a Hebel-Slichter peak is expected for unconventional (sign-changing) order parameters as well (d) [53].*

We will now discuss that this conclusion does not generally apply for kagome systems, again the peculiar property of the subblattice weight, Fig. 19 plays an important role. Indeed, one can evaluate the multiband generalization of the susceptibility numerically by employing the $d{+}id$ superconducting order parameter as already discussed in the previous section, the result is shown in Fig. 18. To gain further insights, we here map the problem to an effective single band Hamiltonian. As seen, in Fig. 19(c), only band number 2 crosses the Fermi level. In the weak coupling regime where the order parameter is much smaller than any band energy scale, only the eigenenergies of this band significantly contribute to Eq. (61) for $\omega \to 0$. To understand the effect on the spin relaxation rate in more detail, we start from the BdG Hamiltonian, Eq. (44) which we transform to the band basis by application of the unitary transformation that diagonalizes H_0. Then the order parameter from sublattice space to band space transforms as

$$\Delta_{nm}(\mathbf{k}) = u^*_{n\alpha}(\mathbf{k})\Delta_{\alpha\beta}u^*_{m\beta}(-\mathbf{k}), \tag{67}$$

where $u_{n\alpha}(\mathbf{k})$ is the eigenstate of $H_0(\mathbf{k})$ in band n. For band 2, the effective Hamiltonian now

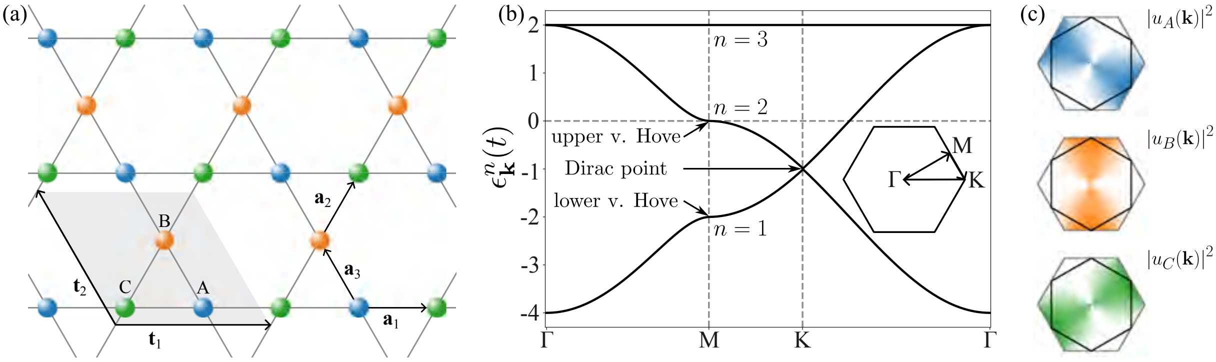

Fig. 19: *Band structure of simple kagome lattice (a) lattice structure with the three sublattices, the lattice vectors* $\mathbf{t}_i$ *and the nearest neighbor vectors* $\mathbf{a}_i$*. (b) Band structure exhibiting van Hove points and a Dirac point. (c) Orbital weight distribution for the* $n = 2$ *band that is crossing the Fermi level close to the upper van Hove point.*

reads

$$H_{\text{eff}}(\mathbf{k}) = \begin{pmatrix} \varepsilon_{2,\mathbf{k}} & -\Delta_{22}(\mathbf{k}) \\ -\Delta^*_{22}(\mathbf{k}) & -\varepsilon_{2,\mathbf{k}} \end{pmatrix}. \tag{68}$$

Evaluating the susceptibility from this effective Hamiltonian, we see that it acquires an additional factor arising from the transformation from sublattice to band space

$$g_{\alpha\beta}(\mathbf{k},\mathbf{q}) = u_{2\alpha}(\mathbf{k}{+}\mathbf{q})u_{2\beta}(\mathbf{k}{+}\mathbf{q})u_{2\alpha}(\mathbf{k})u_{2\beta}(\mathbf{k}). \tag{69}$$

and the dynamical susceptibility in the superconducting state reads

$$\begin{aligned}\chi^{+-}_0(\mathbf{q},\omega) = \frac{1}{\mathcal{N}} \sum_{\mathbf{k},E>0} \Bigg[&\left(1 - \frac{\varepsilon_{\mathbf{k}}\varepsilon_{\mathbf{k}+\mathbf{q}} + \Delta^*_{\mathbf{k}+\mathbf{q}}\Delta_{\mathbf{k}}}{E_{\mathbf{k}}E_{\mathbf{k}+\mathbf{q}}}\right) \frac{1 - f(E_{\mathbf{k}}) - f(E_{\mathbf{k}+\mathbf{q}})}{\omega + E_{\mathbf{k}+\mathbf{q}} + E_{\mathbf{k}} + i\eta} \\ + &\left(1 - \frac{\varepsilon_{\mathbf{k}}\varepsilon_{\mathbf{k}+\mathbf{q}} + \Delta^*_{\mathbf{k}+\mathbf{q}}\Delta_{\mathbf{k}}}{E_{\mathbf{k}}E_{\mathbf{k}+\mathbf{q}}}\right) \frac{f(E_{\mathbf{k}}) + f(E_{\mathbf{k}+\mathbf{q}}) - 1}{\omega - E_{\mathbf{k}+\mathbf{q}} - E_{\mathbf{k}} + i\eta} \\ + &\left(1 + \frac{\varepsilon_{\mathbf{k}}\varepsilon_{\mathbf{k}+\mathbf{q}} + \Delta^*_{\mathbf{k}+\mathbf{q}}\Delta_{\mathbf{k}}}{E_{\mathbf{k}}E_{\mathbf{k}+\mathbf{q}}}\right) \frac{f(E_{\mathbf{k}}) - f(E_{\mathbf{k}+\mathbf{q}})}{\omega + E_{\mathbf{k}+\mathbf{q}} - E_{\mathbf{k}} + i\eta} \\ + &\left(1 + \frac{\varepsilon_{\mathbf{k}}\varepsilon_{\mathbf{k}+\mathbf{q}} + \Delta^*_{\mathbf{k}+\mathbf{q}}\Delta_{\mathbf{k}}}{E_{\mathbf{k}}E_{\mathbf{k}+\mathbf{q}}}\right) \frac{f(E_{\mathbf{k}+\mathbf{q}}) - f(E_{\mathbf{k}})}{\omega + E_{\mathbf{k}} - E_{\mathbf{k}+\mathbf{q}} + i\eta}\Bigg] \sum_{\alpha\beta} g_{\alpha\beta}(\mathbf{k},\mathbf{q}).\end{aligned} \tag{70}$$

In this equation, we have dropped the subscript for the band, i.e., $\varepsilon_{2,\mathbf{k}} \to \varepsilon_{\mathbf{k}}$, $\Delta_{22}(\mathbf{k}) \to \Delta_{\mathbf{k}}$. Similarly to the previous discussion, we can define a (dressed) spin-susceptibility coherence factor given by

$$B_{\text{d}}(\mathbf{q},\mathbf{k}_n) = \frac{\sum_{\alpha\beta} g_{\alpha\beta}(\mathbf{k}_n,\mathbf{q})}{Z} \frac{\Delta^*_{\mathbf{k}_n+\mathbf{q}}\Delta_{\mathbf{k}_n}}{E_{\mathbf{k}_n}E_{\mathbf{k}_n+\mathbf{q}}}, \tag{71}$$

where Z is a normalization factor defined by $Z = \frac{1}{\mathcal{N}^2}\sum_{\mathbf{k},\mathbf{q}}\sum_{\alpha\beta} g_{\alpha\beta}(\mathbf{k},\mathbf{q})$. The crucial property of Eq. (71) is now that it contains a product of the order parameter (in band space) which has sign changing and compensation properties for a d-wave order parameter, but is additionally multiplied by the sublattice weights that vanish in parts of the Brillouin zone, especially where the order parameter has opposite sign. Consequently, the averaging is only partial and an unconventional d (or $d{+}id$) order parameter acquires a finite enhancement factor leading to a sizeable Hebel-Slichter peak just below T_c. In other words for the kagome lattice, one expects Hebel-Slichter peaks for conventional and unconventional order parameters (Fig. 18(d)) and its presence should not be interpreted as evidence against unconventional pairing in these systems [53].

Acknowledgements

I thank Morten Holm Christensen for discussions about the structure of these lecture notes. Thanks to Brian Møller Andersen and Mercè Roig for proofreading and useful comments and to Yi Dai and Sofie Castro Holbæck for the collaboration on the topics of kagome superconductors.

References

[1] F. Steglich, J. Aarts, C.D. Bredl, W. Lieke, D. Meschede, W. Franz, and H. Schäfer, Phys. Rev. Lett. **43**, 1892 (1979)

[2] D. Jérome, A. Mazaud, M. Ribault, and K. Bechgaard, J. Phys. Lett. **41**, 95 (1980)

[3] J.G. Bednorz and K.A. Müller, Z. Phys. B **64**, 189 (1986)

[4] A.F. Hebard, M.J. Rosseinsky, R.C. Haddon, D.W. Murphy, S.H. Glarum, T.T.M. Palstra, A.P. Ramirez, and A.R. Kortan, Nature **350**, 600 (1991)

[5] Y. Maeno, H. Hashimoto, K. Yoshida, S. Nishizaki, T. Fujita, J.G. Bednorz, and F. Lichtenberg, Nature **372**, 532 (1994)

[6] Y. Kamihara, H. Hiramatsu, M. Hirano, R. Kawamura, H. Yanagi, T. Kamiya, and H. Hosono, J. Am Chem. Soc. **128**, 10012 (2006)

[7] J. Nagamatsu, N. Nakagawa, T. Muranaka, Y. Zenitani, and J. Akimitsu, Nature **410**, 63 (2001)

[8] A.P. Drozdov, M.I. Eremets, I.A. Troyan, V. Ksenofontov, and S.I. Shylin, Nature **525**, 73 (2015)

[9] B.R. Ortiz, S.M.L. Teicher, Y. Hu, J.L. Zuo, P.M. Sarte, E.C. Schueller, A.M.M. Abeykoon, M.J. Krogstad, S. Rosenkranz, R. Osborn, R. Seshadri, L. Balents, J. He, and S.D. Wilson, Phys. Rev. Lett. **125**, 247002 (2020)

[10] D.J. Scalapino, Rev. Mod. Phys. **84**, 1383 (2012)

[11] F. Lechermann, Phys. Rev. X **10**, 041002 (2020)

[12] A. Chubukov and P.J. Hirschfeld, Phys. Today **68**, 46 (2015)

[13] P. Coleman: *Introduction to Many-Body Physics* (Cambridge University Press, 2015)

[14] P.J. Hirschfeld, M.M. Korshunov, and I.I. Mazin, Rep. Prog. Phys. **74**, 124508 (2011)

[15] M. Sigrist and K. Ueda, Rev. Mod. Phys. **63**, 239 (1991)

[16] S. Panda and P.J. Hirschfeld, Phys. Rev. B **109**, 174504 (2024)

[17] H. Bruus and K. Flensberg, *Many-body quantum theory in condensed matter physics* (Oxford University Press, 2004)

[18] W. Kohn and J.M. Luttinger, Phys. Rev. Lett. **15**, 524 (1965)

[19] A. Kreisel, Y. Quan, and P.J. Hirschfeld, Phys. Rev. B **105**, 104507 (2022)

[20] A.T. Rømer, T.A. Maier, A. Kreisel, I. Eremin, P.J. Hirschfeld, and B.M. Andersen, Phys. Rev. Res. **2**, 013108 (2020)

[21] A. Kreisel, A.T. Rømer, P.J. Hirschfeld, and B.M. Andersen, J. Supercond. Nov. Magn. **30**, 85 (2017)

[22] S. Graser, T.A. Maier, P.J. Hirschfeld, and D.J. Scalapino, New J. Phys. **11**, 025016 (2009)

[23] Y. Maeno, S. Yonezawa, and A. Ramires, arXiv:2402.12117 (2024)

[24] M.R. Norman, Physics **13**, 85 (2020)

[25] H. Liu, C. Xia, S. Zhou, and H. Chen, arXiv:2311.07316 (2023)

[26] A. Kreisel, R. Nelson, T. Berlijn, W. Ku, R. Aluru, S. Chi, H. Zhou, U.R. Singh, P. Wahl, R. Liang, W.N. Hardy, D.A. Bonn, P.J. Hirschfeld, and B.M. Andersen, Phys. Rev. B **94**, 224518 (2016)

[27] T.A. Maier, S. Graser, P.J. Hirschfeld, and D.J. Scalapino, Phys. Rev. B **83**, 100515 (2011)

[28] K. Kuroki, S. Onari, R. Arita, H. Usui, Y. Tanaka, H. Kontani, and H. Aoki, Phys. Rev. Lett. **101**, 087004 (2008)

[29] A.F. Kemper, T.A. Maier, S. Graser, H.-P. Cheng, P.J. Hirschfeld, and D.J. Scalapino, New J. Phys. **12**, 073030 (2010)

[30] A.T. Rømer, S. Bhattacharyya, R. Valentí, M.H. Christensen, and B.M. Andersen, Phys. Rev. B **106**, 174514 (2022)

[31] C.M. Puetter and H.-Y. Kee, EPL (Europhys. Lett.) **98**, 27010 (2012)

[32] M. Roig, A.T. Rømer, A. Kreisel, P.J. Hirschfeld, and B.M. Andersen, Phys. Rev. B **106**, L100501 (2022)

[33] H. Sun, M. Huo, X. Hu, J. Li, Z. Liu, Y. Han, L. Tang, Z. Mao, P. Yang, B. Wang, J. Cheng, D.-X. Yao, G.-M. Zhang, and M. Wang, Nature **621**, 493 (2023)

[34] F. Lechermann, J. Gondolf, S. Bötzel, and I.M. Eremin, Phys. Rev. B **108**, L201121 (2023)

[35] M. Tomić: *Ab-initio simulations of pressure effects on structural and electronic properties of iron based superconductors* (PhD thesis, Univ. Frankfurt, 2015)

[36] S.K. Ghosh, M. Smidman, T. Shang, J.F. Annett, A.D. Hillier, J. Quintanilla, and H. Yuan, J. Phys.: Condens. Matter **33**, 033001 (2020)

[37] B.M. Andersen, A. Kreisel, and P.J. Hirschfeld, Front. Phys. **12**, 1353425 (2024)

[38] H.S. Røising, M. Geier, A. Kreisel, and B.M. Andersen, Phys. Rev. B **109**, 054521 (2024)

[39] H.-S. Xu, Y.-J. Yan, R. Yin, W. Xia, S. Fang, Z. Chen, Y. Li, W. Yang, Y. Guo, and D.-L. Feng, Phys. Rev. Lett. **127**, 187004 (2021)

[40] C. Mielke, D. Das, J.-X. Yin, H. Liu, R. Gupta, Y.-X. Jiang, M. Medarde, X. Wu, H.C. Lei, J. Chang, P. Dai, Q. Si, H. Miao, R. Thomale, T. Neupert, Y. Shi, R. Khasanov, M.Z. Hasan, H. Luetkens, and Z. Guguchia, Nature **602**, 245 (2022)

[41] J.E. Hoffman, Rep. Prog. Phys. **74**, 124513 (2011)

[42] I. Martin, A.V. Balatsky, and J. Zaanen, Phys. Rev. Lett. **88**, 097003 (2002)

[43] A. Kreisel, P. Choubey, T. Berlijn, W. Ku, B.M. Andersen, and P.J. Hirschfeld, Phys. Rev. Lett. **114**, 217002 (2015)

[44] A.V. Balatsky, I. Vekhter, and J.-X. Zhu, Rev. Mod. Phys. **78**, 373 (2006)

[45] L. Yu, Acta Phys. Sin. **21**, 75 (1965)

[46] H. Shiba, Prog. Theor. Phys. **40**, 435 (1968)

[47] A. Rusinov, Sov. Phys. JETP **29**, 1101 (1969)

[48] P. Anderson, J. Phys. Chem. Solids **11**, 26 (1959)

[49] S.C. Holbæk, M.H. Christensen, A. Kreisel, and B.M. Andersen, Phys. Rev. B **108**, 144508 (2023)

[50] A.A. Abrikosov and L.P. Gor'kov: Zh. Eksp. Teor. Fiz. **39**, 1781 (1960)

[51] T.A. Maier, S. Graser, D.J. Scalapino, and P.J. Hirschfeld, Phys. Rev. B **79**, 134520 (2009)

[52] D. Parker and S. Haas, Phys. Rev. B **75**, 052501 (2007)

[53] Y. Dai, A. Kreisel, and B.M. Andersen, arXiv:2404.10835 (2024)

10 The Berezinskii-Kosterlitz-Thouless Transition and its Application to Superconducting Systems

Lara Benfatto
Sapienza University of Rome
P.le A. Moro 5, 00185 Rome, Italy

Contents

E. Pavarini and E. Koch (eds.)
Correlations and Phase Transitions
Modeling and Simulation Vol. 14
Forschungszentrum Jülich, 2024, ISBN 978-3-95806-751-6
http://www.cond-mat.de/events/correl24

1 Introduction

Almost 50 years after the seminal work by Berezinskii [1] and Kosterlitz and Thouless [2] the Berezinskii-Kosterlitz-Thouless (BKT) transition remains one of the most fascinating examples of topological phase transitions in condensed-matter system, and as such it has been acknowledged by the 2016 Nobel Prize in Physics. Its universality class describes several phenomena ranging from the quantum metal-insulator transition in one dimension to the Coulomb-gas screening transition in 2D, and of course the metal-to-superfluid transition in 2D [3]. As such it has been investigated in neutral superfluids, as, e.g., thin He films [4,5] and cold-atoms systems made of bosons [6] or neutral fermions [7]. Nonetheless, despite the fact that in the original paper by Kosterlitz and Thouless [2] the authors argued that the BKT transition should not be observed in (quasi) two-dimensional (2D) superconductors, this is certainly the field where it has been most widely discussed. As we will see in this Chapter, the conditions under which BKT physics can be seen in quasi-2D superconductors are not always met. Nonetheless, in the past and recent literature the BKT physics has been invoked to explain observations in a wide class of systems: thin films of conventional [8–10] and unconventional [11–13] superconductors, but also to the 2D electron gas confined at the interface between two insulators in artificial heterostructures [14–16], or in the top-most layer of ion-gated superconducting (SC) systems [17]. Due to the breadth of literature on the subject, the references provided in the present lecture cannot be at any extent exhaustive: the reader must be conscious that they just reflect the personal choice of the author in providing few (over many) examples for each category of problems that will be discussed.

The aim of this lecture is twofold. From one side, I will provide a general introduction to the basic theoretical concepts behind the understanding of the BKT transition, and from the other side I will summarize the efforts done over the years to understand how one can measure and interpret experimental signatures of BKT physics in real materials, especially superconductors.

For the first part, I will start from the description of the BKT transition within the classical XY-model, which describes Heisenberg interactions between two-component classical spins in a 2D lattice. The physical transition behind this model is then the paramagnetic-ferromagnetic transition in 2D, and it allows one to understand easily the basic difference between “order” and “spin rigidity” that is at the heart of the BKT physics. In addition, it allows one to easily visualize the topological excitations as spin vortices that appear in 2D in addition to the more conventional spin waves. As a second step, I will show the formal mapping between this problem and the screening transition for the Coulomb gas, always in 2D. This analogy allows one to grasp an intuition on the role of vortices to break the “quasi-long-range” order of the low-temperature phase as an effect analogous to the screening of Coulomb interaction by charges that are free to move. Finally, I will also mention the mapping into the sine-Gordon model, that describes again a completely different physical problem, i.e., a quantum field in one dimension. Such a mapping turns out to provide an alternative, elegant way to derive the renormalization-group equations of the BKT transition via quantum-field theory techniques, as beautifully described in the book by T. Giamarchi [18], that is also rather powerful to describe the role played by screening currents in a charged superfluid [19,20].

For the second part, I will discuss to what extent the BKT transition can be observed in superconductors, and what we can define as "2D superconductors" within the context of BKT physics. I will then discuss in detail the benchmark experimental determination of the BKT transition, i.e., the well-known BKT universal jump of the superfluid density [21], that has been beautifully confirmed few years after the theoretical prediction by Nelson and Kosterlitz by experiments in He films [5]. After a critical discussion of *what* exactly "universal jump" means within the context of experiments in superconductors, as compared to the case of neutral superfluids, I will review the results of the last ten years or so to identify this signature in real systems. As we shall see, in most of the hypothetical quasi-2D superconductors where a BKT jump could be expected it appears somehow hidden by *inhomogeneity* effects, that systematically smear it out, hindering its observation. Nonetheless, I will present few paradigmatic cases where BKT physics seems to be supported by the experiments, once the "textbook" results are properly analyzed by taking into account the role of inhomogeneity. In the last Section I will also discuss two other celebrated examples of experimental observations of BKT physics connected to vortex transport, i.e., the non-linear I-V characteristics below T_{BKT} and the exponential temperature dependence of the paraconductivity above T_{BKT} [22]. Also in these cases I will point out physical effects present in real materials that can overscreen a pure BKT phenomenon, requiring a careful analysis of the experimental conditions under which BKT physics can be disentangled from other phenomena.

2 The XY-model

The pioneering works of Berezinkii [1] and Kosterlitz and Thouless [2] in the late 70's were originally motivated by the ongoing discussion at the time on the possibility to observe some sort of transition in 2D, that could be still consistent with the expectation of the Mermin-Wagner theorem [23]. The Mermin-Wagner theorem states that a 2D system cannot break spontaneously a continuous symmetry at finite temperature. The reason, as we shall see below via an explicit computation, is that the thermal fluctuations of the Goldstone (massless) mode which emerges when a continuous symmetry is broken completely spoil the order parameter of the transition itself. At that time, the contribution of Berezinkii from one side, and Kosterlitz and Thouless from the other, was to shown that a phase transition can still take place, but it must be identified by starting from a more general definition of "quasi-ordered" state, that is no more characterized by a finite order parameter, but rather by a finite "rigidity" of the state itself. Once established that a phase transition can be identified on the basis of the presence (below T_{BKT}) or the absence (above T_{BKT}) of rigidity, they showed that topological vortex-like excitations play a central role in driving the transition. It must be noted that the concept of rigidity as manifestation of a phase transition is not limited to the BKT case. Just to mention the most intuitive case, when translational symmetry is broken to form a solid the system becomes indeed "rigid" (we can walk on it!). The Goldstone modes of the transition in this case are the acoustic phonons, whose energy scales with the gradient of the lattice deformation. As such, as the wavelength of the deformation goes to infinity, i.e., the momentum goes to zero, it cost nothing to create the phononic distortion, i.e., the mode appears “massless”. This analogy will be useful to understand the results we will derive in this Section.

To start the discussion on the basic concepts behind the BKT transition let us introduce the XY-model, where these effects were originally discussed. The model describes the ferromagnetic interactions between planar spins with fixed modulus ($|\mathbf{S}_i| = 1$), placed on a square lattice. Its Hamiltonian reads

$$H_{XY} = -J \sum_{\langle i,j \rangle} \mathbf{S}_i \cdot \mathbf{S}_j = -J \sum_{\langle ij \rangle} \cos\bigl(\theta_i - \theta_j\bigr), \tag{1}$$

where the sum $\sum_{\langle i,j \rangle}$ is restricted to nearest neighbors spins, J is a positive coupling constant and θ represents the angle that each spin form with the x direction. For convenience of language, and for the sake of the analogy with the role played by θ within the context of the superfluid transition, we will refer to it as to a “phase” variable. From (1), it is straightforward to recognize that the system shows two different symmetries

- q continuous and global symmetry $U(1)$: $\forall i : \theta_i \to \theta_i + c$
- q discrete and local symmetry $\mathbb{Z}^m$: $\theta_i \to \theta_i + 2\pi m$

In the following, we will see that these two symmetries are connected to two different phase excitations below T_{BKT}. Let us start to analyze the Hamiltonian (1) trying to guess the low-temperature ground state. It can be easily understood that the minimum value of the energy corresponds to a situation in which all the spins are aligned in one particular direction, say $\theta_i = 0$ for all spins, breaking in this way the $U(1)$ symmetry of the Hamiltonian itself. Whenever this happens, the system has a finite macroscopic magnetization in the x direction, i.e. $\langle \mathbf{S} \rangle = \hat{x}$. Let us see why this is not possible, as expected on the basis of the Mermin-Wagner theorem.

At finite temperature, the phase θ_i of each site can fluctuate with respect to the ground-state value. We are interested in computing the contribution of such phase fluctuations to $\langle \mathbf{S} \rangle$ in a low-temperature phase, where the difference in phase between neighboring spins is very small, so that we can rewrite the Hamiltonian (1) by expanding the cosine up to the second order in its argument. Furthermore, by taking the continuum limit on the lattice we can approximate $\theta_i - \theta_{i+\hat{\delta}} \approx a\, \partial\theta(\mathbf{r})/\partial\hat{\delta}$, where $\theta(\mathbf{r})$ is a smooth function and $\hat{\delta} = x, y$. Finally, we get

$$H_{XY} \simeq \frac{J}{2} \int d\mathbf{r}\, \bigl(\nabla\theta(\mathbf{r})\bigr)^2 = \frac{J}{2} \int \frac{d\mathbf{q}}{(2\pi)^2}\, \mathbf{q}^2\, |\theta_{\mathbf{q}}|^2. \tag{2}$$

Thanks to the Gaussian approximation (2) to the XY-Hamiltonian we can easily compute the effect of phase fluctuations as

$$\langle \mathbf{S}_i \rangle = \bigl\langle e^{i\theta_i} \bigr\rangle = e^{-\langle \theta_i^2 \rangle /2}\,, \tag{3}$$

where in the last passage we have used a well known property of the average over a Gaussian distribution (see Appendix A), while the average $\langle \cdots \rangle$ is defined as the average over the canonical ensemble of the system

$$\langle A \rangle = \frac{1}{Z} \int_0^{2\pi} d\theta_1 \cdots \int_0^{2\pi} d\theta_N\, A e^{-\beta H_{XY}}, \tag{4}$$

where as usual $\beta = 1/T$. By using the approximation (2) the calculation (3) is straightforward

$$\langle \theta_i^2 \rangle = \int \frac{d\mathbf{q}}{(2\pi)^2} \langle |\theta_\mathbf{q}|^2 \rangle = \int_{1/L}^{1/a} \frac{d\mathbf{q}}{(2\pi)^2} \frac{T}{J\mathbf{q}^2} = \frac{T}{2\pi J} \ln \frac{L}{a}\,, \tag{5}$$

where we used the fact that from Hamiltonian (2)

$$\big\langle \theta_{\mathbf{q}_1} \theta_{\mathbf{q}_2} \big\rangle = \frac{T}{J\mathbf{q}_1^2}\, \delta_{\mathbf{q}_1,-\mathbf{q}_2}, \tag{6}$$

and we denoted with L the linear size of the system and with a the lattice spacing between two neighboring spins. Substituting the result (5) into Eq. (3) we get

$$\langle \mathbf{S}_i \rangle = e^{-\frac{T}{4\pi J} \ln(L/a)} = \left(\frac{a}{L}\right)^{\frac{T}{4\pi J}} \xrightarrow[L\to\infty]{} 0\,. \tag{7}$$

Hence, at any nonzero temperature the system cannot sustain a spontaneous magnetization in the thermodynamic limit, since the spin wave excitations suppress the long-range order. As one can immediately see from Eq. (2), spin waves appear as smooth variations of the phase, that cost no energy in the long-wavelength ($\mathbf{q} \to 0$) limit. Thus, in the 2D XY-model they are indeed “massless” at long-wavelength, and as such they can be recognized as the Goldstone modes of the system. We then proved explicitly the Mermin-Wagner theorem.
However, it is worth to mention that very often real systems are quite far from the thermodynamic limit so that they could exhibit a finite magnetization in the low-temperature regime. Indeed, if we estimate the exponent of (7), using the universal relation between the renormalized stiffness J and the temperature at the critical point (we will come back on this point in the next pages), we obtain that it is $\leq 1/8$. It means that for a microscopic scale $a \sim 10$ nm one would need a system with a linear size $L \sim 100000$ km to have $\langle \mathbf{S}_i \rangle = 0.01$. In short, if a real finite system exhibits a spontaneous symmetry breaking, it does not mean that the Mermin Wagner theorem is violated, but that the system studied is far away from its thermodynamic limit.
Anyway, at the time of its formulation, the generally accepted conclusion was that in the XY-model[1] there is no transition to an ordered state at any nonzero temperature. The merit of Berezinskii, Kosterlitz and Thouless was first of all to overcome this idea, by realizing that a different kind of transition was possible.

2.1 Correlation functions and rigidity

Even though we have explicitly seen that a conventional order-parameter description of the phase transition is not possible, since $\langle \mathbf{S}_i \rangle = 0$ at any temperature, the close investigation of the behavior of the spin correlation functions suggests that a change of behavior should still happen between the low and high-temperature phase. The correlation function between two sites i and j is defined as

$$C(\mathbf{r}_i - \mathbf{r}_j) = \big\langle \mathbf{S}_i \cdot \mathbf{S}_j \big\rangle = \big\langle \cos(\theta_i - \theta_j) \big\rangle. \tag{8}$$

---

[1] More generally in a two-dimensional system with a continuous symmetry and short-range interactions.

Let us try to estimate its behavior in the low-temperature $\beta J \ll 1$ and high temperature limit $\beta J \ll 1$, respectively. At low temperature we can rely on the same approximated Gaussian Hamiltonian (2) used above for the calculation of the average order parameter. Using again the properties of Gaussian averages we get

$$C(\mathbf{r}) = \left\langle e^{i(\theta(\mathbf{r})-\theta(0))}\right\rangle = e^{-\frac{1}{2}\left\langle \theta(\mathbf{r})-\theta(0)^2\right\rangle}, \tag{9}$$

where the quantity in the exponent is computed in Fourier space as

$$\begin{aligned}\left\langle(\theta(\mathbf{r})-\theta(0))^2\right\rangle &= \left\langle \int \frac{d\mathbf{q}_1}{2\pi}\,\theta_{\mathbf{q}_1}\left(e^{i\mathbf{q}_1\mathbf{r}}-1\right)\int \frac{d\mathbf{q}_2}{2\pi}\,\theta_{\mathbf{q}_2}\left(e^{i\mathbf{q}_2\mathbf{r}}-1\right)\right\rangle = \int \frac{d\mathbf{q}}{(2\pi)^2}\left(2-2\cos(\mathbf{q}\cdot\mathbf{r})\right)\left\langle|\theta(\mathbf{q})|^2\right\rangle \\ &= \frac{T}{\pi J}\left(\int_{1/L}^{1/a}\frac{dq}{q}\left(1-\cos(\mathbf{q}\cdot\mathbf{r})\right)\right) \sim \frac{T}{\pi J}\int_{1/r}^{1/a} dq\,\frac{1}{q} = \frac{T}{\pi J}\ln\frac{r}{a}\,, \end{aligned} \tag{10}$$

where the result (6) for the phase correlation function of the Gaussian model has been used. Finally, by substituting this result in Eq. (9) we obtain

$$C(\mathbf{r}) = e^{-\frac{T}{2\pi J}\ln(r/a)} = \left(\frac{a}{r}\right)^{\frac{T}{2\pi J}}\,. \tag{11}$$

In the high-temperature regime one can attempt an estimate of the correlation function in power law of the small parameter $\beta J \ll 1$. In this regime one is not authorized to assume small fluctuations of $\theta_i - \theta_j$, and in general the full cosine structure of Eq. (1) should be retained, along with its periodicity modulo 2π. The details of this calculation can be found in Ref. [24]. The final result is that the correlation function decays in this regime exponentially, with a correlation length ξ depending on the temperature

$$C(\mathbf{r}_i - \mathbf{r}_j) \simeq e^{-|\mathbf{r}_1-\mathbf{r}_2|/\xi}, \quad \xi = \ln\frac{2T}{J}. \tag{12}$$

Let us compare the results (11) and (12) with the standard expectations for a second-order phase transition according to Landau theory. Denoting with $m = \langle \mathbf{S}\rangle$ the average order parameter below T_c, one usually finds

$$C(\mathbf{r}) \simeq \quad A e^{-\mathbf{r}\xi_+}, \quad T > T_c \tag{13}$$

$$C(\mathbf{r}) \simeq \quad m^2 + B e^{-\mathbf{r}\xi_-}, \quad T < Tc \tag{14}$$

where A, A' are constants, and the correlation length above ξ_+ and below ξ_- both diverge as T_c is approached as

$$\xi_\pm(T) \sim \frac{1}{|T-T_c|^\nu}, \quad T \to T_c, \tag{15}$$

with $\nu = 1/2$ in the mean-field case. In other words, the correlation function for the observable that represents the order parameter decays exponentially to zero in the disordered state, while it tends exponentially to the square of the order parameter in the ordered state. The results found above for the XY-model are radically different: at high temperature we recover indeed an exponential decay to zero, Eq. (12), but the correlation length does not diverge at any finite temperature. On the other hand, in the low-temperature expansion (11) the correlation length tends to zero with a power-law instead of an exponential behavior. Strictly speaking, such a scaling implies that $\xi \rightarrow \infty$ in the ordered state. Observe also that both results are consistent with the Mermin-Wagner theorem: the system does not display a non-zero order parameter at any finite temperature. On the other hand, such a drastic change of behavior of the correlation functions cannot occur without the emergence of a phase transition in between: the transition in this case cannot be characterized by a vanishing of the order parameter (that is always zero at finite temperature in the thermodynamic limit), but by the change of scaling of the system correlation functions. At low temperature, the long-wavelength spin fluctuations, or spin waves, have a finite spin (or phase) stiffness, encoded in the finite coefficient of the $\left(\nabla\theta\right)^2$ term of Eq. (2). The direct consequence of this rigidity against phase fluctuations is the (weak) power-law decay of correlation functions at large distances, encoded into Eq. (11). On the other hand, at high temperature, a full cosine-like interaction term should be considered in the Hamiltonian, and the system recovers a standard exponential decay (12) of the correlation function, and the phase rigidity, that controls the power-law decay of the low-temperature expansion (11), is lost. To understand how this transition occurs, we must take into account vortices, not considered so far.

2.2 The role of vortices

Let us tackle the problem starting from the low-temperature expansion (2). It is clear that this approximation cannot be the end of the story: the model (2) is purely Gaussian, and as such it cannot induce any transition. On the other hand, as emphasized above, the pure exponential decay (12) of the correlation functions can only be recovered by retaining the full cosine structure of the Hamiltonian. As a consequence, one recognizes that while going from the original model (1) to the approximated one (2) we have lost one important *discrete* symmetry of the original XY-model, mentioned at the beginning: the invariance under a *local* transformation

$$\theta_i \rightarrow \theta_i \pm 2\pi m\,, \tag{16}$$

with $m \in \mathbb{Z}$, for each site i of the lattice. The presence of this discrete symmetry leads to the existence of a new kind of phase excitations that are topological in character and cannot be smoothly connected to the unperturbed ground state. These are vortices, characterized by a winding of the phase by $\pm 2\pi$ by going around their center

$$\oint \nabla\theta \cdot \vec{d\ell} = 2\pi n\,. \tag{17}$$

It is clear that if a vortex excitation is present in the system, one cannot make the assumption of smoothness of the phase variations in neighboring sites, that led us to the approximate form (2). Thus, vortices are good candidates to be responsible for the phase transition we are looking for. The question to be answered is then: how much energy does it cost to introduce a vortex in the system? Indeed, the answer to this question can also help us understanding what is the temperature scale where the vortex proliferation occurs.

To make this estimate we would like to keep the continuum notation for $\theta(\mathbf{r})$ but allowing also for configurations that are singular in a position $\mathbf{r}_0$. The easiest way to introduce vortices into the low-temperature model (2) is to assume that the Gaussian Hamiltonian admits both *smooth* solutions θ_{SW}, that represent the longitudinal spin waves, and *singular* solutions θ_V, which represent vortices. These two solutions are obtained by a variational principle applied to the Hamiltonian (2): the variational equation $\delta H = 0$ reads in general

$$\nabla^2\theta(\mathbf{r}) = 0. \tag{18}$$

We will then describe spin-waves as solutions of Eq. (18) in all space, and vortices as solutions that satisfy Eq. (18) everywhere except than in isolated points, that represent the vortex center

$$\begin{aligned}\nabla^2\theta_{SW}(\mathbf{r}) &= 0\,, & (19)\\ \nabla^2\,\theta_V(\mathbf{r}) &= 2\pi q\,\delta(\mathbf{r}-\mathbf{r}_0), & (20)\end{aligned}$$

where q is an integer (positive or negative) number representing the vorticity of the topological excitation at $\mathbf{r}_0$. The solution of Eq. (20) for $q = 1$ in 2D is exactly

$$\theta_V = \arctan\frac{y-y_0}{x-x_0}\,, \tag{21}$$

that is the configuration of a vortex. Indeed, since $\nabla\theta_V{=}\big(-(y-y_0),\,x-x_0\big)/R^2$, with $R{=}|\mathbf{r}-\mathbf{r}_0|$, one immediately sees that by computing, e.g., Eq. (17) along a circle of radius R around $\mathbf{r}_0$ that $\nabla\theta_V \parallel \vec{d\ell}$, so that from Eq. (17) we get

$$\oint \nabla\theta_V\cdot\vec{d\ell} = \frac{1}{R}\oint d\ell = \frac{1}{R}\,2\pi R = 2\pi\,. \tag{22}$$

By inserting the solution (21) into the Hamiltonian (2) we can then calculate the energy of the vortex configuration as

$$E = \frac{J}{2}\int d\mathbf{r}\big(\nabla\theta_V(\mathbf{r})\big)^2 = \frac{J}{2}\int_a^L dr\,2\pi r\frac{1}{r^2} = \pi J\ln\frac{L}{a}\,, \tag{23}$$

where we used the fact that the distance R from the vortex center is limited below by the lattice spacing and above by the system size L. This energy is diverging logarithmically with the system size L, disfavoring the generation of vortices in the thermodynamic limit. However, at finite temperature we must consider also the gain in entropy in forming the vortex configuration. Since the number of independent places where a vortex can be located is $\sim L^2/a^2$, we obtain that also the entropy has a logarithmic dependence on the system size

$$S = \ln\frac{L^2}{a^2} = 2\ln\frac{L}{a}\,. \tag{24}$$

In conclusion we have that the free energy of a vortex configuration is

$$F = E - TS = \big(\pi J - 2T\big)\ln\frac{L}{a}\,, \tag{25}$$

so that as soon as

$$T > T_{BKT} = \frac{\pi J}{2}\,, \tag{26}$$

the emergence of an isolated vortex is entropically convenient. Even though we did not prove it yet, it is physically plausible that when vortices proliferate they destroy the quasi-long-range order encoded in the power-law correlation functions (11). More precisely, we will demonstrate, by means of the renormalization-group equations, that the phase rigidity goes to zero. It is worth stressing where the dimensionality entered crucially in the above argument. The entropic cost to obtain a vortex is always logarithmically increasing with the system size, as in Eq. (24) above. However, in dimensions larger than two the energetic cost of vortex configuration would scale faster than $\log(L)$, making the energy term always predominant over the entropic one. Thus, unless additional effects enter to cut-off at large distance the energetic cost of a vortex (as it happens, e.g., in charged superconductors [25]) the free energy of a vortex configuration cannot spontaneously change sign as temperature increase.

The above argument is the one provided in the original paper by Kosterlitz and Thouless [2]. Even though it is qualitatively correct, it neglects two effects. (i) While going from the lattice to the continuum model one misses the energetic costs to form the vortex at the length-scale of the lattice spacing. This energy, that is usually referred as vortex-core energy μ, is a constant that must be added in Eq. (23). Even though it does not change considerably the estimate (26), where only the terms growing with the system size are relevant, it can be nonetheless relevant if one wants to make a direct comparison with experimental data in real superconducting systems, as we will discuss extensively below. (ii) We estimated the transition temperature by considering a single vortex with infinite size, while the reality could be more complicated, with several vortex excitations occurring on shorter scales. For example, if one puts a vortex at $\mathbf{r}_+$ and an antivortex (with same vorticity) at $\mathbf{r}_-$, at scales larger than $\sim |\mathbf{r}_+ - \mathbf{r}_-|$ the phase configuration remains unperturbed. In the spirit of Eq. (23), the log divergence of the integral is cut-off at a scale or order $|\mathbf{r}_+ - \mathbf{r}_-|$. This implies that such vortex "pairs" are energetically possible also below T_c, and can change the "effective" large-distance J that enters Eq. (26). These additional effects are beautifully explained, as we shall see in the next sections, by the renormalization group (RG) analysis of the BKT transition, that was developed by Kosterlitz [26] right after the publication of the original paper with Thouless. The starting point to carry on this analysis was the explicit construction of the mapping into the Coulomb-gas problem, that we will discuss in the next section.

3 Mapping to the Coulomb-gas and sine-Gordon model

As we discussed in the previous Section, vortex-like fluctuations can be introduced into the Gaussian model (2) by allowing for singular solutions (20) of the $\delta H = 0$ variational equation. We can try to pursue this analogy further by writing down a model that also includes interactions between vortices, mediated by spin-wave excitations. This is the idea that was followed by Kosterlitz [26] to write down a partition function for multiple vortices, to be further studied by means of the RG approach. It turns out that the Hamiltonian describing interactions between vortices is formally equivalent to the Hamiltonian of the Coulomb gas in two dimensions. I will review here in detail the derivation of the mapping, as it is discussed in [24], since it allows one to grasp several aspects of the vortex physics, besides providing an additional example of a completely different problem (the screening transition for the 2D Coulomb gas) that still belongs to the BKT universality class.

Let us start again from the low-temperature model (2) and let us promote the phase gradient to a generic current density $\mathbf{j}$

$$\nabla\theta \;\Rightarrow\; \mathbf{j}\,, \tag{27}$$

so that the Hamiltonian (2) becomes more generally

$$H = \frac{J}{2}\int d\mathbf{r}\,\mathbf{j}^2(\mathbf{r}). \tag{28}$$

Such a terminology is further motivated by the application to the case of superconductors, where $\nabla\theta$ is directly connected to the physical electronic current density in the SC state (see Eq. (64) below). In full generality, we can always decompose $\mathbf{j}$ in its longitudinal $\mathbf{j}_{\parallel}$ and transverse $\mathbf{j}_{\perp}$ components, defined as usual as

$$\mathbf{j} = \mathbf{j}_{\parallel} + \mathbf{j}_{\perp} \quad \text{with} \quad \nabla\times\mathbf{j}_{\parallel} = 0 \quad \text{and} \quad \nabla\cdot\mathbf{j}_{\perp} = 0\,. \tag{29}$$

By close inspection of the spin-wave (19) and vortex-like (20) phase excitations we also realize that the former are connected to the longitudinal component, while the latter represent the transverse components. Indeed we see that only $\mathbf{j}_{\perp}$ contributes to vortices, since

$$\oint \mathbf{j}\cdot d\vec{\ell} = \int_S (\nabla\times\mathbf{j})\cdot d\mathbf{s} = \int_S (\nabla\times\mathbf{j}_{\perp})\cdot d\mathbf{s} = 2\pi\sum_i q_i\,, \tag{30}$$

where q_i is an integer (positive or negative number) defining the vorticity of the i-th vortex. Eq. (30) is a generalization of Eq. (22) in the case where several vortices with different vorticity are present. The longitudinal and transverse components can be defined in terms of scalar functions as

$$\mathbf{j}_{\parallel} = \nabla\theta_{SW} \quad \text{and}\; \mathbf{j}_{\perp} = \nabla\times(\hat{z}W) = \big(\partial_y W,\, -\partial_x W,\, 0\big). \tag{31}$$

In this way we also have that $\nabla\times\mathbf{j}_{\perp} = \big(0,\, 0,\, -\nabla^2 W\big)$. Inserting this relation into Eq. (30) we then conclude that W must satisfy the equation

$$\nabla^2 W(\mathbf{r}) = -2\pi\rho(\mathbf{r}), \tag{32}$$

$$\rho(\mathbf{r}) = \sum_i q_i\,\delta(\mathbf{r}-\mathbf{r}_i). \tag{33}$$

Eq. (32) is exactly the Poisson equation in 2D for the potential W generated by a distribution of point-like charges q_i at the positions $\mathbf{r}_i$. Its solution is in general

$$W(\mathbf{r}) = 2\pi\int d\mathbf{r}'\,V(\mathbf{r}-\mathbf{r}')\rho(\mathbf{r}'), \tag{34}$$

where $V(\mathbf{r})$ is the Green's function of the Poisson equation, i.e., the solution of the homogeneous equation (corresponding to the Coulomb potential in 2D) that reads

$$\nabla^2 V(\mathbf{r}) = -\delta(\mathbf{r}) \quad \Rightarrow V(\mathbf{r}) = \int \frac{d\mathbf{k}}{(2\pi)^2} \cdot \frac{e^{i\mathbf{k}\cdot\mathbf{r}}}{\mathbf{k}^2}. \tag{35}$$

Notice that here we denote as Coulomb potential in 2D the Fourier transform of $1/\mathbf{k}^2$ in two spatial dimensions, so that we obtain $V(r) \simeq -\ln r$ at large distances, instead of the usual $1/r$ of the 3D case. If we use the decomposition (29) in Eq. (28) we immediately see that the mixed terms vanishes since $\int d\mathbf{r}\, \mathbf{j}_\parallel \cdot \mathbf{j}_\perp = \int d\mathbf{r}\, \nabla\theta_L \cdot \big(\nabla\times(\hat{z}W)\big) = \theta_L\big(\nabla\times(\hat{z}W)\big)\cdot \hat{n}_S\big|_{\partial S} = 0$, since the integration surface S can be taken larger than the sample area, leading to a vanishing current at the border ∂S. As a consequence, we obtain that longitudinal and transverse degrees of freedom decouple $H = H_\parallel + H_\perp$, and we can focus on the term $H_\perp = (J/2)\int d\mathbf{r}\, \mathbf{j}_\perp^2$ that describes the interaction between vortices. Thanks to the result (34) it can be written as

$$\begin{aligned} H_\perp &= \frac{J}{2}\int d\mathbf{r}\, \mathbf{j}_\perp^2 = \frac{J}{2}\int d\mathbf{r}\big(\nabla\times(\hat{z}W)\big)^2 = \frac{J}{2}\int d\mathbf{r}\big(\nabla W\big)^2 = -\frac{J}{2}\int d\mathbf{r}\, W\nabla^2 W \\ &= \pi J\int d\mathbf{r}\, W(\mathbf{r})\rho(\mathbf{r}) = 2\pi^2 J\int d\mathbf{r}d\mathbf{r}'\rho(\mathbf{r})V(\mathbf{r}-\mathbf{r}')\rho(\mathbf{r}') = 2\pi^2 J\sum_{ij} q_i q_j V(\mathbf{r}_i-\mathbf{r}_j). \end{aligned} \tag{36}$$

Eq. (36) expresses the interaction energy between vortices in the same form of the electrostatic energy of point-like charges q_i, leading to a global charge density $\rho(\mathbf{r})$, interacting via a 2D Coulomb potential $V(\mathbf{r})$. An interesting outcome of the derivation (36) is that, due to the divergence of the potential $V(\mathbf{r})$ as $r \to 0$, only neutral configurations contribute to the partition function. If we compute $V(\mathbf{r})$ from Eq. (35) we see that at the shortest scale of the system, i.e., when we put two vortices on the same site, it has a contribution diverging with the system size

$$V(r{=}0) = \int_{1/L}^{1/a} dk\, \frac{1}{2\pi k} = \frac{1}{2\pi}\ln\frac{L}{a} \to \infty \quad \text{for } L \to \infty. \tag{37}$$

It we separate this divergent term by defining

$$V(\mathbf{r}) = V(0) + G(\mathbf{r}), \tag{38}$$

where now $G(\mathbf{r}{=}0) = 0$, in Eq. (36) we obtain

$$2\pi^2 J\sum_{ij} q_i q_j \big(V(0){+}G(\mathbf{r}_i{-}\mathbf{r}_j)\big) = 2\pi^2 J V(0)\Big(\sum_i q_i\Big)^2 + 2\pi^2 J\sum_{ij} q_i q_j G(\mathbf{r}_i{-}\mathbf{r}_j). \tag{39}$$

Since the Boltzmann weight of each configuration is $e^{-\beta H_\perp}$ the divergence of $V(0)$ in the thermodynamic limit leads to a vanishing contribution to the partition function, unless

$$\sum_i q_i = 0. \tag{40}$$

Using the neutrality condition (40) and the fact that $G(0) = 0$, the last term of Eq. (39) can be written as

$$2\pi^2 J\sum_{ij} q_i q_j G(\mathbf{r}_i{-}\mathbf{r}_j) = 2\pi^2 J\sum_i q_i^2 G(r{=}0) + 2\pi^2 J\sum_{i\neq j} q_i q_j G(\mathbf{r}_i{-}\mathbf{r}_j) = 2\pi^2 J\sum_{i\neq j} q_i q_j G(\mathbf{r}_i{-}\mathbf{r}_j), \tag{41}$$

such that $\mathbf{r}_i - \mathbf{r}_j$ in the last term is at least of order of the lattice spacing. The precise form of the function $G(\mathbf{r})$ follows from the evaluation of the integral (35) on the lattice, that allows one to define the energetic cost to create the vortex on the shortest scale $r = a$. More specifically, one can promote the continuum gradient into a discrete one, and define the Fourier transform of the potential as $V(\mathbf{k}) = a^2/\big(4-2\cos k_x a - 2\cos k_y a\big)$, that reduces to $V(\mathbf{k}) \sim 1/\mathbf{k}^2$ as $ka \ll 1$. From such a discretization the $G(|\mathbf{r}|{=}a)$ potential reads

$$\begin{aligned} G(\mathbf{r}{=}a\hat{x}) &= V(\mathbf{r}{=}a\hat{x}) - V(0) = \int \frac{d^2\mathbf{k}}{(2\pi)^2}\big(e^{i\mathbf{k}\cdot\mathbf{r}}-1\big)V(\mathbf{k}) = \int \frac{d^2\mathbf{k}}{(2\pi)^2}\,\frac{a^2\big(\cos k_x a - 1\big)}{4-2\cos k_x a - 2\cos k_y a} \\ &= \frac{1}{2}\int \frac{d^2\mathbf{k}}{(2\pi)^2}\,\frac{a^2\big(\cos k_x a + \cos k_y a - 2\big)}{4-2\cos k_x a - 2\cos k_y a} = -\frac{1}{4}\,. \end{aligned} \tag{42}$$

This result allows us to rewrite the $G(\mathbf{r})$ potential at the scale relevant for Eq. (41) as

$$G\big(r \gtrsim a\big) \simeq -\frac{1}{4} - \frac{1}{2\pi}\ln\Big(\frac{r}{a}\Big), \tag{43}$$

so that Eq. (36) can be written as

$$\begin{aligned} H_\perp &= 2\pi^2 J \sum_{i\neq j} q_i q_j G(\mathbf{r}_i - \mathbf{r}_j) = -2\pi^2 J \sum_{i\neq j}\left(\frac{1}{4} + \frac{1}{2\pi}\ln\frac{r_{ij}}{a}\right) q_i q_j \\ &= -\frac{\pi^2 J}{2}\sum_{i\neq j} q_i q_j - \pi J \sum_{i\neq j} q_i q_j \ln\frac{r_{ij}}{a} = \mu \sum_i q_i^2 - \pi J \sum_{i\neq j} q_i q_j \ln\frac{r_{ij}}{a}\,, \end{aligned} \tag{44}$$

where we used $\sum_{i\neq j} q_i q_j {=} -\sum_i q_i^2$ from Eq. (40) and identified the vortex-core energy μ with

$$\mu \equiv \mu_{XY} = \frac{\pi^2 J}{2}\,. \tag{45}$$

Finally, we can use the neutrality condition (40) by imposing that vortices should appear in n pairs of opposite vorticity. Moreover, we shall consider in what follows only vortices of the lowest vorticity $q_i{=}\pm 1$, so that $H_\perp$ reads

$$H_\perp = 2n\mu - \pi J \sum_{i\neq j}^{2n} \varepsilon_i \varepsilon_j \ln\frac{r_{ij}}{a}\,, \qquad \varepsilon_i = \pm 1\,. \tag{46}$$

The above equation (46) shows the complete analogy between the vortex problem in the XY-model and the problem of the Coulomb gas in two dimensions, where the electrostatic interaction between charges is written as

$$U(r) = -q_0^2 \sum_{i<j}^{2n} \varepsilon_i \varepsilon_j \ln\frac{r_{ij}}{a}\,, \tag{47}$$

where the logarithmic Coulomb interaction arises from solving the Poisson equation (35) in strictly 2D, as we mentioned before. This also means that to preserve the correct dimension of $U(r)$ one should assume that the fictitious charge q_0 in Eq. (47) has dimensions of $(\mathit{Energy})^{1/2}$.

This is also consistent with the comparison between Eq. (46) and (47), that allows one to identify the effective charge of the XY-model as

$$q_0^2 = 2\pi J, \tag{48}$$

an equivalence that will be useful below. It is worth discussing what is the physical effect behind the BKT transition within the context of the mapping into the Coulomb-gas problem. As we explained before, we expect that in the low-temperature phase vortices can only exist in pairs, and the correlation function display the quasi-long-range order (11) characterized by a power-law decay. The interaction between charges is provided by Eq. (47) and it is unscreened (in the usual language of charged objects). In contrast, in the high-temperature phase the charges are free to move, leading to the usual metallic screening of the potential. As a consequence, within the context of the Coulomb gas the transition occurs between an unscreened (low-temperature) phase and a screened (high-temperature) phase, where long-range 2D Coulomb interactions are suppressed by the existence of free charges, able to move. Such an analogy is sometimes used to discuss the effect of vortices in terms of an effective dielectric function that screens the bare Coulomb interaction, especially within the context of finite-frequency effects [27, 22].

Eq. (46) describes the interaction between vortices in a given configuration with n vortex pairs. In the partition function of the system we must consider all the possible values of n, taking into account that interchanging the n vortices with same vorticity gives the same configuration (so one should divide by a factor $1/(n!)^2$). In conclusion Z reads (up to an irrelevant multiplicative factor Z_{SW} accounting for the partition function of spin-wave excitations connected to the term $H_{\parallel}$ in the Hamiltonian)

$$Z = \sum_{n=1}^{\infty} \frac{1}{(n!)^2} \int d\mathbf{r}_1 \cdots d\mathbf{r}_{2n} e^{-\beta 2n\mu} e^{\pi\beta J \sum\limits_{i\neq j}^{2n} \varepsilon_i \varepsilon_j \ln \frac{r_{ij}}{a}} = \sum_{n=1}^{\infty} \frac{y^{2n}}{(n!)^2} \int d\mathbf{r}_1 \cdots d\mathbf{r}_{2n} e^{2\pi\beta J \sum_{i<j}^{2n} \varepsilon_i \varepsilon_j \ln \frac{r_{ij}}{a}} \tag{49}$$

where we introduced the vortex fugacity

$$y = e^{-\beta\mu}. \tag{50}$$

The explicit derivation of the partition function (49) has the great advantage to introduce one further formal mapping between the original XY-model and a completely different physical problem, that still belongs to the BKT universality class: the quantum sine-Gordon model, defined by the Hamiltonian:

$$H_{sg} = \frac{v_s}{2\pi} \int_0^L dx \Big(K \big(\partial_x \theta\big)^2 + \frac{1}{K} \big(\partial_x \phi\big)^2 - \frac{2g}{a^2} \cos(2\phi) \Big), \tag{51}$$

where θ and $\partial_x \phi$ represent two canonically conjugated variables for a 1D chain of length L, with $\big[\theta(x'), \, \partial_x \phi(x)\big] = i\pi\delta(x'-x)$, K is the Luttinger-liquid (LL) parameter, v_s the velocity of 1D fermions, and g is the strength of the sine-Gordon potential [18]. In this formulation, the role of the spin angle or phase is played by the field θ. Indeed, when the coupling $g_u = 0$ one can integrate out the dual field ϕ to get the action

$$S_0 = \frac{K}{2\pi} \int dx \, d\tau \, \Big(\big(\partial_x \theta\big)^2 + \big(\partial_\tau \theta\big)^2 \Big), \tag{52}$$

equivalent to the gradient expansion (2) of the model (1), once considered that the rescaled time $\tau \to v_s \tau$ plays the role of the second (classical) dimension. The dual field ϕ describes instead the transverse vortex-like excitations. This can be easily understood by considering the quantum nature of the operators within the usual language of the sine-Gordon model. Indeed, a vortex configuration requires that $\oint \nabla\theta \cdot \vec{d\ell} = \pm 2\pi$ over a closed loop, see Eq. (22) above. Since ϕ is the dual field of the phase θ, a 2π kink in the field θ is generated by the operator $e^{i2\phi}$, [18] i.e., by the sine-Gordon potential in the Hamiltonian (51). More formally, one can show that the partition function of the ϕ field in the sine-Gordon model corresponds to the (49) derived above. To see this, let us first of all integrate out the θ field in Eq. (51), to obtain

$$S_{SG} = \frac{1}{2\pi K}\int d\mathbf{r}\big(\nabla\phi\big)^2 - \frac{g}{\pi}\int d\mathbf{r}\cos(2\phi). \tag{53}$$

The overall factor $Z_{\parallel} = \Pi_{q>0}\big(1/\beta J \mathbf{q}^2\big)$ due to the integration of the θ field (corresponding to the longitudinal excitations $Z_{\parallel} = \int \mathcal{D}\theta_{\parallel} e^{-\beta H_{\parallel}}$ in Eq. (28) above) will be omitted in what follows. We can treat the first term of the above action as the free part

$$S_0 = \frac{1}{2\pi K}\int d\mathbf{r}\big(\nabla\phi\big)^2, \tag{54}$$

and expand the exponential of the interacting part in series of powers, so that

$$Z = \int \mathcal{D}\phi\, e^{-S_0}\sum_{p=0}^{\infty}\frac{1}{p!}d\mathbf{r}_1\cdots d\mathbf{r}_p\left(\frac{g}{\pi}\right)^p \cos\big(2\phi(\mathbf{r}_1)\big)\cdots\cos\big(2\phi(\mathbf{r}_p)\big). \tag{55}$$

Here $\int\mathcal{D}\phi$ is the functional integral over the ϕ field. When we decompose each cosine term as

$$\cos\big(2\phi(\mathbf{r}_i)\big) = \frac{e^{i\phi(\mathbf{r}_i)} + e^{-i\phi(\mathbf{r}_i)}}{2} = \sum_{\epsilon=\pm 1}\frac{e^{i\epsilon\phi(\mathbf{r}_i)}}{2}, \tag{56}$$

we recognize that in Eq. (55) we are left with the calculation of average value of exponential functions over the Gaussian weight S_0, i.e of factors

$$\left\langle e^{2i\sum_i \epsilon_i\phi(\mathbf{r}_i)}\right\rangle = e^{2K\sum_{i<j}\varepsilon_i\varepsilon_j \ln\frac{r_{ij}}{a}}\,. \tag{57}$$

Here we followed the analogous steps leading to Eq. (11) above, by recognizing that the above expectation value computed over the Gaussian model (54) is non zero only for neutral configurations $\sum_{i=1}^{p}\varepsilon_i = 0$, in full analogy with the result found above for the vortices. We then put again $p = 2n$. Taking for instance $\varepsilon_1, \ldots \varepsilon_n = +1$ while $\varepsilon_{n+1}, \ldots \varepsilon_{2n} = -1$ the combinatorial prefactor $1/p! \equiv 1/(2n)!$ in Eq. (55) should be multiplied times the number $\binom{2n}{n} = (2n)!/(n!)^2$ of possibilities to choose the n positive ε_i values over the $2n$ ones. Thus, Eq. (55) reduces to

$$Z = \sum_{n=1}^{\infty}\frac{1}{(n!)^2}\left(\frac{g}{2\pi}\right)^{2n}\int d\mathbf{r}_1\cdots d\mathbf{r}_{2n}\, e^{2K\sum_{i<j}^{2n}\varepsilon_i\varepsilon_j\ln\frac{r_{ij}}{a}}\,. \tag{58}$$

By comparing Eq. (49) and Eq. (58) we see that the vortex problem (as well as the Coulomb-gas problem) is fully mapped into the sine-Gordon model, provided that we identify

$$K = \frac{\pi J}{T} \quad \text{and} \quad g = 2\pi e^{-\beta\mu}\,. \tag{59}$$

Once more, we have shown that the partition function (58) bears the same structure of the partition function of the interacting system of vortices, or the interacting 2D Coulomb gas. The same equation corresponds however to different physical problems: within the 1D case, we are dealing with a *quantum* phase transition in $1{+}1$ dimension, that describes how the properties of the one-dimensional Luttinger liquid get modified by the interaction term controlled by g. In general, when g increases the ϕ field tends to get trapped in one of the minima of the $\cos(\phi)$ term, and the field becomes “massive”. As a consequence, the correlation function of the Luttinger liquid lose the power-law decay characteristic of the “massless” phase, and the system typically describes a (spin or charge) ordered state. Further details on the physical aspects of the 1D analogy are discussed in Ref. [18].

As it is clear from the above derivation, within the XY-model there exists a precise relation (45) between the value of the vortex-core energy μ and the value of the superfluid coupling J. This is somehow a natural consequence of the fact that the XY-model (1) has only *one* coupling constant, J. Thus, when deriving the mapping on the continuum Coulomb-gas problem (46), μ is fixed by the short length-scale interaction, that determines the behavior of $G(r)$ in Eq. (43) and consequently the vortex-core energy (45). In contrast, within the sine-Gordon language μ is determined by the value of the interaction g for the model (53), that can attain in principle arbitrary values. This aspect will be relevant later-on when we discuss the *non-universal* properties of the BKT transition observed in real systems, that do not necessarily follow the same expectations of the XY-model, which is only one of the possible models admitting a BKT transition.

4 BKT physics in superfluids and superconductors

Before discussing the renormalization-group (RG) equations for the BKT model, I will first clarify why BKT physics should be relevant for the superfluid to metal transition in 2D. To understand it, one can start from the very basic consideration [24, 25] that a superconductor develops below T_c a complex order parameter $\psi = \Delta_0 e^{i\theta_0}$, whose amplitude Δ_0 is connected to the SC gap appearing in the quasiparticle spectrum $E_{\mathbf{k}} = \sqrt{\xi_{\mathbf{k}}^2 + \Delta_0^2}$, where $\xi_{\mathbf{k}}$ is the excitation energy above the Fermi level. Below T_c then two possible collective fluctuations [28] of the order parameter are possible, related either to its amplitude Δ or to its phase θ

$$\psi(\mathbf{r}) = \big(\Delta_0 + \Delta(\mathbf{r})\big) e^{i(\theta_0 + \theta(\mathbf{r}))}. \tag{60}$$

In analogy with the assumption made before for the XY-model that the modulus of the spins is fixed, under certain circumstances we can assume that the amplitude fluctuations are frozen, and only the phase of the order parameter fluctuates. In this view (that intrinsically assume some form of “preformed” pairing above T_{BKT}, as we shall discuss below) the phase fluctuations are described at Gaussian level by a kinetic-energy term completely analogous to Eq. (2) above. The simplest way to understand this is to start from the order parameter (60) and interpret it as a collective electronic wave function. Within the standard Ginzburg-Landau description of the SC transition [28] one directly expresses the current density in the form analogous to the particle current in first quantization

$$\mathbf{j} = \frac{\hbar q}{2m^*}\left(-i\psi^*\nabla\psi + i\psi\nabla\psi^*\right) - \frac{q^2|\psi|^2}{m^*c}\mathbf{A} = \frac{q|\psi|^2}{m^*}\left(\hbar\nabla\theta - \frac{q}{c}\mathbf{A}\right) \tag{61}$$

where $\mathbf{A}$ is the gauge potential. As usual, in the absence of phase fluctuations ($\nabla\theta = 0$) one recovers the standard diamagnetic response of the superconductor, as given by the London equation [25]

$$\mathbf{j} = -\frac{e^2 n_s}{mc}\mathbf{A} = -\frac{c}{4\pi\lambda^2}\mathbf{A}, \tag{62}$$

where n_s is the superfluid density, m the electronic mass and λ the penetration depth. As it is well known [25,28], the value of the charge $q = -2e$ in Eq. (61) is fixed by the flux quantization, and it physically represents the fact that the SC order parameter is formed by a Cooper pair. The ratio $|\psi|^2/m^*$ is then equivalent to the combination $n_s/4m$ in the London equation (62). One usually defines $m^* = 2m$ and $|\psi|^2| \equiv n_s/2$ so that Eq. (61) reads

$$\mathbf{j} = -\frac{e n_s}{2mc}\left(\hbar\nabla\theta + \frac{2e}{c}\mathbf{A}\right) \equiv -e n_s \mathbf{v}_s, \tag{63}$$

with $\mathbf{v}_s$ superfluid velocity. Once established, the relation (63) between the superfluid current and the phase gradient, one can write down the kinetic energy of superfluid electrons in 2D at $\mathbf{A} = 0$ as

$$H_s = \frac{1}{2} m n_s^{2d} \int d\mathbf{r}\, v_s^2(\mathbf{r}) = \frac{\hbar^2 n_s^{2d}}{8m} \int d\mathbf{r} \big(\nabla\theta\big)^2, \tag{64}$$

where we made explicit the emergence of a 2D superfluid electron density n_s^{2d} such that the quantity $\hbar^2 n_s^{2d}/m$ has the dimension of an energy. By direct comparison between Eq. (64) and Eq. (2) we understand that Gaussian fluctuations of the SC phase of the order parameter are described by the same model obtained by a low-energy approximation to the XY-model. In this case, the role of the coupling J of the XY-model is played by the energy scale connected to the superfluid density in 2D. To make a further connection to the physically-measured penetration depth λ, appearing in the London equation (62), we must convert the 3D superfluid density n_s given in Eq. (62) to an effective 2D one, by using a transverse dimension d. This can represent the film thickness in a thin film, or the distance between planes in weakly coupled layered superconductors (as it is the case for cuprate superconductors). We can then identify the so-called superfluid rigidity or stiffness as the energy scale set by the superfluid density in 2D

$$J = \frac{\hbar^2 n_s^{2d}}{4m} = \frac{\hbar^2 c^2 d}{16\pi e^2 \lambda^2}. \tag{65}$$

To get an idea of the energy scales, it can be useful to express J in Kelvin: since usually the penetration depth is given in microns, one obtains

$$J = 0.62 \times \frac{d[\text{Å}]}{\lambda^2[\mu\text{m}^2]}[K] \tag{66}$$

Typical values [25] of the penetration depth at $T{=}0$ can range from around $\lambda(T{=}0) \sim 0.045$ µm in conventional BCS superconductors, like Al, to $\lambda(T{=}0) \sim 0.16$ µm in cuprate superconductors. As a consequence, if one computes the stiffness per plane in a typical cuprate system, putting the inter-plane distance at $d \sim 5$ Å in Eq. (65), one gets a stiffness of the order of $J_s \sim 120$ K, i.e., not far from the critical temperature of these materials, and much smaller than the pseudogap scale measured above T_c (that can be as large as 20–30 meV). Such an observation motivated, in a milestone paper in the middle 90ties, the proposal that phase fluctuations (and eventually BKT physics) could be relevant for this class of materials [29]. However, as we shall discuss below, the expectation that a layered superconductor with weakly-coupled planes should behave as a quasi-2D system is not always obviously realized, and nowadays convincing evidence of the occurrence of a BKT transition in *bulk* layered cuprates is still lacking.

It is worth stressing that the Gaussian phase-only model (64), that we discussed within a classical Ginzburg-Landau picture, can be derived by starting from a microscopic BCS model by integrating our the fermionic degrees of freedom, as discussed, e.g., in Ref. [24, 30] and references therein. More specifically, one can show in full generality that in the SC state the coefficient of the $\left(\nabla\theta\right)^2$ term in the effective phase-only action is given by the physical superfluid density, defined as the static transverse limit of the current-current correlation function, as it is implicit in the London equation (62). This has also the relevant consequence that J from Eq. (65) should already include the temperature depletion due to *quasiparticle* excitations, not captured by the BKT physics, that only deals with the temperature effects due to proliferation of vortexes. This point will be relevant below while discussing the physical conditions for the observation of BKT physics in effectively 2D superconductors. Indeed, while in 3D the superfluid density is expected to go to zero continuously at the BCS transition T_c, that we will denote in what follows as the mean-field one, within the BKT theory the hallmark of vortex proliferation will be the emergence of a discontinuous jump of the superfluid density at T_{BKT}, as we shall see in the next Section.

Finally, it is crucial to realize that the BKT physics only deals with *classical transverse* phase fluctuations, as it is evident from the phase-only model (64), where no dynamics of the phase degrees of freedom is included. We then expect that such a description can only be valid near T_c, where quantum effects are suppressed and phase fluctuations can be treated as classical. In contrast, as $T \to 0$ one should promote the classical model (64) to a *quantum* one, adding to Eq. (64) the energetic cost to perform a phase gradient *in time* , that is controlled by the charge compressibility κ_0 [24, 31], so that Eq. (64) is replaced at $T = 0$ by the quantum action

$$S = \frac{\hbar^2}{8}\int dt\, d\mathbf{x} \left(\kappa_0 \left(\partial_t\theta\right)^2 - \frac{n_s}{m}\left(\nabla\theta\right)^2\right). \tag{67}$$

For weakly-interacting *neutral* systems κ_0 in the static long-wavelength limit can be approximated with the density of states at the Fermi level, and by Fourier transforming Eq. (67) one recognizes the so-called [31] Anderson-Bogoliubov sound mode

$$\omega^2 = v_s^2|\mathbf{k}|^2, \tag{68}$$

where $v_s^2 = n_s/m\kappa_0$ is the sound velocity. The appearance of the charge compressibility as a coefficient of the time gradient in Eq. (67) is a direct consequence of the fact that density and phase are quantum-mechanically conjugate variables [28]. However, in the case of *charged* superconductors this also implies that the charge compressibility at long wavelength is modified, as compared to the neutral case, by he presence of long-range Coulomb interactions, so the term κ_0 in Eq. (67) is replaced in Fourier space by $\kappa(\mathbf{k}) = \kappa_0/\big(1{+}V(\mathbf{k})\kappa_0\big)$, where $V(\mathbf{k})$ is the Coulomb potential in generic D dimensions. Since for $\mathbf{k} \to 0$ one has $\kappa \to 1/V(\mathbf{k})$ the spectrum of the phase mode, that reflects the one of density fluctuations, identifies now a plasma mode, whose energy vs. momentum dispersion depends on the dimensions. In the standard isotropic three-dimensional (3D) case one recovers [30,31] the well-known dispersion

$$\omega^2 = \omega_p^2 + v_s^2\,|\mathbf{k}|^2, \tag{69}$$

where $\omega_p^2 = 4\pi e^2 n_s/m$ is the isotropic plasma frequency. The main consequence of the emergence of a gapped plasmon in the phase spectrum is that the longitudinal phase fluctuations, that are the main source of the low-T suppression of the stiffness within the classical XY-model [24,32] (see also next Section), are converted from the sound-like mode of Eq. (68) to a gapped plasma mode, leading to a thermal suppression of any contribution to the stiffness due to anharmonic phase fluctuations beyond Gaussian level [30], due to the fact that the plasma frequency at zero temperature can be as large as the normal-state one, that is of the order of eV. This is the main reason why the BCS theory, that only accounts for the effects of quasiparticle excitations on the temperature depletion of the superfluid stiffness, successfully describes the temperature dependence of $J_s(T)$ in all 3D superconductors: quantum phase fluctuations beyond Gaussian level barely contribute to deplete the superfluid density, due to the large energetic cost of their thermal excitation. On the other hand, as T approaches T_c the energy scale of Eq. (65) is progressively suppressed by thermal quasiparticle excitations, the phase fluctuations recover a classical behavior, and transverse vortex-like excitations can become relevant in 2D systems. Their effect will then add to the one of quasiparticle excitations, as we will discuss in the next Section.

5 Renormalization-group equations for the BKT transition

I will not derive here the renormalization-group (RG) equations of the BKT model, but I will rather discuss their consequences. Their derivation can be found in the original paper [26] and in various book, like, e.g., in Ref. [18]. On very general grounds, the RG equations represent the result of a coarse-graining procedure: the physical goal is to integrate out the interaction effects at the short scale, in order to capture the long-scale behavior of the system, that is the relevant one in the thermodynamic limit. To fix also the language once and for all, I will discuss the RG results within the context of 2D superconductors, referring then to a transition from a superfluid state, where the superfluid stiffness (65) is finite, to a metallic one, where $n_s^{2d} = 0$ and the system is no more superfluid.

The derivation of the partition function for the Coulomb-gas model (49) and for the sine-Gordon model (58) has shown that in both cases it can be expressed in terms of the two quantities K and g defined in Eq. (59). Within the context of the SC transition, the large-distance behavior of K defines the large-distance behavior of the phase rigidity J, that tells us if the system remains superfluid in the thermodynamic limit [21]: in other words, the physical value of the superfluid density J_s, that is the quantity experimentally accessible, is obtained under RG flow from the limiting value of K as $\ell \to \infty$

$$J_s \equiv \frac{TK(\ell{\to}\infty)}{\pi}\,. \tag{70}$$

On the other hand, the behavior of the vortex-fugacity g at large distances will tell us if vortices proliferate, leading to a growing of g, or remain bound in pairs, that slightly renormalize J_s with respect to the short-scale value J, without suppressing the superfluid behavior. We will use here the two variables from (59), that naturally occur as coupling constant in the sine-Gordon model. We will assume at each temperature as starting values

$$K(\ell{=}0) = \frac{\pi J(T)}{T} \quad \text{and} \quad g(\ell{=}0) = 2\pi e^{-\beta\mu(T)}\,, \tag{71}$$

where $J(T)$ is given by the value of the stiffness including all other thermal effect besides vortex excitations. For example, within the context of superconductors it will be the stiffness (65) at a given temperature, including the thermal suppression due to quasiparticles. For what concerns the vortex-core energy $\mu(T)$ we will always assume a constant ratio $\mu(T)/J(T) = const$, so that $\mu(T)$ also includes thermal effects due to other excitations of the system. Eqs. (71) identify a line in the (K, g) plane where the RG flow starts, as shown in Fig. 1. Using these two variables the RG equations read

$$\frac{dK}{d\ell} = -K^2 g^2 \quad \text{and} \quad \frac{dg}{d\ell} = \big(2{-}K\big)g\,. \tag{72}$$

By direct inspection of Eqs. (72) one sees that there are two main regimes, represented in Fig. 1: for $K \gtrsim 2$ the r.h.s. of Eq. (72) is negative, so that $g \to 0$ and K tends to a finite value $K \to K^*$ that determines the physical stiffness J_s, according to Eq. (70). Instead for $K \lesssim 2$ the vortex fugacity grows under RG flow, K in Eq. (72) scales to zero, and $J_s = 0$. The BKT transition temperature is defined as the highest value of T such that K flows to a finite value. This occurs at the fixed point $K = 2, g = 0$, so that at the transition one always has

$$K(\ell{\to}\infty,\, T_{BKT}) = 2 \quad \Rightarrow \quad \frac{\pi J_s(T_{BKT})}{T_{BKT}} = 2. \tag{73}$$

As soon as the temperature grows above T_{BKT}, $K \to 0$, so also $J_s \to 0$. As a result, one finds $J(T^+_{BKT}) = 0$, i.e., the superfluid density jumps discontinuously to zero right above the transition. The equation (73) describes the so-called universal relation between the transition temperature T_{BKT} and the value of the superfluid stiffness J_s at the transition, and represents a more refined version of the relation (26) based on the balance between the energy and the entropy of a single-vortex configuration.

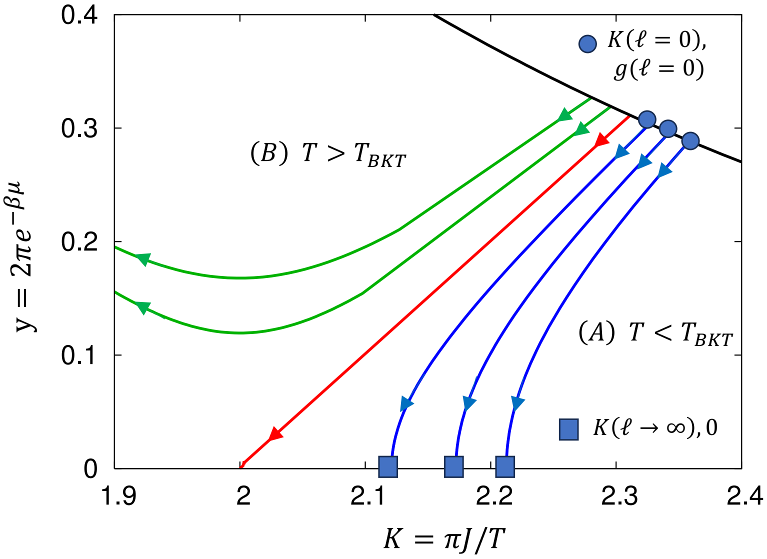

Fig. 1: *RG flow for the BKT problem. The solid black line identifies, for each temperature, the starting values of $K(\ell{=}0)$ and $g(\ell{=}0)$ (denoted with circles) given by Eq. (71). Under the RG flow $K(\ell), g(\ell)$ evolve along the lines shown in blue (for $T{<}T_{BKT}$) and green (for $T{>}T_{BKT}$). For $T{<}T_{BKT}$ the flow at $\ell{\to}\infty$ reaches the point $(K^*, 0) = \big(K(\ell{\to}\infty), 0\big)$, denoted with squares, where vortices disappear and the system has a finite stiffness. At $T{=}T_{BKT}$ the RG equations flow to the fixed point $K{=}2$, $g{=}0$, that allows one to establish the universal relation (73). Above T_{BKT} the flow tends to $(0, \infty)$, so free vortices proliferate and the stiffness goes to zero.*

To better visualize the role of vortex-antivortex pairs it is instructive to derive the temperature dependence of $J_s(T)$ as obtained by numerical solutions of the RG equations. As an example we show in Fig. 2 the expected temperature dependence in the XY-model. As explained above, the BKT RG equations account only for the effect of vortex excitations, so that any other excitation that contributes to the depletion of the superfluid stiffness must be introduced by hand in the initial values of the running couplings. For example, in real superconductors there are also quasiparticle excitations, as we explained above, while in the XY-model there are also longitudinal phase fluctuations, that give rise to a linear depletion to the superfluid stiffness at low temperature $J(T) = J_0\big(1{-}T/4J\big)$ (see e.g. Ref. [32] and references therein). One could then be tempted to use the relation (73) to estimate the T_{BKT} value by looking for the intersection between the universal line $2T/\pi$ and the $J(T)$ expected from the remaining excitations except the vortices. However, such a procedure can only be approximate, since in relation (73) the temperature dependence of $J_s(T)$ is determined also by the presence of bound vortex-antivortex pairs, which can renormalize J_s already *below* T_{BKT}. This effect is connected to the difference between the initial value of $K(0)$ at each temperature, and its asymptotic value $K^* = K(\ell{\to}\infty)$, that determines J_s according to Eq. (70). The crucial observation at this point is that the difference between K and K^* quantitatively depends on the value of μ: as μ decreases the renormalization of J_s due to bound vortex pairs below T_{BKT} increases, the $J_s(T)$ curve starts to deviate from the bare dependence of $J(T)$ (due to other excitations besides vortices) and consequently T_{BKT} is further reduced with respect to the mean-field critical temperature T_c (i.e. the one where $J(T_c){=}0$). As an example we show in Fig. 2 the behavior of $J_s(T)$ using a bare temperature

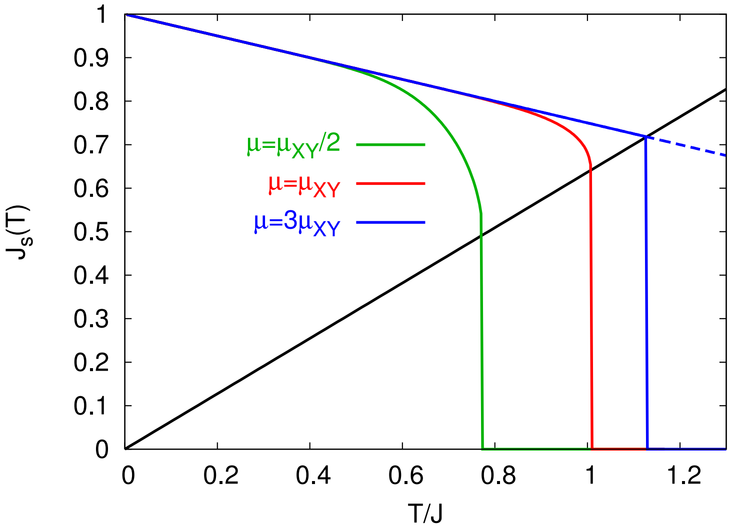

Fig. 2: *Solution of the RG equations by using a linear temperature dependence for* $J(T) = J_0(1-T/4)$*, with* $J_0 = 1$*, to mimic the behavior of the bare stiffness within the* XY*-model. Different curves correspond to different values of the ratio* μ/J*, measured in units of the value (45) it has within the* XY*-model. Notice that for small* μ *values the deviation of* $J_s(T)$ *from* $J(T)$ *starts much before than the temperature where the universal jump occurs: this is due to the larger density of vortex-antivortex pair present below* T_{BKT}*, due to smaller the energetic cost to create them on the shortest length scale.*

dependence as in the XY-model and switching the vortex-core energy from the value (45) to values smaller or larger. As one can see, for decreasing μ the effect of bound vortex-antivortex pairs below T_{BKT} is significantly larger, moving back the transition temperature to smaller values. In the light of this observation, one must be very careful in defining what is universal: T_{BKT} is *not* universal, what is universal in the relation between the *renormalized* superfluid density and the transition temperature, as encoded in Eq. (73).

Finally, it is worth spending still some time on the RG equations (72) to derive the expression of the correlation length ξ close to the BKT critical point. Let us start with a convenient change of variables

$$x = K-2 \quad \text{and} \quad y = 2g\,, \tag{74}$$

so that the RG equations with this choice read

$$\frac{dx}{d\ell} = -(x+2)^2\,\frac{y^2}{4} \simeq -y^2, \tag{75}$$

$$\frac{dy}{d\ell} = -xy, \tag{76}$$

where we approximated the first RG equation around the fixed point $x = 0$, $y = 0$. We can easily solve these differential equations by noticing that they can be rewritten as

$$x\frac{dx}{d\ell} - y\frac{dy}{d\ell} = 0, \tag{77}$$

whence

$$x^2 - y^2 = A^2. \tag{78}$$

Eq. (78) is nothing but the RG flow, close to the fixed point (x,y)=$(0,0)$, in the new x-y plane. The resulting flow lines are hyperbolas, whose symmetry axis can be: $y=0$ if $A^2>0$ (equivalent to the green lines in the region (B) of Fig. 1) or $x=0$ if $A^2<0$ (region (A) of Fig. 1). The critical line corresponds obviously to $A^2=0$.
Approaching the critical point $A\to 0^+$, Eq. (75), can be rewriten as

$$\frac{dx}{d\ell}=-x^2, \tag{79}$$

whose solution is

$$x=\frac{1}{\ell+c}, \tag{80}$$

where c is a constant connected with the initial value of the RG flow $\ell=0$ and $x(0)$. Along the critical line x will finally flow to zero but in an extremely slow fashion, i.e., with the log of the rescaled lattice spacing $\ell=\ln(a'/a)$. Analogously we find in the regime $A^2>0$ that x (and then K) flows to a finite value: it then corresponds the low-temperature region, having a finite superfluid stiffness and vanishing g. Indeed, by substituting $x^2=y^2$+A^2 in (76), we get a first-order differential equation for y

$$\frac{dy}{d\ell}=-y\sqrt{y^2+A^2}, \tag{81}$$

whose solution is

$$y(\ell)=\frac{A}{\sinh\big(A\ell+\operatorname{arcsinh}(A/y_0)\big)}\xrightarrow[\ell\to\infty]{}0. \tag{82}$$

On the other hand, following the same procedure, the solution for x will be

$$x(\ell)=\frac{A}{\tanh\big(A\ell+\operatorname{arcsinh}(A/y_0)\big)}\xrightarrow[\ell\to\infty]{}A. \tag{83}$$

Hence, as expected the superfluid stiffness tends to a finite value, while the coupling accounting for the vortices vanishes under coarse graining.
The opposite regime, the one where $A^2<0$, corresponds to the region $T>T_{BKT}$. Here the superfluid stiffness goes to zero, and we can definite the correlation length as the scale where this happens. In other words, the correlation length can then be estimated as the scale ℓ^* at which $x(\ell^*)=0$. For simplicity let us introduce another constant C, such that: $-A^2=C^2>0$. After having expressed $y^2=x^2+C^2$, we can solve the differential equation (75):

$$\frac{dx}{d\ell}=-\big(x^2+C^2\big)\implies\frac{x}{C}=\tan\big(-C\ell+\arctan(x_0/C)\big). \tag{84}$$

From (84), we then have that x vanishes at the scale

$$\arctan\frac{x}{C}=c\ell^*. \tag{85}$$

Near the transition, we also know that $x_0\sim y_0$, hence: $C^2=y_0^2-x_0^2=(y_0-x_0)(y_0+x_0)\simeq 2y_0(y_0-x_0)$. Since at the transition is x=y, the difference between the initial values y_0-x_0 is at leading order proportional to the distance from the transition temperature, i.e. $(y_0 - x_0) \propto (T - T_{BKT})/T_{BKT}$. Thus we obtain

$$C = \alpha\sqrt{t}, \tag{86}$$

where α is a constant of order one and t is the reduced critical temperature

$$t = \frac{T - T_{BKT}}{T_{BKT}}. \tag{87}$$

Finally, since we are working in the limit $t \ll 1 \to \arctan(x_0/C) \simeq \pi/2$, from Eq. (84) we derive that

$$C\ell^* \sim O(1) \implies \ell^* = \frac{b}{\sqrt{t}}. \tag{88}$$

Since $\ell^* = \ln(\xi/a)$, we have that

$$\xi/a = e^{b/\sqrt{t}}. \tag{89}$$

The parameter b in Eq. (89) depends on the specific model studied. Eq. (89) shows one of the most prominent hallmarks of the BKT transition: by approaching the critical temperature from above the correlation length displays an exponential divergence in the reduced critical temperature t, instead of the usual power-law divergence observed in ordinary Ginzburg-Landau transition, see Eq. (15) above.

6 Superfluid density in thin films of superconductors

In the previous Section we identified at least two typical signatures of BKT physics that are significantly different from the analogous expectations for 3D superconductors: the discontinuous and universal jump (73) of the superfluid stiffness J_s at T_{BKT}, to be contrasted with the continuous suppression of J_s at the critical temperature T_c in 3D, and the exponential activation (89) of the correlation length as T_{BKT} is approached from above. Let us first discuss under which conditions the universal jump of J_s has been measured in real systems, where additional effects not discussed so far very often make such a jump rather elusive.

The first experimental observation of the universal jump (73) has been actually done in thin films of superfluid helium [4, 5]. An example is shown in Fig. 3. Here the experimentally accessible quantity is the shift of the rotation period $\Delta P(T)$ of a torsion pendulum immersed in liquid helium. The rotation period depends on the inertia momentum of the pendulum, that changes below T_{BKT} due to the fact that it cannot drag anymore with it the superfluid fraction of the liquid. As a consequence $\Delta P(T) \propto J_s(T)$, so that the ΔP jump corresponds to the jump (73) of the superfluid stiffness due to the free-vortices proliferation. As one can see, regardless of the $T = 0$ value of J_s the jump always occurs when $J_s(T)$ intersects the BKT line $2T/\pi$: thus, as evidenced above, T_{BKT} is not by itself universal, but the universal relation (73) is always satisfied.

As mentioned at the beginning, in the original paper by Kosterlitz and Thouless [2] it was questioned the possibility to realize a BKT transition in SC films. The objection arises from the fact that in a *charged* superfluid, as is the case for superconductors, a vortex carries a supercurrent,

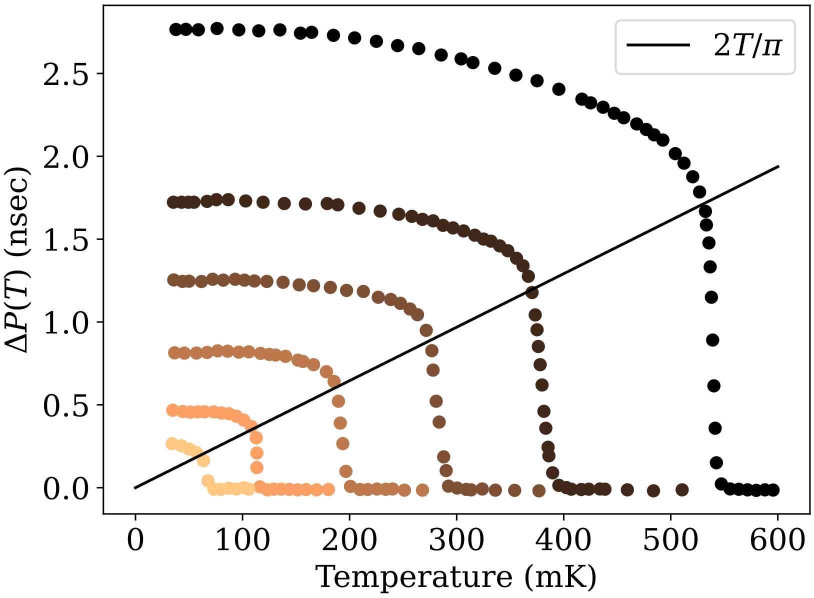

Fig. 3: *Superfluid-density measurements via the oscillator period shift $\varDelta P(T)$ of a torsion pendulum for different films of pure ^{4}He. Each curve corresponds to a different value of the thickness d, such that $\varDelta P(T{=}0)$ decreases with decreasing d. The intersection with the solid line $2T/\pi$ represent the T_{BKT} temperature as defined by the universal-jump relation* (73). *The experimental data have been taken from Ref. [5].*

that contributes itself to the interaction between vortices. In the usual 3D case this mechanism cut-offs the interaction between vortices at a scale λ fixed by the penetration depth [25], leading to a failure of the long-distance $\log$ interaction between vortices that is at the heart of the interacting Hamiltonian (46). However, a crucial observation [33, 22] in this respect is that when the SC system becomes a *thin* film, the interaction between vortices is screened by the supercurrents at a much larger distance $\varLambda = \lambda^2/d$, set by the film thickness d itself, the so-called Pearl length from the name of the scientist who discussed this issue for the first time [34]. An additional effect is that when the film thickness decreases also the relative effects of disorder increase, contributing to a significant increase of λ due to the paramagnetic suppression of the superfluid density [25]. This implies that in practice, for sufficiently thin films with large disorder, where λ is very large, and for temperatures near the mean-field critical temperature T_c, where J is further suppressed by thermal quasiparticle excitations, the electromagnetic screening effects come in at a scale $\varLambda$ even larger than the system size, making the occurrence of a BKT transition possible. It is worth noting that, on very general grounds, this discussion implies that the BKT transition in charged superconductors is possible whenever d is very small or λ is very large. From the relation (65) it follows that whatever mechanism suppresses n_s^{2d}/m it also leads to a large λ, allowing one for a description of the vortex interaction as the one expected in a neutral superfluid. While in thin films of conventional superconductors [10] this usually happens as an effect of disorder on n_s^{2d}, in unconventional superconductors like the cuprates this suppression is observed by proximity to a Mott phase, loosely speaking as an effect of mass-renormalization enhancement [29]. In other words, systems with low intrinsic superfluid rigidity are better candidates for the observation of BKT physics, since screening effects are

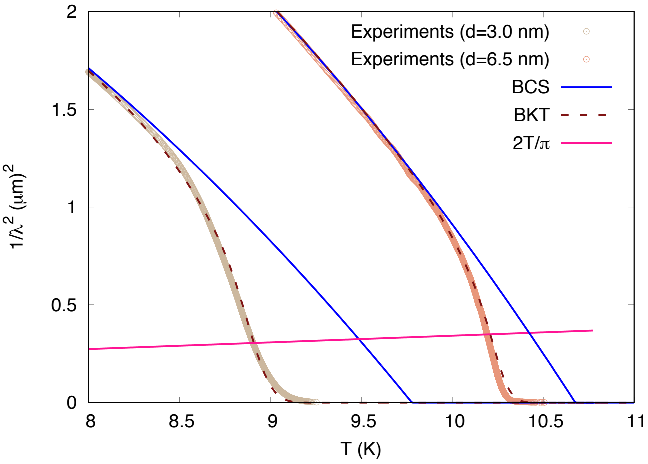

Fig. 4: *Measured temperature dependence of the superfluid density in thin NbN films with different thickness. Data are taken from Ref. [10], along with the BCS fit and the theoretical BKT fit, obtained by using* $\mu/J = 1.19$ *for* $d = 3$ *nm and* $\mu/J = 0.61$ *for* $d = 6.5$ *nm. Notice that the jump here is further smeared out by the inhomogeneity.*

relevant only above a very large Pearl length Λ. In addition, as we commented already before in relation to Eq. (66), a low stiffness implies an energy scale for J_s comparable to the mean-field T_c, making in practice the intervale T_c–T_{BKT} *larger*. To understand this, we should consider that within BCS theory [25] the temperature-dependent bare stiffness $J(T)$ which enters the BKT RG equations vanishes near T_c in a Ginzburg-Landau fashion [28] as

$$J(T) \simeq J_0 \left(1 - \frac{T}{T_c}\right), \tag{90}$$

where

$$J_0 \sim \gamma J(T{=}0), \tag{91}$$

and γ is a constant of order 1. As a consequence, an order-of-magnitude estimate of the T_{BKT} temperature obtained by the universal relation (73) is

$$J_0 \left(1 - \frac{T}{T_c}\right) = \frac{2}{\pi} T_{BKT} \quad \Rightarrow \quad \frac{T_c - T_{BKT}}{T_c} = \frac{1}{1 + \frac{\pi}{2}\frac{J_0}{T_c}}\,. \tag{92}$$

One then understands that as J_0/T_c decreases, as it happens when the film thickness decreases or the superfluid fraction is suppressed by disorder and/or correlations, the distance between T_c and T_{BKT} increases, making it easier to discriminate the two in experiments. In this view, the mean-field temperature T_c can be interpreted as the temperature where pairing forms, so that the amplitude fluctuations can be neglected at $T < T_c$ and one goes back to an effective phase-only model as the one assumed within the BKT approach. In this sense the BKT physics implies a "preformed pairing" in a rather small temperature range, i.e., between T_c and T_{BKT}.

The first observations of BKT physics in thin films of SC date back to the late 80's. However, they were not based on the direct measurement of J_s, but rather to its indirect estimate via I-V characteristics [8, 9], that we will discuss below. This is due to the fact that only in the late nineties emerged an experimental technique able to measure the penetration depth of thin films via the so-called two-coil mutual inductance technique [35] (an experimental technique triggered, as many others, mostly by the investigation of high-temperature cuprate superconductors). Fig. 4 shows one example of λ^{-2} measured in thin films of NbN, a conventional s-wave superconductors, taken from Ref. [10]. As established in Eq. (65) above, this is directly proportional to the superfluid stiffness $J_s(T)$ of the system. Here one can recognize two different theoretical curves: the fit of the low-temperature part $J_{BCS}(T)$, which is based on a standard BCS-like suppression of $J_s(T)$, present also in 3D samples, and the BKT fit, that reproduces the experimental observations, along with the universal $2T/\pi$ line, rescaled to get an inverse length squared. As one can see, $J_s(T)$ displays a rapid downturn around the intersection with the $2T/\pi$ line, but this is not the sharp jump predicted by Eq. (73). This experimental finding has been interpreted [10] as an effect of sample *inhomogeneity*, that one can phenomenologically model as a finite probability P_i of having a range of possible $J_s^i(0)$ values, leading to different T_{BKT}^i temperatures. The measured $J_s(T)$ appears then as an average of the different $J_s^i(T)$ realizations: since, according to Eq. (92), smaller $J_s^i(0)$ lead to smaller T_{BKT}^i, the averaged $J_s(T)$ will display a smeared jump, as observed experimentally. Even though the concept of inhomogeneity has been introduced at the beginning as phenomenological, more recently [36] we worked on a theoretical validation of it based on Monte Carlo simulations on a disordered version of the XY-model (1)

$$H_{XY} = -\sum_{\langle ij\rangle} J_{ij} \cos\big(\theta_i - \theta_j\big), \tag{93}$$

where the local couplings J_{ij} have a finite randomness around an average value $\bar{J}_{ij}$ that sets the scale of the transition. The main point is that in principle one would expect that the universal jump (73) is insensitive to the presence of randomness on the J_{ij} coupling. The reason relies on the so-called Harris criterium [37], which establishes under which condition finite-size effects due to disorder are more relevant that the finite size L of the system itself. This estimate can be done by considering that T_c can still be well identified if the temperature indetermination $|T - T_c|$ itself is larger that the T_c indetermination $\varDelta T_c$ due to disorder, i.e. $|T - T_c| \gg \varDelta T_c$ as $T \to T_c$. In D dimensions one can estimate $\varDelta T_c$ by the following argument: let us assume that the system is ordered on a typical scale of size ξ, the correlation length of the pure system, and let us estimate the variance of the local values of T_c in the disorder system via the central theorem, stating that it scales with the square root of the N possible values of the variable itself, that in turn scales with the volume ξ^D. Thus we could say that

$$\varDelta T_c \sim \frac{1}{\sqrt{\xi^D(T)}} = \frac{1}{\xi^{D/2}(T)}\,. \tag{94}$$

If we plug into Eq. (94) the usual power-law scaling of $\xi(T)$ from Eq. (15) we obtain that disorder-induced uncertainty in the transition is irrelevant when

$$|t| \gg 1/|t|^{\nu D/2} \quad \Rightarrow \qquad \nu > 2/D\,, \tag{95}$$

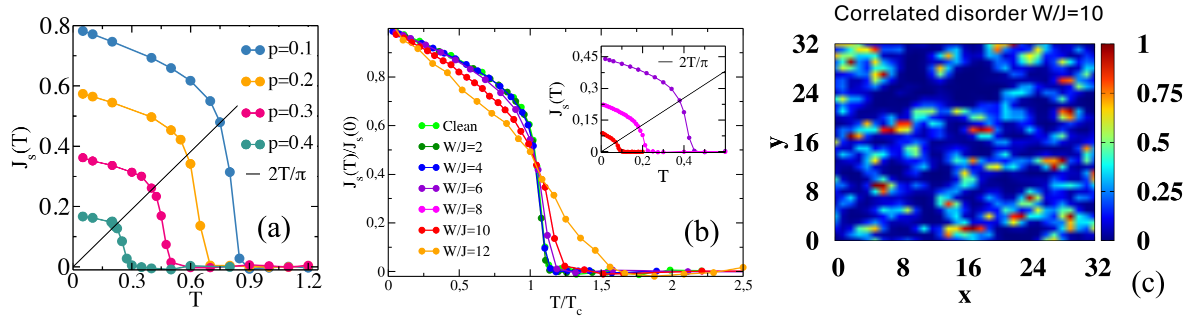

Fig. 5: *Monte Carlo simulations on the disordered* XY*-model (93) for different types of disorder, implemented via the space structure of the local couplings* J_{ij}*. (a) Diluted* XY*-model. In this case* $P(J_{ij}) = 1$ *with probability p. As one can see, as disorder increases the* $J_s(T{=}0)$ *is suppressed, along with* T_{BKT}*, but the universal relation (73) is always observed. Figure adapted from Ref. [32]. (b) Correlated disorder, as generated via a quantum* XY*-model in random transverse field. A typical map of the local coupling at the disorder level* $W/J = 10$ *is shown in panel (c). More details on the generation of the maps of local couplings can be found in Ref. [36]. In this case as the disorder strength* W/J *increases not only the overall scale of the stiffness is suppressed (see inset), but the universal jump is progressively smeared out by disorder. Figures adapted from Ref. [36]*

with $t = (T - T_c)/T_c$. The reasoning is that under the condition (95) weak disorder decreases under coarse graining and becomes unimportant on large length scales, making the clean critical point stable against weak disorder. As we have seen before, in the BKT transition the correlation length $\xi(T)$ diverges *exponentially* as $T \to T_{BKT}$, which means that $\nu = \infty$ within the context of the Harris criterium (the exponential is faster than any power law). One would then conclude that the Harris criterium (95) is always satisfied for BKT physics, disorder is always irrelevant, and the BKT jump (73) should be robust against disorder. Such a result holds indeed for *uncorrelated short-range* disorder, as it is shown in Fig. (5)a, where we show results for a disordered XY-mode with link dilution [36]. However, when disorder is *correlated*, as it happens, e.g., when the local coupling constants J_{ij} have a "granular" structure, see Fig. 5c, the Harris criterium does not hold and one could expect modifications of the BKT jump. Such an effect has been proved by means of Monte Carlo simulations in Ref. [36]: here it has been shown that when the J_{ij} couplings realize a fragmented SC state the BKT jump is symmetrically smeared out with respect to the expected transition, see Fig. 5b, in strong analogy with the experimental observations in thin SC films as the one reported in Fig. 4. This result has been explained in terms of an unconventional vortex-pairs nucleation in the granular SC state. Indeed, the presence of large regions with low couplings J_{ij} allows the system to nucleate several vortex-antivortex pairs already well below T_{BKT}, leading to a continuous downturn of the $J_s(T)$ instead of the expected jump.

A second aspect relevant for the understanding of the BKT transition in real materials is the role played by the vortex-core energy. Indeed, apart from the smearing of the jump, the measured $J_s(T)$ appears to deviate from the BCS behavior significantly before the intersection with the BKT line $2T/\pi$. As we discussed within the context of Fig. 2, this is an effect of the vortex-antivortex pair renormalization of the stiffness that occurs already below T_{BKT}, and it depends on the value of the vortex-core energy. Within the XY-model (1) there exists a single energy scale, J, so that, when we mapped it into the continuum Coulomb-gas problem, the ratio μ/J simply followed from the regularization of the function $G(r)$ at the length scale a of the original lattice model, see Eqs. (42), (43) and (45). However, in a BCS superconductor one would rather fix the value of the vortex-core energy by computing exactly the energy per unit-length of a vortex line [25]

$$I = \left(\frac{\Phi_0}{4\pi\lambda}\right)^2 \left(\log\frac{\lambda}{\xi_0} + \epsilon\right) \equiv \pi J \left(\log\frac{\lambda}{\xi_0} + \epsilon\right)$$

so that according to our definition $\mu = \pi\epsilon J$. A precise estimate of $\epsilon \simeq 0.497$ for the vortex core in three-dimensional geometry is given in Refs. [38, 39], so that within BCS theory one could eventually expect values of μ significantly smaller than within the XY-model,

$$\mu_{BCS} \simeq \pi J/2 \simeq \mu_{XY}/\pi. \tag{96}$$

A similar result can be obtained by using a different argument, i.e., by estimating μ from the condensation energy lost in creating the vortex core [10]. In this case one would put

$$\mu_{BCS} = \pi\xi_0^2\varepsilon_{cond}, \tag{97}$$

where ε_{cond} is the condensation-energy density. In the clean case Eq. (97) can be expressed in terms of J_s by means of the BCS relations for ε_{cond} and ξ_0. Indeed, since $\varepsilon_{cond} = dN(0)\Delta^2/2$, where $N(0)$ is the density of states at the Fermi level, Δ is the BCS gap, and $\xi_0{=}\xi_{BCS}{=}\hbar v_F/\pi\Delta$, where v_F is the Fermi velocity, assuming that $n_s{=}n$ at $T{=}0$, where $n{=}2N(0)v_F^2 m/3$, one has

$$\mu_{BCS} = \frac{\pi\hbar^2 n_s d}{4m}\frac{3}{\pi^2} = \pi J_s\,\frac{3}{\pi^2} \simeq 0.95 J_s\,, \tag{98}$$

that is again of the same order of magnitude of Eq. (96) above. Interestingly, in Ref. [10] it was observed that as the film thickness decreases, the ratio μ/J_s extracted from the fitting of the $J_s(T)$ curve increases. This effect can be understood within a model for disordered superconductors, resulting from an increasing separation between the energy scales associated with the gap and the stiffness, that emerged as a signature of the superconductor-to-insulator transition induced by disorder [40].

The possibility of observing BKT jumps has been discussed in a wide variety of thin films of superconductors: besides the conventional NbN mentioned above, one could list InO$_x$ films, cuprate superconductors, but also the 2D electron gas formed at the interface between artificial heterostructures made of insulating oxides as LaAlO$_3$/SrTiO$_3$, LaTiO$_3$/SrTiO$_3$ [14,15] and more recently even Al/KTiO$_3$ interfaces [16]. A review of these systems and some relevant references can be found in [20]. A related but slightly different issue is instead the observation of BKT physics in *bulk* cuprate superconductors. In this case, one is dealing with a full 3D system, but with weakly coupled SC layers. As we mentioned before, one could argue [29] that each unit behaves as a 2D superconductor, with a characteristic effective thickness d corresponding to the interlayer distance, with the interlayer coupling leading simply to a rounding of the BKT jump. However, as we discussed in Ref. [19], this expectation is only partly realized, and actually the effective BKT temperature of a layered 3D system can move considerably away from the BKT temperature of each isolated unit as the vortex-core energy increases.

7 Signature of BKT physics in other experimental quantities

7.1 I-V characteristics

As mentioned in the previous Section, direct measurements of the universal jump (73) of the superfluid density were possible only from the middle nineties. Nonetheless, Halperin and Nelson in their milestone paper on the applicability of BKT physics to superconductors [22] proposed to access indirectly the J_s jump via a measurement of the I-V characteristics below T_{BKT}. The basic idea is that below T_{BKT} the vortices are bound in pairs: however, a large enough applied current can unbind a certain fraction of vortices, leading to a power-law dependence of V on I that is controlled by the superfluid stiffness. To understand how these two quantities are related, let us consider a film of length L along x and width W along y, and let us consider a finite current I along x, corresponding to a current density $\mathbf{j} = I/(Wd)\hat{x}$. This current produces a force (Magnus force or Lorentz force) per unit length of the vortex line that moves vortices perpendicularly with respect to $\mathbf{j}$, with a direction determined by the sign of the vorticity $\varepsilon_i=\pm 1$

$$\mathbf{f} = \varepsilon_i \, \mathbf{j}_s \times \hat{z} \, \frac{\Phi_0}{c} \, . \tag{99}$$

There are several way to derive Eq. (99): the easiest is to think that this is just a consequence of the Lorentz force between the current and the magnetic field carried by the vortex [25], or that $\mathbf{f}$ is analogous to the usual Magnus effect, where a lift force acts on a spinning object moving through a fluid. The movement of vortices along y causes in turn an electric field E_x along x that contrasts the applied current, giving rise to power dissipation to maintain a steady state. In particular, E_x can be estimated as follows: each time a vortex drifts across the sample width W, a phase slip of 2π occurs through the sample. The number of vortices that escape the sample in the interval Δt is $n_v v_L \Delta t$, where v_L is the drift velocity of vortices along y and n_v is the (two-dimensional) density of free vortices. Thus the rate of phase slip is

$$\frac{d\Delta\theta}{dt} = 2\pi n_v L v_L \, . \tag{100}$$

Thanks to the Josephson relation $\Delta V = (\hbar/2e)\, d\Delta\theta/dt$, this corresponds to a field $E_x = \Delta V/L$ equal to

$$E_x = \frac{\Phi_0}{c} n_v v_L \, . \tag{101}$$

Notice that Eq. (101) can also be seen as a consequence of Faraday law: as soon as a vortex escapes the sample there is a flux variation of Φ_0, so that the induced electric field is $\mathbf{E} = \mathbf{B}\times\mathbf{v}_L/c$, that corresponds to Eq. (101), with $B = n_v\Phi_0$. In the steady state the drift velocity v_L will be simply proportional to the applied Magnus force (99), so that

$$\mathbf{v}_L = \mu_V \mathbf{f} = -\varepsilon_i \mu_V \frac{j\Phi_0}{c} \, \hat{y} \, , \tag{102}$$

where $\mu_V = D/k_B T$ is the vortex mobility and D is the diffusion constant of vortices. In summary, we obtain that free-vortex motion gives a contribution to the resistivity of the material as

$$\rho = \frac{E_x}{j} = \left(\frac{h}{2e}\right)^2 n_v \mu_V \,. \tag{103}$$

It is worth noting that Eq. (103) is a typical example of duality relation: indeed, the resistivity of the real (electronic) charges is expressed as a "conductivity" of the dual vortex charges $h/2e$, given as usual by the charge squared times the density of charges and their mobility. Eq. (103) can be further simplified by using the Bardeen-Stephen [25] expression for the vortex mobility μ_V, derived by an estimate of the dissipation due to the (normal) vortex core

$$\mu_V = 2\pi\xi_0^2 c^2 \rho_n \Phi_0^2, \tag{104}$$

where ρ_n is the normal-state resistivity and ξ_0 is the correlation length, which sets the size of the vortex core. By inserting Eq. (104) into Eq. (103) one obtains

$$\rho = \rho_n 2\pi\xi_0^2 n_v. \tag{105}$$

All the above discussion assumes that one has a finite density n_v of free vortices. However, below T_{BKT} vortices are bound in pairs, and one would then expect to have zero resistance. Nonetheless, when the applied current is large enough a finite free vortex density n_v can be induced even below T_{BKT}. To understand it, we should consider how the magnus force (99) modifies the interaction energy between vortices that we derived in Eq. (46): in particular, the energy per unit length in a film of thickness d of a vortex-antivortex pair at distance r will now read

$$\frac{E}{d} = \frac{2\pi J_s}{d}\ln\frac{r}{\xi_0} - \mathbf{f}\cdot\mathbf{r} = \frac{2\pi J_s}{d}\ln\frac{r}{\xi_0} - \frac{I}{Wd}\frac{\Phi_0}{c}y. \tag{106}$$

As one can see, the log potential tends to confine (i.e. bind) the vortexes, while the current tends to unbind them. The energy has a maximum at the scale where its derivative vanishes, i.e., when $\partial E(y^*)/\partial y = 0$, where

$$y^* = \frac{2\pi J_s c W}{I\Phi_0} \,. \tag{107}$$

This means that for separations $y > y^*$ it becomes energetically favorable for a vortex pair to unbind. Since the maximum separation between vortices is cut-off by the sample width W, whenever $y^* > W$ the vortex pair cannot be dissociated within the sample. In contrast, when the current is large enough to get $y^* \leq W$ free vortexes are generated. The minimum current required to unbind the vortices is then such that $y^* = W$, so that

$$I^* = 2\pi J_s \frac{c}{\Phi_0}, \tag{108}$$

and for $I > I^*$ a free vortex density $n_v(I)$ will be present. To estimate it one can use a kinetic-like equation for n_v such that

$$\frac{dn_v}{dt} = \Gamma(T,I) - n_v^2 \tag{109}$$

where Γ is the rate at which vortices are unbound, and can be taken as $e^{-E(y^*)/T}$, where $E(y^*)$ is the energy of a vortex pair at the threshold instability determined above. The second term in

Eq. (109) accounts for the vortices recombining to form pairs again. In the steady state then one has

$$n_V = \Gamma^{1/2} = e^{-E(y^*)/2T}. \tag{110}$$

From Eq. (105) we already established that $\rho \sim n_v$, where $\rho = E_x/j \propto V/I$. We conclude that

$$V \sim n_v I. \tag{111}$$

Let us then estimate n_v by means of Eq. (110). By using the y^* value (107) in Eq. (106) we get

$$E(y^*) = 2\pi J_s \ln \frac{2\pi J_s c W}{\xi_0 \Phi_0 I} - \frac{2\pi J_s c}{d} = 2\pi J_s \ln \frac{I^* W}{I \xi_0} - \frac{2\pi J_s c}{d}\,. \tag{112}$$

Since only the first term depends on the applied current, we obtain from Eq. (110) that the vortex density scales with the current I as

$$n_v = e^{-E(y^*)/2T} \sim e^{-\pi J_s \ln(I^*/I)/T} = \left(\frac{I}{I^*}\right)^{\pi J_s/T}\,. \tag{113}$$

When replaced into Eq. (111) this implies that above I^* one should observe a non-linear I-V characteristic controlled by the exponent

$$V \propto I^{a(T)}, \quad a(T) = \frac{\pi J_s(T)}{T} + 1\,. \tag{114}$$

From Eq. (73), it follows then that a should jump discontinuously from $a = 3$ at $T = T_{BKT}^-$ to $a = 1$ at $T = T_{BKT}^+$. Below T_{BKT}, the exponent a is expected to increase with decreasing T since the superfluid density increases. The extraction of the superfluid-density jump from the exponent of I-V characteristics has been one of the very first demonstration of BKT physics in thin films of superconductors [8, 9]. Later on, it has been used to characterize the BKT transition in several systems, even when its application can be questioned (see Ref. [41] and discussion therein). The main problem is the identification of the correct range of temperatures and currents where Eq. (114) should be applied. As explained above, non-linearity is expected only *below* T_{BKT} and *above* I^*. In real samples even below T_{BKT} finite-size effects always lead to a finite n_v even for $I \to 0$, that is orders of magnitude smaller than the normal-state one [42]. So the effect of vortex unbinding will manifest in the experiments as a deviation from a linear characteristic to a non-linear one as I overcomes the threshold value I^* for vortex-pair proliferation [13, 41, 42]. To get an idea of its value, one can use the universal relation (73) to replace $2\pi J_s$ with $4k_B T_{BKT}$ in the previous equation. Then using $c/\Phi_0 = 0.5{\cdot}10^{15}$ A / J one has

$$I^*[A] = \frac{c}{\Phi_0} 4 k_B T_{BKT} \simeq 2.67 \cdot 10^{-8}\, T_{BKT}[K] \tag{115}$$

In conventional superconductors where $T_{BKT} \sim 10$ K this corresponds to a current of order of 10^{-7} A. In experiments the crossover is observed for larger currents (usually around 10^{-5} A), an effect that has been ascribed to sample inhomogeneity [42]. However, this also implies that one should avoid to confuse the threshold current for vortex-pair unbinding with the real critical current of the superconductor, where Cooper pairs break down. In Ref. [41] it has been shown how taking into account the effect of inhomogeneity on the smearing of the superfluid-density jump, that we described before, one can get an excellent agreement between the $J_s(T)$ dependence extracted from direct measurements of the inverse penetration depth via two-coils mutual inductance in NbN (see Fig. 4) and the one extracted from the I-V exponent (114). On the other hand, as discussed in Ref. [41], there have been several examples in the literature where the existence of BKT physics has been claimed based on the analysis of I-V non-linearity in a *wrong* temperature/current regime. One paradigmatic example is provided by SrTiO$_3$-based oxide interfaces, where the SC transition has a considerable broadening, that seems to indicate a percolative transition in a network of SC islands of micrometer size, rather that the inhomogeneity on nanometer scales observed in thin films of conventional superconductors, as NbN. In this case non-linear I-V characteristics have been actually measured, but at temperatures *larger* than the real T_c. In Ref. [41] we then argued that in these systems the non-linearity of the I-V characteristics cannot be simply ascribed to vortex-antivortex unbinding triggered by a large current, as it happens within the BKT scheme, since this would lead to dramatically overestimate the BKT transition temperature. In contrast, the observed I-V characteristics can be well reproduced theoretically by modeling the effect of mesoscopic inhomogeneity of the superconducting state, as a consequence of pair-breaking effects in the weaker SC regions, that leads to a progressive non-linear increase of the voltage as the driving current increases, see Fig. 6. In general, one should be very careful in drawing any conclusion about BKT physics for non-linear characteristics measured above the real transition temperature, i.e., the one where resistivity drops to zero (within the available experimental resolution).

7.2 Vortex contribution to transport: paraconductivity

A second possible identification of a BKT transition, still related to vortex transport, is connected to the temperature dependence of the resistivity as one approaches T_{BKT} from above, that can be used to experimentally determine the characteristic exponential divergence of $\xi(T)$ that we derived in Eq. (89) above. As we mentioned, this temperature variation is radically different from the usual power-law divergence (15) observed for ordinary Ginzburg-Landau (GL) fluctuations, where $\xi_{GL}^2 \sim T_c/(T-T_c)$ as one approaches T_c from above. The difference between the two regimes can be eventually tested experimentally by extracting the temperature dependence of the so-called paraconductivity, i.e., the contribution of SC (amplitude and phase) fluctuations to the conductivity. Indeed, both within GL and BKT theory [22] the contribution σ_s of SC fluctuations to the normal-state conductivity σ_N diverges as T approaches the transition temperature as ξ^2

$$\frac{\sigma_s}{\sigma_N} = \left(\frac{\xi(T)}{\xi_0}\right)^2. \tag{116}$$

Within GL theory the above result is the consequence of SC fluctuations of the order parameter, that can be technically understood as the so-called Aslamazov-Larkin correction to the bare current-current correlation function with Cooper-pair fluctuations above the critical temperature

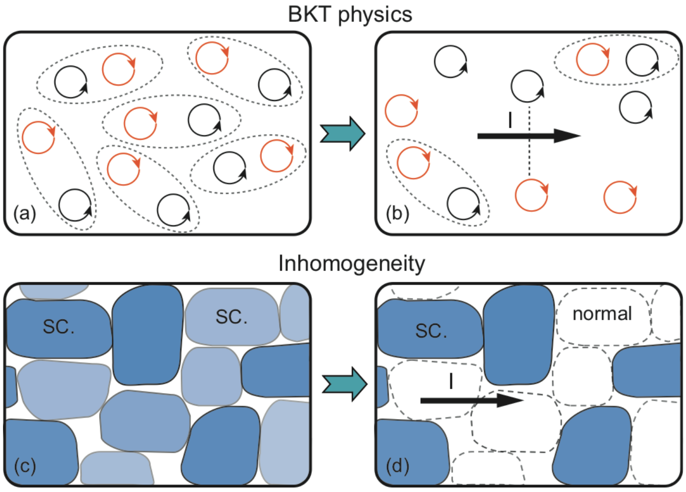

Fig. 6: *Adapted from Ref. [41]. Sketch of the difference between I-V non-linearity arising from BKT physics and from inhomogeneity. In the BKT case, the vortices, which are bound below T_{BKT} in pairs with opposite vorticity (a), get unbound by a sufficiently large current I (b). This generates an extra voltage drop proportional to the average density of unbound vortices, leading to nonlinear characteristics, as given by Eq. (114). In the case of inhomogeneous superconductors, instead, the system segregates into puddles with different strength of the local SC condensate (c). As a consequence, a finite applied current I can turn weak SC puddles into normal ones (d), nonlinearly increasing the global resistivity.*

T_c [43]. The main theoretical paradigm behind this result is the idea that one can describe SC fluctuations above T_c via a Gaussian GL functional, where the fluctuations of the complex order parameter are described by a diffusive mode, that dresses the metallic fermionic response. In this view such Gaussian fluctuations do not distinguish the amplitude from the phase (a distinction that is only possible below T_c), and essentially describe the incipient formation of Cooper pairs with size $\xi(T)$ above T_c. The progressive divergence of σ as $\xi(T)$ increases by approaching T_c, encoded in Eq. (116), is an indication of the formation of fluctuating Cooper pairs with increasing size. As a consequence the resistivity, given by $\rho = 1/(\sigma_N + \sigma_s)$, decreases continuously to zero in the range of temperatures where $\xi(T)$ increases. This effect is then expected to be present regardless of the dimensionality of the system: all non-universal effects, that account for example for the range of temperatures where the paraconductivity can be appreciated experimentally, depend on the specific parameters of the GL functional, that are not universal. A detailed description of GL fluctuations can be found in Ref. [43].

Within the BKT theory one should then expect, as suggested by Halperin and Nelson in [22], that as T decreases one first observes a regime of GL fluctuations, and then a BKT fluctuation regime between the mean-field temperature T_c (that one would observe in the 3D case) and the 2D BKT temperature T_{BKT}. This corresponds to the same range of temperatures where the stiffness is suddenly suppressed by vortex proliferation, as discussed above. To make a correspondence between the GL and the BKT result for the paraconductivity let us go back to Eq. (105) above, where we established a general relation between the dissipative motion of free vortices and the vortex density n_v. While in the previous Section we derived the vortex density induced below T_{BKT} by a large current $n_v(I)$, above T_{BKT} we already have a finite $n_v(T)$ due to the thermal dissociation of vortex-antivortex pairs. In particular, since ξ is the scale where the superfluid density vanishes above T_{BKT}, we can identify

$$n_v \equiv \frac{1}{2\pi\xi^2(T)} \tag{117}$$

so that from Eq. (105) we obtain exactly the form (116), provided that $\xi(T)$ is given by eq. (89). In principle, the experimental determination of such exponential behavior via paraconductivity measurements could represent a clear signature of BKT physics. However, as the above discussion demonstrates, the validity of Eq. (89) is limited to a narrow range of temperatures between T_c and T_{BKT}. In addition, the value of the parameters appearing in the BKT correlation length $\xi \sim ae^{-b/\sqrt{t}}$ are *not* arbitrary, since they depend on the distance (92) between T_c and T_{BKT}, as originally discussed in Ref. [22], and on the value μ of the vortex-core energy, as more recently discussed in Ref. [42], where it has been shown that

$$b = 2\frac{\mu}{\mu_{XY}}\sqrt{\frac{T_c - T_{BKT}}{T_{BKT}}}. \tag{118}$$

For conventional superconductors, such as NbN, usually $\sqrt{\frac{T_c - T_{BKT}}{T_{BKT}}} \sim 0.1$, while $\mu/\mu_{XY} \sim 0.5$, as estimated by the fit of $J_s(T)$ in [10]. In general, all these parameters are constrained one to the other. However, it is not uncommon in the literature that a fit to the resistivity $\rho(T)$ above T_c is attempted with a BKT formula like Eq. (116), without a check a-posteriori that the obtained b value is consistent with its expression via Eq. (118). Some examples of potential problems of this kind are discussed in Ref. [42, 41].

8 Conclusions

In this lecture I gave an introductory overview on the properties of the BKT transition, as it was originally formulated within the classical XY-model, the Coulomb-gas model and the sine-Gordon model. The mapping among these physically different problems turned out to be useful for the analytical derivation of various properties, including the celebrated RG equations. The two most spectacular effects obtained by the RG equations are the universal and discontinuous jump of the superfluid stiffness as the transition is approached from below, and the exponential divergence of the correlation length as the transition is approached from above. I then discussed how these rather specific signatures can be observed in real materials, focusing in particular on the case of superconducting systems. My personal view after several years of intense work in close connection with experiments is that BKT physics has been clearly observed in some cases, but often in the literature the observation of BKT signatures has been based on a naive application of the celebrated BKT formulas. This caveat should be taken by the readers to develop a critical attitude towards the identification of BKT signatures in experiments.

Appendix

A Averages over Gaussian variables

To understand Eq. (11) let us consider a generic Gaussian model with real variables $u(r) \equiv (1/\Omega)\sum_{\mathbf{q}} e^{i\mathbf{q}\cdot\mathbf{r}} u_{\mathbf{q}}$ (where Ω is the volume) whose Hamiltonian in momentum space reads

$$H = \frac{1}{2}\sum_{\mathbf{q}} G(q)\,|u_{\mathbf{q}}|^2. \tag{119}$$

To compute the partition function let us define the integrals over the complex variables $u_{\mathbf{q}}$ in the usual way

$$\int \frac{du_{\mathbf{q}}du^*_{\mathbf{q}}}{2\pi i} \quad e^{-au_{\mathbf{q}}u^*_{\mathbf{q}}} \equiv \int \frac{d\,\mathrm{Re}\,u_{\mathbf{q}}\,d\,\mathrm{Im}\,u_{\mathbf{q}}}{\pi} e^{-au_{\mathbf{q}}u^*_{\mathbf{q}}} = \frac{1}{a}, \tag{120}$$

$$\int \frac{du_{\mathbf{q}}du^*_{\mathbf{q}}}{2\pi i}\, u_{\mathbf{q}}u^*_{\mathbf{q}} e^{-au_{\mathbf{q}}u^*_{\mathbf{q}}} = \quad \frac{1}{a^2}. \tag{121}$$

Since we have only N independent $u(r)$ variables we use the relation $u^*_{\mathbf{q}} = u_{-\mathbf{q}}$ to halve the number of allowed $\mathbf{q}$ values in Eq. (119), so that

$$H = \frac{1}{\Omega}\sum_{\mathbf{q}>0} G(q)\big((\mathrm{Re}\,u_{\mathbf{q}})^2 + (\mathrm{Im}\,u_{\mathbf{q}})^2\big), \tag{122}$$

where we used the symbolic short-hand notation "$\mathbf{q} > 0$". We can then easily compute the partition function as

$$Z = \int \mathcal{D}u\, e^{-\beta H[u]} = \prod_{\mathbf{q}>0}\left(\frac{\Omega}{\beta G(\mathbf{q})}\right), \tag{123}$$

while the average values read

$$\langle u_{\mathbf{q}}u_{\mathbf{q}'}\rangle = \delta_{\mathbf{q}+\mathbf{q}'}\,\frac{\Omega}{\beta G(\mathbf{q})}\,. \tag{124}$$

Finally, one can easily get the average values of exponential of linear functions in the u variables. Indeed, if we define in general

$$R(\mathbf{r}) = \frac{1}{\Omega}\sum_{\mathbf{q}} u_{\mathbf{q}}\,C_{-\mathbf{q}}(\mathbf{r}), \tag{125}$$

we see that

$$\begin{aligned}\left\langle e^{iR(r)}\right\rangle &= \frac{1}{Z}\int \mathcal{D}u\, e^{-\frac{1}{\Omega}\sum_{\mathbf{q}>0} G(q)u_{\mathbf{q}}u_{-\mathbf{q}} + \frac{i}{2\Omega}\sum_{\mathbf{q}>0} u_{\mathbf{q}}C_{-\mathbf{q}}(\mathbf{r}) + \frac{i}{2\Omega}\sum_{\mathbf{q}>0} u_{-\mathbf{q}}C_{\mathbf{q}}(\mathbf{r})}\\ &= \frac{1}{Z}\int \mathcal{D}u\, e^{-\frac{1}{\Omega}\sum_{\mathbf{q}>0} G(q)[u_{\mathbf{q}}-iC_{\mathbf{q}}/2G(q)][u_{-\mathbf{q}}-iC_{-\mathbf{q}}/2G(q)]} e^{-\frac{1}{2\Omega}\sum_{\mathbf{q}}\frac{C_{\mathbf{q}}C_{-\mathbf{q}}}{G(q)}} = e^{-\frac{1}{2}\langle [R(r)]^2\rangle}\end{aligned} \tag{126}$$

References

[1] V.L. Berezinsky, Sov. Phys. JETP **34**, 610 (1972)

[2] J.M. Kosterlitz and D.J. Thouless, J. Phys. C **6**, 1181 (1973)

[3] J.V. José: *40 Years of Berezinskii-Kosterlitz-Thouless Theory* (World Scientific, Singapore, 2013)

[4] M.H.W. Chan, A.W. Yanof, and J.D. Reppy. Phys. Rev. Lett., **32** 1347, (1974)

[5] D. McQueeney, G. Agnolet, and J.D. Reppy. Phys. Rev. Lett., **52** 1325, (1984)

[6] Z. Hadzibabic, P. Kruger, M. Cheneau, B. Battelier, and J. Dalibard, Nature, **44**, 1118 (2006)

[7] P.A. Murthy, I. Boettcher, M. Holzmann L. Bayha, D. Kedar, M. Neidig, M.G. Ries, A.N. Wenz, G. Zurn, and S. Jochim. Phys. Rev. Lett., **115**, 010401 (2015)

[8] K. Epstein, A.M. Goldman, and A.M. Kadin, Phys. Rev. Lett. **47**, 534 (1981)

[9] A.T. Fiory, A.F. Hebard, and W.I. Glaberson. Phys. Rev. B **28**, 5075, (1983)

[10] A. Kamlapure, M. Mondal, M. Chand, A. Mishra, J. Jesudasan, V. Bagwe, L. Benfatto, V. Tripathi and P. Raychaudhuri, Appl. Phys. Lett. **96**, 072509 (2010); M. Mondal, S. Kumar, M. Chand, A. Kamlapure, G. Saraswat, G. Seibold, L. Benfatto, P. Raychaudhuri, Phys. Rev. Lett. **107**, 217003 (2011)

[11] I. Hetel, T.R. Lemberger and M. Randeria, Nat. Phys. **3**, 700 (2007)

[12] Jie Yong, M.J. Hinton, A. McCray, M. Randeria, M. Naamneh, A. Kanigel, and T.R. Lemberger, Phys. Rev. B **85**, 180507(R) (2012)

[13] P.G. Baity, Xiaoyan Shi, Zhenzhong Shi, L. Benfatto, and Dragana Popovic, Phys. Rev. B **93**, 024519 (2016)

[14] J.A. Bert, K.C. Nowack, B. Kalisky, H. Noad, J.R. Kirtley, C. Bell, H.K. Sato, M. Hosoda, Y. Hikita, H.Y. Hwang, and Kathryn A. Moler. Phys. Rev. B (R) **86**, 060503 (2012)

[15] A. Caviglia *et al.*, Nature **456**, 624 (2008)

[16] S. Mallik, G. Menard, G. Saiz, H. Witt, J. Lesueur, A. Gloter, L. Benfatto, M. Bibes, and N. Bergeal, Nat. Comm. **13**, 4625 (2022)

[17] Y. Saito, Y. Kasahara, J. Ye, Y. Iwasa, and and T. Nojima, Science **350**, 409 (2015)

[18] T. Giamarchi: *Quantum physics in one dimension* (Clarendon Press, 2004)

[19] L. Benfatto, C. Castellani and T. Giamarchi, Phys. Rev. Lett. **99**, 207002 (2007)

[20] L. Benfatto, C. Castellani and T. Giamarchi: *Beresinskii-Kosterlitz-Thouless transition within the sine-Gordon approach: the role of the vortex-core energy*, in [3]

[21] D.R. Nelson and J.M. Kosterlitz, Phys. Rev. Lett. **19**, 1201 (1977)

[22] B.I. Halperin and D.R. Nelson, J. Low Temp. Phys. **36**, 590 (1979)

[23] N.D. Mermin and H. Wagner. Phys. Rev. Lett., **17**, (1966)

[24] N. Nagaosa: *Quantum field theory in condensed matter physics* (Springer, 1999)

[25] M. Tinkham: *Introduction to Superconductivity* (Dover Publications, New York, 2004)

[26] J.M. Kosterlitz, J. Phys. C: Solid State Phys. **7**, 1046 (1974)

[27] V. Ambegaokar, B.I. Halperin, D.R. Nelson, and E.D. Siggia, Phys. Rev. B **21**, 1806 (1980)

[28] P. Coleman: *Introduction to Many-Body Physics* (Cambridge University Press, 2016)

[29] V. Emery and S. Kivelson, Nature **374**, 434 (1995)

[30] L. Benfatto, A. Toschi, and S. Caprara, Phys. Rev. B. **69**, 184510 (2004)

[31] P.W. Anderson, Phys. Rev. **112**, 1900 (1958)

[32] Ilaria Maccari, Lara Benfatto, and Claudio Castellani, Phys. Rev B **99**, 104509 (2019)

[33] S. Doniach and B.A. Huberman, Phys. Rev. Lett. **42**, 1169, (1979)

[34] J. Pearl, Appl. Phys. Lett. **5**, 65, (1964)

[35] S.J. Turneaure, E.R. Ulm, and T.R. Lemberger, J. Appl. Phys. **79**, 4221, (1996)

[36] I. Maccari, L. Benfatto and C. Castellani, Phys. Rev. B **96**, 060508 (2017)

[37] A.B. Harris, J. Phys. C **7**, 1671 (1974)

[38] C.R. Hu, Phys. Rev. B **6**, 1756 (1972)

[39] S. Alama and A.J. Berlinsky, and L. Bronsard and T. Giorgi, Phys. Rev. B **60**, 6901 (1999)

[40] M. Chand, G. Saraswat, A. Kamlapure, M. Mondal, S. Kumar, J. Jesudasan, V. Bagwe, L. Benfatto, V. Tripathi, P. Raychaudhuri, Phys. Rev. B **85**, 014508 (2012)

[41] G. Venditti, J. Biscaras, S. Hurand, N. Bergeal, J. Lesueur, A. Dogra, R.C. Budhani, M. Mondal, J. Jesudasan, P. Raychaudhuri, S. Caprara, and L. Benfatto, Phys. Rev. B **100**, 064506 (2019)

[42] L. Benfatto, C. Castellani, and T. Giamarchi, Phys. Rev. B **80**, 214506 (2009)

[43] Anatoly Larkin and Andrei Varlamov: *Theory of Fluctuations in Superconductors* (Clarendon, Oxford, 2005)

11 Polar Quantum Criticality: Challenges and Opportunities

Premala Chandra
Rutgers University
136 Frelinghuysen Road, Piscataway NJ 08854, USA

Contents

E. Pavarini and E. Koch (eds.)
Correlations and Phase Transitions
Modeling and Simulation Vol. 14
Forschungszentrum Jülich, 2024, ISBN 978-3-95806-751-6
http://www.cond-mat.de/events/correl24

1 Quantum criticality and polar materials?

Intuitively the link between polar materials and quantum criticality is not at all obvious. Polar materials are mostly insulators with discontinuous classical transitions, whereas quantum criticality is often studied in itinerant magnetic systems towards the characterization of novel metallic behaviors. Nonetheless I hope to convince you that there is much to be gained at the confluence of these two research areas. After unpacking the title, I will present a theoretical basis for how the interplay of classical first-order transitions with quantum fluctuations can restore quantum criticality in compressible insulators. Next we will turn to strongly correlated phases in quantum critical polar metals, including non-Ferm liquids. The miracle and the mystery of unconventional superconductivity in the nearly quantum critical system n-doped $\mathrm{SrTiO_3}$ will be our last topic. We will end with a summary and outlook for future work.

In the course of our discussion, I will make an effort to present a more expansive treatment of topics that may not be in the mainstream lexicon; these include simple ways to determine the temperature-dependence of observables near quantum critical points, crossover scaling for when both quantum and classical critical fluctuations are present, and subtleties involving $q = 0$ and $q \neq 0$ elastic degrees of freedom. Naturally I will be sharing with you a very personal perspective, and I will do my best to provide references whenever appropriate to provide more details and to broaden the viewpoints expressed here for the curious reader.

1.1 Quantum criticality primer

At classical phase transitions, thermal fluctuations melt the long-range order. By contrast quantum criticality, associated with continuous quantum phase transitions, occurs at zero temperature where thermal fluctuations are absent; here the phase change is driven by zero-point fluctuations whose magnitude can be tuned by pressure or field. My aim here is to present the key ideas of quantum criticality with minimal formalism, using familiar concepts whenever possible; there are several excellent resources for readers eager for more specifics [1–5]. My emphasis will be on determining the temperature-dependence of observable quantities near quantum critical points, and our discussion here will follow closely an approach that three experimental colleagues (G.G. Lonzarich, S.E. Rowley and J.F. Scott) and I have developed together [6].

Aren't quantum fluctuations only present at zero temperature? According to the Heisenberg uncertainty principle, temporal uncertainty is inversely proportional to that in the energy

$$\varDelta t \propto \hbar/\varDelta E \qquad \Rightarrow \qquad \tau_P \propto \hbar/k_B T \tag{1}$$

so that the decoherence timescale, the Planck time τ_P, of the quantum fluctuations, is inversely proportional to the temperature. Fluctuations are purely quantum up to τ_P, and are classical beyond it. At a $T = 0$ quantum critical point, τ_P is infinite so the fluctuations are purely quantum. The Planck time-scale decreases with increasing temperatures and quantum fluctuations remain important roughly up to the Debye temperature, determined by phonon frequencies, that can be several hundred Kelvin. Thus, unlike its classical counterpart, the quantum critical region can have significant presence in a temperature-pressure phase diagram indicating the important influence of the zero-temperature critical point. From another perspective, quantum fluctuations are important for temperatures bounded by the condition

$$\hbar\omega \sim k_B T \quad (\omega \propto q^z) \quad \Rightarrow \quad \xi_Q \propto (\tau_P)^{1/z} \quad \text{and} \quad q_T \propto T^{\frac{1}{z}} \tag{2}$$

which, combined with the dispersion ($\omega \propto q^z$), leads to a corresponding quantum correlation length ξ_Q where z is the dynamical exponent; fluctuations are classical on length-scales greater than ξ_Q with a corresponding thermal momentum cutoff q_T for thermally activated modes. Therefore, for temperatures where ξ_Q is greater than the lattice spacing, the thermal correlation volume contains a quantum mechanical core on length-scales and time-scales determined by ξ_Q and τ_P; in momentum space the thermal wavevector q_T is a cutoff for classical fluctuations when their quantum counterparts are present [6], as we shall discuss shortly.

What defines the quantum critical region? It is crucial to note that temperature is *not* a simple tuning parameter at a quantum phase transition. Indeed T provides the low-energy cutoff for quantum fluctuations through the Planck time-scale τ_P so that temperature plays the role of a finite-size effect in time at a quantum critical point [4, 7]. The quantum critical region is defined by the interplay between the scale-invariant order parameter fluctuations and the temporal boundary conditions imposed by finite temperature; here a system's thermodynamic behavior depends on both space and time, observable experimentally with signatures distinct from its classical counterpart.

Can one see the coexistence of quantum and classical fluctuations in a simple example? Let us illustrate these concepts by considering the amplitude fluctuations of a one-dimensional harmonic oscillator (1d SHO) as a function of temperature whose variance is

$$\langle x^2 \rangle = \frac{\Omega}{\mathcal{K}}\Big(n_\Omega + \frac{1}{2}\Big) \tag{3}$$

where $n_\Omega = 1/\big(\exp(\Omega/T) - 1\big)$ is the Bose factor and we have set the constants $\hbar = k_B = 1$ (see Fig. 1). Here the important energy scales are the temperature T and the oscillator frequency Ω. If $T \gg \Omega$, then $n_\Omega \sim T/\Omega$ and the variance $\langle x^2 \rangle$ scales with T and Ω drops out completely. In this instance, the total variance results from purely classical (thermal) fluctuations. However for lower temperatures, specifically in the interval $0 \le T \le \Omega$, there is another contribution to $\langle x^2 \rangle$ due to quantum fluctuations. The total variance then becomes the sum of the quantum and classical components, where at $T = 0$ only the quantum component survives.

What does the behavior of a 1d SHO have to do with quantum phase transitions? Let me explain the conceptual connection. Order parameter fluctuations play an important role at phase transitions, and we can consider the variance of each of their Fourier components one at a time. Let us call each of these Fourier components a mode of wavevector q whose behavior can be mapped onto that of a simple harmonic oscillator of amplitude x with oscillator frequency Ω. At a continuous transition, the mode stiffness $\mathcal{K}$ vanishes for modes close to the ordering wavevector and the amplitude fluctuations diverge. If this occurs at $T \gg \Omega$, then the transition may be driven by essentially classical fluctuations. However at lower temperatures

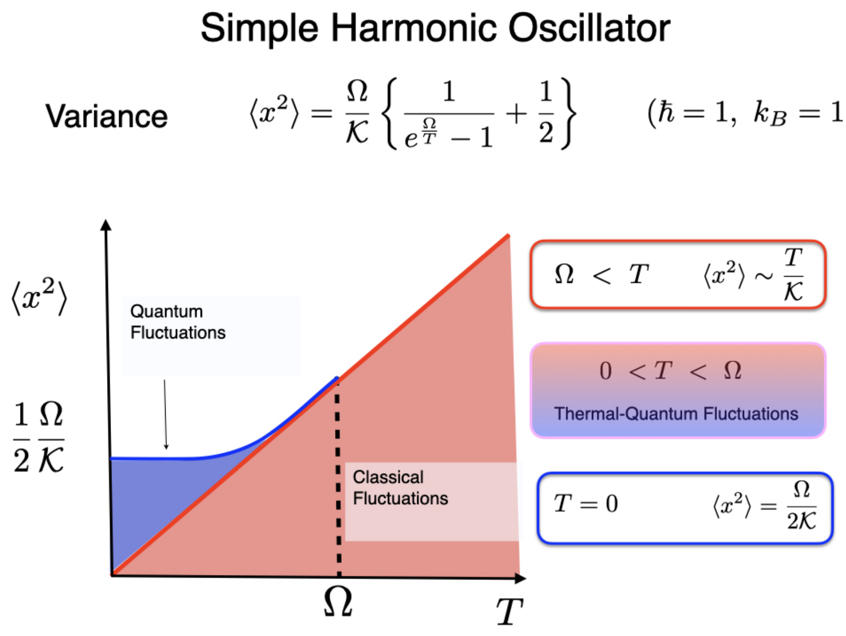

Fig. 1: *Amplitude of a simple harmonic oscillator with frequency Ω and stiffness $\mathcal{K}$ as a function of temperature.*

where $0 \leq T \leq \Omega$, both classical and quantum fluctuations are present and these "hybrid" fluctuations lead to behaviors and orderings distinct from those driven solely by their classical counterparts. Again $\mathcal{K}$ is zero at the ordering wavevector but now there are both quantum and classical contributions to $\langle x^2\rangle$. Of course at strictly $T = 0$ the fluctuations are purely quantum.

Why is "$d+z$" the effective dimension of a quantum critical system? Since for purely classical fluctuations, the amplitude of each mode of wavevector q depends only on the temperature, its statistical mechanical description involves d spatial dimensions. However when quantum fluctuations are present, both the mode frequency and T are important. More generally each mode has a power spectrum of frequencies that results in a statistical mechanical description involving the summation over both the wavevectors and the frequency. The number of dimensions associated with the dynamics is associated with the frequency-wavevector dispersion relation; then the overall effective dimensionality will be $D = d{+}z$, referring to d space and z time dimensions, where z is the dynamical exponent associated with the dispersion of the mode frequency.

Our focus here is on the temperature-behavior of observable quantities near a quantum critical point. Towards this goal, let us resume our discussion of order parameter fluctuations where we treated each Fourier mode as a simple harmonic oscillator of amplitude x with frequency Ω. The total variance in the mode amplitude is then

$$\langle x^2\rangle = \left(n_\Omega + \frac{1}{2}\right)\Omega\,\chi \tag{4}$$

where n_ω refers to the Bose function and $\chi = \frac{1}{\mathcal{K}} = \mathrm{Re}\,\chi_{\omega=0}$ where $\mathcal{K}$ is the stiffness. We recall that for a simple harmonic oscillator

$$\mathrm{Im}\,\chi_\omega = \frac{\pi}{2}\,\omega\,\chi\,\delta(\omega{-}\Omega) \qquad (\omega > 0) \tag{5}$$

so that we can rewrite (4) as

$$\langle x^2 \rangle = \frac{2}{\pi} \int_0^\infty d\omega \Big(n_\omega + \frac{1}{2} \Big) \, \mathrm{Im} \, \chi_\omega \, . \tag{6}$$

We note that this link between the variance of amplitude fluctuations and the imaginary part of the response, here derived for a simple harmonic oscillator, is actually a much more general result associated with the fluctuation dissipation (Nyquist) theorem [8].

We can generalize (6) to a sum of all wavevector q modes, for example, over the entire Brillouin zone. In anticipation of our discussion of polar quantum criticality, let us now transition to the amplitude of the scalar order parameter ϕ that is an electric dipole moment density. Then, following our previous line of reasoning, the variance of the amplitude fluctuations of the moment is

$$\big\langle \delta\phi^2 \big\rangle = \frac{2}{\pi} \sum_q \int_0^\infty d\omega \Big(n_\omega + \frac{1}{2} \Big) \, \mathrm{Im} \, \chi_\omega = \big\langle \delta\phi_T^2 \big\rangle + \big\langle \delta\phi_{ZP}^2 \big\rangle \tag{7}$$

where $\phi = \bar{\phi} + \delta\phi$, $\bar{\phi}$ is the average, $\big\langle \delta\phi \big\rangle = 0$ and

$$\mathrm{Im} \, \chi_{q\omega} = \frac{\pi}{2} \, \omega_q \, \chi \, \delta(\omega - \omega_q) \qquad (\omega > 0) \tag{8}$$

in the propagating limit where ω_q is the oscillator frequency of the mode of wavevector q, though of course more general power spectra are also possible.

We note that in (7) there are two contributions: (1) $\big\langle \delta\phi_T^2 \big\rangle$ that involves the Bose factor and is strongly temperature-dependent and (2) $\big\langle \delta\phi_{ZP}^2 \big\rangle$ due to zero-point fluctuations. Here we focus on $\big\langle \delta\phi_T^2 \big\rangle$ since it will be crucial in determining the temperature-dependence of any measured quantity. At high temperatures ($T \gg \omega$), $n_\omega \equiv T/\omega$ we obtain, by invoking causality in the form of the Kramers-Kronig relations, a generalized equipartition theorem

$$\big\langle \delta\phi_T^2 \big\rangle \approx T \sum_{q < q_{BZ}} \chi_q \qquad (T \gg \omega_q \text{ for } q < q_{BZ}) \tag{9}$$

where all the modes up to the Brillouin wavevector q_{BZ} are excited; here the dynamics drop out completely of the classical equilibrium description. We note that in (9) we have a d-dimensional wavevector summation over the Brillouin zone that implies a d-dimensional theory in real space. Once quantum fluctuations are important ($T \ll \omega$), $n_\omega \approx e^{-\omega/T}$ and the dynamics remain. Now the modes will be classical up to a thermal wavevector cutoff (q_T) determined by quantum mechanics and the dispersion (see Fig. 2). More specifically the relevant wavevectors are the Brillouin zone (q_{BZ}) and the thermal (q_T) wavevectors, where the latter's temperature-dependence, determined by the condition $\omega \sim T$ and the dispersion $\omega \propto q^z$, is $q_T \propto T^{\frac{1}{z}}$; we note that $1/q_T$ is a generalized deBroglie wavelength that corresponds to the usual free-particle case when $z = 2$. We emphasize that the smaller of the two wavevector scales, q_T and q_{BZ}, serves as a cutoff for the classical fluctuations. If $q_T < q_{BZ}$ then not all the modes in the Brillouin zone are thermally excited; in this case the dynamical exponent enters via q_T and thus quantum fluctuations contribute to the variance of the order parameter fluctuations. Applying these ideas to (6) and again invoking Kramers-Kronig relations, we obtain

$$\langle \delta\phi_T^2 \rangle \approx T \sum_{q < q_T} \chi_q \qquad (T \gg \omega_q \text{ for } q < q_{BZ}). \tag{10}$$

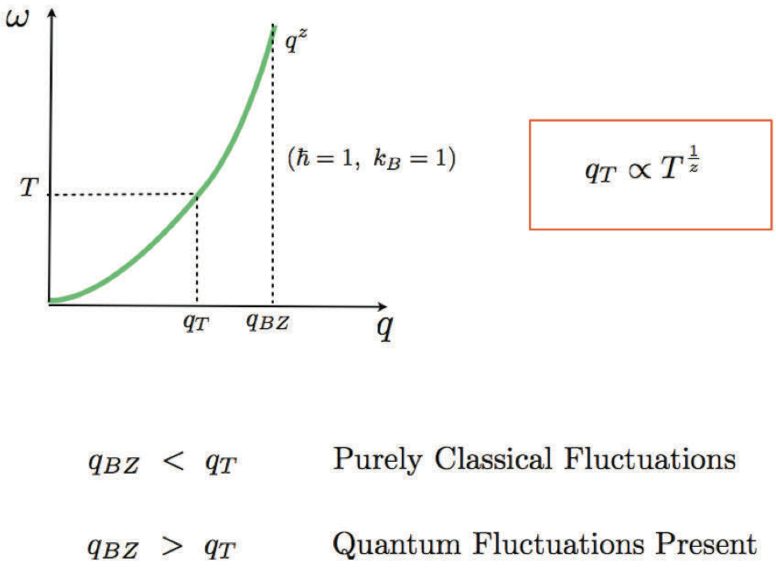

Fig. 2: *Schematic of the dispersion and the important wavevectors associated with the presence of classical and quantum fluctuations.*

Can we please use this approach to calculate a measurable quantity? Using a Landau-Ginzburg approach to phase transitions combined with (9) and (10), we can related the variance $\langle \delta\phi_T^2 \rangle$ to the susceptibility χ, an observable quantity [6]; though this is currently a general discussion, we note that this treatment is appropriate for polar materials [9]. Since

$$\chi_q^{-1} \propto q_\xi^2 + q^2 \quad \Rightarrow \quad \lim_{q \to 0} \chi^{-1} \propto q_\xi^2 \tag{11}$$

where q_ξ is the inverse (classical) correlation length; we note that the latter is often denoted as κ in the literature, but we will not use this notation here since κ will be used later for other purposes. We recall that Landau theory is a symmetry-based description of macroscopic properties near a phase transition. This coarse-graining procedure ensures that the main effects of zero-point fluctuations are absorbed in the Landau coefficients, and that thermal effects appear through fluctuations of the order parameter field coarse-grained over $1/q_T$. We will assume that this scale is large enough so that a Taylor expansion of the free energy is still reasonable for our applications.

The Landau free energy density for a system with moment density ϕ and conjugate field $\mathcal{E}$ is

$$f = \frac{1}{2}\alpha\phi^2 + \beta\frac{1}{4}\phi^4 + \frac{1}{2}\gamma\left|\nabla\phi\right|^2 - \mathcal{E}\phi \tag{12}$$

where $\alpha \to 0$ at the transition and β and γ are constants. Minimizing this free energy with respect to the order parameter ϕ, we obtain

$$\mathcal{E} = \alpha\phi + \beta\phi^3 - \gamma\nabla^2\phi. \tag{13}$$

In order to obtain $\langle \delta\phi^2 \rangle$, we follow the standard prescription of adding a random (Langevin) field to $\mathcal{E}$; next we average over the random fluctuations in (13) using $\phi \to \bar{\phi} + \delta\phi$ where $\bar{\phi}$ is the average and $\langle\phi\rangle = 0$ to obtain to lowest order

$$\mathcal{E} = \big(\alpha + 3\beta\langle\delta\phi^2\rangle\big)\bar{\phi} - \gamma\nabla^2\bar{\phi} \tag{14}$$

where we note that the variance emerges from the anharmonic cubic contribution in (13). In the limit of small $\bar{\phi}$ and $\mathcal{E}$, we can Fourier transform this expression to obtain

$$\chi_q^{-1} = \big(\alpha + 3\beta\langle\delta\phi^2\rangle\big) + q^2. \tag{15}$$

If we consider the $q \to 0$ limits of both (11) and (15), retaining the most temperature-dependent terms, we obtain

$$\lim_{T\to 0} q_\xi^2 \propto \langle\delta\phi_T^2\rangle \tag{16}$$

where we have assumed a quantum critical point (QCP) so that $\alpha \to 0$ as $T \to 0$. We note that (16) is only valid near a $T_c = 0$ phase transition since for a nonzero T_c there are additional terms proportional to $T_c \neq 0$ so that this expression of proportionality is no longer valid [6].
We can now combine (10), (11) and (16) to determine the temperature-dependence of the susceptibility near a quantum critical point, obtaining the expression

$$q_\xi^2 \propto \sum_{q<q_T} \frac{T}{q_\xi^2 + q^2} \approx T \int_{q_\xi}^{q_T} \frac{q^{d-1}\, dq}{q^2} \approx T\, q_T^{d-2}\left(1 - \left(\frac{q_\xi}{q_T}\right)^{d-2}\right) \tag{17}$$

where, using $q_T \propto T^{1/z}$, we would like to disregard the q_ξ/q_T term on the right-hand side of (17) so that we can write

$$\chi^{-1} \propto q_\xi^2 \propto T^{\frac{(d+z-2)}{z}} \qquad \Rightarrow \qquad \chi^{-1} \propto T^2 \qquad (d = 3, z = 1). \tag{18}$$

where we anticipate the situation for $d = 3$ quantum paraelectrics with $z = 1$ ($\omega \propto q$). We note that this situation ($d{+}z = 4$) is marginal, so technically there will be logarithmic corrections though they are not observed experimentally [6, 10]. We take a moment to note that (18) is distinct from the Curie behavior ($\chi^{-1} \propto T$) observed in the approach to the classical transition.
When is this assumption valid ? We can address this question by rearranging (17) to yield

$$\left(\frac{q_\xi}{q_T}\right)^2 \propto T^{\frac{(d+z-4)}{z}}\left(1 - \left(\frac{q_\xi}{q_T}\right)^{d-2}\right) \tag{19}$$

From (19) we see that

$$\lim_{T\to 0}\left(\frac{q_\xi}{q_T}\right) = 0 \qquad \text{if } d_{\mathit{eff}} = d{+}z > 4; \tag{20}$$

in this case (18) is true, and no further fluctuation effects need to be considered; there will be weak logarithmic corrections for $d{+}z = 4$. The upper critical dimension of this quantum theory is thus $D^u = 4{-}z$. In other words the inclusion of dynamics in quantum critical phenomena reduces the upper critical dimension from $d^u = 4$ in the purely classical limit; from this standpoint in experiment we are often above the upper critical dimension near a quantum phase transition in real materials.

1.2 Polar quantum criticality?

Polar materials undergo inversion symmetry-breaking transitions to phases characterized by polar space groups. Insulating ferroelectrics are among the simplest polar materials; they host spontaneous polarizations that can be switched by electric fields of practical magnitude. Furthermore ferroelectrics are in a class of polar materials whose electromechanical properties are important for transducers, passive memory components and infrared sensors. As a result of their many practical applications, they are predominantly studied at room temperature [11–15]. **Can these functional materials "teach" us about some fundamental physics?** Indeed historically ferroelectrics played an important role in our collective understanding of classical critical phenomena in the pioneering work of A.I. Larkin and D.E. Khmelnitskii (LK) [16, 17]. In the sixties it was known that Landau theory breaks down for the Ising model in four or fewer dimensions, and that this model's universal behavior was equivalent to that of a ϕ^4 field theory. Exploiting this link, LK applied the renormalization methods of quantum electrodynamics to the ϕ^4 model in $d = 4$, finding clear singularities in the exponents of the specific heat and other quantities. Finally they noted that the four-dimensional Ising model is realized in a three-dimensional uniaxial ferroelectric, and indeed their results were confirmed experimentally, first in a dipolar Ising ferromagnet [18] and then later in a uniaxial ferroelectric [19].

Let us take a moment to get a flavor for the LK argument about the effective dimensionality of a uniaxial ferroelectric. Ferroelectrics are well-described by $O(n)$ (spherical) models where $d^u = 4$ is the upper critical dimension; this of course means that interactions are relevant for $d < d^u$, whereas mean-field (Landau) theory is fine for $d > d^u$ and $d^u = 4$ is marginal. Let us assume that all dipoles are in the z direction with a dipole potential $W(q) \propto q_z^2/q^2$ so that the resulting action is

$$S = \int \frac{d^3q}{(2\pi)^d} \left|\phi_q\right|^2 \left(q^2 + \frac{q_z^2}{q^2} + \Delta^2\right) \tag{21}$$

where Δ refers to its gap. If we assume

$$q^2 \approx q_x^2 + q_y^2 = q_\perp^2 \tag{22}$$

and apply the simple scaling expressions

$$x \to bx, \quad q_\perp \to \frac{q_\perp}{b}, \quad q_z \to \frac{q_z}{b^k}(b, k{>}1) \tag{23}$$

then we obtain

$$S \approx \int \frac{d^2q_\perp dq_z}{b^{2+k}} \left|\phi_q\right|^2 \left(\frac{q^2}{b^2} + \frac{q_z^2}{q^2}\frac{b^2}{b^{2k}} + \Delta^2\right). \tag{24}$$

We see that, in order for (24) to have the same form as (21), we require

$$2{-}2k = -2 \quad \to \quad k = 2 \tag{25}$$

so that q_z "counts" for effective two dimensions. In this sense the effective dimension of the uniaxial ferroelectric is $d_{\mathit{eff}} = d{+}1$ so that a three-dimensional uniaxial ferroelectric has an effective dimension of four and is thus a setting to test predictions for the upper critical dimension of the Ising model. More specifically, in Landau theory the specific heat has only a discontinuity ($\alpha = 0$) and LK were able to calculate the critical logarithmic corrections for the marginal case $d^u = 4$. The LK results were the first exact calculations of non-mean field exponents in an experimentally realizable systems, that subsequent measurements confirmed [18, 19].

Fine, but what can polar materials bring to the field of quantum criticality? The emergence of complex states of quantum matter in the neighborhood of zero-temperature phase transitions suggests that such quantum phenomena should be explored in a variety of settings [6]. Paraelectric (disordered) materials in close proximity to polar quantum critical points can be viewed as "economy" quantum critical systems whose propagating dynamics and few degrees of freedom allow for detailed interplay between analytic approaches, first-principles approaches and laboratory measurements. From an experimental standpoint, the pressure-sensitivity of polar transition temperatures is very appealing. For example, in order to cover a 300 K range in magnetic T_c's, hundreds of kilobars must be applied, whereas in ferroelectrics the same temperature range can be covered with an order of magnitude less pressure. Furthermore the electric field as another "tuning knob" is significantly easier to apply than is its magnetic counterpart. Finally the dispersion $\omega \propto q$ in most ferroelectrics so that $z = 1$ which means that these materials can be studied and probed below, at and above their upper critical dimension in contrast to magnetic materials where z is typically of higher values. Additional degrees of spin and charge can be added to these polar materials, leading to rich phase behavior mostly as yet to be explored.

How old is the study of polar quantum criticality? There has been tremendous "historical entanglement" between the fields of ferroelectrics and criticality, beginning with the calculation of non-mean field exponents at marginal dimensionality that we have just discussed. Similarly the transverse-field Ising model, one of the simplest settings for a quantum critical point, was first developed to describe an order-disorder transition in the ferroelectric KH_2PO_4 [20]. Indeed there have been several "waves" of interest in low-temperature polar materials and here, for the sake of completeness and compactness, I refer interested readers elsewhere to read about these developments [6, 21].

For our purposes, let us consider a paper in 1971 by A.B. Rechester where he calculates the temperature-dependence of the dielectric susceptibility (χ) near a continuous polar phase transition [22]; to do this, he employs a parquet approximation, valid because he is working in a marginal dimension, to obtain $\chi^{-1} \propto T^2$. The key question here is whether there is a simpler way to get this result. First, we note that in our previous treatment relating $\langle \delta\phi_T^2 \rangle$ to $\chi(T)$, we obtained this same result in (18), setting $d = 3$ and $z = 1$. Strictly speaking this approach is only valid for $d+z > 4$, but since we are in the marginal dimension ($d+z = 4$) we are using it assuming, it turns out correctly, that the logarithmic corrections will not be important experimentally. We should add that long-range dipolar interactions have been neglected as their main effect near a QCP is to produce a gap in the longitudinal fluctuations; the transverse fluctuations however remain critical [16, 23].

We have already discussed the fact that temperature is *not* a tuning parameter in the vicinity of a quantum phase transition, but rather plays the role of a *finite-size boundary effect* on time. Indeed we can adapt finite-size scaling (FSS) approaches near classical phase transitions to study

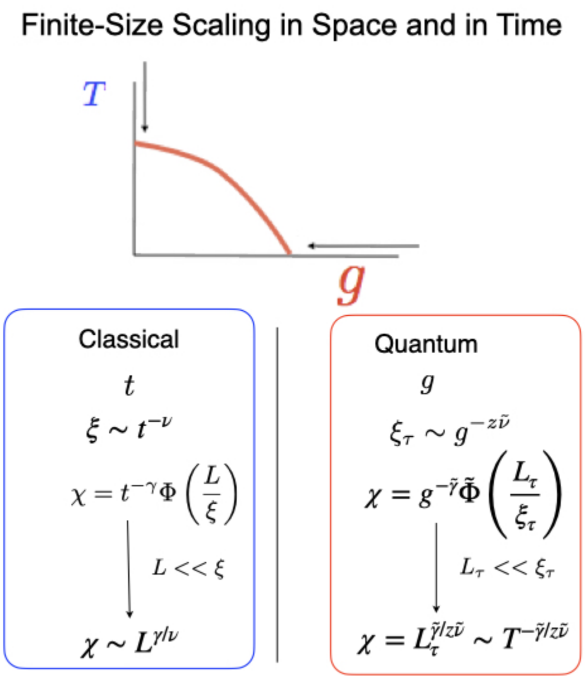

Fig. 3: *Schematic of finite-size scaling at classical and at quantum critical points.*

the influence of temperature near a QCP. This scaling approach is strictly valid in dimensions for $d+z < 4$, so again we will argue that because $d = 3$ quantum critical paraelectrics are marginal ($d+z = 4$), the scaling results are valid up to logarithmic corrections. Following the standard FSS procedure [24], we impose boundaries on the system near its critical point. For a classical system with tuning parameter $t = T/(T-T_c)$ and correlation length $\xi \sim t^{-\nu}$, we confine it in a box of size L and then write the standard FSS scaling form

$$\chi \sim t^{-\gamma}\Phi\left(\frac{L}{\xi}\right) \sim t^{-\gamma}\Phi\left(\frac{L}{t^{-\nu}}\right). \tag{26}$$

For $L \ll \xi$, we must have $\chi = \chi(L)$ and assuming that $\Phi(x) \sim x^p$, we obtain

$$\chi \sim t^{-\gamma}\left(\frac{L}{\xi}\right)^p \sim t^{-\gamma}\left(\frac{L}{t^{-\nu}}\right)^{\frac{\gamma}{\nu}} \sim L^{\frac{\gamma}{\nu}}. \tag{27}$$

Now let us apply the analogous finite-size scaling to time near a quantum critical point. We note that

$$\xi \sim g^{-\tilde{\nu}} \quad \rightarrow \quad \xi_\tau \sim g^{-z\tilde{\nu}} \qquad (\omega \propto q^z \rightarrow [\xi_\tau] = [\xi^z]) \tag{28}$$

where g is the tuning parameter of the quantum phase transition, ξ_τ is the correlation time, and we write the exponents for the quantum transition with a tilde (e.g. $\tilde{\nu}$) to distinguish them from their classical counterparts (ν); we now have the boundary cutoff in time $L_\tau = \tau_P = \hbar/(k_B T)$ that is inversely proportional to temperature. Then the scaling expression for the susceptibility is

$$\chi \sim g^{-\tilde{\gamma}}\Phi\left(\frac{L_\tau}{\xi_\tau}\right) \sim g^{-\tilde{\gamma}}\Phi\left(\frac{L_\tau}{g^{-z\tilde{\nu}}}\right). \tag{29}$$

Then for $L_\tau \ll \xi_\tau$ we must have $\chi = \chi(L_\tau)$ so that we obtain

$$\chi \sim g^{-\tilde{\gamma}} \left(\frac{L_\tau}{\xi_\tau}\right)^{p} \sim g^{-\tilde{\gamma}} \left(\frac{L_\tau}{g^{-z\nu}}\right)^{\frac{\tilde{\gamma}}{z\tilde{\nu}}} \sim L^{\frac{\tilde{\gamma}}{z\tilde{\nu}}} \sim T^{-\frac{\tilde{\gamma}}{z\tilde{\nu}}} \tag{30}$$

at finite temperature near a polar QCP; here $z = 1$, $\tilde{\nu} = \frac{1}{2}$ and $\tilde{\gamma} = 1$ so that $\tilde{\gamma}/(z\tilde{\nu}) = 2$ and $\chi^{-1} \propto T^2$.

In summary, exploiting the fact that the $d = 3$ quantum critical paraelectrics reside in its marginal dimension, we have used both mean-field and scaling arguments to recover the $1/T^2$ behavior of the dielectric susceptibility near a polar quantum critical point that was previously derived using more technical diagrammatic, large N and renormalization group methods [6]; it has also been observed experimentally, validating our neglect of logarithmic corrections [6,10].

The Rundown. So why should we explore polar quantum criticality? Of course in our collective quest for universality, it is important to study quantum phase transitions in many different settings. Furthermore polar quantum critical materials offer the following opportunities:

- Simple “economy” examples with few degrees of freedom and non-dissipative dynamics.
- Their linear dispersion ($z = 1$) means that they can be studied at, below and above their upper critical dimension allowing for a detailed interplay between theory and experiment.
- Additional degrees of freedom like spin and charge can be added systematically.

However there are also outstanding conceptual questions that include

- How can systems that display classical first-order phase transitions display quantum criticality?
- Can metals near polar quantum criticality host novel strongly correlated phases?

These issues motivate our discussion in the subsequent sections of this chapter.

2 Quantum annealed criticality

2.1 The challenge: classical first-order transitions!

Let us start simply with polar insulators. At finite temperatures and ambient pressure these materials typically display first-order transitions due to strong electromechanical coupling [11–13]; yet in many cases their dielectric susceptibilities indicate the presence of pressure-induced quantum criticality associated with zero-temperature quantum phase transitions [6,10]. The interplay of first-order phase transitions with quantum fluctuations is known to lead to exotic quantum states near quantum critical points In many metallic quantum ferromagnets, coupling of the local magnetization to the low-energy particle-hole excitations transforms a high-temperature continuous transition into a low-temperature discontinuous one, and the resulting classical tricritical points have been observed in many systems [25].

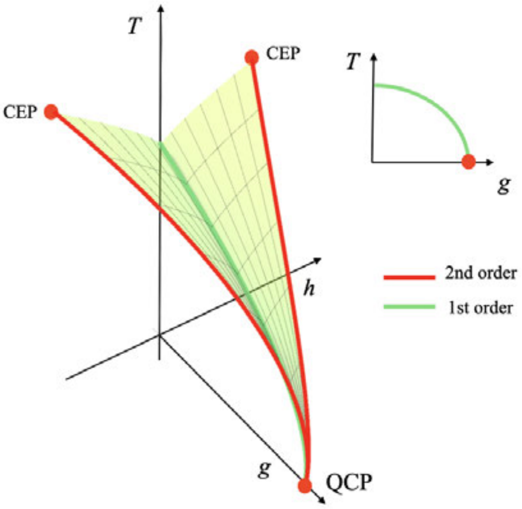

Fig. 4: *Temperature (T)-Field (h)-Tuning Parameter (g) Phase Diagram with a sheet of first-order transitions bounded by critical end-points (CEP) terminating at a zero temperature quantum critical point (QCP); here g tunes the quantum fluctuations and h is the field conjugate to the order parameter. Inset: Temperature-Tuning Parameter "slice" indicating a line of classical phase transitions ending in a "quantum annealed critical point" where the underlying order parameter criticality is restored by zero-point fluctuations.*

In this section, we will discuss a theoretical basis for the observation that many polar insulators display quantum critical behavior despite hosting classical first-order transitions. Experimentally it is known that classical ferroelectric transitions, for example in $BaTiO_3$, are continuous when clamped and become first-order when unclamped [12]. In magnetic systems there is a mechanism, studied by A.I. Larkin and S.A. Pikin (LP), where strain-energy density coupling is known to drive discontinuous transitions in compressible systems that are critical when clamped [26]. We will adapt this Larkin-Pikin approach to (compressible) polar systems and ask what happens in the approach to zero temperature. In a nutshell, we will show that as the temperature is lowered, quantum fluctuations reduce the amplitudes of their thermal counterparts, weakening the first-order transition and "annealing" the system's elastic response, ultimately resulting in a $T = 0$ "quantum annealed" critical point. As we will see, this is because fluctuations at finite temperature are more singular than at $T = 0$ where the effective dimension is higher than in the classical case. The general temperature (T)-tuning parameter (g)-field (h) phase diagram that emerges is presented in Fig. 4 where the field (h) is conjugate to the order parameter. A flavor of this theoretical underpinning to the observed behavior will be given here where details are available elsewhere for the interested reader [27].

2.2 Adaptation of the Larkin-Pikin approach

Before we adapt it, what is the classical Larkin-Pikin approach? At a first-order transition the quartic mode-mode coupling of the effective action becomes negative. One mechanism for this phenomenon, studied by Larkin and Pikin [26] (LP), involves the interaction of strain with the fluctuating energy density of a critical order parameter. LP found that a diverging specific heat in the "clamped" (fixed volume) system leads to a first-order transition in the unclamped system at constant pressure. The Larkin-Pikin criterion [26] for a first order phase transition is

$$\kappa \lesssim \frac{\Delta C_V}{T_c}\left(\frac{dT_c}{d\ln V}\right)^2 \tag{31}$$

where V is the volume, ΔC_V is the singular part of the specific heat capacity in the clamped critical system, T_c is the transition temperature and $dT_c/d\ln V$ is its volume strain derivative. The effective bulk modulus κ is defined by $\kappa^{-1} = K^{-1} - \big(K{+}4\mu/3\big)^{-1}$ where K and μ are the bare bulk and the shear moduli in the absence of coupling between the order parameter and strain; physically $\kappa \sim K c_L^2/c_T^2$ where c_L and c_T are the longitudinal and the transverse sound velocities. More specifically, LP considered the coupling

$$\mathcal{L}_I = \lambda e_{ll}(\vec{x}\,)\psi^2(\vec{x}\,) \tag{32}$$

between the volumetric strain field e_{ll} and the squared amplitude ψ^2 of the critical order parameter. In a critical system, the singular fluctuations of the energy density are directly proportional to ψ^2; thus (32) corresponds to a strain-energy coupling. Naively (32) is expected to induce a short-range attractive order parameter interaction. LP showed that (32) also leads to an anomalous long-range interaction between order parameter fluctuations; careful integration, as we shall discuss, over the elastic degrees of freedom results in a qualitative transformation of the action

$$S \longrightarrow S - \frac{\lambda^2}{2T\kappa}\left[\frac{1}{V}\int d^3x \int d^3x'\, \psi^2(\vec{x}\,)\psi^2(\vec{x}')\right] \quad \text{with} \quad \frac{1}{\kappa} = \left(\frac{1}{K} - \frac{1}{K+4\mu/3}\right) \tag{33}$$

where μ is the shear modulus [26, 27]. This long-range interaction is finite if $\mu > 0$, i.e., if the medium is a solid. LP showed that this induced long-range interaction in (33) generates positive feedback to the tuning parameter, leading to a multi-valued free energy surface and a resulting first order phase transition.

To summarize the situation more conceptually, we note that in the LP scenario the strain-energy density coupling results in a renormalized effective bulk modulus

$$\tilde{\kappa} \equiv \kappa - \Delta\kappa \tag{34}$$

in the unclamped system where the shift in the effective bulk modulus is related to the singular part of the (clamped) specific heat

$$\Delta\kappa = \frac{\Delta C_V}{T_c}\left(\frac{dT_c}{d\ln V}\right)^2 . \tag{35}$$

The condition for a macroscopic instability, and hence a first-order transition, is when the renormalized bulk modulus is negative

$$\kappa - \Delta\kappa = 0 \quad \Rightarrow \kappa \lesssim \frac{\Delta C_V}{T_c}\left(\frac{dT_c}{d\ln V}\right)^2 \tag{36}$$

and we see that we have recovered the LP criterion (31). Here we note that it is the divergence of $\Delta\kappa$ that is crucial to this result.

The LP criterion in its current form is not appropriate for T=0! When we generalize the Larkin-Pikin approach to include quantum zero-point fluctuations of the energy density, we show that it is the divergence of the energy fluctuations, both quantum and classical, that is crucial for the LP mechanism [27]. When we sum over all possible spacetime configurations in the action, we obtain a generalized LP criterion

$$\kappa \lesssim \left(\frac{dg_c}{d\ln V}\right)^2 \chi_{\psi^2} \tag{37}$$

where

$$\chi_{\psi^2} = \int_0^\beta d\tau \int d^3x \, \langle \delta\psi^2(\vec{x},\tau)\, \delta\psi^2(0)\rangle \tag{38}$$

is the space-time average of the quantum and thermal "energy" fluctuations, $\beta = \frac{1}{k_B T}$ and g is the tuning parameter for the quantum phase transition, with the convention that $g_c(T=0)=0$. At zero temperature, this expression extends the original LP criterion (36) to quantum phase transitions. As we will discuss further shortly, at finite temperatures, the critical quantum and classical tuning parameters are related by $g_c(T_c) = uT_c^{1/\tilde{\Psi}}$, where $\tilde{\nu}$ and z are the exponents associated with the quantum correlation length and the dynamics respectively and $\tilde{\Psi} = \tilde{\nu}$ is called the shift exponent [4]; therefore $d\ln g_c = \frac{1}{\tilde{\Psi}} d\ln T_c$ and the LP criterion becomes

$$\kappa - \Delta\kappa = 0 \quad \Rightarrow \quad \kappa \lesssim \left(\frac{dT_c}{d\ln V}\right)^2 \overbrace{\left(\frac{g}{2T_c}\right)^2 \chi_{\psi^2}}^{\Delta C_V/T_c}, \tag{39}$$

where we have identified $\Delta C_v/T_c = (g/2T_c)^2\chi_{\psi^2}$ with the specific heat capacity. In this way, we see that the generalized Larkin Pikin equation encompasses the original criterion (31) in addition to being applicable at low temperatures [27]. Due to their additional time dimension, quantum fluctuations are typically less singular than are their classical counterparts. As the temperature is lowered, the correlation volume of the zero-point fluctuations grows, reducing the amplitudes of the singular thermal fluctuations in the clamped system. The induced first order transition thus becomes progressively weaker with decreasing temperature, leading to a continuous "quantum annealed" transition at $T=0$.

Is there a simple way to get a sense of the quantum Larkin-Pikin result? We have seen that the LP criterion can be reexpressed as

$$\kappa - \Delta\kappa = 0 \tag{40}$$

We can use a scaling argument to get a flavor for the key quantum LP result. Let us rewrite (39) as

$$\tilde{\kappa} = \kappa - \Delta\kappa = \kappa - \gamma^2 \chi_{\psi^2} \tag{41}$$

with

$$\chi_{\psi^2} = \int_0^\beta d\tau \int d^dx \, \langle \delta\psi^2(\vec{x},\tau)\, \delta\psi^2(0)\rangle, \tag{42}$$

where we have generalized the expression (38) to d spatial dimensions. If we make the Gaussian approximation $\langle \delta\psi^2(\vec{x}\,)\,\delta\psi^2(0)\rangle \approx \big(\langle \delta\psi(\vec{x}\,)\,\delta\psi(0)\rangle\big)^2$, then the zero-temperature limit of χ_{ψ^2} is

$$\lim_{T\to 0}\chi_{\psi^2} \approx \int d\tau d^dx \big(\langle \delta\psi(\vec{x}\,)\,\delta\psi(0)\rangle\big)^2 = \int \frac{d\nu}{2\pi}\frac{d^dq}{(2\pi)^d}\big(\chi_\psi(\vec{q},\nu)\big)^2 \tag{43}$$

where we have Fourier transformed into momentum space, and $\chi_\psi(\vec{q},\nu) = \langle \delta\psi(-q)\,\delta\psi(q)\rangle$, the order parameter susceptibility, is the space-time Fourier transform of the correlator $\langle \psi(\vec{x}\,)\psi(0)\rangle$. It then follows that

$$\lim_{T\to 0}\varDelta\kappa \propto \int dq\,d\nu\,q^{d-1}\big(\chi_\psi(\vec{q},i\nu)\big)^2. \tag{44}$$

To examine how this quantity behaves in the approach to the quantum critical point of the clamped system, we can use dimensional power-counting. Since $[\chi] = \left[\frac{1}{q^2}\right]$ and $[\nu] = [q^z]$,

$$\lim_{T\to 0}[\varDelta\kappa] = \frac{[q^{d+z}]}{[q^4]} \sim \xi_Q^{4-(d+z)}$$

where we have replaced $[q^{-1}] = [\xi_Q]$, the quantum correlation length. As the quantum critical point of the clamped system is approached, $\xi_Q \to \infty$, so that the quantum corrections to κ are non-singular for $d{+}z > 4$; in this case $\varDelta\kappa$ does not diverge so a continuous transition is possible. Of course for three-dimensional polar insulators with a linear dispersion $d{+}z = 4$ is marginal, so there will be logarithmic corrections; this suggests that the quantum phase transition will be very weakly first-order which may be indistinguishable from continuous in experiment. Basically here we are arguing that if the $T = 0$ compressible system lies above its upper critical dimension, the line of first-order transitions can end in a “quantum annealed critical point” where zero-point fluctuations restore the underlying criticality of the order parameter.

How can this scaling argument be substantiated? This scaling logic can be supported by a more technical argument which we will now outline; here we consider the simplest case: isotropic elasticity and a scalar order parameter ψ. The action, $\mathcal{S}[\psi,u]$ is then a function of ψ and u, the lattice displacement; it has three distinct components corresponding to the physics of ψ, a description of the elastic degrees of freedom and finally the strain-energy density coupling with strength λ [26,27]. The generalized LP argument is subtle and proceeds in three steps:

- Careful integration of the $q = 0$ and $q \neq 0$ Gaussian strain contributions distinctly.
- Identification of an expression relating the unclamped and the clamped free energies.
- Use of crossover scaling [4] to determine $T \to 0$ phase behavior when both classical and quantum critical fluctuations are present.

Here the key first step is to integrate out the Gaussian elastic degrees of freedom from the action

$$Z = \int \mathcal{D}[\psi]\int \mathcal{D}[u]\,e^{-\mathcal{S}[\psi,u]} \quad\to\quad Z = \int \mathcal{D}[\psi]\,e^{-S[\psi]} \tag{45}$$

where the actions involve integrals over spacetime. This procedure must be performed with some care because of the special role of boundary normal modes. In a solid of volume L^3, the normal modes can be separated into two components according to their wavelength λ: sound waves with $\lambda \ll L$ and boundary waves with $\lambda \sim L$. From another perspective, we can understand this distinction by noting that the strain only couples to the longitudinal modes; however at $q = 0$ there is no distinction between transverse and longitudinal modes so this case must be treated separately from the finite-q situation.

The generalized Larkin-Pikin action, following careful integration of the Gaussian strain to include both thermal and quantum fluctuations, is

$$S[\psi] = S_L[\psi, \tilde{g}, b^*] - \frac{\lambda^2}{2}\left(\frac{1}{K} - \frac{1}{K + 4\mu/3}\right)\frac{1}{\beta V}\int d^4x \int d^4x'\, \psi^2(\vec{x}\,)\,\psi^2(\vec{x}'). \tag{46}$$

with the local contribution

$$S_L[\psi, \tilde{g}, b^*] = \int d^4x\, \mathcal{L}_L[\psi, \tilde{g}, b^*] = \int d^4x \left(\frac{1}{2}(\partial_\mu \psi)^2 + \frac{\tilde{g}}{2}\psi^2 + \frac{b^*}{4!}\psi^4\right) \tag{47}$$

where

$$b^* = b - \frac{12\lambda^2}{K + 4\mu/3}. \tag{48}$$

(46) is a $d{+}z$-dimensional generalizations of the classical LP action where all spacetime configurations are summed. The essence of the Larkin-Pikin effect is the appearance of a distance-independent interaction between the energy densities of the order parameter field that appears in (46). Since the Larkin-Pikin argument is valid for arbitrarily small coupling λ, the perturbative $O(\lambda^2)$ renormalization of the short-range interaction in (48) becomes negligibly small in this limit and can be safely neglected.

The Larkin-Pikin term in (46) is a kind of "elastic anomaly", whereby the integration over boundary modes generates nonlocal interactions between energy densities of the order parameter similar in form to (42). Indeed this distance-independent term in (46) can be written as the spacetime volume average of the energy density

$$\Psi^2 \equiv \frac{1}{\beta V}\int d^4x\, \psi^2(x) \tag{49}$$

that is an intensive variable with small fluctuations about its thermal average $\langle \Psi^2 \rangle$. We perform a Hubbard-Stratonovich transformation of the spacetime-independent interaction in (46)

$$-\frac{\lambda^2}{2}\frac{1}{\kappa}\frac{1}{\beta V}\int d^4x \int d^4x'\, \psi^2(\vec{x}\,)\,\psi^2(\vec{x}') \to \int d^4x \left((\lambda\phi)\psi^2(\vec{x}\,) + \frac{\kappa}{2}\phi^2\right) \tag{50}$$

where we have introduced an auxiliary "strain" field

$$\phi = -\frac{\lambda\langle \Psi^2 \rangle}{\kappa} \tag{51}$$

that is independent of space and time. Then we may write

$$\mathcal{Z} = e^{-\beta\tilde{\mathcal{F}}} = e^{-\tilde{S}(\phi)} = \int \mathcal{D}\psi\, e^{-S[\psi,\phi]}\,, \tag{52}$$

where $\tilde{\mathcal{F}}$ is the free energy of the unclamped system; here

$$S[\psi,\phi] = \int d^4x \left(\mathcal{L}_L(\psi,\tilde{g}) + \lambda\phi\psi^2 + \frac{\kappa}{2}\phi^2\right) \tag{53}$$

that can be reexpressed as

$$S[\psi,\phi] = \int d^4x\, \mathcal{L}_L(\psi,\tilde{g}{+}2\lambda\phi) + \frac{\kappa V\beta}{2}\phi^2\,. \tag{54}$$

In their original classical treatment, Larkin and Pikin observed that the main effect of elasticity in the unclamped system is to make a parametrized shift of the original tuning parameter to a parametrized variable X; we can see this in our generalized LP equations. From (52) and (54), we can write the free energy for our unclamped system as

$$\tilde{\mathcal{F}}[\phi,\tilde{g}] = \mathcal{F}[X] + \frac{\kappa V}{2}\phi^2 \tag{55}$$

where $\mathcal{F}$ is the free energy of the clamped system and

$$X = \tilde{g} + 2\lambda\phi \tag{56}$$

indicates the shift of the tuning parameter $\tilde{g}$ due to the presence of energy fluctuations. Now

$$\frac{1}{V}\frac{\partial\mathcal{F}}{\partial X} = \frac{\langle\Psi^2\rangle}{2} \tag{57}$$

so that

$$\phi = -\frac{\lambda\langle\Psi^2\rangle}{\kappa} = -\frac{2\lambda}{V\kappa}\left(\frac{\partial\mathcal{F}}{\partial X}\right) \equiv -\frac{2\lambda}{V\kappa}\,\mathcal{F}'[X] \tag{58}$$

where we have defined $\mathcal{F}'[X] \equiv \left(\frac{\partial\mathcal{F}}{\partial X}\right)$ for simplicity. Therefore

$$\tilde{\mathcal{F}} = \mathcal{F}[X] + \frac{2\lambda^2}{V\kappa}\big(\mathcal{F}'[X]\big)^2 \tag{59}$$

and

$$X = \tilde{g} - \frac{4\lambda^2}{V\kappa}\mathcal{F}'[X]. \tag{60}$$

Let us define

$$\tilde{f} \equiv \frac{2\lambda}{V\kappa}\tilde{\mathcal{F}} \quad \text{and} \quad f \equiv \frac{2\lambda}{V\kappa}\mathcal{F}\,. \tag{61}$$

Here we recall that the integrals in the action involve an integral over time, $\int d^4x = \int_0^\beta d\tau \int d^3x$ where $\beta = 1/T$ is a boundary term, so that these free energies are determined at fixed temperature. Therefore the two equations describing the unclamped system are

$$\tilde{f} = f[X,T] + \lambda\big(f'[X,T]\big)^2 \tag{62}$$

and

$$\tilde{g} = X + 2\lambda f'[X,T] \tag{63}$$

which have to be solved self-consistently.

Although the phase transition of the unclamped system is continuous in X, the physical tuning parameter, $\tilde{g}[X]$, can become a non-monotonic function of X, leading to a first-order transition. Thus the Larkin-Pikin criterion is

$$\frac{d\tilde{g}}{dX} = 1 - \frac{\lambda^2 V}{\kappa}\chi_{\psi^2} \tag{64}$$

where

$$\chi_{\psi^2} = \int_0^\beta d\tau \int d^3x \big\langle \delta\psi^2(\vec{x}\,)\,\delta\psi^2(0)\big\rangle \tag{65}$$

is the space-time average of the quantum and thermal "energy" fluctuations that is familiar from our previous discussion. The condition $\frac{d\tilde{g}}{dX} \leq 0$ corresponds to the development of a first-order transition; we already know that for $d{+}z > 4$ the term χ_{ψ^2} does not diverge so there is the possibility of a continuous transition. We note that in the physically important case of $d{+}z = 4$ there will be weak logarithmic effects that are probably not observable experimentally. Again here a flavor for the technical argument has been presented as a sketch, and more details are available for the curious reader [27].

2.3 Quantum annealing of the first-order transition

A crucial feature of the LP approach is that the feedback of the energy fluctuations can be understood purely by studying the critical behavior of the clamped system. In order to illustrate this, let us return to the original LP classical version of the two equations, (62) and (63)

$$\tilde{f} = f[x] + \lambda\big(f'[x]\big)^2 \tag{66}$$

and

$$t = x + 2\lambda f'[x] \qquad t \equiv \frac{T - T_c}{T_c} \tag{67}$$

describing the unclamped system that must be solved self-consistently. In the classical clamped system, we assume a continuous transition so we can write

$$f \propto -|t|^{2-\alpha} \qquad (\alpha > 0). \tag{68}$$

Combining (67) and (68), we obtain

$$t = x + 2\lambda f'[x] = x - 2\lambda(2{-}\alpha)\,|x|^{1-\alpha}\,\mathrm{sign}(x) \tag{69}$$

that is non-monotonic leading to a first-order transition for the unclamped system (see Fig. 5). Therefore, in order to generalize the Larkin-Pikin argument to $T \to 0$, we need to introduce a crossover scaling form for the clamped free energy f in (62) and (63) that is applicable near both the classical and the quantum critical points. The approach we outline here that describes both the quantum and classical cases was adapted from an earlier study used to describe Ising anisotropy at a Heisenberg critical point [4]. From our previous discussion, we recall that at a finite temperature T, the criticality of quantum fluctuations is cut off by the Planck time $\tau_P = \hbar/(k_B T)$ with a corresponding quantum correlation length $\xi_Q \sim \tau_P^{1/z}$ Near the quantum

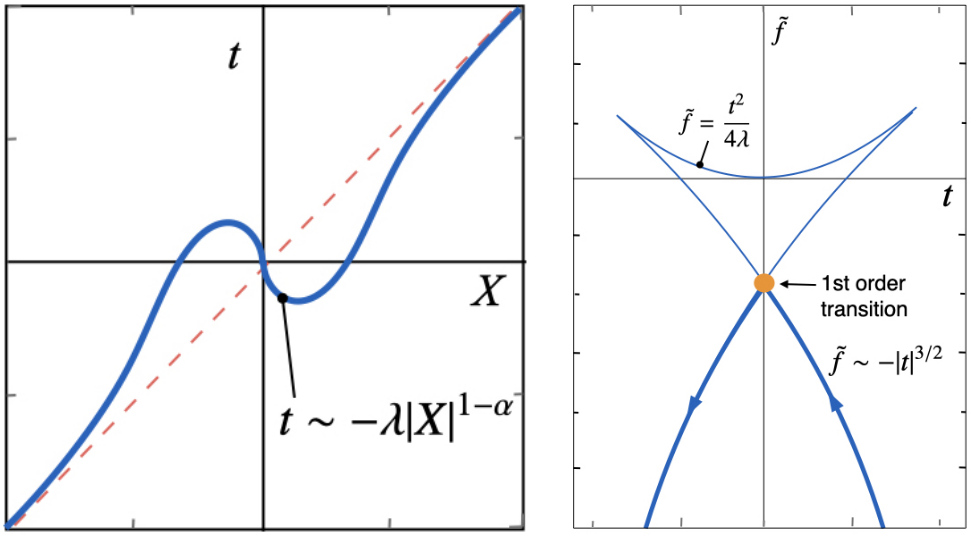

Fig. 5: *Schematic of the (left) nonmonotonic relationship between the reduced temperature (t) and the parametrized variable (X) shifted by energy fluctuations for the unclamped LP problem and (right) the free energy of the unclamped compressible system for $\alpha = 1/2$ as in the original LP paper [26].*

critical point at $T = 0$, the zero-point fluctuations are governed by a finite correlation length $\xi_Q \sim \big(g - g_c(0)\big)^{-\tilde{\nu}}$, where g is the parameter that tunes the quantum transition and $g = g_c(0)$ is the location of the quantum critical point. If we combine our expressions for the quantum correlation length in the ordered phase close to the line of phase transitions, we find

$$(g - g_c)^{-\tilde{\nu}} \sim \left(\frac{\hbar}{k_B T_c}\right)^{1/z} \tag{70}$$

which leads to

$$T_c \sim (g - g_c)^{\tilde{\nu} z} \equiv (g - g_c)^{\tilde{\Psi}} \tag{71}$$

where $\tilde{\Psi}$ is called the shift exponent that we have discussed earlier. Therefore at finite temperature, the location of the phase transition is shifted by the thermal fluctuations, so that

$$g_c(T) = g_c(0) - uT^{1/\tilde{\Psi}}. \tag{72}$$

For convenience, we will shift the definition of g to absorb the zero temperature QCP critical coupling constant, $g_c(0)$, i.e. $g - g_c(0) \rightarrow g$, so that $g_c(T) = -uT^{1/\tilde{\Psi}}$. Now temperature is a finite size correction to the quantum critical point, and the free energy is determined by a crossover function

$$f(g, T) = g^{2-\tilde{\alpha}}\, \Phi\left(\frac{T^{1/\tilde{\Psi}}}{g}\right). \tag{73}$$

which describes both the quantum critical point, and the finite temperature classical critical point of the clamped system (see Figure 6); here we will use the convention that an exponent with a tilde refers to the quantum case so that α and $\tilde{\alpha}$ are classical and quantum exponents, respectively. A key point is that at finite temperature, critical behavior now occurs at the shifted

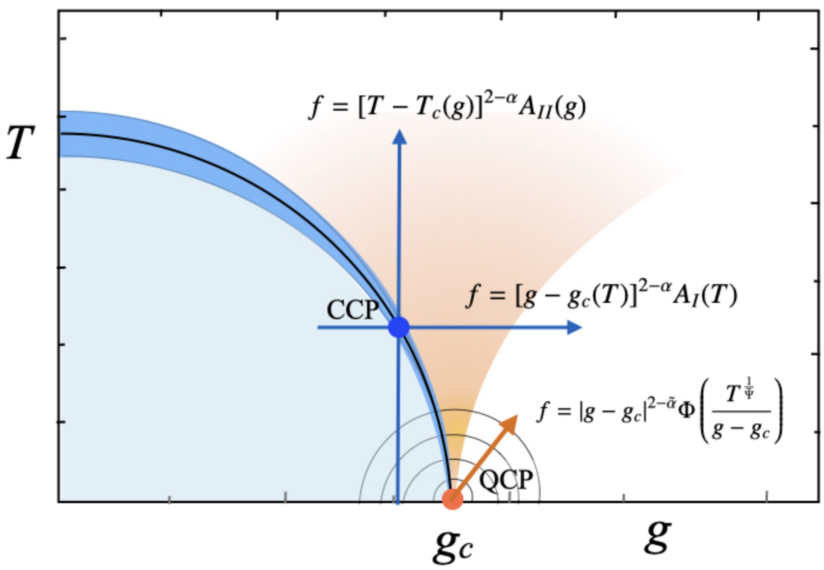

Fig. 6: *Schematic showing the dependence of the free energy of the clamped system in the vicinity of the quantum critical point. The scaling function about the QCP determines the amplitude factors for the finite temperature classical critical point (CCP), given by* $A_I(T)$ *for a constant temperature sweep and* $A_{II}(g)$ *for a sweep at constant tuning parameter. Here the location of the quantum critical point at* $g_c(0)$ *is labelled as simply* g_c.

value of $g_c(T)$, and the scaling behavior is governed by the finite temperature critical exponents. Therefore for a fixed temperature scan (Fig. 6) for small $g - g_c(T)$,

$$f(g,T) = \big(g - g_c(T)\big)^{2-\alpha} A_I(T). \tag{74}$$

where $A_I(T)$ is the amplitude factor for the classical critical point occurring at $g = g_c(T)$. Similarly if we perform a sweep through the phase transition at constant coupling constant g (Fig. 6), then we can write

$$f[g,T] \sim \big(T - T_c[g]\big)^{2-\alpha} A_{II}(g), \tag{75}$$

where $A_{II}(g)$ is amplitude factor for the quantum transition at $T_c[g] = (-g/u)^{\tilde{\Psi}}$. The scaling form (73) allows us to determine the form of these amplitude factors.

Using this crossover approach, we can study how the discontinuities in the entropy and the volume, $\Delta S(T_c)$ and $\Delta V(T_c)$, evolve along the first order phase boundary as the transition T_c is lowered towards zero. In this discussion, we shall identify the tuning parameter g with the pressure P, $g \equiv P - P_c$. Using Maxwell's relations we have

$$\frac{dT_c}{dP_c} \equiv \frac{dT_c}{dg_c} = -\left.\frac{\Delta V}{\Delta S}\right|_{T=T_c} \qquad \longrightarrow \qquad \frac{dT_c}{dg_c} \propto -T_c^{1-1/\Psi}. \tag{76}$$

where we have used (72) to obtain the right-hand expression in (76). For the case of polar insulators, $\tilde{\Psi} = \tilde{\nu} z = 1/2$, and we see that this $dT_c/dP_c \propto T_c^{-1}$; naively this implied divergence of $\Delta V/\Delta S$ as $T_c \to 0$ might be taken as evidence that the tendency towards a first order transition increases as the temperature goes to zero. However the paradox is resolved by noting that ΔS and ΔV simply vanish at different rates, still signifying an approach to a continuous

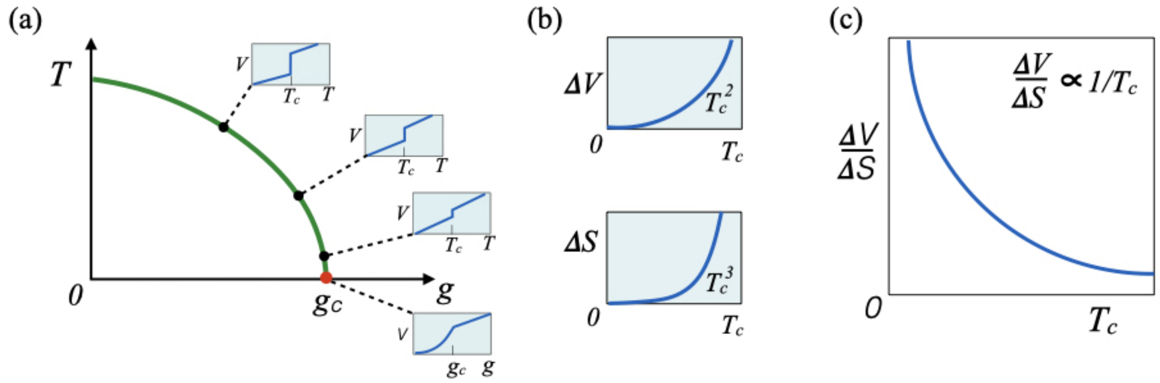

Fig. 7: *Schematic figure showing the evolution of the first order phase transition in the approach to the quantum annealed critical point for the case* $\tilde{\Psi} = \tilde{\nu} z = 1/2$, $\alpha = 1/2$, $\tilde{\alpha} = 0$. *(a) Evolution of jump in volume (b) dependence of* ΔV *and* ΔS *on* T_c *and (c)* T_c *dependence of* $\Delta V/\Delta S$.

quantum phase transition. In particular using this crossover scaling we can show [27]

$$\Delta V(T_c) \propto -T_c^{\frac{\alpha-\tilde{\alpha}}{\alpha\tilde{\Psi}}}, \tag{77}$$

so that as long as $\alpha > \tilde{\alpha}$,

$$\lim_{T_c \to 0} \Delta V \to 0 \tag{78}$$

and there is no latent work as T_c goes to zero, indicating that quantum fluctuations "anneal" the zero-temperature quantum phase transition to become continuous (Fig. 7).

The Rundown. In summary, we have developed a theoretical framework to describe compressible insulating systems that have classical first-order transitions and display pressure-induced quantum criticality. We have generalized the Larkin-Pikin approach [26] to the quantum case using crossover scaling forms that can describe both its classical and its quantum critical behavior. In particular when the system is above its upper critical dimension, there is no latent work at the quantum transition indicating that it is continuous. The key point is that a compressible material can host a quantum critical phase even if it displays a first-order transition at ambient pressure. More generally the order of a lattice-sensitive system's classical phase transition can be different from its quantum counterpart. As always there are always outstanding questions that emerge; they include:

- Lines of discontinuous classical transitions ending in quantum critical points have now also been observed in several metallic systems; can this quantum annealed criticality approach be generalized to include electronic degrees of freedom?
- Can this LP mechanism be understood in a broader field-theoretic context? It has a topological flavor since a $q = 0$ "boundary component of the strain drives the long-range interaction; when integrated around a closed loop on a torus, it is a topological invariant that counts the number of enclosed defect [27]. This appears to be a sort of bulk-boundary correpondance thus suggesting a phenomenon that is topological in character and should be explored.

3 Novel metallicity

So far, we have only discussed polar insulators. However now let us turn to the other conceptual question we posed earlier: Can metals near polar quantum criticality host novel strongly correlated phases?

What exactly is a polar metal and do they exist? A polar metal undergoes a continuous transition from a non-polar to a polar crystal structure; there is no macroscopic polarization due to screening by the conduction electrons [30–32]. Though predicted some time ago [30], it is only relatively recently that such polar metals have been identified experimentally and there exist both intrinsic and engineered varieties with many more predicted [31, 32]. In the extrinsic case, charge can be added to a polar insulator by either chemical and/or gate doping. The Mott criterion for the critical dopant concentration (n_c) for a metal-insulator transition in doped (3d) semiconductors occurs when the average dopant-dopant distance $\left(d = n^{-1/3}\right)$ is a significant fraction of the effective Bohr radius $\left(a_B^* = \epsilon\hbar^2/(m^* e^2)\right)$ where ϵ is the dielectric constant; more concretely the critical concentration n_c is defined as $a_B^* n_c^{1/3} \approx 0.26$, consistent with experiment in many semiconductors [28]. Since the effective Bohr radius is proportional to the dielectric constant (ϵ), it is much larger in materials near polar transitions like n-doped STO than in doped semiconductors based on silicon or germanium (see Figure 8); therefore a lower n_c is expected, consistent with observation [29, 28]. Polar metals can thus have very low carrier concentrations.

Is polar quantum criticality experimentally accessible? Polar transition temperatures of metallic systems have been controllably suppressed, driving them into observed quantum critical regimes [33, 34]. Metals close to quantum critical points are known to be strongly correlated systems that host exotic phases including non-Fermi liquids and unconventional superconductivity where specifics depend on the nature of the quantum criticality involved [25, 35]. The vicinities of polar quantum critical points thus present new settings to explore such novel metallicities [36].

3.1 The challenge: how to couple electrons to a soft polar mode?

In quantum critical polar metals, the $q = 0$ soft mode is an inversion symmetry-breaking transverse optical phonon that has no direct coupling to the charge density. Furthermore the usual Fröhlich electron-phonon coupling vanishes for $q \to 0$. Quantum critical polar metals thus offer opportunities to study novel electron-phonon interactions and their resulting collective behaviors. A key challenge in studying novel metallicity near polar quantum critical points is how to promote strong electronic coupling to the critical polar mode. Conversely, the region around a polar quantum critical point presents an opportunity to explore nontraditional electron-phonon interactions; proposed couplings that include order parameter gradients and/or nonlinearities are usually irrelevant in the scaling sense at a QCP, leading to Fermi liquid behavior. Additionally, Coulomb interactions play a special role here, gapping the longitudinal mode when the screening is weak [16, 23].

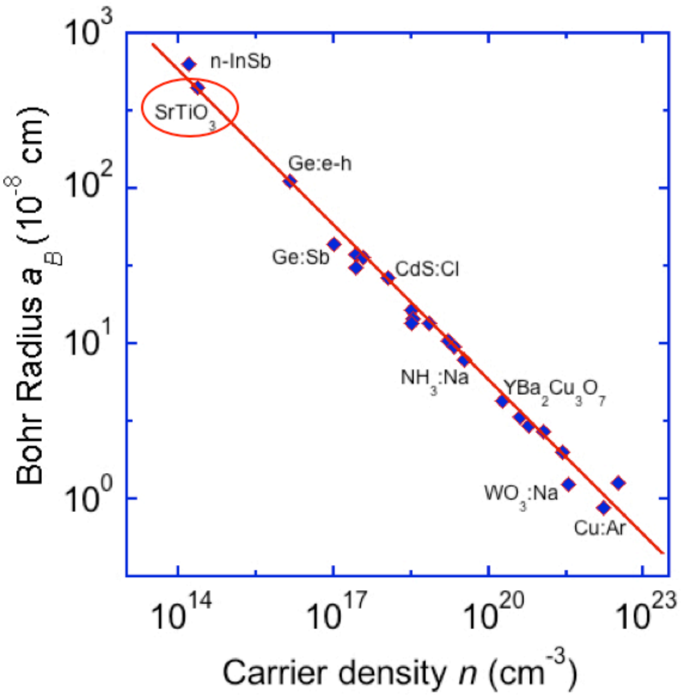

Fig. 8: *A plot of the effective Bohr radius (a_B) vs. carrier density (n) indicating good comparison between the Mott criterion $\left(n_c^{1/3} a_B = 0.26\right)$ for the metal-insulator transition in a number of experimental systems. Here $a_B = \epsilon\hbar^2/(m^* e^2)$ is determined experimentally whenever possible using spectra, otherwise computationally, and the critical carrier density (n_c) for metallicity is measured [28]. Because the effective Bohr radius is proportional to the dielectric constant, it is large for a doped nearly polar material like n-SrTiO$_3$; this results in a low critical carrier concentration for the metal-insulator transition consistent with observation [29]. (Adapted from [28] with permission from the American Physical Society.)*

3.2 Spin-orbit assisted electron-phonon interactions

Many anomalous properties of quantum critical polar metals, particularly in the superconducting state, have been predicted [37–42] by invoking a spin-orbit interaction mediated coupling between polar fluctuations and electrons in the vicinity of a polar quantum critical point (PQCP) with the appropriate interaction Hamiltonian

$$\hat{H}_{\text{int}} = \lambda \sum_{\mathbf{k},\mathbf{q}} \sum_{s,s'} c^\dagger_{\mathbf{k}+\mathbf{q}/2,s} \big((\mathbf{k} \times \hat{\boldsymbol{\sigma}}_{ss'}) \cdot \mathbf{P}_\mathbf{q} \big) c_{\mathbf{k}-\mathbf{q}/2,s'}, \tag{79}$$

where λ is the electron-phonon coupling constant, $c^\dagger_{\mathbf{k},s}(c_{\mathbf{k},s})$ is the electron creation (annihilation) operator with momentum $\mathbf{k}$, spin $s = \uparrow, \downarrow$, $\hat{\boldsymbol{\sigma}}$ is the Pauli matrix for spin and $\mathbf{P}_\mathbf{q}$ describes the polar order fluctuation field at a finite momentum $\mathbf{q}$. Here we note that the fluctuating phonon couples to the electronic spin current; since this coupling remains finite in the limit of $q \to 0$, it allows direct coupling to the critical mode, leading to a range of interesting phenomena emerging close to quantum criticality [37–42]. To date there is no consensus about the magnitude of this coupling in specific polar materials. Interestingly, very recent ab initio studies suggest a reasonable coupling of this type in doped strontium titanate [43], where it was previously not expected to be large [44]; this nearly polar metal has several unconventional

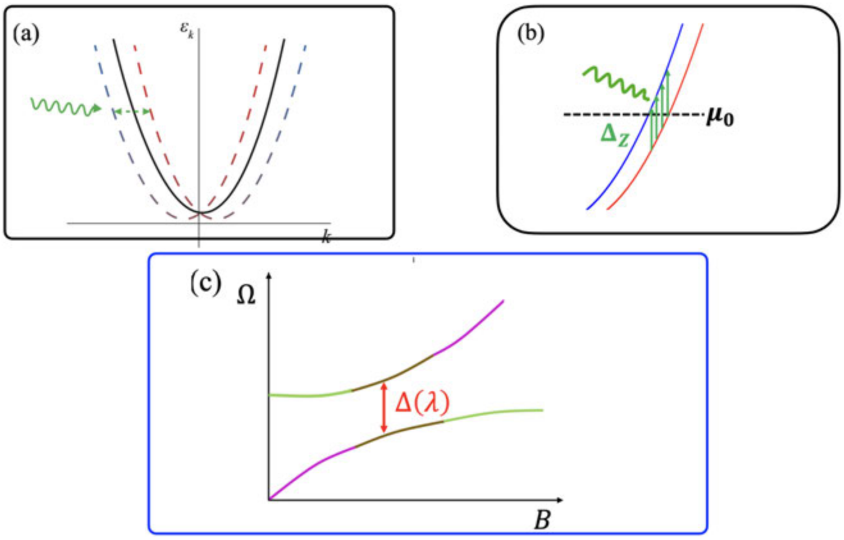

Fig. 9: *Schematics of (a) the virtual spin-orbit assisted electron-phonon interaction, where the green (squiggly) line is the soft TO phonon, (b) the virtual spin-orbit mediated electron-TO phonon interaction in the presence of a magnetic field near the chemical potential μ_0, (c) the avoided crossing of the soft polar and the electronic collective modes where Ω is frequency, B is magnetic field and Δ is a function of the Rashba-type electron-phonon coupling strength λ that can be extracted experimentally.*

properties [34], possibly related to quantum critical polar fluctuations [45–47].

Is there any way to determine the strength of this type of coupling from experiment? The spin-assisted electron-phonon interaction influences the collective modes of a nearly polar metal in an applied magnetic field [48]. Here the soft polar phonon hybridizes with spin-flip electronic excitations of the Zeeman-split bands leading to an anticrossing in the spectra (see Figure 9). The associated splitting energies at the anticrossings can be used to determine the strength of the spin-orbit coupling mediated interactions between electrons and phonons in spectroscopic experiments, such as inelastic neutron scattering or IR spectroscopy, where estimates on known polar materials suggest that such measurements are currently experimentally accessible [48]; such measurements are in progress and will provide important constraints on theoretical descriptions of polar metals, particularly in their superconducting states where there are many mysteries [34, 40].

3.3 Multiband strongly correlated electronic phases

The Yukawa coupling of the order parameter (φ) to carriers

$$H_Y = \lambda \int d\mathbf{r}\ \varphi(\mathbf{r})\, c^\dagger(\mathbf{r}) c(\mathbf{r}) \tag{80}$$

is known to induce strong correlations for other types of quantum critical points, and so naturally we can ask whether it can also do so near a PQCP [25, 35]. As we will discuss in this section, a robust Yukawa coupling (80) to a soft polar mode can be generically realized in multiband systems even without spin-orbit coupling (SOC) leading to pronounced interaction effects at band crossings.

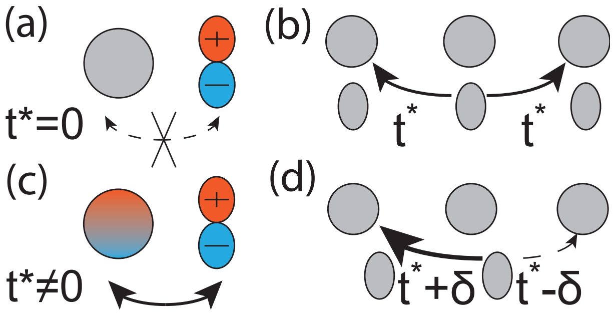

Fig. 10: *Schematic of the coupling to the polar order parameter for two orbitals having (a,c) opposite and (b,d) same parity under inversion. (a) and (b) show the symmetric phase* $\varphi^i = 0$*, while (c) and (d) show the state for* $\varphi^i \neq 0$*. In both cases the interorbital hoppings change.*

So how do the electrons here couple to an inversion symmetry-breaking field? What is wanted is a fermionic bilinear $\hat{O}^i(\mathbf{k})$ that breaks inversion symmetry ($\mathcal{P}$) leading to the coupling

$$H_{\text{coupling}} = \lambda \int d\mathbf{k}\, \varphi(\mathbf{k})\, \hat{O}^i(\mathbf{k}), \tag{81}$$

first assuming time-reversal symmetry ($\mathcal{T}$). For a single conduction band without SOC, the only possible form of

$$\hat{O}(\mathbf{k}) = \hat{c}^\dagger_{\mathbf{k}}\, f_0(\mathbf{k})\, \hat{c}^\dagger_{\mathbf{k}} \qquad \mathcal{P}, \mathcal{T} \quad \rightarrow \quad f_0\,. \tag{82}$$

Since both $\mathcal{P}$ and $\mathcal{T}$ require f_0 to be even, it is not possible for $\hat{O}(\mathbf{k})$ to break only inversion-symmetry. Yukawa polar coupling in a single-band model thus requires SOC.

By contrast, in a multiband system a Yukawa coupling can exist without SOC. In a two-band model $\mathcal{T}$ is complex conjugation and $\mathcal{P}$ acts in band space: $\mathcal{P} \sim \sigma_0$ for bands with the same parity or $\mathcal{P} \sim \sigma_3$ (up to a unitary transformation) in the opposite case. Writing a generic fermionic bilinear as $\hat{c}^\dagger_{\mathbf{k}}\big(f_0(\mathbf{k}) + \sum_{i=1}^3 f_i(\mathbf{k})\sigma_i\big)\hat{c}^\dagger_{\mathbf{k}}$, we find that the terms breaking inversion, but not time-reversal, symmetries are even in $\mathbf{k}$: $f_1(\mathbf{k})$ for $\mathcal{P} \sim \sigma_3$ or odd in $\mathbf{k}$: $f_2(\mathbf{k})$ for $\mathcal{P} \sim \sigma_0$. We can thus have the following Yukawa couplings to the polar mode at $\mathbf{q} \approx 0$

$$\begin{aligned} H^{(a)}_{\text{coupl}} &= \textstyle\sum_{i,\mathbf{q},\mathbf{k}} f^i_a(\mathbf{k})\, \varphi^i_{\mathbf{q}}\, c^\dagger_{\mathbf{k}+\mathbf{q}/2}\, \sigma_1\, c_{\mathbf{k}-\mathbf{q}/2}, \quad \mathcal{P} \sim \sigma_3 \\ H^{(b)}_{\text{coupl}} &= \textstyle\sum_{i,\mathbf{q},\mathbf{k}} f^i_b(\mathbf{k})\, \varphi^i_{\mathbf{q}}\, c^\dagger_{\mathbf{k}+\mathbf{q}/2}\, \sigma_2\, c_{\mathbf{k}-\mathbf{q}/2}, \quad \mathcal{P} \sim \sigma_0, \end{aligned} \tag{83}$$

where $f^i_{a(b)}(\mathbf{k})$ is even(odd) in $\mathbf{k}$, and the order parameter couples to an *interband* bilinear (Fig.11(a), inset). If we assume the bands to originate from two distinct orbitals, the physical mechanism of this Yukawa polar coupling can be illustrated (Fig. 10). If the orbitals have different parity (e.g. s and p) (Fig.10 (a)), they are mixed linearly by an inversion-breaking perturbation. This mixing is reflected in a nonzero hybridization between the resulting bands, forbidden in the symmetric phase (Fig.10 (a)). Due to the necessity of $\mathbf{k}$-dependence, the similar parity case (Fig.10 (b)) cannot be viewed as local. We illustrate it by a nearest-neighbor hopping between the orbitals (Fig.10 (b)); absence of inversion symmetry yields distinct left and right interorbital hoppings from a given site.

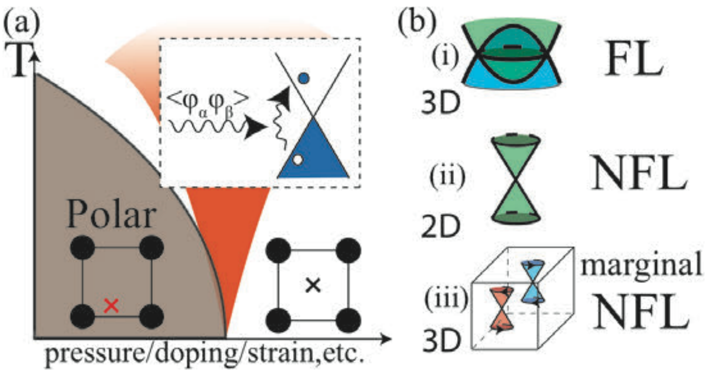

Fig. 11: *(a) Schematic phase diagram of a polar metal with a critical region around the QCP. Inset illustrates that the critical fluctuations couple to an interband excitation. (b) Summary of the QCP behaviors near typical band crossing: (i) a 3D nodal line, (ii) a 2D nodal point, and (iii) 3D Weyl points. (N)FL is (non-)Fermi liquid, and in all cases the polar mode is strongly renormalized. Coulomb interactions introduce anisotropy for (i) and (ii), and gaps the longitudinal mode for (iii).*

Can metals near polar quantum points host novel correlated phases? In order to drive unconventional metallic behavior already at weak coupling, the interband particle-hole excitations coupled to the critical mode with (83) need to be gapless. The best case scenario occurs when the two bands cross close to the Fermi energy, a situation that can be realized by carrier doping, where a low energy theory can be constructed. The critical behavior for three distinct cases (2D Dirac and 3D Weyl points, and 3D nodal lines) with and without interactions has been studied with and without Coulomb interactions. For all band crossing types, the critical polar mode is strongly renormalized and there is the emergence of non-Fermi liquid behavior for the two nodal point cases (Fig. 11). Details for the curious reader are available elsewhere along with experimental signatures for thermodynamic and transport properties [36].

The Rundown. In a nutshell, quantum critical polar metals provide settings to study exotic electron-phonon couplings due to the symmetry of the critical mode. Even in the absence of spin-orbit assisted interactions, nodal multiband metals provide promising platforms for novel metallic behaviors near polar quantum points. More specifically here we have discussed a generic mechanism for Yukawa-type coupling of the electronic density to the critical polar mode accessible even at weak coupling. We have identified novel interacting phases, including non-Fermi liquids, when band crossing are close to the Fermi level, with experimental signatures for generic types of band crossings [36]. As always these results prompt more questions; they include

- A number of polar materials with multiband electronic structures, including $LiOsO_3$ [49], $MoTe_2$ [50] and WTE_2 [51], have been recently discovered with many more predicted [32]. Can application of realistic pressures, external or chemical, drive these polar system to quantum criticality? How do spin-orbit effects, not considered here but present in several of these materials, compete with the Yukawa phases we have discussed here?
- Can new "flavors" of superconductivity emerge from the exotic metallic states we have discussed and, if so, what would be their key distinctive experimental signatures?

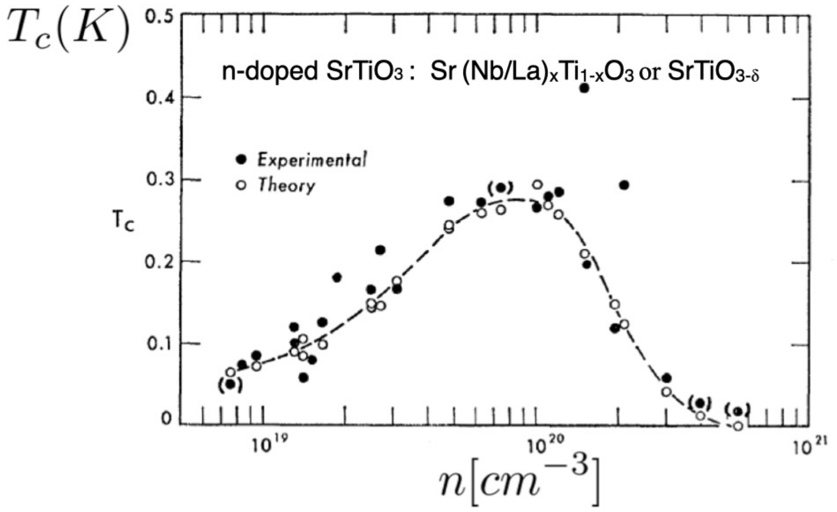

Fig. 12: *The first study of the transition temperature as a function of carrier concentration for n-doped SrTiO*$_3$ *with good fit between the Cohen theory and experiment. Reprinted from [54] with permission from the American Physical Society.*

4 Unconventional superconductivity (with only phonons!)

4.1 The challenge: anti-adiabatic and isotropic!

We have just seen that novel metallic states can occur near polar QCPs and we have even wondered whether such phases can lead to novel types of superconductivity. **A simpler question: can polar quantum criticality drive dilute (unconventional) superconductivity from a parent Fermi liquid state?** In conventional superconductors, electrons exploit the electron-phonon attraction to overcome the Coulomb repulsion by producing a highly retarded attraction that pairs electrons [52], a process that requires a large ratio between the Fermi and Debye energies $E_F/\omega_D \gg 1$. A challenge to this mechanism is posed by superconductivity in low carrier density metals near polar quantum critical points (PQCPs). Such materials, typified by n-doped SrTiO$_3$ (nSTO) [34], exhibit bulk superconductivity down to carrier densities of order 10^{19} cm^{-3}, where the relevant phonon frequency significantly exceeds the Fermi energy [34]. Proximity to the polar quantum critical point has been observed to enhance superconductivity in nSTO [53], suggesting that the underlying polar quantum criticality is a key driver to the pairing despite the decoupling of the critical polar modes from the electrons at low momenta [40,45,47]. Finally, despite this inversion of energy scales, experiments on nSTO indicate a conventional s-wave condensate, with a ratio of gap to transition temperature $2\Delta/T_c \approx 3.5$ in agreement with BCS theory and the normal state is a good Fermi liquid [34].

4.2 Historical context

Historically superconductivity in dilute nSTO was predicted based on an extension of conventional BCS theory to include multivalley phonons as a way to overcome Coulomb repulsion. The predicted transition temperature T_c versus doping, shown in Fig. 12, fit very well with experiment [54]. There was just one rub: band-structure calculations, performed after the original prediction, indicated that nSTO has just one valley, so the theoretical premise of the prediction/confirmation by experiment needed reassessment and the mystery continues [34]. We note that in nSTO the enigmatic superconductivity emerges from a well-behaved Fermi liquid [34]. Over the years many theories have been developed to explain superconductivity in nSTO and other quantum critical polar metals using novel electron-phonon interactions with generalizations to include plasmons. More recently the importance of quantum criticality has been incorporated into theories with multiband effects and spin-orbit coupling; the curious reader is referred to an excellent recent review that surveys these different approaches [40].

4.3 Superconductivity with transverse phonons

Here we revisit superconductivity in quantum critical polar metals, particularly nSTO, guided by two key observations: first, that the strong ionic screening associated with the enhanced dielectric constant severely weakens the electronic Coulomb interaction (Fig. 13(a)); second, that in the absence of strong spin-orbit coupling the transverse optical phonon modes, decoupled from the electron charge, can be likened to dark matter, for like baryons in the cosmos, the electrons do not directly interact with the intense background of zero-point dipole fluctuations. Furthermore like dark matter, the presence of the TO modes is only revealed to the electrons via their stress-energy tensor. In particular, the electrons interact with the energy density of the TO phonons. We model this coupling by the Hamiltonian

$$H_{\mathrm{En}} = g \int d^3x \, \rho_e(\mathbf{x}) (\vec{P}(\mathbf{x}))^2 \tag{84}$$

where $\rho_e(\mathbf{x}) = \psi^\dagger(\mathbf{x})\psi(x)$ is the electron density, $\big(\vec{P}(\mathbf{x})\big)^2$ is proportional to the energy density of the local polarization $\vec{P}$ and g is a coupling constant with the dimensions of volume. Microscopically, this interaction can arise from the short-range effects of the Coulomb force within a unit cell of the material.The presence of an additional charge at the conduction electron site modifies the potential profile for the ions. A local increase in the electron density attracts the surrounding positively charged ions, reducing the distance between them. This causes the local "effective spring constant" of the phonons to rise in regions of high electron density. The natural units for this interaction are therefore atomic ones, i.e., unit cell volume, and should not be extremely different between different materials.

This coupling suppresses the zero-point fluctuations of the polarization in the vicinity of electrons, which in turn lowers the chemical potential of nearby electrons (Fig. 13(b)), creating an attractive potential well. To leading order, the resulting attractive potential is described by the virtual exchange of pairs of transverse optical phonons [47]: this approach is supported by other results:

- According to Equation (84), the presence of a finite electron density $n_e = \langle \rho_e(x) \rangle$ leads to a shift in the phonon frequency

$$\omega_T^2(n_e) = \omega_{T0}^2 + 2 g n_e \varepsilon_0 \Omega_0^2 \, , \tag{85}$$

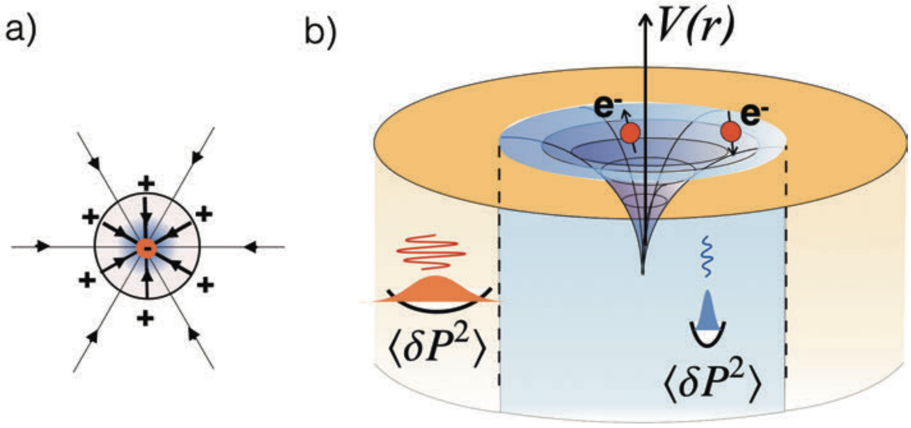

Fig. 13: *Interactions between electrons in a quantum critical polar metal: (a) the electric lines of force around an electron are ionically screened, (b) the fluctuations of the phonon energy density around electrons (see Eq.*(84)*) create an attractive potential well.*

which naturally explains the observed suppression of the polar state by charge doping in polar metals; neutron scattering measurements that probe the hardening of the polar mode with doping indicate that the charge density couples to the phonon energy rather than to its displacement [33,55].

- Many quantum critical polar metals display "high-temperature" T^2 resistivity well above their Fermi temperatures [34], and a two-phonon exchange mechanism has been proposed to describe this anomalous transport [46].

Reviving an old idea [56,57] and generalizing it to include polar quantum criticality, we now explore whether two-phonon processes can drive superconductivity in a quantum critical polar metal from a Fermi liquid state. [47,58].

In this scenario, what is the interaction relevant for electron pairing?? Typically dilute systems require strong coupling approaches since the ratio of the Coulomb to the kinetic energy $r_s = 1/(k_F a_B) \gg 1$ since $k_F \propto n^{1/3}$. However in dilute quantum critical polar metals $a_B \propto \epsilon$ and thus is very large leading to $r_s \ll 1$; quantum critical polar metals then are weakly interacting and thus can be treated by considering perturbative effects. To lowest order, the virtual exchange of critical phonon pairs is the electron-electron interaction from two-phonon exchange. Close to the PQCP, the interaction relevant for electron pairing, averaged over the Fermi surface, is

$$\langle V(k-k') \rangle = \langle V(k_F, \theta) \rangle_\theta \sim -\frac{g^2}{c_S^3} \log \frac{\Omega_T}{\max(\omega_T, c_s k_F, E_f)} \tag{86}$$

where $\Omega_T = \max_{\vec{q}} \omega_T(\vec{q})$ cutoff and we see that large momenta contribute; ω_T is the soft (transverse) polar phonon. This interaction is dependent on carrier density since $k_F \propto n^{1/3}$ and $E_F \propto n^{2/3}$. At low densities close to the PQCP we have $E_F < c k_F$, so the interaction can be considered as instantaneous.

Can this interaction overcome Coulomb repulsion to lead to superconductivity? For carrier densities where $c_s k_F$ is the dominant energy scale, this attractive electron-electron interaction will indeed overcome the Coulomb repulsion leading to superconductivity. The attractive part of the effective electron coupling is

$$\lambda_{att} \sim k_F \left[\log\left(\frac{\Omega_T}{2c_s k_F}\right) + 1\right] \tag{87}$$

that has the form $\lambda(x) = -x\log x + x$. Inclusion of Coulomb repulsion results in

$$\lambda \sim k_F \left(\left[\log\left(\frac{\Omega_T}{2c_s k_F}\right) + 1\right] - \frac{C}{\epsilon_0}\right). \tag{88}$$

that leads to

$$T_c \propto E_F\, e^{-1/\lambda} \qquad \frac{2\Delta}{T_c} = 3.5 \tag{89}$$

using a previously known approach [59]. The key take-home message here is that T_c has dome-like behavior as a function of the carrier density n_e and details of this approach are available elsewhere for a curious reader [47].

4.4 Comparison with experiment ... and homework!

Because filamentary superconductivity is suspected for very low carrier density superconducting n-doped SrTiO$_3$ (nSTO), detailed comparison here will be made to experiment for densities greater than $5 \cdot 10^{-18}$ cm^{-3}, corresponding to where $c_s k_F$ is the dominant energy scale and where bulk effects are observed [34]. As shown in Figure 14, the agreement between theory (solid line) and experiment (crosses) is reasonably good for a decade up to densities of roughly $5 \cdot 10^{-19}$ cm^{-3}, corresponding to its region of validity ($2c_s k_F > E_F$). It is to be noted that a better fit to the experimental data (crosses) for a larger density range is achieved by neglecting Coulomb interactions (dashed gray lines in Figure 14) but this is completely unjustified [47].
For densities higher than $5 \cdot 10^{-19}$ cm^{-3}, E_F is the dominant energy scale and dynamical aspects of the interaction cannot be ignored. At these densities, electronic as well as ionic contributions to the screening of the Coulomb interaction must be included, and we expect the Coulomb repulsion to increase as a function of frequency whereas the electron-electron attraction will behave in the opposite manner. We thus expect the overall interaction to change sign as a function of frequency, allowing for the enhancement of pairing by retardation effects [60]. However such a dynamical approach by itself does not lead to an attractive interaction in the dilute case; thus both energy fluctuations and dynamical screening, must be included to describe the full range of carrier concentrations where bulk superconductivity in n-doped SrTiO$_3$ is observed.

The Rundown. Typified by anti-adiabatic behavior and a "domed" T_c as function of carrier density, unconventional superconductivity (with only phonons!) has been observed in several low-density polar metals near polar quantum critical points, though there is still no consensus on the underlying mechanisms involved. Motivated by an approach that unifies different properties, here we have explored electron pairing mediated by energy fluctuations; it is already known to

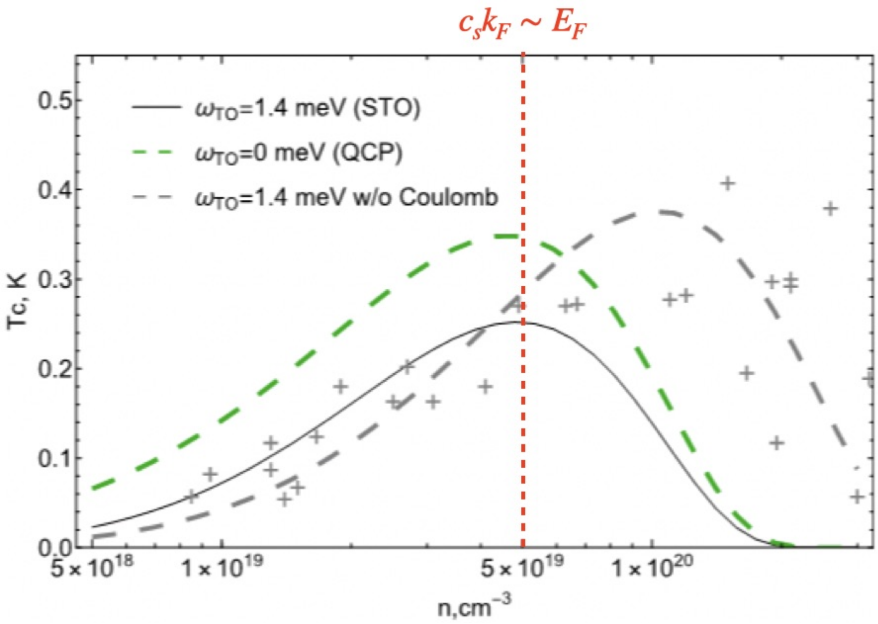

Fig. 14: *The superconducting T_c for n-doped SrTiO$_3$ as a function of carrier concentration where the crosses and lines refer to experiment and theory respectively; the instantaneous approach taken ($c_S k_F$ is dominant energy-scale) is only valid up to $n \sim 5 \cdot 10^{-19}$ cm^{-3}, so for higher densities dynamical effects must be included.*

describe the shift of the quantum critical point with doping [55] and anomalous normal state transport at high temperatures [46]. We find that this approach leads to a superconducting dome, $T_c(n_e)$, that is in good agreement with experiment at low doping. However for higher carrier densities E_F is the dominant energy scale in (86) and dynamical effects should be included. Yet signatures of the two-phonon mechanism including the soft phonon hardening and $\rho \propto T^2$ persist [33, 34, 55], suggesting that both energy fluctuations and dynamical screening contribute to the superconductivity in nSTO and in other quantum critical polar metals for a broad range of carrier concentrations.

Let us now step back and think more generally. Transverse modes are traditionally absent in theories of phonon-based superconductivity, as they do not couple to the charge density. However our discussion of doped quantum paraelectrics has revealed that superconductivity can be driven by multiple critical transverse phonons, a new channel for superconductivity in materials with large anharmonicity. The $3d$ electron pairing mediated by quantum energy fluctuations, an exchange of two critical transverse phonons at leading order, describes the dome-line structure of the superconducting phase diagram at low doping. In order to describe the observed superconducting behavior of the full range of carrier concentrations, this energy fluctuation pairing mechanism must be generalized dynamically, requiring the inclusion of longitudinal fluctuations. The resulting theory that includes both transverse and longitudinal phonons should be applicable well beyond the realm of quantum critical polar superconductors; it may be helpful to describe quantum materials with light electrons including magnesium diboride and the superconducting hydrides where significant nonlinear elasticity is present.

5 Summary and outlook

In these Lecture Notes, I have tried to convey my excitement and enthusiasm for the area of polar quantum criticality, emphasizing aspects that may not be part of the mainstream literature. We began by unpacking the title, discussing key concepts in quantum criticality, particularly phenomenological approaches towards determining measured low-temperature quantities. Next we presented polar materials, and we floated concerns about introducing these systems as research settings for quantum criticality which we subsequently addressed. Experimentally many compressible polar materials are found to have discontinuous finite-temperature transitions coexisting with quantum critical behavior, and we discussed a theoretical basis for this phenomenon. Because the approach here is subtle and not that well known, we have spent some effort outlining the arguments carefully. The quest for novel metallicity and unconventional superconductivity is a key motivation for research activity on quantum criticality, so next we show that both occur near polar quantum critical points. Furthermore symmetry demands that nontraditional electron-phonon interactions can be explored in this setting with implications beyond the original realm.

More generally we recall that polar phenomena are classical examples of emergent behavior in solids that have been important for many technological applications. Recently polar phenomena have been observed in several correlated materials where quantum effects dominate, including frustrated magnets, Mott insulators, non-Fermi liquid and Moire superlattices and there is much to be done towards understanding and harnessing the rich polar properties of quantum materials. The presence of polar behavior in these strongly correlated quantum materials provides opportunities to

- Identify and characterize new electrically active states of quantum matter including electron dipole liquids and quantum critical multiferroics
- Probe quantum matter using electric field-based tools
- Develop quantum states of matter that can be tuned and controlled by electric fields towards practical quantum device applications

and the study of these fascinating materials at cryogenic temperatures near quantum criticality is a way to focus on their predominantly quantum behaviors. In addition, the neighborhood of a polar quantum critical point is a good setting for these explorations since it is a scale-free zone where the Coulomb repulsion is significantly weakened. Possible research directions for the future include:

- Mixed parity states in polar superconductors. Polar superconductors are by definition non-centrosymmetric and thus defy standard classification schemes; exotic properties like unusual surface states and magnetoelectric effects could occur.
- The relation between polarization and band topology. Because the Coulomb interaction is weak near a polar quantum critical point, this could be an excellent setting to study polarization textures.

- Dynamical quantum criticality has been studied in synthetic quantum systems. Since polar materials have soft optical modes, they are good settings for photoinduced classical transitions [61]. What experimental signatures would be expected at a dynamical quantum critical point?

- Interfacial and stacked ferroelectricity has been recently demonstrated in layered van der Waals structures that depend sensitively on the stacking configurations of the layers involved [62], and I would be remiss if I did not mention this fascinating development. Because the nature of these polar system is so different than that which we have discussed so far, there are bound to be fascinating new phenomena here to study, particularly related to the electrooptical properties of these heterostructures.

The list can of course go on and on. I hope that I have given you a flavor for polar quantum criticality with its many challenges and its many opportunities. Please come and join the fun!

Acknowledgements

This work is result of many wonderful collaborations with P. Coleman, M.A. Continentino, A. Kumar, G.G. Lonzarich, L. Palova, S.E. Rowley, J.F. Scott, P.A. Volkov and of course many stimulating discussion with countless colleagues. I am grateful to them all for sharing their knowledge and their insights with me in this fascinating area and more. I have tried to provide references whenever possible for further reading/clarification; due to space restrictions naturally the bibliography is not exhaustive, and I apologize in advance to colleagues whose research may be inadvertently not represented. This work was performed in part at the Aspen Center for Physics, which is supported by National Science Foundation grant PHY-2210452.

References

[1] S. Sachdev: *Quantum Phase Transitions* (Cambridge University Press, 1999)

[2] P. Coleman and A. Schofield, Nature **433**, 226 (2005)

[3] S. Sachdev, Nat. Phys. **4**, 173 (2008)

[4] M.A. Continentino: *Quantum Scaling in Many-Body Systems* (World Scientific, Singapore, 2001)

[5] M. Vojta, Rep. Prog. Phys. **66**, 2069 (2003)

[6] P. Chandra, G. Lonzarich, S. Rowley, and J. Scott, Rep. Prog. Phys. **80**, 112502 (2017)

[7] L. Palova, P. Chandra, and P. Coleman, Phys. Rev. B **79**, 075101 (2009)

[8] L. Landau and E. Lifshitz: *Statistical Physics* (Pergamon Press, Oxford, 1980)

[9] P. Chandra and P. Littlewood, pp. 69–115 in [63]

[10] S. Rowley, L. Spalek, R. Smith, M. Dean, M. Itoh, J. Scott, G. Lonzarich, and S. Saxena, Nat. Phys. **10**, 367 (2014)

[11] E. Fatuzzo and W. Merz: *Ferroelectricity* (North-Holland, Amsterdam, 1967)

[12] M. Lines and A. Glass: *Principles and Applications of Ferroelectrics and Related Materials* (Clarendon Press, Oxford, 1977)

[13] F. Jona and G. Shirane: *Ferroelectric Crystals* (Dover Publications, New York, 1993)

[14] B. Strukov and A. Levanyuk: *Ferroelectric Phenomena in Crystals: Physical Foundations* (Springer, Heidelberg, 1998)

[15] K.M. Rabe, M. Dawber, C. Lichtensteiger, C.H. Ahn, and J.M. Triscone, pp. 1–29 in [63]

[16] A. Larkin and D. Khmelnitskii, Sov. Phys. JETP **29**, 11231128 (1969)

[17] P. Chandra, Nat. Phys. **19**, 1525 (2023)

[18] G. Ahlers, A. Kornbilt, and H. Guggenheim, Phys. Rev. Lett. **34**, 1227 (1975)

[19] E. Sandvold and E. Courtens, Phys. Rev. B **27**, 5660 (1983)

[20] B. Chakrabati, A. Dutta, and P. Sen: *Quantum Ising Phases and Transitions in Transverse Ising Models* (Springer, Heidelberg, 1996)

[21] O. Kvyatkovskii, Phys. Solid State **43**, 1401 (2001)

[22] A. Rechester, Sov. Phys. JETP **33**, 423 (1971)

[23] R. Roussev and A. Millis, Phys. Rev. B **67**, 014105 (2003)

[24] J. Cardy: *Scaling and renormalization in statistical physics*, Vol. 5 (Cambridge University Press, 1996)

[25] M. Brando, D. Belitz, F.M. Grosche, and T.R. Kirkpatrick, Rev. Mod. Phys. **88**, 025006 (2016)

[26] A. Larkin and S. Pikin, Sov. Phys. JETP **29**, 891 (1969)

[27] P. Chandra, P. Coleman, M.A. Continentino, and G. Lonzarich, Phys. Rev. Res. **2**, 043440 (2020)

[28] P.P. Edwards and M.J. Sienko, Phys. Rev. B **17**, 2575 (1978)

[29] X. Lin, Z. Zhu, B. Fauqué, and K. Behnia, Phys. Rev. X **3**, 021002 (2013)

[30] P.W. Anderson and E.I. Blount, Phys. Rev. Lett. **14**, 217 (1965)

[31] N. Benedek and T. Birol, J. Mat. Chem. C **4**, 4000 (2016)

[32] S. Bhowal and N.A. Spaldin, Annu. Rev. Mat. Res. **53**, 53 (2023)

[33] C.W. Rischau, X. Lin, C.P. Grams, D. Finck, S. Harms, J. Engelmayer, T. Lorenz, Y. Gallais, B. Fauque, J. Hemberger, and K. Behnia, Nat. Phys. **13**, 643 (2017)

[34] C. Collignon, X. Lin, C.W. Rischau, B. Fauque, and K. Behnia, Annu. Rev. Condens. Matter Phys. **10**, 25 (2019)

[35] A. Abanov, A.V. Chubukov, and J. Schmalian, Adv. Phys. **52**, 119 (2003)

[36] P.A. Volkov and P. Chandra, Phys. Rev. Lett. **124**, 237601 (2020)

[37] V. Kozii and L. Fu, Phys. Rev. Lett. **115**, 207002 (2015)

[38] J. Ruhman, V. Kozii, and L. Fu, Phys. Rev. Lett. **118**, 227001 (2017)

[39] S. Kanasugi and Y. Yanase, Phys. Rev. B **100**, 094504 (2019)

[40] M.N. Gastiasoro, J. Ruhman, and R.M. Fernandes, Ann. Phys. **417**, 168107 (2020)

[41] M.N. Gastiasoro, M.E. Temperini, P. Barone, and J. Lorenzana, Phys. Rev. Res. **5**, 023177 (2023)

[42] A. Klein, V. Kozii, J. Ruhman, and R.M. Fernandes, Phys. Rev. B **107**, 165110 (2023)

[43] M.N. Gastiasoro, M.E. Temperini, P. Barone, and J. Lorenzana, Phys. Rev. B **105**, 224503 (2022)

[44] J. Ruhman and P.A. Lee, Phys. Rev. B **100**, 226501 (2019)

[45] J.M. Edge, Y. Kedem, U. Aschauer, N.A. Spaldin, and A.V. Balatsky, Phys. Rev. Lett. **115**, 247002 (2015)

[46] A. Kumar, V.I. Yudson, and D.L. Maslov, Phys. Rev. Lett. **126**, 076601 (2021)

[47] P. Volkov, P. Chandra, and P. Coleman, Nat. Commun. **13**, 4599 (2021)

[48] A. Kumar, P. Chandra, and P.A. Volkov, Phys. Rev. B **105**, 125142 (2022)

[49] Y. Shi, Y. Guo, X. Wang, A.J. Princep, D. Khalyavin, P. Manuel, Y. Michiue, A. Sato, K. Tsuda, S. Yu, M. Arai, Y. Shirako, M. Akaogi, N. Wang, K. Yamaura, and A.T. Boothroyd, Nat. Mat. **12**, 1024 (2013)

[50] J. Jiang, Z. Liu, Y. Sun, H. Yang, C. Rajamathi, Y. Qi, L. Yang, C. Chen, H. Peng, C. Hwang et al., Nat. Commun. **8**, 13973 (2017)

[51] Z. Fei, W. Zhao, T.A. Palomaki, B. Sun, M.K. Miller, Z. Zhao, J. Yan, X. Xu, and D.H. Cobden, Nature **560**, 336 (2018)

[52] P. Coleman: *Introduction to Many-Body Physics* (Cambridge University Press, 2015)

[53] M.J. Coak, C.R. Haines, C. Liu, S.E. Rowley, G.G. Lonzarich, and S.S. Saxena, Proc. Nat. Acad. Sci. U.S.A. **117**, 12707 (2020)

[54] C.S. Koonce, M.L. Cohen, J.F. Schooley, W.R. Hosler, and E.R. Pfeiffer, Phys. Rev. **163**, 380 (1967)

[55] D. Bäuerle, D. Wagner, M. Wöhlecke, B. Dorner, and H. Kraxenberger, Z. Phys. B Condens. Matter **38**, 335 (1980)

[56] K.L. Ngai, Phys. Rev. Lett. **32**, 215 (1974)

[57] D. van der Marel, F. Barantani, and C.W. Rischau, Phys. Rev. Res. **1**, 013003 (2019)

[58] D.E. Kiselov and M.V. Feigel'man, Phys. Rev. B **104**, L220506 (2021)

[59] L.P. Gor'kov, Phys. Rev. B **93**, 054517 (2016)

[60] D. Pimenov and A.V. Chubukov, Ann. Phys. **447**, 169049 (2022)

[61] Z. Zhuang, A. Chakraborty, P. Chandra, P. Coleman, and P.A. Volkov, Phys. Rev. B **107**, 224307 (2023)

[62] E.Y. Tsymbal, Science **372**, 1389 (2021)

[63] K. Rabe, C. Ahn, and J. Triscone (Eds.): *Physics of Ferroelectrics: A Modern Perspective* (Springer, Heidelberg, 2007)

12 Competition between Kondo Effect and RKKY Coupling

Stefan Kettemann
Constructor University Bremen
Campus Ring 1, 28759 Bremen

Contents

E. Pavarini and E. Koch (eds.)
Correlations and Phase Transitions
Modeling and Simulation Vol. 14
Forschungszentrum Jülich, 2024, ISBN 978-3-95806-751-6
http://www.cond-mat.de/events/correl24

1 Introduction

Localized magnetic moments in metals, for example formed by Fe-atoms in gold, interact with the spins of itinerant electrons in the Fermi sea via exchange couplings J. This results in spin dependent electron scattering, in addition to potential scattering from the impurity potential. Depending on magnetic moment density n_{M}, magnetic impurity spin S, magnitude and sign of exchange couplings J and temperature T, the metal settles for one of a diverse set of quantum phases, each with very different degrees of spin and charge correlations. If the exchange coupling J with impurity spin $S = 1/2$ is antiferromagnetic, all conduction electrons compete to form a singlet with this localized spin, if J is not sufficiently strong to bind and localize one of the electrons completely into a singlet. This competition leads to strongly enhanced magnetic and normal scattering, measurable as enhanced electrical resistivity, as the temperature is lowered towards and below a temperature T_{K}. This effect was explained by Kondo [1] and is now known as the Kondo effect. The resistance minimum as function of temperature close to the Kondo temperature T_{K} [2] occurs since above T_{K} the resistance decays with temperature, as typical for a metal, while it increases at and below T_{K} due to Kondo enhanced scattering rate. While such magnetic moments are paramagnetic, contributing a Curie magnetic susceptibility $\chi \sim 1/T$ at higher temperature $T > T_{\mathrm{K}}$, at lower temperature their contribution to the magnetic susceptibility saturates to $\chi \sim 1/T_{\mathrm{K}}$. More recently, it was found that mesoscopic metal wires with dilute magnetic impurities show a pronounced peak at T_{K} in the temperature dependent dephasing rate, which governs quantum corrections to the conductance, the so called weak localization corrections [3–5], allowing high precision studies of the Kondo screening. The Kondo temperature T_{K} is a functional of the local exchange coupling J and the local density of states ρ, at and in the vicinity of the Fermi energy ε_F. Remarkably, as the temperature is lowered further, a portion of the conduction electrons settle for a joint screening of the magnetic impurity spin and form the so called Kondo singlet, a highly correlated many body state. For the remaining conduction electrons the magnetic impurity spin seemingly disappears. The electrons settle then again to form a Fermi liquid, albeit with enhanced density of states at the Fermi energy, forming a narrow resonance peak of width $k_B T_{\mathrm{K}}$, as sketched in Fig. 1 (upper Right). As a consequence, the spin scattering from the magnetic impurity decays to zero, as the temperature is lowered further. The remaining enhanced potential scattering from the Kondo impurities then contributes to the enhanced low temperature resistance.

When the concentration of magnetic moments in a metallic host is high, and they form a regular lattice, all Kondo impurities can conspire to form a narrow band at the Fermi energy, as sketched in Fig. 1 (lower Right), at sufficiently low temperature, below a critical temperature $T_c < T_{\mathrm{K}}$. Then, the itinerant electrons at the Fermi energy are no longer scattered from the potential of the Kondo impurities but move through the lattice formed by the Kondo impurities as dressed quasiparticles with strongly enhanced mass, accordingly called *heavy fermions*. This transition to a new state of heavy but itinerant fermions is experimentally seen, when the Fermi energy is in that narrow band, in a sudden drop of the resistivity below a critical temperature T_c, where the low temperature coherence sets in, while at higher temperatures still the typical Kondo enhanced

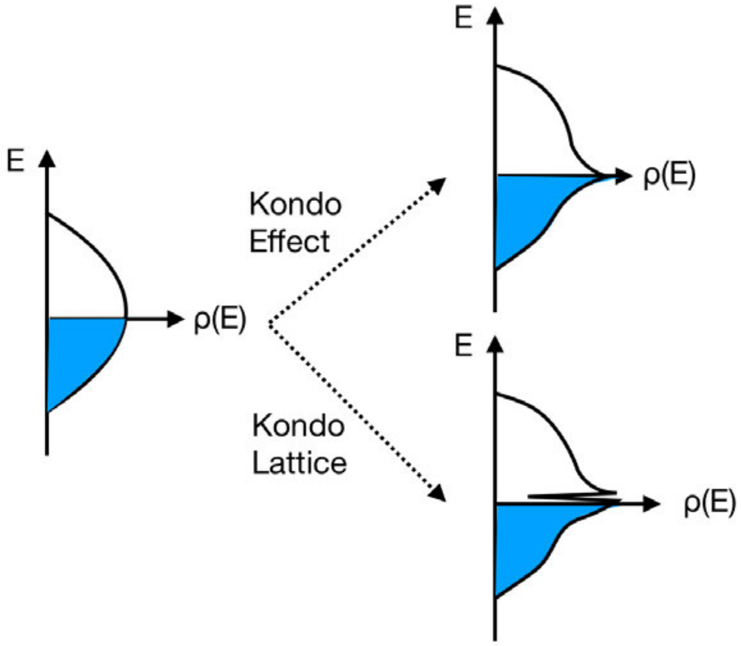

Fig. 1: *Left: Sketch of typical density of states $\rho(E)$ of a metal as function of energy E, with states filled up to the Fermi energy ε_{F}, as colored in blue. Upper Right: For dilute magnetic impurities with spin $S = 1/2$, coupled by an antiferromagnetic exchange coupling to the conduction electron spins, a Kondo resonance of width $k_{\mathrm{B}}T_{\mathrm{K}}$ forms. Lower Right: At sufficiently large impurity density a Kondo lattice forms with a narrow band at the Fermi energy.*

resistivity from individual Kondo impurities is observable. This is observed for example in the intermetallic crystal CeCu_6, where the Ce^{3+}-ions form at high temperature a dense lattice of magnetic moments in the metallic copper host, while at low temperatures a transition to a coherent state of heavy electrons occurs with a sharp drop of resistivity [6–9].

However, localized magnetic moments in metals interact with each other. Their magnetic dipole interaction is finite, but is typically exceeded by far by indirect exchange couplings between them, the so called RKKY couplings, mediated by conduction electrons [10–12]. In metals, RKKY coupling decays slowly, with a power law of distance R between two magnetic moments. The RKKY coupling is a functional of exchange couplings J, local density of states at the Fermi energy at the locations of the magnetic impurities $\rho(\mathbf{r}, E_F)$, and their distance R. Since these couplings tend to quench their spins, it may prevent the Kondo screening by the conduction electrons partially, or even completely, depending on the amplitude of local exchange coupling J, the distance R between them and temperature T.

Thus, there is a competition between Kondo screening and RKKY coupling. Depending on which one wins, the system will find itself in very different quantum states. This competition can be studied systematically by increasing the density of magnetic impurities. Increasing their concentration, decreases their average distance R and thereby the typical RKKY coupling between them increases. In the very dilute limit RKKY couplings can be neglected, and magnetic impurities can be treated as a dilute set of single Kondo spins, as shown in Fig. 2a). Increasing

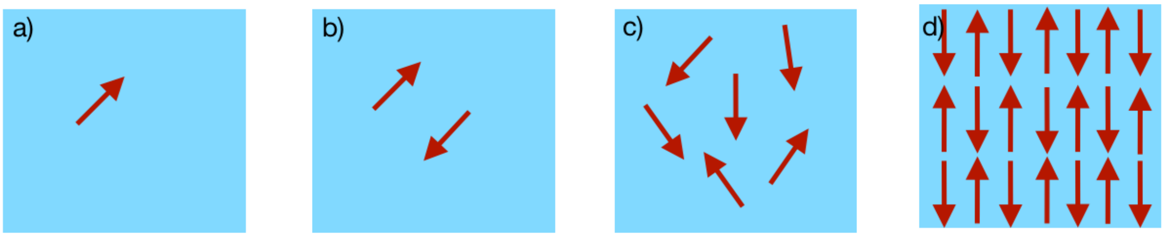

Fig. 2: *Kondo impurity spins (red) in a metal host (blue): a) Single Kondo impurity, b) Pair of Kondo impurities, c) Dilute Kondo system, d) Kondo lattice.*

their concentration further, randomly placed magnetic impurities may be modeled by a set of pairs of magnetic impurities, formed by those spins which are closest to each other, as shown in Fig. 2b). At higher concentrations larger clusters of spins, shown in Fig. 2c) have to be considered to model their quantum state, and at still higher concentrations a connected random network of them. When the density of magnetic moments is so high that they form a regular lattice, as it occurs in f-band materials, a coherent Kondo lattice can form. The competition between the Kondo effect in this Kondo lattice and the RKKY coupling gives rise to a quantum phase transition between a heavy fermion state and an ordered state, which, when mapped as function of exchange coupling J, is called the Doniach diagram [13, 14].

In these lecture notes we give an introduction to the theory of this rich competition between Kondo screening and RKKY coupling. In section 2 we review the formation of magnetic moments as modeled by the Anderson model. In section 3 we review the theory of the Kondo effect for a single magnetic impurity in a metal host. In section 4 we derive the RKKY coupling between magnetic impurities in a metal host. In section 5 we review the Doniach diagram, and give an introduction to a self consistent renormalization group theory which takes into account both Kondo effect and RKKY coupling between magnetic impurities, and explain the results obtained thereby. In section 6 we review the effect of gaps and pseudo-gaps on both Kondo effect and RKKY couplings, and accordingly on their competition. Especially for dilute concentration of magnetic moments, the disorder effects from randomly distributed impurities result in a distribution of both Kondo temperatures and RKKY couplings. Then, their competition becomes an even more complex problem, as reviewed in section 7. Moreover, disorder induced Anderson localization transitions may occur, which effect both Kondo effect and RKKY coupling severely, and changes their competition, as we review in that section, as well. We conclude with an outlook and list the, in our view, most pressing and interesting open problems.

2 Formation of magnetic moments

The first microscopic model for the formation of magnetic moments in metals was formulated by P.W. Anderson [15]. He showed that local moments can form from localized d- or f-levels which are weakly coupled by hybridization to the conduction electrons, when the repulsive Coulomb interaction $U > 0$ between two electrons on these localized levels is sufficiently large. He found furthermore, quite surprisingly, that the resulting local moments develop an antiferromagnetic coupling with the spins of the surrounding electron liquid. The formation of magnetic moments is described by the Anderson model, where a d- or f-level is weakly coupled to conduction band electrons, as modelled by the Hamiltonian [15]

$$H = \sum_{n,\sigma} E_{n\sigma}\,\hat{n}_{n\sigma} + \sum_{\sigma} \varepsilon_{d\sigma}\,\hat{n}_{d\sigma} + U\,\hat{n}_{d+}\hat{n}_{d-} + \sum_{n,\sigma} \big(t_{nd}\,c^{\dagger}_{n\sigma} d_{\sigma} + t_{dn}\,d^{\dagger}_{\sigma} c_{n\sigma}\big), \tag{1}$$

where electrons in a conduction band state $|n\rangle$ with eigenenergy $E_{n\sigma}$ are annihilated and created by fermion operators $c_{n\sigma}$, $c^{\dagger}_{n\sigma}$ with spin index $\sigma = \pm$. The corresponding density operator is $\hat{n}_{n\sigma} = c^{\dagger}_{n\sigma} c_{n\sigma}$. In the following, we assume spin degeneracy of the conduction band states $E_{n\sigma} = E_n$. The annihilation and creation operators of electrons in the d-level are d_{σ}, $d^{\dagger}_{\sigma}$ with density operator $\hat{n}_{d\sigma} = d^{\dagger}_{\sigma} d_{\sigma}$. The d-level can either be in a magnetic state, when it is occupied by a single electron with energy $\varepsilon_{d\sigma}$, which can be in one of two spin states $\sigma = \pm$. We assume that these two states form a Kramers doublet, with energy ε_d, degenerate in the spin σ. Furthermore, it can be in a nonmagnetic state when unoccupied or when doubly occupied, with vanishing total spin and total energy $2\varepsilon_d + U$. In order that the ground state is magnetic, the energy of the singly occupied states must be lower than the energy of the unoccupied state, as well as the one of the doubly occupied state, requiring $\varepsilon_d < 0$ and $\varepsilon_d + U > 0$. Thus, the repulsion must be stronger than the bound state energy of a single electron, $U > -\varepsilon_d$. At finite temperature T, the d-level remains magnetic as long as T is lower than the energy cost for such valence fluctuations, $T < \min(\varepsilon_d + U,\, -\varepsilon_d)$. However, the hybridization between the d-level and the conduction band state $|n\rangle$, as given by the matrix elements $t_{dn} = t^{*}_{nd}$, may change this ground state. To study its effect on the magnetic states, one can project nonmagnetic higher energy states, where the d-level is doubly occupied or unoccupied, out of the Hilbert space of the d-level. This was done by Schrieffer and Wolff [16], who thereby showed that the spin on the d-level is coupled by an antiferromagnetic exchange interaction J with the spins of the conduction electrons. Performing this, so called Schrieffer-Wolff transformation one obtains the Kondo Hamiltonian in its most general form

$$H_K = \sum_{n,\sigma} E_n \hat{n}_{n\sigma} + \sum_{n,n'} J_{nn'} \left(S^{+} c^{\dagger}_{n+} c_{n'-} + S^{-} c^{\dagger}_{n-} c_{n'+} + S_z \big(c^{\dagger}_{n+} c_{n'+} - c^{\dagger}_{n-} c_{n'-} \big) \right), \tag{2}$$

where $\mathbf{S}$ is the spin vector operator of the localized moment, written here in terms of the ladder operators $S^{\pm} = S_x \pm \mathrm{i} S_y$ and its z-component S_z. The matrix elements of the exchange coupling in the basis of the conduction electron eigenstates $|n\rangle$ are found to be given by

$$J_{nn'} = t_{nd}\, t_{dn'} \left(\frac{1}{U + \varepsilon_d - E_{n'}} + \frac{1}{-\varepsilon_d + E_n} \right). \tag{3}$$

The hopping matrix element connecting the localized d-state $\phi_d(\mathbf{r})$ to the conduction band state $\psi_n(\mathbf{r})$ is related to the atomic potential $\hat{V}$ by the hybridization integral

$$t_{dn} = \langle d|\hat{V}|n\rangle = \int d^d r\ \phi^{*}_d(\mathbf{r})\, V(\mathbf{r})\, \psi_n(\mathbf{r}). \tag{4}$$

For an impurity state strongly localized on a length scale a_0 at position $\mathbf{r}$ in a d-dimensional sample, one can simplify that expression with the hybridization parameter t to

$$t_{dn} \approx t a_0^d \phi_d^*(\mathbf{r})\, \psi_n(\mathbf{r}). \tag{5}$$

Assuming that both nonmagnetic states have the same energy $U/2$, one arrives at the symmetric Kondo model. In this approximation, the Kondo Hamiltonian can be written with the superexchange term in the form of a Heisenberg Hamiltonian [1,8],

$$H_K^0 = \sum_{n,\sigma} E_n \hat{n}_{n\sigma} + J\, \vec{\mathbf{S}}\, \vec{\mathbf{s}}(\mathbf{r}), \tag{6}$$

where $J = 4t^2/U > 0$. Thus, the superexchange interaction is indeed antiferromagnetic. The matrix elements of the conduction band spin density vector operator $\vec{\mathbf{s}}(\mathbf{r})$ at the site of the d-level, $\mathbf{r}$ are given by

$$\vec{\mathbf{s}}_{\alpha\beta}(\mathbf{r}) = \sum_{n,n'} \psi_{n'}^*(\mathbf{r}) \psi_n(\mathbf{r})\, c_{n\alpha}^\dagger \vec{\sigma}_{\alpha\beta} c_{n'\beta}, \tag{7}$$

where $\vec{\sigma}$ is the vector of Pauli matrices $\vec{\sigma} = (\sigma_x, \sigma_y, \sigma_z)$. Here, we used $a_0^d \left|\phi_d(\mathbf{r})\right|^2 = 1$, since the intensity $|\phi_d(\mathbf{r})|^2$ in the d-level is localized in the volume a_0^d.

3 Kondo effect: screening of magnetic moments

When the bare antiferromagnetic exchange interaction J is too weak to bind a single conduction electron into a singlet state, all conduction electrons in the vicinity of the Fermi energy become excited by scattering from the magnetic impurity spin. Integrating out all these excitations, of conduction electrons to energy levels E_m above the Fermi energy and of hole excitations below the Fermi energy, one finds that the exchange interaction J becomes thereby enhanced. Performing perturbation theory to second order in J, there are two processes to be considered: (i) The scattering due to the exchange coupling J of an electron from initial state $|n\rangle$ to a state $|l\rangle$ at the Fermi energy via an intermediate state $|m\rangle$, which can be of either spin. This process is proportional to the probability that state $|m\rangle$ is not occupied, $1-f(E_m)$, where $f(E)$ is the Fermi distribution function. (ii) The reverse process, in which a hole is scattered from the state $|l\rangle$ to the state $|n\rangle$ via the occupied state $|m\rangle$ which is accordingly proportional to the occupation factor $f(E_m)$. Thereby, one finds that the Kondo exchange Hamiltonian acquires an additional term so that the total exchange coupling becomes

$$\tilde{J}_{nl} = J_{nl} \left[1 + \frac{J}{2N} \sum_{m,\sigma} \frac{L^d \left|\psi_m(\mathbf{r})\right|^2}{E_m - E_F} \tanh\!\left(\frac{E_m - E_F}{2T} \right) \right]. \tag{8}$$

For positive exchange coupling, $J > 0$, the correction term is positive as well. Moreover, this perturbation theory diverges as the temperature is lowered. Defining the Kondo temperature as the temperature where perturbation theory breaks down since the second-order correction to the exchange coupling becomes equal to the bare coupling, we find in this 1-loop approximation, that the Kondo temperature at site $\mathbf{r}$ of a spin-$1/2$-impurity is determined by the equation [17,18]

$$1 = \frac{J}{2N} \sum_{m,\sigma} \frac{L^d \left|\psi_m(\mathbf{r})\right|^2}{E_m - E_F} \tanh\left(\frac{E_m - E_F}{2T_\mathrm{K}(\mathbf{r})}\right), \tag{9}$$

with N the total number of energy levels, including spin degeneracy, in a finite sample of linear size L and dimension d. $|\psi_m(\mathbf{r})|^2$ is the probability density of the eigenstate at site $\mathbf{r}$.
An equivalent expression can be derived from a renormalization group analysis. Integrating successively high energy excited states at energy scale Λ above and below the Fermi energy yields the renormalized coupling $\tilde{J}(\Lambda)$, governed by the RG flow equation [19, 20]. For a magnetic moment at site $\mathbf{r}$ with exchange coupling J and local density of states at energy ε, $\rho(\mathbf{r}, \varepsilon)$, the renormalization of the effective coupling $\tilde{J}(\Lambda)$ at energy scale Λ, above and below the Fermi energy, is found in 1-loop approximation to be given by

$$\frac{d\tilde{J}}{d \ln \Lambda} = -\tilde{J}^2 \, \frac{V_a}{2} \big(\rho(\mathbf{r}, \varepsilon_F + \Lambda) + \rho(\mathbf{r}, \varepsilon_F - \Lambda)\big), \tag{10}$$

where$V_a = L^d/N$ is the atomic volume, which is often set equal to one, we will keep it for clarity. The solution of Eq. (10) diverges for small energy scales $\Lambda \to 0$. Defining the Kondo temperature by the scale $\Lambda_K = k_B T_K$ at which the correction to the renormalized coupling is equal to the bare coupling, we recover Eq. (9), when approximating $\tanh(x) \approx \mathrm{sign}(x)$ for $|x| > 1$, and 0 otherwise, noting that the local density of states, the number of states per energy and volume, can be written in terms of the eigenstates of the conduction electrons as

$$\rho(\mathbf{r}, \varepsilon) = \sum_{n,\sigma} \left|\psi_n(\mathbf{r})\right|^2 \delta(\varepsilon - E_n). \tag{11}$$

In terms of the local density of states, we can thus rewrite Eq. (9) as

$$1 = \frac{V_a}{2} J \int_0^D dE \, \frac{\rho(E, \mathbf{r})}{E - E_F} \tanh\left(\frac{E - E_F}{2T_\mathrm{K}(\mathbf{r})}\right). \tag{12}$$

Since perturbation theory breaks down at temperatures of the order of T_K, a nonperturbative treatment is needed to be able to derive lower temperature properties. This is possible with the Wilson numerical renormalization group method [21, 22] and analytically with the exact Bethe-Ansatz method [23, 24]. Both methods show that the temperature T- and magnetic field H-dependence of the free energy, and thus all thermodynamic observables, as well as transport properties like the resistivity, scale with the Kondo temperature, depending only on the ratios T/T_K and H/T_K. Thus, thermodynamic observables like the magnetic susceptibility are for single Kondo impurities proportional to known universal scaling functions of T/T_K and H/T_K, and it only remains to find the Kondo temperature for specific magnetic impurities in a metal. The low temperature phase can thus be described by a state where the magnetic impurity spins are screened by Kondo clouds formed by the conduction electrons whose effective mass is thereby enhanced, but still forming a Fermi liquid [25].

Therefore, let us first proceed to review the calculation of the Kondo temperature T_K. For a clean metal the eigenstates are plane waves with uniform density $|\psi_n(\mathbf{r})|^2 = 1/L^d$, independent of position $\mathbf{r}$. For a smooth density of states $\rho(\varepsilon_F) = \rho_0$, we denote the number of states per energy and spin as $N_0 = V_a \rho_0/2$, with $V_a = L^d/N$. Then, Eq. (12) simplifies to

$$1 = J \int_0^D dE \, \frac{N_0}{E - E_F} \, \tanh\left(\frac{E - E_F}{2T_{\mathrm{K}}}\right). \tag{13}$$

Noting that $\tanh(x) \to \mathrm{sign}(x)$ for $|x| \gg 1$, and assuming that the Fermi energy is in the middle of the band $E_F = D/2$, we find $1 \approx J\, 2N_0 \ln(D/T_K)$, yielding the Kondo temperature

$$T_{\mathrm{K}}^0 = cDe^{-1/2N_0 J}, \tag{14}$$

where $c = 0.57$ is found by a more accurate integration of the $\tanh$-function. Higher order corrections in J lead only to pre-exponential corrections which depend weakly on J. Thus, the 1-loop result T_K^0 yields already the dominant dependence on the exchange coupling J.

The Kondo effect can also occur in semimetals, semiconductors and even insulators, where the density of states at the Fermi energy is vanishing, when the exchange coupling exceeds a critical value J_c. At first sight, Eq. (14) seems to imply, that the Kondo temperature is vanishing when $\rho(\varepsilon_F) = 0$. However, then the assumption of smooth density of states is no longer valid and we need to start rather from the general self consistency equation, Eq. (9). In section 6 we will therefore consider and review the derivation of the Kondo temperature and J_c for two generic cases: a) when the Fermi level is in a pseudo-gap and b) when it is in a hard gap.

In a real material there are spatial variations of local density of states $\rho(\mathbf{r})$ and exchange coupling J due to inhomogeneities and disorder, both from nonmagnetic and magnetic impurities. According to Eq. (9) this results in Kondo temperatures which vary with spatial position, $T_{\mathrm{K}}(\mathbf{r})$, since the intensity $|\psi_n(\mathbf{r})|^2$ may vary spatially. Moreover the intensity of each state $|n\rangle$ at different energy E_n at the site of a magnetic moment may be different, making it a complex problem to evaluate the sum over all eigenstates. In fact, already in a weakly disordered metal one finds that the Kondo temperature is distributed with a finite width [26–28]. In section 7 we will therefore consider and review the Kondo effect in disordered systems in more detail.

4 RKKY coupling between magnetic moments

A magnetic impurity never comes alone. Thus, we need to consider what happens when more than one magnetic impurity is in the metal. Naturally, the Anderson impurity model Eq. (1) can be extended to any number M of localized level sites, summing over their M positions $\mathbf{r}_j$,

$$H = \sum_{n,\sigma} E_{n\sigma} \hat{n}_{n\sigma} + \sum_{j,\sigma} \varepsilon_{d_j\sigma} \hat{n}_{d_j\sigma} + \sum_j U_j \hat{n}_{d_j+} \hat{n}_{d_j-} + \sum_{n,j,\sigma} \left(t_{nd_j} c^\dagger_{n\sigma} d_{j\sigma} + t_{d_j n} d^\dagger_{j\sigma} c_{n\sigma} \right), \tag{15}$$

where the energy of localized levels $\varepsilon_{d_j\sigma}$, onsite interaction U_j, and hopping elements $t_{d_j n}$ may depend on the positions $\mathbf{r}_j$, where $j = 1, \ldots, M$. Nothing prevents us, to perform again a

Schrieffer-Wolff transformation to the Kondo Hamiltonian in the basis of the singly occupied states of the M magnetic moments, which yields

$$H_K = \sum_{n,\sigma} E_n \hat{n}_{n\sigma} + \sum_{j,n,n'} J_{j,nn'} \Big(S_j^{\dagger} c_{n+}^{\dagger} c_{n'-} + S_j^{-} c_{n-}^{\dagger} c_{n'+} + S_{jz}\big(c_{n+}^{\dagger} c_{n'+} - c_{n-}^{\dagger} c_{n'-}\big)\Big), \quad (16)$$

where $\mathbf{S_j}$ is now the spin vector operator of the localized moment at position $\mathbf{r}_j$. Accordingly, the matrix elements of the exchange coupling depend on the positions $\mathbf{r}_j$ as

$$J_{j;nn'} = t_{nd_j}\, t_{d_j n'} \left(\frac{1}{U_j + \varepsilon_{d_j} - E_{n'}} + \frac{1}{-\varepsilon_{d_j} + E_n} \right). \quad (17)$$

For the symmetric Kondo model, we then get,

$$H_K = \sum_{n,\sigma} E_n \hat{n}_{n\sigma} + \sum_j J_j \vec{\mathbf{S}}_j \vec{\mathbf{s}}(\mathbf{r_j}) = H_0 + H_J, \quad (18)$$

with $J_j = 4t_j^2/U_j > 0$. To derive the RKKY-coupling at finite temperature T, let us consider the thermodynamic potential $\mathit{\Omega}$ for the Kondo model Eq. (16). The correction $\Delta\mathit{\Omega}$ due to the exchange interaction between magnetic moments and the Fermi sea is given by

$$\Delta\mathit{\Omega} = -T \ln \langle S \rangle = -T \ln \big(\mathrm{Tr}(S \cdot e^{-H_0/T})/Z_0 \big), \quad (19)$$

where Z_0 is the grand canonical partition function of the Fermi sea, and S the correction factor due to the exchange interaction term in the Hamiltonian, H_J, $S = \exp\Big(-\int_0^{1/T} H_J(\tau)\, d\tau\Big)$. Performing perturbation theory in J to second order we obtain

$$\Delta\mathit{\Omega} = -\frac{1}{2} T \sum_{i,j;\alpha\beta\gamma\delta} J_i J_j \int_0^{1/T}\!\!\int_0^{1/T} d\tau_1 d\tau_2 \left\langle \vec{\mathbf{S}}_i \vec{\sigma}_{\alpha\beta} \vec{\mathbf{S}}_j \vec{\sigma}_{\gamma\delta} T_\tau \big(c_{i\alpha}^{\dagger}(\tau_1) c_{i\beta}(\tau_1) c_{j\gamma}^{\dagger}(\tau_2) c_{j\delta}(\tau_2) \big) \right\rangle . \quad (20)$$

where $\langle \cdots \rangle = \mathrm{Tr}\,\big(\cdots \exp(-H_0/T)\big)/Z_0$. Here, we assumed that the conduction electron spins are not polarized, $\big\langle \vec{\mathbf{s}}(\mathbf{r}) \big\rangle = 0$. Terms proportional to $\vec{\mathbf{S}}_i^2$ and $\vec{\mathbf{S}}_j^2$ yield only corrections to the local energy, not to the nonlocal interaction J_{RKKY}. With Wick's theorem we can present the correlator in Eq. (20) in the form $-\mathcal{G}_{\beta\gamma}(i,j;\tau_1{-}\tau_2)\, \mathcal{G}_{\delta\alpha}(j,i;\tau_2{-}\tau_1)$, where

$$\mathcal{G}_{\beta\gamma}(i,j,\tau_1{-}\tau_2) = -\Big\langle T_\tau \big(c_{i\beta}(\tau_1) c_{j\gamma}^{\dagger}(\tau_2) \big) \Big\rangle \quad (21)$$

is the Matsubara Green function [29]. Since we perform perturbation theory in J to 2nd order only, and as long as there are no other spin dependent couplings in the Hamiltonian, the propagator $\mathcal{G}_{\beta\gamma}$ is proportional to $\delta_{\beta\gamma}$ which allows us to perform the summation over spin indices in Eq. (20) explicitly to get $\sum_{\alpha\beta} \mathbf{S}_i \vec{\sigma}_{\alpha\beta} \mathbf{S}_j \vec{\sigma}_{\beta\alpha} = \mathbf{S}_i {\cdot} \mathbf{S}_j$, Thus, we find in second order perturbation theory in J that there is an indirect exchange coupling term in the Hamiltonian, the RKKY coupling between the magnetic impurity spin operators $\vec{\mathbf{S}}_i$, $\vec{\mathbf{S}}_j$, given by

$$H_{\mathrm{RKKY}} = \sum_{i,j} J_i J_j \chi_{ij} \vec{\mathbf{S}}_i \vec{\mathbf{S}}_j, \quad (22)$$

with the non local, temperature dependent susceptibility matrix

$$\chi_{ij} = -\frac{1}{2}\int_0^{1/T} \mathcal{G}(i,j;\tau)\,\mathcal{G}(j,i;-\tau)\,d\tau\,. \tag{23}$$

Writing the Green function in the representation of eigenvectors $|n\rangle$,

$$\mathcal{G}(i,j;\tau) = \sum_n \psi_n^*(\mathbf{r}_i)\,\psi_n(\mathbf{r}_j)\,e^{-(E_n-\mu)\tau} \times \begin{cases} -\big(1-f(E_n)\big), & \tau > 0 \\ \quad f(E_n)\,, & \tau < 0 \end{cases}, \tag{24}$$

we find the RKKY coupling between the magnetic impurity spin operators $\vec{\mathbf{S}}_i, \vec{\mathbf{S}}_j$,

$$J_{\mathrm{RKKY}}(\mathbf{r}_{ij}) = J_i J_j \chi_{ij} = J_i J_j \frac{V_a^2}{4\pi}\,\mathrm{Im}\!\int dE\, f(E) \sum_{n,l} \frac{\psi_n^*(\mathbf{r}_i)\psi_n(\mathbf{r}_j)}{E - E_n + \mathrm{i}\varepsilon}\,\frac{\psi_l(\mathbf{r}_i)\psi_l^*(\mathbf{r}_j)}{E - E_l + \mathrm{i}\varepsilon}, \tag{25}$$

where $V_a = L^d/N$. Note that often when discussing the RKKY coupling, the magnetic impurity spins are treated classical. Then, the coupling has to be multiplied by $S(S+1)/S^2$ to account for quantum fluctuations of the magnetic impurity spins. Here, we keep the quantum spin operators, since we want to consider the competition with the Kondo effect, for which quantum spin fluctuations are essential. We see that the RKKY coupling depends not only on the local intensities of the conduction electrons $|\psi_n(\mathbf{r}_i)|^2$, but also on the phase difference between the eigenfunctions at the different locations $\mathbf{r}_i, \mathbf{r}_j$. Inserting plane-wave states $\psi_n(\mathbf{r}_i) \sim \exp(i\mathbf{k}\mathbf{r}_i)$ into Eq. (25) one finds at large distances $k_{\mathrm{F}} r_{ij} \gg 1$ the RKKY coupling in d dimensions [30],

$$J^0_{\mathrm{RKKY}}(\mathbf{r}_{kl}) \to -c_d N_0 J_i J_j \sin\!\big(2k_{\mathrm{F}} r_{ij} + d\pi/2\big)\frac{V_a}{r_{ij}^d}, \tag{26}$$

with $r_{ij} = |\mathbf{r}_i - \mathbf{r}_j|$, k_{F} the Fermi wave number, $V_a = V/N$, $c_{d=2} = 1/\pi, c_{d=3} = 1/(2\pi)$, and $N_0 = 1/D$. Here, $N_0 = V_a\rho_0/2$ is the number of states per energy and spin with total density of states (including the factor 2 for spin) $\rho_0 = m/\pi$ in $d = 2$ dimension and $\rho_0 = mk_{\mathrm{F}}/\pi^2$ in $d = 3$, where m is the effective electron mass. In Fig. 3 results for the coupling between two magnetic adatoms on a metal surface are plotted for various distances $\mathbf{r}$, as extracted from spin dependent scanning tunnelling microscopy measurements [31].

5 Spin competition: the Doniach diagram

Knowing the Kondo temperature T_{K} and the RKKY coupling we can now study their competition as function of the local exchange coupling J and the concentration of magnetic moments n_{m}. The amplitude of the oscillatory RKKY coupling Eq. (26) can be rewritten as $J^0_{\mathrm{RKKY}}/D = c_d J^2 n_{\mathrm{m}}$. Noting that the coupling is dominated by nearest neighbored magnetic moments, we wrote it in terms of the density of magnetic moments $n_{\mathrm{M}} = V_a/R^d$, where R is the average distance between next neighbored magnetic moments. In Fig. 4 (left) we plot both energy scales in $d = 3$ dimensions. For the RKKY-coupling we plot it both for a dense system of magnetic impurities $n_{\mathrm{M}} = 1$ (blue), and for a more dilute case, $n_{\mathrm{M}} = 0.5$ (dashed blue).

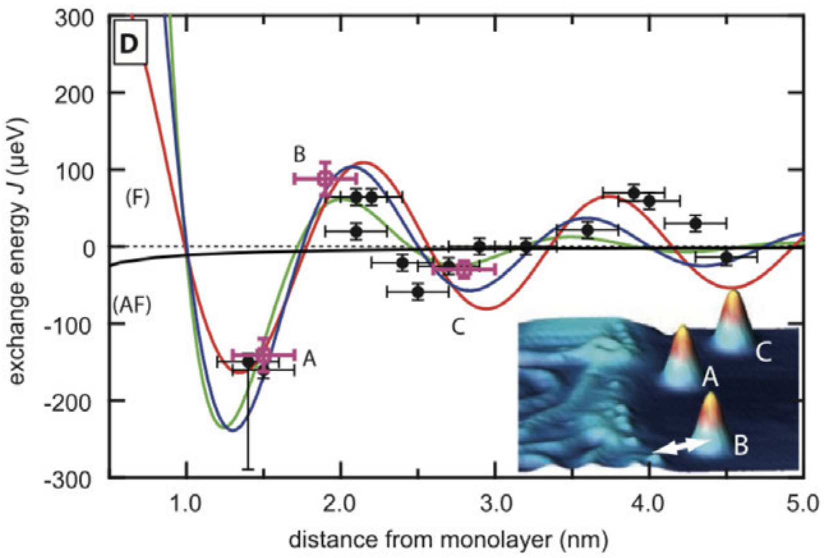

Fig. 3: *Magnetic exchange interaction between adatoms on a monolayer stripe. Dots show the measured exchange energy as function of the distance from the monolayer, indicated in the inset. Lines are fits to the 1D, 2D and 3D RKKY-coupling Eq. (26). Figure taken from Ref. [31].*

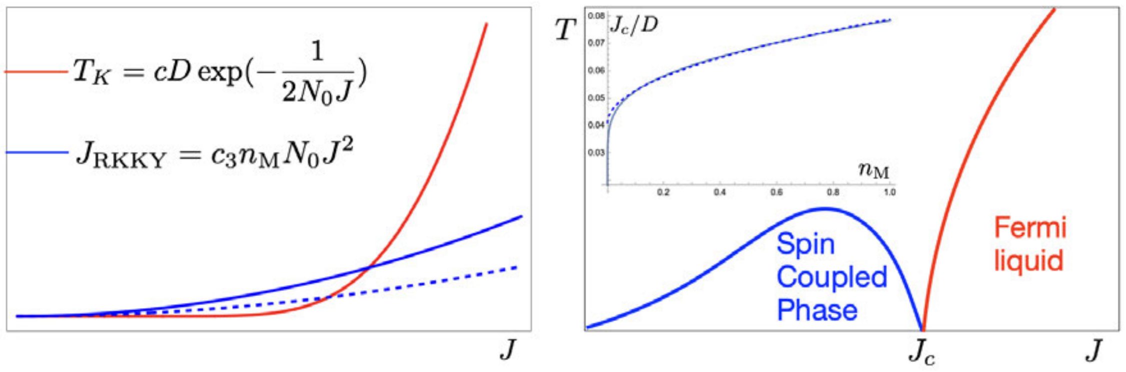

Fig. 4: *Left: Kondo temperature* $T_{\rm K}$ *with* $c = 0.57$ *(red) and RKKY coupling* $J_{\rm RKKY}$ *with* $c_3 = 1/(2\pi)$ *for (dense, dilute) magnetic impurities,* $n_M = (1, 0.5) \equiv$ *(blue, blue dashed) as function of exchange coupling* J*. Right: Doniach diagram, qualitative sketch of transition temperature to a spin coupled state (blue), and to the low temperature Fermi liquid (red), as function of* J*. The critical coupling* J_c/D*, Eq. (27), is plotted in the inset as function of magnetic moment density* $n_{\rm M}$ *(blue line), together with the fit* $J_c/D \approx 0.041 + 0.038\sqrt{n_{\rm M}}$ *(dashed blue).*

Thus, we see that there is a critical coupling J_c below which the RKKY coupling exceeds the energy scale for Kondo screening $T_{\rm K}$, so that the magnetic impurity spins can be coupled with each other. That critical coupling J_c is seen to increase with the concentration of the magnetic moments. Solving the nonlinear equation analytically, we find

$$J_c = -\frac{D}{4W\big(-1, -\sqrt{(c_d/c)n_{\rm M}}/4\big)}, \tag{27}$$

where $W(k,z)$ is the k-th branch of the Lambert W-function, also known as ProductLog-function, plotted for $d = 3$ in the inset of Fig. 4 (right), blue line. We find for the whole range of concentrations $0 < n_{\rm M} < 1$, $J_c/D \approx 0.041 + 0.038\sqrt{n_{\rm M}}$ a good fit (dashed blue line).

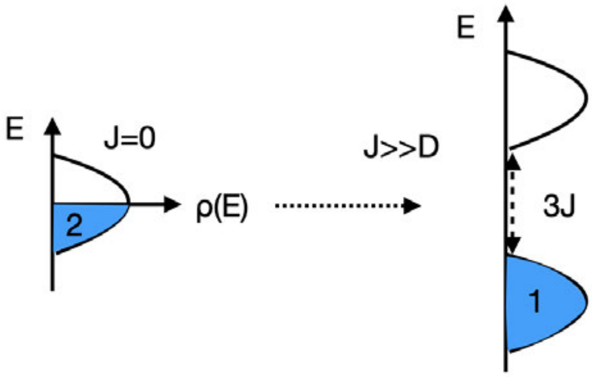

Fig. 5: *Left: Sketch of typical density of states $\rho(E)$ of a metal as function of energy E. The band of width D is half filled with N electrons (blue). Each state is doubly spin degenerate as indicated by 2. Right: Density of states in the presence of a lattice of N magnetic moments, coupled by strong antiferromagnetic exchange coupling $J > D$ to the conduction electron spins, forming N non degenerate Kondo singlet states, as indicated by 1, thereby enlarging the Fermi surface. There is a charge transfer gap $3J$, making that system for $J > D$ a Kondo insulator.*

Doniach argued in Ref. [13] that the critical coupling J_c marks a quantum phase transition between a heavy fermion state and an ordered, typically antiferromagnetic, phase in the Kondo lattice limit $n_{\mathrm{M}} = 1$, where nearest neighbor RKKY coupling is antiferromagnetic. This gives a good description of quantum phase transitions in heavy fermion materials that contain rare earth elements like Ce, Sm, and Yb or actinides like U and Np, where local magnetic moments originate from localized f-orbitals and antiferromagnetic order is observed at sufficiently low temperature. As pressure or external magnetic field is changed, the Néel temperature T_N reaches a maximum, before it is suppressed at the quantum critical point. This has been measured in detail for Cerium compounds, such as $\mathrm{CeAl_2}$, CeAg or $\mathrm{CeRh_2Si_2}$, as well as in $\mathrm{YbRh_2Si_2}$ under pressure and in a magnetic field [32], for a review see [8].

In order to derive that quantum phase transition at $T = 0K$ one needs to find the ground state of the Anderson model with a finite number of M Anderson impurity sites, Eq. (15) or, alternatively, solve the Kondo model of M impurity spins, Eq. (18) as coupled to the conduction band by the antiferromagnetic exchange couplings $J_j = 4t_j^2/U_j > 0$ at the M impurity sites $j = 1, \ldots, M$. In a dense Kondo lattice, where $n_M = 1$, the number of impurity spins M equals the number of occupied conduction band states N.

Let us start by looking at a simpler state, a Kondo insulator, which can, for example, form when the uniform coupling is strong $J{=}J_j \gg D$, exceeding the conduction band width D. Then, the exchange coupling J is so strong that each impurity spin localizes one of the conduction electrons, so that the ground states is given simply by a product of singlet states, $|\psi_0\rangle = \sum_{j=1}^N |0_i\rangle$, where $|0_i\rangle = \big(|\uparrow_{di}\rangle|\downarrow_{ci}\rangle - |\downarrow_{di}\rangle|\uparrow_{ci}\rangle\big)/\sqrt{2}$, is the singlet state formed by the impurity spin (indexed by d) and a conduction electron spin (indexed by c) at site i. The ground state energy is then given by $E_0 = -N(3/2)J$. The lowest spin excitation energy gap ΔE_s is obtained by exciting one of the spin pairs to a triplet state of energy $J/2$, thus $\Delta E_s = 2J$. However, there is also a finite charge transfer gap ΔE_q, which is obtained by transferring one of the conduc-

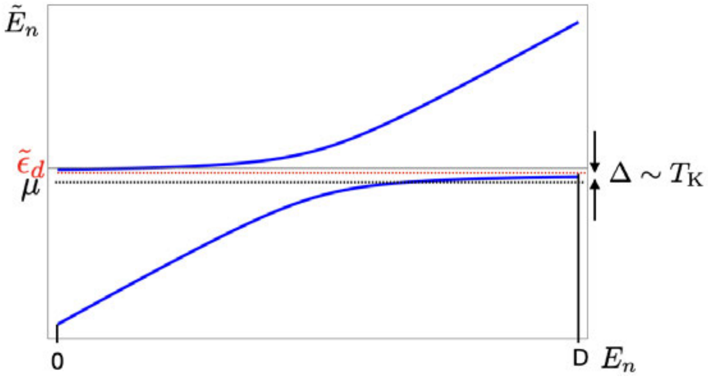

Fig. 6: *Quasi particle eigenenergies* $\tilde{E}_n$ *as function of bare eigenenergies without Kondo coupling* E_n. μ *is the chemical potential, the energy level of the localized level becomes shifted upward into the gap,* $\tilde{\varepsilon}_d$. *The indirect gap* Δ *is of the order of* T_{K},

tion electrons from site i to site j. Consequently, at site i the impurity spin is left alone $|\uparrow_{di}\rangle$, breaking up the singlet state $|0_i\rangle$, and shifting its energy to $E_i = 0$, while at site j the singlet state is also broken up to accommodate the second electron, exciting the state to $|\uparrow_{di}\rangle|\downarrow_{ci}\rangle|\uparrow_{ci}\rangle$, with energy $E_j = 0$, since the spins of the two conduction electrons compensate each other to $s_{\mathrm{tot\ j}} = 0$, so that the magnetic impurity spin at site j cannot couple to them. As a consequence, a transfer of a single electron from site i to site j costs in total $\Delta E_q = 2(3/2)J$. Thus, the exchange coupling J to localized magnetic moments prevents charge transfer, opening a large gap $\Delta E_q = 3J$. Taking into account the finite band width D due to the dispersion of the conduction electrons, each of the N Kondo singlets is formed rather by electrons in superpositions of conduction band states. Thus, these Kondo clouds overlap strongly in space. To accommodate all N conduction electrons in these N Kondo singlets, the Fermi surface expands to embrace all states in the conduction band, as compared to the half filled conduction band with doubly occupied states, which is the ground state without the exchange coupling J, see Fig. 5 and the discussion in Refs. [7,8]. Above this ground state of Kondo singlets, the gap $\Delta E_q = 3J$ opens, the energy needed to transfer one electron from one Kondo singlet to another, making the system an insulator. In fact, this is the mechanism for the formation of a Kondo insulator, which has been experimentally observed, first in SmB$_6$ [33].

When the exchange coupling is smaller than the band width $J < D$, the ground state is no longer a simple product of Kondo singlets. One way to derive the ground states then is by a mean-field treatment of a generalized Kondo lattice Hamiltonian with degeneracy $N_K \gg 1$, the Coqblin-Schrieffer Hamiltonian [34], performing a $1/N_K$-expansion, as done first in Refs. [35] and [36]. Thereby one finds the quasi particle eigenenergies $\tilde{E}_n$ as function of the eigenenergies of the conduction band without Kondo coupling, E_n,

$$\tilde{E}_n = \frac{1}{2}(E_n + \tilde{\varepsilon}_d) \pm \frac{1}{2}\sqrt{(E_n - \tilde{\varepsilon}_d)^2 + 4V^2}. \tag{28}$$

as plotted in Fig. 6 as function of E_n Thus, there opens a gap $\Delta = T_{\mathrm{K}}$, relating the mean-field order parameter V to the Kondo temperature T_{K} by $4V^2 = DT_{\mathrm{K}}$, when $\tilde{\varepsilon}_d \approx D/2$. The density of states above and below the gap is seen to be strongly enhanced. The chemical potential is located in the lower band, so that the exchange coupling transformed the Fermi sea of conduction electrons to a Fermi sea of heavy holes. The energy level of the localized level ε_d becomes shifted upward into the gap, $\tilde{\varepsilon}_d$. With the invention of dynamical mean-field theory, exploiting the fact that mean-field theory becomes exact in infinite dimension $d \to \infty$ [37], another route to solve the Kondo lattice model and the periodic Anderson model opened, which allows the calculation of self energies [38, 39] and of the resistivity. Thereby, the decay of the resistivity was shown as coherent heavy fermions form at low temperature [40], in agreement with experiments on heavy fermion compounds, as reviewed above.

However, in order to allow the study of the competition between the Kondo screening and the RKKY-coupling both approaches need to be modified. By adding the RKKY-coupling between the magnetic moments to the Kondo lattice hamiltonian, the quantum phase diagram can be studied in mean-field theory, when combined with the $1/N_K$-expansion [41–44].

A system of two magnetic impurities in a metal has been studied in detail with nonperturbative methods like the numerical renormalization group [45–49]. Such a system has also been realized experimentally by Co atoms on a gold surface and studied varying their distance with scanning tunnelling microscopy [50]. One finds a crossover between a state where both magnetic moments are Kondo screened by the conduction electrons and a state where the impurity spins are coupled. Depending on their distance, they form either a singlet, enforced when RKKY coupling is antiferromagnetic, or a triplet state, when the coupling is ferromagnetic. Building on these studies, DMFT has been extended to Cluster-DMFT, where the exact results for a cluster of few spins, in particular two magnetic impurities are used to enhance the DMFT and to derive the phase diagram of the Kondo lattice model with RKKY coupling [51].

Further insights into this competition comes from exact analytical results for the 1D Kondo lattice and the 1D periodic Anderson model employing the bosonization technique, see Refs. [52] and [53] and references therein. At half filling a Kondo insulator is found, and both the spin and charge transfer gaps have been derived [52].

Recently, Nejati *et al.* extended the renormalization group equations for a Kondo lattice incorporating self consistently the RKKY coupling between magnetic moments [54]. Thereby they could show that the Kondo temperature is decreased as the exchange coupling J is decreased, as found with diagrammatic methods in Refs. [55–57]. Furthermore, it was found in Ref. [54] that the Kondo screening is quenched at a critical coupling J_c. Since this approach to the spin competition problem is very insightful let us review it in the remainder of this section.

The renormalization of the effective coupling $\tilde{J}(\Lambda)$ at energy Λ, above and below the Fermi energy, Eq. (10), is modified by the RKKY coupling as derived first in Ref. [54] and generalized in Ref. [58] to account for an energy dependent local density of states $\rho(E, \boldsymbol{r}_i)$, yielding

$$\begin{aligned}\frac{d\tilde{J}_i}{d\ln\Lambda} = & -\tilde{J}_i^2\frac{V_a}{2}\sum_{\alpha=\pm}\rho(\mu{+}\alpha\Lambda, \boldsymbol{r}_i)\\ & +\frac{4}{\pi}\tilde{J}_i^2 J_i^0\sum_{\alpha=\pm}\sum_{j\neq i}J_j^0\,\mathrm{Im}\left(e^{i\mathbf{k}_F\mathbf{r}_{ij}}\chi_c(\mathbf{r}_{ij},\mu{+}\alpha\Lambda)G_c^R(\mathbf{r}_{ij},\mu{+}\alpha\Lambda)\chi_f(\mathbf{r}_j,\mu{+}\alpha\Lambda)\right),\end{aligned} \quad (29)$$

where Λ is the effective band cutoff for the renormalization group flow. While the first term on the right hand side is the well known 1-loop RG for the Kondo problem with energy dependent density of states, Eq. (10) [18, 20], the second term describes the correction due to RKKY-coupling. Here, $\chi_f(\mathbf{r}_j, E)$ is the spin susceptibility of the magnetic moment at site $\mathbf{r}_j$. $G_c^R(\mathbf{r}_{ij}, E)$ is the retarded conduction electron propagator from site $\mathbf{r}_i$ to $\mathbf{r}_j$ and we defined the distance vector $\mathbf{r}_{ij} = \mathbf{r}_i - \mathbf{r}_j$. $\chi_c(\mathbf{r}_{ij}, E)$ denotes the conduction electron correlation function between sites $\mathbf{r}_i$ and $\mathbf{r}_j$. Solving Eq. (29) we can thus derive the position dependent Kondo temperatures for a given configuration of magnetic moments.

When the magnetic moment density n_M is not too large, $\chi_f(\mathbf{r}_j, E)$ can be approximated by the Bethe-Ansatz solution for a single Kondo impurity [23, 24]. In Ref. [54] this approximation has been used. Then, only its real part contributes, as given by $\mathrm{Re}\,\chi_f(\mathbf{r}_j, \mu + D) = \mathcal{W}/(\pi T_{Kj}\sqrt{1 + D^2/T_{Kj}^2})$. Here, $\mathcal{W}$ is the Wilson ratio. T_{Kj} is the Kondo temperature at site $\mathbf{r}_j$. Since it is well known that the energy dependence of the density of states changes the Kondo renormalization [59], it is in general important to keep the energy dependence of all functions and not to replace it with their value at the chemical potential, when the density of states is strongly varying with energy, as in the presence of a pseudo-gap, or in disordered systems.

But, let us first consider the simpler case of magnetic moments in a clean metal, with slowly varying density of states. Then, we can furthermore assume that all conduction electron properties, the local density of states, the propagator $G_c^R(\mathbf{r}_{ij}, E)$ and the correlation function $\chi_c(\mathbf{r}_{ij}, E)$ depend only weakly on energy, and therefore can be replaced by its value at the chemical potential μ, as has been done in Ref. [54]. Then, we can define the effective Kondo coupling $g_i = N(\mu) J_i$ of the Kondo impurity at site $\mathbf{r}_i$, where $N(\mu) = V_a \rho(\mu)/2$, and find the renormalization group equation for g_i, as modified by the RKKY coupling [54],

$$\frac{dg_i}{d \ln \Lambda} = -2 g_i^2 \left(1 - y_i g_0^2 \frac{D}{2T_K} \frac{1}{\sqrt{1 + (\Lambda/T_K)^2}} \right), \tag{30}$$

where D is the bare bandwidth and $g_0 = N(\mu) J^0$ is the bare, unrenormalized Kondo coupling, y_i is the effective dimensionless RKKY interaction strength at site $\mathbf{r}_i$, given by [54]

$$y_i = -\frac{8W}{\pi^2 \rho(\mu)^2} \,\mathrm{Im} \sum_{j \neq i} e^{i\mathbf{k}_F \mathbf{r}_{ij}} G_c^R(\mathbf{r}_{ij}, \mu) \Pi(\mathbf{r}_{ij}, \mu), \tag{31}$$

where W is the Wilson ratio as determined by the Bethe Ansatz solution of the Kondo problem [23, 24]. $G_c^R(\mathbf{r}_{ij})$ is the single particle propagator in the conduction band from site $\mathbf{r}_i$ to $\mathbf{r}_j$. The summation is over all other magnetic moments at positions $\mathbf{r}_j$. $\Pi(\mathbf{r}_{ij}, \mu)$ is the RKKY correlation function of conduction electrons between sites $\mathbf{r}_i$ and $\mathbf{r}_j$. y_i is found to be always positive [54], while the RKKY correlation function can be positive or negative.

It is interesting to observe that the effective Kondo interaction renormalized by the RKKY interaction is a function of Λ/T_K, where Λ is the renormalization group energy scale and T_K is the renormalized Kondo temperature to be determined self-consistently.

For two magnetic moments in a clean system, where the bare couplings g_0 are the same at both sites, and $y_i = y$, one can solve this differential equation to obtain [54]

$$\frac{1}{g} - \frac{1}{g_0} = 2 \ln \frac{2\Lambda}{D} - y g_0^2 \frac{D}{2T_K} \ln \frac{\sqrt{1 + (\Lambda/T_K)^2} - 1}{\sqrt{1 + (\Lambda/T_K)^2} + 1}\,. \tag{32}$$

When the energy scale Λ coincides with the Kondo temperature, i.e., $\Lambda \to T_K$, the correction to the effective Kondo interaction is large. Therefore, setting $g(T_{\mathrm{K}}) = \infty$ we get the self-consistent equation for the effective Kondo temperature as a function of the RKKY interaction,

$$T_K(y, g_0) = T_K^0(g_0) \exp\Big(-ykg_0^2 \frac{D}{T_K(y)}\Big), \tag{33}$$

where $T_K^0(g_0) = cD \exp\big(-1/(2g_0)\big)$ is the bare Kondo temperature in the absence of the RKKY interaction and the numerical constant is $k = \ln(\sqrt{2}+1)$. Its solution is

$$T_K(y, g_0) = -\frac{ykg_0^2}{W\big(-ykg_0^2/T_K^0(g_0)\big)}, \tag{34}$$

for $y < y_c$ with the critical coupling [54]

$$y_c = T_K^0/(k\, eg_0^2 D). \tag{35}$$

Noting that the coupling y is related to the magnetic moment density as $y \sim n_{\mathrm{M}}$, and that $g_0 = N_0 J$, we find that the exchange coupling has to exceed the critical coupling $J_c(n_{\mathrm{M}})$. Thus, it agrees with the result obtained above, when using the Doniach argument, Eq. (27), up to a numerical constant of order 1. As the exchange coupling J is diminished towards that critical value, J_c, the Kondo temperature T_K becomes diminished continuously, as plotted in Fig. 7. At the critical value, however, it is found to take a finite value $T_K^* = T_{Kc}(J_c) = e^{-1}T_K^0(J_c)$, about one third of its value without the RKKY coupling, before it jumps to zero at smaller J.

For two magnetic Co atoms on a gold surface such a suppression of T_K was observed experimentally in Ref. [50] at varying distance R, as measured in the width of the tunnelling peak with scanning tunnelling microscopy [50]. In that case, one finds a crossover between a state where both magnetic moments are Kondo screened by the conduction electrons and a state where the impurity spins form a singlet, enforced when RKKY coupling is antiferromagnetic.

Applying that to a system of dense magnetic moments, like heavy fermion materials, this result is remarkably different from the Doniach diagram, Fig. 4, where it was assumed that both the Kondo temperature and the critical temperature T_c on the spin coupled side of the transition would decay continuously towards the critical point J_c. However, to conclude on the nature of the quantum phase diagram one would have to include self consistently the change in the spin polarization function in the derivation due to an ordering transition of the unscreened or partially screened magnetic moments or by a spin wave instability of the conduction electrons.

The result Eq. (34) also implies that by taking into account the RKKY-coupling, the Kondo temperature becomes dependent explicitly on the distance R between the magnetic moments, and thereby on the density of magnetic moments n_{M}.

However, when the magnetic impurity concentration n_{M} is lowered, not only is $J_c \sim \sqrt{n_{\mathrm{M}}}$ diminished, and thereby the parameter range of the ordered phase reduced, but the positions of magnetic moments become distributed randomly. Thus, for $n_{\mathrm{M}} < 1$, the distance between magnetic moments R is random. Thereby, both the sign and amplitude of the RKKY coupling is randomly distributed. This may give rise to the appearance of a richer quantum phase diagram with a spin coupled phase without long range order, such as a *spin glass* state [60], which

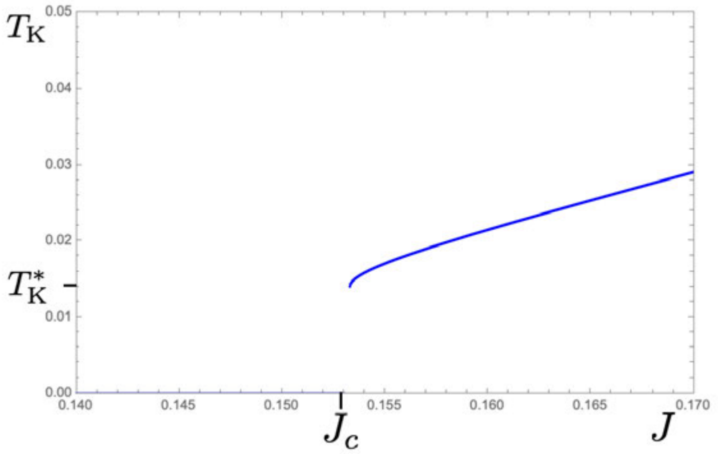

Fig. 7: *Kondo temperature as function of J in units of D, $T_K(J)$, Eq. (34), as modified by RKKY coupling for $y = 0.6/k < y_c$. Note that $T_K(J)$ jumps discontinuously from T_K^* to zero at J_c.*

competes with an ordered state [41]. In metal wires with dilute magnetic impurities, such as $Ag_{1-x}Mn_x$, a transition from a Kondo phase to a spin glass phase has been detected in transport experiments, as the Mn concentration x is enhanced [61]. Spin glass phases have also been found in alloys with rare earth elements, such as $CeNi_{1-x}Cu_x$ [62], where the competition between Kondo and RKKY coupling is studied as function of x: CeCu (x=1) is at low temperature an antiferromagnet and the alloy remains one up to $x = 0.7$, while CeNi (x=0) is a heavy fermion material. Thus, lowering x corresponds to an increase of the local Kondo coupling J, inducing a Doniach like quantum phase transition. However, at intermediate values of x, disorder is relevant, and spin glass behavior is found [62], as reviewed and modelled in [44]. Similar successions of quantum phase transitions between heavy fermion, spin glass and ordered phases have been found in $CeRh_xPd_{1-x}$ as function of x [63]. We will consider the effect of disorder on the competition between Kondo screening and RKKY coupling in section 7, where we will find that new effects introduced by randomness, like Anderson localization and multifractality have to be taken into account in strongly disordered systems with magnetic moments, which profoundly change the quantum phase diagram.

In the next section we consider the effect of a strongly varying density of states on both the Kondo screening and the RKKY-coupling and thereby on the quantum phase diagram.

6 Spin competition in presence of a spectral (pseudo) gap

In semiconductors and insulators the density of states at the Fermi energy is vanishing. At first sight, Eq. (14) seems to imply, that the Kondo temperature is vanishing in such a situation, when $\rho(\varepsilon_F) = 0$. However, the assumption of a smooth density of states is no longer valid and we need to start from the general self consistency equation, Eq. (9). We find that the Kondo effect occurs provided the exchange coupling J exceeds a critical value J_c. Let us review the derivation of the Kondo temperature and J_c for two generic cases when the Fermi level is in a pseudogap and when it is in a hard band gap.

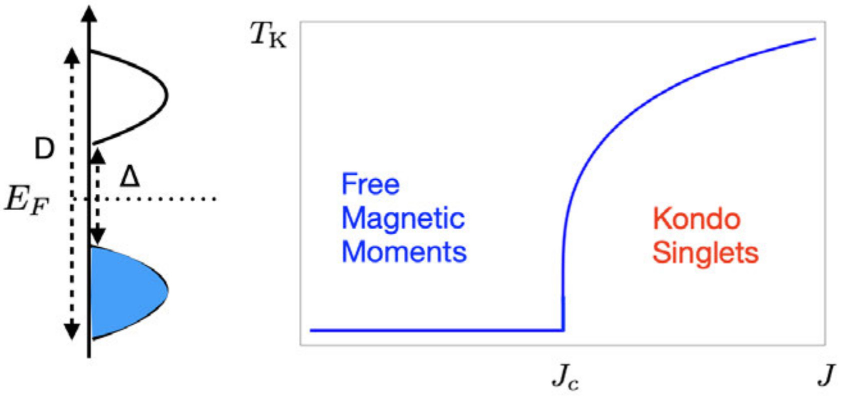

Fig. 8: *Left: Schematic density of states with gap $\varDelta$, total bandwidth D, Fermi energy E_F in the middle of the gap. Right: Kondo temperature $T_{\mathrm{K}}(J)$ as function of J in units of D, Eq. (38). Note that it decays continuously to zero at the critical coupling $J_c(\varDelta)$. Eq. (37).*

6.1 Band insulator, semiconductor

Here, we derive the Kondo temperature in a band insulator with a gap $\varDelta$, where the Fermi level is in the middle of the gap, as sketched in Fig. 8(left), by inserting the gapped density of states into Eq. (12). For a small gap $\varDelta < T_{\mathrm{K}}$, assuming that the density of states is constant and the same in the upper and lower band, ρ_0, the functional dependence of the Kondo temperature on the exchange coupling J remains the same as in a metal, $T_{\mathrm{K}} \approx c(\varDelta)\exp\big(-1/(2N_0J)\big)$, where N_0 is the number of states per energy and spin, but the pre-factor $c(\varDelta) < c$ is diminished compared to a metal, $c = c(\varDelta{=}0) \approx 0.57$. When the gap is larger $\varDelta > T_{\mathrm{K}}$, the functional dependence on J changes. Integration of Eq. (12), using that $\tanh(x) \approx 1 - 2\exp(-2x)$ for $x > 1$, we find the Kondo temperature as a solution of the equation

$$\frac{\varDelta}{4}\left(\ln\frac{D}{\varDelta} - \frac{1}{2N_0J}\right) = T_{\mathrm{K}}\exp\left(-\frac{\varDelta}{T_{\mathrm{K}}}\right). \tag{36}$$

We see that, only when the left side is positive, there can be a real solution for T_{K}. Thus, the Kondo temperature can only be finite when $J > J_c(\varDelta)$, with critical exchange coupling

$$J_c^{\varDelta} = \frac{1}{2N_0}\frac{1}{\ln(D/\varDelta)}. \tag{37}$$

As $J \to J_c^{\varDelta}$ the Kondo temperature is found to decay continuously to zero as

$$T_{\mathrm{K}} = \frac{\varDelta}{2}\frac{1}{W\big(4N_0J/(J/J_c^{\varDelta}-1)\big)}. \tag{38}$$

For $J \gtrsim J_c^{\varDelta}$ that decay can be approximated as $T_{\mathrm{K}} \approx \varDelta/2/\ln\big(4N_0J/(J/J_c^{\varDelta}-1)\big)$. Thus, for $J > J_c^{\varDelta}$ magnetic moments are Kondo screened for temperatures below $T_{\mathrm{K}}(J)$, in spite of the large band gap $\varDelta > T_{\mathrm{K}}$. For $J < J_c^{\varDelta}$ all magnetic moments remain unscreened.

Since RKKY couplings, Eq. (25), are dominated by the density of states at the Fermi energy, in an insulator they are small and decay exponentially with distance R. However, when an insulator or semiconductor is doped, there exist other forms of magnetic coupling between magnetic

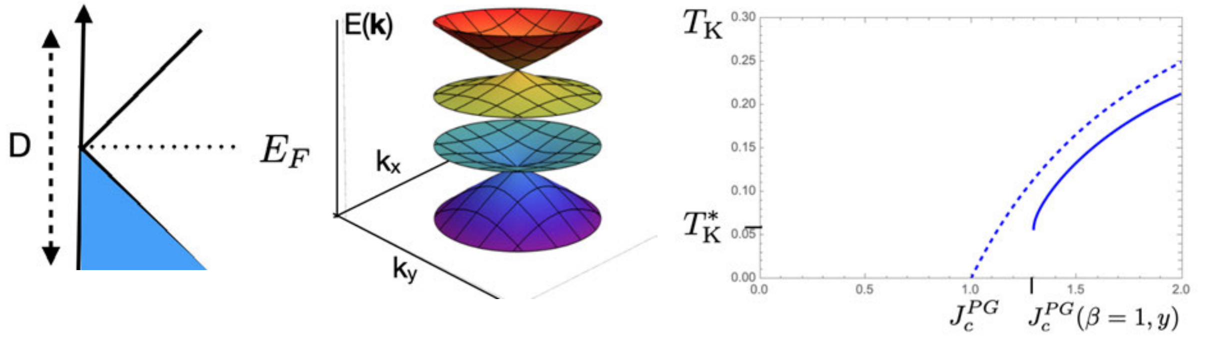

Fig. 9: *Left: Schematic density of states with pseudo-gap at Fermi energy E_F, bandwidth D. Middle: Quasiparticle dispersion of a 2D honeycomb Kondo lattice. Fig. taken from Ref. [72]. Right: Kondo temperature in the presence of a pseudo-gap with power $\beta = 1$ with RKKY coupling $y = 1/(32k)$ Eq. (44) (full line) and without, Eq. (40) (dashed line). The Kondo temperature in the presence of RKKY coupling y terminates at the critical coupling Eq. (43) $J_c^{PG}(\beta{=}1,y) > J_c^{PG}(\beta{=}1)$, Eq. (39) at the value $T_{\rm K}^*$, Eq. (45) and jumps then to zero.*

dopants. For spin-½ dopants, like P in Si, they are known to be coupled by antiferromagnetic superexchange interaction, caused by the overlap of dopant eigenfunctions. Then, dopant spins are in a random singlet state for dilute doping [64], see Ref. [65] for a review. But there can be other exchange mechanisms in dilute magnetic semiconductors, for example the Zener's double exchange coupling and the p-d coupling, which are ferromagnetic. See Ref. [66] for a review.

6.2 Pseudo-gap semimetal

A pseudo-gap opens at the Fermi energy when the density of states vanishes at the Fermi energy as $\rho(E) \sim |E{-}E_F|^\beta$ with a power $\beta > 0$, as shown schematically in Fig. 9 (left). This occurs in numerous materials, like at the surface of topological insulators [67] and in graphene [68], where the electrons are confined to a 2-dimensional honeycomb lattice. The low-energy excitations in graphene are fermionic quasiparticles described by relativistic massless Dirac fermions, as characterized by a linear dispersion relation, with two Dirac points, where the density of states vanishes linearly with energy ($\beta{=}1$). Thus, the question arises, what happens when these massless fermions are coupled to local magnetic moments. The answer depends strongly on the magnitude of the exchange coupling J. Plugging in the pseudo-gap density of states $\rho(E) = \rho_0 \big|(E{-}E_F)2/D\big|^\beta$ in the equation for the Kondo temperature, Eq. (12), for $E_F = D/2$, we find for $J > J_c^{PG}(\beta)$ with critical exchange coupling

$$J_c^{PG}(\beta) = \beta/(2N_0) = \beta D/2, \tag{39}$$

the Kondo temperature

$$T_{\rm K} = \frac{D}{2}\left(1 - \frac{J_c^{PG}(\beta)}{J}\right)^{1/\beta}. \tag{40}$$

Note that for $J \gg J_c^{PG}$, Eq. (40) converges to $T_{\rm K}^0 \sim D/2\exp\big(-1/(2N_0J)\big)$, the Kondo temperature in a metal. There is for $J < J_c^{PG}(\beta)$ no Kondo screening, as has been confirmed with non perturbative methods like the numerical renormalization group method in Refs. [59,69,70], and the concentration of free, unscreened magnetic moments $n_{\rm FM}(J)$ at $T = 0K$ is a step function, $n_{\rm FM}(J) = n_{\rm M}$ for $J < J_c^{PG}(\beta)$ and zero otherwise.

It has been shown in Ref. [71] with a large N_K-expansion that there is a quantum phase transition in the Kondo lattice on a 2-dimensional honeycomb lattice at critical coupling J_c, even when neglecting the RKKY coupling. Remarkably, the energy dispersion of quasiparticles in such a system with a pseudo-gap has a direct gap, see Fig. 9 [72], where it was shown that the Kondo-insulator gap is observable in the optical conductivity, in stark contrast to the conventional Kondo lattice system where the Kondo-insulator gap is indirect, see Fig. 6. The Dirac cones become duplicated and shifted up and down in energy, respectively, as seen in Fig. 9.

The RKKY coupling in presence of a pseudo-gap at the Fermi energy is shorter ranged,

$$J_{\rm RKKY}(\mathbf{R}) = \frac{g(\mathbf{R})}{R^{d+\beta}}, \tag{41}$$

where $g(\mathbf{R})$ is an oscillatory, non decaying function of $\mathbf{R}$ which may be anisotropic, depending on the specific lattice. Here, $R = |\mathbf{R}|$. As an example, in a 2D honeycomb lattice like graphene, where there are two sub-lattices A and B, the RKKY coupling is decaying with power $d+\beta = 3$. The oscillatory function is different, when the magnetic moments are placed on the same sub-lattices, as given by [73] $g_{AA}(\mathbf{R}) = -J^2(1+\cos\big(\varDelta\mathbf{K}\cdot\mathbf{R})\big)$, while on different sub-lattices, $g_{AB}(\mathbf{R}) = J^2 3\big(1-\cos(\varDelta\mathbf{K}\cdot\mathbf{R}-2\vartheta_R)\big)$, where $\varDelta\mathbf{K} = \mathbf{K}^{\dagger}-\mathbf{K}^{-}$, with $\mathbf{K}^{\dagger}, \mathbf{K}^{-}$ the reciprocal lattice vectors of the two Dirac points. ϑ_R is the angle between the armchair direction and the position vector of the magnetic moment on the lattice.

Thus, both Kondo temperature and RKKY coupling are diminished in the presence of a pseudo-gap. This raises the question how the pseudo-gap modifies their competition. As there is no Kondo screening for $J < J_c^{PG}(\beta) = \beta D/2$, while the RKKY-coupling is finite for all J, magnetic moments couple in that regime. To find out whether RKKY-coupling is dominating the Kondo screening even for larger exchange couplings $J > J_c^{PG}(\beta)$, we need to solve the RG-equation, Eq. (29) with RKKY interaction with a pseudo-gap. Inserting the density of states $\rho(E) = \rho_0\big|(E-E_F)2/D\big|^{\beta}$ into Eq. (29) and integration over $\varLambda$ up to the breakdown of perturbation theory at scale $T_{\rm K}$, yields the equation for the Kondo temperature

$$\frac{J_c(\beta)}{J} - 1 + \left(\frac{2T_K}{D}\right)^{\beta} + k\beta y_\beta J^2 N_0^2 \frac{D}{2T_K} = 0, \tag{42}$$

where $k = \ln(\sqrt{2}+1)$, y_β the RKKY coupling function as modified by a pseudo-gap with power β, and $J_c^{PG}(\beta)$ the critical coupling in absence of y_β, Eq. (39).

Let us consider as an example a pseudo-gap with power $\beta = 1$, as it occurs in graphene and on the surface of topological insulators. For $J > J_c^{PG}(\beta{=}1, y)$ with critical exchange coupling

$$J_c^{PG}(\beta{=}1, y) = J_c^{PG}\,\frac{1-\sqrt{1-4\sqrt{ky}}}{2\sqrt{ky}}, \tag{43}$$

where $J_c^{PG} = J_c^{PG}(\beta{=}1, y{=}0) = D/2$, is the critical coupling when neglecting the RKKY-coupling, we find the Kondo temperature

$$T_K = \frac{D}{4}\left(1 - \frac{J_c^{PG}}{J} + \sqrt{\left(1-\frac{J_c^{PG}}{J}\right)^2 - ky\left(\frac{J}{J_c^{PG}}\right)^2}\right). \tag{44}$$

Note that at the critical coupling $J_c^{PG}(\beta{=}1, y)$ it has a finite value,

$$T_K^* = \frac{D}{4}\left(1 - \frac{J_c^{PG}}{J_c^{PG}(\beta{=}1, y)}\right), \tag{45}$$

one half of the value it has at that exchange coupling $J_c^{PG}(\beta{=}1, y) > J_c^{PG}$, without RKKY-coupling. Thus, even in the presence of a pseudo-gap, the Kondo temperature jumps discontinuously to zero at $J_c^{PG}(\beta{=}1, y)$ as seen in Fig. 9(right), similar to what was found in a metal, Fig. 7. The critical coupling $J_c^{PG}(\beta{=}1, y)$ is an increasing function of the RKKY-coupling y_1 for $0 < y < 1/(16k)$, varying from $D/2$ to D. For stronger coupling $y > 1/(16k)$ there is no finite Kondo temperature and thus no Kondo screening for any coupling J.

7 Spin competition in the presence of disorder

Any real material has some degree of disorder. In doped semiconductors it arises from the random positioning of the dopants themselves, in heavy fermion materials it may in addition arise from structural defects or impurities caused by atomic defects. Disorder can cause Anderson localization, trapping electrons in the disorder potential. Thus, in order to fully understand the physics of electron systems with magnetic moments, we need to understand how Anderson localization affects the competition between Kondo screening and RKKY coupling, and how that in turn affects Anderson localization. Moreover, as noted already early [74], the physics of random systems is fully described only by probability distribution functions, not just averaged quantities. Thus, for electron systems with randomly located magnetic moments the derivation of physical properties requires the knowledge of distribution functions of both the Kondo temperature and the RKKY coupling [75], not just their averages. In fact, anomalous distributions of the Kondo temperature T_{K} and the RKKY coupling can give rise to non-Fermi-liquid behavior, as measured for example in the low-temperature power-law divergence of the magnetic susceptibility in doped semiconductors close to the metal-insulator transition [65].

7.1 Distribution of Kondo temperature and RKKY couplings

Since the Kondo temperature depends on the product of the local exchange coupling J and the density of states at the Fermi energy ρ [1, 17, 18], it is natural to expect a distribution of the Kondo temperature, $P(T_K)$, when J and ρ are distributed due to the random placement of the dopants, as has been pointed out in Refs. [74–79].

Indeed, the disorder potential results in wave function amplitudes which vary randomly, both spatially and with energy. In a weakly disordered metal different wave functions are correlated with each other in a macroscopic energy interval of the order of the elastic scattering rate $1/\tau$. This results already in weakly disordered metals in a Kondo temperature distribution of finite width in the thermodynamic limit [27, 28]. To model the disorder one adds a disorder potential $V(\mathbf{r})$ to the one particle Hamiltonian, which can be assumed to be spatially uncorrelated and white noise distributed with width given by the elastic scattering rate $1/\tau$. Using the 1-loop equation for the Kondo temperature written in terms of the local density of states $\rho(E,\mathbf{r})$, Eq. (12), let us rewrite it in terms of the disorder induced local deviations $\delta\rho(E,\mathbf{r}) = \rho(E,\mathbf{r}) - \langle\rho(E,\mathbf{r})\rangle$, where $\langle\cdots\rangle$ denotes the average over the disorder potential. Denoting $T_K^{(0)}$ as the Kondo temperature obtained with the average local density of states, $\nu = \langle\rho(E,\mathbf{r})\rangle$ we find the Kondo temperature for a given realization of the disorder potential [20]

$$T_K = T_K^{(0)} \exp\left(\int_0^D dE\, \frac{\delta\rho(\mathbf{r},E)}{2\nu(E-E_F)} \tanh\left(\frac{E-E_F}{2T_K}\right)\right). \tag{46}$$

Taking the square of the logarithm of Eq. (46) and

$$\left\langle \ln^2\left(\frac{T_K}{T_K^{(0)}}\right)\right\rangle = \int_0^D dE \int_0^D dE' \left\langle \tanh\left(\frac{E-E_F}{2T_K^{(0)}}\right) \tanh\left(\frac{E'-E_F}{2T_K^{(0)}}\right) \frac{\delta\rho(\mathbf{r},E)}{2\nu(E-E_F)} \frac{\delta\rho(\mathbf{r},E')}{2\nu(E'-E_F)}\right\rangle. \tag{47}$$

The disorder averaged correlation function of local density of states $\langle\rho(\mathbf{r},E)\,\rho(\mathbf{r},E')\rangle$ is governed at weak disorder $E_F\tau > 1$ by diffusion and Cooperon modes, as obtained by summing up ladder diagrams, describing multiple elastic scattering of the electrons from the impurity potential. For a review see [80]. Physically, these diffusion modes account for the fact that electrons in a disorder potential do not move ballistically along straight paths, but rather diffusively, such that the average square of the path length $\mathbf{r}(\mathbf{t})$ on which an electron moves within a time t is given by $\langle\mathbf{r}(\mathbf{t})^2\rangle = D_e t$, where $D_e = v_F^2\tau/d$, is the diffusion constant. Thereby one finds for the standard deviation of the Kondo temperature in the thermodynamic limit [27, 28]

$$\delta T_K \approx T_K^{(0)} \begin{cases} \frac{c_3}{(E_F\tau)\sqrt{\beta}} \ln\left(\frac{1}{\tau T_K^{(0)}}\right) & \text{in } d=3, \\ \frac{1}{\sqrt{3\pi E_F\tau\beta}} \left[\ln\left(\frac{1}{\tau T_K^{(0)}}\right)\right]^{3/2} & \text{in } d=2, \\ 2\sqrt{\frac{\pi\sqrt{3}}{k_F^2 A\beta}}\, (\tau T_K^{(0)})^{-1/4} & \text{in quasi 1-d wire of cross section } A, \end{cases} \tag{48}$$

with c_3 a constant. Note that it is larger with time-reversal symmetry $\beta = 1$ than when it is broken by a magnetic field $\beta = 2$, which diminishes weak localization corrections. In the weak disorder limit, the Kondo temperature has a Gaussian distribution with width given by Eq. (48). However, its distribution becomes strongly bimodal as disorder is increased further with an increasing weight at small Kondo temperature, see Fig. 10(left), where the distribution of T_K is plotted, obtained numerically for a tight binding model on a square lattice with potential disorder of box distribution and width W [72]. Furthermore, a finite concentration of *free* magnetic moments is found when electrons at the Fermi energy are localized. Since these effects can be explained by Anderson localization and multifractality, we will return to the Kondo temperature distribution after introducing these phenomena in the next chapters.

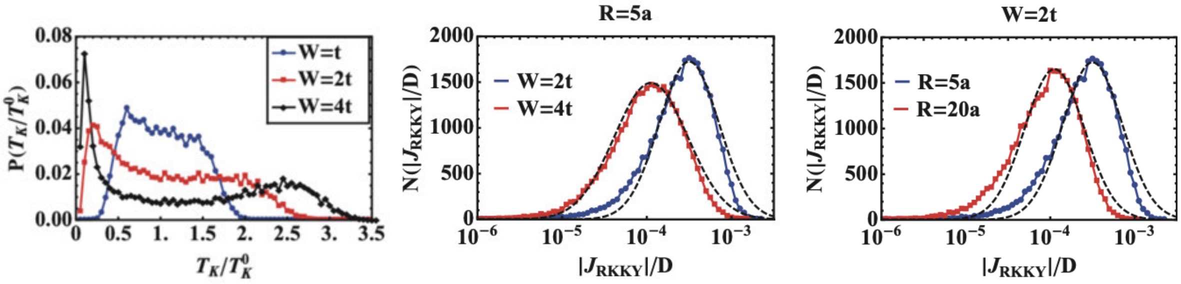

Fig. 10: *Left: Distribution of Kondo temperature for different disorder strengths W. Middle: distribution of absolute value of the RKKY coupling at fixed distance $R = 5a$ for different disorder strengths W. Right: at fixed $W = 2t$ for distances $R = 5a, 20a$. Dashed lines: lognormal distribution with fitted parameters. All results are obtained a for 2D tight binding model on a square lattice, with lattice spacing a, with potential disorder, box distribution of width W in units of hopping amplitude t, Fermi energy $E_F = t$. All Figs. taken from Ref. [72].*

As the RKKY coupling is mediated by conduction electrons, it is strongly affected by their elastic scattering from the disorder, as well. Indeed, the disorder averaged RKKY coupling decays exponentially for distances larger than the mean free path $l_e = v_F\tau$ [81]. This can be understood from the fact that it depends on the product of the electron wave function amplitudes at the locations $\mathbf{r}_i$ and $\mathbf{r}_j$, see Eq. (25), and thereby on the electron phase difference between these two locations, which the elastic scattering from disorder randomizes. However, its geometrical average is hardly changed from its value in the clean limit [82–84], which is valid even at stronger disorder, as long as the distance between the magnetic moments is not larger than the localization length. The distribution of the RKKY coupling deviates from a normal distribution already at weak disorder and converges to a log-normal distribution at stronger disorder, $P(x = \ln\big(|J_{\mathrm{RKKY}}|/D\big) = \exp\big(-(x-x_0)^2/(2\sigma^2)\big)/(\sqrt{2\pi}\sigma)$, with x_0 and σ disorder dependent parameters, as was derived with a field-theoretical approach [85]. That was confirmed numerically for 2D disordered metals in Refs. [86–88], as seen in Fig. 10(middle and right). There, the distribution of $|J_{\mathrm{RKKY}}|$ is plotted as obtained numerically for a tight binding model on square lattice with potential disorder and box distribution of width W for various distances between the magnetic moments R as compared to the lognormal distribution with fitted parameters (dashed lines) [72]. This is expected, since the amplitude of the RKKY coupling, Eq. (25), is dominated by the local density of states at the Fermi energy, which has at strong disorder and close to the Anderson localization transition a lognormal distribution [80]. The width σ of the lognormal distribution has been derived in Ref. [85] to scale with the elastic scattering rate as $1/\tau$ as $\sigma \sim \tau^{-1/2}$, which has been confirmed numerically in 2D disordered systems [88], noting that $1/\tau = \pi W^2/(6D)$ with $D = 8t$ the band width of the 2D tight binding model.

7.2 Anderson localization – local spectral gaps

Disorder can result in Anderson localization, where states are exponentially localized with localization length ξ, forming a discrete spectrum with local level spacing Δ_ξ as sketched in Fig. 11(left). Since electrons need then to be thermally activated to contribute to a current, their resistivity is found at low temperature to increase exponentially. The interplay of Anderson

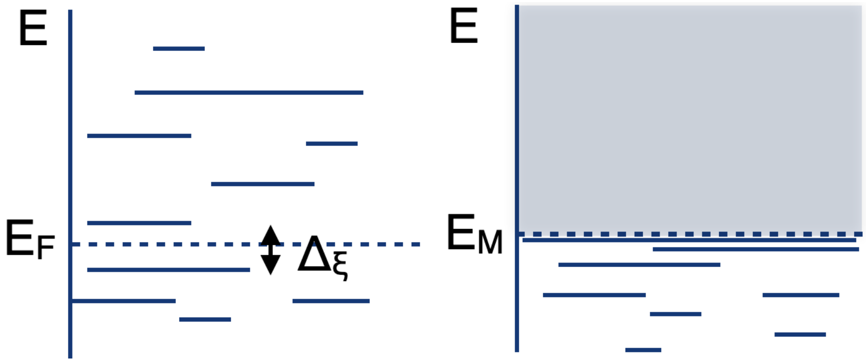

Fig. 11: *Left: Spectrum of localized states with local level spacing Δ_ξ. Right: Spectrum with mobility edge $E_{\rm M}$, where for $E < E_{\rm M}$ all states are localized, while for $E > E_{\rm M}$ there is a continuum of extended states. At the mobility edge $E = E_{\rm M}$ there is a critical state.*

localization with spin correlations like Kondo effect and RKKY interaction, has only recently received increased attention, even though both spin correlations and disorder effects are relevant for many materials, including doped semiconductors close to the metal-insulator transition [89,65], and typical heavy Fermion systems like materials with $4f$ or $5f$ atoms [90,44].
In $d = 3$ and higher dimensions mobility edges E_M appear in the band of eigenstates of a Hamiltonian of electrons moving in a disorder potential $V(\mathbf{r})$. Then, the eigenstates are found to be localized with energy dependent localization length $\xi(E)$ at the band edges. There is a delocalization transition at E_M to a continuum of extended states, as sketched in Fig. 11(right). where the localization length diverges with a power law $\xi(E) \sim |E - E_M|^{-\nu}$ with critical exponent ν. For $d < 2$ all states are localized for a Hamiltonian of noninteracting disordered electrons. For $d = 2$ all states are localized in a disorder potential without magnetic field, or in weak magnetic field. In the presence of a strong perpendicular magnetic field in two dimensions, critically extended states appear in the middle of Landau bands, which is known as the integer quantum Hall transition. In presence of spin-orbit interaction in two dimensions there is a critical delocalization transition. Also, long range interactions may cause a delocalization transition in two dimensions. For reviews on Anderson localization, see Refs. [91–97].
When eigenstates are localized with localization length $\xi(E)$, the spectrum is discrete with a local spacing between the energy levels $\Delta_\xi = 1/(\rho(E)\xi(E)^d)$, where $\rho(E)$ is the density of states at energy E and d is the dimension. Thus, when placing magnetic moments in a disordered electron system, and the Fermi energy E_F is in the band of localized states, the Kondo renormalization of exchange couplings stops at energy scale $\Delta_\xi(E_F)$, since there are no states coupling to the magnetic moment at lower energy. Even though the gap is local, as the exchange coupling is local as well, this problem is equivalent to the Kondo effect in the presence of a spectral gap, which we reviewed in section 6. Thus, we can conclude that there is a critical exchange coupling J_c^A below which the magnetic moment remains unscreened, where

$$J_c^A(\Delta_\xi) = \frac{1}{2N_0} \frac{1}{\ln(D/\Delta_\xi(E_F))}, \tag{49}$$

where $N_0 = N(E_F) = V_a \rho(E_F)/2$ is the number of states per energy and spin at the Fermi energy.

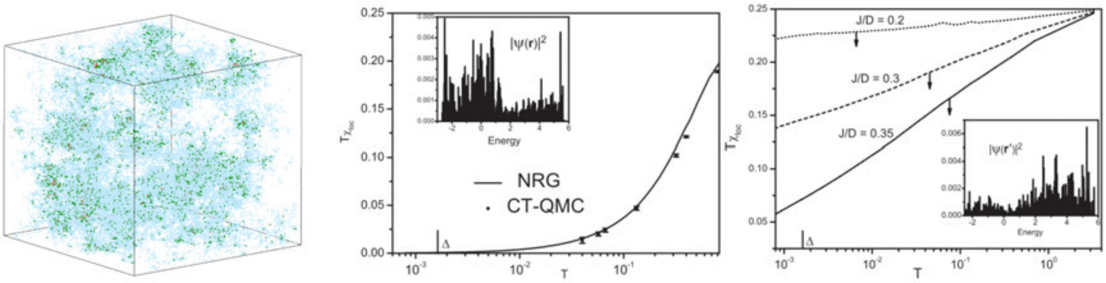

Fig. 12: *Left: Critical state intensity at $E = 2t$ on $d = 3$ Anderson tight binding model ($N = 10^6$ sites, disorder amplitude $W = 16.5t$), obtained by exact diagonalization. Coloring denotes $\alpha = -\ln|\psi|^2/\ln L$ with $\alpha \in [1.2, 1.8]$ (red), $\alpha \in [1.8, 2.4]$ (green), $\alpha \in [2.4, 3.0]$(blue). Sites with higher intensity $\alpha{<}1.2$ and lower intensity $\alpha{>}3$ are not shown. Thereby, 80 $\%$ of total state intensity is visible. Fig. taken from Ref. [103]. Middle and Right: Local spin susceptibility as function of temperature T for spin $S = 1/2$ coupled by exchange coupling $J = 0.35D$, disorder amplitude $W = 2t$ in 2D lattice ($L{=}\,70$), obtained with numerical renormalization group (lines) and continuous time quantum Monte Carlo (dots) method, at sites where Kondo temperature T_K is maximal (middle) and where the magnetic moment remains free (right). Arrows indicate $T_K^{(0)}(J)$. Insets: Intensity as function of E ($E_F{=}\,0$). Fig. taken from Ref. [102].*

The RKKY coupling, on the other hand, is cut off for length scales exceeding the localization length at the Fermi energy $R > \xi(E_F)$, but remains finite between magnetic moments whose distance is smaller, $R < \xi(E_F)$. At and in the vicinity of the mobility edge E_M, another phenomenon has to be taken into account, to understand the competition between Kondo effect and RKKY-coupling: there the eigenfunction intensities have multifractal distributions and the intensities at different energy are power law correlated. We give a brief introduction to multifractality in the next chapter, before reviewing its effects on spin correlations.

7.3 Multifractality – local pseudo-gaps

Multifractality has been observed experimentally in disordered thin film systems measuring the local density of states by scanning tunnelling microscopy [98, 99]. In the vicinity of the Anderson delocalization transition wave functions have been shown to be strongly inhomogeneous, multifractal [96] and power law correlated in energy [100, 101]. Since the delocalization transition is a 2nd order quantum phase transition, the localization length ξ on the localized side of the transition, and the correlation length ξ_c on the metallic side, diverge at E_M as $\xi(E) \sim |E{-}E_M|^{-\nu}$ and $\xi_c(E) \sim |E{-}E_M|^{-\nu_c}$, where universality implies $\nu = \nu_c$. Thus, at the mobility edge there is a critical state, which is very sparse, but spread over the whole sample, see Fig. 12(left), where the intensity $\left|\psi_n(\mathbf{r})\right|^2$ is plotted for all sites of a finite sample of the 3-dimensional tight binding model with onsite disorder potential. The critical eigenfunction intensities $\left|\psi_l(\mathbf{r})\right|^2$ are found to scale linearly with size L as,

$$P_q = L^d \big\langle\, |\psi_l(\mathbf{r})|^{2q} \big\rangle \sim L^{-d_q(q-1)}. \tag{50}$$

Critical states are characterized by multifractal dimensions $d_q < d$, smaller than spatial dimension d and changing with power q. The local intensity distribution of s a critical state is close to a log-normal distribution function, as given by [96]

$$P\big(|\psi_l(\mathbf{r})|^2\big) \sim L^{\alpha_\psi-(\alpha_\psi-\alpha_0)^2/(2\eta)}, \tag{51}$$

where $\alpha_\psi = -\ln\big|\psi_l(\mathbf{r})\big|^2/\ln L$ and $\eta = 2(\alpha_0 - d)$ with $\alpha_0 > d$. Then, $d_q = d - q(\alpha_0 - d)$ for $q < q_c$. For $q > q_c = \alpha_0/\eta$ it terminates at τ_{q_c} [96]. Away from criticality wave functions show multifractality at length scales smaller than the localization length $\xi(E)$ and the correlation length $\xi_c(E)$, respectively, where moments scale with $\xi(E)$, $\xi_c(E)$ in multifractal dimensions d_q.

Another consequence of multifractality is that intensities are power law correlated in energy [100, 101] within correlation energy $E_c \sim 1/\tau$. Given that the intensity at the critical energy $E_k = E_M$ is $\big|\psi_M(\mathbf{r})\big|^2 = L^{-\alpha_\psi}$ the conditional intensity of a state at energy E_l, is relative to the intensity of an extended state L^{-d} given by [103]

$$I_\alpha = L^d \big\langle|\psi_l(\mathbf{r})|^2\big\rangle_{|\psi_M(\mathbf{r})|^2=L^{-\alpha_\psi}} \sim \left|\frac{E_l - E_M}{E_c}\right|^{\beta_\alpha}, \tag{52}$$

for $|E_l - E_M| < E_c \sim 1/\tau$. Thus the intensity varies with a power law with power $\beta_\alpha = (\alpha_\psi - \alpha_0)/d$ for $|E_l - E_M| > \mathit{\Delta}$ (when E_l is closer to E_M than the level spacing $\mathit{\Delta}$, the conditional intensity reduces to the intensity itself, $L^{-\alpha_\psi}$). At positions where the intensity is small, $\alpha > \alpha_0$, it remains suppressed within an energy range of order $1/\tau$ around E_M forming a *local pseudo-gap* with power $\beta_\alpha > 0$. Indeed, such local pseudo-gaps are found numerically with only small fluctuations, see the inset of Fig. 12(right) for a 2D disordered system with linear size $L < \xi$ at $E_F = 0$. When the intensity is larger than its typical value $L^{-\alpha_0}$, $\alpha < \alpha_0$, it remains enhanced within an energy range of order $1/\tau$ around E_M, increasing as a power law when E_l approaches the mobility edge. An example of such strong enhancement at $E_F = 0$, as obtained numerically for a 2D system with linear size $L < \xi$, is shown in the inset of Fig. 12(middle).

Implementing multifractality and power law correlation of intensities, the Kondo temperature T_K is found by inserting the conditional intensity of state l, Eq. (52) into Eq. (9),

$$1 = \frac{J\mathit{\Delta}}{2DE_c} \sum_{|\varepsilon_l|<E_c} \left|\frac{\varepsilon_l}{E_c}\right|^{\beta_\alpha - 1} \tanh\left(\frac{\varepsilon_l}{2T_K}\right), \tag{53}$$

where the summation over l is restricted to energies within the energy interval of the correlation energy $E_c \sim 1/\tau$ around the mobility edge. The power is given by $\beta_\alpha = (\alpha_\psi - \alpha_0)/d$ for $\mathit{\Delta} < |E_l - E_M| < E_c$. Thus, Eq. (53) defines the Kondo temperature in a system with *pseudo-gaps* of power β_α, in the local density of states when it is positive [59] and the Kondo temperature is reduced at such sites. On the other hand, at sites where β_α is negative T_K is enhanced. Eq. (53) can be solved analytically yielding [103]

$$\frac{T_K}{E_c} = \left[\left(1 - \frac{J_c^{PG}(\beta_\alpha)}{J}\right) c_\alpha\right]^{\frac{1}{\beta_\alpha}}, \tag{54}$$

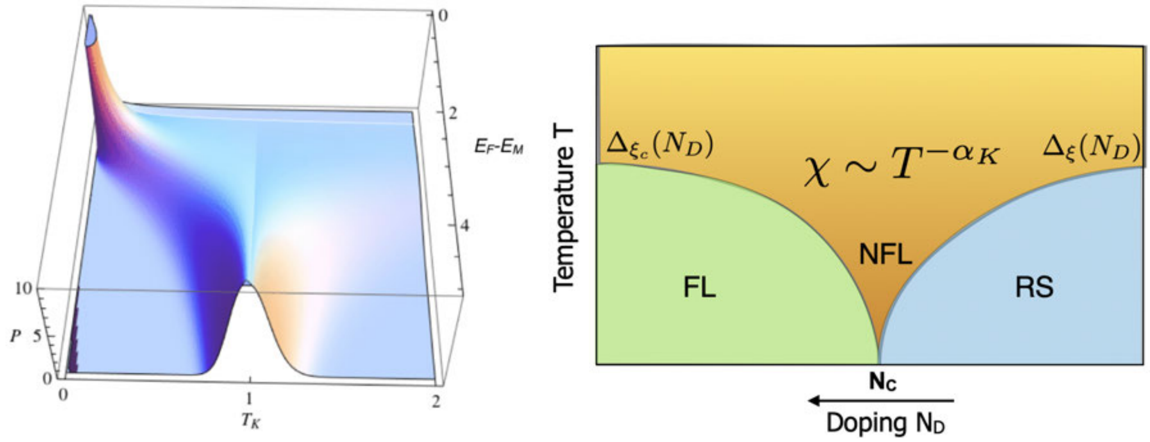

Fig. 13: *Left: Kondo temperature T_K-distribution in units of $T_K^{(0)}$ as function of distance to the mobility edge $E_F{-}E_M$ in units of E_c for exchange coupling $J = D/5$, derived analytically. Fig. taken from Ref. [103]. Right: Schematic phase diagram as function of doping concentration N_D, near critical doping N_c. Non-Fermi liquid behavior at temperatures exceeding the scale $\Delta_{\xi_c}(N_D)$ on the metallic side and $\Delta_{\xi}(N_D)$ below which there is a Fermi liquid (FL) due to Kondo screening, and a random singlet state (RS), respectively.*

where $\beta_\alpha = (\alpha_\psi{-}\alpha_0)/d$, and the critical exchange coupling is $J_c^{PG}(\beta_\alpha) = \beta_\alpha D/2$ and $c_\alpha = (2\alpha_\psi{-}\eta)/(\alpha_\psi{-}\eta/2{+}d)$. Thus, the Kondo temperature has the form we found in the presence of a pseudo-gap Eq. (40), with power β_α. For $J < J_c^{PG}(\beta_\alpha)$ the magnetic moment remains unscreened. Since $\alpha_\psi \in [0, \infty]$ is distributed, we find that $J_c^{PG}(\beta_\alpha)$ and thereby $T_K(\alpha)$ are distributed, accordingly. For the typical value $\alpha_\psi = \alpha_0$ we recover T_K of a clean system $T_K(\alpha_\psi{=}\alpha_0) \sim E_c \exp\big(-1D/(2J)\big) \sim T_K^{(0)}$. The derivation can be extended into the vicinity of the mobility edge, where the (localization, correlation) lengths (ξ, ξ_c) are finite, respectively by substituting in α_ψ the system size L by (ξ, ξ_c). Thereby, using a normal distribution of α_ψ, the distribution of the Kondo temperature can be derived analytically, as plotted in Fig. 13(left) [103] as function of energy distance to the mobility edge E_M. It evolves from a Gaussian distribution with finite width in the weakly disordered metal regime to a bimodal distribution with a divergent power law tail at the mobility edge. The enhanced weight at low Kondo temperatures was shown in Ref. [103] to origin from the opening of the local pseudogaps and is given by

$$P\big(0{<}T_K{\ll}T_K^0\big) \sim T_K^{-\alpha_K}, \tag{55}$$

with universal power $\alpha_K = 1 - \eta/(2d)$, with multifractal correlation exponent $\eta = 2(\alpha_0{-}d)$. The magnetic susceptibility $\chi(T) \sim n_{FM}(T)/T$ with density of free moments $n_{FM}(T) = n_M \int_0^T dT_K P(T_K)$, at temperature T is found at the mobility edge as [103],

$$\chi(T) \sim \left(\frac{T}{E_c}\right)^{-\alpha_K}, \tag{56}$$

diverging with a universal power law, in good agreement with experimentally observed Non-Fermi liquid behavior in the magnetic susceptibility and specific heat [89] to which the magnetic moments contribute $C(T) \sim T dn_{FM}(T)/dT$ as $C(T) \sim T^{\eta/(2d)}$. This result is also valid on the insulating side for $T > \Delta_\xi$ and on the metallic side for $T > \Delta_{\xi_c}$, yielding the phase diagram shown in Fig. 13(right) with a Non-Fermi liquid fan, caused by the distribution of Kondo temperatures due to the multifractality in the vicinity of the mobility edge.

Numerical calculations of the T_K-distribution confirm the anomalous power [79, 104] with a power which is very close to the analytical result Eq. (55). In Ref. [102] the magnetic susceptibility was obtained by a full Wilson renormalization group (RG) calculation [21] for a 2D disordered system finding the anomalous power law divergence, shown in Fig. 12 at sites where the intensity is suppressed as in a local pseudo-gap. Recently, it was pointed out that a more realistic model of the Kondo impurity which takes into account anisotropies yields a modified distribution of Kondo temperatures [105]. It remains to be explored whether this will affect the low T_K tail at the AMIT and thereby the anomalous power of the magnetic susceptibility α_K.

On the insulating side of the transition there remains a finite density of magnetic moments in the low temperature limit, since the Kondo screening becomes quenched by Anderson localization, where renormalization of the Kondo coupling becomes cutoff by the local level spacing $\Delta_\xi = 1/(\rho\xi^3)$ [106]. Since these free moments are still weakly coupled to the electron system, they interact with each other in the vicinity of the mobility edge by RKKY- like exchange interactions, extending up to distances of the order of the localization length ξ. In the dilute doping limit the indirect exchange interaction becomes the superexchange interaction due to the overlap of hydrogen like impurity states, which is known to be antiferromagnetic. These randomly positioned magnetic moments have been modelled by a Heisenberg spin model with random antiferromagnetic short range, exponentially decaying exchange interaction [64]. In agreement with experiments, numerical simulations and the implementation of a cluster renormalization group, no evidence for a spin glass transition, at which the magnetic susceptibility would peak and then decay to lower temperatures is found [64]. Rather, the magnetic susceptibility diverges at low temperature with a power law $\chi(T) \sim T^{-\alpha_J}$, with $\alpha_J \leq 1$ [64]. In one dimension, the random antiferromagnetic short range Heisenberg model is known to flow at low temperature to the infinite randomness fixed point, where the ground state is formed of randomly placed spin singlets [107]. When the localization length ξ exceeds the Fermi wave length, however, the indirect exchange interaction oscillates in sign with distance, as the RKKY interaction in the metallic regime, but decays exponentially beyond ξ. In the next section we will address the question, whether the RKKY interaction or the Kondo effect wins the spin competition in disordered electron systems in the vicinity of the delocalization transition.

7.4 Doniach diagram of disordered systems

Extending the argument of Doniach [13] to disordered systems where both Kondo temperature T_K and RKKY couplings are distributed, it is natural to study next the distribution of the ratio of both energy scales, $J_{\text{RKKY}}(\mathbf{r}_{ij})$ and T_{Ki}. This has been done in Ref. [88], as shown in Fig. 14(left) for four distances R between two magnetic moments, placed randomly in a 2D disordered tight binding model. While it is found to have a wide distribution for all R, there

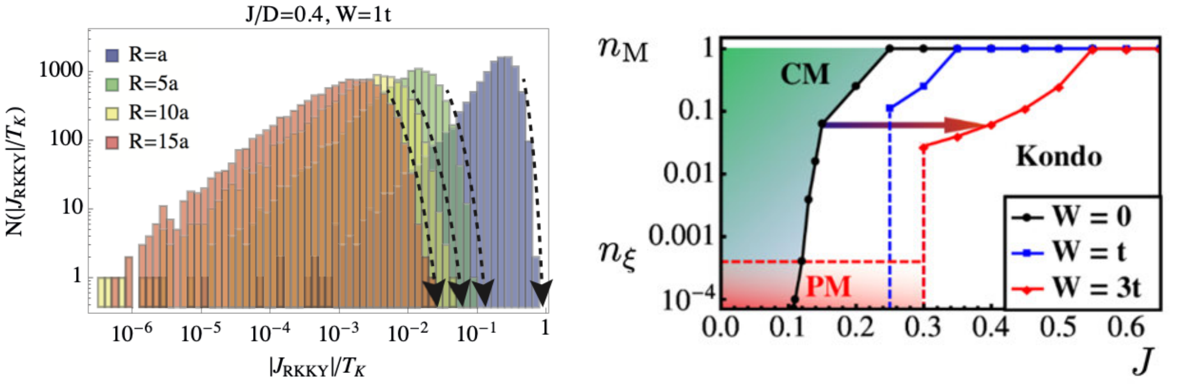

Fig. 14: *Left: Distribution of ratio* $|J_{RKKY}(R)|/T_K$ *for two magnetic moments at distance* R*, placed randomly in a 2D disordered lattice. Black arrows: sharp cutoff. Right: Magnetic quantum phase diagram, critical density of magnetic moments* n_c *as function of* J *for various disorder strengths* W*, as derived numerically from that cutoff, separating a coupled moment (CM) from a Kondo screened phase. Horizontal dashed line separates the free moment phase (PM) for* $J < J_c(W)$*, and* $n_M < n_\xi$*, where* n_ξ *is the concentration, when there is no more than one magnetic moment within a localization length* ξ*. Linear system size* $L = 100a$*, number of disorder configurations* $M = 30000$*. Figs. taken from Ref. [88].*

is a sharp cutoff, indicated by the black arrows. From the condition that $|J_{\mathrm{RKKY}}(R)/T_K| < 1$ for all concentrations $n_M = 1/R^d$ below a critical value $n_c = 1/R_c^d$, we can derive n_c accurately as function of exchange coupling J. The resulting quantum phase diagram is shown in Fig. 14(right) for three disorder strengths W. The Kondo dominated regime is pushed to larger J as the disorder strength W is increased. At strong disorder a phase of uncoupled, paramagnetic local moments (PM) appears at small $n_M < n_\xi$, where n_ξ is the concentration, when there is no more than one magnetic moment within the range of a localization length ξ, as shown in Fig. 14(right) (horizontal red dashed line) [88].

In Fig. 15 we show the critical coupling $J_c^{(1)}$ as function of disorder amplitude W, as defined to be the coupling above which there remain no unscreened magnetic moments in the sample. It is derived for a 2D disordered tight binding model as function of disorder amplitude W with (left figure) numerical exact diagonalization for several lengths L. The full line is a plot of $J_c^A(W)$, Eq. (49), with 2D localization length $\xi = l_e \exp(\pi E_F \tau)$, where $1/\tau = \pi W^2/(6D)$. The dashed line is a guide to the eye. In Fig. 15(right) we show results obtained by employing the Kernel polynomial method for Eq. (9) for system size $L = 100$ [88]. The dashed line is the analytical function $J_c^{(1)}(W)$, obtained from deriving the density of free moments due to local pseudo-gaps, yielding $J_c^{(1)} = \sqrt{\eta} D/2$, with $\eta = 2(\alpha_0 - d)/d$. In $d = 2$, expansion in $1/g$, with $g = E_F \tau$, yields $\eta = 2/(\pi g)$ and thus

$$J_c^{(1)}(W) = \sqrt{\frac{D}{3E_F}}W. \tag{57}$$

The good agreement with numerical results supports the result that the formation of free moments is due to local pseudo-gaps formed by multifractal intensity distribution and correlations. To go beyond the Doniach argument for disordered systems let us next apply and extend the self

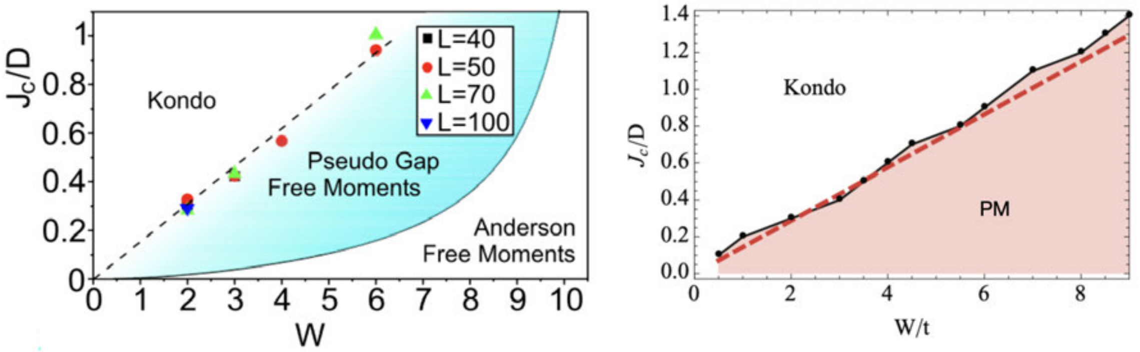

Fig. 15: *Left: Critical coupling $J_c^{(1)}$ as function of disorder amplitude W, derived for a 2D disordered tight binding model as function of disorder amplitude W with numerical exact diagonalization for sizes L, defined such that for $J > J_c^{(1)}$, there is no unscreened magnetic moment in the sample. Full line: $J_c^A(W)$, Eq. (49), with 2D localization length $\xi = l_e \exp(\pi E_F \tau)$, where $1/\tau = \pi W^2/(6D)$. Dashed line: guide to the eye. Fig. taken from Ref. [102]. Right: Same as left figure, but derived by employing Kernel polynomial method to Eq. (9) for $L = 100$ [88]. Dashed line: analytical function $J_c^{(1)}(W)$, Eq. (57). Fig. taken from Ref. [88].*

consistent approach of Ref. [54], reviewed in section 5. Placing two magnetic moments at sites of a disordered electron system with different local density of states yields different bare Kondo temperatures $T_{Ki}^0 = D_0 \exp\big(-1/(2g_i^0)\big)$, $i = 1, 2$ [58]. By solving the coupled RG-Eqs. (29) for two magnetic moments numerically, we find that both Kondo temperatures are reduced in the presence of RKKY-coupling, see Fig. 16. The initially smaller Kondo temperature T_{K_2} is suppressed more than the larger one T_{K_1}. Thereby, their ratio $x = T_{K_2}/T_{K_1}$ decreases. Thus, we find that the inequality between Kondo temperatures becomes enhanced by RKKY coupling. Moreover, the quenching of the Kondo screening by the RKKY coupling occurs already for smaller RKKY coupling, as seen in Fig. 16(left), the stronger the inhomogeneity and the smaller the ratio of the bare Kondo temperature x_0. For the smallest value, $x_0 = 0.1$, the breakdown occurs at a critical value $y_c(x_0 \ll 1) = 0.88 y_c$, where y_c is the one in the homogeneous system, Eq. (35). The discontinuous jump of both Kondo temperatures T_{K_1} and T_{K_2} at $y_c(x_0)$ are seen in Fig. 16(right), plotted relative to their bare values as function of bare Kondo temperature ratio x_0 and dimensionless RKKY coupling parameter $\tilde{y}$. Thus, we conclude that disorder makes Kondo screening more easily quenchable by RKKY coupling.

For a finite density of randomly distributed magnetic moments n_M, coupled by random local exchange couplings J_i^0 to conduction electrons with random local density of states $\rho(E, \mathbf{r}_i)$, one can extend this approach, solving the coupled RG-Eqs. (29). Every magnetic moment has then, in general, a different Kondo temperature, as they are placed at different positions with different local couplings $g_0(\boldsymbol{r}_i) = J_i^0 \rho(E, \mathbf{r}_i)$. As the RKKY coupling is itself distributed widely in disordered systems [85, 88] the long range function $y(\boldsymbol{r}-\boldsymbol{r}')$ is distributed as well. We can thus derive the distribution function of Kondo temperatures T_K from Eqs. (29). We note that the random distribution of RKKY-couplings is mainly due to the distribution of local couplings $g_0(\boldsymbol{r})$ [88], while the function $y(\boldsymbol{r}-\boldsymbol{r}')$ is only weakly affected by the disorder.

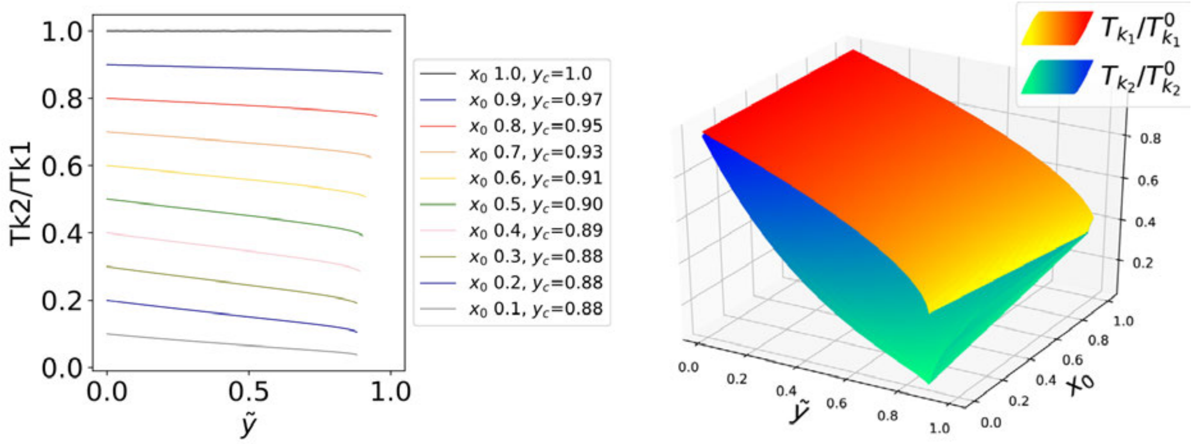

Fig. 16: *Left: The ratio of Kondo temperatures of two magnetic moments* $x = T_{K2}/T_{K1}$ *as function of dimensionless RKKY coupling parameter* $\tilde{y}$*, relative to its critical value* y_c *for the homogenous system, for different bare Kondo temperature ratios* $x_0 = T^0_{K_2}/T^0_{K_1}$*. It stops at a critical value* $\tilde{y}_c(x_0)$*, relative to* y_c *for the homogenous system. Right: Kondo temperatures* T_{K_1} *and* T_{K_2} *relative to their bare values as function of bare Kondo temperature ratios* x_0 *and the dimensionless RKKY coupling parameters* $\tilde{y}$*. Figs. are taken from Ref. [58].*

Without the RKKY-coupling we found at the mobility edge a bimodal distribution of T_K with one peak close to the Kondo temperature of the clean system and a power law divergent tail at low T_K [88, 103, 104], see Fig. 13. Since the RKKY-interaction enhances inequalities between Kondo temperatures, we expect that it shifts more weight to the low Kondo temperature tail. This could be checked quantitatively by the solution of Eqs. (29), but still needs to be done.

Anderson localization is weakened when time reversal and spin symmetry are broken by magnetic scattering from magnetic moments [108, 109]. A finite magnetic scattering rate τ_s^{-1} enhances the localization length through the parameter $X_s = \xi^2/L_s^2$, where $L_s = \sqrt{D_e \tau_s}$ is the spin relaxation length [110] and $D_e = v_F^2\, \tau/3$ the electron diffusion coefficient. When $X_s \geq 1$ the electron spin relaxes before it covers the area limited by ξ, and Anderson localization is weakened. In 3D the mobility edge is thereby shifted towards stronger disorder by magnetic scattering. As Kondo screening of magnetic moments diminishes magnetic scattering, while RKKY coupling tries to quench their spins, resulting in magnetic scattering, the competition between these effects governs Anderson localization and the position of the delocalization transition. Treating the interplay between Anderson localization and Kondo screening, novel effects like a giant magneto resistance [106, 103], finite temperature delocalization transitions and the emergence of a critical band [103] have been derived. Experimentally, the interplay of Kondo effect, indirect exchange interaction and Anderson localization has recently been studied in a 2D experimental setup in a controlled way [111]. Thus, it remains an important and experimentally relevant problem, to develop a self consistent treatment of Anderson localization, Kondo screening and RKKY-coupling. This problem has been studied with the disordered Kondo lattice and the Anderson-Hubbard model with a variety of numerical methods. Each method comes with different approximations, providing different insights. These include mean-field theories of the Kondo lattice with an added RKKY coupling term [44, 112–117], where fluctuations around the mean-field theory have been studied with Ginzburg-Landau and nonlinear sigma model type

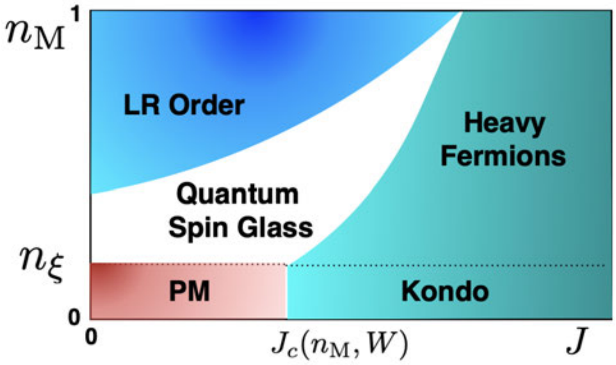

Fig. 17: *Schematic quantum phase diagram of Kondo lattice systems as function of magnetic moment density* n_{M} *and exchange coupling* J *for fixed disorder* W. *The critical coupling* $J_c(n_{\mathrm{M}}, W)$ *separates spin coupled from Kondo screened phases. Dark blue indicates higher transition temperatures to the long range ordered state (LR). Dark red indicates higher concentrations of free magnetic moments (PM), when electrons are localized and there is not more than one magnetic moment within the localization length* ξ, $n_{\mathrm{M}} < n_\xi = \xi^{-d}$. *Dark petrol indicates higher Kondo and coherence temperatures in the dilute Kondo phase and heavy fermion phase.*

actions. Statistical dynamical mean-field theory based approaches [118–125], Hartree-Fock based methods [126–128], quantum Monte Carlo method [129–132], typical medium dynamics cluster approximations [133, 134] and cluster extensions of the numerical renormalization group method [135] have been applied. While we cannot review all results, some of them have been reviewed in Ref. [90], we would like to mention that in Refs. [133, 134] the quasiparticle self energy of the Anderson-Hubbard model was derived as function of excitation energy $\operatorname{Im} \Sigma(\omega) \sim \omega^{\alpha_\Sigma}$. It was found to behave as a non-Fermi liquid with power $\alpha_\Sigma(W) < 2$, which becomes smaller with stronger disorder amplitude W. The non-Fermi liquid phase extends down to lowest energies at the mobility edge. Away from it, it is cutoff by $\Delta_\xi = 1/(\rho\xi^d)$, and $\Delta_{\xi_c} = 1/(\rho\xi_c^d)$, respectively. This is in agreement with the phase diagram derived from the magnetic properties, reviewed above, Fig. 13(right). The typical medium dynamics cluster approximation employed in Ref. [133] does not include long range indirect exchange interactions. Thus, the study of the competition between Anderson localization, Kondo screening and RKKY-coupling, remains a challenging problem.

8 Conclusions and open problems

To conclude, when magnetic moments are immersed into the Fermi sea of itinerant electrons, rich quantum physics emerges, which is relevant for a wide range of materials including heavy Fermion systems, materials with $4f$ or $5f$ atoms, notably Ce, Yb, or U, high temperature superconductors like the cuprates, but also good metals with magnetic impurities, doped semiconductors like Si:P close to the metal-insulator transition, 2D materials like graphene and topological insulators. While each material has its specific properties, requiring detailed modelling, their electronic properties are to some degree governed by the competition between Kondo screening and indirect exchange couplings, which can be modelled by (disordered) Kondo lattices. We summarize the main results in the schematic quantum phase diagram Fig. 17.

While the Doniach argument gives a good idea of the competition between Kondo screening and RKKY coupling, a self consistent renormalization theory which implements the RKKY coupling into the Kondo renormalization yields a remarkably different result: the Kondo temperature jumps discontinuously to zero at a critical exchange coupling which is larger than expected with the Doniach argument. We reviewed the extension of that framework to a finite density of magnetic moments n_{M} to systems with a spectral (pseudo) gap and to disordered systems, where the Kondo temperature is different for every magnetic moment. We have seen that disorder leads to a wide distribution of both Kondo temperature and RKKY couplings and tends to diminish the Kondo dominated phase, enhancing the critical coupling $J_c(n_{\mathrm{M}}, W)$. In the dilute limit we identified a paramagnetic phase, even at zero temperature, where the Kondo screening is prevented by local pseudo-gaps, and the RKKY coupling between the dilute magnetic moments is cutoff by Anderson localization. In that regime, the density of free magnetic moments is found to decrease continuously with increasing J. There, an analytical formula for the increase of the critical coupling $J_c^{(1)}(n_{\mathrm{M}}, W)$ with disorder W is available, Eq. (57), which was found in 2D to be in good agreement with numerical results, see Fig. 15.

As the density of magnetic moments is increased, there is a succession of quantum phase transitions between quantum spin glass and ordered phases for couplings $J < J_c(n_{\mathrm{M}}, W)$, as shown schematically in Fig. 17. Since we cannot review here the rich physics and variety of these spin coupled phases, let us refer to the literature cited above and recent reviews [8, 90, 44, 65]. For $J > J_c(n, W)$, a transition between a phase of dilute Kondo singlets and a heavy fermion state is expected as n_{M} is increased. Experimentally, even for dilute densities of about $n_{\mathrm{M}} = 0.05$, indications of a coherent Kondo lattice were found in Si:P deep in the metallic phase [136] and in the dilute Kondo lattice CeIn$_3$ [137]. The theory of the transition from dilute Kondo singlets to heavy Fermions is still a challenging problem, as it requires to solve the dilute Kondo lattice model, as studied for example in [132]. Taking fully into account the disorder introduced by the random placements of magnetic moments is still a challenge. Last but not least, even in the dense magnetic moment limit $n_{\mathrm{M}} \to 1$, the mechanism for the emergence of long range order at the Kondo breakdown is under debate. Is it due to the ordering of emerging local moments, or a spin-density wave transition [8] or a more complex mechanism, where ordered magnetic moments and Kondo screening coexist in a spatially modulated state [138]?

Acknowledgements

These lecture notes are dedicated to the memory of Peter Fulde. We thank Hans Kroha and Keith Slevin for critical reading and feedback

References

[1] J. Kondo, Prog. Theor. Phys **32**, 37 (1964)

[2] A.C. Hewson: *The Kondo Problem to Heavy Fermions* (Cambridge Univ. Press, 1993)

[3] P. Mohanty and R.A. Webb, Phys. Rev. Lett. **84**, 4481 (2000); *ibid.* **91**, 066604 (2003)

[4] F. Pierre and N.O. Birge, Phys. Rev. Lett. **89**, 206804 (2002)

[5] F. Mallet, J. Ericsson, D. Mailly, S. Ünlübayir, D. Reuter, A .Melnikov, A.D. Wieck, T. Micklitz, A. Rosch, T.A. Costi, L. Saminadayar, and C. Bäuerle, Phys. Rev. Lett. **97**, 226804 (2006)

[6] P. Nozières, J. Low Temp. Phys. **17**, 3 (1974)

[7] P. Nozières, Eur. Phys. J. B **6**, 447 (1998)

[8] P. Coleman: *Heavy Fermions: electrons at the edge of magnetism*, in H. Kronmüller and S. Parkin (eds.): *Handbook of Magnetism and Advanced Magnetic Materials, Vol 1: Fundamentals and Theory* (Wiley, New York, 95-148, 2007)

[9] P. Fulde: *Correlated Electrons in Quantum Matter* (World Scientific, Singapore, 2012)

[10] M.A. Ruderman and C. Kittel, Phys. Rev. **96**, 99 (1954)

[11] T. Kasuya, Prog. Theor. Phys. **16**, 45 (1956)

[12] K. Yosida, Phys. Rev. **106**, 893 (1957)

[13] S. Doniach, Physica B+C **91** 231(1977)

[14] J. Kroha: *Interplay of Kondo effect and RKKY interaction*, in E. Pavarini, Erik Koch, R. Scalettar, and R.M. Martin (eds.): *The Physics of Correlated Insulators, Metals, and Superconductors* Modeling and Simulation, Vol. 7 (Forschungszentrum Jülich, 2017)

[15] P.W. Anderson, Phys. Rev. **124**, 41 (1961)

[16] J.R. Schrieffer and P. Wolff, Phys. Rev. **149**, 491 (1966)

[17] Y. Nagaoka, Phys. Rev. **138**, 1112 (1965)

[18] H. Suhl, Phys. Rev. **A 138**, 515 (1965)

[19] P.W. Anderson, G. Yuval, and D.R. Hamann, Phys. Rev. B **1**, 4464 (1970)

[20] G. Zarand and L. Udvardi, Phys. Rev. **B 54**, 7606 (1996)

[21] K. G. Wilson, Rev. Mod. Phys. **47**, 773 (1975)

[22] H.R. Krishna-murthy, J.W. Wilkins, and K.G. Wilson, Phys. Rev. B **21**, 1003 (1980); *ibid.* **21**, 1044 (1980)

[23] A.M. Tsvelick and P.B. Wiegmann, Adv. Phys. **32**, 453 (1983)

[24] N. Andrei, K. Furuya, and J.H. Lowenstein, Rev. Mod. Phys. **55**, 331 (1983)

[25] P. Nozières, J. Phys. **C, 37**, 1 (1976)

[26] S. Kettemann, E.R. Mucciolo, JETP Lett. **83**, 240 (2006)

[27] T. Micklitz, A. Altland, T.A. Costi, and A. Rosch, Phys. Rev. Lett. **96**, 226601 (2006)

[28] S. Kettemann and E.R. Mucciolo, Phys. Rev. B**75**, 184407 (2007)

[29] A.A. Abrikosov, L.L.P. Gorkov, I.E. Dzialosinskij, and I.I.E. Dzialoshinskii:
Methods of Quantum Field Theory in Statistical Physics (Dover Publications, 1975)

[30] D.N. Aristov, Phys. Rev. **B 55**, 8064 (1997)

[31] F. Meier, L. Zhou, J. Wiebe and R. Wiesendanger, Science **320**, 82 (2008)

[32] S. Seiro, L. Jiao,S. Kirchner *et al.*, Nat Commun. **9**, 3324 (2018)

[33] A. Menth, E. Buehler, and T.H. Geballe, Phys. Rev. Lett. **22**, 295 (1969)

[34] B. Coqblin and J.R. Schrieffer, Phys. Rev. **185**, 847 (1969)

[35] N. Read and D.M. Newns, J. Phys. C **16**, L1055 (1983); *ibid.* **16**, 3273 (1983)

[36] A. Auerbach and K. Levin, Phys. Rev. Lett. **57**, 877 (1986)

[37] W. Metzner, and D. Vollhardt, Phys. Rev. Lett. **62**, 324 (1989)

[38] M. Jarrell, Phys. Rev. **B, 51**, 7429 (1995)

[39] A. Georges, G. Kotliar, W. Krauth, and M. Rozenberg, Rev. Mod. Phys. **68**, 13 (1996)

[40] H. Schweitzer and G. Czycholl, Phys. Rev. Lett. **67**, 3724 (1991)

[41] A.Theumann, B. Coqblin, S.G. Magalhaes and A.A. Schmidt,
Phys. Rev. **B 63**, 054409 (2001)

[42] B. Coqblin, J.R. Iglesias, N.B. Perkins, S.G. Magalhaes and F.M. Zimmer,
J. Magn. Magn. Mater. **320**, 1989 (2008)

[43] S.G. Magalhaes, F.M. Zimmer, and B. Coqblin, Phys. Rev. **B 81**, 094424 (2010)

[44] S.G. Magalhaes, F. Zimmer and B. Coqblin, Int. J. Mod. Phys. Conf. Ser. **11**, 38 (2012)

[45] B.A. Jones and C.M. Varma, Phys. Rev. Lett. **58**, 843 (1987)

[46] R. Bulla, T.A. Costi, and T. Pruschke, Rev. Mod. Phys. **80**, 395 (2008)

[47] F. Eickhoff, B. Lechtenberg, and F.B. Anders, Phys. Rev. **B 98**, 115103 (2018)

[48] A.K. Mitchell and R. Bulla, Phys. Rev. **B 92**, 155101 (2015)

[49] F. Eickhoff and F.B. Anders, Phys. Rev. **B 102**, 205132 (2020)

[50] J. Bork, Y.-H. Zhang, L. Diekhöner, L. Borda, P. Simon, J. Kroha, P. Wahl, and K. Kern, Nat. Phys. **7**, 901 (2011)

[51] A. Gleis, S.-S.B. Lee, G. Kotliar, and J. von Delft, arXiv:2310.12672 (2023)

[52] S. Fujimoto and N. Kawakami, J. Phys. Soc. Jpn. **66**, 2157 (1997)

[53] H. Tsunetsugu, M. Sigrist, and K. Ueda, Rev. Mod. Phys. **69**, 809 (1997)

[54] A. Nejati, K. Ballmann, and J. Kroha, Phys. Rev. Lett. **118**, 117204 (2017)

[55] K. Matho and M.T. Béal-Monod, Phys. Rev. **B 5**, 1899 (1972); *ibid.* **B 6**, 2888 (1972)

[56] Y.C. Tsay and M.W. Klein, Phys. Rev. **B 7**, 352 (1973)

[57] Y.C. Tsay and M.W. Klein, Phys. Rev. **B 11**, 318 (1975)

[58] K.-Y. Park, I. Jang, K.-S. Kim and S. Kettemann, Ann. Phys. **435**, 168501 (2021)

[59] D. Withoff and E. Fradkin, Phys. Rev. Lett. **64**, 1835 (1990); K. Ingersent, Phys. Rev. B **54**, 11936 (1996); S. Florens and M. Vojta, Phys. Rev. B **72**, 115117 (2005); L. Fritz, S. Florens, and M. Vojta, Phys. Rev. B **74**, 144410 (2006)

[60] D. Sherrington and S. Kirkpatrick, Phys. Rev. Lett. **35**, 1792 (1975)

[61] G. Forestier, M. Solana, C. Naud, A.D. Wieck, F. Lefloch, R. Whitney, D. Carpentier, L.P. Lévy and L. Saminadayar, Phys. Rev. **B 102**, 024206 (2020)

[62] J.C. Gomez Sal, J. Garcia Soldevilla, J.A. Blanco, J.I. Espeso, J. Rodriguez Fernandez, F. Luis, F. Bartolome, Phys. Rev. B **56**, 11741 (1997)

[63] T. Westerkamp, M. Deppe, R. Kuchler, M. Brando, C. Geibel, P. Gegenwart, A.P. Pikul and F. Steglich, Phys. Rev. Lett. **102**, 206404 (2009)

[64] R.N. Bhatt, P.A. Lee, Phys. Rev. Lett. **48**, 344 (1982)

[65] S. Kettemann, Special Issue in memory of K.B. Efetov, Ann. Phys. **456**, 169306 (2023)

[66] K. Sato, L. Bergqvist, J. Kudrnovský, P.H. Dederichs, O. Eriksson, I. Turek, B. Sanyal, G. Bouzerar, H. Katayama-Yoshida, V.A. Dinh, T. Fukushima, H. Kizaki, and R. Zeller, Rev. of Mod. Phys. **82**, 1633 (2010)

[67] M.Z. Hasan and C.L. Kane Rev. Mod. Phys. **82**, 3045 (2010)

[68] A.H. Castro Neto, F. Guinea, N.M.R. Peres, K.S. Novoselov, and A.K. Geim, Rev. Mod. Phys. **81**, 109 (2009)

[69] M.T. Glossop and K. Ingersent, Phys. Rev. B. **75** 104410 (2007)

[70] M. Vojta and R. Bulla, Eur. Phys. J. B **28**, 283 (2002)

[71] S. Saremi and P.A. Lee, Phys. Rev. **75**, 165110 (2007)

[72] H.Y. Lee and S. Kettemann, Phys. Rev. B **91**, 205109 (2015)

[73] M. Sherafati and S. Satpathy, Phys. Rev. **B 83**, 165425 (2011)

[74] P.W. Anderson, Nobel Lectures in Physics **1980**, 376 (1977)

[75] N.F. Mott, J. Phys. Colloques **37**, C4 (1976)

[76] E. Miranda, V. Dobrosavljevic, and G. Kotliar, J. Phys.: Condens. Matter **8**, 9871 (1996)

[77] R.N. Bhatt and D.S. Fisher, Phys. Rev. Lett. **68**, 3072 (1992)

[78] A. Langenfeld and P. Woelfle, Ann. Phys. **507**, 43 (1995)

[79] P.S. Cornaglia, D.R. Grempel, and C.A. Balseiro, Phys. Rev. Lett. **96**, 117209 (2006)

[80] A.D. Mirlin, Phys. Rep. **326**, 259 (2000)

[81] P.G. de Gennes, J. Phys. Radium **23**, 630 (1962)

[82] A.Y. Zyuzin and B.Z. Spivak, JETP Lett. **43** 234 (1986)

[83] L.N. Bulaevskii and S.V. Panyukov, JETP Lett. **43**, 240 (1986)

[84] G. Bergmann, Phys. Rev. **B 36**, 2469 (1987)

[85] I.V. Lerner, Phys. Rev.**B 48**, 9462 (1993)

[86] H.Y. Lee, E.R. Mucciolo, G. Bouzerar, S. Kettemann, Phys. Rev. **B 86**, 205427 (2012)

[87] H.Y. Lee, J.H. Kim, E.R. Mucciolo, G. Bouzerar, and S. Kettemann, Phys. Rev. **B 85**, 075420 (2012)

[88] H.Y. Lee and S. Kettemann, Phys. Rev. **B 89**, 165109 (2014)

[89] H. von Löhneysen, Ann. Phys. (Berlin) **523**, 599 (2011)

[90] E. Miranda and V. Dobrosavljevic, Rep. Prog. Phys. **68**, 2337 (2005)

[91] P. A. Lee and T.V. Ramakrishnan, Rev. Mod. Phys. **57**, 287 (1985)

[92] B. Kramer and A. MacKinnon, Rep. Prog. Phys. **56**, 1469 (1993)

[93] D. Belitz and T. Kirkpatrick, Rev. Mod. Phys. **66** (1994)

[94] K.B. Efetov: *Supersymmetry in Disorder and Chaos*, (Cambridge Univ. Press, 1997)

[95] B. Kramer, T. Ohtsuki, and S. Kettemann, Phys. Rep. **417**, 211 (2005)

[96] F. Evers and A. Mirlin, Rev. Mod. Phys. **80**, 63 (2008)

[97] R.N. Bhatt and S. Kettemann, Special Issue Localization 2020: Editorial Summary, Ann. Phys. **435**, 168664 (2021)

[98] A. Richardella, P. Roushan, S. Mack, B. Zhou, D.A. Huse, D.D. Awschalom, A. Yazdani, Science **327**, 665 (2010)

[99] J. Gao, J.W. Park, K.-S. Kim, S.K. Song, H.R. Park, J. Lee, J. Park, F. Chen, X. Luo, Y. Sun, and H.W. Yeom, Nano Lett. **20**, 6299 (2020)

[100] J.T. Chalker, Physica A **167**, 253 (1990); V.E. Kravtsov and K.A. Muttalib, Phys. Rev. Lett. **79**, 1913 (1997); J.T. Chalker *et al.*, JETP Lett. **64**, 386 (1996); T. Brandes, B. Huckestein, and L. Schweitzer, Ann. Phys. (Leipzig) **5**, 633 (1996)

[101] E. Cuevas and V.E. Kravtsov, Phys. Rev. B **76**, 235119 (2007)

[102] A. Zhuravlev, I. Zharekeshev, E. Gorelov, A.I. Lichtenstein, E.R. Mucciolo, and S. Kettemann, Phys. Rev. Lett. **99**, 247202 (2007)

[103] S. Kettemann, E.R. Mucciolo, I. Varga, and K. Slevin, Phys. Rev. **B 85**, 115112 (2012)

[104] K. Slevin, S. Kettemann, and T. Ohtsuki, Eur. Phys. J. **B 92**, 281(2019)

[105] M. Debertolis, I. Snyman, and S. Florens, Phys. Rev. **B 106** 125115 (2022)

[106] S. Kettemann and M.E. Raikh, Phys. Rev. Lett. **90**, 146601 (2003)

[107] F. Igloi and C. Monthus, Phys. Rep. **412**, 277 (2005)

[108] D. Khmel'nitskii and A. Larkin, Solid State Commun. **39**, 1069 (1981)

[109] F.J. Wegner, Nucl. Phys. B **270**, 1 (1986)

[110] S. Hikami, A. Larkin, and Y. Nagaoka, Prog. Theor. Phys. **63**, 707 (1980)

[111] W. Zhang, E.R. Brown, and R.P. Mirin, Phys. Rev. Res. **4**, 043040 (2022)

[112] A.H. Castro Neto, G. Castilla and B.A. Jones, Phys. Rev. Lett. **81**, 3531 (1998); A.H. Castro Neto and B.A. Jones, Phys. Rev. **B 62**, 14975 (2000)

[113] M.N. Kiselev, K. Kikoin, and R. Oppermann, Phys. Rev. B **65**, 184410 (2002)

[114] S. Burdin and P. Fulde, Phys. Rev. **B 76**, 104425 (2007)

[115] M.-T. Tran and K.-S. Kim, Phys. Rev. Lett. **105**, 116403 (2010)

[116] M.-T. Tran and K.-S. Kim, J. Phys.: Condens. Matter **23** 425602 (2011)

[117] B. Poudel, G. Zwicknagl, C. Lacroix, and S. Burdin, J. of Magn. Magn. Mater. **520**, 167405 (2021)

[118] K. Byczuk, W. Hofstetter, U. Yu, and D. Vollhardt, Eur. Phys. J. Spec. Top. **180**, 135 (2009)

[119] M. Ulmke, V. Janis, and D. Vollhardt, Phys. Rev. **B 51**, 10411 (1995)

[120] M.C.O. Aguiar, V. Dobrosavljevic, E. Abrahams, and G. Kotliar, Phys. Rev. **B 73**, 115117 (2006)

[121] M.C.O. Aguiar, V. Dobrosavljevic, E. Abrahams, and G. Kotliar, Phys. Rev. Lett. **102**, 156402 (2009)

[122] D.Tanaskovic,V.Dobrosavljevic, E.Abrahams, and G. Kotliar, Phys. Rev. Lett. **91**, 066603 (2003)

[123] M.C.O. Aguiar and V. Dobrosavljevic, Phys. Rev. Lett. **110**, 066401 (2013)

[124] K. Byczuk, W. Hofstetter, and D. Vollhardt, Phys. Rev. Lett. **94**, 056404 (2005)

[125] A. Weh, Y. Zhang, A. Östlin, H. Terletska, D. Bauernfeind, K.-M. Tam, H.G. Evertz, K. Byczuk, D. Vollhardt, and L. Chioncel, Phys. Rev. **B 104**, 045127 (2021)

[126] M. Milovanović, S. Sachdev, and R. N. Bhatt, Phys. Rev. Lett. **63**, 82 (1989)

[127] S. Sachdev, Phil. Trans. R. Soc. **A 356**, 173 (1998)

[128] M.A. Tusch and D.E. Logan, Phys. Rev. **B 48**, 14843 (1993)

[129] P.B. Chakraborty, K. Byczuk, and D. Vollhardt, Phys. Rev. **B 84**, 035121 (2011)

[130] M. Ulmke and R.T. Scalettar, Phys. Rev. B 55, 4149 (1997)

[131] M.E. Pezzoli and F. Becca, Phys. Rev. **B 81**, 075106 (2010)

[132] N.C. Costa, T. Mendes-Santos, T. Paiva, N.J. Curro, R.R. dos Santos, and R.T. Scalettar, Phys. Rev. **B 99**, 195116 (2019)

[133] S. Sen, N.S. Vidhyadhiraja, M. Jarrell, Phys. Rev. **B 98**, 075112 (2018)

[134] C.E. Ekuma, H. Terletska, K.-M. Tam, Z.-Y. Meng, J. Moreno, and M. Jarrell, Phys. Rev. **B 89**, 081107 (2014)

[135] A.K. Mitchell, P.G. Derry, and D.E. Logan, Phys. Rev. **B 91**, 235127 (2015)

[136] H. Im, D.U. Lee, J. Jo, Y. Chong, W. Song, H. Kim, E.K. Kim, T. Yuk, S.-J. Sin, S. Moon, J.R. Prance, Y.A. Pashkin, J.S. Tsai, Nat. Phys. **19**, 676 (2023)

[137] C.-K. Park, S. Park, H. Jang, T.B. Park, I.C. Kim, S. Shin, T. Lee, T. Fennell, U. Stuhr, M. Kenzelmann, H. Lee, and T. Park, J. Korean Phys. Soc. **84**, 446 (2024)

[138] P. Li, H. Ye, Y. Hu, Y. Fang, Z. Xiao, Z. Wu, Z. Shan, R.P. Singh, G. Balakrishnan, D. Shen, Y-f. Yang, C. Cao, N.C. Plumb, M. Smidman, M. Shi, J. Kroha, H. Yuan, F. Steglich, and Y. Liu, Phys. Rev. B **107**, L201104 (2023)

13 Quantum Magnetism In and Out of Equilibrium

Salvatore R. Manmana
Institute for Theoretical Physics
Georg-August-University Göttingen

Contents

E. Pavarini and E. Koch (eds.)
Correlations and Phase Transitions
Modeling and Simulation Vol. 14
Forschungszentrum Jülich, 2024, ISBN 978-3-95806-751-6
http://www.cond-mat.de/events/correl24

1 Quantum magnetism and strongly correlated systems

An exceptional and widely known quantum state of matter is superconductivity. It is realized by the spontaneous breaking of a (gauge) symmetry, in which (in the simplest theory) the interaction between the electrons and lattice degrees of freedom leads to this peculiar 'macroscopic' behavior of certain materials. Other systems, in which the interaction between the constituent particles leads to a variety of interesting phenomena, are quantum magnets: these are quantum many-body systems, in which the interplay between immobile spin degrees of freedom (typically the spins of the electrons in a material, or pseudo-spin degrees of freedom, e.g., in cold gases experiments) leads to unconventional quantum phases. In this chapter, I will present various aspects of the phenomenology of quantum magnetism, the unconventional states of matter that can be realized, and how to characterize them. The topic is too vast to cover all essential aspects in a single book chapter. Therefore, most of the sections are summaries of (review) articles, text books, or from the introduction of PhD theses on related topics, and are intended as a starting point for further reading.

To start with, I will first put quantum magnetism in the context of strongly correlated quantum many-body systems and discuss typical models and examples. In order to understand what kind of states of matter can be obtained in such correlated systems, the basic notions of spontaneous symmetry breaking, order parameters, long-range order and topological order are discussed. Important experimental tools are spectroscopic measurements (e.g. inelastic neutron scattering), which will lead us to the notion of dynamical structure factors. At the end, I will give a glimpse onto recent developments, where the dynamical properties are further studied by going out of equilibrium and directly measuring the time evolution of the observables – typically, the demagnetization dynamics on very short time scales, or the time evolution of order parameters, which show that one can realize (transient) magnetically ordered states when exciting certain materials with a laser pulse.

1.1 Quantum many-body systems

Quantum many-body effects come into play in certain materials and in systems of ultracold atomic and molecular gases on optical lattices [1]. Prominent examples for strongly correlated materials are high-temperature superconductors [2, 3] and Mott insulators [4]. Using ultracold atoms, a breakthrough experiment was the realization of a Mott-insulating state of ultracold bosons in 2002 [5]. These systems are described by microscopic quantum mechanical models of interacting particles on various lattice geometries. Interesting effects arise due to competing interactions or geometrical frustration, which typically does not allow for the realization of a simple ground state that satisfies all bonds equally well. Examples for such frustrated geometries are shown in Fig. 1.

An interesting class of strongly correlated materials, in which such competing interactions lead to novel and interesting states of matter, are (frustrated) quantum magnets [11–14]. These systems can be described as networks of interacting quantum mechanical spins on a lattice, and

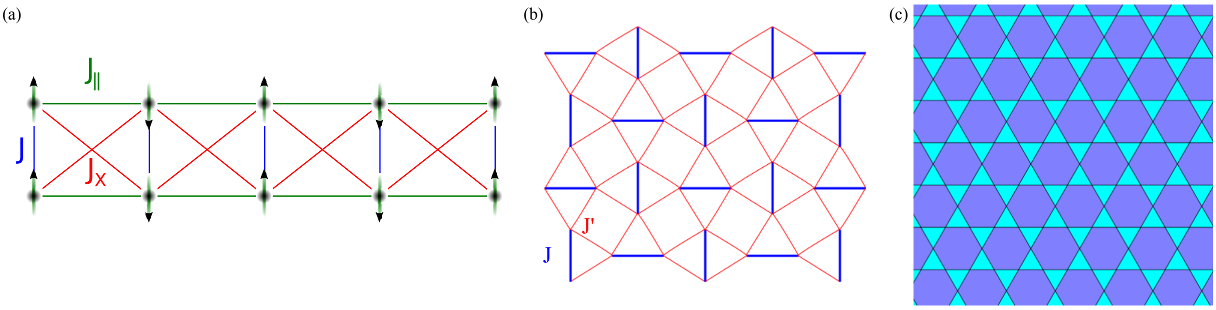

Fig. 1: *Examples of frustrated lattice geometries realized in quantum magnetic materials. (a) Frustrated ladder, realized in various materials, e.g., $TlCuCl_3$ [6, 7]. (b) Shastry-Sutherland lattice, a network of orthogonal dimers. This geometry is realized, e.g., in $SrCu_2(BO_3)_2$ [8, 9]. (c) Kagome lattice of corner-sharing triangles. This system is realized, e.g., in Herbertsmithite* $\big(ZnCu_3(OH)_6Cl_2\big)$ *[10].*

the underlying microscopic model typically is a variant of the Heisenberg Hamiltonian,

$$\mathcal{H}_{\text{Heisenberg}} = \sum_{\langle i,j \rangle} J_{i,j}\, \vec{S}_i \cdot \vec{S}_j, \tag{1}$$

where the operator $\vec{S}_i \equiv \begin{pmatrix} S_i^x \\ S_i^y \\ S_i^z \end{pmatrix}$ describes a localized spin on the lattice site i, and $S_i^{x,y,z}$ are the usual spin operators. In principle, any magnitude of $S \equiv \left|\vec{S}\right|$ can be considered, but the most appealing effects due to the quantum nature of the spins are expected for small values of S, e.g., $S = 1/2$ or $S = 1$. Many quantum magnetic materials can be described using the Heisenberg model or one of its variants and a rich bouquet of interesting phenomena is found, which are often revealed in the presence of an external magnetic field. For example, an *a priori* not necessarily expected realization of an unconventional phase of matter in a magnetic material is the Bose-Einstein-condensation (BEC) of triplet excitations (see, e.g. [7, 15–17]). Since these excitations are of bosonic nature, at temperatures low enough, they can form a BEC, so that quantum magnets can host this peculiar state of matter, which was first realized in the lab in experiments with ultracold gases [1]. Other quantum states of matter realized in these materials are Mott-insulators on magnetization plateaux [8, 9, 18, 19], and the proposed spin-equivalent [20–25] of a supersolid phase [26, 27], which is characterized by the simultaneous spontaneous breaking of the translational symmetry of the underlying lattice and of a U(1) symmetry associated to the formation of a superfluid. These effects most prominently appear at low temperatures, at which quantum fluctuations dominate over thermodynamic fluctuations, and which drive quantum phase transitions [28, 29].

Quantum states of matter are either described by local order parameters, which are due to the spontaneous breaking of a symmetry of the Hamiltonian, or by topological properties. The Heisenberg model (1) contains a scalar product of two vectors $\vec{S}$ and is, hence, invariant against rotation in spin-space, i.e., it possesses a SU(2) symmetry. An important question for quantum magnets is, therefore, if and how this symmetry (and possibly other symmetries) of the system is broken spontaneously. The most prominent way of breaking the SU(2) symmetry is by realizing a finite magnetization, i.e., the expectation value of the spin in (at least) one direction in space gets finite, e.g. $\langle S_i^z \rangle \neq 0$. Since the magnetization is a vector and points in a specific direction, a finite magnetization implies a broken time-reversal symmetry. The question arises, if other (for quantum magnets less obvious) types of order can be realized. A prominent example is realized for $S > 1/2$: In this case, the SU(2) symmetry of the Heisenberg Hamiltonian can spontaneously be broken *without* resulting finite local magnetizations. This leads to a rather unconventional ordered phase which in an experimental investigation would appear disordered, if only (local or total) magnetizations are measured. Indeed, the resulting type of order is reminiscent of liquid crystals, which realize nematic states with a broken spin-rotational symmetry but unbroken time reversal symmetry [30,13]. Correspondingly, such states are called *spin-nematic states* and have been explored in a large number of theoretical approaches (a nice summary is sketched in the introduction of [31] and references therein). Recently, the observation of such a spin-nematic state in an iridate material was reported [32].

One particular playground for quantum magnetic systems are phases in which, despite the presence of strong correlations in the system, *no* long-range order is induced at zero temperature. These phases are called *spin liquids* and can be pictured as a superposition of many spins which simultaneously point in different directions. They show exotic behavior and possess a number of interesting properties such as excitations with fractional quantum numbers [33]. There exists a vast literature on this topic, for an introduction see [34]. The search for realizations of this type of unconventional states is motivating a lot of ongoing research. For example, numerical methods based on tensor network states (TNS), in particular matrix product state (MPS) approaches, have provided evidence for the existence of such a spin liquid phase in the kagome lattice [35–37]. This highly frustrated geometry is depicted in Fig. 1(c) and has been identified, e.g., in the natural mineral Herbertsmithite [10,38].

While the interacting spins in the Heisenberg model remain localized, in many materials the electrons are itinerant. This is addressed, e.g., by the Hubbard model [39–42], which is one of the simplest models taking into account the effects of spin and of electron motion. Both, the fermionic version[1]

$$\mathcal{H}_{\text{Hubbard}}^{\text{Fermions}} = -t \sum_{\langle i,j \rangle,\, \sigma} \left(c_{i,\sigma}^\dagger c_{j,\sigma} + h.c. \right) + U \sum_i n_{i,\uparrow} n_{i,\downarrow} \tag{2}$$

as well as the bosonic variant [28,43]

$$\mathcal{H}_{\text{Hubbard}}^{\text{Bosons}} = -J \sum_{\langle i,j \rangle} \left(b_i^\dagger b_j + h.c. \right) + \frac{U}{2} \sum_i n_i (n_i - 1) \tag{3}$$

are relevant for the description of strongly correlated materials or for systems of ultracold atoms on optical lattices, respectively. Using degenerate perturbation theory, the Hamiltonian (2) in

---

[1] Standard notation for the operators is used, i.e., $c_{i,\sigma}^{(\dagger)}$ represents a fermionic annihilation (creation) operator, $b_i^{(\dagger)}$ the corresponding bosonic one, and $n_{i,\sigma} = c_{i,\sigma}^\dagger c_{i,\sigma}$ or $n_i = b_i^\dagger b_i$ the densities in the fermionic or bosonic case, respectively. In the case of the t-J-model, the operators $f_{i,\sigma}^{(\dagger)}$ are fermionic ones, but act on a restricted Hilbert space in which double occupancies are forbidden.

the strong coupling limit $U/t \gg 1$ can be mapped to the Heisenberg model (1) [44] with antiferromagnetic (AFM) interactions ($J > 0$ in the convention used in Eq. (1)). In this way, studying Hubbard systems allows one to study quantum magnetism. Due to the difficulties to treat in particular the fermionic variant of the Hubbard model beyond 1D using analytical or numerical approaches, experiments on optical lattices have got the particular motivation to *emulate* the behavior of this microscopic model [45], so that its phase diagram can be investigated in such experiments. This is in the spirit of Feynman's proposal from the early 1980s[2] to use some well controlled quantum systems to simulate other ones, eventually leading to the development of a quantum computer [47–49]. In this way, for $U/t \gg 1$ quantum magnetism can be studied, and the realization of a controlled quantum simulator for quantum magnetism in cold gases experiments is a central topic of ongoing research. Interestingly, there are further proposals for how to realize Heisenberg-type models in cold gases experiments based on ultracold polar molecules, e.g., where internal degrees of freedom of the molecules can be used as pseudo-spin degrees of freedom (see, e.g., [50, 51]).

One interesting hybrid of itinerant electrons and Heisenberg exchange is the so-called t-J model

$$\mathcal{H}_{\mathrm{tJ}} = -t \sum_{\langle i,j \rangle,\sigma} \left(f^\dagger_{i,\sigma} f_{j,\sigma} + h.c. \right) + J \sum_{\langle i,j \rangle} \left(\vec{S}_i \cdot \vec{S}_j - \frac{1}{4} n_i n_j \right) , \tag{4}$$

which, similarly to the Heisenberg model, can be obtained from the fermionic Hubbard model in degenerate perturbation theory in the limit $U/t \to \infty$ [44] and by excluding double occupancies on the lattice sites. One possible way to look at the t-J model is to imagine a lattice with initially one spin per site, in which the spins interact via Heisenberg exchange, but then *dope* it (i.e. remove more and more of the electrons). In this way, empty lattice sites are formed, and the spins can 'hop around' in addition to experiencing the spin exchange interaction. Since in cuprates high-temperature superconductivity is obtained by doping an AFM, there are proposals to understand high-temperature superconductors based on spin fluctuations, and the t-J model (which describes such a doped quantum magnet) is considered a minimal model [3, 52].

The fermionic and spin systems considered so far have a SU(2) symmetry and are invariant under the corresponding transformations. From the theoretical side, it is tempting to enhance this symmetry from SU(2) to SU(N). This has attracted considerable theoretical attention. There is a long history of studies of SU(N) spin systems (see, e.g., [53–55]) since they become analytically tractable in the large-N limit, and rich phase diagrams have been identified. In 1D, the aforementioned spin-nematic phases have been predicted as well as generalizations of the so-called AKLT state, which is an archetypical example for topological phases which are briefly revisited in Sec. 2.2.

Since no exact SU(N) models have been identified in nature, these efforts were broadly considered a theoretical playground. However, it has been proposed that systems with such a high symmetry (up to $N = 10$) can be realized in quantum simulators with ultracold alkaline earth

---

[2] The possibility to exploit quantum speed up was actually first envisaged by Y.I. Manin [46] in a radio interview with Radio Moscow in 1980; it is unclear to me whether Feynman was aware of this. In any case, he seems to be the first one to promote these ideas in the public in the western hemisphere and pursue them.

atoms [56]. More specifically, these experiments can realize SU(N) symmetric generalizations of fermionic Hubbard models

$$\mathcal{H}^{\mathrm{SU}(N)}_{\text{Hubbard}} = -t \sum_{\langle i,j \rangle} \sum_{\alpha=1}^{N} \left(f^{\dagger}_{\alpha,i} f_{\alpha,j} + h.c. \right) + \frac{U}{2} \sum_{i,\alpha \neq \alpha'} f^{\dagger}_{\alpha,i} f^{\dagger}_{\alpha',i} f_{\alpha',i} f_{\alpha,i} \,. \tag{5}$$

Here, $f^{(\dagger)}_{\alpha,i}$ is a fermionic annihilation (creation) operator for a particle with flavor α on lattice site i. Similarly to the SU(2) case, in the limit $U/t \to \infty$ an effective SU(N) symmetric Heisenberg model can be derived

$$\mathcal{H}^{\mathrm{SU}(N)}_{\text{Heisenberg}} = \frac{2t^2}{U} \sum_{\langle i,j \rangle} \sum_{\alpha,\beta} S^{\beta}_{\alpha}(i) S^{\alpha}_{\beta}(j) \,, \tag{6}$$

with the spin operators $S^{\beta}_{\alpha}(i) = f^{\dagger}_{\alpha,i} f_{\beta,i}$. This opens the door to studying SU(N) quantum magnetism. Having this and the specific experimental implementation in mind, exotic new phases have been predicted. An example, which has intrigued researchers, is the possibility to realize chiral spin liquids [57, 58] in such systems [59]. These are spin liquids with certain topological properties, which can be of relevance for the realization of topological quantum computers [60, 33].

These findings underline the recent focus of research on the uncovering of new and unconventional behavior in microscopic models and their possible experimental detection. Since most of the models are non integrable,[3] numerical methods play an important role in the investigation of quantum magnetism. A very powerful approach is using *quantum Monte Carlo* techniques [61], which, in principle, can be applied to arbitrary situations. However, fermionic and AFM frustrated spin systems are affected by what is known as ‘the sign problem’, which leads to negative probabilities in the course of the Monte Carlo sampling, and which makes it essentially impossible to control the calculations for many interesting situations. Therefore, other, wave-function based approaches have been developed. For quasi-1D systems (i.e., chains and ladder geometries), efficient approaches are *tensor network methods*, in particular *matrix product state* methods (MPS) and one of the realizations in terms of the density matrix renormalization group method (DMRG) [62], which are explained in detail in various review articles (e.g. [63]). This method has been applied very successfully for the investigation of phase diagrams and of quantum critical behavior of a multitude of (quasi-)1D systems (see the website [64] for a collection of the publications relying on this method). However, for 2D systems, the area law of entanglement growth [65, 66] is a major obstacle for an efficient treatment of the microscopic models of interest. Since also other numerical methods are limited, it is an ongoing challenge to develop numerical and analytical approaches for 2D quantum magnetic systems.

---

[3] An important exception is the Heisenberg model and its generalization to the XXZ-model by allowing the spin-exchange in the z-direction to have a different strength than in the x-y-plane in 1D, which is integrable using the Bethe ansatz [42].

1.2 Basic properties of $S = 1/2$ quantum magnets, magnetization curves

In order to get a better intuition for the behavior of quantum magnets, it is useful to start with a small number of quantum spins, which can serve as building blocks to understand the large interacting networks of spins realized in quantum magnets. To do so, let us consider a $S = 1/2$ Heisenberg model with interactions between nearest neighboring spins in a magnetic field $\vec{B}$,

$$\mathcal{H} = J \sum_{\langle i,j \rangle} \vec{S}_i \cdot \vec{S}_j - \vec{B} \sum_j \vec{S}_j \,. \tag{7}$$

To simplify the discussion, we assume the magnetic field $\vec{B}$ to point in z-direction.

1. One single spin-$1/2$:
   The Hamiltonian is simply $\mathcal{H}{=}{-}BS_i^z$, i.e., in its ground state the spin can take one of the two possible configurations $|\uparrow\rangle$, $|\downarrow\rangle$, depending on the direction the magnetic field is pointing at.
   Note: for $B = 0$, any superposition of both states is a possible ground state, $|\psi\rangle = \alpha\,|\uparrow\rangle + \beta\,|\downarrow\rangle$ with $\alpha^2 + \beta^2 = 1$, and for $\alpha = \beta$ a so-called "cat state" is realized.[4] This can be relevant for quantum computation, where you can associate the two spin states to the two possible internal states of a *qubit* (e.g., $|\uparrow\rangle \equiv |1\rangle$, $|\downarrow\rangle \equiv |0\rangle$).

2. Two spin-$1/2$ objects interacting via Heisenberg exchange (spin-$1/2$ dimer):
   The Hamiltonian now is

$$\mathcal{H} = J\vec{S}_1 \cdot \vec{S}_2 - B\,(S_1^z{+}S_2^z) = J\Big(\frac{1}{2}\big(S_1^+S_2^-{+}S_1^-S_2^+\big) + S_1^zS_2^z\Big) - B\big(S_1^z{+}S_2^z\big)\,, \tag{8}$$

   with ladder operators $S^\pm = S^x{\pm}iS^y$.
   Let us first consider the case $B = 0$. In this case, the Hamiltonian has the full SU(2) symmetry, and we can rewrite

$$\vec{S}_{total} = \vec{S}_1{+}\vec{S}_2 \;\Rightarrow\; \vec{S}_1 \cdot \vec{S}_2 = \frac{1}{2}\left(\big(\vec{S}_{total}\big)^2 - \big(\vec{S}_1\big)^2 - \big(\vec{S}_2\big)^2\right)\,.$$

   Realizing that $\vec{S}^2 = S(S{+}1)$, we obtain for the Hamiltonian (8) for $S = 1/2$ at $B = 0$

$$\mathcal{H} = \frac{J}{2}\Big(\big(\vec{S}_{total}\big)^2 - \frac{3}{2}\Big).$$

   Since for $S = 1/2$ the only possible values for $\vec{S}_{total}$ are 0 or 1, respectively, we see immediately that the Hamiltonian has only two eigenvalues

$$E_{S_{total}=0} = -3J/4 \quad \text{and} \qquad E_{S_{total}=1} = J/4\,.$$

   Depending on the sign of J, either of the two values is the ground state. Due to the degeneracy (see below) the state with $S_{total}{=}0$ is called *singlet state* (it is not degenerate), and the other one is threefold degenerate and accordingly the eigenstates are called *triplet states*.

---

[4] Named after the famous gedankenexperiment with "Schrödinger's cat".

We now turn to the Hamiltonian matrix, i.e., we need to introduce a suitable many-body basis, which can be obtained by the tensor product of single-spin basis states, leading to the basis states $\{\,|{\downarrow\downarrow}\rangle\,,\,|{\downarrow\uparrow}\rangle\,,\,|{\uparrow\downarrow}\rangle\,,\,|{\uparrow\uparrow}\rangle\,\}$. Note that the number of basis states compared to one spin-$1/2$ particle has *doubled*. This is at the heart of why it is so complicated to numerically treat large quantum many-body systems: here, the dimension d of the basis grows exponentially with the number N of spins in the system, $d = 2^N$, so that only small systems can be treated exactly [61].

For the dimer, the Hamiltonian in this basis is represented by the matrix

$$\mathbf{H} = \begin{pmatrix} \frac{J}{4}+B & 0 & 0 & 0 \\ 0 & -\frac{J}{4} & \frac{J}{2} & 0 \\ 0 & \frac{J}{2} & -\frac{J}{4} & 0 \\ 0 & 0 & 0 & \frac{J}{4}-B \end{pmatrix} . \tag{9}$$

Note the *block structure* on the diagonal of the matrix. This is due to symmetries and conserved quantities (here: conservation of the z-component of the total spin of the system) and follows from Schur's Lemma [67]. It can be exploited to speed up the diagonalization of the matrix, since one needs to explicitly diagonalize only the smaller 'blocks' of the matrix, i.e., for Hamiltonian (9) we need to diagonalize only a 2×2 matrix. This leads to the following eigenstates and eigenvalues:

- Singlet-state $|s\rangle = \big(|{\uparrow\downarrow}\rangle - |{\downarrow\uparrow}\rangle\big)/\sqrt{2}$, with energy $E_s = -3J/4$. This is the state with $S_{total} = 0$, which we encountered above, and also the z-component $S^z_{\text{total}} \equiv \big\langle S^z_1 + S^z_2 \big\rangle = 0$, so that the magnetic field B does not contribute to the energy.
  Note: This state is a *maximally entangled* state and is *antisymmetric* when swapping the position of the two spins. Indeed, it is one of the *Bell states* and can be useful for quantum information aspects.
- Triplet-states:

  $$|t_1\rangle = |{\uparrow\uparrow}\rangle \qquad |t_0\rangle = \big(|{\uparrow\downarrow}\rangle + |{\downarrow\uparrow}\rangle\big)/\sqrt{2} \qquad |t_{-1}\rangle = |{\downarrow\downarrow}\rangle$$
  $$E_{t_1} = J/4 - B \qquad E_{t_0} = J/4 \qquad E_{t_{-1}} = J/4 + B$$

  For all three states we have $S_{\text{total}} = 1$, but $S^z_{\text{total}} = +1$, 0, or -1, respectively. We see that at $B = 0$ the three states are degenerate, but that turning on a magnetic field removes this degeneracy: depending on the sign of B, the energy of one of the triplet states $|t_1\rangle$ or $|t_{-1}\rangle$ will grow linearly with B, the other one decreases linearly with B; the energy of $|t_0\rangle$ remains unchanged. Using this, we obtain our first magnetization curve: for $J > 0$ (AFM) the singlet state is the lowest energy state for $|B| < J$, but then one of the triplet states takes over, so that we have a jump in the total magnetization from $M = 0$ to $M = 1$ at this 'critical field strength'.

  Note: The states $|t_1\rangle$ and $|t_{-1}\rangle$ are product states with zero entanglement, but $|t_0\rangle$ is maximally entangled, as is also the singlet state (it is another Bell state); however, all three triplet states are symmetric when swapping the positions of the spins.

The physics of such spin-$^1/_2$ dimers is the building block for various quantum magnets. A prominent example is the Shastry-Sutherland lattice depicted in Fig. 1(b), and which can be seen as a system of orthogonal dimers, where the coupling between the dimers can vary. Other systems are, e.g., spin ladders (see Fig. 1(a)), in which the interaction on the rungs is stronger than on the legs. For weak inter-dimer coupling, the physics of such quantum magnetic systems is determined by the properties of the singlet and triplet states discussed here. The inter-dimer coupling will lead to a 'dressing' of the triplet states (resulting in so-called 'triplons'), which then form the building block for the system's behavior. When such a system with AFM interactions on the dimers is put in a magnetic field, the ground state at $B = 0$ is determined by the singlets, but the magnetization curve will mainly be determined by the magnetization of the individual dimers: the dimers, which at $B = 0$ are in a singlet state, are 'populated' by the triplets (or triplons) upon increasing B, leading to particular behavior of the magnetization curve. For example, one can derive effective models $\big($e.g. using perturbative unitary transformations, PCUTs; see, e.g., [68]$\big)$, in which the triplons interact via long-range interactions, and which can form Wigner-type crystals. If this happens, a gap opens, and a magnetization plateau is stabilized, which hosts a Mott insulator, which is formed by the crystal of triplons. Other examples are the aforementioned possible Bose-Einstein condensation of these triplet or triplon excitations at finite B.

3. Three spin-$^1/_2$ objects interacting via Heisenberg exchange:

   As before, at $B = 0$, we can rewrite using $\vec{S}_{total}$ and obtain

$$\mathcal{H} = \frac{J}{2}\Big(\big(\vec{S}_{\text{total}}\big)^2 - \frac{9}{4}\Big) \quad \text{for } S = 1/2\,.$$

   We realize that, as in the system with 2 spins, the ground state for the ferromagnetic (FM) case $J < 0$ is obtained by maximizing $\vec{S}_{\text{total}}$, while for the AFM case $J > 0$, $\vec{S}_{\text{total}}$ needs to be minimized. For $S = 1/2$, the maximal value of $|\vec{S}_{\text{total}}| = 3/2$, and all spins point in the same direction. All the interactions on the bonds are satisfied. However, in the AFM case, the ground state energy is minimal for the smallest possible value $|\vec{S}_{\text{total}}| = 1/2$. We realize the following two aspects:

   i) There are in total *6 configurations*, which all result in $|\vec{S}_{\text{total}}| = 1/2$, i.e., the ground state of the AFM case will be a superposition of the corresponding 6 states: it is *highly* degenerate, since in total we have only $2^3 = 8$ basis states, and hence the largest part of the Hilbert space contributes to the ground state manifold!

   ii) There is no way to simultaneously satisfy all the three interaction terms (i.e., minimize the energy of each of the three bonds): the system is the simplest example for a *geometrically frustrated* quantum magnet. One effect of such geometrical frustration is that the spins try to find a new configuration, in which none of the bonds is fully satisfied, but which minimizes the total energy. As such, qualitatively new behavior can be realized when comparing to non-frustrated geometries. One example is the classical Heisenberg model on a triangle, where the three spins align in the plane and point outwards, forming a $120°$ angle between each other.

> There are many quantum magnetic materials with such AFM triangles as building blocks, see Fig. 1 for example geometries. Particularly interesting situations are obtained when a lattice consists of corner-sharing triangles, such as the kagome lattice depicted in Fig. 1(c). Here, the degree of frustration in the extended lattice is very high and determines the ground state physics. As we have seen for a single triangle, ground states of frustrated AFM are typically very highly degenerate. Due to this degeneracy, the spins fluctuate strongly, so that under circumstances they cannot realize long-range order. This leads to a peculiar situation: the ground state and the excited states are governed by the interactions between the spins, but, due to the strong fluctuations, any attempt to stabilize long-range order is suppressed. Such a state is called a *spin liquid*. Such spin liquid states can also host topological phases of matter (which do not rely on the existence of a finite local order parameter, but are described by global quantities), and due to their rich and unconventional behavior have been a focus of intense studies.

We could, of course, go on, and discuss larger and larger building blocks. Noteworthy are lattices, in which the building blocks are tetrahedrons; for ferromagnetic Ising-type interactions $\mathcal{H}^{\text{Ising}} = J \sum_{\langle i,j \rangle} S_i^z S_j^z$, again a highly frustrated geometry can be realized, e.g., on so-called pyrochlore lattices. The spins align according to so-called 'spin-ice rules' (two spins point into the tetraeder, two point outwards), and due to the high frustration, unconventional states can be realized. Indeed, such systems can even host excitations, which can be described as magnetic monopoles, which in vacuum cannot exist, but are realized and measured in these systems [69, 70].

The generic question is how to deal with a large number of spins on an arbitrary graph. Since in most cases there is no analytical solution, but we are dealing with finite-dimensional Hilbert spaces, we can use the matrix representation of the Hamiltonian in an appropriately chosen basis and diagonalize this on a computer. We refer the reader to, e.g., Refs. [61, 71].

1.2.1 Magnetization curves

An important quantity to study in quantum magnets is the dependence of the magnetization on the applied magnetic field $\vec{B}$, which typically is included in the Hamiltonian as a Zeeman-type term (see Eq. (7)) and which, for the sake of simplicity, we will assume is pointing in z-direction. In this case, the original SU(2) symmetry of the Heisenberg model is broken down to U(1), which can be exploited for investigating the system. Note that, however, the most general form of the Zeeman term is $\sim \vec{B}\mathrm{g}\vec{S}$, with the so-called '$g$-tensor' g, which captures a possibly anisotropic response of the material to the applied magnetic field. If a material has a non-trivial g-tensor, also the remaining U(1) symmetry is broken, and the magnetization will not point in parallel direction to $\vec{B}$. This can lead to further interesting behavior as, e.g., a torque on the sample. Here, however, for the sake of simplicity we assume a simple g-tensor and hence a response only in parallel direction to $\vec{B}$, so that the U(1) symmetry prevails. Then, it suffices to treat the magnetization $M{=}\langle S^z_{total} \rangle$, which can have nontrivial behavior. For example, if there is an excitation gap, then increasing the magnetic field will not change the value of M, leading to

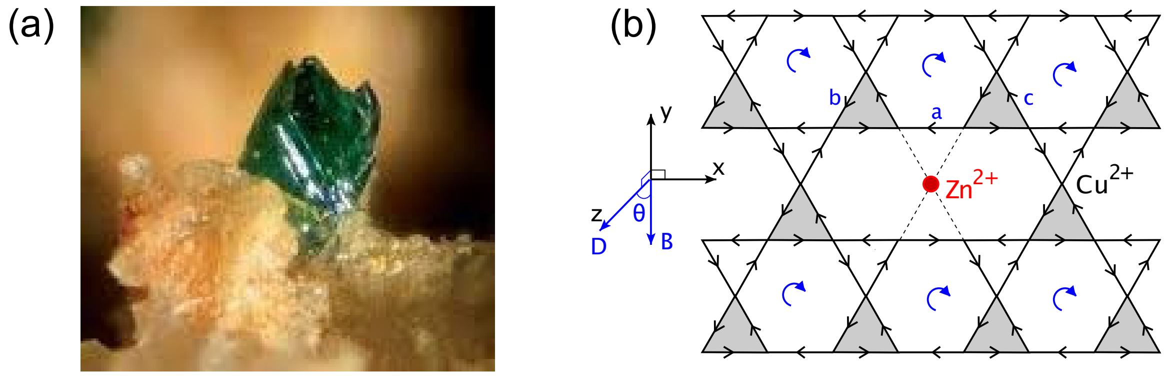

Fig. 2: *(a) The natural mineral Herbertsmithite is a realization of a Heisenberg spin-*$^1/_2$ *system on the kagome lattice [10]. However, the material contains* $\sim 5\%$ *nonmagnetic impurities and anisotropic DM interactions due to spin-orbit coupling. (b) The lattice with one impurity and the orientation of the DM-vectors used in [74].*

a *magnetization plateau*, as already illustrated further above in the context of the spin-$^1/_2$ dimer. These plateaux can host interesting Mott phases (e.g., crystals of triplets). In the vicinity of these magnetization plateaux, it is interesting to study how the plateau 'melts', and the resulting phase can host unconventional states, like the BEC of triplets, or even supersolid phases.

For systems with U(1) symmetry in a magnetic field, the total value of S^z_{total} is conserved, so that one does not need to compute explicitly $M(B)$ via expectation values. Instead, at zero temperature,[5] one computes the ground state energies $E_0(S^z_{total})$ in all possible sectors of S^z_{total} and obtains the Magnetization via a Legendre-transform:

$$M(B) = \left\langle S^z_{total} \right\rangle \Big|_{\left[E_0(S^z_{total}, B=0) - B\cdot S^z_{total}\right]=\min} .$$

Therefore, it is important to have methods to efficiently compute the ground state energy for systems as large as possible in order to be as close as possible to the thermodynamic limit. Two such approaches are the aforementioned exact diagonalizations (ED) and tensor network states, such as the MPS or the Projected Entangled Pair States (PEPS) [72]. Both methods also exist in a version, which works directly in the thermodynamic limit as iMPS and iPEPS, respectively. In particular the iPEPS has been successful in investigating magnetic properties of dimer-based quantum magnets such as the Shastry-Sutherland lattice, see, e.g. [73].

1.3 Effect of spin-orbit coupling at high magnetic fields

The models mentioned so far are often minimal models. However, in real materials additional effects like the anisotropic g-tensor mentioned above, or other anisotropies due to spin-orbit coupling (SOC) are present. In a magnetic field, SOC can alter the physics of the system significantly [75], but is often neglected, since its magnitude typically is only a few percent of the magnitude of the Heisenberg exchange in the system. However, since its effect can be

---

[5] Remember that we are interested in low temperature properties, since here quantum fluctuations will have a stronger effect than thermal ones.

important, in order to obtain a more realistic description, it is necessary to consider SOC by treating additional anisotropic interactions, e.g., of Dzyaloshinskii-Moriya (DM) type [76,77],

$$\mathcal{H}_{\rm DM} = \sum_{\langle i,j \rangle} \vec{D}_{i,j} \cdot \big(\vec{S}_i \times \vec{S}_j\big). \tag{10}$$

This term arises in the strong coupling limit of the fermionic Hubbard model (2) when taking into account spin orbit coupling $\sim \vec{L} \cdot \vec{S}$. Note that, in contrast to the Heisenberg term (1), the DM interaction is antisymmetric upon exchange of the spins and breaks the SU(2) symmetry. On dimers, this leads to a mixing of the singlet and the triplet sectors and can so lead to new interesting effects. An example for DM interactions in a kagome system is depicted in Fig. 2.

2 Unconventional phases and quantum critical behavior

In the previous section, we have seen the most important microscopic models for quantum magnetism (in particular the Heisenberg model (1)), and related models of itinerant fermions or bosons. Most of these models are inspired by quantum magnetic materials. One such material, which hosts unconventional behavior in magnetic fields, is $\mathrm{SrCu_2(BO_3)_2}$, which is a very good realization of the AFM Heisenberg Hamiltonian on the Shastry-Sutherland lattice [78] depicted in Fig. 1(b) [8,9], with additional DM interactions. Using a combination of various numerical methods, the magnetization curve up to 118 T has been compared to experimental data [79], and interesting Mott insulators on magnetization plateaux have been found (see Fig. 3), e.g., one which is formed by bound states of triplons [73]. Another example for a quantum magnetic material, which hosts an unconventional phase, is the ground state of the kagome lattice in Hebertsmithite, which realizes the Heisenberg Hamiltonian with additional DM interactions on this lattice. However, a large number of non-magnetic impurities is present in this material, so that additional effects close to the impurity sites come into play (see Fig. 2).

Many studies are performed on a large variety of further quantum magnetic materials. However, also beyond their possible realization in a material it is interesting *per se* to formulate models with competing interactions based on mathematical insights and to investigate their properties. An example we already encountered in Sec. 1.1 is to enhance the SU(2) symmetry to SU(N). Another model that can be introduced in this line of thinking is the $S = 1$ Heisenberg chain with additional biquadratic interactions in a magnetic field,

$$\mathcal{H} = \sum_i \Big(\cos(\theta)\, \vec{S}_i \cdot \vec{S}_{i+1} + \sin(\theta) \big(\vec{S}_i \cdot \vec{S}_{i+1}\big)^2\Big) - B \sum_i S_i^z\,, \tag{11}$$

the so called *bilinear biquadratic* Hamiltonian (BLBQ). Here, at $B = 0$, the simple Heisenberg model of Eq. (1) has been extended by a term in such a way that the resulting Hamiltonian still possesses the SU(2) symmetry of the Heisenberg model,[6] but the Hamiltonian now has two competing interaction terms. That the two terms compete with each other can be seen by considering a spin-1 dimer: while for the bilinear term (the Heisenberg term) the ground state

---

[6] The biquadratic term itself has, actually, SU(3) symmetry.

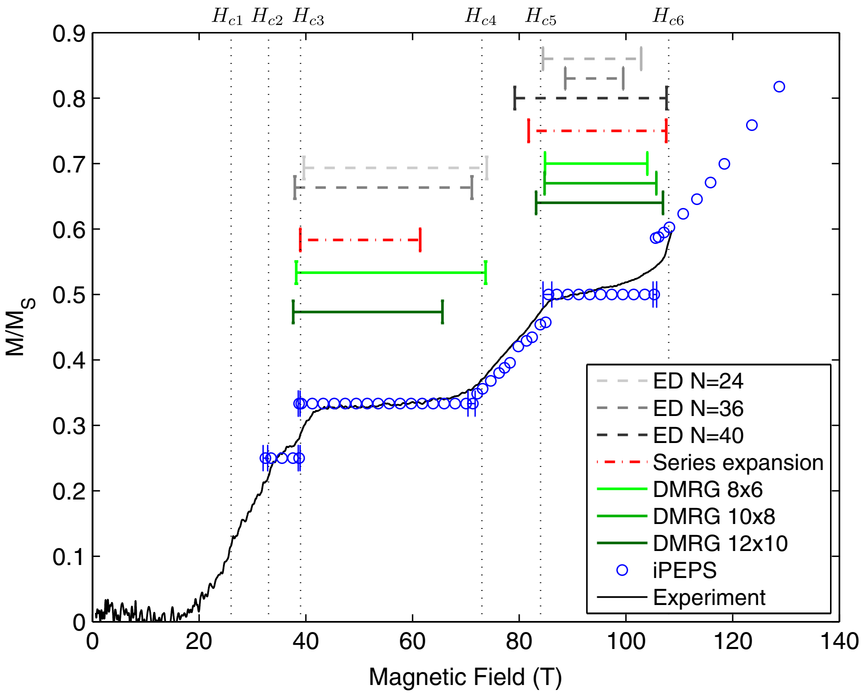

Fig. 3: *Comparison of the experimental data for the magnetization curve of SrCu$_2$(BO$_3$)$_2$ to theoretical results obtained with different approaches (Fig. taken from [79]).*

is either a singlet or a triplet, for the biquadratic term it can be a *quintet* state with $S_{total} = 2$. Going to an extended lattice, one can therefore expect that at zero and at finite B different types of ground states will compete with each other, depending on the strength and the sign of the respective bilinear or biquadratic term. As discussed in [80], the resulting phase diagram of (11) is, indeed, rich. Interestingly, one of the phases realizes spin-nematic quasi long range order (QLRO, see further below). The question arises, how to systematically characterize the different types of order that can emerge in such systems.

2.1 Equilibrium: order parameters from symmetry considerations

Here we give a summary of important aspects concerning spontaneous symmetry breaking. For further reading, I suggest, e.g., the excellent lecture notes ‘An introduction to spontaneous symmetry breaking’ by A.J. Beekman *et al.* [81].

In Landau’s theory of phase transitions, spontaneous symmetry breaking (SSB) leads to a finite local order parameter. In such a scenario, the state of the system[7] is not symmetric under a symmetry transform U, which leaves the Hamiltonian $\mathcal{H}$ invariant $\big($i.e. $[\mathcal{H}, U] = 0\big)$; the symmetry of the state is ‘lower’ than the symmetry of the Hamiltonian. Since symmetries are mathematically described by groups, the state can then still be symmetric under a transform corresponding to a subgroup H of the original symmetry group G of the Hamiltonian, if it preserves any symmetry at all.

---

[7] Typically, we are interested in the ground state $|\psi_0\rangle$ since many of the phenomena discussed here are realized at low temperatures, but the considerations also hold for the thermal equilibrium state.

Is such a symmetry broken state unique? To answer this, consider the following: $[\mathcal{H},\, U] = 0$, so we know that an eigenstate $|\psi\rangle$ of $\mathcal{H}$ and $U\,|\psi\rangle$ must have the same energies, since $|\psi\rangle$ is a simultaneous eigenstate of $\mathcal{H}$ and U. However, $|\psi\rangle \neq U\,|\psi\rangle$ if the symmetry is spontaneously broken, i.e., in the case of SSB, multiple related states exist, which all share the same energy. Indeed, there exists a whole set of distinct symmetry-broken states with the same energy, which can be obtained by performing all possible symmetry transforms U on the symmetry broken state $|\psi\rangle$. These states are, hence, all related to each other by the symmetry G. This allows us to define the order parameter $\mathcal{O}$: it is the operator, whose eigenstates are the inequivalent states in the set of symmetry related states, and whose eigenvalues are different *and* non-zero for each of these states. $\mathcal{O}$ is constructed in such a way, that it has eigenvalue zero for states, which are symmetric under the transform U. Note however, that due to the so-called orthogonality catastrophe, for a finite system, $\langle\psi\,|\mathcal{O}|\,\psi\rangle = 0$ [81]. We will come back to this later, when we ask how to investigate order parameters in practice.

How to think about order parameters? Can we find a way to construct them? This is not straightforward to answer, and we have to dive a little deeper into the mathematics of symmetry transformations. From group theory we learn that in the thermodynamic limit (we will come back to this further below), one can classify the symmetry broken states by the *cosets* gH, which are elements of the *quotient set* G/H, if G is the group of all symmetry transforms, $H \subset G$ is the subgroup of unbroken transformations, and $g \in G$. H is then also called the *residual symmetry group*. For example, let us have a closer look at the SU(2) symmetry of the AFM Heisenberg model. Consider a Néel state $|\uparrow\downarrow\uparrow\downarrow\ldots\rangle$, in which the symmetry is broken down to rotations around a single axis, e.g., in z-direction. Hence, $G =$ SU(2), while the residual symmetry group is $H =$ U(1). One finds for the quotient set $G/H =$ SU(2)/U(1) $\simeq S^2$, which gives all the points on the surface of a sphere. The direction of the sublattice magnetization is then one of these points on the sphere; hence, without applying an external field, infinitely many directions are possible, and the symmetry broken state will pick one of these.

For continuous symmetries, we consider the generators Q of the group, which can be introduced by considering transformations $U(d\theta)$ by an infinitesimally small value of a parameter θ (e.g., for rotations θ is the rotation angle), so that one can write $U(d\theta) \approx 1 + i\, d\theta\, Q$. This allows one to write for arbitrary angles $U(\theta) = e^{i\theta Q}$, which is obtained by subsequently applying transforms $U(d\theta)$ until the desired value θ of the parameter is obtained [67]. Consider a broken-symmetry state $|\psi\rangle$. Then, generators Q, of which $|\psi\rangle$ is an eigenstate, are called *unbroken generators*, and conversely generators, which do not leave the state invariant, are called *broken*. The dimension of the quotient set G/H is then said to equal the number of broken generators.

It would now be useful to identify an operator, whose expectation value can be used to distinguish between the symmetry broken states, and which has zero expectation value in the symmetric state. For each of the sets of equivalent symmetry-broken states, it should have a unique non-zero expectation value. This leads us to the question of how to identify suitable order parameters.

Let $U = e^{i\alpha Q}$ be a symmetry transform such that $[\mathcal{H},\, U] = 0$. Since $U|\psi\rangle \neq |\psi\rangle$ for a symmetry broken state, this also holds for the generator, $Q\,|\psi\rangle \neq |\psi\rangle$, so that we cannot simply consider

the expectation value $\langle\psi\,|Q|\,\psi\rangle$. Instead, one proceeds as follows:
A state $|\psi\rangle$ breaks this symmetry, if there exists any operator Φ such that

$$\langle\psi\,|[Q,\,\Phi]|\,\psi\rangle \neq 0\,. \tag{12}$$

If no such operator exists, $|\psi\rangle$ is symmetric under U. $\Phi(x)$ is called interpolating field,[8] and allows us to introduce the order parameter operator $\mathcal{O}(x)$ and its expectation value, which then is the local order parameter:

$$\mathcal{O}(x) = \big[Q,\,\Phi(x)\big] \quad \text{and} \qquad O(x) = \langle\psi\,|\mathcal{O}(x)|\,\psi\rangle\,.$$

Due to Eq. (12), $O(x)$ is automatically zero if $|\psi\rangle$ is a symmetric state, and finite otherwise, so that it, indeed, distinguishes symmetric from symmetry-breaking states. Note that $\Phi(x)$ and $\mathcal{O}(x)$ are not necessarily hermitian, but one can always construct an observable from this operator, e.g., $\mathcal{O}+\mathcal{O}^\dagger$ or $\mathcal{O}\mathcal{O}^\dagger$.
It is possible to always find an operator $\mathcal{O}$ such that $O(x)$ will be different for distinct broken-symmetry states and equal for states related by residual symmetry transforms, since Eq. (12) does not uniquely determine $\mathcal{O}$ and Φ (e.g, construct an alternative interpolating field by multiplying Φ by a constant, then the equation can still be fulfilled). In almost all cases, the physics of the symmetry-breaking system itself suggests a convenient choice for $\mathcal{O}$, which maps onto the quotient space G/H. Furthermore, it inherits the structure of the quotient space.
Let us consider a concrete example for quantum magnets and go back to the Heisenberg AFM. The Hamiltonian has SU(2) symmetry, which is broken down in the AFM state to U(1). Inequivalent broken-symmetry states correspond to AFM configurations with the sublattice magnetization pointing in different directions – all possibilities together constitute the points on the surface of a sphere, S^2, as discussed above, and which coincides with the quotient SU(2)/U(1)$\simeq S^2$. We now choose the pointer along the z-direction. Hence, the symmetry generators S^x and S^y are broken, but not S^z. How to introduce an interpolating field? We expect for the AFM state the spins to alternately point in the up- and down-direction, respectively, so that it is natural to introduce the *staggered magnetization* $N_i^a = (\pm 1)^i S_i^a$, with i the position on the lattice, and $a = x, y, z$. Can we use N_i^a as interpolating field? Let us consider the breaking of rotations generated by S^x. We see after a short calculation, that $\sum_{ij}[S_i^x,\,N_j^y] = i\sum_i N_i^z$. Similarly, choosing S^y and N_j^x also leads to $\sum_{ij}[S_i^y,\,N_j^x] = i\sum_i N_i^z$. Hence, it seems plausible that the choice $\mathcal{O} = N^z = \sum_i N_i^z$ gives a suitable order parameter operator. Its expectation value then is the expectation value for the staggered magnetization, which can be measured in experiments (e.g. by measuring spin structure factors) – and which also would be the natural choice for an AFM state, since there we expect the spins to alternate, as in the classical Néel state. Note, however, that the classical Néel state is *not* an eigenstate of the AFM Heisenberg model, but, in the thermodynamic limit, if SSB takes place, the expectation value of the staggered magnetization is finite, *like* in a Néel state. This brings us to the following considerations:
In general, $[\mathcal{H},\,\mathcal{O}] \neq 0$, which would imply that the symmetry broken states are not eigenstates of $\mathcal{H}$, contradicting our above statement. In particular, for numerical methods, which treat finite

---

[8] We work for the moment with continuous variables x and will go back to lattice positions later.

system sizes, this implies that the expectation value $\langle\psi_0|\mathcal{O}|\psi_0\rangle = 0$ for all system sizes, so the question arises, how to investigate for the order characterized by $\mathcal{O}$, a topic we will return to later. The solution to this puzzle lies in the necessity of taking the *thermodynamic limit* $N \to \infty$ and $V \to \infty$, with $N/V =$ *const*. It turns out that in this limit $\big\langle[\mathcal{H},\, \mathcal{O}]\big\rangle$=0, and the symmetry-broken states become orthogonal to one another in this limit, as well as degenerate with the symmetric exact eigenstates of $\mathcal{H}$. If in this limit, the symmetry-broken states are eigenstates of $\mathcal{H}$. The thermodynamic limit is, hence, always different to any finite volume (irrespective of its size), and makes it a *singular* limit. Care needs to be taken, when computing quantities in this limit. Often, in order to have some finite expectation value, one applies a small field[9] h, which induces the order one wants to investigate, but which one needs to 'remove' again. Hence, when studying observables in the thermodynamic limit, two limits need to be taken, and since the thermodynamic limit is singular, the order cannot be exchanged. Hence, the order parameter can be obtained as

$$\langle\mathcal{O}\rangle = \lim_{h\to 0}\lim_{N\to\infty} \langle\psi_0(h,N)|\mathcal{O}|\psi_0(h,N)\rangle \ ,$$

with $|\psi_0(h,N)\rangle$ being the ground state for a system with N spins and when applying a small field h.

From these considerations, two questions are imminent: i) how to compute order parameters numerically, if one treats finite systems? ii) which order parameters can we realize in a quantum magnetic system?

We first turn to the latter. As we have seen above, this needs some careful thought. Since we are dealing with systems on lattices, one can consider the breaking of the lattice symmetries, like translational, rotational, or parity symmetry. Since this is not peculiar for spin systems (also itinerant electrons on such lattices can undergo the corresponding SSB), we focus here on the SSB associated to the spin degrees of freedom, and discuss the above mentioned example of spin-nematic order as an unconventional way to realize SSB in quantum magnets.

2.1.1 Spin-nematic order

We start by describing an $S = 1$ object by the three S^z eigenstates $|{\downarrow}\rangle$, $|0\rangle$, $|{\uparrow}\rangle$. From these, we can construct basis states (see also the Suppl. Material of [82] and the PhD thesis of T. Tóth (EPF Lausanne, 2011) [83])

$$|x\rangle = \frac{i}{\sqrt{2}}\big(|{\uparrow}\rangle - |{\downarrow}\rangle\big)\,, \quad |y\rangle = \frac{1}{\sqrt{2}}\big(|{\uparrow}\rangle + |{\downarrow}\rangle\big) \quad \text{and} \qquad |z\rangle = -i\,|0\rangle\,.$$

We see that $S^x|x\rangle$=$S^y|y\rangle$=$S^z|z\rangle$=0, and that these basis states are invariant against time reversal operation. The action of the spin operators in this basis can be written in a compact form

$$S^\alpha|\beta\rangle = i\sum_{\gamma=x,y,z}\varepsilon_{\alpha\beta\gamma}|\gamma\rangle \ .$$

---

[9] What exactly this field is depends on the situation.

Now, every hermitian operator O can be written as

$$O = \sum_{\alpha,\beta=1}^{3} A_{\alpha,\beta} \left|\alpha\right\rangle \left\langle\beta\right| \,,$$

where $|1\rangle$, $|2\rangle$, $|3\rangle$ are basis states describing the $S = 1$ object (e.g., the ones defined above), and $A^*_{\alpha\beta} = A_{\beta\alpha}$, and which by the above construction is a quadratic form in the spin operators S^α. Such a self-adjoint 3×3 matrix is described by 9 real-valued parameters, from which we can introduce eight non-trivial, independent operators (the trace is held fixed, so that it is one parameter less than the number of entries in the matrix). These entries can be interpreted as possible on-site order parameters for systems, which are built up from $S = 1$ objects. More general, we can introduce a rank-k tensor operator $\mathbf{T}^k$, whose entries T^k_q satisfy the commutation relations

$$\left[S^z,\, T^k_q\right] = qT^k_q \quad \text{and} \qquad \left[S^\pm,\, T^k_q\right] = \sqrt{k(k{+}1) - q(q{\pm}1)}\, T^k_{q\pm1}\,.$$

From this, the 'highest' entry is a product of k operators S^+; for example, we obtain for $k = 1$ the components of $T^1_q = (S^+,\, S^z,\, S^-)$, which, because $S^\pm = S^x \pm iS^y$, are the three order parameters for local magnetizations in the three spatial directions (dipolar order). For $S = 1/2$, this exhausts all possibilities, since there we can apply the ladder operators $S^\pm$ maximally once, before the result is zero, i.e., $\mathbf{T}^2 = 0$ for $S = {}^1\!/\!_2$ systems. However, for $S = 1$ this is not true, and for $k = 2$ we find

$$\begin{aligned}
T^2_2 &= S^+S^+ & T^2_{-2} &= S^-S^- \\
T^2_1 &= -\big(S^+S^z{+}S^zS^+\big) & T^2_{-1} &= \big(S^-S^z{+}S^zS^-\big) \\
T^2_0 &= \sqrt{\frac{2}{3}}\big(3(S^z)^2{-}S(S{+}1)\big).
\end{aligned}$$

The elements T^2_q are not automatically hermitian. Since the order parameter is an observable and hence hermitian, we can use the T^2_q to form suitable linear combinations, which then can be interpreted as local order parameters. We thus obtain the 5-component order parameter for spin-nematic or spin-quadrupolar order:

$$\mathbf{Q} = \begin{pmatrix} Q^{x^2-y^2} \\ Q^{3z^2-r^2} \\ Q^{xy} \\ Q^{yz} \\ Q^{zx} \end{pmatrix} = \begin{pmatrix} (S^x)^2 - (S^y)^2 \\ \frac{1}{\sqrt{3}}\big(2(S^z)^2{-}(S^x)^2{-}(S^y)^2\big) \\ S^xS^y + S^yS^x \\ S^yS^z + S^zS^y \\ S^zS^x + S^xS^z \end{pmatrix} .$$

The components of $\mathbf{Q}$ are called quadrupolar order parameters. Their expectation value can be finite also for states, which are invariant under time-reversal symmetry, for which the dipolar (magnetic) order parameters have zero expectation value. Hence, this construction lead us to a new type of order parameter, which is beyond the 'standard' view onto magnetic systems, in which only the dipolar (magnetic) order parameters are considered.

An alternative way to obtain the quadrupolar order parameters is the following: The quadratic form $A_{\alpha,\beta} = S^\alpha S^\beta$ is decomposed into a scalar $S(S{+}1)\delta^{\alpha\beta}/3$ (trace – corresponding to the length of the spin), a three-component vector $(S^{\alpha\beta}{-}S^{\beta\alpha})/2$ (antisymmetric representations: dipolar operators, pointing to a certain direction and thus breaking time-reversal symmetry – corresponding to the local magnetization), and a symmetric, traceless, tensor of rank two, $(S^{\alpha\beta}{+}S^{\beta\alpha})/2 - S(S{+}1)\delta^{\alpha\beta}/3$, corresponding to the five quadrupolar operators. How many local order parameters one can obtain in a quantum magnetic system then depends on the value of the spin S and, in general, the underlying symmetry, which typically for spin systems describing electronic systems is SU(2), but can be larger, SU($N{>}2$), as described in the introduction.

Note that a similar construction can be done for bond-order [82]: when summing the spins on neighboring bonds, then even for a $S = {}^1\!/_2$ system we obtain $S_{Bond} > 1/2$, and a similar construction for higher-order order parameters can be done. The local order parameters for quadrupolar order then live on the bonds rather than on the sites, and hence this type of order is also called 'bond-nematic order'.

The number of possible order parameters is determined by the extent, to which one can apply the ladder operators $S^\pm$ without getting zero. For the SU(2) case, we see that for $S = 1$, similarly to the $S = {}^1\!/_2$ case, we have $T_q^{k>2} = 0$, so the local magnetization and the quadrupolar order exhaust the possibilities to construct local order parameters related to the spin degrees of freedom. However, for $S > 1$, again further order parameters can be realized, named multipolar states of degree $k \leq 2S$, and the order parameters are rank-k tensor operators.

Since the so-constructed local order parameters rely on symmetry considerations, one can ask for possible relations between them. Indeed, one finds for the SU(2), $S = 1$ case

$$\langle \mathbf{S} \rangle^2 + \langle \mathbf{Q} \rangle^2 = \frac{4}{3},$$

and that any state $|S,\, S^z\rangle$ is an eigenstate of $\mathbf{Q}^2$ for any spin S,

$$\mathbf{Q}^2\, |S,\, S^z\rangle = \frac{4}{3} S(S{+}1)\Big(S(S{+}1) - \frac{3}{4}\Big)\, |S, S^z\rangle$$

and hence

$$\big(\mathbf{Q}^2 + \mathbf{S}^2\big)\, |S, S^z\rangle = \frac{4}{3} S^2 (S{+}1)^2\, |S, S^z\rangle\,.$$

2.1.2 How to identify long-range order

As mentioned before, the order parameter is finite only in the thermodynamic limit. The question arises, how to compute it in practical calculations, which often imply finite size systems. To do so, one can investigate the behavior of two-point correlation functions,

$$C(x, x') = \left\langle \psi \left| \mathcal{O}^\dagger(x) \mathcal{O}(x') \right| \psi \right\rangle\,.$$

Typically, one encounters the following behavior:

$$\lim_{|x-x'|\to\infty} C(x, x') \propto \begin{cases} \langle \mathcal{O}^\dagger(x) \rangle \langle \mathcal{O}(x') \rangle = \mathit{const.} & \text{long-range ordered} \\ e^{-|x-x'|/l} & \text{disordered,} \end{cases} \tag{13}$$

with l the *correlation length*. In the presence of long-range order (LRO), the spatial average of the local order parameter will be finite: assuming locality,[10] the correlation function in Eq. (13) *factorizes*, and hence $C(x, x')$ approaches a constant, finite value when increasing the distance $|x - x'| \to \infty$. This corresponds to a divergent correlation length l, since the values of the order parameter at two points in space are correlated to each other for arbitrary separations between them. What is interesting is that, while the order parameter $O(x) = \langle \mathcal{O}(x) \rangle$ for a finite system is exactly zero, the two-point functions *can* show a finite value for *finite,* large enough separations! This opens the door to investigate LRO by working on finite systems by making sure that one treats systems large enough so that over a wide range of distances larger than a typical length scale determined by the details of the system, $|x-x'| > l_c$, the value of $C(x, x')$ is constant. This is, in particular, important for numerical approaches, where often one works with a finite lattice size.

Note that correlation functions can also decay to zero *algebraically*, $C(x, x') \propto |x-x'|^c$, with some exponent c. In this case, one speaks of *algebraic* or quasi long-range order, since the order parameter will have zero expectation value also in the thermodynamic limit. This happens, in particular, for low dimensional systems like spin-1 chains due to the *Hohenberg-Mermin-Wagner* theorem, according to which systems with short-range interactions in low dimensions cannot realize SSB of a continuous symmetry (essentially because fluctuations are too large). Therefore, in this case, the phases are not characterized by a finite order parameter, but by the *dominant* correlation function, i.e., the one, which decays *slowest*. An interesting scenario is realized in quantum magnets in so-called *Berezinskii-Kosterlitz-Thouless* (BKT) phase transitions: here, on one side of the transition, $C(x, x') \propto \exp\left(-|x-x'|/l\right)$, while on the other side of the transition $C(x, x') \propto |x-x'|^c$. On both sides of the transition, the order parameter is zero, but nevertheless the physics is different. Because one cannot analytically continue a power law to an exponential function, one encounters a real, thermodynamic transition between two states of matter, where $C(x, x')$ is nonanalytic at the critical point. This type of transition is not due to SSB, since the order parameter is zero on both sides. One example system for such a BKT transition is the classical XY-model on a square lattice, where as a function of temperature the binding or unbinding of *topological defects* causes this transition. Such an effect can be expected in XY-type models or models with U(1) symmetry. For quantum magnets, one often speaks of a BKT-type transition, if a gapless phase (with algebraically decaying correlation functions) is connected to a gapped phase (with exponentially decaying correlation functions), and at which the gap opens exponentially slowly: the transition is continuous, but in this case there is no thermodynamic potential (e.g. the free energy, which at zero temperature is the ground state energy), whose n-th derivative is nonanalytical, which is required by Ehrenfest's classification of a phase transition to be of n-th order. Therefore, one sometimes speaks of 'infinite-order transitions'.

---

[10] This is also referred to as the *cluster decomposition theorem*, according to which measurements of observables 'distant enough' from each other should be independent of each other.

2.1.3 What can be learned from correlation matrices

Let us have a closer look at the correlation function introduced in Eq. (13) (see, e.g., [84]). Let us switch from the continuous variable x to lattice positions i, j, so that we consider a correlation function $C_{i,j} = \left\langle \mathcal{O}_i^\dagger \mathcal{O}_j \right\rangle$. This is an hermitian matrix, and it is a valid question to ask, what we may learn from its eigenvectors and eigenvalues. Indeed, they give a valuable tool to investigate LRO in the following way: Let us consider the global order parameter $O = \sum_j O_j$. In the presence of translational invariance, we can write $O_j \equiv O/N = \bar{O}$. According to Eq. (13), we can write

$$\lim_{|i-j|\to\infty} \left\langle \mathcal{O}_i^\dagger \mathcal{O}_j \right\rangle = \overline{O}^2 \neq 0. \tag{14}$$

Let us consider a concrete example and choose $\mathcal{O}_j = S_j^+ = S^x + iS^y$, which addresses the question for finite in-plane magnetization. We see immediately, that (if S^z_{total} is a good quantum number) $\left\langle \psi \left| S_j^+ \right| \psi \right\rangle = 0$ for any finite system. However, $C_{ij} = \left\langle \psi \left| S_i^+ S_j^- \right| \psi \right\rangle$ can take a finite value even for small lattice sizes. Diagonalizing the hermitian matrix C_{ij} for such a finite system, we obtain real eigenvalues λ_ν and eigenvectors $\mathbf{v}_\nu$, and we can rewrite

$$C_{ij} = \sum_\nu \mathbf{v}_\nu \underbrace{\left\langle \psi \left| \Big(\sum_i v^*_{\nu,i} S_i^+ \Big) \Big(\sum_i v_{\nu,j} S_j^- \Big) \right| \psi \right\rangle}_{\lambda_\nu} \mathbf{v}_\nu^\dagger \,.$$

Introducing operators $\eta_\nu = \sum_i v_{\nu,i} S_i^-$, we obtain

$$\mathbf{v}_\nu^\dagger C_{ij} \mathbf{v} = \left\langle \psi \left| \eta_\nu^\dagger \eta_\nu \right| \psi \right\rangle = \lambda_\nu \geq 0 \,,$$

the eigenvalues are therefore strictly positive. How does this relate to the order parameters? Let us apply the cluster decomposition theorem, then

$$\lim_{|i-j|\to\infty} C_{ij} = \lim_{|i-j|\to\infty} \sum_\nu v_{\nu,i} \underbrace{\left\langle \psi \left| \sum_k v^*_{\nu,k} S_k^+ \right| \psi \right\rangle}_{\sqrt{\lambda_\nu}^*} \underbrace{\left\langle \psi \left| \sum_l v_{\nu,l} S_l^- \right| \psi \right\rangle}_{\sqrt{\lambda_\nu}} v^\dagger_{\nu,j} = \lim_{|i-j|\to\infty} \langle S_i^+ \rangle \langle S_j^- \rangle.$$

However, the last equality can only be true if there is only *one* eigenvalue $\lambda_\nu = \lambda_{max}$, which is not vanishing. On the other hand, we see that $\langle S_j^+ \rangle = \sqrt{\lambda_{max}}$. For finite systems, these relations are not exact, but in the limit of infinite system size, there has to be asymptotically one dominant eigenvalue λ_L, so that for large systems of size L one can approximate

$$\lim_{|i-j|\to\infty} C_{ij} \approx \lambda_L v_{L,i} v^*_{L,j} \,.$$

Since the eigenvectors $\mathbf{v}_\nu$ are normalized, their coefficients scale $\sim 1/\sqrt{L}$. Hence, in order to have a finite value in the thermodynamic limit, the dominant eigenvalue has to scale $\lambda_L \sim L$, giving a condition on the largest eigenvalue of C_{ij}, which can be tested numerically.

Fig. 4 shows an example for the kagome lattice in the presence of DM interactions and of a non-magnetic impurity (see Fig. 2), for which this analysis was performed. For this system it

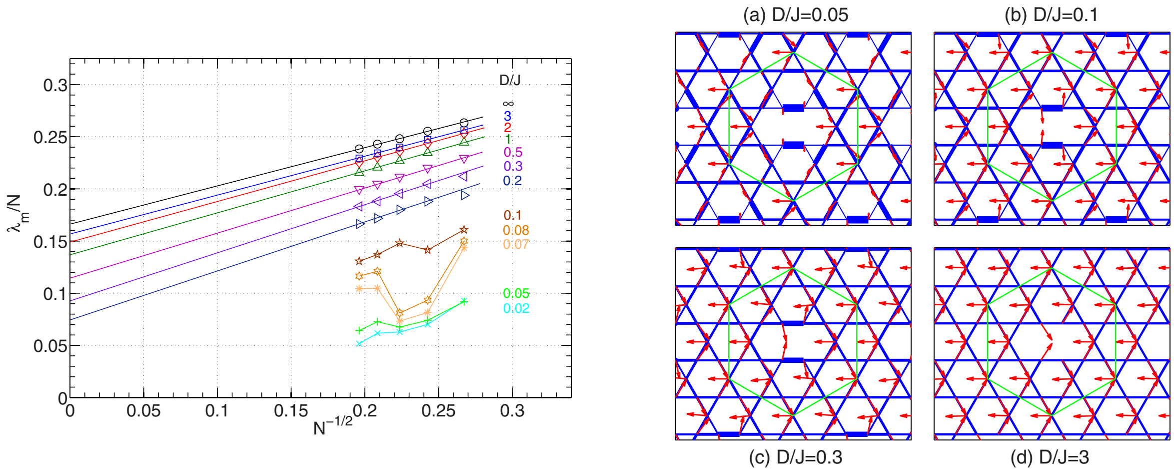

Fig. 4: *Correlation matrix analysis of the local magnetizations for the AFM Heisenberg model on a kagome lattice with DM interactions. Left: scaling of the largest eigenvalue of C_{ij} with system size. Right: Magnetization profile obtained from the eigenvector of C_{ij} belonging to the largest eigenvalue for different values of the DM interaction. The red arrows indicate the in-plane moments, given by the real and imaginary part of the entries of the eigenvector, respectively; the blue lines are the local bond strengths, which are computed separately (Figures taken from [74]).*

is very difficult to treat large system sizes due to the lack of symmetries. Nevertheless, using this analysis, it is possible to gain information on the possible LRO realized in the thermodynamic limit, which illustrates that this approach to computing LRO is suitable also for difficult situations.

2.2 Symmetry protected topological phases in quantum magnets: the AKLT state

As we have seen, states of matter are usually characterized by the Landau paradigm, in which a continuous phase transition and the associated phases are obtained by the SSB of one (or more) symmetries of the Hamiltonian and the emergence of a *local* order parameter [85]. This paradigm has been *the* framework for understanding phases of matter and phase transitions, until in the 1980s experiments discovered the integer [86] and later the fractional quantum Hall effect [87, 88]. These systems possess transitions between states with different conductivities, which apparently are not associated to any SSB. Subsequently, and also motivated by the discovery of high-temperature superconductivity [2], a new type of 'order' was proposed whose phenomenology is not due to the finiteness of some local order parameter, but in which the phases are characterized by *global* characteristics, like the degeneracy of the ground state or entanglement of the system. This type of order has been coined *topological order* [89,90,33] since the behavior is captured by topological field theories [91]. The main characteristics of topologically ordered phases are the presence of degenerate ground states, of gapless edge states, and the characterization in terms of *topological invariants* which are integer numbers capturing 'topological' properties of the system and which vary in the different phases. One characteristic of topological phases is that they do not change under continuous deformations of the system (i.e., the topological invariant does not change unless one hits a critical point at which the system experiences singular behavior) and are, hence, protected against local perturbations like, e.g., noise. This makes these states very interesting for quantum computation in which one of the biggest challenges is to protect the entanglement between qubits from decoherence effects due to local noise induced by the environment. This approach is coined *topological quantum computation* and is described in the review article [33]. A lot of research is, therefore, devoted to uncovering such topological phases in quantum magnets.

At the present, obtaining a complete characterization of topological phases (including interacting systems) is an ongoing topic of research. However, one can use the following approach to distinguish between different gapped phases [92, 93]: a gapped quantum phase is characterized by ground states of Hamiltonians, which can be smoothly deformed into each other without closing the gap. An illustrative example is the $S = 1$ BLBQ chain (11), which at zero magnetic field displays a gapped phase for $-\pi/4 < \theta < \pi/4$; even though at $\theta = 0$ the Hamiltonian looks much simpler, the system in this parameter range is in the same phase since the gap closes only at the endpoints of this region. This property can be rephrased by saying that two ground states belong to the same phase if they are related by a *local* unitary transformation. Since local unitary transformations can only change local entanglement properties but not global ones, states in the same topological phase are characterized by the same 'long-range entanglement'. Based on these considerations, the following gapped phases can be identified:

1. Phases with 'short-range entanglement':
   (a) Topologically 'trivial' product states.
   (b) Symmetry protected topological phases (SPT). In these phases, local unitary transformations exist which preserve the symmetry of the state. Short-range entangled phases in which such a symmetry is broken are well described by Landau theory. Note that phases without local order parameter can still belong to different SPT phases if they are characterized by different symmetries, even though in Landau classification they would belong to the same 'disordered' phase.
2. 'True' topological order with 'long-range' entanglement, existing only in spatial dimensions $D \geq 2$ [92]. These phases are characterized by *anyonic* fractionalized excitations, which obey a generalized quantum statistics and are neither fermions nor bosons [33].

It is possible to characterize topological order by considering entanglement properties [94, 95], and tensor-network approaches have been introduced (see, e.g. [96] and the viewpoint [97]). While it is possible to investigate for 'true' topological order in 2D using the DMRG (for studies on the kagome lattice see, e.g. [35, 37, 36]), often SPT phases are investigated, which, according to the above said, are the only type of topological phases encountered in 1D. A prototypical example for an SPT state in quantum magnets is the so-called AKLT state [98] (named after the authors of the original publication, Affleck, Kennedy, Lieb, and Tasaki), which is depicted in

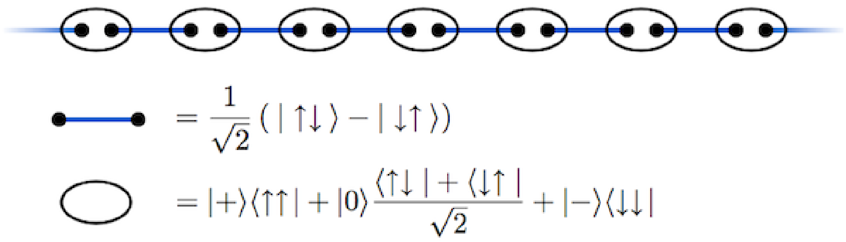

Fig. 5: *Sketch of the AKLT state (figure taken from Wikipedia).*

Fig. 5. It is the ground state of the BLBQ model (11) for $B = 0$ and $\tan(\theta) = 1/3$. It has several peculiar properties: the spin-1 degrees of freedom on the lattice sites are understood as being composed of two spin-$^1\!/_2$ degrees of freedom, which *between* neighboring lattice sites form singlets. At the edges, effective, free spin-$^1\!/_2$ degrees of freedom remain and form edge states – the spin-1 degrees of freedom 'fractionalize' to the 'smaller' spin-$^1\!/_2$ degrees of freedom. Since the presence of such edge states is typical for an SPT phase, one can use this to identify and characterize such phases, as seen further below.

SPT phases can numerically be detected by identifying an excitation gap, zero local order parameters, and degeneracy of the *entanglement spectrum* [99]. As discussed in [100, 95], in an SPT phase all states of the entanglement spectrum are non-trivially degenerate due to the symmetry in the system. Other indications for topological properties can be obtained from diagonalizing transfer matrices from which one can obtain directly the projective representations of the symmetry group [101], which can be used to further characterize SPT phases (see also [102] for a nice discussion of this aspect). According to [102–104], it is possible to distinguish between different SPT phases by applying the corresponding *active operators* on the edge states: if the correct active operator is coupled to the edge of the system, the ground state degeneracy is lifted. This can indeed be used to distinguish the different SPT phases in quantum magnetic systems obtained from the projective representations [105]. Numerically, it is easily seen that applying the 'wrong' active operator does not lift the ground state degeneracy, while applying the correct one leads to different energies of the ground states with a difference far greater than the numerical accuracy.

2.3 Dynamical properties: inelastic neutron scattering, electron spin resonance

One way to characterize a state is to weakly perturb it and to monitor its response. In this way, information beyond the LRO in the system can be obtained, and an insight about the elementary excitations in the system can be obtained. This is the realm of linear response theory. To study such a situation is interesting from many points of view. For example, the aforementioned spin liquids do not show any sign of LRO. Any investigation based on this will, therefore, not find any interesting properties and overlook that we are, indeed, facing a very rich quantum state of matter. However, the response of such states to weak perturbations is determined by the interactions in the system, hence these type of experiments are helpful for gaining insight into the true nature of the system.

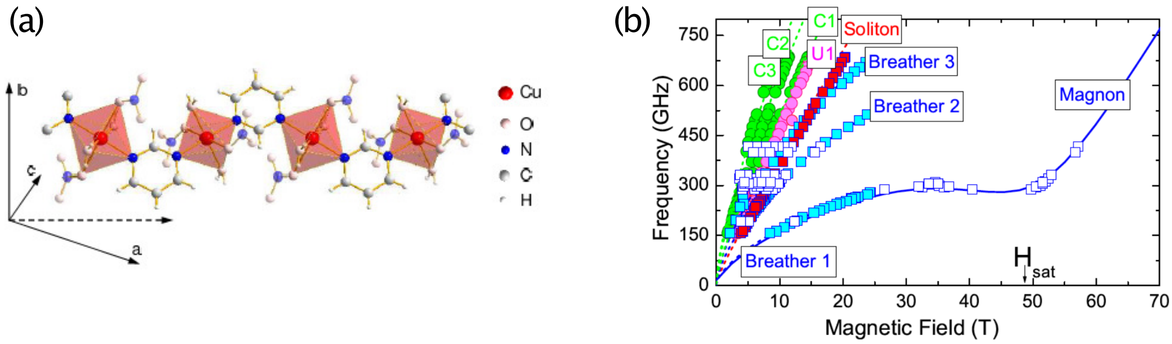

Fig. 6: *(a) Crystal structure of Cu-PM (copper pyrimidine dinitrate), a $S = 1/2$ spin chain material with DM interactions and alternating g-tensor. (b) Comparison of ESR spectra (symbols) and DMRG results (solid line) (Figures taken from Ref. [106]).*

From the experimental side, inelastic neutron scattering is one of the most important, direct probes for dynamical properties of quantum magnets. Since the neutron is charge neutral, one can perform the investigation such that only magnetic degrees of freedom are probed. The coupling of the magnetic moment of the neutron to the magnetic moments in the material allows one to measure the *dynamical structure factor*, which can be defined via

$$S^{\alpha,\alpha}(k,\omega) = \frac{1}{N}\sum_{j=1}^{N} e^{-ik(j-N/2)} \int_{-\infty}^{\infty} dt\, e^{i\omega t} \left\langle S_j^\alpha(t) S_{N/2}^\alpha(0)\right\rangle \, .$$

Here, the system contains N spins, $\alpha = x, y, z$, and we assume translational invariance. These experiments can be performed also at high magnetic fields, so that the excitation spectrum of quantum magnets for different phases can be investigated.

Another interesting type of experiments are electron spin resonance experiments (ESR), which give access to the imaginary part of the dynamical structure factor in the long wavelength limit $k \to 0$. An example for the ESR spectrum of a spin-chain material with DM interactions is shown in Fig. 6. As can be seen, different types of excitations (e.g. solitons, breathers) can be identified by comparing to an effective field theory (in this case a sine-Gordon theory).

3 Nonequilibrium dynamics

So far we considered static properties of quantum magnets, which uncover a multitude of interesting phenomena. It is only natural to ask what happens if one now excites such a system, e.g., with a laser pulse, so that its state evolves in time. The typical questions one can ask is how the order parameters decay in time, and what nature the equilibrium state will be. Also, one can ask the reverse question: is it possible to induce order (e.g. magnetization) by exciting the system? These are recent topics of study and in this final section of this book chapter we give a short glimpse on some of the ongoing developments.

In the mid 1990s, investigations were performed on thin magnetic films, which were excited with an ultrashort laser pulse of duration 60 fs (see, e.g., [107] for a review). The magnetization was measured using the magneto-optical Kerr effect (MOKE), and, since the signal was thought to be proportional to the magnetization, they were able to measure the time evolution of the magnetization after such a short excitation. Interestingly, they found that the magnetization decreased very quickly (on a time scale < 1 ps), but then recovered again. Later, it was argued that the MOKE signal is not necessarily proportional to the magnetization in such a nonequilibrium situation, but these results were reproduced using other techniques. This behavior raises many questions. One main point is to understand where the angular momentum, which is underlying to the magnetization, dissipates to, and how the light-matter interaction triggers the dynamics. Typically, a *three temperature model* is introduced: the energy absorbed from the laser flows to (i) the electrons, (ii) the lattice vibrations, i.e., creation of phonons, and (iii) the spin degrees of freedom of the system, by creating magnons. Often, in the theoretical studies, time-dependent density functional theory is applied. However, despite now about 30 years of research, no consensus has been reached on the mechanism of the demagnetization dynamics [107]. One possibility would be to address many-body spin systems like the ones described in this book chapter; however, since the electron and phonon degrees of freedom also seem to play an important role in the magnetization dynamics, one would need to extend the models correspondingly. Treating such complicated many-body models is a challenge for ongoing and future research. However, it would be interesting to see if other types of order, e.g., spin-quadrupolar order in spin-1 systems, could show similar time dependence, or if the demagnetization dynamics only affects magnetic order.

In materials with two different types of magnetic ions (e.g. Heusler compounds), optical excitation can lead to an effective transfer of spins from one atomic species to the other [108]. This effect was coined ‘optically induced spin transfer’ (OISTR) [109, 110] and builds on the observation that, even in the presence of SOC (which, as discussed in Sec. 1.3, does not preserve S^z as good quantum number) on very fast time scales $\lesssim 11$ fs no spin flips happen. Instead, the spin is simply transferred to the neighboring ion, leading to a change in the magnetization pattern, and the charge distribution on the lattice. At later times, SOC may come into play and may cause demagnetization dynamics, but at least on the very short time scale the OISTR mechanism leads to a metastable or transient state, which is different from the initial state. Such a situation can also be studied in Hubbard-type models with an underlying magnetic microstructure, where OISTR leads to the weakening of the original spin structure, but induces charge density wave type structures, which prevail until further effects like SOC or phonons come into play [111].

Other interesting effects when going out-of-equilibrium are the possibility to realize (transient) long-range order. A famous example is the description of transient superconductivity in pump-probe experiments [112]. Also, the formation of magnetic LRO has been reported [113]. For example, in the manganite material GdSrMnO$_3$, a photo-induced transition to a ferromagnetic metallic phase within 200 fs has been observed [114] and can be described by first-principles approaches [115]. It will be interesting to further study the possibility to realize (transient) LRO in quantum magnets, in particular regarding the realization of the unconventional states discussed in this contribution. Maybe some of the LRO that is possible in interacting spin systems, but hard to realize in ground states, can be found in such nonequilibrium setups in future investigations.

4 Conclusions and outlook

Quantum magnetism is a vast field of research, and in this contribution only some aspects could be discussed. What remains appealing is the possibility to identify by mathematical considerations further order parameters, which can help to identify novel types of LRO, for which the spin-nematic order is one example. The newer developments for nonequilibrium systems are a promising way to go, since there many basic questions on the nature of transient order are still under investigation. It will be interesting to see whether in such situations novel behavior can be identified, and if it will be long-lived, so that it does not vanish in less then a blink of the eye, but can be enjoyed on a useful time scale.

Acknowledgements

I thank Daniel Steil for hinting Ref. [107] to me, and all co-authors, with whom I have had the big pleasure to work on quantum magnetism and related topics.

References

[1] I. Bloch, J. Dalibard, and W. Zwerger, Rev. Mod. Phys. **80**, 885 (2008)

[2] J.G. Bednorz and K.A. Müller, Z. Phys. B **64**, 189 (1986)

[3] E. Dagotto, Rev. Mod. Phys. **66**, 763 (1994)

[4] F. Gebhard, *The Mott Metal-Insulator Transition* (Springer, Berlin, 1997)

[5] M. Greiner, O. Mandel, T. Esslinger, T.W. Hänsch, and I. Bloch, Nature **415**, 39 (2002)

[6] K. Takatsu, W. Shiramura, and H. Tanaka, J. Phys. Soc. Jpn. **66**, 1611 (1997)

[7] C. Rüegg, N. Cavadini, A. Furrer, H.-U. Güdel, K. Krämer, H. Mutka, A. Wildes, K. Habicht, and P. Vorderwisch, Nature **423**, 62 (2003)

[8] H. Kageyama, K. Yoshimura, R. Stern, N.V. Mushnikov, K. Onizuka, M. Kato, K. Kosuge, C.P. Slichter, T. Goto, and Y. Ueda, Phys. Rev. Lett. **82**, 3168 (1999)

[9] K. Kodama, M. Takigawa, M. Horvatic, C. Berthier, H. Kageyama, Y. Ueda, S. Miyahara, F. Becca, and F. Mila, Science **298**, 395 (2002)

[10] M.P. Shores, E.A. Nytko, B.M. Bartlett, and D.G. Nocera, J. Am. Chem. Soc. **127**, 13462 (2005)

[11] H.T. Diep (ed.): *Frustrated Spin Systems* (World Scientific, Singapore, 2004)

[12] U. Schollwöck, J. Richter, D. Farnell, and R. Bishop (eds.): *Quantum Magnetism*, Lecture Notes in Physics Vol. 645 (Springer, Heidelberg, 2004)

[13] C. Lacroix, P. Mendels, and F. Mila (eds.): *Introduction to Frustrated Magnetism*, Springer Series in Solid-State Sciences Vol. 164 (Springer, Heidelberg, 2011)

[14] P. Fazekas: *Lecture Notes on Electron Correlation and Magnetism* (World Scientific, Singapore, 1999)

[15] M. Matsumoto, B. Normand, T.M. Rice, and M. Sigrist, Phys. Rev. Lett. **89**, 077203 (2002)

[16] M. Jaime, V.F. Correa, N. Harrison, C.D. Batista, N. Kawashima, Y. Kazuma, G.A. Jorge, R. Stern, I. Heinmaa, S.A. Zvyagin, Y. Sasago, and K. Uchinokura, Phys. Rev. Lett. **93**, 087203 (2004)

[17] T. Giamarchi, C. Rüegg, and O. Tchernyshyov, Nat. Phys. **4**, 198 (2008)

[18] M. Oshikawa, M. Yamanaka, and I. Affleck, Phys. Rev. Lett. **78**, 1984 (1997)

[19] T.M. Rice, Science **298**, 760 (2002)

[20] T. Momoi and K. Totsuka, Phys. Rev. B **62**, 15067 (2000)

[21] K.-K. Ng and T.K. Lee, Phys. Rev. Lett. **97**, 127204 (2006)

[22] K. Ng and T. Lee, J. Magn. Mag. Mat. **310**, 1371 (2007)

[23] P. Sengupta and C.D. Batista, Phys. Rev. Lett. **98**, 227201 (2007)

[24] N. Laflorencie and F. Mila, Phys. Rev. Lett. **99**, 027202 (2007)

[25] K.P. Schmidt, J. Dorier, A.M. Läuchli, and F. Mila, Phys. Rev. Lett. **100**, 090401 (2008)

[26] O. Penrose and L. Onsager, Phys. Rev. **104**, 576 (1956)

[27] N. Prokof'ev, Advances in Physics **56**, 381 (2007)

[28] S. Sachdev: *Quantum Phase Transitions* (Cambridge University Press, 1999)

[29] M. Vojta, Reports on Progress in Physics **66**, 2069 (2003)

[30] M.J. Stephen and J.P. Straley, Rev. Mod. Phys. **46**, 617 (1974)

[31] A. Smerald and N. Shannon, Phys. Rev. B **88**, 184430 (2013)

[32] H. Kim, J.-K. Kim, J. Kwon, J. Kim, H.-W.J. Kim, S. Ha, K. Kim, W. Lee, J. Kim, G.Y. Cho, H. Heo, J. Jang, C.J. Sahle, A. Longo, J. Strempfer, G. Fabbris, Y. Choi, D. Haskel, J. Kim, J.W. Kim, and B.J. Kim, Nature **625**, 264 (2024)

[33] C. Nayak, S.H. Simon, A. Stern, M. Freedman, and S.D. Sarma, Rev. Mod. Phys. **80**, 1083 (2008)

[34] L. Balents, Nature **464**, 199 (2010)

[35] S. Yan, D.A. Huse, and S.R. White, Science **332**, 1173 (2011)

[36] S. Depenbrock, I. Mcculloch, and U. Schollwöck, Phys. Rev. Lett. **109**, 067201 (2012)

[37] H.-C. Jiang, Z. Wang, and L. Balents, Nat. Phys. **8**, 902 (2012)

[38] P. Lee, Science **321**, 1306 (2008)

[39] J. Hubbard, Proc. R. Soc. (London) A **276**, 238 (1963)

[40] M.C. Gutzwiller, Phys. Rev. Lett. **10**, 159 (1963)

[41] J. Kanamori, Prog. Theor. Phys. **30**, 275 (1963)

[42] F.H.L. Essler, H. Frahm, F. Göhmann, A. Klümper, and V.E. Korepin: *The One-Dimensional Hubbard Model* (Cambridge University Press, 2005)

[43] M.P.A. Fisher, P.B. Weichman, G. Grinstein, and D.S. Fisher, Phys. Rev. B **40**, 546 (1989)

[44] A. Auerbach: *Interacting Electrons and Quantum Magnetism* (Springer, 1994)

[45] T. Esslinger, Annu. Rev. Condens. Matter Phys. **1**, 129 (2010)

[46] Y.I. Manin: *Computable and uncomputable* (in Russian); Moscow, Sovetskoye Radio 1980. See appendix of arXiv:quant-ph/9903008 for an english translation.

[47] R.P. Feynman, Int. J. Theor. Phys. **21**, 467 (1982)

[48] R.P. Feynman, Found. Phys. **16**, 507 (1985)

[49] R.P. Feynman, Optics News **11**, 11 (February 1985)

[50] A.V. Gorshkov, S.R. Manmana, G. Chen, J. Ye, E. Demler, M.D. Lukin, and A.M. Rey, Phys. Rev. Lett. **107**, 115301 (2011)

[51] A.V. Gorshkov, S.R. Manmana, G. Chen, E. Demler, M.D. Lukin, and A.M. Rey, Phys. Rev. A **84**, 033619 (2011)

[52] F.C. Zhang and T.M. Rice, Phys. Rev. B **37**, 3759 (1998)

[53] B. Sutherland, Phys. Rev. B **12**, 3795 (1975)

[54] N. Read and S. Sachdev, Phys. Rev. Lett. **62**, 1694 (1989)

[55] I. Affleck and J.B. Marston, Phys. Rev. B **37**, 3774 (1988)

[56] A.V. Gorshkov, M. Hermele, V. Gurarie, C. Xu, P.S. Julienne, J. Ye, P. Zoller, E. Demler, M.D. Lukin, and A.M. Rey, Nat. Phys. **6**, 289 (2010)

[57] V. Kalmeyer and R.B. Laughlin, Phys. Rev. Lett. **59**, 2095 (1987)

[58] X.G. Wen, F. Wilczek, and A. Zee, Phys. Rev. B **39**, 11413 (1989)

[59] M. Hermele, V. Gurarie, and A.M. Rey, Phys. Rev. Lett. **103**, 135301 (2009)

[60] A. Kitaev, Ann. Phys. **321**, 2 (2006)

[61] A.W. Sandvik, AIP Conf. Proc. **1297**, 135 (2010)

[62] S.R. White, Phys. Rev. Lett. **69**, 2863 (1992)

[63] U. Schollwöck, Ann. Phys. **326**, 96 (2011)

[64] `quattro.phys.sci.kobe-u.ac.jp/dmrg/condmat.html`, maintained by T. Nishino, updated daily.

[65] M.B. Hastings, J. Stat. Mech.: Theor. Exp. **2007**, P08024 (2007)

[66] J. Eisert, M. Cramer, and M.B. Plenio, Rev. Mod. Phys. **82**, 277 (2010)

[67] A. Zee: *Group Theory in a Nutshell for Physicists* (Princeton University Press, 2016)

[68] G.R. Foltin, S.R. Manmana, and K.P. Schmidt, Phys. Rev. B **90**, 104404 (2014)

[69] C. Castelnovo, R. Moessner, and S.L. Sondhi, Nature **451**, 42 (2008)

[70] D.J.P. Morris, D.A. Tennant, S.A. Grigera, B. Klemke, C. Castelnovo, R. Moessner, C. Czternasty, M. Meissner, K.C. Rule, J.-U. Hoffmann, K. Kiefer, S. Gerischer, D. Slobinsky, and R.S. Perry, Science **326**, 411 (2009)

[71] R.M. Noack and S.R. Manmana, AIP Conf. Proc. **789**, 93 (2005)

[72] F. Verstraete, V. Murg, and J.I. Cirac, Adv. Phys. **57**, 143 (2008)

[73] P. Corboz and F. Mila, Phys. Rev. Lett. **112**, 147203 (2014)

[74] I. Rousochatzakis, S.R. Manmana, A.M. Läuchli, B. Normand, and F. Mila, Phys. Rev. B **79**, 214415 (2009)

[75] K. Penc, J.-B. Fouet, S. Miyahara, O. Tchernyshyov, and F. Mila, Phys. Rev. Lett. **99**, 117201 (2007)

[76] I. Dzyaloshinskii, J. Phys. Chem. Solids **4**, 241 (1958)

[77] T. Moriya, Phys. Rev. Lett. **4**, 228 (1960)

[78] B.S. Shastry and B. Sutherland, Physica B+C **108**, 1069 (1981)

[79] Y.H. Matsuda, N. Abe, S. Takeyama, H. Kageyama, P. Corboz, A. Honecker, S.R. Manmana, G.R. Foltin, K.P. Schmidt, and F. Mila, Phys. Rev. Lett. **111**, 137204 (2013)

[80] S.R. Manmana, A.M. Läuchli, F.H.L. Essler, and F. Mila, Phys. Rev. B **83**, 184433 (2011)

[81] A.J. Beekman, L. Rademaker, and J. van Wezel, SciPost Phys. Lect. Notes **11** (2019)

[82] S. Jiang, J. Romhányi, S.R. White, M.E. Zhitomirsky, and A.L. Chernyshev, Phys. Rev. Lett. **130**, 116701 (2023)

[83] T. Tóth: *Quadrupolar Ordering in Two-Dimensional Spin-One Systems* (doi.org/10.5075/epfl-thesis-5037)

[84] S. Paeckel: *Topological and non-equilibrium superconductivity in low-dimensional strongly correlated quantum systems* (doi.org/10.53846/goediss-7971)

[85] N. Goldenfeld: *Lectures on Phase Transitions and the Renormalization Group*, Frontiers in Physics Vol. 85 (Addison-Wesley, Boston, 1992)

[86] K. v. Klitzing, G. Dorda, and M. Pepper, Phys. Rev. Lett. **45**, 494 (1980)

[87] D.C. Tsui, H.L. Stormer, and A.C. Gossard, Phys. Rev. Lett. **48**, 1559 (1982)

[88] R.B. Laughlin, Phys. Rev. Lett. **50**, 1395 (1983)

[89] X.G. Wen, Phys. Rev. B **40**, 7387 (1989)

[90] X.G. Wen, Int. J. Mod. Phys. B **04**, 239 (1990)

[91] E. Witten, Commun. Math. Phys. **117**, 353 (1988)

[92] X. Chen, Z.-C. Gu, and X.-G. Wen, Phys. Rev. B **83**, 035107 (2011)

[93] X. Chen, Z.-C. Gu, and X.-G. Wen, Phys. Rev. B **82**, 155138 (2010)

[94] M. Levin and X.-G. Wen, Phys. Rev. Lett. **96**, 110405 (2006)

[95] A.M. Turner, F. Pollmann, and E. Berg, Phys. Rev. B **83**, 075102 (2011)

[96] Z.-C. Gu and X.-G. Wen, Phys. Rev. B **80**, 155131 (2009)

[97] S. Sachdev, Physics **2**, 90 (2009)

[98] I. Affleck, T. Kennedy, E.H. Lieb, and H. Tasaki, Phys. Rev. Lett. **59**, 799 (1987)

[99] H. Li and F.D.M. Haldane, Phys. Rev. Lett. **101**, 010504 (2008)

[100] F. Pollmann, A.M. Turner, E. Berg, and M. Oshikawa, Phys. Rev. B **81**, 064439 (2010)

[101] F. Pollmann and A.M. Turner, Phys. Rev. B **86**, 125441 (2012)

[102] Z.-X. Liu, Z.-B. Yang, Y.-J. Han, W. Yi, and X.-G. Wen, Phys. Rev. B **86**, 195122 (2012)

[103] Z.-X. Liu, M. Liu, and X.-G. Wen, Phys. Rev. B **84**, 075135 (2011)

[104] Z.-X. Liu, X. Chen, and X.-G. Wen, Phys. Rev. B **84**, 195145 (2011)

[105] S.R. Manmana, E.M. Stoudenmire, K.R.A. Hazzard, A.M. Rey, and A.V. Gorshkov, Phys. Rev. B **87**, 081106 (2013)

[106] S.A. Zvyagin, E. Čižmár, M. Ozerov, J. Wosnitza, R. Feyerherm, S.R. Manmana, and F. Mila, Phys. Rev. B **83**, 060409(R) (2011)

[107] P. Scheid, Q. Remy, S. Lebègue, G. Malinowski, and S. Mangin, J. Magn. Magn. Mat. **560**, 169596 (2022)

[108] D. Steil, J. Walowski, F. Gerhard, T. Kiessling, D. Ebke, A. Thomas, T. Kubota, M. Oogane, Y. Ando, J. Otto, A. Mann, M. Hofherr, P. Elliott, J.K. Dewhurst, G. Reiss, L. Molenkamp, M. Aeschlimann, M. Cinchetti, M. Münzenberg, S. Sharma, and S. Mathias, Phys. Rev. Res. **2**, 023199 (2020)

[109] P. Elliott, T. Müller, J.K. Dewhurst, S. Sharma, and E.K.U. Gross, Sci. Rep. **6**, 38911 (2016)

[110] J.K. Dewhurst, P. Elliott, S. Shallcross, E.K.U. Gross, and S. Sharma, Nano Lett. **18**, 1842 (2018)

[111] T. Köhler, S. Paeckel, C. Meyer, and S.R. Manmana, Phys. Rev. B **102**, 235166 (2020)

[112] D. Fausti, R.I. Tobey, N. Dean, S. Kaiser, A. Dienst, M.C. Hoffmann, S. Pyon, T. Takayama, H. Takagi, and A. Cavalleri, Science **331**, 189 (2011)

[113] T. Jauk, H. Hampel, J. Walowski, K. Komatsu, J. Kredl, E.I. Harris-Lee, J.K. Dewhurst, M. Münzenberg, S. Shallcross, S. Sharma, and M. Schultze, arXiv:2405.12690 (2024)

[114] M. Matsubara, Y. Okimoto, T. Ogasawara, Y. Tomioka, H. Okamoto, and Y. Tokura, Phys. Rev. Lett. **99**, 207401 (2007)

[115] S. Rajpurohit, C. Jooss, and P.E. Blöchl, Phys. Rev. B **102**, 014302 (2020)

14 High-Pressure Phases of Hydrogen

Markus Holzmann
Univ. Grenoble Alpes, CNRS
LPMMC, 38000 Grenoble, France

Contents

E. Pavarini and E. Koch (eds.)
Correlations and Phase Transitions
Modeling and Simulation Vol. 14
Forschungszentrum Jülich, 2024, ISBN 978-3-95806-751-6
http://www.cond-mat.de/events/correl24

1 Introduction

The single hydrogen atom has a special significance in quantum mechanics, as exact analytical solutions to the Schrödinger equation can be presented already in elementary introductory courses. Small, but important deviations between theory and experiment have also played a central role in the development of quantum field theory and quantum electrodynamics. However, under normal conditions on earth, atomic hydrogen, H, is unstable forming molecules, H_2. The theoretical description of molecular hydrogen is immediately getting more challenging than the atom, as the quantization of the nuclear motion must be taken into account. Separation of electronic and nuclear degrees of freedom can be achieved within the adiabatic or Born-Oppenheimer approximation [1], based on the high mass ratio $m_p/m_e \approx 1836$ between protons and electrons of mass m_p and m_e, respectively. Vibrational excitation energies of the isolated H_2 molecule are around ~ 6000 K, whereas rotational energies are much smaller ~ 200 K.

Since the nuclei of the molecule are identical, the nuclear spin has to be taken into account as well, leading to two different molecular species. Para (ortho) H_2 is characterized by even (odd) rotational quantum numbers. A distinction between these molecular species becomes important around and below room temperature, whereas nuclear quantum effects may extend up to several thousands of Kelvin.

At zero pressure and low temperatures, hydrogen is in the solid state forming a molecular crystal with almost freely rotating molecules, translationally localized around crystalline lattice sites but with large zero point motion [2]. Up to at least six different solid phases are experimentally known [3]. A sketch of the phase diagram for temperatures and pressures reached by static diamond anvil cell (DAC) experiments is shown in Fig. 1. Most of the transition lines are inferred from changes in infrared or Raman spectra whereas direct information on the crystal structures is almost entirely missing. Only in phase I, measurements of the Bragg peaks by X-ray spectroscopy have recently confirmed m-HCP at 300 K up to 250 GPa [4,5].

Increasing pressure an insulator to metal (IM) transition is expected. Originally predicted around 25 GPa [6], the search for metallic hydrogen has been one of the main driving forces in high-pressure physics. Evidence for a semi-metallic state at 350 GPa below 200 K has been reported [7], a discontinuous change of the direct gap observed near 425 GPa [8] indicates the transition to a "good" metal. Earlier reports of metallic hydrogen at 495 GPa [9] has received strong criticism [10,11]. Whether the IM transition occurs within the molecular solid or whether it coincides together with a molecular dissociation transition to atomic hydrogen remains still an open question.

Disappearance of lattice modes of Raman spectroscopy signalling melting of the crystalline state [12] with a maximum around 1000 K showing a reentrant behavior of the liquid phase at higher pressure. This experimental line coincides astonishingly well with theoretical predictions based on Born-Oppenheimer molecular dynamics (BOMD) calculations with DFT-PBE electronic energies using classical nuclei [13]. However, more recent calculations for quantum nuclei using Path-Integral molecular dynamics with a machine learned force-field trained on QMC data indicate melting at considerable higher temperatures [14].

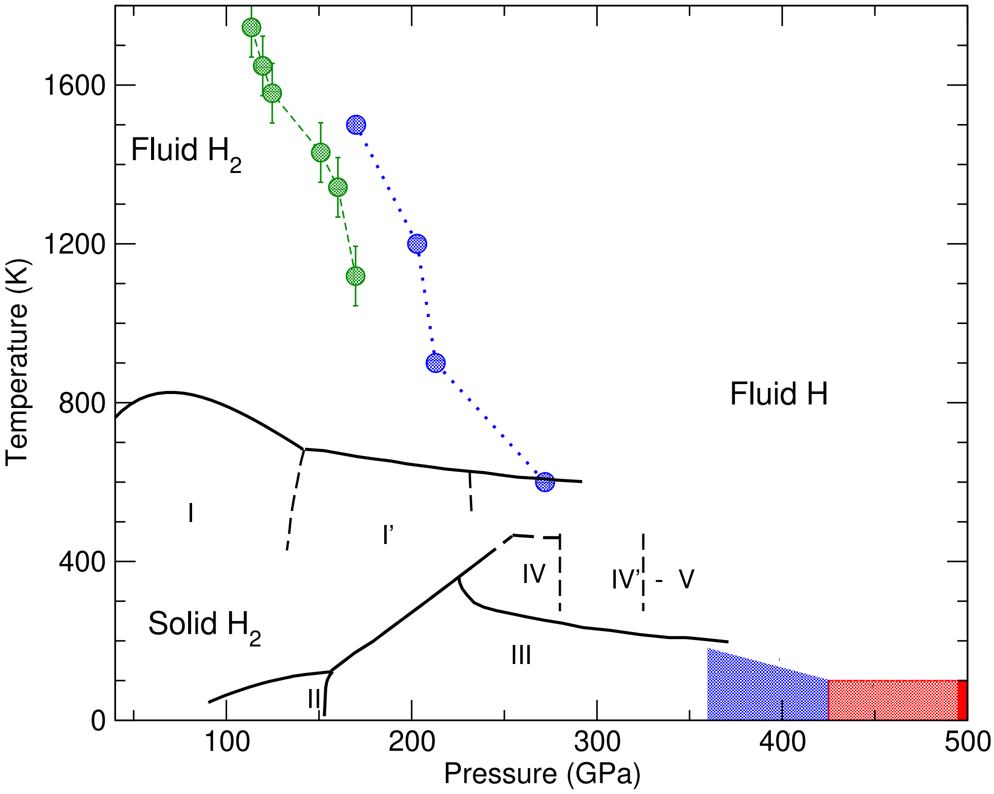

Fig. 1: *Phase diagram of solid hydrogen as inferred from static compression experiments (solid and dashed black lines). The solid black line shows the melting of the crystal as identified by the disappearance of Raman active lattice modes [12]. The blue area indicates a semimetallic state [7], with the closure of the direct gap [8] signalling the transition to metallic solid hydrogen (red area). A reflective sample has been reported at 495 GPa [9–11]. Green circles report signatures of a liquid-liquid phase transition from diamond anvil cell (DAC) experiments [15], blue circles are CEIMC predictions [18] from the molecular (insulating) to the atomic (metallic) liquid (Figure courtesy of C. Pierleoni).*

Above melting, the fluid may either be in the molecular or atomic state with a possible first order phase transition and a critical point at higher temperatures. Static compression experiments using DAC [15] and dynamic shock wave experiments [16, 17] report evidence for this liquid-liquid phase transition, supported by Coupled-Electron-Ion Monte Carlo (CEIMC) calculations [18–20] and molecular dynamics calculations based on electronic variational Monte Carlo energies [21, 22].

A proper discussion of the phase diagram of hydrogen can be found in Refs [2, 3, 23] and references therein. The above discussion mainly serves to illustrate some of the main difficulties and challenges theoretical and computational physics has to face when studying hydrogen. In the following, I will give an overview over various Monte Carlo methods and the approximations underlying CEIMC calculations, before briefly discussing some of the results obtained with.

2 Computational methods – overview

In the region of phase diagram discussed above, the properties of hydrogen are up to very high accuracy described within the following non-relativistic Hamiltonian

$$H = T + V \tag{1}$$

$$T = T_N + T_e \quad \text{with} \quad T_N = -\frac{\hbar^2}{2m_p}\sum_I \nabla_I^2 \quad \text{and} \quad T_e = -\frac{\hbar^2}{2m_e}\sum_i \nabla_i^2 \tag{2}$$

$$V(\mathbf{r},\mathbf{R}) = \sum_{i<j}\frac{e^2}{|\mathbf{r}_i - \mathbf{r}_j|} + \sum_{I<J}\frac{e^2}{|\mathbf{R}_I - \mathbf{R}_J|} - \sum_{i,I}\frac{e^2}{|\mathbf{r}_i - \mathbf{R}_J|} \tag{3}$$

where $\mathbf{r}$ and $\mathbf{R}$ denotes the set of electronic and nuclear positions, $\mathbf{r}_i$ ($\mathbf{R}_I$) labels the individual coordinate of electron i (nucleon I) and summations over i (I) extend over all N_e electrons (N_n nuclei). Electrons and nucleons interact via the Coulomb interactions between themselves and each other, e is the electron charge. The physical problem is then set up by the Schrödinger equation for the many-body wave function, imposing appropriate boundary conditions and symmetries due to particle statistics.

We are interested in the description of a macroscopic system characterized by the electronic density $n{=}N_e/V$, equal to the atomic number density due to charge neutrality, and temperature T. Density is frequently parametrized by the Wigner-Seitz parameter $r_s = a/a_B$ where $n = 3/(4\pi a^3)$ and a_B is the Bohr radius. At zero pressure and 4.2 K, the density corresponds to $r_s \simeq 1.768$ for p-H_2. Periodic boundary conditions on the density distribution in the simulation cell are used to eliminate surface effects, and the Coulomb $1/r$ interaction in Eq. (3) has to be replaced by the appropriate expressions, e.g., using Ewald's expressions [24–26].

Despite the simplicity of the Hamiltonian, Eq. (1), the extremely rich phase diagram indicates to us that a quantitative description/prediction will be challenging. In fact, straightforward approaches to directly determine hydrogen properties in a large part of the phase diagram are beyond our actual capacities, and we will introduce several approximations. These approximations are in general uncontrolled, in the sense that we will not be able to improve them systematically until a given precision is reached. However, our aim should be to estimate and quantify the systematic uncertainty stemming from the various approximation, if necessary. Experimental data should not be used to validate these approximations, rather, deviations with experiment should trigger reexaminations, as well as questioning the underlying description and modelling of experimental setups and their interpretation.

2.1 Path-integral Monte Carlo calculations

Path-Integral Monte Carlo (PIMC) methods give access to sample the elements of the thermal density matrix

$$\rho\big(\mathbf{R}'\mathbf{r}', \mathbf{R}\mathbf{r}; \beta\big) = \big\langle \mathbf{R}'\mathbf{r}' | e^{-\beta H} | \mathbf{R}\mathbf{r} \big\rangle \tag{4}$$

from which we can calculate static expectation values of any operator at inverse temperature $\beta = 1/k_B T$.

However, since functions of operators are in general defined via their spectral representation, a direct evaluation of Eq. (4) requires knowledge of all energy eigenfunctions. Based on the Trotter formula [27]

$$e^{-\beta H} = \lim_{M\to\infty} \left(e^{-\tau T} e^{-\tau V} \right)^M , \quad \tau = \beta/M \tag{5}$$

the path integral formulation [28] circumvents explicit diagonalizations and the density matrix can be written as

$$\rho\big(\mathbf{R}'\mathbf{r}', \mathbf{R}\mathbf{r}; \beta\big) = \lim_{M\to\infty} \sum_{\mathcal{P}} (\pm 1)^{|\mathcal{P}|} \int_{\mathbf{R}\mathbf{r}}^{\mathcal{P}(\mathbf{R}'\mathbf{r}')} D\mathbf{R}[\tau]\, D\mathbf{r}[\tau] \left(\frac{\sqrt{m_e m_p}}{2\pi\hbar^2 \beta/M} \right)^{3M} e^{-S_M^p(\mathbf{R}[\tau]\mathbf{r}[\tau];\beta)} \tag{6}$$

with $\int D\mathbf{R}[\tau]\, D\mathbf{r}[\tau] = \prod_{m=1}^{M-1} \int d\mathbf{R}^m \int d\mathbf{r}^m$ and

$$S_M^p(\mathbf{R}[\tau]\mathbf{r}[\tau];\beta) = \sum_{m=0}^{M-1} \left(\frac{m_p \big(\mathbf{R}^{m+1} - \mathbf{R}^m\big)^2}{2\hbar^2(\beta/M)} + \frac{m_e \big(\mathbf{r}^{m+1} - \mathbf{r}^m\big)^2}{2\hbar^2(\beta/M)} + (\beta/M) V(\mathbf{r}^m, \mathbf{R}^m) \right) \tag{7}$$

setting $(\mathbf{R}^0, \mathbf{r}^0) = (\mathbf{R}, \mathbf{r})$ and $(\mathbf{R}^M, \mathbf{r}^M) = \mathcal{P}(\mathbf{R}', \mathbf{r}')$ and the summation extends over all possible permutations $\mathcal{P}$ for correct (anti-)symmetrization. Integrals involved in the discretized path integral as well as the summation over permutations can then be sampled by Monte Carlo methods [29, 30].

The negative sign occurring for odd permutations of fermions will strongly affect the signal to noise ratio of direct Monte Carlo evaluations [23]. Such quantum statistical effects will be important below the Fermi temperature. For an ideal gas of electrons, we have $T_F^e \simeq 581\,454\, r_s^{-2}$ Kelvin, such that $T/T_F^e \lesssim 1\%$ in the our region of interest, Fig. 1. The Fermi temperature of free protons, T_F^p, is considerably lower, $T_F^p = (m_e/m_p) T_F^e \simeq T_F^e/1836$, so that inter-molecular exchange effects are expected to be negligible for establishing the phase diagram in the central region of Fig. 1. However, proper intra-molecular exchanges for para and ortho H_2 may need to be taken into account, certainly at the lower temperatures around and below the rotational energy excitations ~ 200 K.

2.2 Adiabatic approximation

The path-integral expression above, Eq. (6) with Eq. (7), is based on the so-called primitive approximation of the short time (or high temperature) density matrix

$$\rho\big(\mathbf{R}'\mathbf{r}', \mathbf{R}\mathbf{r}; \tau\big) \approx \big\langle \mathbf{R}'\mathbf{r}' \big| e^{-\tau T} e^{-\tau V} \big| \mathbf{R}\mathbf{r} \big\rangle \sim e^{-S_1^p(\mathbf{R}'\mathbf{r}', \mathbf{R}\mathbf{r}; \tau)} \tag{8}$$

choosing τ sufficiently small, such that residual effects due to the commutator $[T,\, V]$ can be neglected. Different short-time approximations can be chosen which may allow us to reach the same precision within larger time steps, τ, so that less discretizations M of the path are needed for our computations [29].

From physical considerations we expect that the Born-Oppenheimer approximation should provide an excellent description in our region of interest. We therefore choose a different short time approximation, $\rho(\mathbf{R}'\mathbf{r}', \mathbf{R}\mathbf{r}; \tau) \approx \rho_{BO}(\mathbf{R}'\mathbf{r}', \mathbf{R}\mathbf{r}; \tau)$ with

$$\rho_{BO}\big(\mathbf{R}'\mathbf{r}', \mathbf{R}\mathbf{r}; \tau\big) = \big\langle \mathbf{R}'\mathbf{r}' \big| e^{-\tau T_N} e^{-\tau H_e} \big| \mathbf{R}\mathbf{r} \big\rangle = \big\langle \mathbf{R}'\mathbf{r}' \big| e^{-\tau T_N} \big| \mathbf{R}\mathbf{r}' \big\rangle \big\langle \mathbf{R}\mathbf{r}' \big| e^{-\tau (T_e + V)} \big| \mathbf{R}\mathbf{r} \big\rangle \tag{9}$$

where matrix elements of $e^{-\tau T_N}$ are independent of electronic degrees of freedom and those of $e^{-\tau(T_e+V)}$ are now diagonal in the nuclear coordinates. Denoting $\Psi_n(\mathbf{r}|\mathbf{R})$ the eigenfunctions of energy $E_n(\mathbf{R})$ of the Born-Oppenheimer Hamiltonian $H_e = T_e + V$, the dependence on $\mathbf{R}$ enters only parametrically, we get

$$\rho_{BO}\big(\mathbf{R}'\mathbf{r}', \mathbf{R}\mathbf{r}; \tau\big) \sim \left(\frac{m_p}{2\pi\hbar^2\tau}\right)^{3/2} \sum_n e^{-m(\mathbf{R}-\mathbf{R}')^2/2\hbar^2\tau - \tau E_n(\mathbf{R})} \Psi_n^*(\mathbf{r}'|\mathbf{R}) \Psi_n(\mathbf{r}|\mathbf{R}). \tag{10}$$

In the resulting discretized path integral, we can then integrate out the electronic degrees of freedom (setting $\mathbf{r}^M{=}\mathbf{r}^0$ and integrating over $\mathbf{r}^0$)

$$\begin{aligned}\rho(\mathbf{R}', \mathbf{R}; \beta) &= \lim_{M\to\infty} \sum_{\mathcal{P}} (\pm 1)^{|\mathcal{P}|} \int_{\mathbf{R}}^{\mathcal{P}(\mathbf{R}')} D\mathbf{R}[\tau]\, D\mathbf{r}[\tau] \prod_m \rho_{BO}(\mathbf{R}^m\mathbf{r}^m, \mathbf{R}^{m+1}\mathbf{r}^{m+1}; \tau) \\ &= \lim_{M\to\infty} \sum_{\mathcal{P}} (\pm 1)^{|\mathcal{P}|} \int_{\mathbf{R}}^{\mathcal{P}(\mathbf{R}')} D\mathbf{R}[\tau] \left(\frac{m_p}{2\pi\hbar^2\beta/M}\right)^{3M/2} \sum_n e^{-S_{Mn}^{BO}(\mathbf{R}[\tau];\beta)}\end{aligned} \tag{11}$$

with

$$S_{Mn}^{BO}(\mathbf{R}[\tau]; \beta) = \sum_{m=0}^{M-1} \left(i(\mathbf{R}^{m+1}{-}\mathbf{R}^m) \cdot \mathbf{A}_n(\mathbf{R}^{m+1}, \mathbf{R}^m) + \frac{m_p(\mathbf{R}^{m+1}{-}\mathbf{R}^m)^2}{2\hbar^2(\beta/M)} + (\beta/M) E_n(\mathbf{R}^m) \right) \tag{12}$$

where the (real-valued) vector potential $\mathbf{A}_n$ is defined by the electronic overlap integrals

$$\int d\mathbf{r}\; \Psi_n^*(\mathbf{r}|\mathbf{R}')\, \Psi_n(\mathbf{r}|\mathbf{R}) \simeq e^{-i(\mathbf{R}'-\mathbf{R})\cdot\mathbf{A}_n(\mathbf{R}',\mathbf{R})} \tag{13}$$

for $\mathbf{R}' \to \mathbf{R}$ and we have neglected non-adiabatic transitions between different electronic states. In general, we should have kept terms of order $(\mathbf{R}'{-}\mathbf{R})^2 \sim \hbar^2\beta/Mm_p$ to recover the exact path-integral in the limit $M \to \infty$. Neglecting these terms which are suppressed by $1/m_p$ corresponds to the Born-Oppenheimer approximation.

In the following, we will focus on the diagonal part of the density matrix, $\rho(\mathbf{R}, \mathbf{R}; \beta)$ which determines most of the basic thermodynamic observables. Further, we will assume sufficiently high temperatures to neglect proton exchanges, and all proton paths are closed. Then, the phase term in Eq. (12) only contributes when a Berry phase is acquired during the trajectory in imaginary time. In general, this requires exceptionally high symmetry configurations, so that this adiabatic phase is frequently dropped in the Born-Oppenheimer sampling of solids and liquids.

For $T \ll T_F^e$, we may further neglect any contributions from electronic excitations, $n > 0$, and restrict to configurations within the ground state Born-Oppenheimer surface $E_0(\mathbf{R})$. However, we still have to resolve the electronic ground state problem to obtain $E_0(\mathbf{R})$ for given nuclear positions.

Ab-initio or first-principles molecular dynamics methods [31] are frequently based on electronic structure calculations using density functional theory (DFT). How to decide which DFT functional should be used? Frequently, comparisons with experiments gauges the choice of DFT functional. Since we want to avoid this criterium, we need some other strategies to calculate the Born-Oppenheimer electronic energies.

2.3 Quantum Monte Carlo calculations at zero temperature

2.3.1 Variational principle

Quantum Monte Carlo methods at zero temperature are based on the variational principle

$$E_0 \leq E_T \equiv \frac{\langle \Psi_T | H_e | \Psi_T \rangle}{\langle \Psi_T | \Psi_T \rangle} \tag{14}$$

where Ψ_T is any trial wave function obeying the same boundary conditions as our true (Born-Oppenheimer) ground state wave function Ψ_0. Here, and in the following we suppress the parametric dependence on the nuclear coordinates.

The simplest anti-symmetric trial wave function for N electrons is $\det_n \varphi_n(\mathbf{r}_i)$, a Slater determinant, for spin-polarized electrons, whereas it reduces to a product of two determinants, one for each spin-component, for a gas of unpolarized electrons. Optimizing the variational energy obtained by a Slater determinant with respect to the orbitals, $\varphi_n(\mathbf{r})$ gives the Hartree-Fock energy. To go beyond the Hartree-Fock approximation, we can add explicit pair correlations [32–35] to our wave function

$$\Psi_{SJ}(\mathbf{r}) = \det_{ni} \varphi_n(\mathbf{r}_i)\, e^{-U(\mathbf{r})}. \tag{15}$$

The frequently called Jastrow factor $U(\mathbf{r})$ is symmetric under electron exchanges, e.g. $U = \sum_{i<j} u_{ee}(|\mathbf{r}_i - \mathbf{r}_j|) + \sum_{iJ} u_{ep}(|\mathbf{r}_i - \mathbf{R}_J|)$ provides an explicit, size consistent and translational invariant form containing electron-electron and electron-proton correlations. In addition to the orbitals $\varphi_n(\mathbf{r})$, the one dimensional functions $u_{ee}(r)$ and $u_{ep}(r)$ need also to be determined by minimizing the resulting energy expectation value.

Backflow wave functions introduce an explicit dependence on all electron coordinates $\mathbf{r}$ into the Slater determinant [36–38]

$$\Psi_{bf}(\mathbf{r}) = \det_{ni} \varphi_n(\mathbf{q}_i(\mathbf{r}))\, e^{-U(\mathbf{r})} \tag{16}$$

by the use of backflow coordinates $\mathbf{q}_i(\mathbf{r})$ which need to be symmetric with respect to electron exchange holding i fixed. A simple form for liquid and solid hydrogen [39] is

$$\mathbf{q}_i = \mathbf{r}_i + \sum_{j \neq i} (\mathbf{r}_i - \mathbf{r}_j) b_{ee}\big(|\mathbf{r}_i - \mathbf{r}_j|\big) + \sum_J (\mathbf{r}_i - \mathbf{R}_J) b_{ep}\big(|\mathbf{r}_i - \mathbf{R}_J|\big)$$

with one dimensional functions $b_{ee}(r)$ and $b_{ep}(r)$, ultimately determined by energy minimization. Systematic improvement for many-body correlations either explicitly [40] or implicitly via an iterative (deep) structure [41–44] are possible, as well as combined with neural network representations [45–50]. In addition to providing lower energy expectation values, better trial wave functions also lower the variance of the energy,

$$\sigma_T^2 = \frac{\langle \Psi_T | H^2 | \Psi_T \rangle}{\langle \Psi_T | \Psi_T \rangle} - \left(\frac{\langle \Psi_T | H | \Psi_T \rangle}{\langle \Psi_T | \Psi_T \rangle} \right)^2 \tag{17}$$

which vanishes in case Ψ_T coincides with an exact energy eigenstate. Calculations with different classes of trial wave functions can be used for heuristic extrapolations of E_T to zero variance, thus providing an estimate for the residual energy error of the best trial wave function [41–43].

2.3.2 Variational Monte Carlo calculations

All of the wave functions described before have in common that the evaluation for a given configuration $\mathbf{r}$ is sufficiently fast for systems ranging from around ten to thousands of electrons. However, we still have to calculate and optimize E_T. Whereas the Hartree-Fock energy can still be calculated by deterministic quadrature, the integrals involved in the calculations based on correlated wave functions, e.g., the Slater-Jastrow and backflow forms, involve integrations over $3N$ dimensions

$$E_T = \frac{\int d\mathbf{r}\, |\Psi_T(\mathbf{r})|^2 E_L(\mathbf{r})}{\int d\mathbf{r}\, |\Psi_T(\mathbf{r})|^2} \tag{18}$$

where we have introduced the so-called local energy

$$E_L(\mathbf{r}) \equiv \frac{\langle \mathbf{r}|H|\Psi_T\rangle}{\langle \mathbf{r}|\Psi_T\rangle} = \frac{H\Psi_T(\mathbf{r})}{\Psi_T(\mathbf{r})} \tag{19}$$

in the position representation $\Psi_T(\mathbf{r}) \equiv \langle \mathbf{r}|\Psi_T\rangle$.

In variational Monte Carlo (VMC) calculations [51–53], the standard Metropolis algorithm is used to sample the $3N$ dimensional configuration space $\mathbf{r}$ according to a weight $\sim |\Psi_T(\mathbf{r})|^2$ via Markov chains. An estimate of the trial energy is then obtained by averaging the local energy over the sampled configurations

$$E_T = \mathbb{E}_{\mathbf{r}\sim\Psi_T^2}[E_L(\mathbf{r})]. \tag{20}$$

This estimate is unbiased, but affected by a stochastic error of order $\sim \sqrt{\sigma_T^2/N_{MC}}$, controlled by the number of independent Monte Carlo samples, N_{MC}. Better wave functions, not only lower the energy expectation value, but also reduce the statistical error of the VMC calculations when reducing the variance towards an exact eigenstate (zero variance principle).

2.3.3 Stochastic optimization

The variational principle is of fundamental importance, since it allows us to compare the "quality" of different trial wave functions and select our "best" one, based on an objective criterium, without invoking comparison with experiment. Within VMC we can evaluate the energy of broad classes of wave functions, those which we can evaluate efficiently on our computer. Above, we have described generic forms of trial wave functions, all of them containing one or several unspecified functions. Any of these (one dimensional) functions can be expanded in a basis set providing a parametrization of the wave function.

Our trial wave function $\Psi_T(\mathbf{r}|\alpha)$ thus contains potentially a very large number of parameters α. The variational principle allows us to fix them by searching for the minimum of the energy expectation value $E_T(\alpha)$. This is almost a standard minimization problem, non-linear in α and intrinsically affected by stochastic noise, since $E_T(\alpha)$ is obtained via Monte Carlo integration. Ignoring the problem of noise for the moment, one would expand $E_T(\alpha+\delta\alpha)$ up to second order in small changes $\delta\alpha$ of our parameters and use some iterative method based on Newton's method

$$\alpha \leftarrow \alpha - \left(\partial_\alpha^2 E_T(\alpha)\right)^{-1} \partial_\alpha E_T(\alpha) \tag{21}$$

where $\partial_\alpha E_T(\alpha)$ denotes the gradient vector and $\partial^2_\alpha E_T(\alpha)$ the second derivative (Hessian) matrix, or some variant of it [54]. Apart that the Hessian might be quite costly to calculate for large number of parameters, the inversion is likely to be corrupted by the stochastic noise. Instead of trying to reduce the noise as much as possible by using long MC runs, a simple gradient descent

$$\alpha \leftarrow \alpha - \epsilon\, \partial_\alpha E_T(\alpha) \tag{22}$$

with learning rate ϵ can be more efficient [55].

For a real trial wave function, the gradient vector of the trial energy is written as

$$\begin{aligned}\partial_\alpha E_T(\alpha) &= 2\,\frac{\int d\mathbf{r}\, \Psi_T(\mathbf{r}|\alpha) H \partial_\alpha \Psi_T(\mathbf{r}|\alpha)}{\int d\mathbf{r}\, \Psi_T^2(\mathbf{r}|\alpha)} - 2\,\frac{\int d\mathbf{r}\, \Psi_T(\mathbf{r}|\alpha) H \Psi_T(\mathbf{r}|\alpha)}{\int d\mathbf{r}\, \Psi_T^2(\mathbf{r}|\alpha)}\,\frac{\int d\mathbf{r}\, \Psi_T(\mathbf{r}|\alpha) \partial_\alpha \Psi_T(\mathbf{r}|\alpha)}{\int d\mathbf{r}\, \Psi_T^2(\mathbf{r}|\alpha)} \\ &= 2\,\mathbb{E}_{\mathbf{r}\sim\Psi_T^2}\left[\big(E_L(\mathbf{r}|\alpha) - E_T(\alpha)\big)\partial_\alpha \log \Psi_T(\mathbf{r}|\alpha)\right]\end{aligned} \tag{23}$$

where we have used that the Hamiltonian is hermitian to obtain an unbiased estimator in the last line. The resulting stochastic gradient descent based on the Monte Carlo estimation of $\partial_\alpha E_T$ is guaranteed to converge to the minimal energy [55], even in the case of large stochastic noise. Strategies based on stochastic gradient descent, also known as stochastic reconfiguration [56], have been successfully used for minimizing very large set of variational parameters, and have been combined with machine learning approaches more recently [57–59].

2.3.4 Projector Monte Carlo methods

Propagating a wave function in imaginary time $\Psi_t(\mathbf{r}) \sim \langle \mathbf{r} | e^{-tH} | \Psi_T \rangle$, the energy expectation value $E_t = \langle \Psi_t | H | \Psi_t \rangle / \langle \Psi_t | \Psi_t \rangle$ approaches the ground state energy of the same symmetry sector exponentially fast in t. Imaginary time projection can be performed stochastically based on the path-integral representation of the propagator $\rho_e(\mathbf{r}', \mathbf{r}; t) = \langle \mathbf{r}' | e^{-tH_e} | \mathbf{r} \rangle$ along the lines discussed above. In the primitive approximation for $\rho_e(\mathbf{r}', \mathbf{r}; t)$ we get the variational path-integral expression (VPIMC or PIGS for path-integral ground state techniques)

$$\Psi_t^2(\mathbf{r}) \sim \frac{\int d\mathbf{r}^0 \int d\mathbf{r}^{2M} \int_{\mathbf{r}^0}^{\mathbf{r}^{2M}} D\mathbf{r}[\tau]\, \pi(\mathbf{r}[\tau])\, \delta(\mathbf{r} - \mathbf{r}^M)}{\int d\mathbf{r}^0 \int d\mathbf{r}^{2M} \int_{\mathbf{r}^0}^{\mathbf{r}^{2M}} D\mathbf{r}[\tau]\, \pi(\mathbf{r}[\tau])} \tag{24}$$

with

$$\pi(\mathbf{r}[\tau]) = \Psi_T(\mathbf{r}^0)\, e^{-S^p_{2M}(\mathbf{r}[\tau];2t)}\, \Psi_T(\mathbf{r}^{2M}). \tag{25}$$

In contrast to PIMC for the diagonal density matrix, Eqs (6) and (7), where the paths are periodic in imaginary time ($\mathbf{r}^0 = \mathbf{r}^M$), in VPIMC, Eq. (24), the paths are open with their ends weighted by the trial wave function, $\Psi_T(\mathbf{r}^0)$ and $\Psi_T(\mathbf{r}^{2M})$, and the ground state distribution is represented in the central slice $\mathbf{r}^M$ of the path.

The primitive approximation is rarely used in this context. As ground state projector Monte Carlo methods are build on top of an optimized trial wave function, one usually wants to take advantage, using it as a guiding wave function for importance sampling. For this we introduce a similarity transformation of our Hamiltonian in the position representation

$$\widetilde{H}_e = e^{U_T(\mathbf{r})} H_e e^{-U_T(\mathbf{r})} = T_e + \frac{\hbar^2}{m_e} \sum_i [\nabla_i U_T(\mathbf{r})] \cdot \nabla_i + E_L(\mathbf{r}) \tag{26}$$

where $\Psi_T(\mathbf{r}) = e^{-U_T(\mathbf{r})}$ is used as a guiding wave function.
The propagator corresponding to $\widetilde{H}$ can then be written as

$$\widetilde{\rho}_T(\mathbf{r}', \mathbf{r}; \tau) = \sum_n \frac{\langle \mathbf{r}' | (-\tau \widetilde{H}_e)^n | \mathbf{r} \rangle}{n!} = \sum_n \frac{e^{U_T(\mathbf{r}')} \langle \mathbf{r}' | (-\tau H_e)^n | \mathbf{r} \rangle e^{-U_T(\mathbf{r})}}{n!} = e^{U_T(\mathbf{r}')} \rho(\mathbf{r}', \mathbf{r}; \tau) e^{-U_T(\mathbf{r})} \tag{27}$$

which shows that $\widetilde{\rho}_T$ and ρ are also related by a similarity transformation.
Let us now apply Trotter's approximation to $\widetilde{\rho}_T$ for small τ

$$\begin{aligned} \widetilde{\rho}_T(\mathbf{r}', \mathbf{r}; \tau) &\approx \langle \mathbf{r}' | e^{-\tau T_e} e^{-i\tau \sum_j (\hbar/m_e)[\nabla_j U_T] \cdot \hat{\mathbf{p}}_j} e^{-\tau E_L} | \mathbf{r} \rangle \\ &\approx \langle \mathbf{r}' | e^{-\tau T_e} | \mathbf{r} - \tau \mathbf{f} \rangle e^{-\tau E_L(\mathbf{r})} \quad \approx \quad e^{-\tau E_L(\mathbf{r}')} \langle \mathbf{r}' + \tau \mathbf{f}' | e^{-\tau T_e} | \mathbf{r} \rangle \\ &\sim e^{-m_e(\mathbf{r} - \mathbf{r}' - \tau \mathbf{f}')^2 / 2\hbar^2 \tau} e^{-\tau [E_L(\mathbf{r}') + E_L(\mathbf{r})]/2} \equiv \widetilde{\rho}_T^D(\mathbf{r}' \to \mathbf{r}; \tau) e^{-\tau [E_L(\mathbf{r}') + E_L(\mathbf{r})]/2} \end{aligned} \tag{28}$$

where $\mathbf{f}_i = (\hbar^2/m_e) \nabla_i \log \Psi_T(\mathbf{r})$ and we have used that $e^{-ip\delta/\hbar} |x\rangle = |x + \delta\rangle$. We have split the propagator into a drifted random walk, $\widetilde{\rho}_T^D$, and a weight according to the local energy of the configurations. However, our approximate expression involving $\widetilde{\rho}_T^D$ violates the exact relation $\widetilde{\rho}_T(\mathbf{r}', \mathbf{r}; \tau) / \widetilde{\rho}_T(\mathbf{r}, \mathbf{r}'; \tau) = \Psi_T^2(\mathbf{r}) / \Psi_T^2(\mathbf{r}')$. It is important to restore this symmetry, e.g. using

$$\widetilde{\rho}_T^{DMC}(\mathbf{r}' \to \mathbf{r}; \tau) = \widetilde{\rho}_T^D(\mathbf{r}' \to \mathbf{r}; \tau) \min \left[1, \frac{\Psi_T^2(\mathbf{r})}{\Psi_T^2(\mathbf{r}')} \frac{\widetilde{\rho}_T^D(\mathbf{r} \to \mathbf{r}'; \tau)}{\widetilde{\rho}_T^D(\mathbf{r}' \to \mathbf{r}; \tau)} \right] \tag{29}$$

which coincides with Eq. (28) up to higher order terms in τ. We can now replace the weight of the path, Eq. (25), involved in the projection with

$$\pi(\mathbf{r}[\tau]) \approx \psi_T^2(\mathbf{r}^0) \prod_{m=0}^{2M-1} \widetilde{\rho}_T^{DMC}(\mathbf{r}^m \to \mathbf{r}^{m+1}; \tau)\, e^{-\tau [E_L(\mathbf{r}^m) + E_L(\mathbf{r}^{m+1})]/2} \tag{30}$$

Reptation Monte Carlo (RMC) [60] adds moves where new configurations are proposed by a global shift in imaginary time, $\mathbf{r}^{m+1} \leftarrow \mathbf{r}^m$ (and, with equal probability, $\mathbf{r}^{m-1} \leftarrow \mathbf{r}^m$), dropping the configuration $\mathbf{r}^m$ with $m > 2M$ ($m < 0$), and creating a new configuration for the freed place $\mathbf{r}^0$ ($\mathbf{r}^{2M}$). This proposition is then accepted or refused following Metropolis' rule according to the change of the weight $\pi(\mathbf{r}[\tau])$. The autocorrelation can be further reduced with minimal modifications implementing an algorithm similar to a directed loop algorithm [61].
PIMC and RMC methods store the (discretized) path $\mathbf{r}[\tau]$, ground state properties are directly accessible in the middle of the path, $\mathbf{r}(t/2)$, Eq. (24), in the limit $t \to \infty$, $\tau = t/2M \to 0$. Both limits must be numerically extrapolated.
Let us now regard the mixed distribution $\Psi_t(\mathbf{r}) \Psi_T(\mathbf{r})$ at the external ends of the path which we write

$$f_t(\mathbf{r}) = \Psi_t(\mathbf{r}) \Psi_0(\mathbf{r}) \sim \frac{\int d\mathbf{r}^0 \int d\mathbf{r}^M \int_{\mathbf{r}^0}^{\mathbf{r}^M} D\mathbf{r}[\tau]\, \pi_M(\mathbf{r}[\tau])\, \delta(\mathbf{r} - \mathbf{r}^M)}{\int d\mathbf{r}^0 \int d\mathbf{r}^M \int_{\mathbf{r}^0}^{\mathbf{r}^M} D\mathbf{r}[\tau]\, \pi_M(\mathbf{r}[\tau])} \tag{31}$$

$$\pi_M(\mathbf{r}[\tau]) = \psi_T^2(\mathbf{r}^0) \prod_{m=0}^{M-1} \widetilde{\rho}_T^{DMC}(\mathbf{r}^m \to \mathbf{r}^{m+1}; \tau)\, e^{\tau \{E_T - [E_L(\mathbf{r}^m) - E_L(\mathbf{r}^{m+1})]/2\}} \tag{32}$$

where we have introduced the trial energy E_T, a so-far arbitrary constant corresponding to a global weight, for later use. By noting that

$$\pi_{M+1}(\mathbf{r}[\tau]) = \pi_M(\mathbf{r}[\tau])\, \widetilde{\rho}_T^{DMC}(\mathbf{r}^M \!\rightarrow \mathbf{r}^{M+1}; \tau)\, e^{\tau\{E_T - [E_L(\mathbf{r}^{M+1}) + E_L(\mathbf{r}^M)]/2\}} \tag{33}$$

we can grow the projection time t based on

$$f_{t+\tau}(\mathbf{r}) \sim \mathbb{E}_{\mathbf{r}' \sim f_t(\mathbf{r}')} \big[\widetilde{\rho}_T^{DMC}(\mathbf{r}' \!\rightarrow \mathbf{r}; \tau)\, e^{\tau\{E_T - [E_L(\mathbf{r}) + E_L(\mathbf{r}')/2\}}\big]. \tag{34}$$

Diffusion Monte Carlo (DMC) calculations directly sample the limiting distribution $t \rightarrow \infty$, iterating Eq. (34). Starting from an initial VMC distribution of N_w "walkers" $\mathbf{r}' \sim f_0(\mathbf{r}') \equiv \Psi_T^2(\mathbf{r}')$, the walkers are displaced by a drifted random walk according to $\widetilde{\rho}_T^{DMC}(\mathbf{r}' \!\rightarrow \mathbf{r}; \tau)$ acquiring a weight $w(\mathbf{r}, \mathbf{r}') = e^{\tau\{E_T - [E_L(\mathbf{r}) + E_L(\mathbf{r}']/2\}}$. A branching process is usually added to take this weight into account by keeping on average $w(\mathbf{r}, \mathbf{r}')$ copies of a propagated walker. The trial energy E_T must be chosen (and eventually adapted) to keep the population of walkers asymptotically stable. The grows process of Eq. (34) will reach a stationary non-vanishing distribution, $f_\infty(\mathbf{r}) \sim \Psi_T(\mathbf{r})\Psi_0(\mathbf{r})$ for a trial energy coinciding with the true ground state energy E_0 [62,63,56].

Since DMC can be implemented on top of VMC with very few modifications, it is by far the most applied zero temperature projection method. However, the stationary distribution $f_\infty(\mathbf{r})$ does not correspond to the ground state density unless $\Psi_T \sim \Psi_0$. Thus, general ground state observables are not directly accessed, apart from the energy where

$$E_0 = \lim_{t \rightarrow \infty} \frac{\langle \Psi_{t/2} | H | \Psi_{t/2} \rangle}{\langle \Psi_{t/2} | \Psi_{t/2} \rangle} = \lim_{t \rightarrow \infty} \frac{\langle \Psi_T | H | \Psi_t \rangle}{\langle \Psi_T | \Psi_t \rangle} = \mathbb{E}_{\mathbf{r} \sim f_\infty} E_L(\mathbf{r}) \tag{35}$$

provides an unbiased estimator of the true ground state energy.

DMC calculations need to be extrapolated to the limit of vanishing time step, $\tau \rightarrow 0$, and an infinitely large population of walkers, $N_w \rightarrow \infty$. In particular, the bias due to the finite size of the population will eventually grow strongly with system size. Depending on the quality of the trial wave function, the scalability of DMC to converge to the ground state energy of large systems may be questionable [64].

2.3.5 Fixed-node approximation

Quite generally, the overall ground state of any (regular) Hamiltonian, is nodeless and symmetric with respect to particle exchange. Thus, all projection Monte Carlo methods described above can be directly applied to obtain the ground state of a system containing N bosons. This is not the case for Fermions, since the ground state wave function of a Fermi system must be anti-symmetric,

$$\Psi_F(\ldots, \mathbf{r}_i, \ldots, \mathbf{r}_j, \ldots) = -\Psi_F(\ldots, \mathbf{r}_j, \ldots, \mathbf{r}_i, \ldots), \quad \text{for any } i, j \tag{36}$$

with nodes where $\Psi(\mathbf{r}) = 0$, e.g., when $\mathbf{r}_i = \mathbf{r}_j$. Thus, in general, the ground state of fermions is never the lowest eigenstate of the Hamiltonian of the system. Only in particular situations which we do not address here, e.g., for some particular Hamiltonian in one spatial dimension, it can be degenerate with the bosonic ground state.

It is possible to extend the variational principle for the energy to some excited states, $|\Psi_m\rangle$ with $E_m > E_0$, imposing orthogonality of the trial wave function to all lower eigenfunctions, $\langle\Psi_T|\Psi_n\rangle = 0$ for all n with $E_n < E_m$. Since the fermionic ground state wave function is the lowest eigenfunction in the space of anti-symmetric wave functions, orthogonality to states with lower energy is guaranteed by symmetry. Since VMC based methods sample $|\Psi_T(\mathbf{r})|^2 \geq 0$, they can be directly applied to Fermions by using anti-symmetric trial wave functions which obey Eq. (36). All of the previously discussed trial wave functions are constructed manifestly anti-symmetric based on determinants.

In contrast to VMC, Projection Monte Carlo methods stochastically sample $\Psi_0(\mathbf{r})$ which now contains negative regions where the wave function cannot be interpreted as probability. Let us try to represent a fermionic wave function, starting with

$$\Psi_T^{\pm} = \frac{1}{2}\big(|\Psi_T|\pm\Psi_T\big) \quad \text{so that} \quad \Psi_T = \Psi_T^{+}-\Psi_T^{-}, \quad \Psi_T^{+} \geq 0, \quad \Psi_T^{-} \geq 0 \tag{37}$$

and diffuse $\Psi_T^{\pm} \geq 0$ separately. Using $|\Psi_T|$ for importance sampling, e.g. in DMC, we obtain the mixed distribution

$$f_t^{\pm}(\mathbf{r}) = \big|\Psi_T(\mathbf{r})\big|\, \Psi_t^{\pm}(\mathbf{r}). \tag{38}$$

However, both $\Psi_T^{\pm}$ do have some overlap with the bosonic ground state, Ψ_B, of energy E_B,

$$\Psi_T^{\pm} = \frac{1}{2}\Big(c_B\, e^{-tE_B}\Psi_B(\mathbf{r}) \pm c_F\, e^{-tE_F}\Psi_F(\mathbf{r}) + \dots\Big) \quad \text{with} \quad c_{B/F} = \int d\mathbf{r}\, \Psi_{B/F}(\mathbf{r})|\Psi_T(\mathbf{r})|. \tag{39}$$

We can now calculate the expectation value of some operator for the fermionic state as

$$\langle O\rangle = \frac{\int d\mathbf{r}\, s(\mathbf{r})\, O(\mathbf{r})(f_t^{+}-f_t^{-})}{\int d\mathbf{r}\, s(\mathbf{r})\ (f_t^{+}-f_t^{-})} = \frac{1}{\bar{s}}\frac{\int d\mathbf{r}\, s(\mathbf{r})\, O(\mathbf{r})\ (f_t^{+}-f_t^{-})}{\int d\mathbf{r}\ (f_t^{+}+f_t^{-})} \tag{40}$$

where $s(\mathbf{r}) \equiv \Psi_T(\mathbf{r})/|\Psi_T(\mathbf{r})| = \pm 1$ and

$$\bar{s} = \frac{\int d\mathbf{r}\, s(\mathbf{r})\, (f_t^{+}-f_t^{-})}{\int d\mathbf{r}\ (f_t^{+}+f_t^{-})} = \frac{c_F^2\, e^{-tE_F} + \dots}{c_B^2\, e^{-tE_B} + \dots}. \tag{41}$$

Therefore, we have

$$\bar{s} \sim \exp\big(-Nt\Delta\mathcal{E}\big) \tag{42}$$

where $\Delta\mathcal{E} = (E_F - E_B)/N$ is independent of N for large systems. The mean sign $\bar{s}$ in general enters in the normalization of expectation values for physical observables. Assuming a finite gap, $\mathcal{E} > 0$, between the fermionic and bosonic ground state energy per particle, $\bar{s}$ vanishes exponentially in $Nt \gg 1$. Since $\langle s^2\rangle = 1$, the variance approaches one in this limit

$$\sigma_s^2 = \overline{s^2} - \bar{s}^2 \approx 1 \gg \bar{s}^2 \sim \exp\big(-2Nt\Delta\mathcal{E}\big). \tag{43}$$

In order to get the error bar of the sign $\sim \sqrt{\sigma_s^2/N_{MC}}$ sufficiently small to resolve the value of the average sign, we roughly need

$$N_{MC} \sim \frac{1}{\bar{s}^2} \sim \exp\big(2Nt\Delta\mathcal{E}\big) \tag{44}$$

independent samples, increasing exponentially with N and t. This is the fermion sign problem. Can we circumvent this exponential signal to noise ratio? Importance sampling DMC is based on the overlap

$$f(\mathbf{r}) = \Psi_T(\mathbf{r})\,\Psi_0(\mathbf{r}). \tag{45}$$

Let us consider that we have found a trial wave function with exactly the same positive and negative regions as the fermionic ground state we are looking for, so that $f(\mathbf{r}) \geq 0$ in the full configuration space. In this case, if we impose $f(\mathbf{r}) \geq 0$ during the time evolution in DMC, we expect that DMC converges to the exact fermionic ground state. What happens? Looking at the drifted random walk created by the importance sampling, imposing $f(\mathbf{r}) \geq 0$ for all $\mathbf{r}$, we reject any move $\mathbf{r} \to \mathbf{r}'$ with $\Psi_T(\mathbf{r})\Psi_T(\mathbf{r}') < 0$. Our population of walkers can be separated into two sets, positive walkers at $\mathbf{r}^+$ which satisfy $\Psi_T(\mathbf{r}^+) \geq 0$, and negative walkers at $\mathbf{r}^-$ with $\Psi_T(\mathbf{r}^-) < 0$. Positive and negative walkers are separated by the nodal surface s where $\Psi_T(\mathbf{r}{=}\mathbf{s}) \equiv 0$, and it is enough to know the exact nodal surface. Note that the nodal surface $\mathbf{r}$ is a hypersphere in $Nd{-}1$ dimensions where d is the spatial dimension. For any sufficiently regular anti-symmetric trial function, applying the permutation operator to any positive configuration, we obtain a negative walker, and vice versa. It is therefore sufficient to sample only the positive space as long as we are only interested in physical observables which commute with the permutation operator.

Everything above is fine, but we still do not know the nodal surface for almost all fermion problems we are interested in, so let us search for the best approximation we can do. In the fixed-node approximation, we simply impose the nodes of a given trial wave function. Once started with positive walkers, our fixed-node DMC algorithm will converge to an eigenfunction of the Hamiltonian

$$H\Psi_{FN}(\mathbf{r}) = E_{FN}\Psi_{FN}(\mathbf{r})\,, \quad \text{for all } \mathbf{r} \text{ in } \mathbf{r}^+, \text{the positive region with } \Psi_T(\mathbf{r}) \geq 0. \tag{46}$$

On the nodes s of Ψ_T we also have $\Psi_{FN}(\mathbf{s}) = 0$, and we can continue the wave function to the negative regions, $\mathbf{r}^-$ using permutations $\Psi_{FN}(\mathbf{r}) = (-1)^{|P|}\,\Psi_{FN}(P\mathbf{r})$, where the permutation P can be determined from solving $\Psi_T(\mathbf{r}) = (-1)^{|P|}\,\Psi_T(P\mathbf{r})$ for P. As long as Ψ_T is a sufficiently regular fermionic trial wave function, we can reach all configuration space by this procedure, and the continued Ψ_{FN} is a continuous anti-symmetric wave function [65].

Unfortunately, the partial derivatives of the constructed FN wavefunction with respect to $\mathbf{r}_i$ are in general not continuous at the nodal surface. The variational principle does not directly apply, since the FN wave function is outside the variational space of wave functions (continuous wave functions with continuous first derivatives). However, we can smear out our wave function at a distance ϵ close to the nodes to make them sufficiently smooth to apply the variational theorem, so that the smoothed function provides an upper bound for the energy. This smoothing will increase the absolute value of the curvature $\sim \epsilon^{-1}$ close to the node and the Laplacian of the kinetic energy will produce large absolute values, $\sim \varepsilon^{-1}$. However, since the wave function vanishes as ϵ, the kinetic energy contribution of the smoothed wave function close to the nodal region $\sim \int_\epsilon \psi\nabla^2\psi \sim \epsilon$ vanishes. Therefore, the energy of our fixed-node wave function provides a true upper bound to the fermion ground state energy, E_F, [66]

$$E_F \leq E_{FN} = \frac{\int d\mathbf{r}\, \Psi_{FN}(\mathbf{r}) E_L(\mathbf{r}) \Psi_{FN}(\mathbf{r})}{\int d\mathbf{r}\, \Psi_{FN}(\mathbf{r}) \Psi_{FN}(\mathbf{r})}\,. \tag{47}$$

For many-body fermion problems, the fixed-node energies are the most accurate variational values and routinely used in electronic structure DMC calculations [67].

As a generalization of the fixed-node approach, the fixed-phase approximation [68] is based on a complex trial wave function

$$\Psi_T(\mathbf{r}) = A(\mathbf{r}) e^{-i\varphi(\mathbf{r})}, \quad \text{with non negative amplitude } A(\mathbf{r}) \geq 0 \text{ and real phase } \varphi(\mathbf{r}). \tag{48}$$

For any given phase, we can then minimize the energy of the trial wave function for an explicitly given phase, $\varphi(\mathbf{r})$. However, since the phase is only well defined for non-vanishing amplitude, we also have to fix the nodes of the amplitude and make the wave function single valued. An argument similar to that above shows that the fixed-phase wave function provides also an upper bound for the ground state energy in the same symmetry class as Ψ_T. Fixed-phase methods are needed for treating twisted boundary conditions, see below, and for systems with broken time-reversal invariance, e.g., including magnetic field effects.

2.4 Finite size effects

With the methods described above, we will be able to simulate systems containing N particles (electrons or protons), typically $N \lesssim 10^3$, and one might ask how such small systems may faithfully reproduce material properties in the bulk. To eliminate surface effects, periodic boundary conditions are in general used. Still, residual effects of the underlying finite simulation cell remain and the extrapolation to the thermodynamic limit represents one of the major sources of bias. Heuristically, for classical particles, interacting via short-range forces exponential convergence may be expected once the size of the simulation cell exceeds the correlation length. Large systems are needed approaching phase transitions where the correlation length diverges, and care is needed to correctly describe ordered phases which are in general sensitive to boundary conditions. Methods to address finite size effects having their origin in structural formation have been developed in the context of classical molecular dynamics or Monte Carlo calculations [25, 26]. In the following we will focus on finite size effects of electronic origin.

As discussed previously, all temperatures shown in Fig. 1 are much lower than the Fermi temperature of electrons, a typical situation in condensed matter physics and material science. In contrast to the nuclei, electrons are in a strongly degenerate quantum state where the wave character dominates and the sensitivity to boundary conditions is strongly enhanced.

To illustrate finite size effects, let us consider a non-interacting gas of electrons at density $N/L^3 \sim k_F^3 \sim r_s^{-3}$ where k_F is the Fermi wave vector corresponding to the highest occupied single particle state. From the ratio of the Fermi wave length $\lambda_F = 2\pi/k_F$ to the size of the box, $\lambda_F/L \simeq 2.03 N^{-1/3}$, we already see that size effects will be far from negligible even for large simulation cells containing thousands of electrons or more.

These size effects are rather well understood. They correspond to shell effects which are already present for an ideal gas with a Slater determinant composed of the first N plane wave orbitals of wave vectors $\mathbf{k}_i$ on a discrete grid of spacing $2\pi/L$. The corresponding kinetic energy per particle, $\mathcal{T}_N^0 = T_N^0/N = N^{-1}\sum_{i=1}^N (\hbar k_i)^2/2m_e$, extrapolates irregularly to the thermodynamic limit due to the sharp Fermi surface. Imposing twisted boundary conditions on the wave function [69], $\Psi(\dots,\mathbf{r}_i{+}L,\dots) = e^{i\vartheta}\Psi(\dots,\mathbf{r}_i,\dots)$, the wave vectors of the plane wave orbitals are collectively deplaced, corresponding to a shifted grid $\mathbf{k}+\vartheta$. Averaging the twist angle ϑ over N_ϑ twists on a dense grid in the Brillouin zone of the simulation cell then mimics the thermodynamic limit integration $\lim_{N_\vartheta\to\infty} N_\vartheta^{-1}\sum_\vartheta\sum_{\mathbf{k}} f(\mathbf{k}{+}\vartheta) = V/(2\pi)^3\int d^3q\, f(\mathbf{q})$ for any function f. However, in a many-body calculation with fixed number of particles, twist averaged boundary conditions (TABC) do not necessarily restore a sharp Fermi surface, since exactly N orbitals of lowest single particle energies are occupied for each twist, ϑ. To reproduce the exact single particle energy with a sharp Fermi surface, the number of particles must be allowed to vary with ϑ. This is implemented in grand-canonical twist averaging (GC-TABC) [70, 71].

Further important size effects are due to the long range Coulomb interactions. Let us write down the potential energy per particle, considering only electron-electron interactions,

$$\mathcal{V}_N \equiv V_N/N = \frac{1}{2V}\sum_{\mathbf{k}\neq 0} v_k\big(S_N(k){-}1\big) \tag{49}$$

where $v_k \sim k^{-2}$ is the Fourier transform of the Coulomb potential, $S_N(k) = \langle \rho_{\mathbf{k}}\,\rho_{-\mathbf{k}}\rangle/N$ the static structure factor, and $\rho_{\mathbf{k}} = \sum_j e^{i\mathbf{k}\cdot\mathbf{r}_j}$ the Fourier transform of the density operator.

Since $S_N(k)$ is a local operator, we may expect fast convergence to the thermodynamic limit, $S_N(k) \simeq S_\infty(k)$, by analogy of $\int d\mathbf{r}\,\Psi_N^2(\mathbf{r})$ to the configuration integral of classical systems. Then, the dominate size error is given by the replacement of the discrete summation in reciprocal space by an integration is

$$\mathcal{V}_\infty - \mathcal{V}_N = \bigg(\int\frac{d\mathbf{k}}{(2\pi)^3} - \frac{1}{V}\sum_{\mathbf{k}\neq 0}\bigg)\frac{v_k}{2}\big(S_\infty(k){-}1\big). \tag{50}$$

Nonanalytical behavior of the integrand will dominate the quadrature error. Since v_k diverges at the origin, leading order corrections can be determined by focusing on the integration around $k \to 0$. The dominating term is actually the Madelung constant, e.g., the contribution of the interaction of one particle with all its periodic imagines,

$$v_M = -\bigg(\int\frac{d\mathbf{k}}{(2\pi)^3} - \frac{1}{V}\sum_{\mathbf{k}\neq 0}\bigg)\frac{v_k}{2} \sim \sum_{\mathbf{n}\neq 0}\frac{1}{|\mathbf{n}|L} \sim N^{-1/3} \tag{51}$$

and Ewald's method should be used for evaluation [24–26].

Since $S(k) \sim k^2$ for charged systems, with the prefactor fixed by sum rules, the next order term corresponds to the missing term with $k = 0$ in the summation on the rhs of Eq. (50), $\lim_{k\to 0} v_k S(k)/V \sim N^{-1}$. Similar to the Madelung constant, this term depends only on the shape of the simulation cell. Both terms are therefore easily corrected for [70].

Seemingly innocent, the quadratic behavior of $S(k)$ around the origin is due to charge density fluctuations, the plasmons. The size correction of the potential energy $\sim N^{-1}$ corresponds to including half of the zero point energy of the long wavelength plasmons which do not fit inside the simulation cell. Kinetic energy corrections will add the missing other half of the plasmon energies [70].

For neutral quantum particles, these size corrections decay slightly faster $\sim N^{-4/3}$, since the energy of the long wave length phonon modes vanish linearly in $|\mathbf{k}|$, and one can show that $S(k) \sim k$ in this case.

Understanding size effects can be a powerful tool. Using all information of calculations at a single system size, allows us to make reliable predictions of thermodynamic limit values. This is particularly important for calculations on hydrogen discussed later, where several calculations varying system sizes are hardly affordable.

We have outlined above, that finite size effects on the electronic ground state energy are intrinsically connected to non-analytical behavior of the wave function. Beyond shell effects, the behavior of the structure factor $S(k) \sim k^\alpha$ for $k \to 0$ determines the exponent of the leading order power law $\mathcal{E}_\infty - \mathcal{E}_N \sim N^{-(\alpha+1)/3}$ for the total energy per particle, $\mathcal{E}_N \equiv E/N$ in the case of Coulomb interactions. Although the exponent as well as the prefactor of $S(k)$ can be determined via general considerations, inaccuracies in the trial wave function, either due to limitations of the functional form or due to insufficient optimization, might lead to deviations which then propagate to size effects.

Of course, such predictions depend crucially on the underlying assumptions, as well as on the actual values for the asymptotics, e.g., extrapolating $\lim_{k\to 0} S(k)/k^2$ from our finite size data. Estimating the error of such procedures is a difficult task. Whenever affordable, numerical extrapolations of different system sizes provide important cross-checks.

Pure numerical extrapolation of size effects is delicate as our computations actually only guarantee upper bounds to the exact ground state energies. As the computational cost for optimization as well as for projection methods like DMC strongly increase with system size, deteriorations of the energies for large system sizes as compared to those predicted based on finite size corrections, may actually indicate convergence problems in the data.

Here, we have focused on the error of the ground state energy. Similar considerations apply for other observables, in particular for the pressure. Using the virial estimator for Coulomb systems, size effects on the pressure can be obtained from the separate information on kinetic and potential energy corrections.

2.5 Monte Carlo calculations with noisy action

Above we have discussed the main systematic errors of QMC calculations together with some strategies to estimate and reduce them. However, when using QMC energies in Born-Oppenheimer calculations for the nuclei, we also have to address the stochastic error. To be concrete, let us discuss Monte Carlo calculations for classical nuclei distributed by the Boltzmann weight $\sim e^{-\beta E_\mathbf{R}}$ according to the Born-Oppenheimer ground state energies $E_\mathbf{R} \equiv E_0(\mathbf{R})$.

Using QMC methods to determine electronic energies we do not have access to $E_{\mathbf{R}}$ with arbitrary precision. Our QMC calculations output $\varepsilon = E_{\mathbf{R}}+r$ where r is the error due to the stochastic noise. Assuming the error is Gaussian distributed, $g(\varepsilon|E_{\mathbf{R}}\sigma^2_{\mathbf{R}}) \sim e^{-(\varepsilon-E)^2/2\sigma^2}$ with variance $\sigma^2_{\mathbf{R}}$, the configuration integral can be written

$$Z = \int d\mathbf{R}\, e^{-\beta E_{\mathbf{R}}} = \int d\varepsilon \int d\mathbf{R}\, e^{-\beta\varepsilon-\beta^2\sigma^2_{\mathbf{R}}/2} g(\varepsilon|E_{\mathbf{R}}\sigma^2_{\mathbf{R}}) \tag{52}$$

where the last equality can be verified by explicit integration over ε. It is then straightforward to perform Monte Carlo calculations using the noisy energies ε. However, we need to replace the (unknown) exact values of the energies, $E_{\mathbf{R}}$, by $\varepsilon+\beta\sigma^2/2$ in the Metropolis acceptance ratio, where ε is our QMC estimate of known variance $\sigma^2 \equiv \sigma^2_{\mathbf{R}}$. We are thus able to obtain unbiased samples of $\mathbf{R}$ according to the Boltzmann weight of the energies $E_{\mathbf{R}}$ without ever calculating them exactly!

It is instructive to formulate such an algorithm in more detail. Our Monte Carlo state vector is actually specified by $(\mathbf{R}, \varepsilon)$ with weight

$$\Pi(\mathbf{R}, \varepsilon) = e^{-\beta\varepsilon-\beta^2\sigma^2_{\mathbf{R}}/2} g(\varepsilon|E_{\mathbf{R}}\sigma^2_{\mathbf{R}}) \tag{53}$$

and our transition probability of the Markov chain is given by

$$T(\mathbf{R}\varepsilon \to \mathbf{R}'\varepsilon') = \mathcal{A}(\mathbf{R} \to \mathbf{R}')\, g(\varepsilon'|E_{\mathbf{R}'}\sigma^2_{\mathbf{R}'})\, a(\mathbf{R}\varepsilon \to \mathbf{R}'\varepsilon') \tag{54}$$

where $\mathcal{A}(\mathbf{R} \to \mathbf{R}')$ is the a-priori probability for the proposed move and the acceptance probability is given by the Metropolis-Hastings rule

$$a(\mathbf{R}\varepsilon \to \mathbf{R}'\varepsilon') = \min\left[1, \frac{\Pi(\mathbf{R}', \varepsilon')}{\Pi(\mathbf{R}, \varepsilon)} \frac{\mathcal{A}(\mathbf{R}' \to \mathbf{R})}{\mathcal{A}(\mathbf{R} \to \mathbf{R}')} \frac{g(\varepsilon|E_{\mathbf{R}}\sigma^2_{\mathbf{R}})}{g(\varepsilon'|E_{\mathbf{R}'}\sigma^2_{\mathbf{R}'})}\right] \tag{55}$$

$$= \min\left[1, e^{-\left(\beta(\epsilon'-\epsilon)+\beta^2(\sigma^2_{\mathbf{R}'}-\sigma^2_{\mathbf{R}})/2\right)} \frac{\mathcal{A}(\mathbf{R}' \to \mathbf{R})}{\mathcal{A}(\mathbf{R} \to \mathbf{R}')}\right] \tag{56}$$

satisfying detailed balance

$$\Pi(\mathbf{R}, \varepsilon)\, T(\mathbf{R}\varepsilon \to \mathbf{R}'\varepsilon') = \Pi(\mathbf{R}', \varepsilon')\, T(\mathbf{R}'\varepsilon' \to \mathbf{R}\varepsilon). \tag{57}$$

Therefore, $\Pi(\mathbf{R}, \varepsilon)$ will be a stationary distribution of our Markov chain, so that the correct unbiased Boltzmann distribution results via integration over ε, yielding unbiased expectation values of all observables involving $\mathbf{R}$ without explicit dependence on $E_{\mathbf{R}}$ (or ε), e.g., nuclear structural properties.

The electronic energies, $E_{\mathbf{R}}$, as well as general electronic properties can be calculated by independent re-sampling of the Born-Oppenheimer wave function at the obtained nuclear configurations. The mere average of ε of the weight $\Pi(\mathbf{R}, \varepsilon)$ will differ from $E_{\mathbf{R}}$ by $\sim \beta\sigma^2$.

But why should we actually store the value of ε, and return to this value whenever our attempted move to a new configuration $(\mathbf{R}'\varepsilon')$ is rejected? After all ε is a gaussian variable which is integrated over stochastically.

We should rather try to construct a Markov chain where our uncertainty is only entering inside a transition probability which depends on the energy difference $\Delta\varepsilon = E_{\mathbf{R}'} - E_{\mathbf{R}} + r$ with gaussian errors r

$$T(\mathbf{R} \to \mathbf{R}') = \int d\Delta\varepsilon \, \widetilde{T}(\mathbf{R} \to \mathbf{R}'; \Delta\varepsilon) \tag{58}$$

Let us plug Eq. (58) into the usual detailed balance condition

$$e^{-\beta E_{\mathbf{R}}} \int d\Delta\varepsilon \, \widetilde{T}(\mathbf{R} \to \mathbf{R}', \Delta\varepsilon) = e^{-\beta E_{\mathbf{R}'}} \int d\Delta\varepsilon \, \widetilde{T}(\mathbf{R}' \to \mathbf{R}; \Delta\varepsilon). \tag{59}$$

As long as $\widetilde{T}$ satisfies Eq. (59), our Markov chain based on the transition probability Eq. (58) will converge to the correct equilibrium distribution. Replacing the deterministic integration in the transition matrix, Eq. (58), with a stochastic evaluation of the integral over the noise cannot affect the asymptotic, stationary distribution of the Markov chain, and we will still converge to the correct, unbiased equilibrium distribution. Therefore, it is enough that our new transition matrix $\widetilde{T}$ is determined by Eq. (59) such that detailed balance for $\widetilde{T}$ needs only to be satisfied on average. In Ref. [72] it has been shown that

$$\widetilde{T}(\mathbf{R} \to \mathbf{R}'; \Delta\varepsilon) = g\big(\Delta\varepsilon | E_{\mathbf{R}'} - E_{\mathbf{R}}, \sigma^2\big) \min\Big(1, \, e^{-\beta\Delta\varepsilon - \beta^2\sigma^2/2}\Big) \tag{60}$$

satisfies detailed balance on average, Eq. (59). Since the variance of the energy difference reduces the acceptance probability, the algorithm for the random walk with uncertain energies has been called penalty method. Uncertainty in the variance can be similarly taken into account, but modifies the acceptance ratio further [72].

3 Coupled electron-ion Monte Carlo calculations

Coupled Electron-Ion Monte Carlo (CEIMC) calculations [73, 74] sample the discretized path-integral representation of nuclei in the Born-Oppenheimer approximation, Eqs (11,12), using Monte Carlo methods, both for the nuclear degrees of freedom, and for the determination of the adiabatic electronic ground state energies $E_0(\mathbf{R})$. So far, calculations have been performed for discernible nuclei, neglecting ionic exchange effects as well as excitations to higher electronic energy surfaces and effects of a possible Berry phase.

Electronic energies are calculated by ground state QMC methods as described above, the penalty methods is used to provide unbiased sampling of the nuclear degrees of freedom despite the intrinsic stochastic error in the Born-Oppenheimer energy surface.

Accuracy of the electronic energies is of crucial importance to provide meaningful comparisons and predictions for experiment. This requires robust high quality trial wave functions for the electronic Born-Oppenheimer ground state, as well as elimination of dominating finite size effects on the fly for each set of nuclear positions, $\mathbf{R}$.

The trial wave functions are build out of orbitals obtained from a separate density-functional (DFT) calculation at each nuclear configuration, many-body correlations are included via analytical expressions for Jastrow, three-body, and backflow potentials with parametric dependence on the nuclear coordinates [39, 75] augmented by simple functional forms which are optimized over representative samples of nuclear positions. This provides an accurate and smooth parametrization of the trial wave functions over all relevant nuclear configurations avoiding on-the-fly optimizations. Although the orbitals have been determined by DFT, the dependence on the underlying DFT functional is weakened by the presence of the explicit many-body correlations in the wave function. Ultimately, the selection of the DFT flavor is based on the variational principle, similar to the functional choice and parametrization of the Jastrow, three-body and backflow functions.

Electronic energies are systematically averaged over twisted boundary conditions (TABC) for each nuclear configuration to reduce the influence of the finite simulation cell. This is particularly important, because shell effects strongly bias nuclear configurations on an energy scale easily exceeding the nuclear temperature. The use of TABC in CEIMC is almost for free, since the averaging of independent calculations with different twists reduces the overall stochastic error and can be implemented massively parallel.

More details concerning the methodology of CEIMC calculations can be found in Ref. [74]. Most of the CEIMC calculations so far have used VMC energies for the Born-Oppenheimer energy surface. Additional projection in imaginary time using RMC or DMC provides an overall lowering of the energies, typically smooth and weakly depend on the nuclear constellation. Such effects can be quantified a-posteriori by reweighting selected configurations of CEIMC trajectories based on VMC energies. Similarly, the influence of different DFT functionals used for the orbitals in VMC, as well as optimization of more flexible functional forms for the many-body correlations can be estimated and quantified, if necessary. Reweighting methods are expected to work, as long as structural properties are not strongly modified, e.g., the energy landscape for the nuclei is not significantly changed.

Since CEIMC calculations are computationally expensive, it is in general not possible to explore a phase diagram like that of hydrogen in Fig. 1 fully from scratch. Rather, less expensive DFT calculations are typically used for structural optimization at fixed pressure either at zero or finite temperatures which provide the shape of the simulation cell used in fixed volume CEIMC calculations. Analyzing the subsequent CEIMC results may then provide indications to either confirm or question such a procedure.

Vice-versa, QMC energies of selected configurations can be used to benchmark DFT functionals [76] or to train a machine-learned effective potential [14, 77, 22] such to fully explore phase diagrams and afford molecular dynamics calculations on much bigger length and time scales. The resulting candidate phases can then be explored more precisely within CEIMC.

One of the most appealing features of CEIMC calculations is the possibility to improve existing results on a long term by separately addressing the various assumptions or simplifications used in practice and outlined in the computational methods section above. The underlying variational principle provides an unambiguous criterium to improve and judge the quality of CEIMC results. Use of Langevin dynamics based on QMC forces within the Born-Oppenheimer approximation has also been developed [78], providing comparable results to CEIMC [21, 22].

4 Hydrogen under pressure: Some CEIMC results

Predicting and exploring phases of high pressure hydrogen and deuterium with particular focus on solid phases and on the liquid-liquid phase transition has been one of the main motivations for developing CEIMC. Further, since the major fraction of hydrogen in the universe is in the fluid phase, establishing an accurate equation of state for hydrogen and hydrogen-helium mixtures, pressure as a function of temperature, density, and composition, is relevant for planetary models. Beyond pure structural properties, e.g., the crystal structure in the various solid phases, the existence and location of possible insulator to metal transitions, and their connection to a molecular to atomic transition is one of the longest outstanding issues of high pressure research.

Since CEIMC calculations are based on the many-body density matrix, electronic properties can be probed beyond the single particle approximation. In particular, off-diagonal matrix elements of the reduced single particle density matrix can be calculated and used to determine localized (insulating) or extended (metallic) behavior of the electrons. Furthermore, electronic excitation gaps can be calculated within QMC accuracy as discussed below, providing more direct information on the transition to metallic hydrogen.

4.1 Electronic band gaps

From a theoretical point of view, band insulators and semiconductors are characterized by a nonvanishing value of the fundamental gap [63]

$$\widetilde{\Delta} = E_0(N_n{+}1) + E_0(N_n{-}1) - 2E_0(N_n) \tag{61}$$

where $E_0(N_e)$ denotes the electronic ground state energy of a system of N_e electrons where the number N_n and positions of nuclei are kept fixed, and charge neutrality is assured by applying a uniform background charge. Since Eq. (61) only involves electronic ground state energies, ground state QMC methods can be applied straightforwardly to obtain upper bounds for $E_0(N_n)$ as well as for $E_0(N_n{\pm}1)$. Although this does not guarantee us an upper bound for the gap, we can still use the variational principle to judge the quality of all the quantities involved.

Above, we have discussed the importance of size effects on the electronic energies per particle, $E(N_e)/N_e$. In Eq. (61) this extensive part of the ground state energies will drop out, since the gap itself is an intensive quantity. Calculations of gaps may therefore require higher control of size effects. A detailed discussion is given in Ref. [79] where it is shown that the fundamental gap approaches slowly its value in the thermodynamic limit, inversely proportional to the linear extension of the simulation cell, $\sim (\epsilon L)^{-1}$. Leading order finite size corrections are given in terms of the dielectric constant, ϵ, and can be determined within calculations of the same system size. Similar to ground state energy calculations, predictions for the thermodynamic limit value of the gap can thus be made without the need to extrapolate numerically results for different system sizes.

For hydrogen, the definition of the fundamental gap, Eq. (61), needs to be modified to take into account nuclear quantum effects

$$\Delta = F(N_n{+}1) + F(N_n{-}1) - 2F(N_n) \tag{62}$$

where $F(N_e) = -T \log Z(N_e)$ denotes the free energy of the system containing N_e electrons and N_n nuclei at temperature T. Within the Born-Oppenheimer approximation, we have

$$Z(N_n{\pm}1) = Z(N_n)\left\langle e^{-\beta[E_{\mathbf{R}}(N_n\pm1)-E_{\mathbf{R}}(N_n)]}\right\rangle \geq e^{-\beta\langle E_{\mathbf{R}}(N_n\pm1)-E_{\mathbf{R}}(N_n)\rangle} \tag{63}$$

where $\langle\cdots\rangle \equiv \mathbb{E}_{\mathbf{R}\sim\pi}[\cdots]$ denotes the averaging over the probability distribution of the nuclei according to the Born-Oppenheimer energies of $N_e = N_n$ electrons.

Due to the homogeneous background charge added to the electron/hole-doped systems with $N_e = N_n{\pm}1$, the density of the additional electron/hole is necessarily smeared out over the whole simulation cell. Therefore, the modification of the Born-Oppenheimer energy surface of the doped system uniformly approaches the one of the neutral system up to corrections of $1/N_n$, so that the equality in Eq. (63) applies in the thermodynamic limit. We thus have

$$\varDelta = \big\langle E_{\mathbf{R}}(N_n{+}1) + E_{\mathbf{R}}(N_n{-}1) - 2E_{\mathbf{R}}(N_n)\big\rangle \equiv \big\langle \widetilde{\varDelta}_{\mathbf{R}}\big\rangle \tag{64}$$

and the fundamental gap is obtained by averaging the Born-Oppenheimer gap, $\widetilde{\varDelta}_{\mathbf{R}}$, over the distribution of the nuclei, baptized "quantum average" [80].

Note, that the definition of the fundamental gap, Eq. (62), is given in terms of thermodynamic quantities and does in general not coincide with the spectroscopic gap entering linear response functions given by the minimal difference between two energy eigenstates of the full electron-proton system. In particular, in the semi-classical region the spectroscopic gap is given by the minimum of the Born-Oppenheimer gap, $\widetilde{\varDelta}_{\mathbf{R}}$ with respect to the nuclear configurations $\mathbf{R}$. Thus, the resulting semi-classical gap is in general smaller than the average value of the fundamental gap, Eq. (64). However, such a semi-classical description looses its meaning when nuclear quantum effects become important. At zero temperature, averaging over nuclear configurations corresponds to taking the nuclear ground state expectation value, and the spectroscopic gap for electron/hole excitations will coincide in that limit with the quantum averaged fundamental gap, Eq. (64).

The above discussion can be extended for neutral (optical) gaps of particle-hole excitations with same number of electrons and nuclei, $N_e = N_n$ [81, 82]. However, electron-hole excitations eventually localize and bind together. Size effects on the neutral gap will eventually differ from those of the fundamental gap when the simulation cell reaches the size of the localization length and the electronic wave function can account for excitonic effects. Further, spatial localization of excitons may then also affect the Born-Oppenheimer energy surface of the excitation, differing from the ground state energy surface in this localized region, an effect not necessarily negligible in the thermodynamic limit. Such a modification is neglected when averaging the neutral Born-Oppenheimer excitation energies over the nuclear configurations of the electronic ground state energy surface, so that the resulting averaged gaps represent in general only upper bounds. Approaching the metallic state, such localization effects will vanish and not affect the determination of the insulator to metal transition.

In Fig. 2 are shown the results of a detailed study of the electronic excitation energies of phase I hydrogen at room temperature [82]. The fundamental (or quasi-particle) gap, $\varDelta_{qp}$, determined

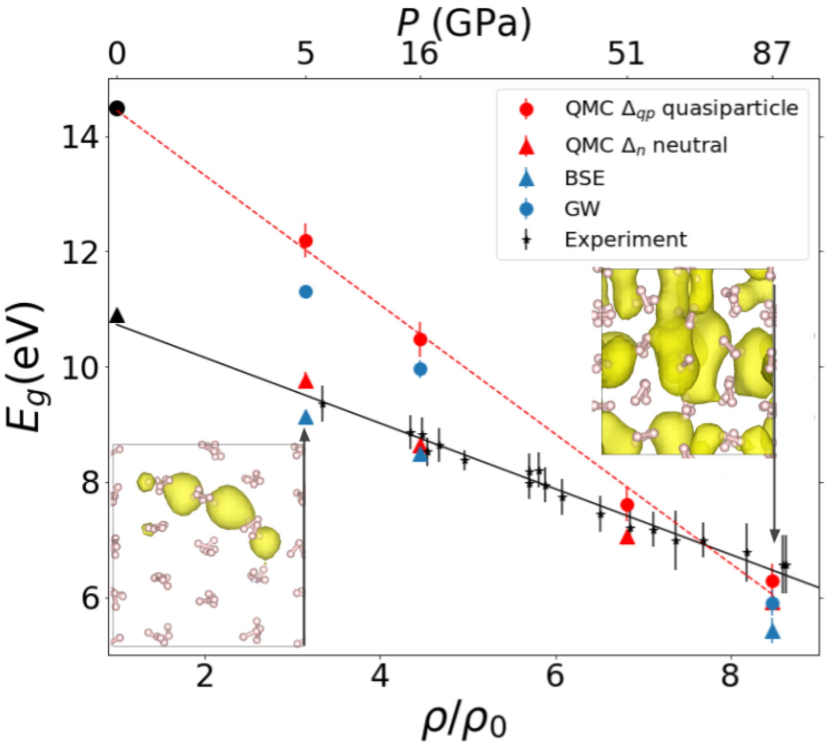

Fig. 2: *Fundamental gap of quasi-particle ($\varDelta_{qp}$) and neutral ($\varDelta_n$) electronic excitations for phase I hydrogen at room temperature from QMC calculations and many-body perturbation theory (GW, BSE) [82]. Experimental values of the gap are determined from IXS spectra [83].*

by Eq. (64), and the corresponding neutral gap $\varDelta_n$ of particle-hole excitations from QMC calculations are compared with those obtained by many-body perturbation theory, charged excitations from GW, and neutral ones from solutions of the Bethe-Salpeter equation (BSE). In the pressure range between 5 and 90 GPa, the system changes from a wide-gap molecular insulator to a semiconductor. Differences between $\varDelta_{qp}$ and $\varDelta_n$ are due to excitonic effects and decrease with pressure, ~ 2 eV at 5 GPa down to ~ 0.5 eV at 90 GPa. Thermal and quantum nuclear motion reduces the gap by ~ 2 eV with respect to the ideal structure, roughly independent of pressure. Experimental values have been obtained by inelastic X-ray scattering (IXS) from the lower limit of the phonon energy-loss spectra [83].

4.2 Approaching metallic solid hydrogen

The metallization of crystalline hydrogen under pressure has been one of the driving forces of high pressure physics. Below 200 K, in phase III, experiments indicate a transition to a semimetallic state at 350 GPa [7], but synchrotron infrared spectroscopy measurements show that the direct gap remains open up to 425 GPa with an abrupt collapse attributed to metallization [8]. Structural information of phase III is indirect via vibrational spectroscopy. In Ref. [80], we have studied two candidate structures, Cmca-12 and C2/c-24, in CEIMC calculations at 200 K including nuclear thermal and quantum effects. The fundamental electronic gap has then been calculated for a subset of the sampled nuclear configurations using reptation

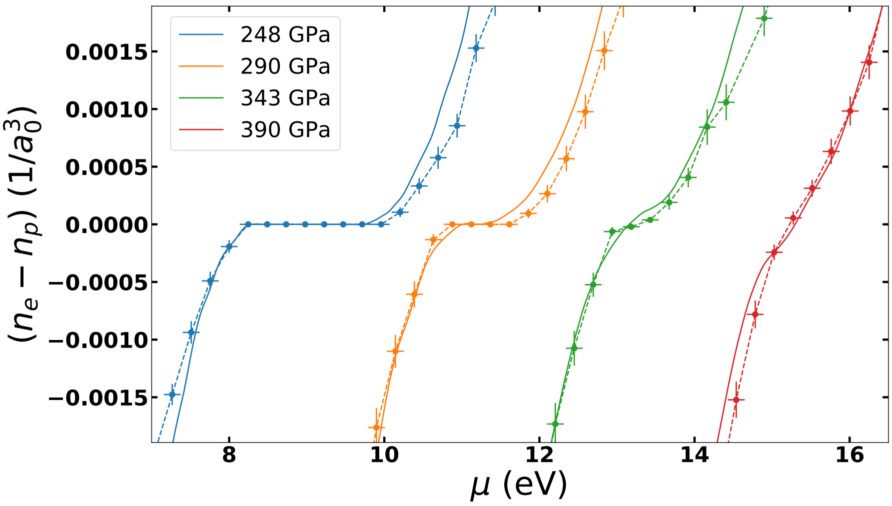

Fig. 3: *Electronic excess density* $n_e - n_p$ *as a function of the chemical potential for solid hydrogen in the C2/c-24 structure (candidate for phase III) at* 200 *K from QMC using GC-TABC (points) compared to DFT-HSE (smooth lines) at various pressures [80]. The observed plateau when the electronic density coincides with the protonic one,* $n_e = n_p$*, at the lower pressures is a signature of the (indirect) gap. It is closing around* $P \approx 370-380$ *GPa.*

Monte Carlo methods combined with grand-canonical twist averaging (GC-TABC) and leading and next-to-leading order finite size corrections.

Figure 3 shows the electronic excess density as a function of the electronic chemical potential in the C2/c-24 structure at 200 K. The incompressible behavior $\partial_\mu n_e = 0$ is characteristic for an insulator, the width of the plateau of the undoped system ($n_e = n_p$) corresponds to the fundamental gap.

Analysis of the electronic states at the edges of the gap shows that the corresponding fundamental gap is indirect [84]. The closure of the indirect gap occurs around 380 GPa for C2/c-24 (340 GPa for Cmca-12). Information on the direct gap can be obtained by unfolding the bandstructure of the simulation cell. The direct gap remains open until ~ 450 GPa for C2/c-24 (500 GPa for Cmca-12). The calculations thus indicate a formation of a bad metal upon closure of the indirect gap, but the solid remains black (absorbing) until closure of the direct gap, a qualitative scenario supporting experimental observations.

4.3 Liquid-liquid phase transition

At higher temperatures, the solid melts to a molecular fluid at the low pressure side, whereas monatomic fluid hydrogen is expected at high pressure. Born-Oppenheimer molecular dynamics simulations using DFT and CEIMC calculations [85, 13, 86, 75] predict a first order liquid-liquid phase transition from the molecular to the atomic fluid below a critical temperature somewhere between 2000 and 3000 K.

The structural transition from the molecular to the atomic liquid is expected to coincide with an insulator to metal transition. Optical conductivity, reflectivity, and absorption can be computed within DFT methods [19], but a dependence on the underlying DFT functional remains.

Within CEIMC, the change of nature from the insulating to the metallic fluid can be detected in the reduced single-body density matrix of the many-electron ground state. Whereas the off-diagonal part, $n(r)$, decays exponentially for large distances r in the insulator, an algebraic decay $\sim r^{-3}$ indicates Fermi-liquid behavior of a metal with a sharp Fermi surface [18, 87]. Calculations of the fundamental electronic gap in the liquid [20] further confirm that molecular-atomic and insulator-metal transition occur together [87, 88].

Experiments probing the liquid-liquid phase transition have been performed with diamond anvil cells (DAC) [15] or by dynamic compression [16, 17], but temperature is not directly measured in the shock wave experiments and the interpretation of the data is sensitive to the adopted model. In Fig. 1, we show the transition from molecular to atomic hydrogen inferred from DAC experiments [15] in comparison with the CEIMC predictions [18].

However, recent calculations of the melting of the solid with a machine learned potential based on QMC Born-Oppenheimer energies [14] (not shown in Fig. 1) have questioned the experimental melting line inferred from Raman spectroscopy [12], predicting melting at considerably higher temperatures with the reentrant part getting very close to the liquid-liquid phase transition indicated by CEIMC. Further studies, theoretical and experimental, will be needed to firmly establish the phase diagram in that region.

4.4 Hugoniot adiabatic

Dynamic compression techniques can be used to experimentally probe the equation of state up to high pressures and temperatures [89]. Assuming that the shock is created by a planar surface, hydrodynamics relates the discontinuity in the energy, pressure, and density occurring at the shock by energy and momentum conservation by [90]

$$E(n,T)-E_0+\frac{1}{2}\left(n^{-1}-n_0^{-1}\right)\left(P(n,T)+P_0\right)=0 \tag{65}$$

where E_0 and n_0^{-1} are the initial values of the energy per atom and volume per atom at the equilibrium pressure P_0 and temperature T_0 before the shock. Only values of the equation of state which satisfy Eq. (65), the so-called shock or Hugoniot adiabatic, can be reached on the other side of the discontinuity surface with energy per particle $E(n,T)$ and pressure $P(n,T)$ at the volume per particle n^{-1} and temperature T.

Given the initial conditions, E_0, n_0, and P_0, and knowledge of the equation of state in the fluid, $E(n,T)$ and $P(n,T)$, the Hugoniot adiabat then determines the line of P vs. n (or compression n/n_0) which can be compared to experimental measurements of P and n at the shock.

CEIMC calculations of the deuterium Hugoniot result in close agreement to measurements at low pressures [91], but predict a larger compression than experiments at higher pressure [91,92]. The origin of the discrepancies remains still unclear as similar differences have been observed by independent calculations of QMC quality [93, 22].

Acknowledgments

I want to thank Carlo Pierleoni and David Ceperley for having introduced me to the physics of hydrogen more than twenty years ago and for ongoing collaborations since then.

References

[1] M. Born and R. Oppenheimer, Ann. Phys. **389**, 457 (1927)

[2] I.F. Silvera, Rev. Mod. Phys. **52**, 393 (1980)

[3] J.M. McMahon, M.A. Morales, C. Pierleoni, and D.M. Ceperley, Rev. Mod. Phys. **84**, 1607 (2012)

[4] J. Cheng *et al.*, Nature **573**, 558 (2019)

[5] J. Cheng *et al.*, Matter and Radiation at Extremes **5**, 038401 (2020)

[6] E. Wigner and H.B. Huntington, J. Chem. Phys. **3**, 764 (1935)

[7] M.I. Eremets, A.P. Drozdov, P.P. Kong, and H. Wang, Nat. Phys. **15**, 1246 (2019)

[8] P. Loubeyre, F. Occelli, and P. Dumas, Nature **577**, 631 (2020)

[9] R.P. Dias and I.F. Silvera, Science **355**, 715 (2017)

[10] P. Loubeyre, F. Occelli, and P. Dumas, arXiv:1702.07192

[11] M.I. Eremets and A.P. Drozdov, arXiv:1601.04479

[12] C.-S. Zha, H. Liu, J.S. Tse, and R.J. Hemley, Phys. Rev. Lett. **119**, 075302 (2017)

[13] M.A. Morales, C. Pierleoni, E. Schwegler, and D.M. Ceperley, Proc. Natl. Acad. Sci. USA **107**, 12799 (2010)

[14] H. Niu, Y. Yang, S. Jensen, M Holzmann, C. Pierleoni, and D.M. Ceperley, Phys. Rev. Lett. **130**, 76102 (2023)

[15] M. Zaghoo, A. Salamat, and I.F. Silvera, Phys. Rev. **B 93**, 155128 (2016)

[16] M.D. Knudson, M.P. Desjarlais, A. Becker, R.W. Lemke, K.R. Cochrane, M.E. Savage, D.E. Bliss, T.R. Mattsson, and R. Redmer, Science **348**, 1455 (2015)

[17] P.M. Celliers, M. Millot, S. Brygoo, R.S. McWilliams, D.E. Fratanduono, J.R. Rygg, A.F. Goncharov, P. Loubeyre, J.H. Eggert, J.L. Peterson, N.B. Meezan, S. Le Pape, G.W. Collins, R. Jeanloz, and R.J. Hemley, Science **361**, 677 (2018)

[18] C. Pierleoni, M.A. Morales, G. Rillo, M. Holzmann, and D.M. Ceperley, Proc. Natl. Acad. Sci. USA **113**, 4954 (2016)

[19] G. Rillo, M.A. Morales, D.M. Ceperley, and C. Pierleoni, Proc. Natl. Acad. Sci. USA 116, 9770 (2019)

[20] V. Gorelov, D.M. Ceperley, M. Holzmann, and C. Pierleoni, Phys. Rev. B **102**, 195133 (2020)

[21] G. Mazzola, R. Helled, and S. Sorella, Phys. Rev. Lett. **120**, 025701 (2018)

[22] G. Tenti, K. Nakano, A. Tirelli, S. Sorella, M. Casula, Phys. Rev. B **110**, L041107 (2024)

[23] M. Bonitz *et al.*, arXiv 2405.106238

[24] P.P. Ewald, Ann. Phys. **64** (1921) 253.

[25] D. Frenkel and B. Smit: *Understanding molecular simulation: from algorithms to applications* (Academic Press, San Diego, 2002)

[26] M.P. Allen and D.J. Tildesley: *Computer Simulation of Liquids* (Oxford Univ. Press, 2017)

[27] H. Trotter, Proc. Am. Math. Soc. **10**, 545 (1959)

[28] R. Feynman: *Statistical Mechanics: A Set of Lectures* (Benjamin, New York, 1972)

[29] D.M. Ceperley, Rev. Mod. Phys. **67**, 279 (1995)

[30] M. Boninsegni, N.V. Prokofev, and B.V. Svistunov, Phys. Rev. **E 74**, 036701 (2005)

[31] D. Marx and J. Hutter, *Ab initio Molecular Dynamics:*
Basic Theory and Advanced Methods, (Cambridge University Press, 2009)

[32] A. Bijl, Physica **7**, 869 (1940)

[33] R.B. Dingle, Phil. Mag. **40**, 573 (1949)

[34] R. Jastrow, Phys. Rev. **98**, 1479 (1955)

[35] E. Feenberg, *Theory of Quantum Fluids* (Academic Press, New York, 1969)

[36] R.P. Feynman and M. Cohen, Phys. Rev. **102**, 1189 (1956)

[37] V.R. Pandharipande and N. Itoh, Phys. Rev. A **8**, 2564 (1973)

[38] K.E. Schmidt and V.R. Pandharipande, Phys. Rev. B **19**, 2504 (1979)

[39] M. Holzmann, D.M. Ceperley, C. Pierleoni, and K. Esler, Phys. Rev. E **68**, 046707 (2003)

[40] M. Holzmann, B. Bernu, and D.M. Ceperley, Phys. Rev. B **74**, 104510 (2006)

[41] M. Taddei, M. Ruggeri, S. Moroni, and M. Holzmann, Phys. Rev. B **91**, 115106 (2015)

[42] M. Ruggeri, S. Moroni, and M. Holzmann, Phys. Rev. Lett. **120**, 205302 (2018)

[43] M. Holzmann and S. Moroni, Phys. Rev. B **99**, 085121 (2019)

[44] M. Holzmann and S. Moroni, Phys. Rev. Lett. **124**, 206404 (2020)

[45] G. Pescia, J. Han, A. Lovato, J. Lu, and G. Carleo, space, Phys. Rev. Res. **4**, 023138 (2022)

[46] X. Li, Z. Li, and J. Chen, Nat Commun. **13**, 7895 (2022)

[47] M. Wilson, S. Moroni, M. Holzmann, N. Gao, F. Wudarski, T. Vegge, and A. Bhowmik, Phys. Rev. B **107**, 235139 (2023)

[48] G. Cassella, H. Sutterud, S. Azadi, N.D. Drummond, D. Pfau, J.S. Spencer, and W.M.C. Foulkes, Phys. Rev. Lett. **130**, 036401 (2023)

[49] H. Xie, Z.-H. Li, H. Wang, L. Zhang, and L. Wang, Phys. Rev. Lett. **131**, 126501 (2023)

[50] G. Pescia, J. Nys, J. Kim, A. Lovato, and G. Carleo, arxXiv:2305.07240

[51] W.L. McMillan, Phys. Rev. **138**, A442 (1965)

[52] D. Ceperley, G.V. Chester, and M.H. Kalos, Phys. Rev. B **16**, 3081 (1977)

[53] D. Ceperley, Phys. Rev. B **18**, 3126 (1978)

[54] W.H. Press, S.A. Teukolsky, W.T. Vetterling, and B.P. Flannery: *Numerical Recipes* (Cambridge University Press, 1992)

[55] H. Robbins and S. Monro, Ann. Math. Stat. **22**, 400 (1951)

[56] F. Becca and S. Sorella, *Quantum Monte Carlo approaches for correlated systems* (Cambridge University Press, 2017)

[57] G. Carleo and M. Troyer, Science **355**, 602 (2017)

[58] D. Pfau, J.S. Spencer, A.G.D.G. Matthews, and W.M.C. Foulkes, Phys. Rev. Res. **2**, 033429 (2020)

[59] J. Hermann, Z. Schätzle, and F. Noé, Nat. Chem. **12**, 891 (2020)

[60] S. Baroni and S. Moroni, Phys. Rev. Lett. **82**, 4745 (1999)

[61] C. Pierleoni and D. Ceperley, Chem. Phys. Chem. **6**, 1872 (2005)

[62] B.L. Hammond, W.A. Lester Jr., and P.J. Reynolds: *Monte Carlo Methods in ab initio Quantum Chemistry* (World Scientific, Singapore, 1994)

[63] R.M. Martin, L. Reining, and D.M. Ceperley, *Interacting Electrons* (Cambridge University Press, 2016)

[64] M. Boninsegni and S. Moroni, Phys. Rev. E **86**, 056712 (2012)

[65] D.M. Ceperley, J. Stat. Phys. **63**, 1237 (1991)

[66] P.J. Reynolds, D.M. Ceperley, B.J. Alder, W.A. Lester, Jr., J. Chem. Phys. **77**, 5593 (1982)

[67] W.M. Foulkes, L. Mitas, R.J. Needs, and G. Rajagopal, Rev. Mod. Phys. **73**, 33 (2001)

[68] G. Ortiz, D.M. Ceperley, and R.M. Martin, Phys. Rev. Lett. **71**, 2777 (1993)

[69] C. Lin, F.-H. Zong, and D.M. Ceperley, Phys. Rev. E **64**, 016702 (2001)

[70] S. Chiesa, D.M. Ceperley, R.M. Martin, M. Holzmann, Phys. Rev. Lett. **97**, 076404 (2006)

[71] M. Holzmann, R.C. Clay, III, M.A. Morales, N.M. Tubman, D.M. Ceperley, and C. Pierleoni, Phys. Rev. B **94**, 035126 (2016)

[72] M. Dewing and D.M. Ceperley, J. Chem. Phys. **110**, 9812 (1999)

[73] C. Pierleoni, D.M. Ceperley, and M. Holzmann, Phys. Rev. Lett. **93**, 146402 (2004)

[74] C. Pierleoni and D.M. Ceperley: *The Coupled Electron-Ion Monte Carlo Method* Lect. Notes Phys. **703**, 641 (2006)

[75] C. Pierleoni, K.T. Delaney, M.A. Morales, D.M. Ceperley, and M. Holzmann, Comp. Phys. Commun. **179**, 89 (2008)

[76] R.C. Clay, M. Holzmann, D.M. Ceperley, M.A. Morales, Phys. Rev. B **93**, 035121 (2016)

[77] A. Tirelli, G. Tenti, K. Nakano, and S. Sorella, Phys. Rev. B **106**, L041105 (2022)

[78] C. Attaccalite and S. Sorella, Phys. Rev. Lett. **100**, 114501 (2008)

[79] Y. Yang, V. Gorelov, C. Pierleoni, D.M. Ceperley, and M. Holzmann, Phys. Rev. B **101**, 085115 (2020)

[80] V. Gorelov, M. Holzmann, D.M. Ceperley, and C. Pierleoni, Phys. Rev. Lett. **124**, 116401 (2020)

[81] V. Gorelov, Y. Yang, M. Ruggeri, D.M. Ceperley, C. Pierleoni, and M. Holzmann, Condens. Matter Phys. **26**, 33701 (2023)

[82] V. Gorelov, M. Holzmann, D.M. Ceperley, C. Pierleoni, Phys. Rev. B **109**, L241111 (2024)

[83] B. Li, Y. Ding, D.Y. Kim, L. Wang, T.-C. Weng, W. Yang, Z. Yu, C. Ji, J. Wang, J. Shu, J. Chen, K. Yang, Y. Xiao, P. Chow, G. Shen, W.L. Mao, and H.-K. Mao, Phys. Rev. Lett. **126**, 036402 (2021)

[84] V. Gorelov, D.M. Ceperley, M. Holzmann, and C. Pierleoni, J. Chem. Phys. **153**, 234117 (2020)

[85] S. Scandolo, Proc. Natl. Acad. Sci. USA **100**, 3051 (2003)

[86] W. Lorenzen, B. Holst, and R. Redmer, Phys. Rev. B **82**, 195107 (2010)

[87] C. Pierleoni, G. Rillo, D.M. Ceperley, and M. Holzmann, J. Phys.: Conf. Ser. **1136**, 012005 (2018)

[88] C. Pierleoni, M. Holzmann, and D.M. Ceperley, Contrib. Plasma Phys. **58**, 99 (2018)

[89] W. Nellis, Rep. Prog. Phys. **69**, 1479 (2006)

[90] L.D. Landau and E.M. Lifshitz: *Fluid Mechanics* (Pergamon, Oxford, 1987)

[91] M. Ruggeri, M. Holzmann, D.M. Ceperley, C. Pierleoni, Phys. Rev. B **102**, 144108 (2020)

[92] N.M. Tubman, E. Liberatore, C. Pierleoni, M. Holzmann, and D.M. Ceperley, Phys. Rev. Lett. **115**, 045301 (2015)

[93] R.C. Clay III, M.P. Desjarlais, and L. Shulenburger, Phys. Rev. B **100**, 075103 (2019)

15 Many-Body Localization

Julian Léonard
TU Wien
Stadionallee 2, 1020 Wien

Contents

E. Pavarini and E. Koch (eds.)
Correlations and Phase Transitions
Modeling and Simulation Vol. 14
Forschungszentrum Jülich, 2024, ISBN 978-3-95806-751-6
http://www.cond-mat.de/events/correl24

1 Introduction

An important class of systems that give rise to new types of order are non-equilibrium systems. An isolated quantum system that is brought far from equilibrium typically relaxes to a state which is locally described by a thermal ensemble. Although the initial global purity persists, the coupling between any subsystem and remainder of the system mimics the contact with a bath, which drives local thermalization. Few exceptions to this paradigm are known. Disorder, for example, can bring non-equilibrium systems into a many-body-localized (MBL) state where thermalization is absent. In those systems, no local order parameter or symmetry breaking is known, and the role of fluctuations at the transition between thermal and localized states remains to be understood. The distinctive feature of the MBL phase, which may be associated with the order in the system, is the evolution of the non-local entanglement, which leads to a characteristic scaling of the entanglement entropy that is logarithmic in time.

In this lecture we will review experimental work on many-body localization, following the path of three key publications. We first discuss the many-body localized state itself, realized as a disordered, isolated quantum system of a controllable number of atoms in an optical lattice. We will then discuss the critical behavior at intermediate disorder and explore the boundary between the classical dynamics at weak disorder,and the quantum dynamics at strong disorder. Finally, we will talk about the robustness of MBL against a thermal inclusion, and quantum avalanches as a possible instability of MBL at long evolution times. The lecture notes have been published as [1–3].

2 Many-body localization

An interacting quantum system that is subject to disorder may cease to thermalize due to localization of its constituents, thereby marking the breakdown of thermodynamics. The key to our understanding of this phenomenon lies in the system's entanglement, which is experimentally challenging to measure. We realize such a many-body-localized system in a disordered Bose-Hubbard chain and characterize its entanglement properties through particle fluctuations and correlations. We observe that the particles become localized, suppressing transport and preventing the thermalization of subsystems. Notably, we measure the development of non-local correlations, whose evolution is consistent with a logarithmic growth of entanglement entropy, the hallmark of many-body localization. Our work experimentally establishes many-body localization as a qualitatively distinct phenomenon from localization in non-interacting, disordered systems.

2.1 Entanglement and quantum thermalization

Isolated quantum many-body systems, undergoing unitary time evolution, maintain their initial global purity. However, the presence of interactions drives local thermalization: the coupling between any subsystem and its remainder mimics the contact with a bath. This causes the

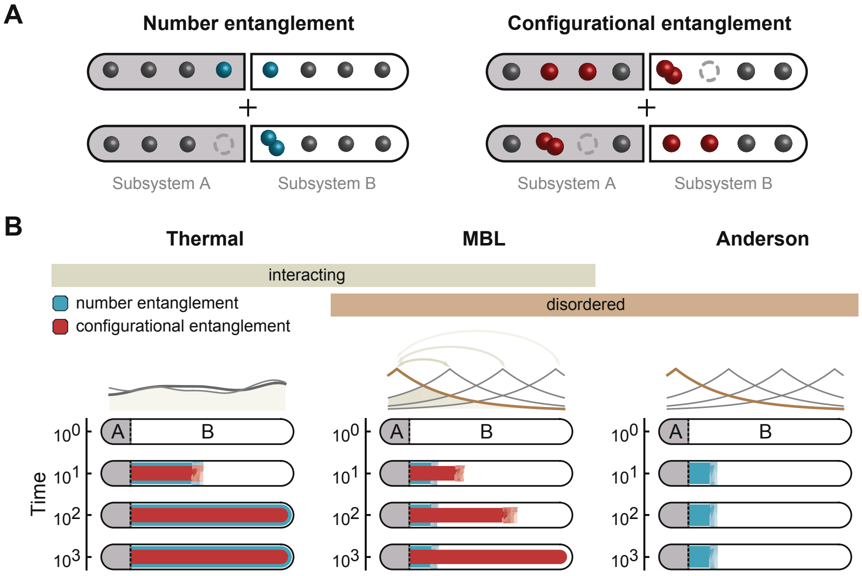

Fig. 1: Entanglement dynamics in non-equilibrium quantum systems. (A) *Subsystems A and B of an isolated system out of equilibrium entangle in two different ways: number entanglement stems from a superposition of states with different particle numbers in the subsystems and is generated through particle motion across the boundary; configurational entanglement stems from a superposition of states with different particle arrangement within the subsystems and requires both particle motion and interactions.* ***(B)*** *In the absence of disorder, both types of entanglement rapidly spreads across the entire system due to delocalization of particles (left panel). The degree of entanglement and the timescales change drastically when applying disorder (central panel): particle localization spatially restricts number entanglement, yet interactions allow configurational entanglement to form very slowly across the entire system. A disordered system without interactions shows only local number entanglement while the slow growth of configurational entanglement is completely absent (right panel).*

subsystem's degrees of freedom to be ultimately described by a thermal ensemble, even if the full system is in a pure state [4–6]. A consequence of thermalization is that local information about the initial state of the subsystem gets scrambled and transferred into non-local correlations that are only accessible through global observables [7–9].

Disordered systems [10–21] can provide an exception to this paradigm of quantum thermalization. In such systems, particles can localize and transport ceases, which prevents thermalization. This phenomenon is called many-body localization (MBL) [9, 10, 22–26]. Experimental studies have identified MBL through the persistence of the initial density distribution [27–32] and two-point correlation functions during transient dynamics [28]. However, while particle transport is frozen, the presence of interactions gives rise to slow coherent many-body dynamics that generate non-local correlations, which are inaccessible to local observables [33–35]. These dynamics are considered to be the hallmark of MBL and distinguish it from its non-interacting counterpart, called Anderson localization [10–14, 17, 18, 21]. Their observation, however, has remained elusive, because it requires exquisite control over the system's coherence.

We study these many-body dynamics by probing the entanglement properties of an MBL system with fixed particle number [33–37]. We distinguish two types of entanglement that can exist between a subsystem and its complement (Fig. 1A): *Number entanglement* implies that the particle number in one subsystem is correlated with the particle number in the other. It is generated through tunneling across the boundary between the subsystems. *Configurational entanglement* implies that the configuration of the particles in one subsystem is correlated with the configuration of the particles in the other. It arises from a combination of particle motion and interaction. The formation of particle and configurational entanglement changes in the presence or absence of interactions and disorder in the system (Fig. 1B). In thermal systems without disorder, interacting particles delocalize and rapidly create both types of entanglement throughout the entire system. Contrarily, for Anderson localization, number entanglement builds up only locally at the boundary between the two subsystems. Here the lack of interactions prevents the substantial formation of configurational entanglement. In MBL systems, number entanglement builds up in a similarly local way as for Anderson localization. However, notably, the presence of interactions additionally enables the slow formation of configurational entanglement throughout the entire system.

In this work, we realize an MBL system and characterize these key properties: breakdown of quantum thermalization, finite localization length of the particles, area-law scaling of the number entanglement, and slow growth of the configurational entanglement that ultimately results in a volume-law scaling. Each property shows a contrasting behavior when the system is prepared at weak disorder in a thermalizing state. While the former three properties are also present for an Anderson localized state, the slowly growing configurational entanglement qualitatively distinguishes our system from a non-interacting, localized state.

2.2 Experimental system

In our experiments, we study MBL in the interacting Aubry-André model for bosons in one dimension [38, 39], which is described by the Hamiltonian

$$\hat{\mathcal{H}} = -J \sum_i \left(\hat{a}_i^\dagger \hat{a}_{i+1} + h.c.\right) + \frac{U}{2} \sum_i \hat{n}_i \left(\hat{n}_i - 1\right) + W \sum_i h_i \, \hat{n}_i \, , \tag{1}$$

where $\hat{a}_i^\dagger$ $\left(\hat{a}_i\right)$ is the creation (annihilation) operator for a boson on site i, and $\hat{n}_i = \hat{a}_i^\dagger \hat{a}_i$ is the particle number operator on that site. The first term describes the tunneling between neighboring lattice sites with the rate $J/\hbar$, where $\hbar$ is the reduced Planck constant. The second term represents the energy shift U when multiple particles occupy the same site. The last term introduces a site-resolved potential offset, which is created with an incommensurate lattice $h_i = \cos\left(2\pi\beta i + \phi\right)$ of period $\beta \approx 1.618$ lattice sites, phase ϕ, and amplitude W. In our experiment, we achieve independent control over J, W, and ϕ (Fig. 2A).

Our experiments begin with a Mott-insulating state in the atomic limit with one ^{87}Rb atom on each site of a two-dimensional optical lattice (Fig. 2B). The system is placed in the focus of a high-resolution imaging system through which we project site-resolved optical potentials [40]. We first isolate a single, one-dimensional chain from the Mott insulator and then add the site-resolved potential offsets W_i with the incommensurate lattice. At this point, the system

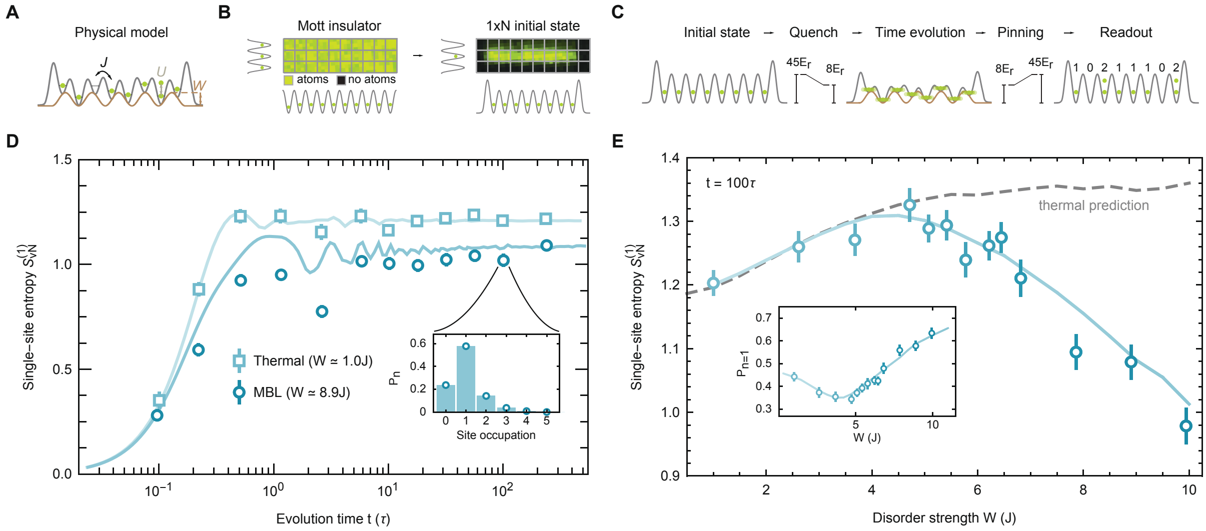

Fig. 2: Site-resolved measurement of thermalization breakdown. **(A)** *One dimensional Aubry-André model with particle tunneling at rate* $J/\hbar$*, on-site interaction energy* U *and quasi-periodic potential with amplitude* W*.* **(B)** *We prepare the initial state of eight unentangled atoms by projecting tailored optical potentials on a two-dimensional Mott insulator at* $45E_r$ *lattice depth, where* $E_r = h\times 1.24\,kHz$ *is the recoil energy.* **(C)** *We create a non-equilibrium system by abruptly enabling tunneling dynamics. Following a variable evolution time, we project the many-body state back onto the number basis by increasing the lattice depth, and obtain the site-resolved atom number from a fluorescence image).* **(D)** *We compute the single-site von Neumann entropy* $S_{vN}^{(1)}$ *from the site-resolved atom number statistics (inset) after different evolution times (scaled with tunneling time* $\tau = \hbar/J$*) in the presence of weak and strong disorder.* **(E)** *Probability* p_1 *to retrieve the initial state (inset) and* $S_{vN}^{(1)}$ *for different* W*, measured after* 100τ *evolution. The deviation from the thermal ensemble prediction for strong disorder signals the breakdown of thermalization in the system. All lines in* **(C-D)** *show the prediction of exact diagonalization calculations without any free parameters. Each data point is sampled from 197 disorder realizations).*

remains in a product state of one atom per lattice site. We abruptly switch on the tunneling by reducing the lattice depth within a fraction of the tunneling time (Fig. 2C). This quench brings the system to a non-equilibrium state and initializes the unitary time dynamics corresponding to the above Hamiltonian. The tunneling time $\tau = \hbar/J = 4.3(1)$ ms and the interaction strength $U = 2.87(3)J$ remain constant in all our experiments. Following a variable evolution time, we abruptly increase the lattice depth and image the system in an atom-number-sensitive way with single-site resolution). This projects the many-body state onto the number basis, which consists of all possible distributions of the particles within the chain.

In some realizations, particle loss during the time evolution and imperfect readout reduce the number of detected atoms compared to the initial state, thereby injecting classical entropy into the system. We eliminate this entropy by post-selecting the data on the intended atom number, thereby reaching a fidelity of $99.1(2)\%$ unity filling in the initial state, which is limited by the fraction of doublon-hole pairs in the Mott insulator. The result is a highly pure state, in which all correlations are expected to stem from entanglement in the system.

2.3 Breakdown of thermalization

We first investigate the breakdown of thermalization in a subsystem that consists of a single lattice site. The conserved total atom number enforces a one-to-one correspondence between the particle number outcome on a single site and the number in the remainder of the system—entangling the two during tunneling dynamics. Ignoring information about the remaining system puts the subsystem into a mixed state of different number states. The associated number entropy is given by $S_{\mathrm{n}}^{(1)} = -\sum_n p_n \log(p_n)$, where p_n is the probability of finding n atoms in the subsystem. Since the atom number is the only degree of freedom of a single lattice site, $S_{\mathrm{n}}^{(1)}$ captures all of the entanglement between the subsystem and its complement, and is equivalent to the single-site von Neumann entanglement entropy $S_{\mathrm{vN}}^{(1)}$.

Counting the atom number on an individual lattice site in different experimental realizations allows us to obtain the probabilities p_n and compute $S_{\mathrm{vN}}^{(1)}$. We perform such measurements for various evolution times. At low disorder depth $\big(W = 1.0(1)J\big)$, the entropy grows over a few tunneling times and then reaches a stationary value (Fig. 2D). The stationary value is reduced for deep disorder $\big(W = 8.9(1)J\big)$ and remains constant over two orders of magnitude, up to several hundred tunneling times. The lack of entropy increase indicates the absence of heating in the system. The excellent agreement of the measured entropy with *ab initio* calculations up to the longest measured evolution times suggests a highly unitary evolution of the system.

We perform measurements of $S_{\mathrm{vN}}^{(1)}$ at different disorder strengths following an evolution of one hundred tunneling times (Fig. 2E). To evaluate the degree of local thermalization, we compare the results with the prediction of a thermal ensemble for our system. For weak disorder, the measured entropy agrees with the predicted value, whereas the entropy is significantly reduced for strong disorder—signaling the absence of thermalization in the system. As a consequence, the system retains some memory of its initial conditions for arbitrarily long evolution times. We indeed find that the probability to retrieve the initial state of one atom per site increases for strong disorder (inset Fig. 2E).

2.4 Spatial localization

The breakdown of thermalization is expected to be a consequence of the spatial localization of the particles. Previous experiments have determined the decay length of an initially prepared density step into empty space [30]. We measure the localization by directly probing density-density correlations within the system. They are captured by $G^{(2)}(d) = \langle n_i n_{i+d}\rangle - \langle n_i\rangle\langle n_{i+d}\rangle$, where $\langle\cdots\rangle$ denotes averaging over different disorder realizations as well as all sites i of the chain. The particle numbers on two sites at distance $d > 0$ are uncorrelated for $G^{(2)}(d) = 0$. If a particle moves a distance d, the sites become anti-correlated, and the correlator decreases to $G^{(2)}(d) < 0$.

We measure the density-density correlations $G^2(d)$ for different disorder strengths in the stationary regime (Fig. 3A). For low disorder, we find the correlations to be independent of distance and below zero. This indicates that the particles tunnel across the entire system and hence are delocalized. On the other hand, at strong disorder, only nearby sites show significant correla-

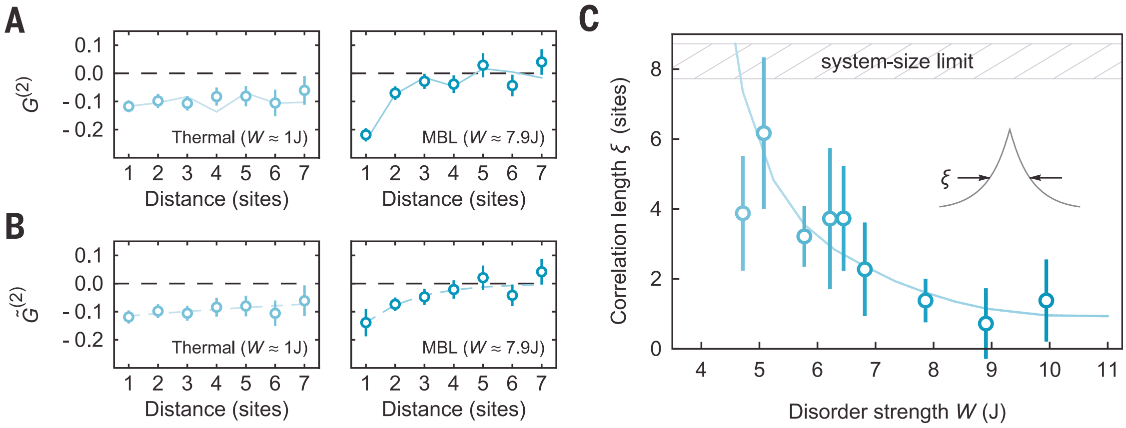

Fig. 3: Spatial localization of the particles. **(A)** *The density-density correlations* $G^{(2)}(d)$ *as a function of distance* d *at weak and strong disorder after an evolution time of* 100τ*. The alternating nature of the density-density correlations is imprinted by the autocorrelation function of the quasiperiodic potential.* **(B)** *Subtracting the influence of the quasiperiodic potential reveals the exponential decay of the correlation function.* **(C)** *Particle motion is confined within the correlation length* ξ*. We use a fit to extract* ξ *for different disorder strengths. The fit function is a product of an exponential decay with the autocorrelation function of the quasiperiodic potential. Each measurement is sampled from 197 disorder realizations. The solid lines show the prediction of exact diagonalization—calculated without any free parameters. Error bars denote the standard error of the mean in* **(A-B)***, and the fit error in* **(C)***.*

tions, signaling the absence of particle motion across large distances. We thus conclude that the particles are localized. We extract the correlation length by fitting an exponentially decaying function to the data (Fig. 3B). For increasing disorder, the correlation length decreases from the entire system size down to around one lattice site (Fig. 3C).

Our observation of localized particles is consistent with the description of MBL in terms of local integrals of motion [33–35]. It describes the global eigenstates as product states of exponentially localized orbitals. The correlation length extracted from our data is a measure of the size of these orbitals. Since the latter form a complete set of locally conserved quantities, this picture connects the breakdown of thermalization in MBL with non-thermalizing, integrable systems.

2.5 Dynamics and spreading of entanglement

We now turn to a characterization of the entanglement properties of larger subsystems, starting with a subsystem covering half the system size. As for the case of a single lattice site, the particle number in the subsystem can become entangled with the number in the remaining system through tunneling dynamics, resulting in the number entropy $S_{\mathrm{n}} = -\sum_n p_n \log(p_n)$. However, subsystems which extend over several lattice sites, with a given particle number, offer the particle configuration as an additional degree of freedom for the entanglement. Configurational entanglement only builds up substantially in interacting systems, since configurational correlations require several particles. The associated configurational entropy S_{c}, together with the number entropy, forms the von Neumann entropy, $S_{\mathrm{vN}} = S_{\mathrm{n}} + S_{\mathrm{c}}$. An analogous relation exists for spin systems with conserved total magnetization instead of the particle number.

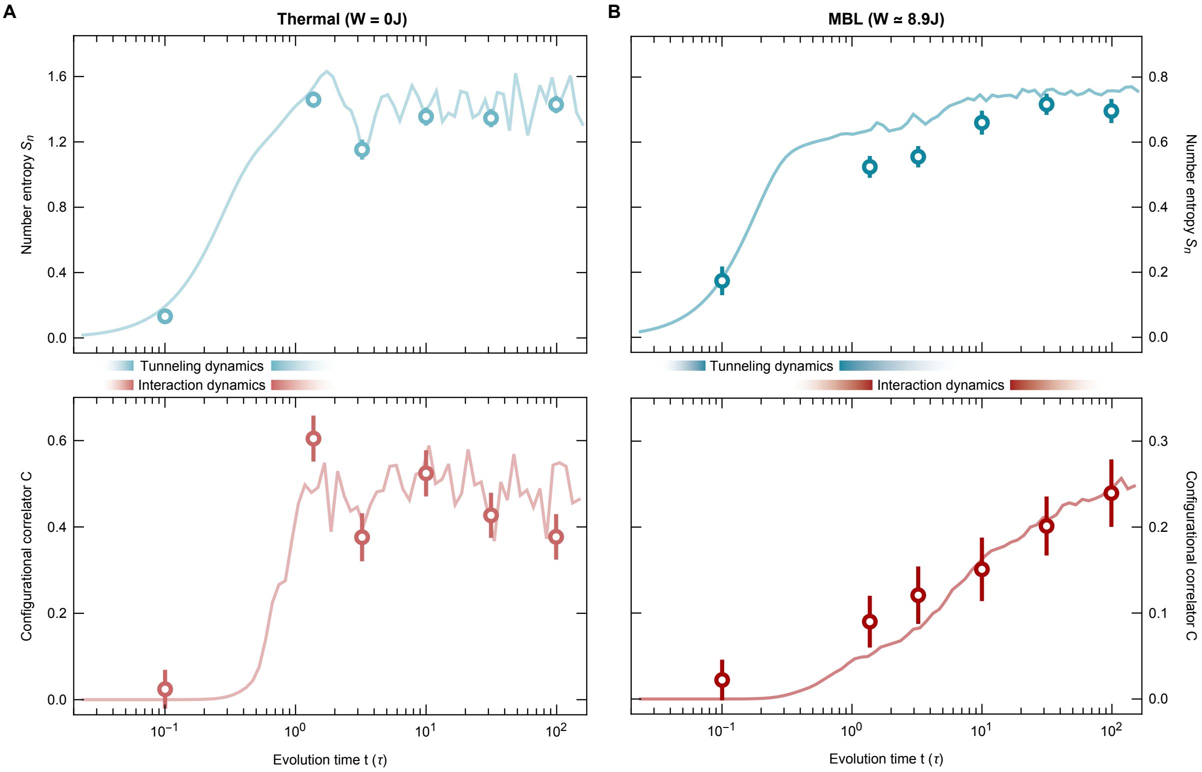

Fig. 4: Dynamics of number and configurational entanglement. **(A)** *In the thermal regime, both the number entropy S_n and the configurational correlator C quickly rise and reach a stationary value after thermalization.* **(B)** *We observe different time scales in the MBL regime. S_n increases for a longer time and reaches a stationary value that is suppressed compared to the thermal one. C shows a persistent slow increase that is consistent with a logarithmic growth, until the longest evolution times covered by our measurements. The solid lines show the prediction of exact diagonalization calculations without any free parameters. The above data was taken on a six-site system and averaged over four disorder realizations.*

The dynamics of S_n and S_c in the MBL regime (Fig. 4A) can be understood in the picture of localized orbitals. Since the localized orbitals restrict the particle motion, the number entropy can only develop within the localization length and hence S_n saturates at a lower value than for the thermal case. In the MBL regime, disorder suppresses the tunneling. Therefore, saturation is reached at a later time. However, the dynamics of S_c are strikingly different. The bare on-site interaction and particle tunneling combine into an effective interaction among localized orbitals, which decays exponentially with the distance between them. As a consequence, entanglement between distant orbitals forms slowly, causing a logarithmic growth of S_c, even after S_n has saturated [33–37].

In our experiment, we can independently probe both types of entanglement. We obtain the number entropy S_n through the probabilities p_n by counting the atom number in the subsystem in different experimental realizations. The configurational entropy S_c, in contrast, is challenging to measure in a many-body system since it requires experimental access to the coherences between a large number of quantum states [41,42]. Here we choose a complementary approach to probe the configurational entanglement in the system. It exploits the configurational correlations between the subsystems, quantified by the correlator

$$C = \sum_{n=0}^{N} p_n \sum_{\{A_n\},\{B_n\}} \big| p(A_n \otimes B_n) - p(A_n)\, p(B_n) \big|, \tag{2}$$

where $\{A_n\}$ (and $\{B_n\}$) is the set of all possible configurations of n particles in subsystem A (and $N-n$ in B), where N is total number of particles in the system. All probability distributions are normalized within the subspaces of n particles in A and the remaining $N-n$ particles in B. The configuration $A_n \otimes B_n$ is separable if $p(A_n \otimes B_n) = p(A_n)\, p(B_n)$. The correlator therefore probes the entanglement through the deviation from separability between A and B. In the MBL regime, for sufficiently small amounts of entanglement, we numerically find C to be proportional to S_c, and hence it inherits its scaling properties. This criterion is independent of the system size. Our measurements lie within the numerically verified parameter regime.

We study the time dynamics of S_n and C with and without disorder (Fig. 4B, C). Without disorder, both S_n and C rapidly rise and reach a stationary value within a few tunneling times (insets). In the presence of strong disorder, we find a qualitatively different behavior for the two quantities: S_n reaches a stationary state within few tunneling times, although after longer evolution time due to reduced effective tunneling. Additionally the stationary value is significantly reduced, indicating suppressed particle transport through the system. The correlator C, in contrast, shows a persistent slow growth up to the longest evolution times reached by our measurements. The growth is consistent with logarithmic behavior over two decades of time evolution. We conclude that we observe interaction-induced dynamics in the MBL regime, which are consistent with the phenomenological model [33–35]. The agreement of the long-term dynamics of S_p and C with the numerical calculations in the MBL regime confirms the unitary evolution of the system over $100\,\tau$. The system remains in the finite-time limit, not in the finite-size limit, since the spread of entanglement has not yet stopped at the longest studied evolution times.

Considering the entropy in subsystems of different size gives us insights into the spatial distribution of entanglement in the system: in a one-dimensional system, locally generated entanglement results in a subsystem size independent entropy, whereas entanglement from non-local correlations causes the entropy to increase in proportion to the size of the subsystem. In reference to the subsystem's boundary and volume, these scalings are called area law and volume law. We find almost no change in S_n for different subsystems of an MBL system (Fig. 5A), indicating an area law scaling due to localized particles and confirming that particle transport is suppressed. In contrast, the configurational correlations C increase until the subsystem reaches half the system size (Fig. 5B). Such a volume-law scaling is also expected for the entanglement entropy and demonstrates that the observed logarithmic growth indeed stems from non-local correlations across the entire system.

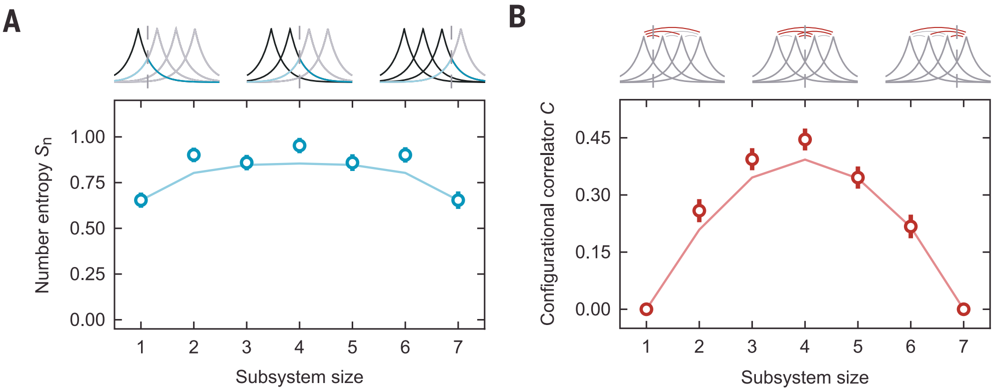

Fig. 5: Spatial distribution of the entanglement. *Number entropy and configurational correlator in the MBL regime ($W = 8.9\,J$) after an evolution time of 100τ.* **(A)** *In an MBL system, number fluctuations between two subsystems only stem from local orbitals near the boundary. Consequentially, the number entropy S_n does not depend on the subsystem size, i.e., follows an area law..* **(B)** *After long evolution times, each local orbital is configurationally entangled with every other. Hence, the configurational correlator C increases almost linearly with the subsystem size, showing a volume-law behavior. The solid lines show the prediction of exact diagonalization calculations without any free parameters. The above data was averaged over four disorder realizations.*

2.6 Conclusion

Investigating the growth of non-local quantum correlations has been a long-standing experimental challenge for the study of MBL systems. In addition to achieving exceptional isolation from the environment and local access to the system, such a measurement requires access to the entanglement entropy [41]. Our work provides a novel method to characterize the entanglement properties of MBL systems. Since it is based on measurements of the particle number fluctuations and their configurations, the method is experimentally accessible and can be generalized to higher dimensions and different experimental platforms, where a direct measurement of entanglement entropy remains challenging, e.g., trapped ions, neutral atoms, and superconducting circuits. The observation of slow coherent many-body dynamics along with the breakdown of thermalization coincides with the expected behavior for larger systems, and allows us to unambiguously identify and characterize the MBL state in our system.

The eight-site system constrained to unity filling, which is studied in this work, spans a 6435-dimensional Hilbert space—larger than for a system of 14 spin-1/2 particles constrained to zero total magnetization. In the future, experiments at even larger system sizes will be of interest to shed light on the critical properties of the thermal-to-MBL phase transition, which are the subject of ongoing studies [43–46]. In our system, it is experimentally feasible to increase the system size at unity filling to a numerically intractable regime. Additionally, we have full control over the disorder potential on every site, which opens the way to studying the role of rare regions and Griffiths dynamics as well as the long-time behavior of an MBL state with a link to a thermal bath [47–49]. Ultimately, these studies will further our understanding of quantum thermodynamics and whether such systems are suitable for future applications as quantum memories [9].

3 Critical behavior

Phase transitions are driven by collective fluctuations of a system's constituents that emerge at a critical point [50]. This mechanism has been extensively explored for classical and quantum systems in equilibrium, whose critical behavior is described by a general theory of phase transitions. Recently, however, fundamentally distinct phase transitions have been discovered for out-of-equilibrium quantum systems, which can exhibit critical behavior that defies this description and is not well understood [50]. A paradigmatic example is the many-body-localization (MBL) transition, which marks the breakdown of quantum thermalization [23, 51, 34, 35, 52, 26–28, 30, 53]. Characterizing quantum critical behavior in an MBL system requires probing its entanglement properties over space and time [34, 35, 26], which has proven experimentally challenging due to stringent requirements on quantum state preparation and system isolation. Here, we observe quantum critical behavior at the MBL transition in a disordered Bose-Hubbard system and characterize its entanglement properties via its quantum correlations. We observe strong correlations, whose emergence is accompanied by the onset of anomalous diffusive transport throughout the system, and verify their critical nature by measuring their system-size dependence. The correlations extend to high orders in the quantum critical regime and appear to form via a sparse network of many-body resonances that spans the entire system [44, 45]. Our results connect the macroscopic phenomenology of the transition to the system's microscopic structure of quantum correlations, and they provide an essential step towards understanding criticality and universality in non-equilibrium systems [50, 45, 26].

3.1 The many-body localization transition

The many-body-localization (MBL) transition describes the breakdown of thermalization in an isolated quantum many-body system as disorder is increased beyond a critical value [27, 28, 30, 53]. It represents a novel type of quantum phase transition that fundamentally differs from both its classical and quantum ground-state counterparts [23, 51, 26]. Instead of being characterized by an instantaneous thermodynamic signature, it is identified by the system's inherent dynamic behavior. In particular, the MBL transition manifests itself through a change in entanglement dynamics [26, 53]. Recent years have seen tremendous progress in our understanding of both the thermal and the MBL phases within the frameworks of quantum thermalization [52, 7, 8] and emergent integrability [34, 35, 27, 28, 30, 53], respectively.

The quantum critical behavior at this transition, however, has remained largely unresolved [26]. In particular, it is unclear whether the traditional association of collective fluctuations with static and dynamic critical behavior can be applied to this transition. The high amount of entanglement found at the MBL transition limits numerical studies due to the required computational power [54, 55]. Several theoretical approaches, despite using disparate microscopic structures, suggest anomalous transport as the macroscopic behavior at the quantum critical point [43, 44, 56, 57]. Experimental studies indeed indicate a slowdown of the dynamics at intermediate disorder [46, 58]. However, identifying anomalous transport as quantum criti-

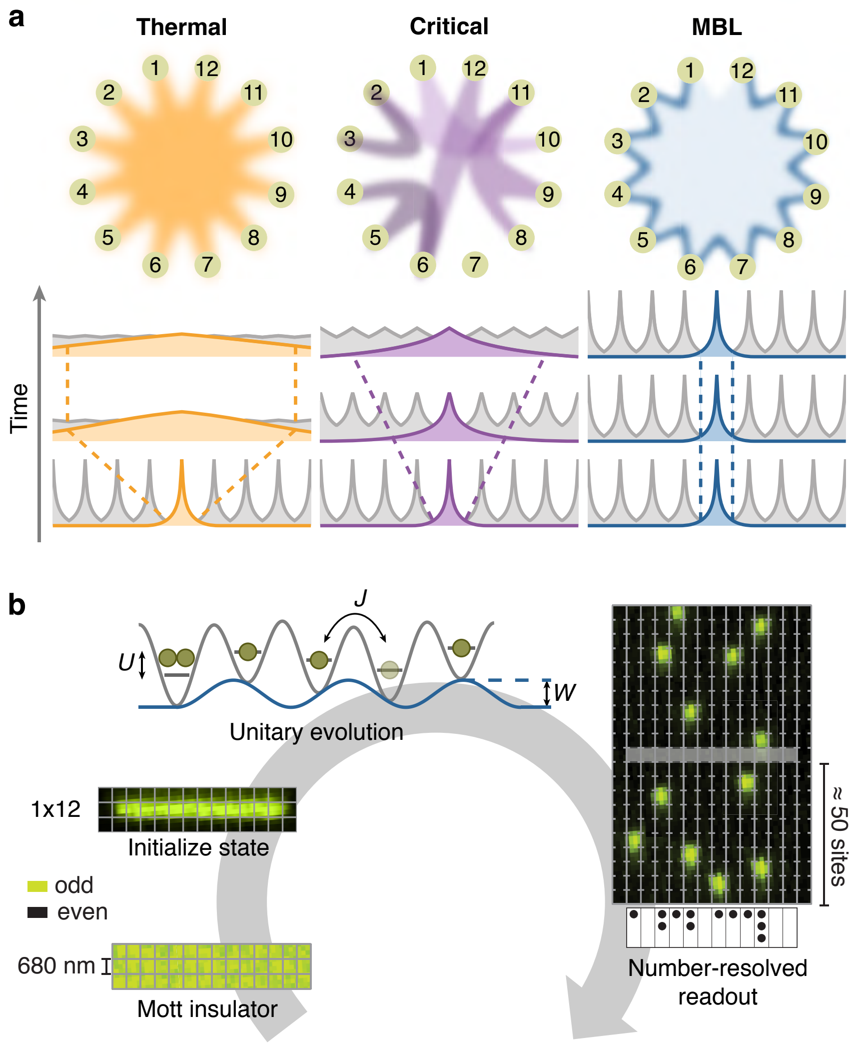

Fig. 6: ***Microscopy of the many-body localization transition.*** ***a:*** *The quantum state at the critical point takes on a complex pattern of strong multi-particle correlations at all length scales, visualized by shaded links between different lattice sites. In contrast, it simplifies in the thermal and the MBL phases to maximal entanglement and predominantly local correlations, respectively. A consequence is a change in the transport properties from diffusive to anomalous before ceasing completely in MBL.* ***b:*** *We initialize the system as a pure product state of up to twelve lattice sites at unity filling. The system becomes entangled under the unitary, non-equilibrium dynamics of the bosonic, interacting Aubry-André model with on-site interaction energy* U*, particle tunneling at rate* $J/\hbar$ *(with the reduced Planck constant* $\hbar$*), and quasi-periodic potential with amplitude* W*. After a variable evolution time, we obtain the full atom-number distribution from site-resolved fluorescence imaging after expansion.*

cal dynamics is experimentally challenging, since similar behavior can also originate from stochastic effects such as inhomogeneities in the initial state [59], or the coupling to a classical bath [60, 31]. Additionally, in the case of random disorder, the presence of rare-regions admits several microscopic mechanisms that may govern this critical behavior and therefore makes identifying this mechanism challenging [47–49]. Our experimental protocol overcomes these challenges by using a quasi-periodic potential, which is rare-region free, as well as by evolving a pure, homogeneous initial state under unitary dynamics. Using this protocol, we observe quantum critical dynamics via anomalous transport, enhanced quantum fluctuations, and system-size dependent thermalization. In addition, we microscopically resolve and characterize the structure of the entanglement in the many-body states through their multi-particle quantum correlations.

Our experiments start with a pure state of up to twelve unentangled lattice sites at unity filling. We study its out-of-equilibrium evolution after a rapid increase of the tunneling in the bosonic, interacting Aubry-Andre Hamiltonian

$$\hat{\mathcal{H}} = -J\sum_i \left(\hat{a}_i^\dagger \hat{a}_{i+1} + h.c.\right) + \frac{U}{2}\sum_i \hat{n}_i \left(\hat{n}_i - 1\right) + W\sum_i h_i \hat{n}_i \, ,$$

where $\hat{a}_i^\dagger$ $\left(\hat{a}_i\right)$ is the creation (annihilation) operator for a boson on site i, and $\hat{n}_i$ is the corresponding particle number operator. The tunneling time $\tau = \hbar/J = 4.3(1)\,\mathrm{ms}$ (with the reduced Planck constant $\hbar$) between neighboring sites and the pair-wise interaction energy $U = 2.87(3)J$ remain constant for all experiments. The potential energy offset $h_i = \cos\left(2\pi\beta i + \phi\right)$ on site i follows a quasi-periodic distribution of amplitude W, period $1/\beta \approx 1.618$ lattice sites, and phase ϕ. After a variable evolution time, we obtain full counting statistics of the quantum state through a fluorescence imaging technique. The applied unitary evolution preserves the initial purity of $99.1(2)\%$ per site, such that all correlations are expected to stem from entanglement in the system [8, 53].

3.2 Transport properties

We first characterize the system's dynamical behavior by studying its transport properties for different disorder strengths. Since the initial state has exactly one atom per site, the system starts with zero density correlations at all length scales. However, during the Hamiltonian evolution, tunneling dynamics build up anti-correlated density fluctuations between coupled sites of increasing distance (Fig. 7a). Motivated by this picture, we quantify the particle dynamics by defining the transport distance, $\Delta x \propto \sum_d d\,\langle G_\mathrm{c}^{(2)}(i, i{+}d)\rangle_i$, as the first moment of the disorder-averaged two-point density correlations, $G_\mathrm{c}^{(2)}(i, i{+}d) = \langle \hat{n}_i \hat{n}_{i+d}\rangle - \langle \hat{n}_i\rangle\langle \hat{n}_{i+d}\rangle$ (Fig. 7a). At low disorder, we observe these anti-correlations rapidly build up and saturate over a time scale of $t/\tau \approx L/2$. With increasing disorder, we observe a slowdown of particle transport that is consistent with a power-law growth $\Delta x \sim t^\alpha$ (Fig. 7b) [61]. We extract the anomalous diffusion exponent α from a subset of the data points that exclude the initial transient dynamics in the system ($L/2 < t/\tau \leq 100$) (Fig. 7b inset). The exponent α is reduced by successively higher disorder, demonstrating the suppression of transport in the MBL regime.

In order to identify the anomalous diffusion as a signature of quantum critical dynamics, we measure the system-size dependence of two observables in the long-time limit ($t = 100\tau$): the on-site number fluctuations $\mathcal{F} \equiv G_\mathrm{c}^{(2)}(d{=}0)$ as a probe of local thermalization, and the transport distance Δx as a localization measure (Fig. 7c). At low disorder, the fluctuations agree with those predicted by a thermal ensemble and particles are completely delocalized for both system

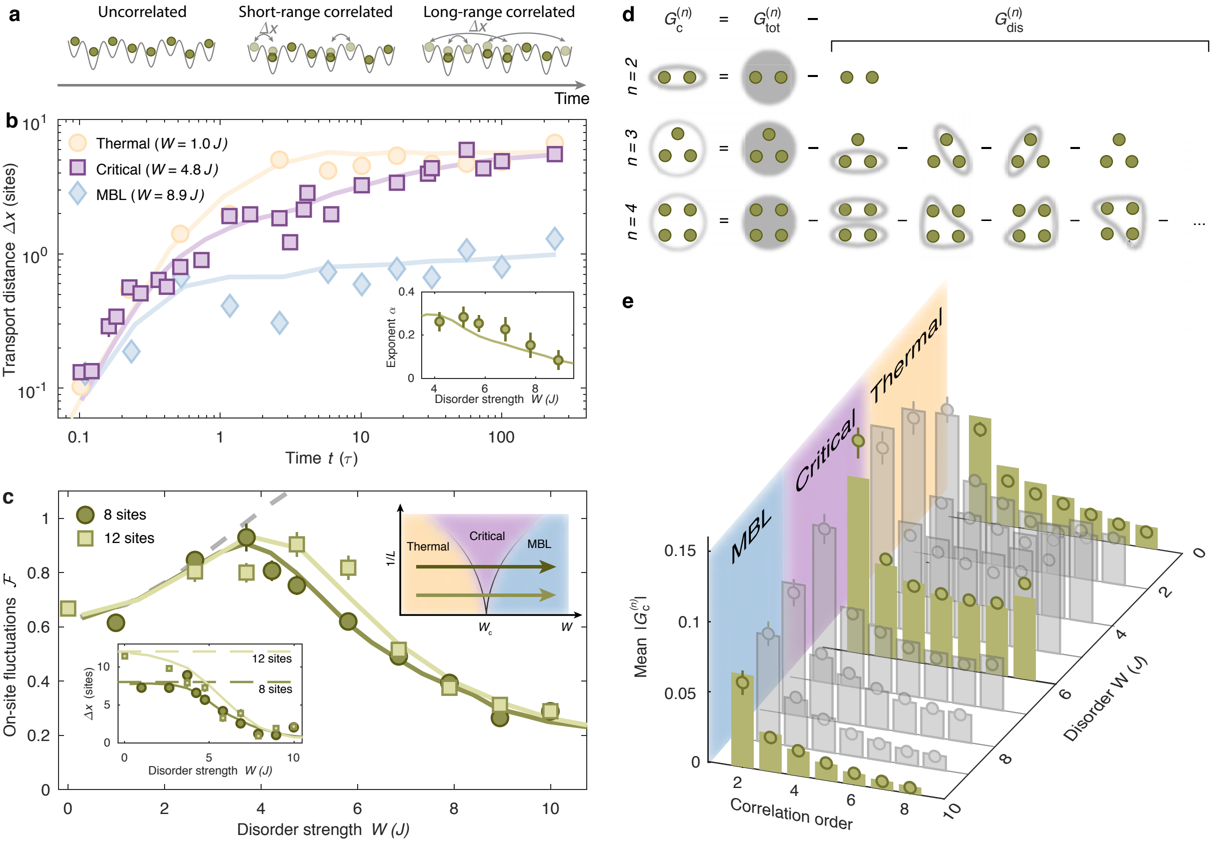

Fig. 7: ***Quantum critical dynamics at the MBL transition.*** ***a:*** *The initially uncorrelated system develops two-point density correlations under its transport dynamics. Short-range correlations emerge within one tunneling time* $\tau = \hbar/J$*, whereas the diffusion exponent* α *determines the time scale over which correlations form across the system size* L*.* ***b:*** *Particle transport slows down at intermediate disorder, consistent with a power-law evolution with exponent* $\alpha < 0.5$*, demonstrating subdiffusive dynamics (inset). These data were taken on an eight-site system.* ***c:*** *The critical nature of these dynamics is determined from the behavior of on-site density fluctuations* $\mathcal{F}$ *and transport distance* $\Delta\tilde{x}$ *(lower left inset) for both considered system sizes. The thermal regime is determined by the agreement of the measured* $\mathcal{F}$ *with the prediction from a thermal ensemble (dashed grey). The system-size dependence at intermediate disorder is consistent with the reduced size of a quantum critical cone (upper right inset). These data were measured for both an eight-site and twelve-site system.* ***d:*** *We obtain the genuine many-body processes of order* n *from connected correlations* $G_c^{(n)}$ *by subtracting all lower order contributions* $G_{dis}^{(n)}$ *from the total correlation function* $G_{tot}^{(n)}$*.* ***e:*** *In the quantum critical regime, we find enhanced collective fluctuations at all measured orders by computing the mean absolute value of* $G_c^{(n)}$ *for different disorder strengths. These data were measured on a twelve-site system. The solid lines (**b,c**) and bars (**e**) denote the prediction of exact numeric time calculations without any free parameters. The errorbars are the standard error of the mean and are below the marker size in **b**.*

sizes. This demonstrates that local quantum thermalization occurs independently of system size at low disorder and establishes that this regime corresponds to the system being in the thermal phase. At strong disorder, the physics is governed by the formation of an intrinsic length scale, namely the localization length $\xi \sim \Delta\tilde{x}$ [30, 53]. We observe system-size independent, subthermal fluctuations and measure an intrinsic length scale $\Delta\tilde{x}$. This indicates that the strong disorder regime corresponds to the system being in the localized phase. However, at intermediate disorder, we find a system-size dependence for both observables. This demonstrates the absence of an intrinsic length scale and the presence of finite-size-limited fluctuations, identifying that the system is in a critically thermalizing regime. These measurements of system-size-dependent thermalization can be visualized as two horizontal cuts in a finite-size phase diagram. The observed finite-size dependence is consistent with the physics associated with a critically thermalizing intermediate phase and a shrinking quantum critical cone (Fig. 7c inset) [50].

3.3 Multi-particle correlations

We then investigate the multi-particle correlations in the system to probe the presence of enhanced quantum fluctuations in the quantum critical regime (Fig. 7d). For this study, we employ the n-point connected density-correlation functions [62–64],

$$G_{\text{c}}^{(n)}(\mathbf{x}) = G_{\text{tot}}^{(n)}(\mathbf{x}) - G_{\text{dis}}^{(n)}(\mathbf{x}),$$

which act on lattice sites with positions $\mathbf{x} = (x_1, \ldots, x_n)$. The disconnected part of this function, $G_{\text{dis}}^{(n)}$, is fully determined by all lower-order correlation functions, and therefore does not contain new information at order n. By removing it from the total measured correlation function, $G_{\text{tot}}^{(n)}(\mathbf{x}) = \left\langle \prod_{k=1}^{n} \hat{n}\left(x_k\right) \right\rangle$, we isolate all n-order correlations that are independent of lower-order processes. This approach gives a direct handle on the level of complexity of the underlying many-body wave function and characterizes its entanglement via its non-separability into subsystems of size $< n$. We quantify the relevance of order n processes by computing the mean absolute value of all correlations arising from both contiguous and non-contiguous n sites in the system (Fig. 7e). We find that in the thermal and the many-body-localized regimes, the system becomes successively less correlated at higher order. The behavior in the quantum critical regime is strikingly different: we observe that the system is strongly correlated at all measured orders.

3.4 Site-resolved correlations

In order to reveal the microscopic origin for the anomalous transport, we now investigate the site-resolved structure of the many-body state (Fig. 8a). We first study how much each lattice site contributes to the transport by considering the site-resolved two-point correlations in the long-time limit ($t = 100\tau$). In the thermal regime, we find similar correlations between all lattice sites, which correspond to uniformly delocalized atoms. In contrast, density correlations are restricted to nearby sites in the MBL regime due to localization. Intriguingly, we observe a sparse structure of correlations at intermediate disorder, which involves only specific distances between lattice sites, yet spans the entire system size.

The sparse structure is expected to be linked to the applied quasi-periodic potential. The average energy offsets of sites d apart in the system are correlated by this potential. This correlation is

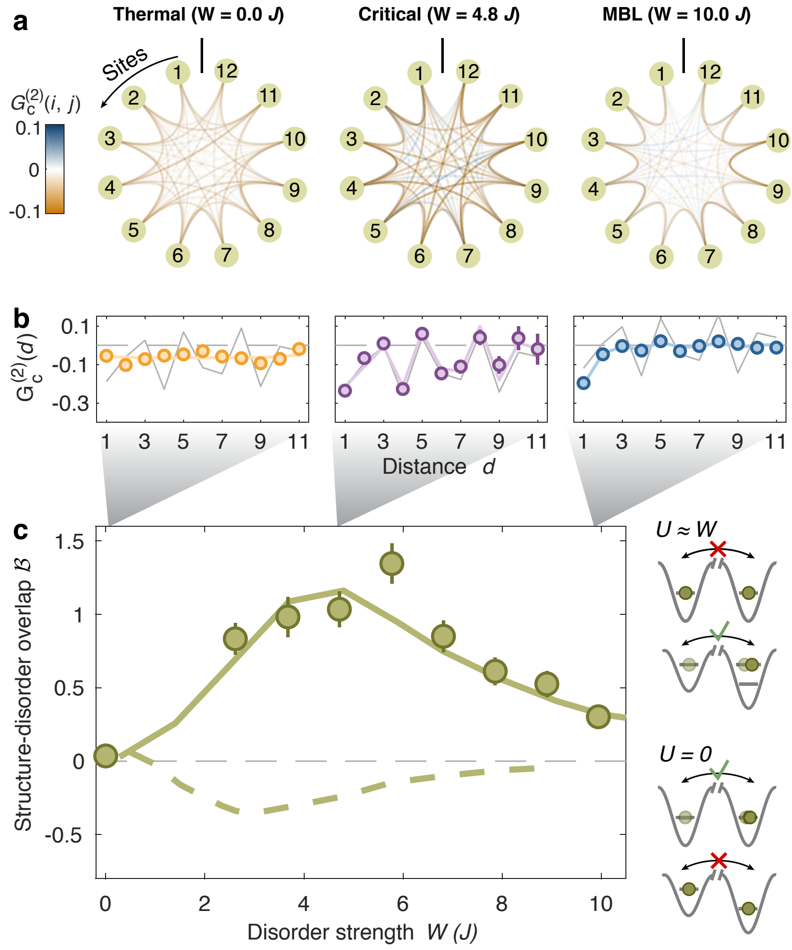

Fig. 8: ***Sparse network of resonances.*** ***a:*** *The measured site-dependent two-point correlations $G_c^{(2)}(i,j)$ are plotted for all inter-site combinations, whose amplitudes are represented by the colored lines connecting the lattice sites-i,j. In the quantum critical regime, correlations preferably form at specific distances, showing a network-like structure. This contrasts with homogeneous correlations in the thermal regime and nearest-neighbor correlations in the MBL regime.* ***b:*** *The structure of the correlation network is revealed by the averaged correlation function $G_c^{(2)}(d) = \left\langle G_c^{(2)}(i,i{+}d)\right\rangle_i$. Its similarity to the autocorrelation $A(d) = \langle h_i h_{i+d}\rangle_i$ of the quasi-periodic potential (solid grey) indicates interaction-induced tunneling processes that are enhanced when the interaction energy compensates for the potential energy difference.* ***c:*** *We quantify the similarity by the overlap $\mathcal{B} = \Sigma_d G_c^{(2)}(d)A(d)$, which is maximal in the quantum critical regime. The sign of the overlap would be opposite for non-interacting particles (dashed line), which favors tunneling between sites with similar potential energies. The solid lines in* ***b,c*** *and the dashed line in* ***c*** *denote the prediction of exact numeric time evolution calculations without any free parameters.*

then inherited by the system's fluctuations when the interaction energy U compensates for these correlated offsets. To investigate this structure, we compare the two-point density correlations with the autocorrelation function, $A(d) = \langle h_i h_{i+d}\rangle_i$, of the quasi-periodic potential. Indeed, we find that the site-averaged density correlations $G_c^{(2)}(d) = \langle G^{(2)}(i,i{+}d)\rangle_i$ inherit their spatial structure from $A(d)$ (Fig. 8b). We find that this contribution is maximal in the critical regime but

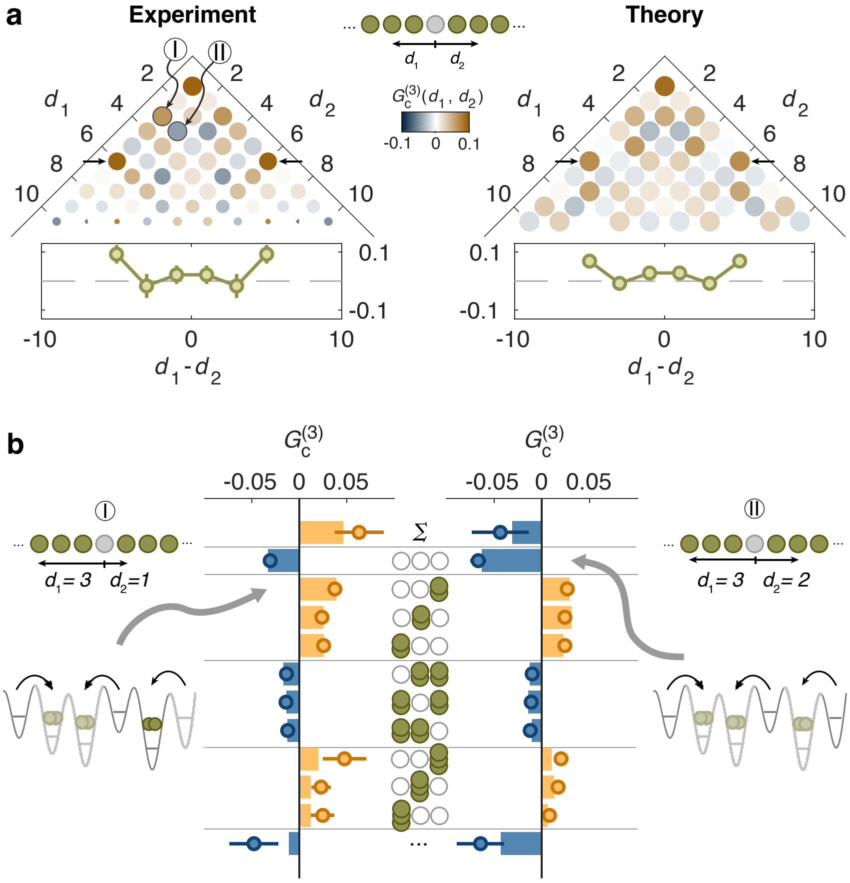

Fig. 9: ***Many-body correlations in the quantum critical regime. a:*** *The connected correlation function,* $G_c^{(3)}(d_1, d_2)$*, for three lattice sites spaced by distances* d_1 *and* d_2 *in the quantum critical regime* $(W = 4.8J)$*, showing the strongly interacting nature of the state. We find that the three-point correlations show a characteristic structure that is governed by the contribution of the number states on the considered sites. The arrows indicate the cut in* d_1, d_2 *space plotted below.* ***b:*** *To exemplify the relevant processes of order* $n = 3$*, we show the contributions of the number states on lattice sites at distance* $d_1 = 3$*,* $d_2 = 1$ *(left) and* $d_1 = 3$*,* $d_2 = 2$ *(right). While there is a wide distribution of contributing configurations, the relative dominance of a particular process provides the overall structure in* ***a****. The illustration of atoms undergoing a highly correlated hopping process in the lattice describe how such correlations can contribute to either positive or negative correlations among the three considered sites. The theory plot in* ***a*** *and bars in* ***b*** *are calculated from exact numeric time calculations without any free parameters. The inverse marker size in the experimental plot in* ***a****, and the error bars in both* ***a*** *and* ***b*** *denote the standard error of the mean.*

is strongly reduced in the thermal and MBL regimes (Fig. 8c). These observations contrast with the behavior of a non-interacting system, where the sign of the structure is opposite since resonant tunneling is favored for zero potential energy difference (Fig. 8c). These results illustrate microscopically how the interplay of strong interactions and disorder can lead to anomalous diffusion. However, this picture of effective single-particle hopping that couples distant sites neglects the many-body nature of these systems.

3.5 Site-resolved detection of three-body processes

In order to investigate the system's many-body structure, we examine the site-resolved contributions of the three-point correlations. Since all non-zero contributions to the three-point correlations involve correlated hopping of at least two particles, they are a signature for multiparticle entanglement [63]. In the quantum critical regime, we find that these correlations span the entire system and are highly structured, taking on both positive and negative values (Fig. 9a). In contrast to the pattern in the second-order correlation function, this third-order structure is not directly recognizable as the quasi-periodic-potential correlations. In order to gain further insight into the structure, we analyze the contributions of all possible particle configurations in Fig. 9b. In particular, for $G_c^{(3)}(d_1{=}3, d_2{=}1)$, which is positive, we see that the dominant contribution comes from a particular process that favors multiple atoms hopping to the same site. In contrast, $G_c^{(3)}(d_1{=}3, d_2{=}2)$, which is negative, has a dominant process that favors all atoms leaving the three sites considered. While this provides some intuition for the emergent many-body resonances, the three-point correlations are, in fact, the result of a superposition of many correlated processes. These observations further demonstrate how the interactions between multiple atoms can compensate for the disorder via correlated tunneling of several atoms. In this way, we can see the additional role interactions play in the disordered system: they supply higher-order many-body resonances that preserve transport where lower-order processes are energetically suppressed.

3.6 Discussion and outlook

Our results demonstrate how a many-body, sparse resonant structure drives the quantum critical behavior at the MBL transition. This observed microscopic description is consistent with the theoretically suggested mechanisms of a sparse *backbone* of resonances that can act as a functional bath for the system [65, 44, 45]. However, our results provide a new perspective on this description by mapping out the prevalence of high-order processes in the system that facilitate this critical thermalization.

In future experiments, the tunability of our system will allow us to address further open questions on the MBL transition, such as possible discontinuities of the entanglement entropy [45], the potential emergence of new dynamic phases near the critical point, and the influence of rare-regions in the disorder potential [48, 49]. Furthermore, the demonstrated techniques pave the way to explore the role of universality in non-equilibrium systems. From a computational perspective, our system's Hilbert space dimension is comparable to the dimension of 22 spins with zero total magnetization. A moderate increase of the system's spatial dimension beyond this experiment results in numerically intractable sizes.

4 Quantum avalanches

Strongly correlated systems can exhibit unexpected phenomena when brought in a state far from equilibrium. An example is many-body localization, which prevents generic interacting systems from reaching thermal equilibrium even at long times [66, 67]. The stability of the many-body localized phase has been predicted to be hindered by the presence of small thermal inclusions that act as a bath, leading to the delocalization of the entire system through an avalanche propagation mechanism [48, 49, 68–71]. Here we study the dynamics of a thermal inclusion of variable size when it is coupled to a many-body localized system. We find evidence for accelerated transport of the thermal inclusion into the localized region. We monitor how the avalanche spreads through the localized system and thermalizes it site by site by measuring the site-resolved entropy over time. Furthermore, we isolate the strongly correlated bath-induced dynamics with multipoint correlations between the bath and the system. Our results have implications on the robustness of many-body localized systems and their critical behavior.

4.1 Stability of many-body localized systems

One of the founding principles of statistical physics is that a generic macroscopic system can equilibrate on its own. This means that local fluctuations of energy, magnetization, or particle density can relax towards thermal equilibrium because interactions allow different parts of the system to serve as reservoirs to each other. This universal picture has been challenged by the idea of many-body localization (MBL), which suggests that systems with strong disorder can evade thermalization even in the presence of interactions [66, 67, 72, 73, 27, 30, 46, 1, 2]. In one-dimensional systems, a stable MBL phase can be argued for as follows: the matrix elements of local operators decay exponentially with the separation between two points, whereas the density of states increases exponentially with the system size. For strong disorder, matrix elements can thus be argued to decay faster than the density of states increases, ultimately inhibiting relaxation.

However, the existence of MBL remains a subject of debate, since it is unclear when those conditions are fulfilled [74–82]. For instance, by introducing a small region with weak disorder, part of the system may be delocalized and thus give rise to local operators with non-exponential decay [54, 83–89, 43–45, 47]. Those local weakly disordered regions occur naturally in randomly disordered systems, when potential offsets on consecutive lattice sites accidentally coincide [90, 91, 54, 85, 47]. The dynamics in MBL systems in the presence of a thermal region have been predicted to occur in so-called quantum avalanches, which imply that these regions grow by absorbing nearby disordered regions [48, 49, 68–70]. Under which conditions quantum avalanches can arise, run out of steam, or propagate without halt determines the fate of MBL at long evolution times. Their understanding is thus closely connected to discerning thermalization in interacting many-body systems.

4.2 Quantum avalanches

Perturbative bath-induced relaxation can often be captured in the context of Fermi's golden rule (Fig. 10a, left). In this picture, the relaxation rate $\Gamma_i = g_i^2 \rho_{\text{bath}}$ at a distance of i sites away from the bath is given by the product of the bath's constant density of states ρ_{bath} and the coupling rate $g_i \propto J e^{-i/\xi_{\text{loc}}}$, where ξ_{loc} is the localization length of the MBL system, and J is the

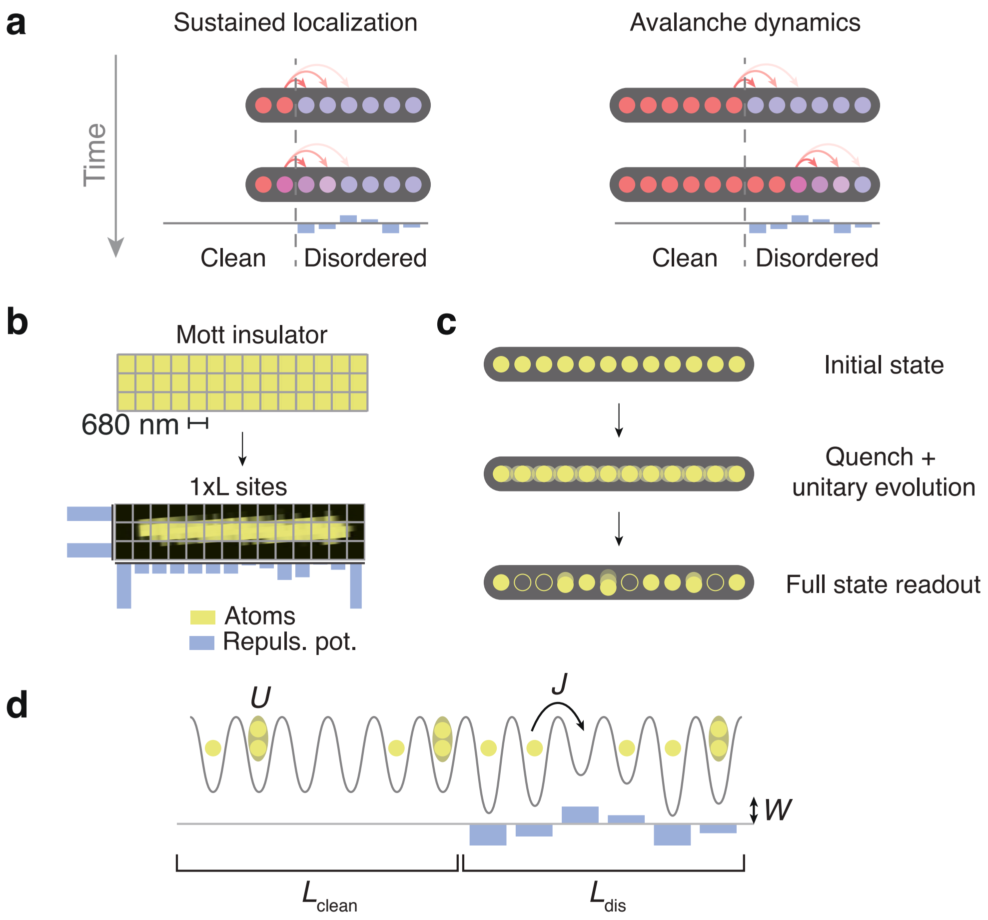

Fig. 10: ***Bath-induced quantum avalanches.*** ***a:*** *Two scenarios at an interface of a thermal bath (clean) and a localized (disordered) region: the bath penetrates logarithmically slow and localization remains robust (left), or an avalanche from a strong bath thermalizes the disordered region site by site (right).* ***b:*** *Fluorescence pictures of a two-dimensional Mott insulator at unity filling, and of the initialized one-dimensional system of L sites. Projected optical potentials isolate the system and apply site-resolved offsets onto the disordered region (blue).* ***c:*** *The initial state is brought far from equilibrium through a quantum quench by abruptly enabling tunneling along all links, then evolved under the Hamiltonian, until we detect the site-resolved atom number with a fluorescence picture.* ***d:*** *The system's dynamics are governed by the Bose-Hubbard model with tunneling energy J and on-site interaction energy U, extended by a disorder potential with amplitude W in the disordered region.*

tunneling rate between neighboring sites. Consequently, within a perturbative description MBL remains robust against a local bath, with a bath penetration into the MBL region that increases logarithmically in time.

Quantum avalanches, in contrast, are predicted to emerge from dynamics beyond this simple picture (Fig. 10a, right). A more accurate description ought to take into account that the density of states of the bath grows when the first disordered site thermalizes and hence merges with the bath. This feedback effect enhances the relaxation rate Γ_i for the next localized sites, giving rise to accelerated bath penetration into the disordered region faster than logarithmic in time. Eventually, these non-perturbative relaxation processes may lead to a full delocalization of the

system if the density of states grows faster than the decay in the coupling rates.
Studying quantum avalanches within disordered systems remains a challenge due to both the statistical rareness of a sufficiently large thermal inclusion, and the large time scales over which the inclusion spreads through the system. Consequently, theoretical approaches often consider disordered systems that are locally coupled to a thermal bath that represents the rare region [68]. Within this canonical setting, several signatures have been proposed to identify quantum avalanches through their short-term dynamics, including a speedup compared to a logarithmic spreading [70], and a backaction on the bath [49]. However, high demands in local control have so far hindered their experimental observation.

4.3 Accelerating delocalization

In this work we explore the dynamics of an MBL system coupled to a thermal inclusion (Fig. 10) and observe phenomena that suggest the presence of non-perturbative avalanche processes. Our experimental protocol starts by preparing a Mott-insulating state with one ^{87}Rb atom on each site of a two-dimensional optical lattice (Fig. 10b). The system is placed in the focus of a high-resolution imaging system through which we project site-resolved repulsive potentials on individual lattice sites. We isolate a one-dimensional system of L lattice sites from the Mott insulator and add potential offsets to the lattice sites. At this point, the system remains in a product state of one atom per lattice site. We then perform a quantum quench by abruptly reducing the lattice depth (Fig. 10c). The subsequent non-equilibrium dynamics are described by the Bose-Hubbard Hamiltonian:

$$\hat{\mathcal{H}} = -J \sum_i \left(\hat{a}_i^\dagger \hat{a}_{i+1} + h.c. \right) + \frac{U}{2} \sum_i \hat{n}_i \left(\hat{n}_i - 1 \right) + W \sum_{i \in L_{\text{dis}}} h_i \hat{n}_i, \tag{3}$$

where $\hat{a}_i^\dagger$ $(\hat{a}_i)$ is the creation (annihilation) operator for a boson on site i, and $\hat{n}_i = \hat{a}_i^\dagger \hat{a}_i$ is the particle number operator. The first term describes the tunneling between all neighboring lattice sites, and the second term represents the on-site repulsive interactions. The last term introduces a site-resolved energy offset. We set $h_i = 0$ for all lattice sites in the clean region of size L_{clean}, whereas the energy offsets in the disordered region of size L_{dis} follow a quasi-periodic disorder distribution $h_i = \cos(2\pi\beta i + \phi)$ with $1/\beta \approx 1.618$, phase ϕ and amplitude W. The quasi-periodic distribution avoids nearby lattice sites to coincidentally have similar energy offsets, which inhibits the presence of secondary rare regions within the disordered region [55]. After a variable evolution time, we read out the site-resolved atom number by fluorescence imaging. The applied unitary evolution preserves the initial purity of $99.1(2)\%$ per site [8, 1]. All observables are averaged over 200 disorder realizations with different ϕ. The tunneling time $\tau = \hbar/J = 4.3(1)$ ms (with the reduced Planck constant $\hbar$), the interaction strength $U = 2.87(3)\ J$, and the number of disordered sites $L_{\text{dis}} = 6$ remain constant in all experiments.
We first use the full site-resolved readout of our microscope to investigate the local transport dynamics in the system. The connected density-density correlations $\langle \hat{n}_i \hat{n}_j \rangle_c = \langle \hat{n}_i \hat{n}_j \rangle - \langle \hat{n}_i \rangle \langle \hat{n}_j \rangle$ detect correlations between the particle numbers on site i and j [2]. Negative values of $\langle \hat{n}_i \hat{n}_j \rangle_c$

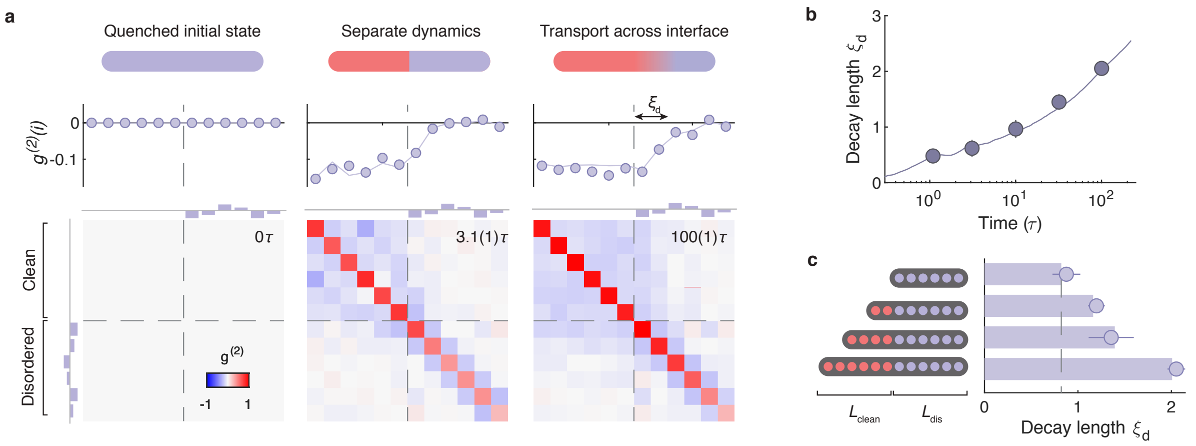

Fig. 11: ***Accelerated transport across the clean-disorder interface.*** ***a:*** *Density correlations for all pairs of sites in a system consisting of $L_{clean} = L_{dis} = 6$ at disorder strength $W = 9.1\,J$. After a quantum quench, an uncorrelated initial state (left) develops separate dynamics within each subsystem (center), followed by particle transport across the clean-disorder interface (grey dashed lines) for evolution times $\gg L_{clean}, L_{dis}$ (right). Cuts show the total density correlations $g^{(2)}(i)$ of the clean region with site i (i.e. average of top six rows, excluding diagonal entries), featuring homogeneous coupling among the clean sites, and exponentially decaying anti-correlations with the distance of the disordered site from the interface.* ***b:*** *The decay length ξ_d of the total density correlations increases first logarithmically in time and accelerates at long evolution times.* ***c:*** *The decay length ξ_d after an evolution time of 100τ grows with L_{clean}, indicating improved particle transport into the disordered region. The data point at $L_{clean} = 0$ and the dashed line show the localization length of an isolated MBL system.*

signal anti-correlated density fluctuations, and thus particle motion between the involved sites (Fig. 11a). In the following, we consider a system with $L_{\text{clean}} = 6$ at disorder strength $W = 9.1\,J$ after different evolution times T after the quantum quench. At the beginning of the evolution ($T = 0\tau$), we do not detect any correlations, because the initial state is a product state. After short evolution times ($T \lesssim \tau L$), we observe the buildup of spatially dependent anti-correlations in the system. Within the clean region all lattice sites develop mutual anti-correlations, signaling delocalized particles. In contrast, the anti-correlations in the disordered region remain short-ranged, indicating localized particles. These properties overall persist up to long evolution times ($T \gg \tau L$). In order to quantify the emergence of a bath, we extract the mean and the variation of the off-diagonal correlations in the clean region (Fig. 11b). We find that within a few tunneling times the clean region reaches its steady state with similar correlations across all pairs of sites, indicating that it starts to act as a thermal bath to the disordered region.

For long evolution times ($T \gg \tau L$) we additionally observe the buildup of anti-correlations between lattice sites in the clean and the disordered region, evidence for transport dynamics across the interface (right panel in Fig. 11a). Each of the disordered sites is similarly anti-correlated to all clean sites, which confirms that the clean region acts as a heat bath for the disordered region. Motivated by this picture, we extract the mean correlations of the clean region $g^{(2)}(i) = \overline{\langle \hat{n}_i \hat{n}_j \rangle_c}\big|_{j \in L_{\text{clean}}}$ by averaging the correlations of each site i with all clean sites j

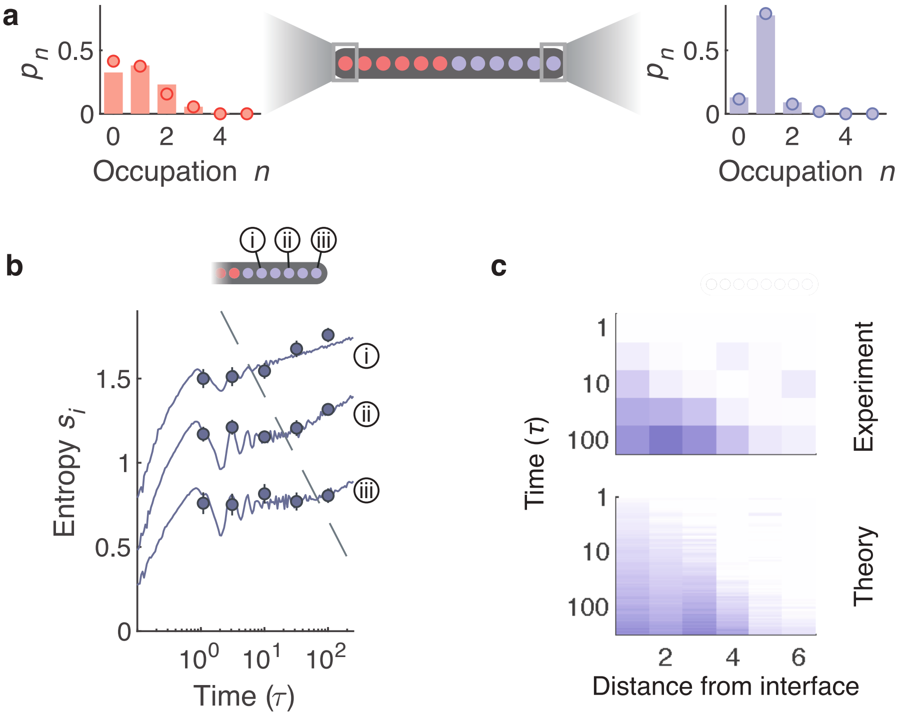

Fig. 12: ***Site-resolved thermalization dynamics.*** ***a:*** *The atom number probability distribution for the edge sites in the clean region (left) and the disordered region (right), measured after* 100τ *in a system consisting of* $L_{clean} = L_{dis} = 6$ *at disorder strength* $W = 9.1\,J$. ***b:*** *Local entropy per particle* $s_i = -\sum_n p_n \log p_n / \langle \hat{n}_i \rangle$ *extracted from the atom number distribution on site* i. *The entropy grows after a stationary evolution whose length depends on the distance from the interface (indicated by the grey dashed line). Traces are vertically offset for better readability.* ***c:*** *Local entropy* s_i *(offset by* $s_i(T = 1\tau)$*) for all disordered sites. Solid lines (bars in panel a) show the prediction from exact numerics without free parameters.*

(Fig. 11a cuts). The results are consistent with an exponential decay with distance from the clean region, in agreement with the Fermi golden rule picture of exponentially decaying couplings between bath and MBL.

While a static bath spectrum causes bath correlations to penetrate MBL logarithmically in time, a signature of the quantum avalanche is an accelerated increase, faster than logarithmically in time. In order to test this picture, we quantify the correlation decay into the disordered region by measuring the average distance $\xi_\mathrm{d} = -\sum_{i \in L_\mathrm{dis}} i\, g^{(2)}(i)$ from the clean region over which anti-correlations form (Fig. 11c). At short times the decay length ξ_d increases logarithmically in time, but accelerates at long evolution times. We contrast this observation with a system with $L_\mathrm{clean} = 2$, where the we do not find any accelerating transport dynamics.

4.4 Site-resolved thermalization

We next examine the local thermalization dynamics across the system. The microscopic readout enables us to measure the full atom number distribution on each site (Fig. 12a). Lattice sites in the clean region show a distribution corresponding to a thermal ensemble, whereas lattice sites

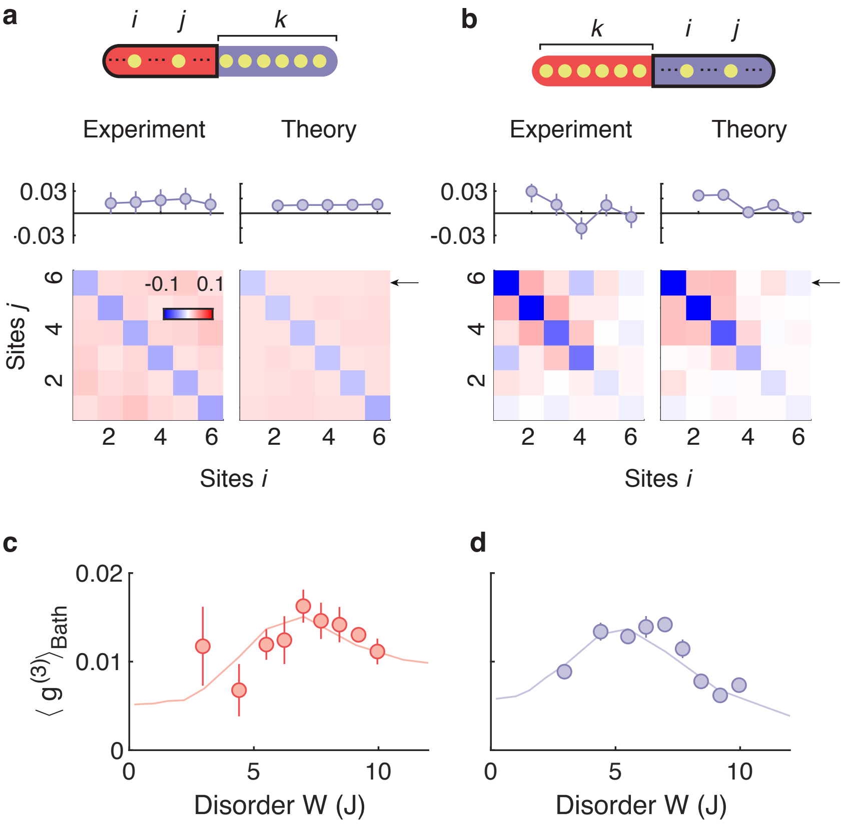

Fig. 13: ***Bath-induced many-body correlations. a:*** *Three-point correlations $\langle \hat{n}_i \hat{n}_j \hat{n}_k \rangle_c$ among pairs of clean sites i, j and one disordered site k (summed over all disordered k) in a system with $L_{clean} = L_{dis} = 6$ at disorder strength $W = 9.1\,J$ and evolution time $T = 100(1)$. Cuts across the site $j = 6$ (arrows) show nonzero entries for all sites, evidence for multi-particle entanglement between all sites in the clean region with the disordered sites. The flat distribution visualizes the homogeneous coupling to the disordered region.* ***b:*** *Correlations $\langle \hat{n}_i \hat{n}_j \hat{n}_k \rangle_c$ among pairs of disordered sites i, j and one clean site k (summed over all clean k) vary strongly with the chosen lattice sites, and decrease with the distance from the clean region. The presence of multi-point correlations demonstrates non-perturbative dynamics: delocalization is driven through many-body processes between the disordered region and the clean region.* ***c:*** *We average over all off-diagonal sites and find a maximum for intermediate disorder for the MBL-bath entanglement.* ***d:*** *The total multi-point correlations among disordered sites with the bath show a similar maximum at slightly lower intermediate disorder. Solid lines show the prediction from exact numerics without free parameters.*

in the disordered region show a distribution with enhanced probability for one particle, the initial state of the system. We quantify the site-resolved thermalization dynamics with the entropy per particle $s_i = -\sum_{n_i} p(n_i) \log p(n_i) / \langle \hat{n}_i \rangle$ on site i from the atom number distributions. We observe reduced thermalization dynamics of the disordered sites with increasing distance from the interface (Fig. 12b, c). Moreover, the data suggest that the dynamics are first stationary until thermalization sets in with a delay that increases with the site's distance from the interface. This picture is confirmed by our exact numerical calculations.

4.5 Many-body processes

The accelerated transport indicates the long-term dynamics are driven by processes that go beyond a perturbative coupling to the bath. We investigate this effect through multipoint correlations [92, 2]. The presence of non-zero three-point connected correlations $\langle\hat{n}_i\hat{n}_j\hat{n}_k\rangle_c$ signals the presence of entanglement among all involved lattice sites, which cannot be explained in a perturbative, semiclassical description. We evaluate the connected correlations $g^{(3)}(i,j) = \overline{\langle\hat{n}_i\hat{n}_j\hat{n}_k\rangle_c}\big|_{k\in L_{\text{clean}}}$ among two disordered sites i, j and a clean site k, averaged over all possible k (Fig. 13a). We find a strong dependence on the involved disordered sites: close to the interface correlations are strong, whereas they become weaker for distant sites. We quantify this behavior by considering the correlations as a function of the mean distance $\bar{d} = (i{+}j)/2$ of the two disordered sites from the clean region (Fig. 13b). Indeed, the correlations decrease with increasing distance from the clean region, comparable to the decay length ξ_{d}. This demonstrates that the accelerated transport is driven by many-body processes, a key property for quantum avalanches. We quantify the presence of many-body correlations at different disorder strengths by taking their average $\overline{g^{(3)}(i,j)}\big|_{i,j\in L_{\text{dis}}}$ (Fig. 13c,d). The correlations are present throughout the covered disorder range with a maximum at intermediate strengths, close to the estimated critical point of the system [2].

In conclusion, we experimentally realized a clean-disordered interface and studied the emerging thermalization dynamics. We observed an accelerated intrusion of the bath in the MBL system, its evolution to thermal equilibrium site after site, and the many-body correlations between the two subsystems, the hallmarks of quantum avalanches. In future, our experiments can be readily extended in many ways. For example, by increasing both the system size of the disordered region, one could explore the interplay at intermediate disorder strengths in a quantitative way through its scaling behavior, i.e., by increasing the system size at constant ratio of L_{clean} and L_{dis}, which may provide insight into the critical behavior of the transition. An interesting extension would also be the influence of the statistical distribution of the disorder on the critical behavior of the system. Furthermore, engineering other heterostructures with quantum gas microscopes may provide an avenue to studying phenomena in the physics of interfaces, or to building atomtronic devices.

References

[1] A. Lukin, M. Rispoli, R. Schittko, M.E. Tai, A.M. Kaufman, S. Choi, V. Khemani, J. Léonard, and M. Greiner, Science **364**, 256 (2019)

[2] M. Rispoli, A. Lukin, R. Schittko, S. Kim, M.E. Tai, J. Léonard, and M. Greiner, Nature **573**, 385 (2019)

[3] J. Léonard, S. Kim, M. Rispoli, A. Lukin, R. Schittko, J. Kwan, E. Demler, D. Sels, and M. Greiner, Nat. Phys. **19**, 481 (2023)

[4] J.M. Deutsch, Phys. Rev. A **43**, 2046 (1991)

[5] M. Srednicki, Phys. Rev. E **50**, 888 (1994)

[6] M. Rigol, V. Dunjko, and M. Olshanii, Nature **452**, 854 (2008)

[7] C. Neill, P. Roushan, M. Fang, Y. Chen, M. Kolodrubetz, Z. Chen, A. Megrant, R. Barends, B. Campbell, B. Chiaro, A. Dunsworth, E. Jeffrey, J. Kelly, J. Mutus, P.J. O'Malley, C. Quintana, D. Sank, A. Vainsencher, J. Wenner, T.C. White, A. Polkovnikov, and J.M. Martinis, Nat. Phys. **12**, 1037 (2016)

[8] A.M. Kaufman, M.E. Tai, A. Lukin, M. Rispoli, R. Schittko, P.M. Preiss, and M. Greiner, Science **353**, 794 (2016)

[9] R. Nandkishore and D.A. Huse, Annu. Rev. Condens. Matter Phys. **6**, 15 (2015)

[10] P.W. Anderson, Phys. Rev. **109**, 1492 (1958)

[11] T. Schwartz, G. Bartal, S. Fishman, and M. Segev, Nature **446**, 52 (2007)

[12] J. Billy, V. Josse, Z. Zuo, A. Bernard, B. Hambrecht, P. Lugan, D. Clément, L. Sanchez-Palencia, P. Bouyer, and A. Aspect, Nature **453**, 891 (2008)

[13] G. Roati, C. D'Errico, L. Fallani, M. Fattori, C. Fort, M. Zaccanti, G. Modugno, M. Modugno, and M. Inguscio, Nature **453**, 895 (2008)

[14] Y. Lahini, A. Avidan, F. Pozzi, M. Sorel, R. Morandotti, D.N. Christodoulides, and Y. Silberberg, Phys. Rev. Lett. **100**, 013906 (2008)

[15] B. Deissler, M. Zaccanti, G. Roati, C. D'Errico, M. Fattori, M. Modugno, G. Modugno, and M. Inguscio, Nat. Phys. **6**, 354 (2010)

[16] B. Gadway, D. Pertot, J. Reeves, M. Vogt, and D. Schneble, Phys. Rev. Lett. **107**, 1 (2011)

[17] S.S. Kondov, W.R. Mcgehee, J.J. Zirbel, and B. DeMarco, Science **334**, 66 (2011)

[18] F. Jendrzejewski, A. Bernard, K. Müller, P. Cheinet, V. Josse, M. Piraud, L. Pezzé, L. Sanchez-Palencia, A. Aspect, and P. Bouyer, Nat. Phys. **8**, 398 (2012)

[19] C. D'Errico, E. Lucioni, L. Tanzi, L. Gori, G. Roux, I.P. McCulloch, T. Giamarchi, M. Inguscio, and G. Modugno, Phys. Rev. Lett. **113**, 1 (2014)

[20] S.S. Kondov, W.R. McGehee, W. Xu, and B. Demarco, Phys. Rev. Lett. **114**, 1 (2015)

[21] G. Semeghini, M. Landini, P. Castilho, S. Roy, G. Spagnolli, A. Trenkwalder, M. Fattori, M. Inguscio, and G. Modugno, Nat. Phys. **11**, 554 (2015)

[22] I.V. Gornyi, A.D. Mirlin, and D.G. Polyakov, Phys. Rev. Lett. **95**, 206603 (2005)

[23] D.M. Basko, I.L. Aleiner, and B.L. Altshuler, Ann. Phys. **321**, 1126 (2006)

[24] V. Oganesyan and D.A. Huse, Phys Rev. B **75**, 115111 (2007)

[25] E. Altman and R. Vosk, Annu. Rev. Condens. Matter Phys. **6**, 383 (2015)

[26] D.A. Abanin, E. Altman, I. Bloch, and M. Serbyn, Rev. Mod. Phys. **91** (2019)

[27] M. Schreiber, S.S. Hodgman, P. Bordia, H.P. Lüschen, M.H. Fischer, R. Vosk, E. Altman, U. Schneider, and I. Bloch, Science **349**, 842 (2015)

[28] J. Smith, A. Lee, P. Richerme, B. Neyenhuis, P.W. Hess, P. Hauke, M. Heyl, D.A. Huse, and C. Monroe, Nat. Phys. **12**, 907 (2016)

[29] P. Bordia, H.P. Lüschen, S.S. Hodgman, M. Schreiber, I. Bloch, and U. Schneider, Phys. Rev. Lett. **116**, 140401 (2016)

[30] J.-Y. Choi, S. Hild, J. Zeiher, P. Schauß, A. Rubio-abadal, T. Yefsah, V. Khemani, D.A. Huse, I. Bloch, and C. Gross, Science **352**, 1547 (2016)

[31] H.P. Lüschen, P. Bordia, S.S. Hodgman, M. Schreiber, S. Sarkar, A.J. Daley, M.H. Fischer, E. Altman, I. Bloch, and U. Schneider, Phys. Rev. X **7**, 011034 (2017)

[32] P. Bordia, H. Lüschen, U. Schneider, M. Knap, and I. Bloch, Nat. Phys. **13**, 460 (2017)

[33] M. Serbyn, Z. Papić, and D.A. Abanin, Phys. Rev. Lett. **110**, 260601 (2013)

[34] M. Serbyn, Z. Papic, and D.A. Abanin, Phys. Rev. Lett. **111**, 127201 (2013)

[35] D.A. Huse, R. Nandkishore, and V. Oganesyan, Phys. Rev. B **90**, 174202 (2014)

[36] M. Žnidarič, T. Prosen, and P. Prelovšek, Phys. Rev. B **77**, 064426 (2008)

[37] J.H. Bardarson, F. Pollmann, and J.E. Moore, Phys Rev. Lett. **109**, 017202 (2012)

[38] S. Aubry and G. André, Ann. Israel Phys. Soc. **3**, 133 (1980)

[39] S. Iyer, V. Oganesyan, G. Refael, and D.A. Huse, Phys. Rev. B **87**, 134202 (2013)

[40] W.S. Bakr, J.I. Gillen, A. Peng, S. Fölling, and M. Greiner, Nature **462**, 74 (2009)

[41] R. Islam, R. Ma, P.M. Preiss, M. Eric Tai, A. Lukin, M. Rispoli, and M. Greiner, Nature **528**, 77 (2015)

[42] A. Elben, B. Vermersch, M. Dalmonte, J.I. Cirac, and P. Zoller, Phys. Rev. Lett. **120**, 50406 (2017)

[43] R. Vosk, D.A. Huse, and E. Altman, Phys. Rev. X **5**, 031032 (2015)

[44] A.C. Potter, R. Vasseur, and S.A. Parameswaran, Phys. Rev. X **5**, 031033 (2015)

[45] V. Khemani, S.P. Lim, D.N. Sheng, and D.A. Huse, Phys. Rev. X **7**, 021013 (2017)

[46] H.P. Lüschen, P. Bordia, S. Scherg, F. Alet, E. Altman, U. Schneider, and I. Bloch, Phys. Rev. Lett. **119**, 260401 (2017)

[47] K. Agarwal, E. Altman, E. Demler, S. Gopalakrishnan, D.A. Huse, and M. Knap, Ann. Phys. (Berlin) **529**, 1 (2017)

[48] W. De Roeck and F. Huveneers, Phys. Rev. B **95**, 155129 (2017)

[49] R. Nandkishore and S. Gopalakrishnan, Ann. Phys. (Berlin) **529**, 1600181 (2017)

[50] U.C. Täuber, Annu. Rev. Condens. Matter Phys. **8**, 185 (2017)

[51] A. Pal and D.A. Huse,Phys. Rev. B.**82**, 174411 (2010)

[52] L.D. Alessio, Y. Kafri, A. Polkovnikov, and M. Rigol, Adv. Phys. **65**, 239 (2016)

[53] A. Lukin, M. Rispoli, R. Schittko, M.E. Tai, A.M. Kaufman, S. Choi, V. Khemani, J. Léonard, and M. Greiner, (2018)

[54] K. Agarwal, S. Gopalakrishnan, M. Knap, M. Müller, and E. Demler, Phys. Rev. Lett. **114**, 160401 (2015)

[55] F. Setiawan, D.-L. Deng, and J.H. Pixley, Phys. Rev. B **96**, 104205 (2017)

[56] P.T. Dumitrescu, R. Vasseur, and A.C. Potter, Phys. Rev. Lett. **119**, 110604 (2017)

[57] A. Goremykina, R. Vasseur, and M. Serbyn, (2018)

[58] P. Bordia, H. Lüschen, S. Scherg, S. Gopalakrishnan, M. Knap, U. Schneider, and I. Bloch, Phys. Rev. X **7**, 041047 (2017)

[59] D.J. Luitz, N. Laflorencie, and F. Alet, Phys. Rev. B **93**, 060201 (2016)

[60] R. Nandkishore, S. Gopalakrishnan, and D.A. Huse, Phys. Rev. B **90**, 064203 (2014)

[61] E. Lucioni, B. Deissler, L. Tanzi, G. Roati, M. Zaccanti, M. Modugno, M. Larcher, F. Dalfovo, M. Inguscio, and G. Modugno, Phys. Rev. Lett. **106**, 230403 (2011)

[62] H.C. Liu, Phys. Rev. A **94**, 023827 (2016)

[63] T. Schweigler, V. Kasper, S. Erne, I. Mazets, B. Rauer, F. Cataldini, T. Langen, T. Gasenzer, J. Berges, and J. Schmiedmayer, Nature **545**, 323 (2017)

[64] S.S. Hodgman, R.I. Khakimov, A.G. Truscott, and K.V. Kheruntsyan, Phys. Rev. Lett. **118**, 240402 (2017)

[65] T. Grover, arXiv:1405.1471v1 (2014)

[66] F. Alet and N. Laflorencie, Comptes Rendus Phys. **19**, 498 (2018)

[67] D.A. Abanin, E. Altman, I. Bloch, and M. Serbyn, Rev. Mod. Phys. **91**, 021001 (2019)

[68] D.J. Luitz, F. Huveneers, and W. De Roeck, Phys. Rev. Lett. **119**, 150602 (2017)

[69] T. Thiery, F. Huveneers, M. Müller, and W. De Roeck, Phys. Rev. Lett. **121**, 140601 (2018)

[70] P.J. Crowley and A. Chandran, Phys. Rev. Res. **2**, 033262 (2020)

[71] A. Morningstar, L. Colmenarez, V. Khemani, D.J. Luitz, and D.A. Huse, Phys. Rev. B **105**, 174205 (2022)

[72] J. Smith, A. Lee, P. Richerme, B. Neyenhuis, P.W. Hess, P. Hauke, M. Heyl, D.A. Huse, and C. Monroe, Nat. Phys. **12**, 907 (2016)

[73] A. Rubio-Abadal, J.Y. Choi, J. Zeiher, S. Hollerith, J. Rui, I. Bloch, and C. Gross, Phys. Rev. X **9**, 041014 (2019)

[74] D.A. Abanin, J.H. Bardarson, G. De Tomasi, S. Gopalakrishnan, V. Khemani, S.A. Parameswaran, F. Pollmann, A.C. Potter, M. Serbyn, and R. Vasseur, Ann. Phys. **427**, 168415 (2021)

[75] R.K. Panda, A. Scardicchio, M. Schulz, S.R. Taylor, and M. Žnidarič, EPL **128**, 67003 (2019)

[76] P. Sierant, D. Delande, and J. Zakrzewski, Phys. Rev. Lett. **124**, 186601 (2020)

[77] J. Šuntajs, J. Bonča, T. Prosen, and L. Vidmar, Phys. Rev. E **102**, 062144 (2020)

[78] J. Šuntajs, J. Bonča, T. Prosen, and L. Vidmar, Phys. Rev. B **102**, 064207 (2020)

[79] D.J. Luitz and Y.B. Lev, Phys. Rev. B **102**, 100202 (2020)

[80] M. Kiefer-Emmanouilidis, R. Unanyan, M. Fleischhauer, and J. Sirker, Phys. Rev. Lett. **124**, 243601 (2020)

[81] M. Kiefer-Emmanouilidis, R. Unanyan, M. Fleischhauer, and J. Sirker, Phys. Rev. B **103**, 024203 (2021)

[82] D. Sels, Phys. Rev. B **106**, L020202 (2022)

[83] Y. Bar Lev, G. Cohen, and D.R. Reichman, Phys. Rev. Lett. **114**, 100601 (2015)

[84] M. Žnidarič, A. Scardicchio, and V.K. Varma, Phys. Rev. Lett. **117**, 040601 (2016)

[85] S. Gopalakrishnan, K. Agarwal, E.A. Demler, D.A. Huse, and M. Knap, Phys. Rev. B **93**, 134206 (2016)

[86] S. Gopalakrishnan, M. Müller, V. Khemani, M. Knap, E. Demler, and D.A. Huse, Physical Review B **92**, 104202 (2015)

[87] F. Weiner, F. Evers, and S. Bera, Phys. Rev. B **100**, 104204 (2019)

[88] V. Khemani, D.N. Sheng, and D.A. Huse, Phys. Rev. Lett. **119**, 075702 (2017)

[89] S.P. Kelly, R. Nandkishore, and J. Marino, Nucl. Phys. B **951**, 114886 (2020)

[90] R.B. Griffiths, Phys. Rev. Lett. **23**, 17 (1969)

[91] B.M. McCoy, Phys. Rev. Lett. **23**, 383 (1969)

[92] R. Kubo, J. Phys. Soc. Jpn. **17**, 1100 (1962)

Index